

# AJNR

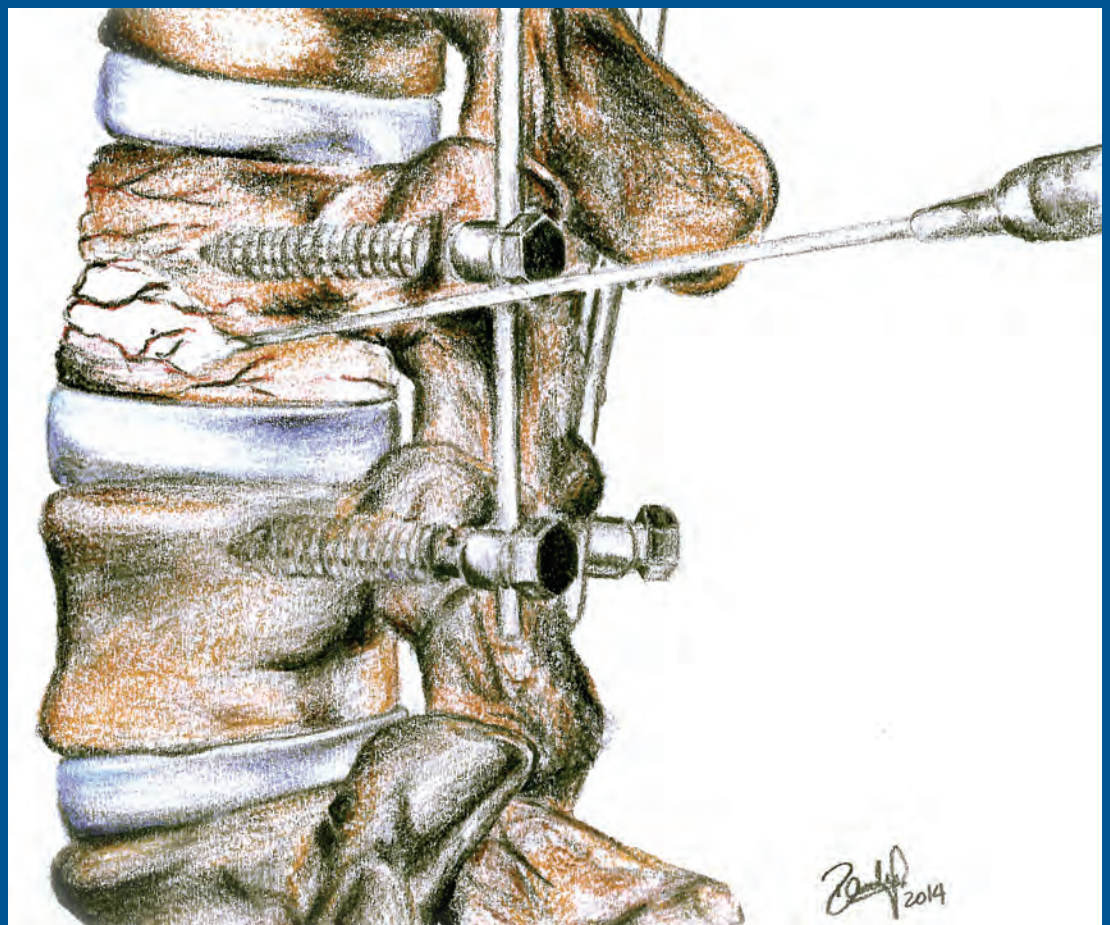
## AMERICAN JOURNAL OF NEURORADIOLOGY

NOVEMBER 2014  
VOLUME 35  
NUMBER 11  
WWW.AJNR.ORG

THE JOURNAL OF DIAGNOSTIC AND  
INTERVENTIONAL NEURORADIOLOGY

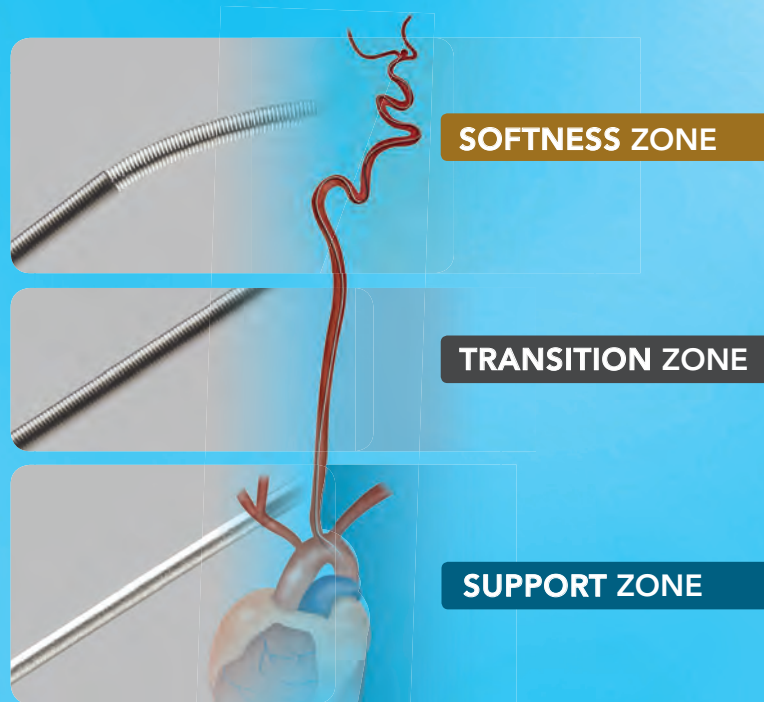
PET approaches for diagnosis of dementia  
Imaging of diving-related decompression illness  
Treatment of cerebral hemorrhage in the  
angiographic suite

Official Journal ASNR • ASFNR • ASHNR • ASPNR • ASSR



# Advanced

by MicroVention



ENHANCED CONTROL TO MAXIMIZE COIL PERFORMANCE

The V-Trak<sup>®</sup> Advanced Coil System, the next generation to power the performance of our most technically advanced line of coils. Offering the optimal combination of support and flexibility.

[microvention.com](http://microvention.com)

MICROVENTION, V-Trak, LVIS and Headway are registered trademarks of MicroVention, Inc. Scientific and clinical data related to this document are on file at MicroVention, Inc. Refer to Instructions for Use for additional information. Federal (USA) law restricts this device for sale by or on the order of a physician.  
© 2014 MicroVention, Inc. 9/14

# Support

by MicroVention



## LOW-PROFILE VISUALIZED INTRALUMINAL SUPPORT

The LVIS® and LVIS® Jr. devices are the next generation technology for optimal intraluminal support and coverage for stent-assist coil procedures.

Used with  Headway  
Microcatheter

*\*Humanitarian Device:*

*Authorized by Federal Law for use in the treatment of wide-necked aneurysms in the neurovasculature.  
The effectiveness of this device for this use has not been demonstrated.*

**For more information or a product demonstration,  
contact your local MicroVention representative:**



**MicroVention, Inc.**

**Worldwide Headquarters**

1311 Valencia Avenue

Tustin, CA 92780 USA

MicroVention UK Limited

MicroVention Europe, S.A.R.L.

MicroVention Deutschland GmbH

PH +1.714.247.8000

PH +44 (0) 191 258 6777

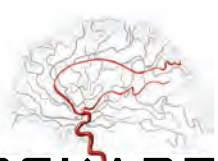
PH +33 (1) 39 21 77 46

PH +49 211 210 798-0



# BARRICADE™ COIL SYSTEM

PERFORMANCE AND VALUE DELIVERED



**BLOCKADE**  
M E D I C A L

18 TECHNOLOGY DRIVE #169, IRVINE CA 92618 | P 949.788.1443  
[WWW.BLOCKADEMEDICAL.COM](http://WWW.BLOCKADEMEDICAL.COM)

 MADE IN AMERICA

**CE**  
0297  
MKTG-020 REV. B



# AJNR

## AMERICAN JOURNAL OF NEURORADIOLOGY

NOVEMBER 2014  
VOLUME 35  
NUMBER 11  
WWW.AJNR.ORG

Publication Preview at [www.ajnr.org](http://www.ajnr.org) features articles released in advance of print. Visit [www.ajnrblog.org](http://www.ajnrblog.org) to comment on AJNR content and chat with colleagues and AJNR's News Digest at <http://ajnrdigest.org> to read the stories behind the latest research in neuroimaging.

### EDITORIALS

#### PERSPECTIVES

- 2027 **Dress for Success** *M. Castillo*

#### EDITORIAL

- 2029 **Lumbar Disc Nomenclature: Version 2.0** *A.L. Williams, F.R. Murtagh, S.L.G. Rothman, and G.K. Sze*

### REVIEW ARTICLES

- 2030 **PET Approaches for Diagnosis of Dementia** *K. Ishii*
- 2039 **Neuroimaging of Diving-Related Decompression Illness: Current Knowledge and Perspectives** *J. Kamtchum Tatuene, R. Pignel, P. Pollak, K.O. Lovblad, A. Kleinschmidt, and M.I. Vargas*

### PATIENT SAFETY

- 2045 **Whole-Brain Adaptive 70-kVp Perfusion Imaging with Variable and Extended Sampling Improves Quality and Consistency While Reducing Dose** *I. Corcuera-Solano, A.M. McLellan, A.H. Doshi, P.S. Pawha, and L.N. Tanenbaum*
- 2052 **Dental Flat Panel Conebeam CT in the Evaluation of Patients with Inflammatory Sinonasal Disease: Diagnostic Efficacy and Radiation Dose Savings** *C. Leiva-Salinas, L. Flors, P. Gras, F. Más-Estellés, P. Lemercier, J.T. Patrie, M. Wintermark, and L. Martí-Bonmatí*

### FUNCTIONAL VIGNETTE

- 2058 **Memory Part I: Overview** *F.D. Raslau, A.P. Klein, J.L. Ulmer, V. Mathews, and L.P. Mark*

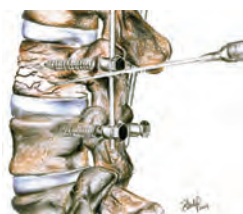
### BRAIN

- 2061 **Susceptibility-Diffusion Mismatch Predicts Thrombolytic Outcomes: A Retrospective Cohort Study** *M. Lou, Z. Chen, J. Wan, H. Hu, X. Cai, Z. Shi, and J. Sun*

#### COMMENTARY

- 2068 **On the Search for the Perfect Mismatch!** *M.A. Almekhlafi*
- 2070 **Leukoaraiosis Predicts a Poor 90-Day Outcome after Endovascular Stroke Therapy** *J. Zhang, A.S. Puri, M.A. Khan, R.P. Goddeau Jr, and N. Henninger*
- 2076 **Whole-Brain Diffusion Tensor Imaging in Correlation to Visual-Evoked Potentials in Multiple Sclerosis: A Tract-Based Spatial Statistics Analysis** *D. Lobsien, B. Ettrich, K. Sotiriou, J. Classen, F. Then Bergh, and K.-T. Hoffmann*

-  Indicates Editor's Choices selection
-  Indicates Fellows' Journal Club selection
-  Indicates open access to non-subscribers at [www.ajnr.org](http://www.ajnr.org)
-  Indicates article with supplemental on-line table
-  Indicates article with supplemental on-line photo
-  Indicates article with supplemental on-line video
-  Indicates Evidence-Based Medicine Level 1
-  Indicates Evidence-Based Medicine Level 2



Needle position for cement salvage of instrumentation-associated vertebral fractures.



## Trevo<sup>®</sup> XP

PROVUE RETRIEVER

### Take Control. Capture More.

The newly designed Trevo<sup>®</sup> XP ProVue Retriever takes proven Trevo Retriever performance to new levels for **easy delivery**, **easy placement**, and **easy visualization**.

When you're in control, it's amazing what you can capture.

**stryker**<sup>®</sup>  
Neurovascular

-  **2082 Utility of Intravoxel Incoherent Motion MR Imaging for Distinguishing Recurrent Metastatic Tumor from Treatment Effect following Gamma Knife Radiosurgery: Initial Experience** *D.Y. Kim, H.S. Kim, M.J. Goh, C.G. Choi, and S.J. Kim*
-   **2091 Comparison of Multiple Parameters Obtained on 3T Pulsed Arterial Spin-Labeling, Diffusion Tensor Imaging, and MRS and the Ki-67 Labeling Index in Evaluating Glioma Grading** *H. Fudaba, T. Shimomura, T. Abe, H. Matsuta, Y. Momii, K. Sugita, H. Ooba, T. Kamida, T. Hikawa, and M. Fujiki*
- 2099 Evaluation of Normal Changes in Pons Metabolites due to Aging Using Turbo Spectroscopic Imaging** *A. Yang, X.h. Xiao, and Z.l. Wang*
- INTERVENTIONAL** *Published in collaboration with Interventional Neuroradiology*
-  **2106 WEB Intrasaccular Flow Disruptor—Prospective, Multicenter Experience in 83 Patients with 85 Aneurysms** *C. Papagiannaki, L. Spelle, A.-C. Januel, A. Benaissa, J.-Y. Gauvrit, V. Costalat, H. Desal, F. Turjman, S. Velasco, X. Barreau, P. Courtheoux, C. Cognard, D. Herbreteau, J. Moret, and L. Pierot*
- 2112 Contrast-Enhanced Time-Resolved MRA for Follow-Up of Intracranial Aneurysms Treated with the Pipeline Embolization Device** *S.R. Boddu, F.C. Tong, S. Dehkharghani, J.E. Dion, and A.M. Saindane*
- 2119 The Success of Flow Diversion in Large and Giant Sidewall Aneurysms May Depend on the Size of the Defect in the Parent Artery** *J.C. Gentric, T.E. Darsaut, A. Makoyeva, I. Salazkin, and J. Raymond*
-  **2125 Modifying Flow in the ICA Bifurcation: Pipeline Deployment from the Supraclinoid ICA Extending into the M1 Segment—Clinical and Anatomic Results** *E. Nossek, D.J. Chalif, S. Chakraborty, and A. Setton*
-   **2130 Morphologic and Hemodynamic Risk Factors in Ruptured Aneurysms Imaged before and after Rupture** *A. Chien and J. Sayre*
-  **2136 Risk Factors for Early Hemorrhagic Complications after Endovascular Coiling of Ruptured Intracranial Aneurysms** *T. Ohta, K. Murao, K. Miyake, K. Takemoto, and K. Nakazawa*
- 2140 Vision Outcomes and Major Complications after Endovascular Coil Embolization of Ophthalmic Segment Aneurysms** *C.R. Durst, R.M. Starke, J. Gaughen, Q. Nguyen, J. Patrie, M.E. Jensen, and A.J. Evans*
-  **2146 Endovascular Treatment of Ophthalmic Artery Aneurysms: Assessing Balloon Test Occlusion and Preservation of Vision in Coil Embolization** *J.H. Ahn, Y.D. Cho, H.-S. Kang, J.E. Kim, W.-S. Cho, S.C. Jung, C.H. Kim, and M.H. Han*
-  **2153 “Y” and “X” Stent-Assisted Coiling of Complex and Wide-Neck Intracranial Bifurcation Aneurysms** *B. Bartolini, R. Blanc, S. Pistocchi, H. Redjem, and M. Piotin*
- 2159 Cerebral Aneurysm Pulsation: Do Iterative Reconstruction Methods Improve Measurement Accuracy In Vivo?** *T. Illies, D. Säring, M. Kinoshita, T. Fujinaka, M. Bester, J. Fiehler, N. Tomiyama, and Y. Watanabe*
- 2164 Evaluation of a Metal Artifacts Reduction Algorithm Applied to Postinterventional Flat Panel Detector CT Imaging** *D.A. Stidd, H. Theessen, Y. Deng, Y. Li, B. Scholz, C. Rohkohl, M.D. Jhaveri, R. Moftakhar, M. Chen, and D.K. Lopes*
- 2170 Treatment of Supratentorial Spontaneous Intracerebral Hemorrhage Using Image-Guided Minimally Invasive Surgery: Initial Experiences of a Flat Detector CT–Based Puncture Planning and Navigation System in the Angiographic Suite** *Z. Yang, B. Hong, Z. Jia, J. Chen, J. Ge, J. Han, J. Beilner, Y. Zhang, Y. Fang, and J. Liu*

Your **single source** for the latest in innovative **solutions.**

Introducing **the most complete and least invasive vertebral augmentation portfolio** on the market today.

**11g iVAS®** Inflatable Vertebral Augmentation System



**VertePort X4 Manifold™**



**Curette**



**TroFlex™**  
Curved Needle



## HEAD & NECK



**2176 Imaging-Detected Incidental Thyroid Nodules that Undergo Surgery: A Single-Center Experience Over 1 Year** *M. Bahl, J.A. Sosa, R.C. Nelson, and J.K. Hoang*

**2181 The “Boomerang” Malleus-Incus Complex in Congenital Aural Atresia**  
*S. Mukherjee, B.W. Kesser, and P. Raghavan*

## PEDIATRICS



**2186 Incidental Radiologic Findings in the 22q11.2 Deletion Syndrome**  
*J.E. Schmitt, J.J. Yi, D.R. Roalf, L.A. Loevner, K. Ruparel, D. Whinna, M.C. Souders, D.M. McDonald-McGinn, E. Yodh, S. Vandekar, E.H. Zackai, R.C. Gur, B.S. Emanuel, and R.E. Gur*

**2192 Pleomorphic Xanthoastrocytoma of Childhood: MR Imaging and Diffusion MR Imaging Features** *W. Moore, D. Mathis, L. Gargan, D.C. Bowers, L.J. Klesse, L. Margraf, and K. Koral*

## SPINE



**2197 Cement Salvage of Instrumentation-Associated Vertebral Fractures**  
*R. Xu, K. O'Connor, G. Krol, Y. Yamada, M. Bilsky, I. Laufer, and E. Lis*



**2202 Safety and Effectiveness of Sacroplasty: A Large Single-Center Experience**  
*A.C. Gupta, R.V. Chandra, A.J. Yoo, T.M. Leslie-Mazwi, D.L. Bell, B.P. Mehta, T.L. Vanderboom, J.D. Rabinov, M. Larvie, and J.A. Hirsch*

## ONLINE FEATURES ([www.ajnr.org](http://www.ajnr.org))

**Lumbar Disc Nomenclature: Version 2.0: Recommendations of the Combined Task Forces of the North American Spine Society, the American Society of Spine Radiology, and the American Society of Neuroradiology**  
**AJNR Am J Neuroradiol 2014 35**

**Citation Only**

Available for download at: <http://dx.doi.org/10.1016/j.spinee.2014.04.022>

## LETTER

**E7 Interventional Neuroradiology on Call: The Need for Emergency Coiling of Ruptured Intracranial Aneurysms**

*W.J. van Rooij, R.S. Bechan, and M. Sluzewski*

**BOOK REVIEWS** *R.M. Quencer, Section Editor*

Please visit [www.ajnrblog.org](http://www.ajnrblog.org) to read and comment on Book Reviews.

# CALL FOR AJNR EDITORIAL FELLOWSHIP CANDIDATES

ASNR and AJNR are pleased once again to join efforts with other imaging-related journals that have training programs on editorial aspects of publishing for trainees or junior staff (3–5 years after training), including Radiology (Olmsted fellowship), AJR (Figley and Rogers fellowships), and Radiologia.

## 2015 Candidate Information and Requirements

### GOALS

- Increase interest in “editorial” and publication-related activities in younger individuals.
- Increase understanding and participation in the AJNR review process.
- Incorporate into AJNR’s Editorial Board younger individuals who have previous experience in the review and publication process.
- Fill a specific need in neuroradiology not offered by other similar fellowships.
- Increase the relationship between “newer” generation of neuroradiologists and more established individuals.
- Increase visibility of AJNR among younger neuroradiologists.

### ACTIVITIES OF THE FELLOWSHIP

- Serve as Editorial Fellow for one year. This individual will be listed on the masthead as such.
- Review at least one manuscript per month for 12 months. Evaluate all review articles submitted to AJNR.
- Access to our electronic manuscript review system will be granted so that the candidate can learn how these systems work.
- Be involved in the final decision of selected manuscripts together with the Editor-in-Chief.
- Participate in all monthly Senior Editor telephone conference calls.
- Participate in all meetings of the Editors and Publications Committee during the annual meetings of ASNR and RSNA as per candidate’s availability. AJNR/ASNR will not provide funding for this activity but may offer a discounted fee for its annual meeting.
- Evaluate progress and adjust program to specific needs in biannual meeting or telephone conference with the Editor-in-Chief.
- Write at least one editorial for AJNR.
- Embark on an editorial scientific or bibliometric project that will lead to the submission of an article to AJNR or another appropriate journal as determined by the Editor-in-Chief. This project will be presented by the Editorial Fellow at the ASNR annual meeting.
- Serve as liaison between AJNR and ASNR’s Young Professionals Network and the 3 YPs appointed to AJNR as special consultants. Participate in meetings and telephone calls with this group. Design one electronic survey/year polling the group regarding readership attitudes and wishes.
- Recruit trainees as reviewers as determined by the Editor-in-Chief.
- Participate in Web improvement projects.
- Potentially become a member of AJNR’s Editorial Board at the end of the fellowship.
- Invite Guest Editors for AJNR’s News Digest to cover a variety of timely topics.

### QUALIFICATIONS

- Be a fellow in neuroradiology from North America, including Canada (this may be extended to include other countries).
- Be a junior faculty neuroradiology member (< 3 years) in either an academic and private environment.
- Provide an “end” of fellowship report to AJNR’s Editor-in-Chief and ASNR’s Publications Committee.
- Be an “in-training” or member of ASNR in any other category.

### APPLICATION

- Include a short letter of intent with statement of goals and desired research project. CV must be included.
- Include a letter of recommendation from the Division Chief or fellowship program director. A statement of protected time to perform the functions outlined is desirable.
- Applications will be evaluated by AJNR’s Senior Editors and the Chair of the Publications Committee prior to the ASNR meeting. The name of the selected individual will be announced at the meeting.
- Applications should be received by March 3, 2015 and sent to Ms. Karen Halm, AJNR Managing Editor, electronically at khalm@asnr.org.

Publication Preview at [www.ajnr.org](http://www.ajnr.org) features articles released in advance of print. Visit [www.ajnrblog.org](http://www.ajnrblog.org) to comment on AJNR content and chat with colleagues and AJNR's News Digest at <http://ajnrdigest.org> to read the stories behind the latest research in neuroimaging.

NOVEMBER 2014 • VOLUME 35 • NUMBER 11 • WWW.AJNR.ORG

### Official Journal:

American Society of Neuroradiology  
American Society of Functional Neuroradiology  
American Society of Head and Neck Radiology  
American Society of Pediatric Neuroradiology  
American Society of Spine Radiology

### EDITOR-IN-CHIEF

#### Mauricio Castillo, MD

Professor of Radiology and Chief, Division of Neuroradiology, University of North Carolina, School of Medicine, Chapel Hill, North Carolina

### SENIOR EDITORS

#### Harry J. Cloft, MD, PhD

Professor of Radiology and Neurosurgery, Department of Radiology, Mayo Clinic College of Medicine, Rochester, Minnesota

#### Nancy J. Fischbein, MD

Professor of Radiology, Otolaryngology-Head and Neck Surgery, Neurology, and Neurosurgery and Chief, Head and Neck Radiology, Department of Radiology, Stanford University Medical Center, Stanford, California

#### Jeffrey S. Ross, MD

Staff Neuroradiologist, Barrow Neurological Institute, St. Joseph's Hospital, Phoenix, Arizona

#### Pamela W. Schaefer, MD

Clinical Director of MRI and Associate Director of Neuroradiology, Massachusetts General Hospital, Boston, Massachusetts, and Associate Professor, Radiology, Harvard Medical School, Cambridge, Massachusetts

#### Charles M. Strother, MD

Professor of Radiology, Emeritus, University of Wisconsin, Madison, Wisconsin

#### Jody Tanabe, MD

Professor of Radiology and Psychiatry, Chief of Neuroradiology, University of Colorado, Denver, Colorado

### EDITORIAL BOARD

Ashley H. Aiken, Atlanta, Georgia  
A. James Barkovich, San Francisco, California  
Walter S. Bartynski, Charleston, South Carolina  
Barton F. Branstetter IV, Pittsburgh, Pennsylvania  
Jonathan L. Brisman, Lake Success, New York  
Julie Bykowski, San Diego, California  
Donald W. Chakeres, Columbus, Ohio  
Alessandro Cianfoni, Lugano, Switzerland  
Colin Derdeyn, St. Louis, Missouri  
Rahul S. Desikan, San Diego, California  
Richard du Mesnil de Rochemont, Frankfurt, Germany  
Clifford J. Eskey, Hanover, New Hampshire  
Massimo Filippi, Milan, Italy  
David Fiorella, Cleveland, Ohio  
Allan J. Fox, Toronto, Ontario, Canada  
Christine M. Glastonbury, San Francisco, California

John L. Go, Los Angeles, California  
Wan-Yuo Guo, Taipei, Taiwan  
Rakesh K. Gupta, Lucknow, India  
Lotfi Hacein-Bey, Sacramento, California  
David B. Hackney, Boston, Massachusetts  
Christopher P. Hess, San Francisco, California  
Andrei Holodny, New York, New York  
Benjamin Huang, Chapel Hill, North Carolina  
Thierry A.G.M. Huisman, Baltimore, Maryland  
George J. Hunter, Boston, Massachusetts  
Mahesh V. Jayaraman, Providence, Rhode Island  
Valerie Jewells, Chapel Hill, North Carolina  
Timothy J. Kaufmann, Rochester, Minnesota  
Kenneth F. Layton, Dallas, Texas  
Ting-Yim Lee, London, Ontario, Canada  
Michael M. Lell, Erlangen, Germany  
Michael Lev, Boston, Massachusetts  
Karl-Olof Lovblad, Geneva, Switzerland  
Franklin A. Marden, Chicago, Illinois  
M. Gisele Matheus, Charleston, South Carolina  
Joseph C. McGowan, Merion Station, Pennsylvania  
Kevin R. Moore, Salt Lake City, Utah  
Christopher J. Moran, St. Louis, Missouri  
Takahisa Mori, Kamakura City, Japan

Suresh Mukherji, Ann Arbor, Michigan  
Amanda Murphy, Toronto, Ontario, Canada  
Alexander J. Nemeth, Chicago, Illinois  
Laurent Pierot, Reims, France  
Jay J. Pillai, Baltimore, Maryland  
Whitney B. Pope, Los Angeles, California  
M. Judith Donovan Post, Miami, Florida  
Tina Young Poussaint, Boston, Massachusetts  
Joana Ramalho, Lisbon, Portugal  
Otto Rapalino, Boston, Massachusetts  
Álex Rovira-Cañellas, Barcelona, Spain  
Paul M. Ruggieri, Cleveland, Ohio  
Zoran Rumboldt, Rijeka, Croatia  
Amit M. Saindane, Atlanta, Georgia  
Erin Simon Schwartz, Philadelphia, Pennsylvania  
Aseem Sharma, St. Louis, Missouri  
J. Keith Smith, Chapel Hill, North Carolina  
Maria Vittoria Spaminato, Charleston, South Carolina  
Gordon K. Sze, New Haven, Connecticut  
Krishnamoorthy Thamburaj, Hershey, Pennsylvania  
Kent R. Thielen, Rochester, Minnesota  
Cheng Hong Toh, Taipei, Taiwan  
Thomas A. Tomsick, Cincinnati, Ohio  
Aquila S. Turk, Charleston, South Carolina  
Willem Jan van Rooij, Tilburg, Netherlands  
Arastoo Vossough, Philadelphia, Pennsylvania  
Elysa Widjaja, Toronto, Ontario, Canada  
Max Wintermark, Charlottesville, Virginia  
Ronald L. Wolf, Philadelphia, Pennsylvania  
Kei Yamada, Kyoto, Japan

### EDITORIAL FELLOW

Asim F. Choudhri, Memphis, Tennessee

### YOUNG PROFESSIONALS ADVISORY COMMITTEE

Asim K. Bag, Birmingham, Alabama  
Anna E. Nidecker, Sacramento, California  
Peter Yi Shen, Sacramento, California

### HEALTH CARE AND SOCIOECONOMICS EDITOR

Pina C. Sanelli, New York, New York

### Founding Editor

Juan M. Taveras

### Editors Emeriti

Robert I. Grossman, Michael S. Huckman,  
Robert M. Quencer

### Special Consultants to the Editor

Sandy Cheng-Yu Chen, Girish Fatterpekar,  
Ryan Fitzgerald, Katherine Freeman,  
Yvonne Lui, Greg Zaharchuk

### INR Liaisons

Timo Krings, Karel terBrugge

### Managing Editor

Karen Halm

### Electronic Publications Manager

Jason Gantenberg

### Editorial Assistant

Mary Harder

### Executive Director, ASNR

James B. Gantenberg

### Director of Communications, ASNR

Angelo Artemakis

**AJNR (Am J Neuroradiol)** ISSN 0195-6108 is a journal published monthly, owned and published by the American Society of Neuroradiology (ASNR), 800 Enterprise Drive, Suite 205, Oak Brook, IL 60523. Annual dues for the ASNR include \$170.00 for journal subscription. The journal is printed by Cadmus Journal Services, 5457 Twin Knolls Road, Suite 200, Columbia, MD 21045; Periodicals postage paid at Oak Brook, IL and additional mailing offices. Printed in the U.S.A. POSTMASTER: Please send address changes to American Journal of Neuroradiology, P.O. Box 3000, Denville, NJ 07834, U.S.A. Subscription rates: nonmember \$370 (\$440 foreign) print and online, \$300 online only; institutions \$430 (\$495 foreign) print and basic online, \$850 (\$915 foreign) print and extended online, \$355 online only (basic), extended online \$770; single copies are \$35 each (\$40 foreign). Indexed by PubMed/Medline, BIOSIS Previews, Current Contents (Clinical Medicine and Life Sciences), EMBASE, Google Scholar, HighWire Press, Q-Sensei, RefSeek, Science Citation Index, and SCI Expanded. Copyright © American Society of Neuroradiology.



# ASNR 53<sup>rd</sup> Annual Meeting & The Foundation of the ASNR Symposium 2015



## ASNR

**CHICAGO ★ 2015**

**April 25-30, 2015**

*Sheraton Chicago Hotel & Towers*

ASFNR ASHNR ASPNR ASSR SNIS

THE FOUNDATION OF THE ASNR



**Request Programming and Registration Materials  
for the ASNR 53<sup>rd</sup> Annual Meeting, Contact:**

ASNR 53<sup>rd</sup> Annual Meeting  
c/o American Society of Neuroradiology  
800 Enterprise Drive, Suite 205  
Oak Brook, Illinois 60523-4216  
Phone: 630-574-0220  
Fax: 630-574-0661  
Email: [meetings@asnr.org](mailto:meetings@asnr.org)  
Website: [www.asnr.org/2015](http://www.asnr.org/2015)

**Scan now to visit our website**



## Abstract Deadline:

Friday, December 12, 2014

Please visit [www.asnr.org/2015](http://www.asnr.org/2015)  
for more information

### **ASNR 2015 Program Chair/President Elect Laurie A. Loevner, MD**

#### **Programming developed in cooperation with the:**

American Society of Functional Neuroradiology (ASFNR)  
Pratik Mukherjee, MD, PhD

American Society of Head and Neck Radiology (ASHNR)  
Richard H. Wiggins, III, MD

American Society of Pediatric Neuroradiology (ASPNR)  
Thierry A.G.M. Huisman, MD

American Society of Spine Radiology (ASSR)  
Adam E. Flanders, MD

American Society of Neuroradiology (ASNR)  
Health Policy Committee  
Robert M. Barr, MD, FACR

Society of NeuroInterventional Surgery (SNIS)  
Donald F. Frei, Jr. MD

## Dress for Success

*It is impossible to wear clothes without transmitting social signals. Every costume tells a story, often a very subtle one, about its wearer.*

Desmond Morris in *A Field Guide to Human Behavior*

M. Castillo, *Editor-In-Chief*

A couple of years ago, I visited the Mayo Clinic in Rochester, Minnesota, and was surprised to see that most physicians still wore suits, while here in Chapel Hill where I work, I am only one of a handful to do so.\* I wear a suit because I feel that it makes for easy choices in the morning, looks respectful and elegant, and after a certain age (mine) it flatters the aging body. The “business suit” (sometimes also called a “lounge suit”) appeared in the late 19th century, and typically all of its pieces (2 or 3) are made of the same cloth. Suits tend to compensate for physical variations by having no indication of a waistline and by adding padding to the shoulders; minor variations such as lapel width go in and out of style regularly. Business suits are a type of uniform, and today uniforms are worn mainly by 3 professions: the armed forces, commercial aviation, and medical staff. Smaller groups of individuals such as sports professionals and hygiene workers and even some students in private schools still wear uniforms. Commonly seen in medicine are 2 types of uniforms: white coats (or laboratory coats) and scrubs.

Most lab coats are knee length and have long sleeves to offer the most protection. Additionally, they are usually made of cotton because of its high capacity to absorb liquids. Professionals for whom sleeves prove uncomfortable or prone to contamination, such as microbiologists and pharmacists, prefer short-sleeve smocks. In a survey of nearly 300 doctors, only 1 in 8 wore a white coat, despite the fact that over 50% thought they should.<sup>1</sup> Specialists who are the least likely to wear white coats include psychiatrists and pediatricians, while those more likely to do so are surgeons and gynecologists. Older physicians are also more likely to wear them than younger ones.

Scrubs were designed for surgical personnel but are now worn by nearly anyone who works in health care (they are also mandated in some prisons). Similar to lab coats, scrubs were initially white, but with the advent of modern operating room illumination, that color resulted in eye strain. During the 1950s and 1960s, most hospitals adopted green scrubs in an attempt to lessen this strain. Today scrubs vary in color, often distinguishing among different specialties, and those used by pediatricians may have cartoon characters printed on them.<sup>2</sup> Because they are very comfortable, they are commonly used outside the hospital as pajamas, for working out, or just hanging out at home (it does upset me when I go to bar or restaurant and see hospital personnel in scrubs there). I also find it unfair to take the hospital germs home and then bring those from home to the hospital.

Wearing a uniform, such as a white coat, alters the perception of those who see us and also affects the way the wearer thinks. In an experiment, students wearing white coats noticed twice as many errors during a test compared with those wearing street clothes. They also did better at spotting differences during tests designed to measure sustained attention.<sup>3</sup> British patients prefer their male physicians in a suit and tie but their female physicians in white coats.<sup>4</sup> In Great Britain, the favorite male attire seems to be a tweed sports jacket and a tie and informal shirt. Overall, 64% percent of patients think that the way their physicians dress is very important, and 41% say they their confidence in their physicians’ abilities is based on appearances. Casual dressing for doctors is a bad tactic: It decreases perceptions of authority regardless of sex, paradoxically decreases perceptions of friendliness and trust, and also lowers attractiveness.<sup>5</sup> There are sex differences in perception, and female patients prefer their physicians in white coats, while male patients prefer them formally dressed. Thus, the best attire may be a white coat over formal wear and removal of the white coat when the occasion calls for it. The attitude toward physicians’ dressing styles may be age-related. In a different study, 43% of teenagers responded that the way their physicians dressed made no difference and only 26% preferred them in white coats.<sup>6</sup> Patients prefer their anesthesiologists to wear the traditional business suit and find blue jeans an undesirable choice.<sup>7</sup>

A different study, also involving anesthetists, found that patients had a preference for name tags, short hair, and white coats but disapproved of clogs, jeans, sneakers, and earrings.<sup>8</sup> In a study done in Italy, patients also preferred formal dressing and name tags.<sup>9</sup> This very complete study of patient preferences also rated the following as very highly favorable: short nails, well-kept teeth, and light makeup on females. The following received very low ratings: tattoos, piercings, obesity, sandals, long hair on men, and heavy makeup on women. In another large study done in South Carolina, all respondents preferred their physicians in white coats, followed by business and surgical (scrubs) attire, and last casually dressed (jeans and polo shirts).<sup>10</sup> In the military where uniforms are standard, patients prefer their doctors in white coats over scrubs.<sup>11</sup> In that same environment, nonwhites and Hispanics had higher rates of preference for more formal dress than other groups.

Not only do most patients show similar preferences but their parents do, too. A study performed at the Children’s Hospital in Cincinnati showed that parents prefer and express more confidence in physicians who are formally dressed than in those without a white coat, no necktie, and tennis shoes. These preferences were independent of the severity of the illness, time of visit, insurance group, race, and sex.<sup>12</sup> Some studies point out that white coats may not be completely innocuous to patients. The “white coat syndrome” is a phenomenon in which patients exhibit high blood pressure when facing someone dressed in a white lab coat. Female students at an American university were asked to rank the same teachers dressed in traditional business and Indian attire,

\*The Mayo Clinic encourages their physicians to wear business suits rather than white coats because suits are thought to convey professionalism and expertise.<sup>20</sup>

<http://dx.doi.org/10.3174/ajnr.A3942>

and not surprisingly, the former received a more positive evaluation.<sup>13</sup> Although females prefer their teachers formally dressed, mixed-sex college classes express positive ratings for instructors dressed in casual clothes (jeans, t-shirts, flannel shirts).<sup>14</sup>

When I was a resident in radiology, the dress code was always a lab coat, a necktie for men, and no scrubs or tennis shoes except when doing procedures. If we arrived at the hospital without a tie, the program director would take us to his office where he had a drawer full of ties from which we chose what to wear that day (I recall that most were ugly, perhaps an incentive not to forget them again). Neckties of different types have been worn since Roman times, but it was not until 1926 that the current necktie (the long one) was designed and became popular. Studies show that about 20% of neckties are contaminated by the third hour worn, often with antibiotic-resistant micro-organisms (the rate of contamination for lab coats is about 25%, more if they contain polyester).<sup>15</sup> Bow ties are also prone to contamination though less often than long ties and because both are seldom washed, colonization with micro-organisms may remain in them forever. Because of this, some companies have started to apply nanoparticles that presumably “lock” the silk fibers found in neckties, preventing bacteria from getting into them. In one study, these so-called “safety ties” were found to have more bacteria than regular ties! Counterintuitively, it was the knots of the ties and not their tips that contained more bacteria (perhaps because we tend to adjust them often).<sup>16</sup> If one is going to wear a tie, it is better to wear a bow tie and change it every day.<sup>17</sup>

White coats also allow one to carry stuff in the pockets. In one study, 70 individuals were asked what their lab coat pockets contained. These were all clinicians, and regardless of their status, stethoscopes, pocket manuals, “to do” lists, and telephone numbers were the items most commonly found in their pockets. Faculty and older staff were not fond of carrying handouts from lectures that were popular among younger staff. Students and faculty both carried family pictures. When asked about the usefulness of these items, obviously medical equipment received higher scores, while lecture handouts were considered less useful than family photographs.<sup>18</sup>

Wearing perfume or cologne at the hospital or clinic, whether you are the physician or the patient, is generally discouraged. A number of workplaces are adopting fragrance-free or scent-reducing policies. It is thought that strong smells may induce allergies or asthma and are frowned on by most hospital safety committees (taking this to an extreme, Harrison Medical Center in Bremerton, Washington, accepts only flowers that are “less” fragrant for their patients). In reality, most allergies are induced by specific proteins that fragrances do not contain because what gives them their odor is actually a series of volatile hydrocarbons, which are not known to stimulate the immune system but, in large concentrations, may result in chemical irritations.<sup>19</sup> Anyway, because most soaps, shower gels, deodorants, and body lotions contain some fragrance nowadays, wearing perfume is less popular (reflected by the decreasing revenues of perfume/cologne sales in the last few years and the fact that most of today’s perfumes and colognes are very mild).

For the time being, I will continue wearing a business suit on most days at work. I generally do not wear a white coat because I

do not see patients, but as the evidence indicates, if you are consulting with patients it is a good idea to wear one and to change it often to keep it clean.

## REFERENCES

1. BBC News. Doctors should wear white coats. <http://news.bbc.co.uk/2/hi/health/3706783.stm>. Accessed March 4, 2014
2. Wikipedia. Scrubs (clothing). [http://en.wikipedia.org/wiki/Scrubs\\_%28clothing%29](http://en.wikipedia.org/wiki/Scrubs_%28clothing%29). Accessed March 4, 2014
3. Adam H, Galinsky AD. **Enclothed cognition.** *J Experimental Social Psychology* 2012;48:918–25
4. McKinstry B, Wang JX. **Putting on the style: what patients think of the way their doctor dresses.** *Br J Gen Pract* 1991;41:275–78
5. Brase GL, Richmond J. **The white-coat effect: physician attire and perceived authority, friendliness, and attractiveness.** *J Appl Soc Psychol* 2004;34:2469–81
6. Neinstein LS, Stewart D, Gordon N. **Effect of physician dress style on patient-physician relationship.** *J Adolesc Health Care* 1985;6:456–59
7. Sanders LD, Gildersleve CD, Rees LT, et al. **The impact of the appearance of the anesthetist on the patient’s perception of the pre-operative visit.** *Anaesthesia* 1991;46:1056–58
8. Hennessy N, Harrison DA, Aitkenhead AR. **The effect of the anaesthetist’s attire on patient attitudes: the influence of dress on patient perception of the anaesthetist’s prestige.** *Anaesthesia* 1993;48:219–22
9. Sotgiu G, Nieddu P, Mameli L, et al. **Evidence for preferences of Italian patients for physician attire.** *Patient Prefer Adherence* 2012;6:36–67
10. Rehman SU, Nietert PJ, Cope DW, et al. **What to wear today? Effect of doctor’s attire on the trust and confidence of patients.** *Am J Medicine* 2005;118:1279–86
11. Lund JD, Rohrer J, Goldfarb S. **Patient attitudes toward the use of surgical scrubs in a military hospital clinic.** *Patient Prefer Adherence* 2008;2:85–88
12. Gonzalez Del Rey JA, Paul RI. **Preferences of parents for pediatric emergency physician’s attire.** *Pediatr Emerg Care* 1995;11:361–64
13. Chowdhary U. **Instructor’s attire as a biasing factor in students’ ratings of an instructor.** *Clothing & Textiles Research Journal* 1988;6:17–22
14. Morris TL, Gorham J, Cohen SH, et al. **Fashion in the classroom: effects of attire on student perceptions of instructors in college classes.** *Communication Education* 1996;45:135–48
15. Abuannadi M. **Should physicians be banned from wearing neckties in medical venues?** *General Surgery News* 2011;38:4. [http://www.generalsurgerynews.com/ViewArticle.aspx?d=In%2Bthe%2BNews&d\\_id=69&i=April%2B2011&i\\_id=719&a\\_id=16975](http://www.generalsurgerynews.com/ViewArticle.aspx?d=In%2Bthe%2BNews&d_id=69&i=April%2B2011&i_id=719&a_id=16975). Accessed March 4, 2014
16. Bosch W, Hedges MS, Cawley JJ, et al. **Do nano-treated neckties reduce the carriage of bacterial pathogens from neckties of physicians?** In: *Proceedings of the 48th Joint Annual Interscience Conference on Antimicrobial Agents and Chemotherapy and the 46th Infectious Diseases Society of America Annual Meeting*, Washington, DC. October 25–28, 2008
17. Biljan MM, Hart CA, Sunderlad D, et al. **Multicentre randomized double blind crossover trial on contamination of conventional ties and bow ties in routine obstetric and gynaecological practice.** *BMJ* 1993;307:1582–84
18. Lynn LA, Bellini LM. **Portable knowledge: a look inside white coat pockets.** *Ann Intern Med* 1999;130:247–50
19. Senger E. **Scent-free policies generally unjustified.** *CMAJ* 2011;183:E315–16
20. Berry L, Bendapudi N. Working Knowledge for Business Leaders. Clueing in customers: why docs don’t wear white coats or polo shirts at the Mayo Clinic. <http://hbswk.hbs.edu/archive/3380.html>. Accessed March 4, 2014

## Lumbar Disc Nomenclature: Version 2.0

A.L. Williams, F.R. Murtagh, S.L.G. Rothman, and G.K. Sze

The above document by Fardon et al, listed in this issue's Table of Contents with links to the full versions recently published by *Spine* and *The Spine Journal*, represents an update to the original article coauthored by David Fardon, MD, and Pierre Milette, MD, entitled "Nomenclature and Classification of Lumbar Disk Pathology: Recommendations of the Combined Task Forces of the American Society of Spine Radiology, the American Society of Neuroradiology and the North American Spine Society" and published in *Spine* in 2001.

Version 2.0 updates the initial article, which provided a standardized nomenclature used extensively by imaging and clinical physicians over the past 13 years. Although the original document has stood the test of time, some sections and definitions were accepted more readily than others. Responding to an initiative from the American Society of Spine Radiology, a task force of spine physicians from the American Society of Spine Radiology, American Society of Neuroradiology, and North American Spine Society has reviewed and modified the original document. This revision represents the end-result of what turned out to be a 10-year process. The revision preserves the format and much of the language of the original document. The general principles that guided the original document remain unchanged. Definitions are based on anatomy and pathology, primarily as visualized on imaging studies. Definitions of diagnoses are not intended to imply external etiologic events such as trauma, do not imply relationship to symptoms, and do not define or imply need for specific treatment.

The modifications to the original document deal primarily with 1) updating and expanding the text, glossary, and references; 2) revision of the distinction between disk herniation and asymmetrically bulging disk; 3) revision of the illustrations; 4) emphasis of the term "annular fissure" in place of "annular tear"; 5) refinement of the definitions of "acute" and "chronic" disk her-

niation and other minor amendments. It is hoped that these disk nomenclature modifications will encourage use by all physicians involved in the diagnosis and treatment of spinal diseases in their daily practice.

Why is disk nomenclature important? In an *AJNR* editorial in January 2007, Reed Murtagh, MD, a senior member of our society, stated that "we need language to communicate precisely and objectively." Galen of Pergamon (129–199 AD), a Roman physician, surgeon, and philosopher, said that "the chief merit of language is clearness, and we know that nothing detracts so much from this as do unfamiliar terms." As neuroradiologists, we communicate with a diverse number of subgroups, including referring physicians, trainees, insurance companies, patients, and attorneys. The key to useful communication with professionals in these groups is the uniformity or standardization of definitions.

The standardization of terms positively impacts our practice of medicine in many ways. With respect to patient care, it is imperative that radiologists and clinicians understand one another. Patient treatment regimens depend on it. Follow-up imaging studies may be read by different radiologists. Different clinicians may be following the same patient. It is important for residents and fellows to learn standardized nomenclature from the outset of their training (eg, Disk Nomenclature 101). Research activities require uniform nomenclature for reliable data collection, indexing, and mining. In the medical-legal realm, attorneys need to understand the content of radiology reports. RadLex, a comprehensive lexicon of radiology terms for the standardized organizing, indexing, and retrieving of radiology information, relies on standardized terms. Structured report templates similar to those used in mammography (eg, BI-RADS) seem to be gaining favor in the "new" medical environment. Disk nomenclature is crucial in such a system.

In conclusion, it is hoped that this revised document will gain even wider acceptance than did the original among all physicians involved in the diagnosis and treatment of spinal diseases. The authors, members of the American Society of Spine Radiology/American Society of Neuroradiology Nomenclature Committee, encourage our neuroradiology colleagues to review the revised document and incorporate this lumbar disk nomenclature in their daily practice.

<http://dx.doi.org/10.3174/ajnr.A4108>

# PET Approaches for Diagnosis of Dementia

K. Ishii



## ABSTRACT

**SUMMARY:** There is increasing use of neuroimaging modalities, including PET, for diagnosing dementia. For example, FDG-PET demonstrates hypometabolic regions in the posterior cingulate gyri, precuneus, and parietotemporal association cortices, while amyloid PET indicates amyloid deposition in Alzheimer disease and mild cognitive impairment due to Alzheimer disease. Furthermore, the use of combination PET with structural MR imaging can improve the diagnostic accuracy of dementia. In other neurodegenerative dementias, each disease exhibits a specific metabolic reduction pattern. In dementia with Lewy bodies, occipital glucose metabolism is decreased, while in frontotemporal dementia, frontal and anterior temporal metabolism is predominantly decreased. These FDG-PET findings and positive or negative amyloid deposits are important biomarkers for various neurodegenerative dementias.

**ABBREVIATIONS:**  $A\beta$  = amyloid  $\beta$  peptide; AD = Alzheimer disease; *APOE* = apolipoprotein E; CBD = corticobasal degeneration; DLB = dementia with Lewy bodies; FTD = frontotemporal dementia; MCI = mild cognitive impairment; PD = Parkinson disease; PIB = Pittsburgh compound-B; PSP = progressive supranuclear palsy; VBM = voxel-based morphometry

The number of patients with dementia is progressively increasing worldwide. Dementia is a clinical diagnosis based on significant and persisting deficits of intellectual function, usually memory. Diagnostic imaging techniques for morphologic examinations (eg, CT and MR imaging) and for functional examinations (eg, SPECT and PET) are now used widely for supporting the diagnosis of dementia. Such imaging techniques can indicate the likely underlying pathology in a patient who meets the clinical criteria for dementia. In particular, amyloid imaging PET has been reported to show the pathophysiologic states of dementia. The PET radiopharmaceutical [ $^{18}\text{F}$ ]fluorodeoxyglucose can detect regional glucose metabolism in patients with dementia and is the most widely available and useful biomarker for dementia diagnosis. However, to exclude several pathologies such as subdural hematoma, vascular dementia, normal pressure hydrocephalus, and brain tumors, clinical examination is first performed by using MR imaging because FDG-PET alone cannot detect these diseases. After this process, FDG-PET is then performed to detect early neu-

rodegenerative dementia, differentiate neurodegenerative dementias,<sup>1</sup> or suggest comorbidity of other neurodegenerative diseases. Herein, I review the various imaging approaches for dementia, with a particular focus on PET and new techniques or tracers.

### Alzheimer Disease

Alzheimer disease (AD) is the most common dementia, which starts with impairment of memory followed by multiple domains of cognitive dysfunction. The 2011 criteria for AD<sup>2,3</sup> was revised from that in 1984,<sup>4</sup> and the recommendations regarding the respective roles of FDG-PET and MR imaging in AD and mild cognitive impairment (MCI) are conflicting. However, PET plays an important role as a biomarker in AD, as well as for functional and molecular imaging. For example, FDG-PET is described as a “neuronal injury” biomarker in AD.<sup>2,3</sup>

### FDG-PET in Alzheimer Disease

FDG-PET can demonstrate a glucose metabolic reduction in the parietotemporal association cortices, posterior cingulate, and precuneus regions at the early stage of AD (Fig 1). By contrast, in the healthy elderly brain, posterior cingulate glucose metabolism is much higher than that in other cortices, while parietal glucose metabolism is the same as that in the primary sensorimotor cortices (Fig 2). In the moderate-to-severe stages of AD, hypometabolic regions spread to the frontal association cortices, while metabolism in the striatum, thalamus, primary sensorimotor cortices, visual cortices, and cerebellum are relatively preserved despite disease progression.

Because the magnitude of glucose metabolic reduction in the medial temporal lobe, including the hippocampus, is not as large

From the Neurocognitive Disorders Center, Kinki University Hospital, Osaka, Japan. This work was supported by JSPS KAKENHI grant number 50534103 and 21st Century Research and Development Incentive Wages at Kinki University.

Paper previously presented at: 98th Scientific Assembly and Meeting of the Radiological Society of North America, November 25–30, 2012; Chicago, Illinois.

Please address correspondence to Kazunari Ishii, MD, Department of Radiology, Kinki University Faculty of Medicines, 377-2 Ohnohigashi, Osakasayama, Osaka 589-8511, Japan; e-mail: kishii@hbhc.jp

Indicates open access to non-subscribers at [www.ajnr.org](http://www.ajnr.org)

<http://dx.doi.org/10.3174/ajnr.A3695>

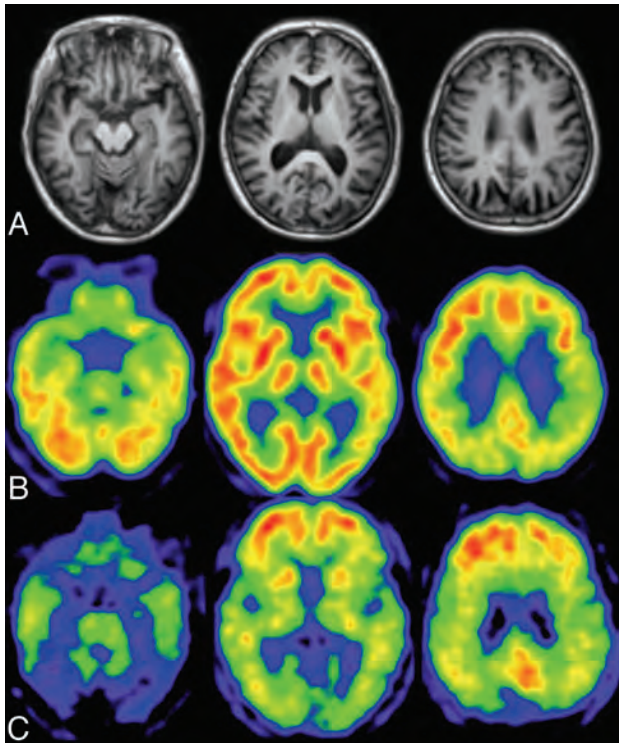


**FIG 1.** A patient with early Alzheimer disease, 77 years of age, Mini-Mental State Examination score = 25. *A*, Minimal atrophy was seen in the right hippocampus. *B*, FDG-PET shows reduced glucose metabolism in the bilateral parietotemporal association cortices and posterior cingulate gyri and precuneus. *C*, PiB accumulations are demonstrated in the cerebral cortices except for the occipital and medial temporal regions. Medial parietal and frontal accumulations of PiB are high, indicative of positive amyloid deposit.

as that in the parietotemporal or posterior cingulate cortices, a decrease in hippocampal glucose metabolism with progression from mild-to-moderate-stage AD is not usually demonstrated,<sup>5</sup> despite obvious hippocampal atrophy at the early stage. Hippocampal glucose metabolism is somewhat decreased at the early stage of AD. However, it is difficult to detect the small reduction of hippocampal glucose metabolism in patients with early AD because the hippocampal glucose metabolism is smaller than the neocortical glucose metabolism, even in healthy subjects, and the magnitude of the decrease is modest. Thus, a method for detecting hippocampal metabolic reduction at an early stage of AD is required.<sup>6-8</sup> However, Karow et al<sup>9</sup> reported that FDG-PET has the same sensitivity as MR imaging for detecting brain degeneration in preclinical and mild AD, suggesting that MR imaging may be a more practical clinical biomarker for early detection of AD.

#### **Mild Cognitive Impairment Due to Alzheimer Disease**

Mild cognitive impairment consists of a heterogeneous pathology, and MCI due to AD is a transitional stage between aging and AD. MCI due to AD demonstrates the same glucose-reduction pattern as early AD (Fig 3), which predicts that the patient will show symptoms of AD in the near future. At the early stage of AD or MCI due to AD, it is difficult to detect the characteristic hypometabolic patterns on FDG-PET images by visual inspection. As such, statistical images are helpful. Nevertheless, FDG-PET generally has a higher accuracy than MR imaging for diagnosing early AD<sup>10,11</sup> and

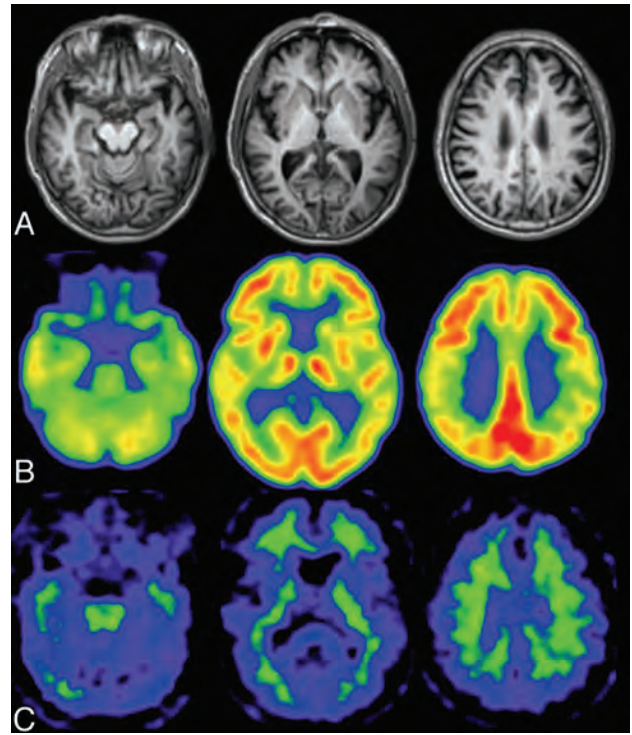


**FIG 2.** Healthy elderly male subject, 78 years of age, Mini-Mental State Examination score = 30. *A*, A slight enlargement of the right inferior horn of the lateral ventricle is seen on the T1-weighted MR image. *B*, The regional glucose metabolism is not reduced on the FDG-PET images. Note that the posterior cingulate glucose metabolism is much larger than that in other regions. *C*, PiB-PET shows non-specific accumulation in the white matter but no PiB accumulation in the gray matter. The amyloid deposit is negative.

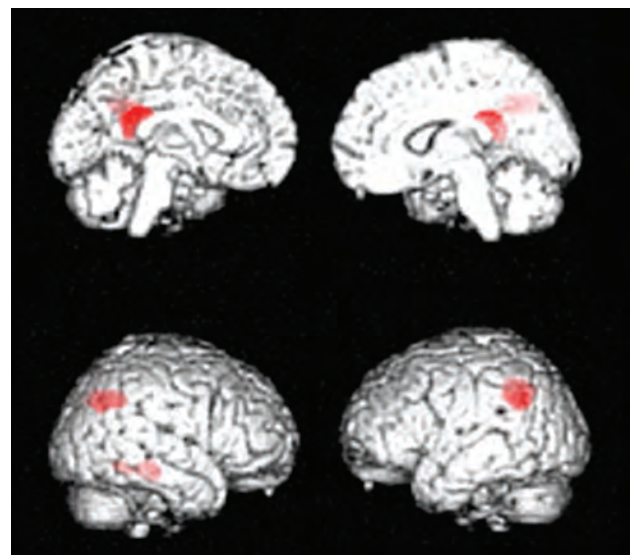


**FIG 3.** MCI due to AD. Regions exhibiting a significant reduction in glucose metabolism in patients with MCI due to AD ( $n = 20$ ) compared with healthy elderly subjects ( $n = 20$ ) are demonstrated by statistical parametric maps. Bilateral parietal and posterior cingulate metabolism is decreased in patients with MCI due to AD. These decreased regions are the same as those in patients with early AD.

for predicting rapid conversion of MCI to early AD.<sup>12</sup> A combination of PET and other biomarkers is important because imaging and CSF biomarkers can improve prediction of conversion from MCI to AD

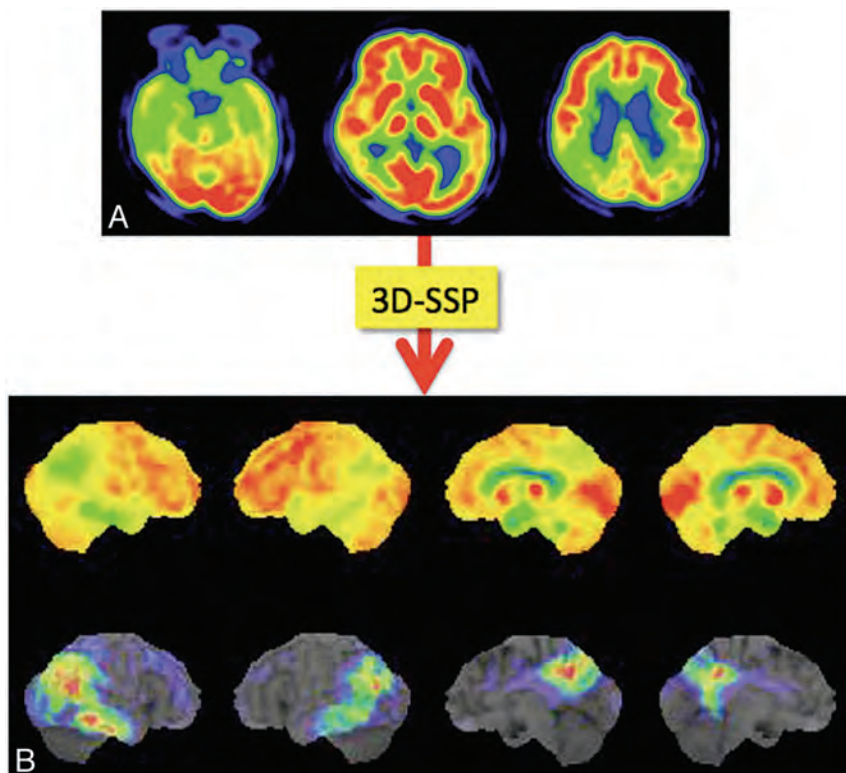


**FIG 4.** Process of voxel-based statistical maps. Original FDG-PET image of a patient with mild AD (A) is analyzed by using the 3D-SSP program, and the 3D-SSP surface map and z score map are produced. The z score map shows the regions with significantly reduced metabolism compared with a normal data base (B), which aid in the diagnosis of AD.

compared with baseline clinical testing. FDG-PET appears to add the greatest prognostic information.<sup>13-16</sup>

#### **Effects of APOE on FDG-PET and Amyloid Imaging of Alzheimer Disease**

The *apolipoprotein E* gene (*APOE*) is a risk factor for late-onset AD, while the *APOE*  $\epsilon 4$  allele ( $\epsilon 4$ ) increases the risk and decreases the average age of dementia onset. Patients with early-onset AD who were *APOE*  $\epsilon 4$ -positive showed a significant decrease in glucose metabolism in the medial temporal lobe compared with patients with *APOE*  $\epsilon 4$ -negative AD.<sup>17</sup> By contrast, in the late-onset group, there were no differences in the glucose-metabolic reduction patterns between patients with *APOE*  $\epsilon 4$ -positive and -negative AD. A similar pattern of cerebral hypometabolism was also detected between patients with *APOE*  $\epsilon 4$ -positive and -negative AD but with stronger abnormalities in  $\epsilon 4$  carriers in the parietal, temporal, and posterior cingulate cortical regions.<sup>18</sup> Recently Ossenkoppele et al<sup>19</sup> found a reversed *APOE*  $\epsilon 4$  dose effect for amyloid deposition in the frontal lobe, whereas *APOE*  $\epsilon 4$  carriage was associated with more profound metabolic impairment in the posterior parts of the cortex. These findings suggest that the *APOE* genotype has a differential effect on the distribution of amyloid plaques and glucose metabolism.

#### **Statistical Voxel-Based Analysis Approach for Alzheimer Disease Diagnosis**

Minoshima et al<sup>20,21</sup> first developed the 3D stereotactic surface projection system (3D-SSP; <http://www.rad.washington.edu/research/>

Research/groups/nbl/neurostat-3d-ssp) and used z score images to aid visual inspection of individual FDG images for diagnosing AD (Fig 4). The Statistical Parametric Mapping program (Wellcome Department of Imaging Neuroscience, London, UK) was developed as a tool for analysis of PET and functional MR imaging images. For automatic diagnosis, Herholz et al<sup>22</sup> proposed the *t*-sum method of calculating the total *t*-values in a region-of-interest template by using the Statistical Parametric Mapping program; by using this method, the parietotemporal and frontal regions were found to be AD-specific compared with healthy elderly subjects. An automatic diagnosis system by using 3D-SSP and a region-of-interest template was proposed for discriminating those with early AD from healthy subjects.<sup>23,24</sup> This system was also applied to distinguish patients with dementia with Lewy bodies (DLB) from those with AD.<sup>24</sup> All these systems require a data base of healthy controls. More recently, however, a data base-independent system was proposed by using *t*-statistics between parietal and sensorimotor glucose metabolism in individual subjects.<sup>25</sup> Mevel et al<sup>26</sup> proposed an automatic system for determining hippocampal metabolism by using a voxel-based method and partial volume correction, which was useful in detecting MCI.

#### **Combination of MR Imaging and PET**

Most of the studies described above have focused on only a single technique such as structural MR imaging or PET. Yuan et al<sup>12</sup> performed a meta-analysis and meta-regression on the diagnostic performance data for MR imaging, SPECT, and FDG-PET in subjects with MCI and reported that FDG-PET performed slightly better than SPECT and structural MR imaging in the prediction of conversion to AD in patients with MCI, while a combination of PET and structural MR imaging improved the diagnostic accuracy of dementia. Kawachi et al<sup>10</sup> also compared the diagnostic performance of FDG-PET and voxel-based morphometry (VBM) on MR imaging in the same group of patients with very mild AD and reported an accuracy of 89% for FDG-PET diagnosis and 83% for VBM-MR imaging diagnosis, while the accuracy of combination FDG-PET and VBM-MR imaging diagnosis was 94%. These studies suggest that a combination of imaging modalities may improve the diagnosis of AD.

#### **Amyloid Imaging in Alzheimer Disease**

The most widely used tracer for amyloid imaging is <sup>11</sup>C-Pittsburgh compound-B (PiB),<sup>27</sup> which has a high affinity to amyloid  $\beta$  peptide ( $A\beta$ ) aggregates. The <sup>11</sup>C-BF 227 ligand is also used for amyloid imaging,<sup>28</sup> though its uptake contrast between amyloid-positive and -negative brain tissue is not as high as that for PiB, and it is used only at a few institutions in Japan. Because the

**Table 1: Representative radiopharmaceuticals for amyloid imaging**

<sup>11</sup> C-PiB	[ <sup>11</sup> C]-2-4-(methylaminophenyl)-6-hydroxybenzothiazole <sup>62</sup>
<sup>11</sup> C-BF227	[ <sup>11</sup> C]-2-[2-(2-Dimethylaminothiazol-5-yl)ethenyl]-6-[2-(fluoro)ethoxy]benzoxazole <sup>28</sup>
<sup>11</sup> C-AZD2184	N-[ <sup>11</sup> C]methyl-2-(6-methylamino-pyridine-3-yl)-benzo[d]thiazole-6-ol <sup>66</sup>
<sup>18</sup> F-FDDNP	2-(1-(6-[(2-[ <sup>18</sup> F]fluoroethyl)(methyl)amino]-2-naphthyl)ethylidene)malononitrile <sup>67</sup>
<sup>18</sup> F-PiB	2-[3-[ <sup>18</sup> F]fluoro-4-(methylamino)phenyl]1,3-benzothiazole-6-ol <sup>68</sup>
<sup>18</sup> F-AV45	(E)-4-(2-(6-(2-(2-(2-[ <sup>18</sup> F]-fluoroethoxy)ethoxy)ethoxy)pyridin-3-yl)vinyl)-N-methyl benzenamine <sup>30</sup>
<sup>18</sup> F-BAY94-9172	4-(N-methylamino)-4'-(2-(2-(2-[ <sup>18</sup> F]fluoroethoxy)-ethoxy)-ethoxy)-stilbene <sup>69</sup>
<sup>18</sup> F-AZD4694	2-(2-[ <sup>18</sup> F]fluoro-6-(methylamino)pyridin-3-yl)benzofuran-5-ol <sup>30</sup>

**Note:**—<sup>18</sup>F-AV45 indicates florbetapir; <sup>18</sup>F-BAY94-9172, florbetaben; <sup>18</sup>F-PiB, flutemetamol.

half-life of the <sup>11</sup>C isotope is short, <sup>11</sup>C-PiB is available only in specific institutions that have a cyclotron and a synthesis system. Conversely, the half-life of the <sup>18</sup>F isotope is 110 minutes, and <sup>18</sup>F-labeled amyloid imaging tracers will become widely used following production by radiopharmaceutical companies. Currently there are a few <sup>18</sup>F-labeled amyloid imaging tracers available (Table 1),<sup>29</sup> though in 2012, <sup>18</sup>F-AV-45 (florbetapir)<sup>30</sup> was approved by the FDA for PET imaging of  $\beta$ -amyloid neuritic plaques in the living brain. <sup>18</sup>F-AZD4694 is also expected to be a good radioligand for both diagnostic use and evaluation of disease-modifying therapies in AD.<sup>31</sup>

Amyloid PET is helpful in the diagnosis of AD. However, the timing of amyloid accumulation is at a preclinical stage of AD.<sup>32</sup> Early A $\beta$  accumulation and increased vulnerability to A $\beta$  pathology play critical roles in the pathogenesis of patients with early-onset AD.<sup>33</sup> A $\beta$  deposition initiates the pathologic cascade but is not the direct cause of cognitive impairment, and intermediate A $\beta$  deposit may represent individuals with AD coexistent with other pathologies.<sup>34</sup> Furthermore, amyloid deposit is not unique to AD and can be found in other diseases or healthy elderly people.

At present, amyloid PET is not indicated in patients with preclinical AD or healthy subjects, except for clinical trials or research studies. The appropriate usage criteria for amyloid PET were proposed by the Amyloid Imaging Task Force, the Society of Nuclear Medicine and Molecular Imaging, and the Alzheimer's Association.<sup>35,36</sup> These criteria indicate that appropriate use of amyloid PET includes the following: 1) patients with persistent or progressive unexplained MCI; 2) patients with possible AD with unclear clinical presentation, either an atypical clinical course or an etiologically mixed presentation; and 3) patients with progressive dementia and atypically early age of onset. Inappropriate use of amyloid PET includes the following: 1) in patients with typical probable AD, 2) for determining the severity of dementia, 3) in subjects with a positive family history of dementia or the presence of APOE  $\epsilon$ 4, 4) in patients with a cognitive problem that is unconfirmed on clinical examination, 5) as a replacement for genotyping for suspected autosomal mutation carriers, 6) in asymptomatic subjects, and 7) for nonmedical use (eg, legal, insurance coverage, or employment screening).

### Dementia with Lewy Bodies

Dementia with Lewy bodies is the second most common neurodegenerative dementia following AD and is characterized pathologically by the presence of Lewy bodies in cortical, subcortical, and brain stem structures. DLB belongs to the spectrum of Lewy body diseases including Parkinson disease (PD), where Lewy bodies remain in the brain stem. PD with dementia has the same

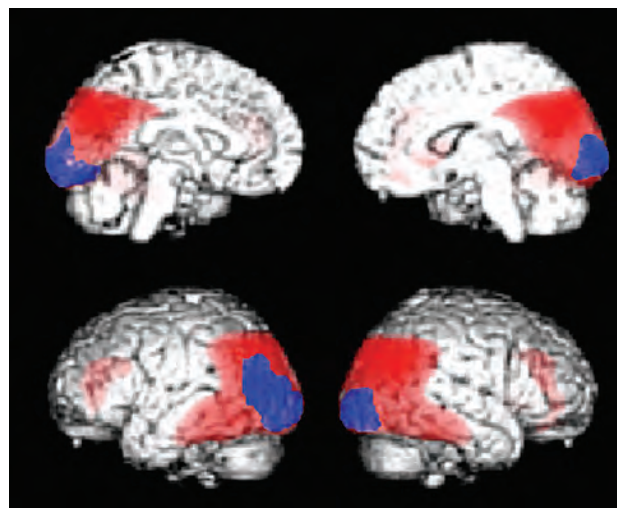


**FIG 5.** Decreased glucose metabolic regions of DLB ( $n = 20$ ). Statistical parametric maps show the areas where glucose metabolism is significantly decreased compared with age-matched healthy controls ( $n = 20$ ). The red area indicates the parietotemporal association area, and the posterior cingulate gyri overlap the area where glucose metabolism is decreased in AD. The blue area indicates occipital cortices that are specific for DLB, where the glucose metabolism is preserved in AD ( $n = 20$ ).

pathology as DLB, though clinical symptoms slightly differ: Parkinsonism appears  $>1$  year earlier than cognitive dysfunctions in PD with dementia.

In 2005, the criteria for clinical and pathologic diagnoses were revised<sup>36</sup> and included an important role for functional and morphologic imaging. For example, low dopamine transporter uptake in the basal ganglia on SPECT and PET imaging scans is regarded as a suggestive feature for DLB, while supportive features include relative preservation of medial temporal lobe structures on CT/MR imaging and generalized low uptake on SPECT/PET, with reduced occipital activity and abnormal (low) uptake on metaiodobenzylguanidine myocardial scintigraphy. Relative preservation of the hippocampus in DLB compared with prominent hippocampal atrophy in AD is also a common finding, though there are many overlapping areas of hippocampal atrophy between patients with DLB and those with AD, making it impossible to distinguish a patient with DLB from one with AD by using only a finding of hippocampal atrophy.

The hypometabolic regions in patients with DLB are similar to those in AD, though patients with DLB exhibit a difference in the involved occipital lobe (Fig 5). The relative metabolic reduction was more severe in the occipital cortices and less severe in the medial temporal lobes in DLB compared with AD, and occipital hypometabolism is a key feature of DLB that discriminates it from

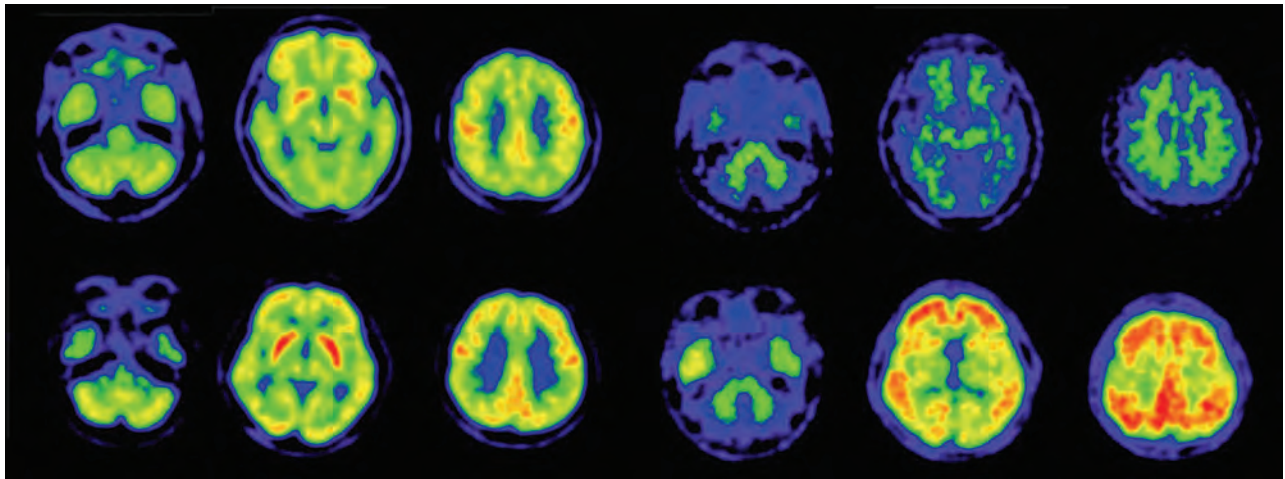


**FIG 6.** PiB-PET and FDG-PET images of patients with DLB. Upper row shows a 76-year-old man with DLB. This patient has Parkinsonism and cognitive fluctuation. His Mini-Mental State Examination score was 19. Diffuse glucose metabolic reduction is demonstrated in all regions apart from the striatum and primary sensorimotor cortices (upper left). PiB-PET (upper right) demonstrates a negative amyloid deposit. Lower row shows a 77-year-old woman with DLB, Parkinsonism, and cognitive fluctuation. Her Mini-Mental State Examination score was 23. FDG-PET demonstrates decreased glucose metabolism in the parietotemporal and frontal association cortices, occipital cortices, and posterior cingulate gyri, while metabolism in the striatum and primary sensorimotor metabolism is spared (lower left). PiB-PET demonstrated diffuse amyloid deposition in the cerebral cortices (lower right).

AD.<sup>7,38,39</sup> Nevertheless, pathologically, the occipital cortices are not as involved in patients with DLB. These findings are also seen in patients with PD and PD with dementia<sup>40</sup> because DLB and PD with dementia are in the same disease entity, involving spread of Lewy bodies in the cerebral cortices.

Dopamine transporter imaging with <sup>123</sup>I-*N*- $\omega$ -fluoropropyl-2 $\beta$ -carbomethoxy-3 $\beta$ -(4-iodophenyl)nortropane ([<sup>123</sup>I] FP-CIT) SPECT imaging is useful for diagnosing DLB and exhibits a diagnostic accuracy sufficient to distinguish DLB from AD.<sup>41</sup> However, this imaging technique cannot distinguish other degenerative dementias with Parkinsonism (eg, progressive supranuclear palsy (PSP) and multiple system atrophy), while FDG-PET imaging can distinguish DLB from PSP and multiple-system atrophy. <sup>123</sup>I-meta-iodobenzylguanidine cardiac scintigraphy, which is typically used for myocardial innervation, also demonstrates a high sensitivity and specificity in patients with suspected DLB and provides an accurate examination for differential diagnosis between DLB and other dementias.<sup>42</sup>

#### **Amyloid Imaging in Dementia with Lewy Bodies**

Shimada et al<sup>43</sup> reported that amyloid deposits are associated with AD-like atrophy in patients with DLB/PD with dementia. Patients with DLB have higher amyloid deposits than patients with PD and PD with dementia. Amyloid deposits have been linked to cognitive impairment in DLB<sup>44,45</sup> and may contribute to the timing of the onset of dementia relative to that of Parkinsonism in Lewy body dementia.<sup>46</sup> However, as shown in Fig 6, severe metabolic reduction was seen in some patients with DLB despite no evidence of amyloid deposits. In particular, regional metabolic reduction in patients with DLB was observed in the parietotemporal, posterior cingulate, and frontal association cortices, which are the same regions affected in AD but are not correlated with amyloid deposit.

#### **Frontotemporal Lobe Degeneration**

Frontotemporal lobe degeneration (FTD) is a heterogeneous group of diseases involving frontal and/or anterior temporal lobe

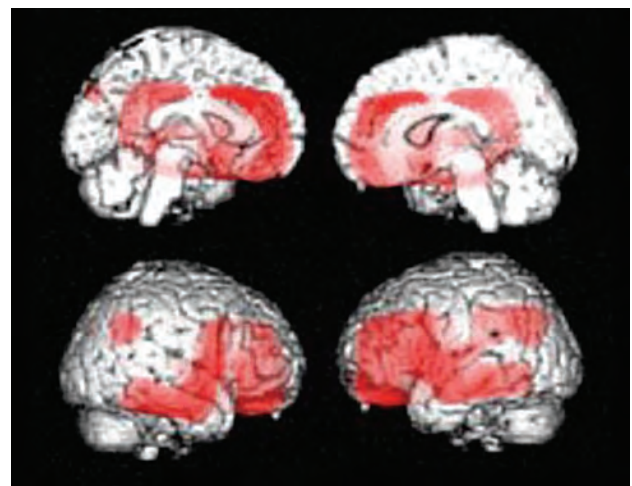


**FIG 7.** Hypometabolic regions in FTD. Statistical parametric mapping analysis shows hypometabolic regions in patients with FTD ( $n = 14$ ) compared with healthy age-matched subjects ( $n = 20$ ). Glucose metabolism in subjects with FTD was significantly decreased in the bilateral lateral and medial frontal cortices, the posterior cingulate gyrus, and small regions in the parietal association cortices.

degeneration and associated dementia. Frontotemporal dementia is a comprehensive clinical entity of primary degenerative dementia characterized by peculiar behavioral changes and includes 3 types of histologic change (pick-type, frontal lobe degeneration type, and motor neuron disease type).<sup>47</sup> Frontotemporal lobe degeneration includes FTD, semantic dementia, and progressive nonfluent aphasia, while FTD is now used clinically to classify patients with frontal and temporal symptoms.

In FTD, frontal and anterior temporal glucose metabolism is decreased, though the medial temporal region and the subcortical structures, including the striatum and thalamus, are also affected (Fig 7).<sup>48</sup> According to a VBM study of FTD,<sup>49</sup> metabolic and atrophic changes occur in the bilateral frontal and temporal lobes,

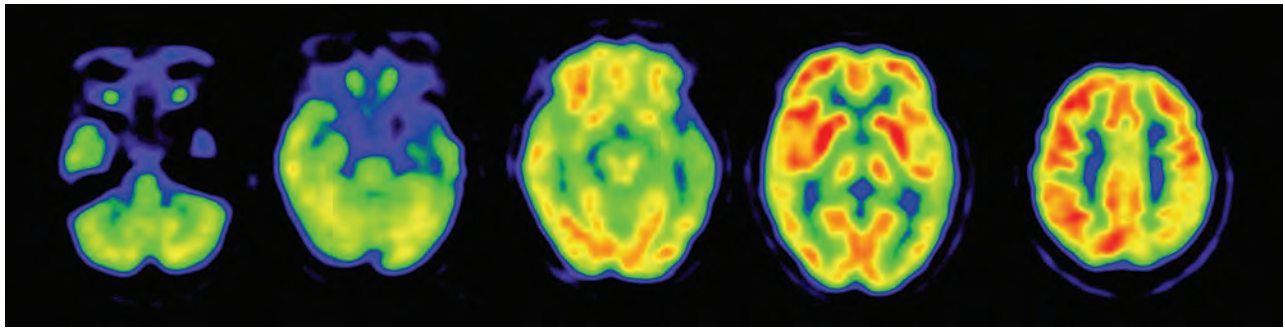


**FIG 8.** FDG-PET image of a 54-year-old female patient with semantic dementia. A marked decreased left anterior temporal metabolism is shown on the FDG-PET image.

whereas the affected regions of metabolism are larger and more severe than those of atrophy in the frontal lobe. In patients with semantic dementia, asymmetrically severely decreased temporal metabolism can be demonstrated on FDG-PET images (Fig 8). These areas can spread to the frontal and parietal cortices, though the degree of metabolism alteration is not as marked as in the anterior temporal cortices.

#### **Amyloid Imaging in Frontotemporal Lobe Degeneration**

In a study of PiB retention in patients with FTD, Engler et al<sup>50</sup> reported that most patients with FTD displayed no PiB retention and that PiB could potentially aid in differentiating FTD and AD. Rabinovici et al<sup>51</sup> also reported that 8/12 patients with frontotemporal lobe degeneration had negative amyloid deposits, and the 4 PiB-positive patients with frontotemporal lobe degeneration may suggest the mimicking of AD pathology.

#### **Progressive Supranuclear Palsy**

Progressive supranuclear palsy is a neurotauopathic degenerative disorder presenting with Parkinsonism and dementia. The neurologic features include impaired ocular motility, pseudobulbar palsy, and axial dystonia. The basal ganglia and brain stem are the main loci of pathologic involvement. MR imaging studies demonstrate brain stem atrophy with a so-called “humming bird” sign, though these findings are not often seen at the early stage of PSP. However, FDG-PET demonstrates decreased glucose metabolism in the midbrain, the lateral and medial frontal lobes, and the caudate nucleus, even at the early stage of PSP (Fig 9)<sup>52,53</sup> and can distinguish PSP from other diseases with Parkinsonism.<sup>54,55</sup>

#### **Corticobasal Degeneration**

Corticobasal degeneration (CBD), which belongs to the corticobasal syndrome, is characterized by akineto-rigid syndrome, dystonia, myoclonus, apraxia, alien limb syndrome, and cortical sensory loss, and typically occurs with asymmetric onset. CBD is pathologically a tauopathic neurodegenerative disease and includes  $\tau$ -immunoreactive neuronal cytoplasmic inclusions, oligodendroglial inclusions, and astrocytic plaques. FDG-PET demonstrates hypometabolism in the frontal and parietal cortices and the subcortical structures, including the thalamus, caudate nucleus, and putamen, with marked asymmetry between the 2 hemispheres. Patients with CBD with symptoms of dementia show an AD-like metabolic reduction pattern but asymmetric glucose-metabolic reduction in the lateral frontal, lateral temporal, medial

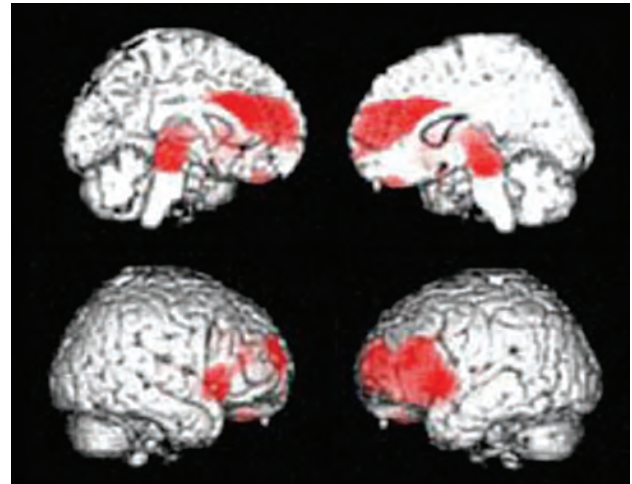


**FIG 9.** Hypometabolic regions in PSP. Statistical parametric mapping analysis shows hypometabolic regions in patients with PSP ( $n = 16$ ) compared with normal age-matched subjects ( $n = 20$ ). Glucose metabolism in subjects with PSP is significantly decreased in the bilateral lateral and medial frontal cortices and midbrain. The significant decreased midbrain metabolism is a hallmark of PSP.

and lateral parietal cortices; the pre- and postcentral gyri; and the thalamus on FDG-PET.<sup>56</sup>

#### **Amyloid Imaging in Progressive Supranuclear Palsy and Corticobasal Degeneration**

PSP and CBD are tauopathic neurodegenerative diseases that exhibit no amyloid deposition. If amyloid deposition is demonstrated with amyloid PET, it should be considered small amyloid deposits with age-related amyloid pathology or extended amyloid deposits similar to those in AD due to comorbidity of AD, which may be associated with *APOE*  $\epsilon 4$ .

#### **Idiopathic Normal Pressure Hydrocephalus**

Idiopathic normal pressure hydrocephalus is characterized by disproportionately enlarged cerebrospinal spaces, ventricle and Sylvian fissure dilation, and tight sulci at high convexity in the medial parietal sulci.<sup>57</sup> To detect these features, morphologic images by using CT or MR imaging are necessary. On the other hand, functional images are not necessary because the glucose metabolic reduction pattern is heterogeneous in idiopathic normal pressure hydrocephalus.<sup>58</sup> Glucose metabolism in idiopathic normal pressure hydrocephalus before and after a

**Table 2: General FDG-PET and amyloid PET findings in neurodegenerative dementia**

	PC	Pari	Lat. Temp	Med. Temp	Fron	Occ	SM	ST	TH	BS	AMY
MCI due to AD	↓	↓	→	→(or ↓)	→	→	→	→	→	→	+ or ++
AD (mild)	↓	↓	↓	→(or ↓)	→	→	→	→	→	→	++
AD (moderate)	↓	↓	↓	↓	↓	↓	→	→	→	→	++
DLB	↓	↓	↓	→	↓	↓	→	→	→	→	+ or -
FTD	→(or ↓)	→(or ↓)	↓	↓	→	→	→	→ or ↓	→	→	-
SD	→	→(or ↓)	↓↓	↓	→	→	→	→	→	→	-
PSP	→	→	→(or ↓)	→	↓	→	→	↓	→	↓	-
CBD 1)	↓	↓	↓	→	↓	→	↓	↓	↓	→	-
VaD 2)	→(or ↓)	→(or ↓)	→ or ↓	→ or ↓	↓	→	→ or ↓	→ or ↓	→ or ↓	→	-

**Note:**—PC indicates posterior cingulate gyrus; Pari, parietal association cortex; Lat. Temp, lateral temporal cortex; Med. Temp, medial temporal cortex; Fron, frontal cortex; Occ, occipital cortex; SM, sensorimotor cortex; ST, striatum; TH, thalamus; BS, brain stem; AMY, amyloid deposition: 1) asymmetric reduction is characteristic, 2) frontal dominant metabolic reduction is often demonstrated in addition to infarction region; SD, semantic dementia; VaD, vascular dementia; ↓, decreased; →, preserved; +, positive; -, negative.

shunt operation is promptly reversible after surgery, and there is a relationship between the early metabolic changes and clinical symptoms that is independent of the simultaneous changes in ventricular size.<sup>59</sup> Because idiopathic normal pressure hydrocephalus occurs in elderly individuals, there is a possibility for concomitant AD. Amyloid imaging with PET may be useful to detect early concomitant AD and other diseases associated with amyloid deposits.<sup>60</sup>

### Vascular Dementia

Vascular dementia is diagnosed with clinical symptoms and by detecting symptoms related to vascular lesions demonstrated by morphologic imaging. As such, pure vascular dementia is not a PET-applicable dementia. However, vascular dementia is sometimes associated with AD or other neurodegenerative pathology, and these patients should be examined with FDG-PET to determine the comorbidity of AD or other neurodegenerative pathology. Amyloid imaging can be used to remove the comorbidity of AD pathology when there is no amyloid deposit.

### Tau Imaging

After amyloid plaques, intracellular neurofibrillary tangles are an important hallmark of AD. Neurofibrillary tangles are preferentially located in the hippocampus and associative cortical regions. <sup>18</sup>F-2-(1-{6-[(2-[F]Fluoroethyl)(methyl)amino]-2-naphthyl}ethylidene)malononitrile or FDDNP was initially developed for Aβ imaging, though this ligand binds to both Aβ plaques and neurofibrillary tangles in the brain. As such, FDDNP was expected to demonstrate both amyloid and neurofibrillary tangle deposits<sup>61</sup> but has limited value for accurate measurement of τ-related pathology in patients with AD. <sup>18</sup>F-THK-523 was developed as a potential in vivo imaging probe for τ pathology and was reported to accumulate in regions containing a high attenuation of τ protein deposits.<sup>62</sup> This tracer is now being used in patients with AD. Some forms of FTD, PSP, and CBD are also characterized by pathologic accumulation of τ protein. Thus, τ imaging will be useful in distinguishing these diseases from AD.

### Cost-Effectiveness of PET Imaging for Dementia

Silverman et al<sup>63</sup> first evaluated the cost and benefit of the diagnosis of early AD by using FDG-PET and reported that appropriate use of FDG-PET can add valuable information to the clinical work-up, without adding to the overall costs of evaluation and management in the United States. In Europe, Moulin-Romsee

et al<sup>64</sup> reported that the introduction of FDG-PET into the clinical work-up of patients with suspected AD can result in substantial benefit in terms of health care cost savings and in benefit for the patient. For the present, there is still no radical treatment for AD because diagnosis of early or preclinical dementia remains controversial. Multicenter cohort studies should be performed to evaluate the cost-effectiveness of new biomarkers such as amyloid PET for early diagnosis of AD and other neurodegenerative dementias and to establish appropriate PET use criteria for the benefit of patients.

### CONCLUSIONS

The use of PET enables the early detection of pathophysiologic changes in patients with dementia and allows differential diagnosis among neurodegenerative dementias. A summary of FDG-PET and amyloid PET findings for each neurodegenerative dementia is shown in Table 2. Each disease has characteristic regional metabolic reduction patterns on FDG-PET. PET is now used as an in vivo imaging technique for examining neurodegenerative dementia including AD and for detecting the early symptomatic and preclinical stages of dementia.

### ACKNOWLEDGMENTS

I thank Takamichi Murakami, MD, PhD, Chisa Hosokawa, MD, PhD, Tomoko Hyodo, MD, PhD, Kenta Sakaguchi, RT, Kimio Usamai, RT, Yoshiyuki Nakayama, Kenji Shimamoto, PhD, and Yuzuru Yamazoe, PhD, for their support for brain FDG-PET and PiB-PET at Kinki University and former staff members at the Hyogo Institute for Aging Brain and Cognitive Disorders.

Disclosures: Kazunari Ishii—RELATED: Grant: JSPS KAKENHI Grant Number 50534103, and 21st century research and development incentive wages at Kinki University.

### REFERENCES

- Ishii K. Clinical application of positron emission tomography for diagnosis of dementia. *Ann Nucl Med* 2002;16:515–25
- McKhann GM, Knopman DS, Chertkow H, et al. The diagnosis of dementia due to Alzheimer's disease: recommendations from the National Institute on Aging-Alzheimer's Association workgroups on diagnostic guidelines for Alzheimer's disease. *Alzheimers Dement* 2011;7:263–69
- Albert MS, DeKosky ST, Dickson D, et al. The diagnosis of mild cognitive impairment due to Alzheimer's disease: recommendations from the National Institute on Aging-Alzheimer's Association workgroups on diagnostic guidelines for Alzheimer's disease. *Alzheimers Dement* 2011;7:270–79

4. McKhann G, Drachman D, Folstein M, et al. **Clinical diagnosis of Alzheimer's disease: report of the NINCDS-ADRDA Work Group under the auspices of Department of Health and Human Services Task Force on Alzheimer's Disease.** *Neurology* 1984;34:939–44
5. Ishii K, Sasaki M, Yamaji S, et al. **Relatively preserved hippocampal glucose metabolism in mild Alzheimer's disease.** *Dement Geriatr Cogn Disord* 1998;9:317–22
6. Maldjian JA, Whitlow CT. **Whither the hippocampus? FDG-PET hippocampal hypometabolism in Alzheimer disease revisited.** *AJNR Am J Neuroradiol* 2012;33:1975–82
7. Ishii K, Soma T, Kono AK, et al. **Comparison of regional brain volume and glucose metabolism between patients with mild dementia with Lewy bodies and those with mild Alzheimer's disease.** *J Nucl Med* 2007;48:704–11
8. Mosconi L, Tsui WH, De Santi S, et al. **Reduced hippocampal metabolism in MCI and AD: automated FDG-PET image analysis.** *Neurology* 2005;64:1860–67
9. Karow DS, McEvoy LK, Fennema-Notestine C, et al. **Relative capability of MR imaging and FDG PET to depict changes associated with prodromal and early Alzheimer disease.** *Radiology* 2010;256:932–42
10. Kawachi T, Ishii K, Sakamoto S, et al. **Comparison of the diagnostic performance of FDG-PET and VBM-MRI in very mild Alzheimer's disease.** *Eur J Nucl Med Mol Imaging* 2006;33:801–09
11. Matsunari I, Samuraki M, Chen WP, et al. **Comparison of <sup>18</sup>F-FDG PET and optimized voxel-based morphometry for detection of Alzheimer's disease: aging effect on diagnostic performance.** *J Nucl Med* 2007;48:1961–70
12. Yuan Y, Gu ZX, Wei WS. **Fluorodeoxyglucose-positron-emission tomography, single-photon emission tomography, and structural MR imaging for prediction of rapid conversion to Alzheimer disease in patients with mild cognitive impairment: a meta-analysis.** *AJNR Am J Neuroradiol* 2009;30:404–10
13. Shaffer JL, Petrella JR, Sheldon FC, et al. **Predicting cognitive decline in subjects at risk for Alzheimer disease by using combined cerebrospinal fluid, MR imaging, and PET biomarkers.** *Radiology* 2013;266:583–91
14. Choo IH, Ni R, Scholl M, et al. **Combination of <sup>18</sup>F-FDG PET and cerebrospinal fluid biomarkers as a better predictor of the progression to Alzheimer's disease in mild cognitive impairment patients.** *J Alzheimers Dis* 2013;33:929–39
15. Westman E, Muehlboeck JS, Simmons A. **Combining MRI and CSF measures for classification of Alzheimer's disease and prediction of mild cognitive impairment conversion.** *Neuroimage* 2012;62:229–38
16. Zhang D, Shen D. **Predicting future clinical changes of MCI patients using longitudinal and multimodal biomarkers.** *PLoS One* 2012;7:e33182
17. Hirono N, Hashimoto M, Yasuda M, et al. **The effect of APOE epsilon4 allele on cerebral glucose metabolism in AD is a function of age at onset.** *Neurology* 2002;58:743–50
18. Drzezga A, Riemenschneider M, Strassner B, et al. **Cerebral glucose metabolism in patients with AD and different APOE genotypes.** *Neurology* 2005;64:102–07
19. Ossenkoppele R, van der Flier WM, Zwan MD, et al. **Differential effect of APOE genotype on amyloid load and glucose metabolism in AD dementia.** *Neurology* 2013;80:359–65
20. Minoshima S, Koeppe RA, Frey KA, et al. **Stereotactic PET atlas of the human brain: aid for visual interpretation of functional brain images.** *J Nucl Med* 1994;35:949–54
21. Minoshima S, Frey KA, Koeppe RA, et al. **A diagnostic approach in Alzheimer's disease using three-dimensional stereotactic surface projections of fluorine-18-FDG PET.** *J Nucl Med* 1995;36:1238–48
22. Herholz K, Salmon E, Perani D, et al. **Discrimination between Alzheimer dementia and controls by automated analysis of multicenter FDG PET.** *Neuroimage* 2002;17:302–16
23. Ishii K, Kono AK, Sasaki H, et al. **Fully automatic diagnostic system for early- and late-onset mild Alzheimer's disease using FDG PET and 3D-SSP.** *Eur J Nucl Med Mol Imaging* 2006;33:575–83
24. Kono AK, Ishii K, Sofue K, et al. **Fully automatic differential diagnosis system for dementia with Lewy bodies and Alzheimer's disease using FDG-PET and 3D-SSP.** *Eur J Nucl Med Mol Imaging* 2007;34:1490–97
25. Uemura T, Ishii K, Miyamoto N, et al. **Computer-assisted system for diagnosis of Alzheimer disease using data base-independent estimation and fluorodeoxyglucose-positron-emission tomography and 3D-stereotactic surface projection.** *AJNR Am J Neuroradiol* 2011;32:556–59
26. Mevel K, Desgranges B, Baron JC, et al. **Detecting hippocampal hypometabolism in mild cognitive impairment using automatic voxel-based approaches.** *Neuroimage* 2007;37:18–25
27. Klunk WE, Engler H, Nordberg A, et al. **Imaging brain amyloid in Alzheimer's disease with Pittsburgh Compound-B.** *Ann Neurol* 2004;55:306–19
28. Kudo Y, Okamura N, Furumoto S, et al. **2-(2-[2-Dimethylaminothiazol-5-yl]ethenyl)-6-(2-[fluoro]ethoxy)benzoxazole: a novel PET agent for in vivo detection of dense amyloid plaques in Alzheimer's disease patients.** *J Nucl Med* 2007;48:553–61
29. Lucignani G. **Clinical applications of PET amyloid imaging: an update.** *Eur J Nucl Med Mol Imaging* 2009;36:1185–90
30. Choi SR, Golding G, Zhuang Z, et al. **Preclinical properties of <sup>18</sup>F-AV-45: a PET agent for Abeta plaques in the brain.** *J Nucl Med* 2009;50:1887–94
31. Cselényi Z, Jonhagen ME, Forsberg A, et al. **Clinical validation of <sup>18</sup>F-AZD4694, an amyloid-beta-specific PET radioligand.** *J Nucl Med* 2012;53:415–24
32. Jack CR Jr, Knopman DS, Jagust WJ, et al. **Hypothetical model of dynamic biomarkers of the Alzheimer's pathological cascade.** *Lancet Neurol* 2010;9:119–28
33. Rabinovici GD, Furst AJ, Alkalay A, et al. **Increased metabolic vulnerability in early-onset Alzheimer's disease is not related to amyloid burden.** *Brain* 2010;133:512–28
34. Jack CR Jr, Wiste HJ, Vemuri P, et al. **Brain beta-amyloid measures and magnetic resonance imaging atrophy both predict time-to-progression from mild cognitive impairment to Alzheimer's disease.** *Brain* 2010;133:3336–48
35. Johnson KA, Minoshima S, Bohnen NI, et al. **Appropriate use criteria for amyloid PET: a report of the Amyloid Imaging Task Force, the Society of Nuclear Medicine and Molecular Imaging, and the Alzheimer's Association.** *J Nucl Med* 2013;54:476–90
36. Johnson KA, Minoshima S, Bohnen NI, et al. **Appropriate use criteria for amyloid PET: a report of the Amyloid Imaging Task Force, the Society of Nuclear Medicine and Molecular Imaging, and the Alzheimer's Association.** *Alzheimers Dement* 2013;9:e-1–16
37. McKeith IG, Dickson DW, Lowe J, et al. **Diagnosis and management of dementia with Lewy bodies: third report of the DLB Consortium.** *Neurology* 2005;65:1863–72
38. Albin RL, Minoshima S, D'Amato CJ, et al. **Fluoro-deoxyglucose positron emission tomography in diffuse Lewy body disease.** *Neurology* 1996;47:462–66
39. Ishii K, Imamura T, Sasaki M, et al. **Regional cerebral glucose metabolism in dementia with Lewy bodies and Alzheimer's disease.** *Neurology* 1998;51:125–30
40. Bohnen NI, Koeppe RA, Minoshima S, et al. **Cerebral glucose metabolic features of Parkinson disease and incident dementia: longitudinal study.** *J Nucl Med* 2011;52:848–55
41. McKeith I, O'Brien J, Walker Z, et al. **Sensitivity and specificity of dopamine transporter imaging with <sup>123</sup>I-FP-CIT SPECT in dementia with Lewy bodies: a phase III, multicentre study.** *Lancet Neurol* 2007;6:305–13
42. Treglia G, Cason E. **Diagnostic performance of myocardial innervation imaging using MIBG scintigraphy in differential diagnosis between dementia with Lewy bodies and other dementias: a systematic review and a meta-analysis.** *J Neuroimaging* 2012;22:111–17
43. Shimada H, Shinotoh H, Hirano S, et al. **Beta-amyloid in Lewy body**

- disease is related to Alzheimer's disease-like atrophy. *Mov Disord* 2013;28:169–75
44. Gomperts SN, Rentz DM, Moran E, et al. **Imaging amyloid deposition in Lewy body diseases.** *Neurology* 2008;71:903–10
  45. Gomperts SN, Locascio JJ, Marquie M, et al. **Brain amyloid and cognition in Lewy body diseases.** *Mov Disord* 2012;27:965–73
  46. Fujishiro H, Iseki E, Higashi S, et al. **Distribution of cerebral amyloid deposition and its relevance to clinical phenotype in Lewy body dementia.** *Neurosci Lett* 2010;486:19–23
  47. **Clinical and neuropathological criteria for frontotemporal dementia; the Lund and Manchester Groups.** *J Neurol Neurosurg Psychiatry* 1994;57:416–18
  48. Ishii K, Sakamoto S, Sasaki M, et al. **Cerebral glucose metabolism in patients with frontotemporal dementia.** *J Nucl Med* 1998;39:1875–78
  49. Kanda T, Ishii K, Uemura T, et al. **Comparison of grey matter and metabolic reductions in frontotemporal dementia using FDG-PET and voxel-based morphometric MR studies.** *Eur J Nucl Med Mol Imaging* 2008;35:2227–34
  50. Engler H, Santillo AF, Wang SX, et al. **In vivo amyloid imaging with PET in frontotemporal dementia.** *Eur J Nucl Med Mol Imaging* 2008;35:100–06
  51. Rabinovici GD, Furst AJ, O'Neil JP, et al. **<sup>11</sup>C-PIB PET imaging in Alzheimer disease and frontotemporal lobar degeneration.** *Neurology* 2007;68:1205–12
  52. Juh R, Pae CU, Kim TS, et al. **Cerebral glucose metabolism in corticobasal degeneration comparison with progressive supranuclear palsy using statistical mapping analysis.** *Neurosci Lett* 2005;383:22–27
  53. Juh R, Kim J, Moon D, et al. **Different metabolic patterns analysis of Parkinsonism on the 18F-FDG PET.** *Eur J Radiol* 2004;51:223–33
  54. Klein RC, de Jong BM, de Vries JJ, et al. **Direct comparison between regional cerebral metabolism in progressive supranuclear palsy and Parkinson's disease.** *Mov Disord* 2005;20:1021–30
  55. Hosaka K, Ishii K, Sakamoto S, et al. **Voxel-based comparison of regional cerebral glucose metabolism between PSP and corticobasal degeneration.** *J Neurol Sci* 2002;199:67–71
  56. Hirono N, Ishii K, Sasaki M, et al. **Features of regional cerebral glucose metabolism abnormality in corticobasal degeneration.** *Dement Geriatr Cogn Disord* 2000;11:139–46
  57. Hashimoto M, Ishikawa M, Mori E, et al. **Diagnosis of idiopathic normal pressure hydrocephalus is supported by MRI-based scheme: a prospective cohort study.** *Cerebrospinal Fluid Res* 2010;7:18
  58. Jagust WJ, Friedland RP, Budinger TF. **Positron emission tomography with [<sup>18</sup>F]fluorodeoxyglucose differentiates normal pressure hydrocephalus from Alzheimer-type dementia.** *J Neurol Neurosurg Psychiatry* 1985;48:1091–96
  59. Calcagni ML, Lavalle M, Mangiola A, et al. **Early evaluation of cerebral metabolic rate of glucose (CMRglu) with <sup>18</sup>F-FDG PET/CT and clinical assessment in idiopathic normal pressure hydrocephalus (INPH) patients before and after ventricular shunt placement: preliminary experience.** *Eur J Nucl Med Mol Imaging* 2012;39:236–41
  60. Rinne JO, Wong DF, Wolk DA, et al. [<sup>18</sup>F]Flutemetamol PET imaging and cortical biopsy histopathology for fibrillar amyloid beta detection in living subjects with normal pressure hydrocephalus: pooled analysis of four studies. *Acta Neuropathol* 2012;124:833–45
  61. Shin J, Kepe V, Barrio JR, et al. **The merits of FDDNP-PET imaging in Alzheimer's disease.** *J Alzheimers Dis* 2011;26(suppl 3):135–45
  62. Fodero-Tavoletti MT, Okamura N, Furumoto S, et al. **<sup>18</sup>F-THK523: a novel in vivo tau imaging ligand for Alzheimer's disease.** *Brain* 2011;134:1089–100
  63. Silverman DH, Gambhir SS, Huang HW, et al. **Evaluating early dementia with and without assessment of regional cerebral metabolism by PET: a comparison of predicted costs and benefits.** *J Nucl Med* 2002;43:253–66
  64. Moulin-Romsee G, Maes A, Silverman D, et al. **Cost-effectiveness of <sup>18</sup>F-fluorodeoxyglucose positron emission tomography in the assessment of early dementia from a Belgian and European perspective.** *Eur J Neurol* 2005;12:254–63
  65. Mathis CA, Wang Y, Holt DP, et al. **Synthesis and evaluation of <sup>11</sup>C-labeled 6-substituted 2-arylbenzothiazoles as amyloid imaging agents.** *J Med Chem* 2003;46:2740–54
  66. Nyberg S, Jonhagen ME, Cselenyi Z, et al. **Detection of amyloid in Alzheimer's disease with positron emission tomography using [<sup>11</sup>C]AZD2184.** *Eur J Nucl Med Mol Imaging* 2009;36:1859–63
  67. Agdeppa ED, Kepe V, Liu J, et al. **Binding characteristics of radio-fluorinated 6-dialkylamino-2-naphthylethylidene derivatives as positron emission tomography imaging probes for beta-amyloid plaques in Alzheimer's disease.** *J Neurosci* 2001;21:RC189
  68. Nelissen N, Van Laere K, Thurfjell L, et al. **Phase 1 study of the Pittsburgh compound B derivative <sup>18</sup>F-flutemetamol in healthy volunteers and patients with probable Alzheimer disease.** *J Nucl Med* 2009;50:1251–59
  69. Rowe CC, Ackerman U, Browne W, et al. **Imaging of amyloid beta in Alzheimer's disease with <sup>18</sup>F-BAY94–9172, a novel PET tracer: proof of mechanism.** *Lancet Neurol* 2008;7:129–35

# Neuroimaging of Diving-Related Decompression Illness: Current Knowledge and Perspectives

J. Kamtchum Tatuene, R. Pignel, P. Pollak, K.O. Lovblad, A. Kleinschmidt, and M.I. Vargas



## ABSTRACT

**SUMMARY:** Diving-related decompression illness is classified into 2 main categories: arterial gas embolism and decompression sickness. The latter is further divided into types 1 and 2, depending on the clinical presentation. MR imaging is currently the most accurate neuroimaging technique available for the detection of brain and spinal cord lesions in neurologic type 2 decompression sickness. Rapid bubble formation in tissues and the bloodstream during ascent is the basic pathophysiologic mechanism in decompression illness. These bubbles can damage the central nervous system through different mechanisms, namely arterial occlusion, venous obstruction, or in situ toxicity. Neuroimaging studies of decompression sickness have reported findings associated with each of these mechanisms: some typical results are summarized and illustrated in this article. We also review the limitations of previous work and make practical methodologic suggestions for future neuroimaging studies.

The term “decompression illness” encompasses all clinical manifestations induced by a rapid decrease of environmental pressure, sufficient to cause the formation of inert gas bubbles previously loaded within tissues or blood as a soluble phase. This can occur in various circumstances, including ascent from diving, flying or climbing mountains immediately after a dive, and exercising in hyperbaric/hypobaric chambers.<sup>1-3</sup> Diving-related decompression illness is classified into 2 main categories: arterial gas embolism due to pulmonary decompression barotrauma and decompression sickness.<sup>4</sup> There are 2 clinically defined types of decompression sickness. Type 1 refers to relatively mild symptoms such as joint pain, skin marbling, small patchy hemorrhages, and lymphatic obstruction. Conversely, type 2 includes more serious and often life-threatening symptoms and can be further divided into 4 subtypes or syndromes according to the organ affected—namely the brain, spinal cord, inner ear, or lung.<sup>5,6</sup> Spinal cord lesions represent the majority of central nervous system insults associated with type 2 decompression sickness.<sup>7-9</sup>

Among the imaging modalities available to study neurologic

type 2 decompression sickness, MR imaging clearly appears to be the most accurate for detecting pathologic changes in the brain and spinal cord.<sup>7,10</sup> To date, several MR imaging studies of neurologic type 2 decompression sickness have been reported with different and often controversial results regarding the sensitivity and utility of this technique in patient evaluation and management.<sup>8,11-16</sup> These discrepancies could be explained by lack of standardized imaging protocols, variable delays between symptom onset and image acquisition, and the high variability of the study design and technical devices. Our aim here is to provide a comprehensive review of neuroimaging studies of neurologic type 2 decompression sickness, discuss their limitations, and make proposals that could help improve the quality of future clinicoradiologic studies in the field.

## Imaging Findings and Related Pathophysiologic Theories

The fundamental reason why decompression illness occurs is that during ascent from depth, gas bubbles form more rapidly in tissues and the bloodstream than the body can eliminate through diffusion and perfusion processes.<sup>8</sup> At this point, some basic physics principles will help in understanding the mechanism of bubble formation. With increasing depth, the pressure of the air found in pulmonary alveoli increases because of compression at relatively constant temperature as stated by Boyle’s law. Therefore, the partial pressure of nitrogen in pulmonary alveoli also increases according to Dalton’s law. This change leads to an increase in nitrogen diffusion into the blood through the alveoli membrane according to Henry’s principle of soluble gas pressure equilibration on either side of a permeable membrane. With time,

From the Neurology Division (J.K.T., P.P., A.K.), Department of Clinical Neurosciences; Hyperbaric Medicine Centre (R.P.), Department of Emergency Medicine; and Neuroradiology Division (K.O.L., M.I.V.), Department of Imaging and Medical Information Sciences, Geneva University Hospitals, Geneva, Switzerland.

Please address correspondence to Maria Isabel Vargas, MD, Geneva University Hospitals, Division of Neuroradiology, DISIM, Rue Gabrielle-Perret-Gentil 4, 1211 Genève 14, Switzerland; e-mail: Maria.I.Vargas@hcuge.ch

Indicates open access to non-subscribers at [www.ajnr.org](http://www.ajnr.org)

Indicates article with supplement on-line table.

<http://dx.doi.org/10.3174/ajnr.A4005>

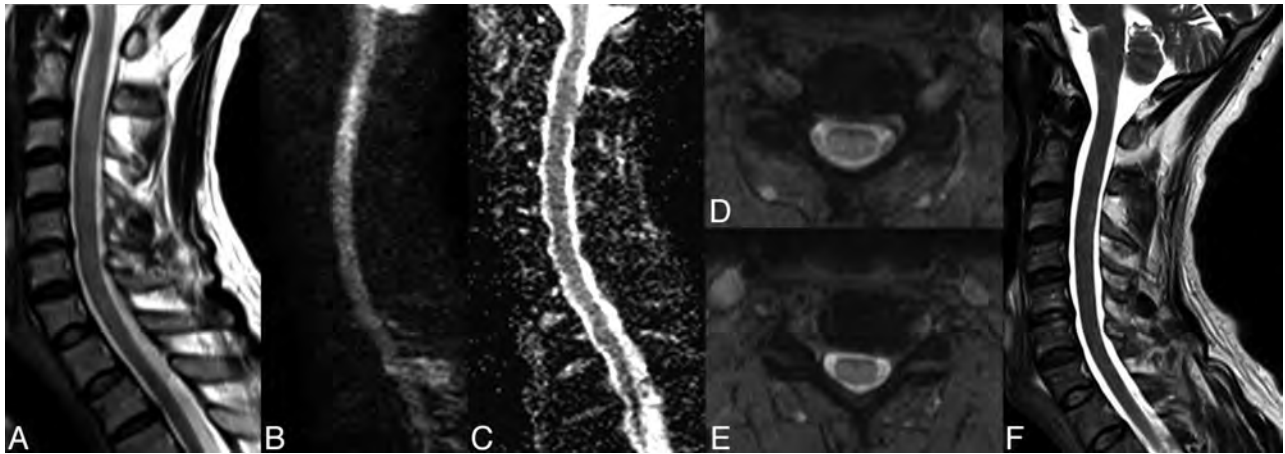


**FIG 1.** Reversible cervical spinal cord lesion due to decompression sickness. MR imaging shows an extensive lesion causing enlargement of the cervical spinal cord. The lesion appears as a high signal on sagittal (A) and axial T2WI (D and E) and on DWI (B) without concomitant signal decrease on the ADC map (C). All these characteristics, with complete healing without a scar as shown on sagittal T2WI (F) obtained 2 weeks later, are consistent with vasogenic edema (referred to as an “ischemic-like” lesion in the On-line Table).

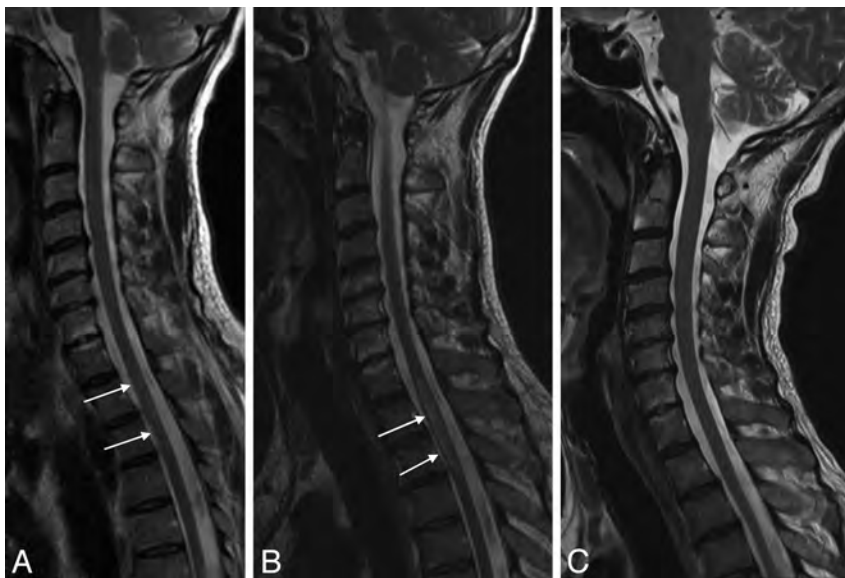


**FIG 2.** Reversible thoracic spinal cord lesion due to decompression sickness. MR imaging performed 24 hours after the diving accident shows a thoracic lesion appearing as a high signal on sagittal T2WI (A, white arrows). The lesion increases in size on the following day (B, white arrows) and subsequently disappears on day 13 (C). This evolution may also be consistent with edema.

increasing amounts of nitrogen dissolve and accumulate in lipid components of tissues. As a diver ascends, there is a sequential well-orchestrated release of the nitrogen dissolved in tissues and blood. The nitrogen in the alveoli expands first and is eliminated; then, the nitrogen in blood is eliminated and its partial pressure in blood decreases, thus allowing saturated tissues to release nitrogen back into the bloodstream for subsequent pulmonary elimination. During fast ascents, the process of progressive nitrogen release does not take place properly and there is premature expansion of the nitrogen trapped in tissues and blood, leading to excessive bubble formation and subsequent tissue damage.<sup>1,17</sup>

The critical role of nitrogen bubbles in tissue damage is highly supported by some typical radiologic findings. First, the high-fat content of the myelin sheath with high solubility of nitrogen in fat explains the preponderance of white matter lesions either in the brain or the spine of patients with neurologic decompression illness

(Figs 1, 2, and 3A). Second, in spinal cord decompression sickness, there is predominant involvement of the thoracic cord segments (Figs 2 and 3B), which may be explained by the following: 1) their high fat content, allowing high concentrations of nitrogen during diving, especially in the lateral and posterior columns<sup>5,7,14,15</sup>; and 2) their relatively low mobility and blood flow, responsible for poor nitrogen bubble wash-out during ascent and hence a higher risk of ischemia.<sup>18–20</sup>

The exact mechanism through which nitrogen bubbles cause brain and spine damage is still highly debated, and there are currently 3 theories supporting 3 different pathophysiologic mechanisms: arterial occlusion, venous infarction, and in situ nitrogen toxicity. The following support the arterial occlusion theory: 1) the predominance of cerebral lesions in arterial gas embolisms with usually a clinical and radiologic stroke-like presentation

(restricted diffusion appearing as hyperintensity on DWI with low values on the ADC map, high signal on T2WI, and usually no contrast enhancement) (Fig 3A).<sup>7,21,22</sup> 2) The finding that nitrogen bubbles can interrupt arterial blood supply to the brain and spine either by direct obstruction of small capillaries or by activation of pathologic clotting at the blood-bubble interface.<sup>23–26</sup> This effect on clotting is increased in case of low hematocrit, explaining the higher risk of severe cardiopulmonary and neurologic decompression sickness in dehydrated divers.<sup>27–30</sup> 3) The higher prevalence of a patent foramen ovale in patients experiencing decompression illness<sup>31–39</sup> could favor paradoxical embolization of either nitrogen bubbles or pathologically formed thrombi with subsequent ischemic infarcts in the brain<sup>40</sup> or spine, where the collateral circulation network is less robust.<sup>41</sup> 4) The presence of extensive gray matter lesions in some neurologic decompression sickness cases—gray matter lesions being typically seen in arterial

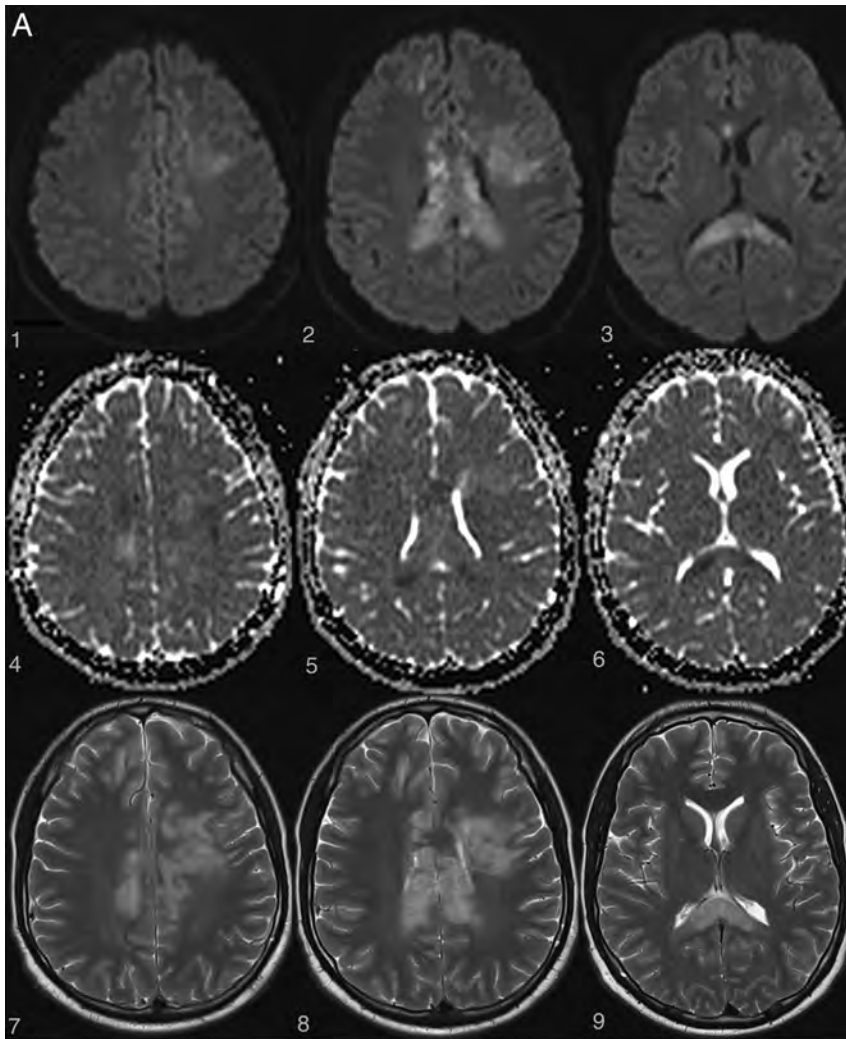


**FIG 3.** Examples of irreversible brain and spinal cord lesions due to decompression sickness (A, B, and C are taken from the same patient). A, On DWI (1, 2, 3, 4, 5, 6), the areas of restricted diffusion correspond to lesions of the corpus callosum and frontal white matter on both sides. They appear as high signal on T2WI (7, 8, 9). B, Sagittal (1 and 2, *white arrows*) and axial (3 and 4, *white arrows*) T2WI shows a cervicothoracic (C7–T1) lesion appearing as high signal without contrast enhancement on T1WI (2). C, On follow-up 1 month later, the lesions described in A and B are still present on these brain (1, 2, 3, 4) and spine (5, 6) images. Note the enhancement of the corpus callosum (3 and 4). Lesions of the right frontal deep white matter and corpus callosum have healed and now appear as “little cavities.” Similar features are usually seen in ischemic or necrotic lesions of the central nervous system.

infarction processes.<sup>11,18,42</sup> 5) Hypoperfused areas compatible with embolic cerebral arterial occlusion are observed in some patients with decompression illness when using SPECT with hexamethylpropyleneamine oxime (HMPAO) marked with a metastable nuclear isomer of the radioisotope technetium Tc99m (the product is sometimes referred to as exametazime).<sup>43,44</sup>

On the other hand, various radiologic and histopathologic findings have been published to support the venous infarction theory. First, the more frequent occurrence of lateral and posterior column white matter lesions compared with gray matter lesions in spinal cord decompression sickness is more likely a consequence of an obstruction of the slow-flowing epidural venous bed by nitrogen bubbles, which leads to vasogenic edema (Figs 1 and 2).<sup>5,8</sup> In some cases, there may be additional venous infarction (Fig 3B, -C). Similar lesions have been provoked experimentally in dogs.<sup>9</sup> Second, several histopathologic studies have dem-

onstrated venous obstruction and white matter congestion.<sup>45,46</sup> Third, vasogenic edema, appearing as high signal on both DWI and ADC maps, was observed by Vollmann et al in 2011<sup>47</sup> in a case of spinal cord decompression sickness, also suggesting a venous rather than arterial pathologic process.

The third theory of in situ nitrogen toxicity is more speculative and posits that nitrogen bubbles found in intercellular spaces may have a direct toxic effect on neurons, causing alterations of the electrical properties of membranes and impairment of ion flow regulation with subsequent cytotoxic edema and cell death. Areas of necrosis may be viewed as high-signal lesions on T2WI and as low signal on T1WI. Additionally, bubbles within the myelin sheath might cause alterations of nerve conduction. This theory of in situ nitrogen toxicity, also called the “autochthonous theory,”<sup>14</sup> may, at least partially, explain symptoms recorded in patients with type 1 decompression sickness, nitrogen narcosis, and type 2 decompression sickness without objective abnormalities on brain or spine MR imaging.<sup>48,49</sup>

Authors of MR imaging studies of decompression illness frequently report that the different clinicoradiologic patterns mentioned above overlap in the same patient, thereby suggesting that no single unifying pathophysiologic mechanism could completely explain this complex condition.<sup>14,16,47</sup> Some have argued that there is a greater participation of arterial occlusion in brain lesions because they are more frequently described in cases of arterial gas embolism, while venous occlusion may play a greater role in spine lesions and may even be favored by local me-

chanical cord compression.<sup>11,15</sup> Whatever the preponderant mechanism involved, the treatment is urgent hyperbaric therapy to allow nitrogen to dissolve and be expelled via the lungs.

Some general rules have been derived from available MR imaging studies. First, any time a lesion is found on radiologic images, there is good correspondence with the clinical symptoms or syndromes described.<sup>8,11</sup> Second, normal MR imaging findings of the spinal cord do not rule out a diagnosis of decompression illness.<sup>15,50,51</sup> Third, in regard to evolution and prognosis, clinicoradiologic discrepancies have been observed (either worsening of lesions on MR imaging despite clinical improvement as shown in Fig 2 or improvement in MR imaging lesions despite neurologic deterioration<sup>19</sup>). Furthermore, patients with hemorrhagic cord injury have the worst neurologic outcome; patients with mere spinal cord edema do better; and patients with normal-appearing spinal cords

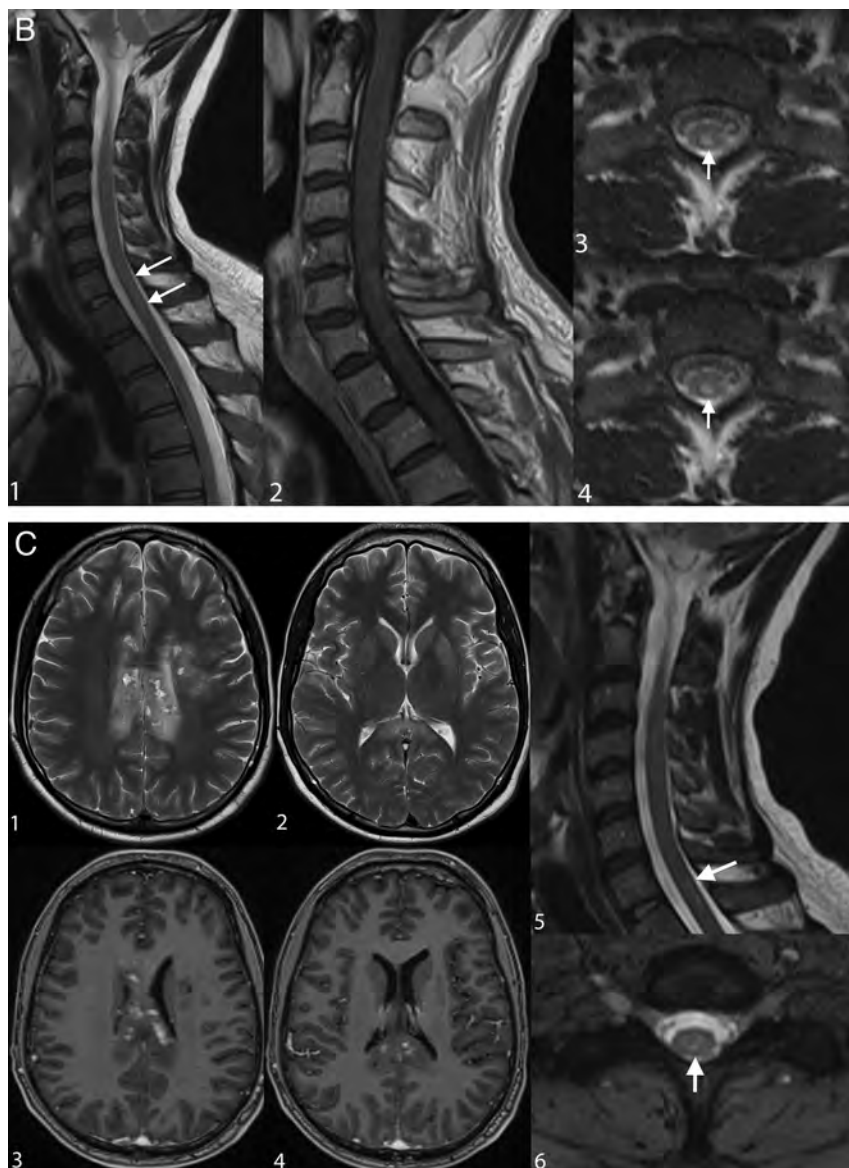


**FIG 3.** Continued.

consistently have a good outcome, though the lack of signal abnormalities on MR imaging does not necessarily mean that the patient will not develop sequelae because the negative predictive value of an investigation with normal findings is 77%.<sup>15,16,52</sup>

Anecdotal findings have been reported in patients with decompression illness. These include intracranial hemorrhages<sup>53</sup> and extensive gas inclusions in CSF spaces.<sup>54</sup> The On-line Table gives an overview of the major characteristics of lesions most frequently found on MR imaging in type 2 decompression sickness.

### **Critical Appraisal of Available Imaging Studies and Suggested Future Directions**

To date, all neuroimaging studies have reported the low sensitivity of MR imaging for detecting central nervous system lesions in patients with decompression sickness.<sup>8,11,49</sup> This could be explained, in part, by the delay between the diving accident and the imaging study because urgent hyperbaric recompression therapy is the priority. The latter could reverse signal alterations in the

brain or spine, which then would not be depicted by posttreatment imaging.

However, several other limitations of available studies could have had a negative impact on the ability to detect central nervous system lesions. First, none of those studies have used high-field magnets (3T). Most of the authors used a 1.5T system,<sup>11,47,49,55</sup> and some even used a 0.5T system, which has a very low sensitivity.<sup>8,56</sup> Second, with the exception of Vollmann et al,<sup>47</sup> no previously published MR imaging studies of decompression sickness used DWI and ADC maps. The use of these sequences could conceivably increase MR imaging sensitivity and even provide additional data on the pathophysiology of brain damage in divers. The same is true for DTI, which has been used only once in animal models of decompression sickness.<sup>57</sup> The third limitation is that only one<sup>56</sup> of the previous MR imaging studies included systematic imaging of both brain and spine. This is probably because they were all retrospective studies in which the part of the central nervous system explored was chosen in accordance with the clinical syndrome. Because subclinical brain lesions have been reported in decompression sickness,<sup>58</sup> we think that the predominance of symptoms and signs related to spinal cord lesions could have obscured the possibility of brain damage, thus leading to underestimation of the overall prevalence of central nervous system lesions, with a negative impact on MR imaging sensitivity.

Taking into consideration all the aforementioned methodologic limita-

tions, we would recommend using higher field strengths (1.5 or 3T) and, systematically, joint brain and spine imaging in future MR imaging studies of decompression illness. We tentatively suggest the following imaging protocol for the brain: T1WI, T2WI, FLAIR, gradient-echo, DWI and ADC mapping, and contrast-enhanced T1WI. For spinal cord exploration, we would recommend the following sequences: sagittal fast spin-echo T2 and spin-echo T1 in the acute phase without and with contrast medium, which may be very useful in the subacute phase. We also encourage clinicians and radiologists to use more sophisticated techniques such as DTI, which could provide deeper insight into pathophysiologic processes.

Some authors have tried to identify prognostic factors in decompression sickness.<sup>59,60</sup> They have even proposed a prospectively validated clinical prognostic score.<sup>61-64</sup> Added to that, the prognostic value of MR imaging findings has been independently evaluated, though in spinal cord decompression sickness only.<sup>15,16</sup> However, there is currently no available study that tried

to integrate neuroimaging findings into a prognostic score. Moreover, the importance of serial brain and spine imaging in the follow-up of patients with decompression sickness has not been studied. Such serial imaging could be used in comparative evaluations of the various treatment protocols currently available because there is no consensus on which is the best.<sup>65</sup>

## CONCLUSIONS

Several neuroimaging studies of decompression illness have been conducted during the past decades. They have helped identify the spectrum of central nervous system lesions in neurologic decompression sickness and have provided useful data for understanding the related possible pathophysiologic mechanisms. However, due to technical and methodologic limitations of the available studies, many questions remain unanswered, especially those pertaining to the role of MR imaging in evaluating treatment protocols and estimating prognosis. Therefore, it seems obvious that well-designed prospective studies integrating new imaging techniques and better designed protocols should be conducted to explore these aspects and eventually provide data that help improve the management of patients with decompression illness.

Disclosures: Andreas Kleinschmidt—UNRELATED: Other: Senior Editor for the journal *Neuroimage* (Elsevier).

## REFERENCES

- Elliott DH, Moon RE. *Manifestations of the Decompression Disorders: The Physiology and Medicine of Diving*. 4th ed. London: Saunders; 1993:481
- Faralli F. **Decompression illness**. In: Oriani G, Marroni A, Wattel F, eds. *Handbook on Hyperbaric Medicine*. Berlin: Springer-Verlag; 1996:135–82
- Pulley SA. Decompression sickness. Medscape. 2012 (updated June 14, 2012). <http://emedicine.medscape.com/article/769717-overview>. Accessed December 2, 2013
- Melamed Y, Shupak A, Bitterman H. **Medical problems associated with underwater diving**. *N Engl J Med* 1992;326:30–35
- Manabe Y, Sakai K, Kashihara K, et al. **Presumed venous infarction in spinal decompression sickness**. *AJNR Am J Neuroradiol* 1998;19:1578–80
- Newton HB. **Neurologic complications of scuba diving**. *Am Fam Physician* 2001;63:2211–18
- Warren LP Jr, Djang WT, Moon RE, et al. **Neuroimaging of scuba diving injuries to the CNS**. *AJR Am J Roentgenol* 1988;151:1003–08
- Sparacia G, Banco A, Sparacia B, et al. **Magnetic resonance findings in scuba diving-related spinal cord decompression sickness**. *MAGMA* 1997;5:111–15
- Hallenbeck JM, Bove AA, Elliott DH. **Mechanisms underlying spinal cord damage in decompression sickness**. *Neurology* 1975;25:308–16
- Hodgson M, Beran RG, Shirtley G. **The role of computed tomography in the assessment of neurologic sequelae of decompression sickness**. *Arch Neurol* 1988;45:1033–35
- Reuter M, Tetzlaff K, Hutzelmann A, et al. **MR imaging of the central nervous system in diving-related decompression illness**. *Acta Radiol* 1997;38:940–44
- Yanagawa Y, Okada Y, Terai C, et al. **MR imaging of the central nervous system in divers**. *Aviat Space Environ Med* 1998;69:892–95
- Hutzelmann A, Tetzlaff K, Reuter M, et al. **Does diving damage the brain? MR control study of divers' central nervous system**. *Acta Radiol* 2000;41:18–21
- Kei PL, Choong CT, Young T, et al. **Decompression sickness: MRI of the spinal cord**. *J Neuroimaging* 2007;17:378–80
- Gempp E, Blatteau JE, Stephant E, et al. **MRI findings and clinical outcome in 45 divers with spinal cord decompression sickness**. *Aviat Space Environ Med* 2008;79:1112–16
- Hennedige T, Chow W, Ng YY, et al. **MRI in spinal cord decompression sickness**. *J Med Imaging Radiat Oncol* 2012;56:282–88
- McMullin AM. **Scuba diving: What you and your patients need to know**. *Cleve Clin J Med* 2006;73:711–12, 714, 716 passim
- Aharon-Peretz J, Adir Y, Gordon CR, et al. **Spinal cord decompression sickness in sport diving**. *Arch Neurol* 1993;50:753–56
- Yoshiyama M, Asamoto S, Kobayashi N, et al. **Spinal cord decompression sickness associated with scuba diving: correlation of immediate and delayed magnetic resonance imaging findings with severity of neurologic impairment: a report on 3 cases**. *Surg Neurol* 2007;67:283–87
- Hierholzer J, Tempka A, Stroszczyński C, et al. **MRI in decompression illness**. *Neuroradiology* 2000;42:368–70
- Moon RE. Gas embolism. In: Oriani G, Marroni A, Wattel F, eds. *Handbook on Hyperbaric Medicine*. Berlin: Springer-Verlag; 1996:229
- Leitch DR, Green RD. **Pulmonary barotrauma in divers and the treatment of cerebral arterial gas embolism**. *Aviat Space Environ Med* 1986;57(10 pt 1):931–38
- Hjelde A, Bergh K, Brubakk AO, et al. **Complement activation in divers after repeated air/heliox dives and its possible relevance to DCS**. *J Appl Physiol* 1995;78:1140–44
- Huang KL, Lin YC. **Activation of complement and neutrophils increases vascular permeability during air embolism**. *Aviat Space Environ Med* 1997;68:300–05
- Dufka AJ, Francis TJ. **Pathophysiology of decompression sickness**. In: Bove AA, ed. *Diving Medicine*. 3rd ed. Philadelphia: Saunders; 1997:159–75
- Boussuges A, Succo E, Juhan-Vague I, et al. **Activation of coagulation in decompression illness**. *Aviat Space Environ Med* 1998;69:129–32
- Fahlman A, Dromsky DM. **Dehydration effects on the risk of severe decompression sickness in a swine model**. *Aviat Space Environ Med* 2006;77:102–06
- Williams ST, Prior FG, Bryson P. **Hematocrit change in tropical scuba divers**. *Wilderness Environ Med* 2007;18:48–53
- Newton HB, Burkart J, Pearl D, et al. **Neurological decompression illness and hematocrit: analysis of a consecutive series of 200 recreational scuba divers**. *Undersea Hyperb Med* 2008;35:99–106
- Gempp E, Blatteau JE, Pontier JM, et al. **Preventive effect of pre-dive hydration on bubble formation in divers**. *Br J Sports Med* 2009;43:224–28
- Germonpré P, Dendale P, Unger P, et al. **Patent foramen ovale and decompression sickness in sports divers**. *J Appl Physiol* 1998;84:1622–26
- Bove AA. **Risk of decompression sickness with patent foramen ovale**. *Undersea Hyperb Med* 1998;25:175–78
- Wilmshurst PT, Nightingale S, Walsh KP, et al. **Effect on migraine of closure of cardiac right-to-left shunts to prevent recurrence of decompression illness or stroke or for haemodynamic reasons**. *Lancet* 2000;356:1648–51
- Schwerzmann M, Seiler C. **Recreational scuba diving, patent foramen ovale and their associated risks**. *Swiss Med Wkly* 2001;131:365–74
- Schwerzmann M, Seiler C, Lipp E, et al. **Relation between directly detected patent foramen ovale and ischemic brain lesions in sport divers**. *Ann Int Med* 2001;134:21–24
- Cartoni D, De Castro S, Valente G, et al. **Identification of professional scuba divers with patent foramen ovale at risk for decompression illness**. *Am J Cardiol* 2004;94:270–73
- Torti SR, Billinger M, Schwerzmann M, et al. **Risk of decompression illness among 230 divers in relation to the presence and size of patent foramen ovale**. *Eur Heart J* 2004;25:1014–20
- Harrah JD, O'Boyle PS, Piantadosi CA. **Underutilization of echocardiography for patent foramen ovale in divers with serious decompression sickness**. *Undersea Hyperb Med* 2008;35:207–11
- Koch AE, Kirsch H, Reuter M, et al. **Prevalence of patent foramen ovale (PFO) and MRI-lesions in mild neurological decompression sickness (type B-DCS/AGE)**. *Undersea Hyperb Med* 2008;35:197–205

40. Palmer AC, Calder IM, Yates PO. **Cerebral vasculopathy in divers.** *Neuropathol Appl Neurobiol* 1992;18:113–24
41. Mastaglia FL, McCallum RI, Walder DN. **Myelopathy associated with decompression sickness: a report of six cases.** *Clin Exp Neurol* 1983;19:54–59
42. McCormac J, Mirvis SE, Cotta-Cumba C, et al. **Spinal myelopathy resulting from decompression sickness: MR findings in a case and review of the literature.** *Emerg Radiol* 2002;9:240–42
43. Macleod MA, Adkisson GH, Fox MJ, et al. **<sup>99</sup>Tcm-HMPAO single photon emission tomography in the diagnosis of cerebral barotrauma.** *Br J Radiol* 1988;61:1106–09
44. Adkisson GH, Macleod MA, Hodgson M, et al. **Cerebral perfusion deficits in dysbaric illness.** *Lancet* 1989;2:119–22
45. Royon M, Wolkiewicz J. **Bilan scanographique et phlébographique d'un accident médullaire de décompression.** *Med Sub Hyp* 1987;4:117–20
46. Kim RC, Smith HR, Henbest ML, et al. **Nonhemorrhagic venous infarction of the spinal cord.** *Ann Neurol* 1984;15:379–85
47. Vollmann R, Lamperti M, Magyar M, et al. **Magnetic resonance imaging of the spine in a patient with decompression sickness.** *Clin Neuroradiol* 2011;21:231–33
48. Levin HS, Goldstein FC, Norcross K, et al. **Neurobehavioral and magnetic resonance imaging findings in two cases of decompression sickness.** *Aviat Space Environ Med* 1989;60:1204–10
49. Grønning M, Risberg J, Skeidsvoll H, et al. **Electroencephalography and magnetic resonance imaging in neurological decompression sickness.** *Undersea Hyperb Med* 2005;32:397–402
50. Tournebise H, Boucand MH, Landi J, et al. **Paraplegia and decompression sickness.** *Paraplegia* 1995;33:636–39
51. Colineau X, Muiyard B, Paoletti H, et al. **Accidents neurologiques de décompression: mise en évidence par IRM.** *Med Armees* 1998;26:371–79
52. White ML, El-Khoury GY. **Neurovascular injuries of the spinal cord.** *Eur J Radiol* 2002;42:117–26
53. Josefsen R, Wester K. **Cerebellar hemorrhage: a rare, but serious complication in decompression disease** [in Norwegian]. *Tidsskr Nor Laegeforen* 1999;119:3901–02
54. Ozdoba C, Weis J, Plattner T, et al. **Fatal scuba diving incident with massive gas embolism in cerebral and spinal arteries.** *Neuroradiology* 2005;47:411–16
55. Gao GK, Wu D, Yang Y, et al. **Cerebral magnetic resonance imaging of compressed air divers in diving accidents.** *Undersea Hyperb Med* 2009;36:33–41
56. Todnem K, Nyland H, Skeidsvoll H, et al. **Neurological long term consequences of deep diving.** *Br J Ind Med* 1991;48:258–66
57. Hutchinson EB, Sobakin AS, Meyerand ME, et al. **Diffusion tensor MRI of spinal decompression sickness.** *Undersea Hyperb Med* 2013;40:23–31
58. Aksoy FG. **MR imaging of subclinical cerebral decompression sickness: a case report.** *Acta Radiol* 2003;44:108–10
59. Dick AP, Massey EW. **Neurologic presentation of decompression sickness and air embolism in sport divers.** *Neurology* 1985;35:667–71
60. Ball R. **Effect of severity, time to recompression with oxygen, and re-treatment on outcome in forty-nine cases of spinal cord decompression sickness.** *Undersea Hyperb Med* 1993;20:133–45
61. Boussuges A, Thirion X, Blanc P, et al. **Neurologic decompression illness: a gravity score.** *Undersea Hyperb Med* 1996;23:151–55
62. Gempp E, Blatteau JE. **Risk factors and treatment outcome in scuba divers with spinal cord decompression sickness.** *J Crit Care* 2010;25:236–42
63. Blatteau JE, Gempp E, Constantin P, et al. **Risk factors and clinical outcome in military divers with neurological decompression sickness: influence of time to recompression.** *Diving Hyperb Med* 2011;41:129–34
64. Blatteau JE, Gempp E, Simon O, et al. **Prognostic factors of spinal cord decompression sickness in recreational diving: retrospective and multicentric analysis of 279 cases.** *Neurocrit Care* 2011;15:120–27
65. Moon RE, Gorman DF. **Treatment of decompression disorders.** In: Bennett PB, Elliott DH, eds. *The Physiology and Medicine of Diving*. 4th ed. London: WB Saunders; 1993:506–41

# Whole-Brain Adaptive 70-kVp Perfusion Imaging with Variable and Extended Sampling Improves Quality and Consistency While Reducing Dose

I. Corcuera-Solano, A.M. McLellan, A.H. Doshi, P.S. Pawha, and L.N. Tanenbaum



## ABSTRACT

**BACKGROUND AND PURPOSE:** Despite common use of CTP to assess cerebral hemodynamics in the setting of ischemia, concerns over radiation exposure remain. Our aim was to evaluate the efficacy of an adaptive 70-kVp (peak) whole-brain CTP protocol with variable sampling intervals and extended duration against an established fixed-sampling, limited-period protocol at 80 kVp.

**MATERIALS AND METHODS:** A retrospective analysis of 37 patients with stroke scanned with conventional ( $n = 17$ ) and variant-protocol ( $n = 20$ ) whole-brain CTP was performed. We compared radiation dose, parametric map quality, and consistency of full-contrast circulation capture between a modified 70-kVp protocol, with 20 whole-brain passes at variable sampling intervals over an extended sampling period, and a conventional 80-kVp CTP examination with 24 passes at fixed-sampling intervals and a more limited scanning window. Mann-Whitney  $U$  test analysis was used to compare both protocols.

**RESULTS:** The 70-kVp CTP scan provided superior image quality at a 45% lower CT dose index volume and 13% lower dose-length product/effective dose compared with the conventional 80-kVp scan. With respect to the consistency of contrast-passage capture, 95% of the adaptive, extended protocol continued through the venous return to baseline, compared with only 47% by using the conventional limited-length protocol. Rapid sampling during the critical arterial arrival and washout period was accomplished in nearly 95% with both the variable and fixed-sampling-interval protocols.

**CONCLUSIONS:** Seventy-kilovolt (peak) CTP with variable and extended sampling produces improved image quality at lower radiation doses with greater consistency of full contrast passage capture.

**ABBREVIATIONS:** CTDI<sub>vol</sub> = CT dose index volume; DLP = dose-length product

CT perfusion studies involve repeated dynamic scanning during the passage of contrast to and through the brain. The derived parametric maps of CBF, CBV, and transit times can be integral to the evaluation and management of acute stroke and

chronic neurovascular steno-occlusive disease. Despite widespread use, concerns over the potential dangers of high radiation exposure remain,<sup>1,2</sup> particularly with more recent 4D or shuttle whole-brain scanning approaches.

Radiation dose is disproportionately dependent on tube voltage, thus the use of lower kilovolt (peak) values has been the principal strategy for managing exposure in CTP.<sup>3</sup> Additional strategies include reducing the temporal resolution<sup>4-6</sup> and limiting the scan duration.<sup>7</sup> Traditionally, CTP studies have been performed at 80 kVp,<sup>3</sup> the lowest energy setting available on most clinical scanners, with a fixed, limited scanning period (40–60+ seconds) and regular sampling intervals (every 1–4 seconds).<sup>4-6</sup> We evaluated radiation dose, image quality, and contrast cycle capture consistency of a variant protocol for whole-brain CTP using 3 innovations—lower 70 kVp, variable sampling intervals, and longer sampling periods—comparing it with the existing, conventional approach used at our institution. We hypothesized that the new 70-kVp protocol would result in a reduced radiation dose while providing comparable parametric image quality and improved consistency of full contrast cycle capture

Received March 19, 2014; accepted after revision May 16.

From the Department of Neuroradiology, Mount Sinai Medical Center, One Gustave L. Levy Place, New York, New York.

I. Corcuera-Solano and A.M. McLellan contributed equally to this work.

Idoia Corcuera-Solano was supported by a grant from the Spanish foundation Fundación Alfonso Martín Escudero.

Paper previously presented as an electronic exhibit at: Annual Meeting of the European Society of Radiology, March 6–10, 2014; Vienna, Austria; and Annual Meeting of the American Roentgen Ray Society, May 4–9, 2014; San Diego, California; and as an oral presentation at Annual Meeting of the American Society of Neuroradiology and the Foundation of the ASNR Symposium, May 17–22, 2014; Montreal, Quebec, Canada.

Please address correspondence to Lawrence N. Tanenbaum, MD, Mount Sinai Medical Center, Department of Radiology, B1234, One Gustave L. Levy Place, New York, NY 10029; e-mail: nuromri@gmail.com; @nuromri

Indicates open access to non-subscribers at www.ajnr.org

<http://dx.doi.org/10.3174/ajnr.A4043>

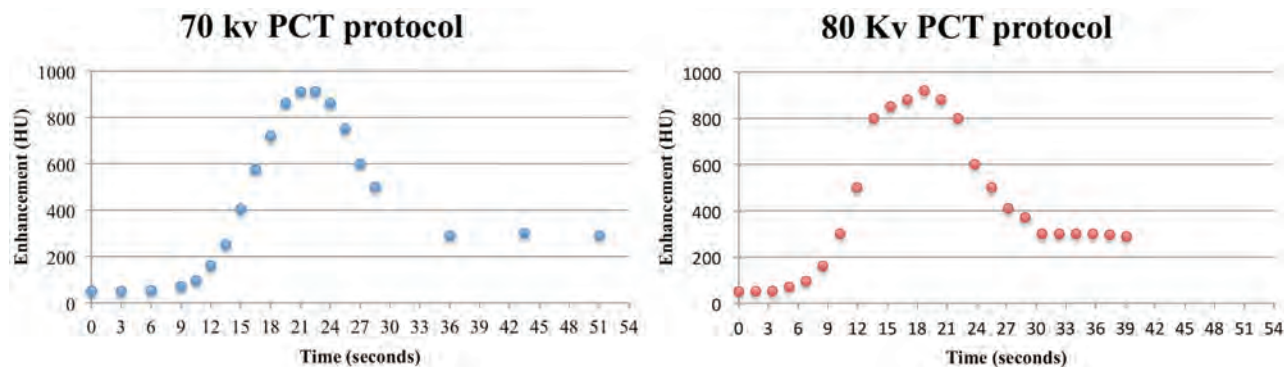


**FIG 1.** Sample middle-brain time-attenuation curves for the 2 CTP protocols.

compared with conventional approaches. To our knowledge, the use of 70-kVp CTP coupled with variable and extended sampling has not been reported.

## MATERIALS AND METHODS

### Patients

The institutional review board approved this retrospective single-center, Health Insurance Portability and Accountability Act-compliant study, with a waiver of informed consent. Our institutional radiology data base was queried to identify patients with a presumptive diagnosis of stroke who underwent clinically indicated head CTP from January 2013 through December 2013.

### Scanning Technique

In our institution, patients with suspected acute stroke who are candidates for thrombolysis undergo unenhanced CT. When appropriate, CTP examinations then follow on one of our 2 capable scanners. Patients scanned on our AS+ 128 scanner (Siemens, Erlangen, Germany) are evaluated with our 70-kVp adaptive 4D spiral CTP protocol. Patients scanned on our LightSpeed VCT (GE Healthcare, Milwaukee, Wisconsin) scanner have a conventional design, helical shuttle 80-kVp examination. Because of scanner limitations, only the 80-kVp examinations benefited from iterative reconstruction (Adaptive Statistical Iterative Reconstruction level 70). The 70-kVp studies were reconstructed with filtered back-projection. All CTPs are performed by using a contrast bolus of 40 mL of nonionic iodinated contrast media (iopamidol, Isovue 370; Bracco Diagnostics, Princeton, New Jersey) administered via a power injector at a rate of 4 mL/s, followed by a saline flush of 40 mL at a 3-mL/s injection rate. Scanning is initiated 8 seconds after the onset of contrast injection in all cases. In the conventional 80-kVp protocol, 24 whole-brain passes are made at a fixed rate of 1.7 seconds per pass (temporal resolution, 1.7–3.4 seconds in a shuttle mode) for 39 seconds. In the adaptive 70-kVp protocol, 20 passes are performed at the following varied intervals: 3 passes every 3 seconds intended for the prearrival baseline, 13 passes every 1.5 seconds targeting the rise and fall of enhancement, and 3 passes at 7.5-second intervals to complete and extend the temporal sampling window for 51 seconds (Fig 1). Detailed technical parameters of the 2 different CTP examinations are given in Table 1. We routinely extract physiologic, time-resolved CTA from all CTP datasets, avoiding the radiation and contrast needed for an additional dedicated study.

**Table 1: CTP parameters**

	70 kVp	80 kVp
Tube current	150 mAs	80 mAs
Section thickness	5 mm	5 mm
Passes	20 passes	24 passes
Range	144 mm	120 mm
Time per pass	3, 1.5, 7.5 seconds	1.7 seconds
Scan window	51 seconds	39 seconds

### Data Processing

All CTP studies were processed at 5-mm thickness with CT Perfusion 4D on an Advantage Workstation 4.6 (GE Healthcare). Arterial and venous input functions were automatically selected by the perfusion software (Perfusion 4D; GE Healthcare) and varied by case, though the algorithm typically defaults to the proximal internal carotid or basilar artery and the sigmoid sinus. Fully automated processing was used unless visual validation by a neuroradiologist suggested the need for semiautomated processing after correction of the arterial and/or venous input over the basilar or internal carotid artery and sigmoid sinus, respectively.

### Image Quality Analysis

All CTP studies were reviewed as saved DICOM datasets on the Advantage 4.6 Workstation.

For quantitative analysis of the parametric images, identical single regions of interest measuring 5 mm<sup>2</sup> were placed in the WM and GM of the medial left occipital lobe on the CBF, CBV, and time-to-maximum maps for both CTP protocols. The medial occipital lobe was chosen because it is less likely to be involved in ischemia than the larger MCA territory. If the left posterior cerebral territory was involved, the region of interest was placed on the contralateral normal side. In addition, single ROI measurements were made on source images at the level of the left thalamus at peak arterial and venous enhancement (Fig 2).

We acquired the following quantitative parameters:

- 1) Signal (*S*), defined as the mean CT attenuation values in Hounsfield units.
- 2) Image noise (*IN*), defined as the SD of CT attenuation values.
- 3) SNR = (Mean WM Region of Interest) / (SD WM Region of Interest) or (*S*) / (*IN*).

Additionally, 3 radiologists with 6, 9, and 20+ years of neuro-radiology experience independently performed a qualitative as-

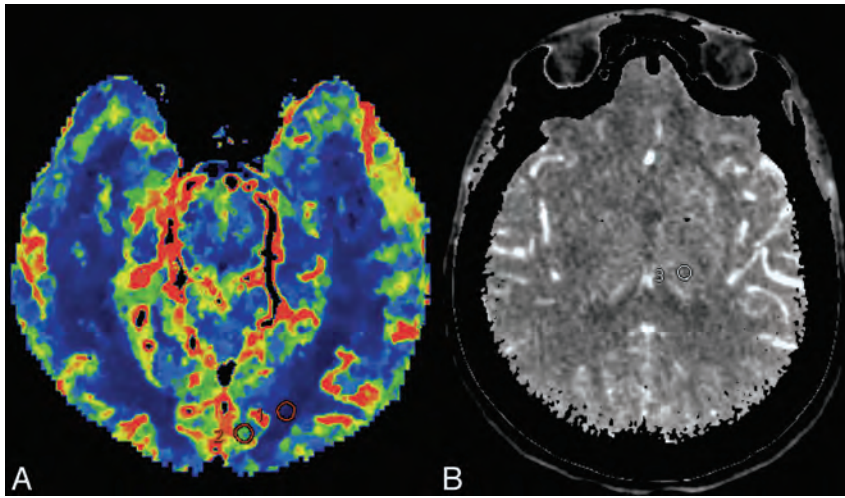


**FIG 2.** A, Parametric map showing placement of regions of interest in the WM and GM of the left medial occipital lobe. B, The region of interest is measured at the peak arterial phase over the left thalamus.

**Table 2: Quantitative analysis<sup>a</sup>**

	70 kVp	80 kVp	P Value
CBF			
WM			
Mean	5.47	8.76	.05
SD	2.26	4.47	.35
SNR	2.81	3.20	.66
GM			
Mean	40.03	40.76	.87
SD	14.84	16.94	.94
SNR	4.38	3.95	.92
CBV			
WM			
Mean	1.50	0.95	.44
SD	0.41	0.35	.21
SNR	3.15	4.97	.07
GM			
Mean	4.88	3.49	.75
SD	1.45	1.08	.21
SNR	5.34	6.53	.18
Tmax			
WM			
Mean	7.81	6.52	.10
SD	1.72	1.63	.47
SNR	6.22	7.08	.96
GM			
Mean	3.94	4.51	.13
SD	0.68	1.03	.31
SNR	6.82	6.72	.82
Arterial max			
Thalamus			
Mean	59.71	50.25	.0005
SD	11.96	11.34	.426
SNR	6.43	4.69	.3316
Venous max			
Thalamus			
Mean	56.72	48.68	.0032
SD	11.67	10.91	.3811
SNR	5.11	4.62	.4738

**Note:**—max indicates maximum; Tmax, time-to-maximum.

<sup>a</sup> Data are presented as mean, SD, and SNR.

assessment of the parametric image sets blinded to the acquisition protocol. Readers were asked to rate overall image quality and gray matter–white matter differentiation of the CBV, CBF, and a variety of transit times maps, including time-to-maximum, time-

to-peak, first moment (impulse residual function at the zero time point), and mean transit time on a 3-point scale: 3 being ideal, 2 being less than ideal, and 1 being nondiagnostic. Window and level settings were standardized for initial review, but each reader was also allowed to vary the settings. Image-quality scores were averaged across readers for analysis and are presented as mean value  $\pm$  SD.

#### Time-Attenuation Curve Analysis

A board-certified radiologist with 1 year of neuroradiology experience analyzed and compared the first-pass perfusion time-attenuation curves to assess the rate at which each protocol imaged the desired portions of the enhancement cycle as intended: capture of the precontrast arrival baseline, fast sampling from the arterial

contrast arrival through the midportion of the downslope back to baseline, and continued sampling through the venous return to baseline.

#### Radiation Dose Assessment

Mean doses of the 2 protocols were recorded and compared. The CT dose index volume (CTDI<sub>vol</sub>) in milligrays and the dose-length product (DLP) were extracted from the scan dose page. The effective dose in millisieverts was estimated by multiplying the DLP by a constant region-specific conversion coefficient of 0.0023 mSv / (mGy·cm).<sup>8</sup> The percentage reduction when comparing the mean CTDI<sub>vol</sub> used in examinations with 80 kVp with the mean CTDI<sub>vol</sub> of 70 kVp was calculated according to the following formula:  $100\% - (\text{CTDI}_{\text{vol}} 70 \text{ kVp} / \text{CTDI}_{\text{vol}} 80 \text{ kVp}) \times 100$ . The same analysis was performed with the DLP and effective dose.

#### Statistical Analysis

Statistical analyses were performed by using the commercial GraphPad Prism, Version 5.00 for Mac OS X (GraphPad Software, San Diego California). Radiation variables were compared by using the Student *t* test for unpaired samples. The Kendall coefficient of concordance was calculated to evaluate the degree of consensus among the 3 observers.<sup>9</sup> The Mann-Whitney *U* test was applied to compare image-quality results between the 70-kVp and 80-kVp CTP protocols. Numeric data were expressed as mean  $\pm$  SD. *P* < .05 was a statistically significant result.

#### RESULTS

Thirty-seven patients (15 men and 22 women), with a mean age of 66 years (range, 48–92 years) and a presumptive diagnosis of stroke, underwent brain CTP in our institution. Of those, 17 cases were performed with the conventional 80-kVp CTP protocol (4 men and 13 women; mean age, 64 years), and 20, with the adaptive 70-kVp CTP (9 men and 11 women; mean age, 66 years). The average NIHSS score was 9.35 for the patients scanned with the 70-kVp and 12.06 for those scanned with the 80-kVp protocol.

The overall incidence of stroke was 70.3% (26/37), with 88.5% (23/26) involving the anterior circulation and 11.5% (3/26), the posterior circulation. Fourteen stroke cases were diagnosed by using 70-kVp protocol: Eleven were anterior circulation strokes (5 left MCA, 1 left ICA, and 5 right MCA), and 3 were posterior strokes, involving the pons, right middle cerebellar peduncle, and bilateral cerebellum. Twelve stroke cases were diagnosed with the 80-kVp protocol: All were anterior strokes, with 7 left MCA, 1 left ICA, 2 right MCA, 1 right anterior cerebral artery/MCA borderzone, and 1 right anterior choroidal artery.

The time from symptom onset to scanning ranged from 25 minutes to 5 hours in the 70-kVp group and 50 minutes to 4 hours at 80 kVp. A stroke alert response time of <20 minutes to CT was maintained in all patients who presented on arrival to the emergency department.

**Table 3: Qualitative analysis of overall quality and gray-white matter differentiation in 80-kVp and 70-kVp whole-brain CTP<sup>a</sup>**

	70 kVp	80 kVp	P Value
Overall quality			
CBF	2.95 ± 0.167	2.81 ± 2.84	.0459
CBV	2.95 ± 0.167	2.76 ± 0.305	.0173
TT	2.89 ± 0.224	2.69 ± 0.276	.0113
GM-WM differentiation			
CBF	2.91 ± 0.187	2.83 ± 0.314	.5598
CBV	2.93 ± 0.178	2.70 ± 0.347	.0278
TT	2.86 ± 0.231	2.69 ± 0.276	.0630

Note:—TT indicates transit time.

<sup>a</sup>Data are presented as means and SD.

### Image Quality

No significant quantitative differences were found on parametric maps between protocols. Source image contrast enhancement was significantly higher at 70 kVp than with 80 kVp, though no significant differences in noise or SNR were found. Quantitative data are summarized in Table 2. The interobserver agreement in the qualitative assessment of parametric maps was good (Kendall coefficient, 0.46).<sup>9</sup> Overall image quality was significantly better by using the 70-kVp CTP protocol for all 3 parameters: CBF ( $P = .02$ ), CBV ( $P = .04$ ), and transit times ( $P = .01$ ), compared with 80 kVp. Scores of the 70-kVp and 80-kVp CTP protocols for GM-WM differentiation were comparable in CBF and transit times, while CBV using 70-kVp CTP was associated with significantly better GM-WM differentiation ( $P = .02$ ) (Table 3 and Figs 3 and 4).

### Time-Attenuation Curves

Time-attenuation curve analysis revealed that by using the adaptively sampled longer 70-kVp CTP technique (sampling extended to 51 seconds), 95% (19/20) of the studies captured the venous return to baseline, compared with only 47% (8/17) of the studies scanned by using the fixed-interval limited-length 80-kVp protocol (39 seconds). Rapid sampling during the critical arterial arrival and washout period was comparable in both protocols, captured at 95% (19/20) with the 70-kVp adaptive protocol and at 94% (16/17) with the 80-kVp fixed protocol.

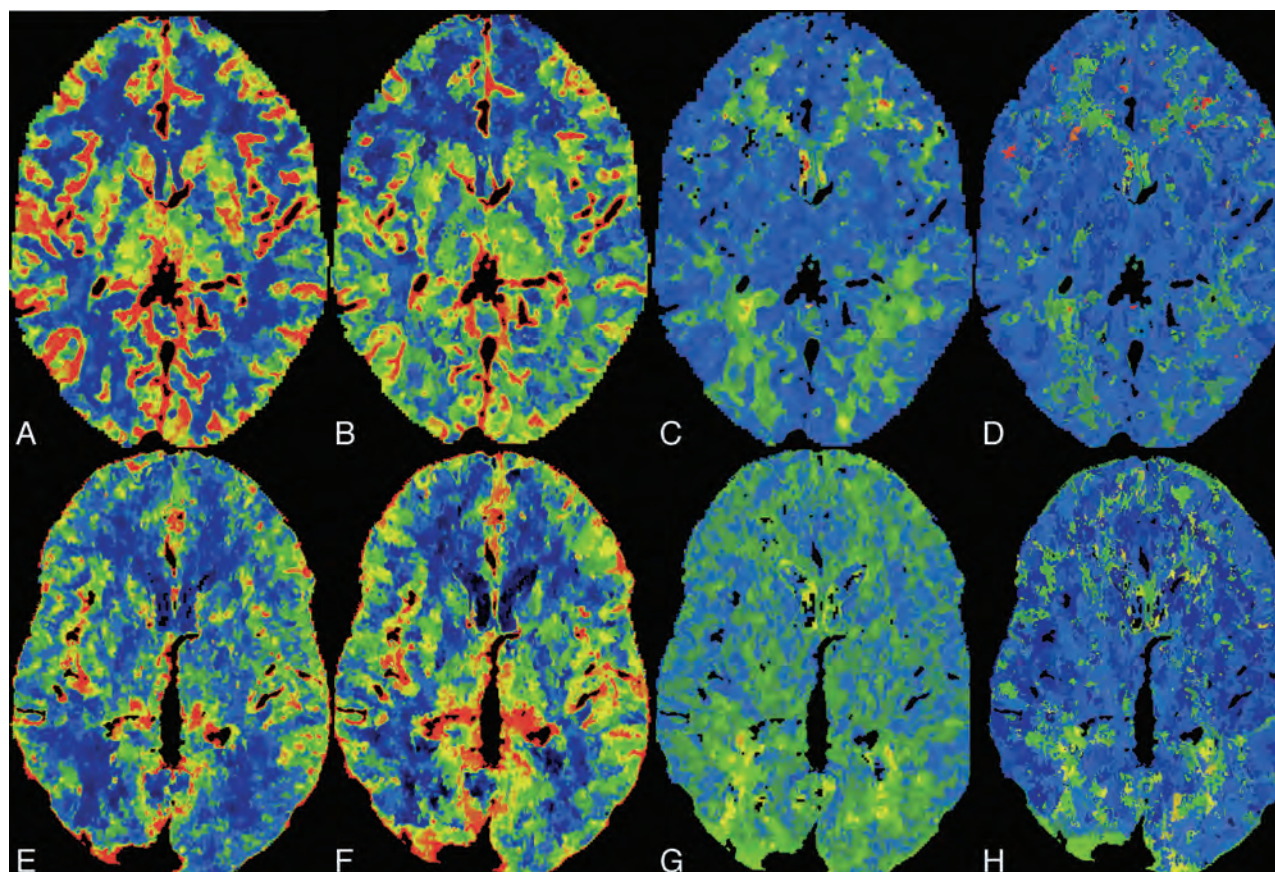


**FIG 3.** Normal-sample CTP datasets from the 70-kVp protocol: CBF (A), CBV (B), time-to-maximum (C), TTP (D). From the 80-kVp protocol: CBF (E), CBV (F), time-to-maximum (G), TTP (H).

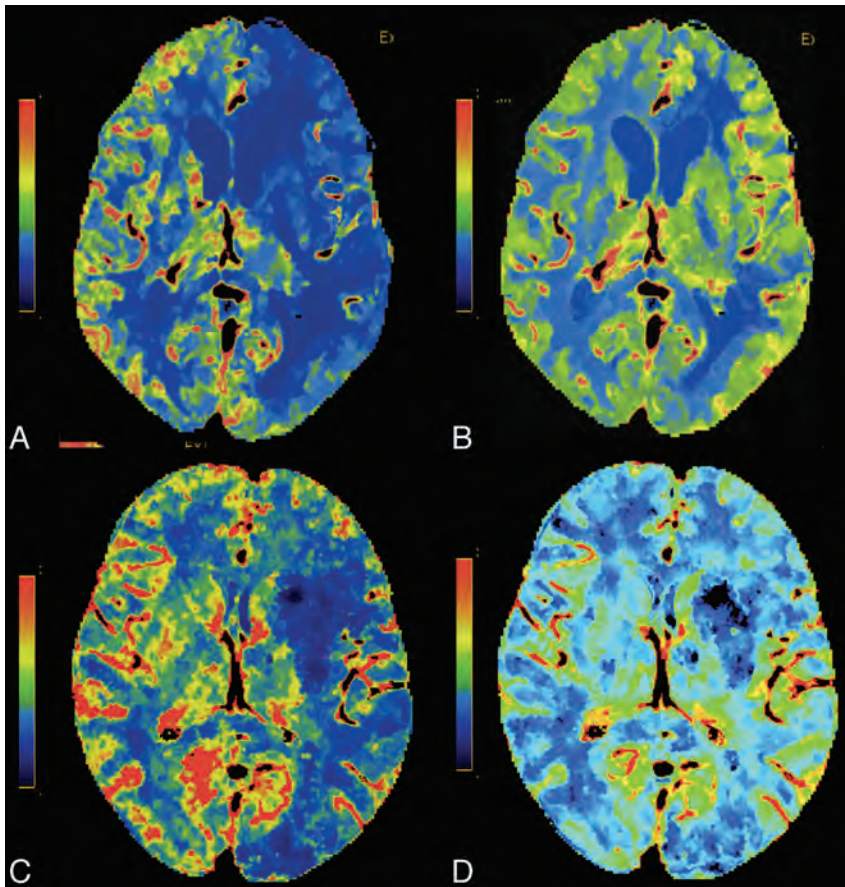


**FIG 4.** Two different patients with left MCA ischemia. CBF (A) and CBV (B) at 70-kVp and CBF (C) and CBV (D) at 80-kVp CTP. Note the decreased CBF and preserved CBV.

**Table 4: CTDI<sub>vol</sub> and DLP/ED values for whole-brain CTP examinations at 80 kVp and 70 kVp with different scanners**

	Percentage Reduction		
	70 kVp	80 kVp	100% - (70 kVp/80 kVp) × 100
CTDI <sub>vol</sub> (mGy)	105	192	45.31
DLP (mGy·cm)	1588	1831	13.27
ED (mSv)	3.65	4.21	13.27

**Note:**—ED indicates effective dose.

### Radiation Dose

Differences in mean CTDI<sub>vol</sub>, DLP, and effective dose between groups were statistically significant (all  $P < .01$ ). At 70 kVp, there was a 45.31% reduction of the mean CTDI<sub>vol</sub> (105 mGy) compared with 80 kVp (192 mGy). Despite an approximately 12-second wider scanning window and greater anatomic coverage (144 versus 120 mm), there was a 13.27% reduction of the mean DLP (1588 mGy·cm) and of the mean effective dose (3.65 mSv) when using the 70-kVp protocol compared with the 1831 mGy·cm and 4.21 mSv at 80 kVp. Table 4 summarizes the radiation dose results.

### DISCUSSION

In this study, we evaluated the efficacy of a 70-kVp whole-brain CTP protocol with variable sampling intervals and extended sampling against our established fixed-sampling, limited-period protocol at 80 kVp. Our protocol goals included reduced dose, matched or superior image quality, and more consistent contrast-

passage capture. To the best of our knowledge, our protocol is an approach that has not yet been reported.

Several methods have been proposed to limit the radiation dose in CTP, including reducing the tube voltage,<sup>3,10,11</sup> lowering the tube current,<sup>10</sup> dropping the temporal resolution,<sup>4-6</sup> and shortening the scan duration.<sup>7</sup> Reducing the tube voltage has a disproportionate effect on dose (eg, there is a 5-fold dose reduction in shifting from 140 to 80 kVp).<sup>12</sup> Wintermark et al<sup>3</sup> demonstrated that moving to 80 kVp from 120 kVp both reduced radiation dose, reporting a CTDI<sub>vol</sub> of 291 mGy, and increased the effectiveness of contrast enhancement in CTP. At present, the widely practiced standard for CTP has been 80 kVp at 200 mAs or less.<sup>3,13</sup> Our study used 70 kVp, a setting available on many clinical scanners, and 150 mAs, resulting in a CTDI<sub>vol</sub> of 105 mGy, 63% lower than the 80-kVp protocol used in the study of Wintermark et al.<sup>3</sup> The use of even lower kilovolt (peak) further enhances the attenuation of contrast because the 70-kVp beam energy even more closely approximates the iodine k-edge (33.2 KeV).<sup>12</sup> The net result is a lower net dose per whole-brain pass.

Another approach to radiation dose limitation is the use of wider sampling intervals. Conventional CTP studies use regular sampling intervals for a fixed period with length limited by dose concerns. The optimal sampling rate remains controversial. Wintermark et al<sup>4</sup> found that a sampling interval of >1 second could be used without altering the quantitative accuracy of CTP and recommended a sampling interval of 3 seconds over 42 seconds if a contrast bolus of 40 mL with an injection rate of 4 mL/s is used. Wiesmann et al<sup>14</sup> also stated that temporal resolution could be reduced to 3 seconds without significant compromise in image quality. In a more recent study, Shankar et al<sup>15</sup> suggested the use of a temporal resolution of up to 4 seconds for whole-brain CTP. However, other groups concluded that sampling intervals longer than 1 second yielded significantly poorer depiction of ischemic areas.<sup>5,6,16</sup>

Traditional fixed-sampling approaches have a uniform scanning rate over the entire CTP acquisition. Because certain portions of the contrast passage are likely less sensitive to sampling frequency, such as the pre-enhancement baseline and the downward slope toward the return to and through baseline, reducing sampling rates during these segments is appealing. The “omitted” samples can be traded for dose reduction or for higher temporal resolution during key segments of arterial tissue passage. Variable sampling for CTP has been reported by investigators working with wide 320-channel detector systems with favorable results.<sup>15</sup> To date, variable intervals have yet to be investigated on the much

more commonly used conventional 64-channel detector systems, despite wide clinical availability.

Overall scanning time can also be reduced in the interest of dose control. With fixed-sampling, the dose is directly proportional to the scanning period, which encourages shorter scans. Shorter scan time increases the risk that due to variability in cardiac output, a number of examinations may not continue through the venous return to baseline; this difference challenges the calculation of parametric maps based on deconvolution principles.<sup>17,18</sup> Longer sampling periods provide greater consistency of capture of the full contrast cycle from arterial arrival through venous return over a broad range of cardiac outputs. Adaptive asymmetric sampling intervals permit extended scan windows with dose neutrality because scans ordinarily taken at close intervals during before, and after arterial passage are traded for those at wide intervals at the end of the scanning period; the trading affords protection against premature termination. With a variable sampling rate, dose is independent of the length of the scanning window and instead is related to the total number of samples.

The classic CTP protocol described by Wintermark et al<sup>4</sup> had only a 40-second scanning window, starting 7 seconds after the contrast injection, similar to the 39-second and 8-second delay for the 24 fixed-rate whole-brain passes of our standard 80-kVp examination. In the variable-rate 70-kVp protocol, the scan window for 20 whole-brain passes was extended to 51 seconds. Analysis of the time-attenuation curve revealed that when scanning with the wider CTP window, nearly all of the studies continued through the venous return to baseline, while only the half of the studies using the limited-length protocol did. Discovery of this failure rate provoked a subsequent change in our clinical 80-kVp protocol, with the sampling time now extended to 43 seconds at the cost of a modest 10% increase in dose.

Previous studies using whole-brain CTP imaging with fixed-sampling rates reported radiation doses of 7.6 mSv,<sup>19</sup> 4.56 mSv,<sup>20</sup> and 4.6 mSv,<sup>21</sup> depending on the protocol. With our 20 whole-brain passes at 70 kVp, we achieved a considerable reduction of the effective dose to 3.65 mSv. Despite a 13% reduction in the effective dose compared with our standard 80-kVp protocol, overall quality was rated significantly better in the 70-kVp protocol and GM-WM differentiation was similar in both the quantitative and qualitative analyses.

We acknowledge several limitations in our study. The retrospective study design and small sample size may have introduced sampling errors or other dataset biases and require a confirmation of our findings in a prospective trial and a larger population. In addition, we compared studies between scanners from different manufacturers with different acquisition methods. We are unable to exclude the possible influence of different technical specifications such as x-ray generator/tube, detection system, and reconstruction algorithm on image quality and radiation dose. Parameters such as z-axis coverage of each acquisition, detector configuration, and the use of shuttle mode are slightly different between scanner models. Finally, while all the parametric maps were processed with a form of 4D noise reduction, because of scanner limitations, the 70-kVp datasets did not benefit from iterative reconstruction as did the CTP studies at 80 kVp; this difference diminished the impact of protocol variation on image

quality and possible dose reduction. A future study might seek to validate our conclusions on a single scanner.

## CONCLUSIONS

Whole-brain adaptive perfusion imaging at 70 kVp produces significant improvement in image quality compared with traditional 80-kVp acquisitions at lower radiation doses while providing greater consistency of full-contrast transit capture.

Disclosures: Idoia Corcuera-Solano—UNRELATED: Grant: Fundación Alfonso Martín Escudero, Comments: The foundation paid my salary as a research fellow in Mount Sinai when I was conducting research for this article. Lawrence N. Tanenbaum—UNRELATED: Payment for Lectures (including service on Speakers Bureaus): Siemens, GE Healthcare.

## REFERENCES

1. Ringelstein A, Lechel U, Fahrendorf DM, et al. **Radiation exposure in perfusion CT of the brain.** *J Comput Assist Tomogr* 2014;38:25–28
2. Imanishi Y, Fukui A, Niimi H, et al. **Radiation-induced temporary hair loss as a radiation damage only occurring in patients who had the combination of MDCT and DSA.** *Eur Radiol* 2005;15:41–46
3. Wintermark M, Maeder P, Verdun FR, et al. **Using 80 kVp versus 120 kVp in perfusion CT measurement of regional cerebral blood flow.** *AJNR Am J Neuroradiol* 2000;21:1881–84
4. Wintermark M, Smith WS, Ko NU, et al. **Dynamic perfusion CT: optimizing the temporal resolution and contrast volume for calculation of perfusion CT parameters in stroke patients.** *AJNR Am J Neuroradiol* 2004;25:720–29
5. Kämena A, Streitparth F, Grieser C, et al. **Dynamic perfusion CT: optimizing the temporal resolution for the calculation of perfusion CT parameters in stroke patients.** *Eur J Radiol* 2007;64:111–18
6. Abels B, Klotz E, Tomandl BF, et al. **CT perfusion in acute ischemic stroke: a comparison of 2-second and 1-second temporal resolution.** *AJNR Am J Neuroradiol* 2011;32:1632–39
7. Hirata M, Sugawara Y, Murase K, et al. **Evaluation of optimal scan duration and end time in cerebral CT perfusion study.** *Radiat Med* 2005;23:351–63
8. Bogartz G, Golding SJ, Jurik AG, et al. **European Guidelines for Multislice Computed Tomography.** 2004. [http://w3.tue.nl/fileadmin/sbd/Documenten/Leergang/BSM/European\\_Guidelines\\_Quality\\_Criteria\\_Computed\\_Tomography\\_Eur\\_16252.pdf](http://w3.tue.nl/fileadmin/sbd/Documenten/Leergang/BSM/European_Guidelines_Quality_Criteria_Computed_Tomography_Eur_16252.pdf). Accessed February 19, 2014
9. Siegel S, Castellan JN. *Nonparametric Statistics for the Behavioral Sciences.* New York: McGraw-Hill; 1988
10. Hirata M, Sugawara Y, Fukutomi Y, et al. **Measurement of radiation dose in cerebral CT perfusion study.** *Radiat Med* 2005;23:97–103
11. Cohnen M, Fischer H, Hamacher J, et al. **CT of the head by use of reduced current and kilovoltage: relationship between image quality and dose reduction.** *AJNR Am J Neuroradiol* 2000;21:1654–60
12. Huda W, Lieberman KA, Chang J, et al. **Patient size and x-ray technique factors in head computed tomography examinations. II. Image quality.** *Med Phys* 2004;31:595–601
13. Wintermark M, Lev MH. **FDA investigates the safety of brain perfusion CT.** *AJNR Am J Neuroradiol* 2010;31:2–3
14. Wiesmann M, Berg S, Bohner G, et al. **Dose reduction in dynamic perfusion CT of the brain: effects of the scan frequency on measurements of cerebral blood flow, cerebral blood volume, and mean transit time.** *Eur Radiol* 2008;18:2967–74
15. Shankar JJ, Lum C, Sharma M. **Whole-brain perfusion imaging with 320-MDCT scanner: reducing radiation dose by increasing sampling interval.** *AJR Am J Roentgenol* 2010;195:1183–86
16. Kloska SP, Fischer T, Sauerland C, et al. **Increasing sampling interval in cerebral perfusion CT: limitation for the maximum slope model.** *Acad Radiol* 2010;17:61–66
17. Konostas AA, Goldmakher GV, Lee TY, et al. **Theoretic basis and tech-**

- nical implementations of CT perfusion in acute ischemic stroke. Part 1: Theoretic basis.** *AJNR Am J Neuroradiol* 2009;30:662–68
18. Fieselmann A, Kowarschik M, Ganguly A, et al. **Deconvolution-based CT and MR brain perfusion measurement: theoretical model revisited and practical implementation details.** *Int J Biomed Imaging* 2011;2011:467563
  19. Page M, Nandurkar D, Crossett MP, et al. **Comparison of 4 cm z-axis and 16 cm z-axis multidetector CT perfusion.** *Eur Radiol* 2010;20:1508–14
  20. Diekmann S, Siebert E, Juran R, et al. **Dose exposure of patients undergoing comprehensive stroke imaging by multidetector-row CT: comparison of 320-detector row and 64-detector row CT scanners.** *AJNR Am J Neuroradiol* 2010;31:1003–09
  21. Wintermark M, Maeder P, Thiran JP, et al. **Quantitative assessment of regional cerebral blood flows by perfusion CT studies at low injection rates: a critical review of the underlying theoretical models.** *Eur Radiol* 2001;11:1220–30

# Dental Flat Panel Conebeam CT in the Evaluation of Patients with Inflammatory Sinonasal Disease: Diagnostic Efficacy and Radiation Dose Savings

C. Leiva-Salinas, L. Flors, P. Gras, F. Más-Estellés, P. Lemerrier, J.T. Patrie, M. Wintermark, and L. Martí-Bonmatí

## ABSTRACT

**BACKGROUND AND PURPOSE:** CT is the imaging modality of choice to study the paranasal sinuses; unfortunately, it involves significant radiation dose. Our aim was to assess the diagnostic validity, image quality, and radiation-dose savings of dental conebeam CT in the evaluation of patients with suspected inflammatory disorders of the paranasal sinuses.

**MATERIAL AND METHODS:** We prospectively studied 40 patients with suspected inflammatory disorders of the sinuses with dental conebeam CT and standard CT. Two radiologists analyzed the images independently, blinded to clinical information. The image quality of both techniques and the diagnostic validity of dental conebeam CT compared with the reference standard CT were assessed by using 3 different scoring systems. Image noise, signal-to-noise ratio, and contrast-to-noise ratio were calculated for both techniques. The absorbed radiation dose to the lenses and thyroid and parotid glands was measured by using a phantom and dosimeter chips. The effective radiation dose for CT was calculated.

**RESULTS:** All dental conebeam CT scans were judged of diagnostic quality. Compared with CT, the conebeam CT image noise was 37.3% higher ( $P < .001$ ) and the SNR of the bone was 75% lower ( $P < .001$ ). The effective dose of our conebeam CT protocol was  $23 \mu\text{Sv}$ . Compared with CT, the absorbed radiation dose to the lenses and parotid and thyroid glands with conebeam CT was 4%, 7.8%, and 7.3% of the dose delivered to the same organs by conventional CT ( $P < .001$ ).

**CONCLUSIONS:** Dental conebeam CT is a valid imaging procedure for the evaluation of patients with inflammatory sinonasal disorders.

**ABBREVIATIONS:** CNR = contrast-to-noise ratio; TLD = thermoluminescent dosimeter

CT is the criterion standard imaging technique for the evaluation of adult patients with suspected sinonasal inflammatory disease.<sup>1</sup> The use of CT has increased dramatically, and it is estimated that approximately 4 million CT scans of the sinuses are currently obtained each year in the United States.<sup>2</sup>

CT involves considerable ionizing radiation. It accounts for 10% of radiology procedures but represents approximately two-thirds of the total medical radiation dose,<sup>3,4</sup> and 2% of all cancers in the United States may be attributable to the radiation derived from CT studies.<sup>5</sup> Patients in whom an inflammatory disorder of the paranasal sinuses is suspected are frequently young,<sup>1,6</sup> and in

this population, radiation-induced cancer risk is considerably higher.<sup>5</sup> Besides carcinogenesis, CT of the paranasal sinuses increases the risk of radiation-induced cataracts because the lens of the eye is a highly radiosensitive organ enclosed in the scanning field.<sup>1,7,8</sup>

One approach to reduce such adverse effects is to decrease the CT-related radiation dose by adjusting downward the scanner settings that determine it. Prior studies<sup>1,4,6,8-11</sup> have shown that, indeed, reducing the radiation dose by 75% does not significantly impact the diagnosis of sinonasal inflammatory diseases. A different approach would be to replace conventional CT with another technique. Dental conebeam CT is an emerging clinical technique. It uses a cone-shaped x-ray beam and an exceptionally radiosensitive flat panel detector to provide high-resolution images with a low radiation dose.<sup>12,13</sup> At present, the clinical use of this technique is largely centered on the dental region, where it is considered more effective and economical than conventional CT.<sup>14</sup> Conebeam CT systems have limited soft-tissue contrast discrimination,<sup>13</sup> compared with conventional CT. This limitation represents the main barrier to the extension of conebeam of into

Received January 6, 2014; accepted after revision April 14.

From the Departments of Radiology and Medical Imaging (C.L.-S., L.F., F.M.-E., P.L., L.M.-B.) and Physics (P.G.), ERESA (F.M.-E.), and GIBI Research Group (L.M.-B.), Hospital Universitario y Politécnico la Fe, Valencia, Spain; and Departments of Radiology and Medical Imaging (C.L.-S., L.F., M.W.) and Public Health Sciences (J.T.P.), University of Virginia, Charlottesville, Virginia.

Please address correspondence to Carlos Leiva-Salinas, MD, Neuroradiology Division, Department of Radiology, Hospital Universitario y Politécnico la Fe, Bulevar Sur s/n, Torre F, Valencia, Spain; e-mail: carlosleivasalinas@gmail.com

<http://dx.doi.org/10.3174/ajnr.A4019>

diagnostic imaging. In the sinonasal region, this technique may not be appropriate for the evaluation of tumors or complicated sinusitis or critical evaluation of small changes in soft-tissue attenuation. The purpose of our investigation was to assess the diagnostic validity and image quality of dental conebeam CT compared with standard CT in the evaluation of inflammatory disorders of the paranasal sinuses and to investigate the potential radiation-dose savings achieved with this technique.

## MATERIALS AND METHODS

### Study Patients and Protocol

We prospectively enrolled all consecutive adult patients (older than 18 years of age) who were referred by the ear, nose, and throat clinic to our department to perform noncontrast CT of the paranasal sinuses due to a clinical suspicion of an inflammatory disorder of the nasal fossae or paranasal sinuses during a 3-month period. Although we had planned to exclude patients in whom a sinonasal neoplasia was discovered, no patient was excluded because we did not find any. CT was performed first. In the hour following the CT, an additional dental conebeam CT scan was obtained.

The institutional ethics committee approved our research protocol. All participants gave written informed consent.

### Image Acquisition

The CT studies were performed on a 64-channel multidetector CT system (Brilliance 64; Philips Healthcare, Best, the Netherlands). We used the following protocol: 120 kV, 120 mAs, 64 × 0.625 mm collimation, 0.75-second rotation time, table feed of 0.7 mm (pitch factor of 0.891), and FOV of 18 cm. This protocol is provided by the manufacturer for this specific diagnostic purpose. No iterative reconstruction technique was used because it is not available in our scanners. All raw datasets were reconstructed at 1-mm section thickness in 0.5-mm increments by using a routine bone reconstruction algorithm. On the basis of the transverse images, coronal reformations were reconstructed at 1-mm section thicknesses.

The conebeam CT studies were performed on a dental conebeam CT (i-CAT Next Generation; Imaging Sciences International, Hatfield, Pennsylvania). We used the following protocol: 120 kV, 5 mA, 0.4-mm collimation, 13-cm scan length, 4.8-second rotation time, 190° tube rotation, 159 basis images, and FOV of 16 cm. Because the system is not designed to image the sinuses, there is no manufacturer-recommended protocol for that purpose; we considered this combination of parameters adequate on the basis of our experience with dental studies. Raw images were reconstructed at 1-mm section thicknesses in 0.5-mm increments. Coronal reformations were reconstructed at 1-mm section thicknesses in 1-mm increments.

### Image Analysis

Two experienced radiologists (C.L.-S. and F.M.-E.) with 4 and 15 years of experience in reading head and neck studies, respectively, assessed the images independently. They were blinded to the clinical information provided in the CT request. In a first session, the studies were randomized and the radiologists evaluated the image

quality of conventional and conebeam CT by using 2 different scoring methods.

Scoring method 1 is a previously published system<sup>1</sup> that takes into account 6 anatomic structures: the osteomeatal unit, uncinate process, infundibulum, frontal recess, attachments of the middle turbinate, and path of the optic nerve. For each structure, the following scores were assigned, depending on how well it was visualized: 0, not demonstrated; 1, demonstrated but not clearly visualized; 2, clearly visualized. The right and left sides were analyzed separately. The maximum score for each of the left and right sides was 12. For analysis purposes, we calculated the mean of the scores of the right and left sides combined.

Scoring method 2 is based on another previously published grading system.<sup>8</sup> It takes into account the radiologist's subjective impression of the overall quality of the study regarding the evaluation of the bony structures described in scoring method 1 by using a 5-point scale: 1, unacceptable noise rendering a study nondiagnostic; 2, low noise resulting in diagnostic uncertainty; 3, average image quality with a correct diagnosis being highly likely; 4, good image quality enabling a confident diagnosis; 5, excellent image quality of the best diagnostic value.

In a separate session, the same radiologists evaluated the diagnostic validity of dental conebeam CT compared with conventional CT by using scoring method 3, in which we randomized the studies and assigned the following scores: 0, not sufficient for diagnosis; 1, sufficient for diagnosis.

### Image Noise and Signal-to-Noise and Contrast-To-Noise Ratios

Image noise, signal-to-noise ratio, and contrast-to-noise ratio (CNR) were used to characterize image quality. These measurements were obtained by a single radiologist (P.L.). The attenuation in the cortical bone of the zygomatic arch, the pterygoid muscles, and air in the oropharynx were measured by drawing circular regions of interest for both CT and dental conebeam CT, according to the patient's individual anatomy. The diameter of the region of interest was made as large as possible, depending on the anatomic region. ROIs of similar size were placed at the same location on both imaging modalities. Image noise ( $N$ ) was calculated as the SD of the voxel values of the region of interest placed in the air. SNR of the bone was calculated by using the following equation:

$$SNR_b = A_b/N,$$

where  $A_b$  is the mean attenuation of the voxel values of the region of interest placed in the bone and  $N$  is the image noise. The contrast between the bone and the muscle-to-noise ratio ( $CNR_{(b/m)}$ ) was calculated by using the following equation:

$$CNR_{(b/m)} = (A_b - A_m)/N,$$

where  $A_b$  and  $A_m$  are the mean attenuation of the voxel values of the region of interest placed in the bone and muscle respectively, and  $N$  is the image noise.  $CNR_{(b/a)}$  (bone and air) and  $CNR_{(m/a)}$  (muscle and air) were calculated similarly.

## Radiation-Dose Analysis

The absorbed radiation dose to the lens of the eye and thyroid and parotid glands was measured by using an adult male skull and a tissue-equivalent phantom (radiation analog dosimetry system; Nuclear Associates, Hicksville, New York). Lithium fluoride thermoluminescent dosimeter (TLD) chips (EXT-RAD, XD-100; Harshaw, Cleveland, Ohio),  $3.2 \times 3.2 \times 0.4$  mm, were used to record the absorbed radiation dose at selected locations in the head and neck region of the phantom. The chips were precalibrated for diagnostic x-ray energies with an accuracy and precision of 5%. At the start of each CT or dental conebeam CT scan, the TLD chips were superficially placed over the right and left lenses of the eye, the left parotid gland, and the thyroid surface. We measured the dose delivered to both lenses, because those were specific targets of interest. TLD doses were assumed equal to the dose delivered to each of the organs. Three scan acquisitions, each by using a different set of 4 TLD chips, were performed to provide a more reliable measure of radiation, and the mean was calculated for each TLD position.

The CT effective dose was calculated from the dose-length product (DLP) recorded from each CT protocol. A normalized conversion factor ( $k$ ) of 0.0023 for the head was used to calculate the effective dose by using the following formula<sup>15</sup>:

$$ED \text{ (mSv)} = DLP \text{ (mGy} \times \text{cm)} \times k \text{ [mSv/(mGy} \times \text{cm)]}.$$

Doses from TLDs at the different positions within tissue or organ were used to express the tissue-absorbed dose in milligrays. The products of these values and the percentage of a tissue or organ irradiated for the dental conebeam CT examination were used to calculate the equivalent dose ( $EqD$ ) in millisieverts. The proportion of the different tissues in the head and neck region, directly exposed to radiation (as a percentage of the total body), was set on the basis of evidence from previous studies.<sup>16,17</sup> The effective dose was calculated by using the following formula<sup>16,17</sup>:

$$ED \text{ (mSv)} = EqD \text{ (mSv)} \times W_T,$$

where  $EqD$  is the equivalent dose and  $W_T$  is a tissue-weighting factor that represents the relative contribution of that organ or tissue to the overall carcinogenic risk.

## Statistical Analysis

The differences in image quality and diagnostic validity scores were compared by using Wilcoxon signed rank tests. The interreader agreement for such scores for both conventional CT and conebeam CT and the intrareader agreement for conventional CT versus conebeam CT were quantified by using a linear-weighted  $\kappa$  analysis.

The differences in effective radiation doses between CT and dental conebeam CT were analyzed by using paired  $t$  tests. The absorbed radiation data were analyzed by using a linear-mixed model. The sources of variation analyzed were the imaging technique (CT, dental conebeam CT) and the anatomic organ (left lens, right lens, right parotid gland, thyroid gland). The null hypothesis decision rule was based on a  $P \leq .05$  criterion with a Bonferroni correction for 4 hypothesis tests.

The difference in image noise between CT and dental

**Table 1: Image-quality scores for scoring method 1 (visualization of 6 bony anatomic structures) and scoring method 2 (subjective impression of the overall quality of the study) for each imaging technique, with left and right sides combined<sup>a</sup>**

	Standard CT	Conebeam CT	Difference
Score 1 <sup>b</sup>			
Reader 1	11 ± 2.8 (3–12)	10.5 ± 3.4 (3–12)	0.5 <sup>c</sup>
Reader 2	11 ± 2.9 (3–12)	10.25 ± 3.5 (3–12)	0.75 <sup>d</sup>
Difference	0	0.25	0.5 <sup>c</sup>
Score 2 <sup>e</sup>			
Reader 1	5 ± 0.45 (4–5)	4 ± 0.7 (4–5)	1 <sup>d</sup>
Reader 2	5 ± 0.22 (3–5)	4 ± 0.54 (3–5)	1 <sup>d</sup>
Difference	0	0	0

<sup>a</sup> Data are median values ± SD (range).

<sup>b</sup> Score 1: 0- to 12-point scale.

<sup>c</sup>  $P < .01$ .

<sup>d</sup>  $P < .001$ .

<sup>e</sup> Score 2: 1- to 5-point scale.

**Table 2: Interreader agreement regarding image-quality scores for CT and conebeam CT**

	$\kappa$ Statistics (95% CI)
CT	
Score 1 <sup>a</sup>	0.78 (0.60–0.80)
Score 2 <sup>b</sup>	0.08 (–0.16–0.32)
Conebeam CT	
Score 1 <sup>a</sup>	0.79 (0.70–0.87)
Score 2 <sup>b</sup>	0.40 (0.22–0.59)

<sup>a</sup> Score 1: 0- to 12-point scale.

<sup>b</sup> Score 2: 1- to 5-point scale.

**Table 3: Intrareader agreement between CT and conebeam CT image-quality scores for each reader**

	$\kappa$ Statistics (95% CI)
Reader 1	
Score 1 <sup>a</sup>	0.82 (0.75–0.90)
Score 2 <sup>b</sup>	0.03 (–0.05–0.12)
Reader 2	
Score 1 <sup>a</sup>	0.70 (0.60–0.80)
Score 2 <sup>b</sup>	0.01 (–0.00–0.01)

<sup>a</sup> Score 1: 0- to 12-point scale.

<sup>b</sup> Score 2: 1- to 5-point scale.

conebeam CT was compared by using Wilcoxon signed rank testing.

The statistical software packages SAS, Version 9.2.2 (SAS Institute, Cary, North Carolina) and Spotfire S+, Version 8.1 (TIBCO, Palo Alto, California) were used.

## RESULTS

We enrolled 40 consecutive patients (mean age,  $44 \pm 15$  years; range, 18–82; female, 57.5%). Sixteen patients (40%) were younger than 40 years of age.

The median score for method 1, regarding identification of anatomic structures, was 11 for standard CT and 10.25 for dental conebeam CT ( $P < .01$ ) (Table 1). Regarding scoring method 1, the average specific scores for the osteomeatal unit, uncinate process, infundibulum, frontal recess, attachments of the middle turbinate, and path of the optic nerve were 1.58, 1.52, 1.46, 1.58, 1.97, and 2 for CT, and 1.56, 1.37, 1.34, 1.44, 1.71, and 1.81 for conebeam CT. The median score for method 2, regarding the subjective quality of the study, was 5 for CT and 4 for dental conebeam CT ( $P < .01$ ) (Table 1). Regarding scoring method 3, both readers judged all the dental conebeam CT studies valid for

**Table 4: Image noise, signal-to-noise ratio, and contrast-to-noise ratio for each imaging technique<sup>a</sup>**

	Noise	SNR <sub>b</sub>	CNR <sub>(b/m)</sub>	CNR <sub>(b/a)</sub>	CNR <sub>(m/a)</sub>
CT	29.28 ± 9.39	100.35 ± 33.1	97.03 ± 31.63	163.80 ± 54.81	66.76 ± 23.31
Conebeam CT	46.76 ± 15.84	25.33 ± 16.73	28.45 ± 18.11	50.46 ± 31.9	22 ± 14
Difference	17.48 <sup>b</sup>	75.02 <sup>b</sup>	68.58 <sup>b</sup>	113.34 <sup>b</sup>	44.76 <sup>b</sup>

**Note:**—SNR<sub>b</sub> indicates SNR of the bone; CNR<sub>(b/m)</sub>, contrast between the bone and the muscle-to-noise ratio; CNR<sub>(b/a)</sub>, contrast between bone and air; CNR<sub>(m/a)</sub>, contrast between muscle and air.

<sup>a</sup>Data are median values ± SD.

<sup>b</sup>*P* < .001.

**Table 5: Absorbed radiation dose to the lenses of the eye and parotid and thyroid glands for each imaging technique<sup>a</sup>**

	Absorbed Dose Right Lens (mGy)	Absorbed Dose Left Lens (mGy)	Absorbed Dose Right Parotid Gland (mGy)	Absorbed Dose Thyroid Gland (mGy)
CT	9.25 ± 1.69	9.69 ± 1.08	8.87 ± 1.68	0.45 ± 0.13
Conebeam CT	0.28 ± 0.01 <sup>b</sup>	0.4 ± 0.03 <sup>b</sup>	0.69 ± 0.05	0.05 ± 0.05
Difference	8.97 <sup>c</sup>	9.29 <sup>c</sup>	8.18 <sup>c</sup>	0.4 <sup>c</sup>

<sup>a</sup>Data are mean values ± SD.

<sup>b</sup>For Conebeam CT, the absorbed radiation dose to the left lens was significantly higher than the dose to the right lens because the x-ray tube describes a 190° rotation around the left side of the patient's face.

<sup>c</sup>*P* < .001.

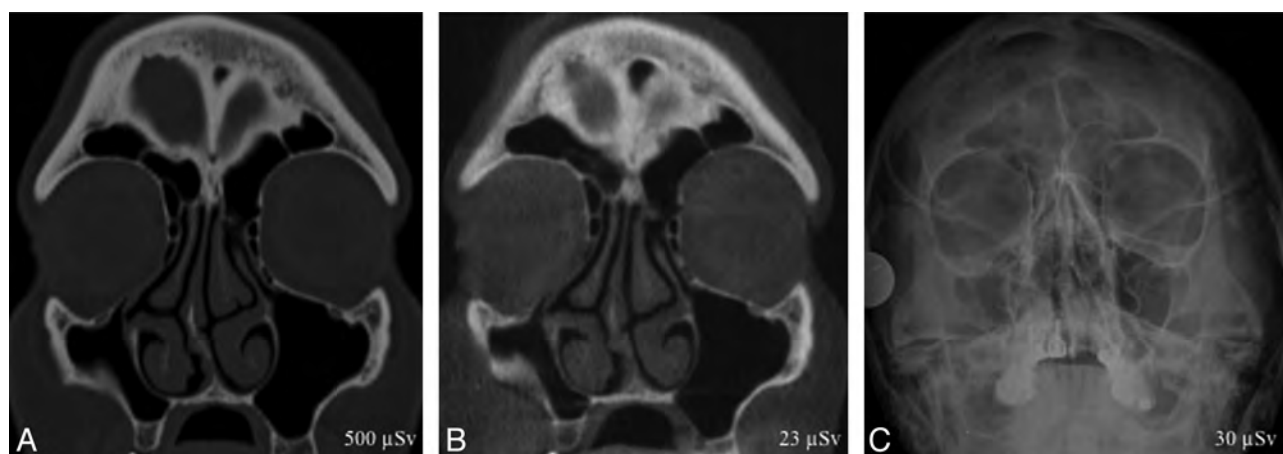


**FIG 1.** A 50-year-old woman with vague facial pain for several months and enophthalmos on physical examination. CT (A) and conebeam CT (B) coronal images show inward retraction of the right maxillary walls and apposition of the right uncinate process into the orbital floor, occluding the maxillary sinus infundibulum. The clinical and CT imaging findings were characteristic of silent sinus syndrome. CT scans delineate anatomic structures and demonstrate disease not shown on the x-ray (C). X-ray shows a small right maxillary sinus but is unable to help in the diagnostic work-up of the patient.

diagnosis. Tables 2 and 3 show the inter- and intrareader agreement for both imaging techniques.

Compared with conventional CT, the dental conebeam CT image noise was 37.3% higher (*P* < .001), the SNR of the bone was 75% lower (*P* < .001), and the CT CNR<sub>(b/m)</sub>, CNR<sub>(b/a)</sub>, and CNR<sub>(m/a)</sub> were 70%, 69.1%, and 67% lower, respectively (*P* < .001) (Table 4).

The mean effective radiation dose for CT was 0.511 ± 0.039 mSv (range, 0.44–0.61 mSv). The calculated effective radiation dose for dental conebeam CT was 0.023 mSv. Compared with CT, the dental conebeam CT effective radiation dose was 95.5% lower (*P* < .001). Compared with CT, the dental conebeam CT absorbed radiation doses to the right lens, left lens, right parotid gland, and thyroid gland were 95.8%, 97%, 92.2%, and 92.7% lower, respectively (*P* < .001) (Table 5).

A representative image from each technique is shown in Fig 1.

## DISCUSSION

Our study suggests that by using conebeam CT technology, it is possible to drastically reduce the radiation dose without compro-

promising the diagnostic capability in screening examination of the paranasal sinuses. While conventional CT better delineated the bony anatomic structures and obtained better objective metrics of image quality (lower image noise, higher SNR and CNR), the overall diagnostic validity of both imaging techniques was considered similar. Conebeam CT image quality was graded as good, compared with excellent for CT, enabling a confident diagnosis. Although CT evaluated the bony structures statistically better than conebeam CT, most bony anatomic structures were perfectly visualized with conebeam CT. That the image quality for CT was graded as excellent and that the SNR and CNR were significantly better for CT than for conebeam CT are evidence that the radiation dose used in the multidetector CT protocol was excessively high, as mentioned in the “Discussion.”

The effective dose of our dental conebeam CT protocol was 23 μSv, lower than the radiation dose from a sinus x-ray, which is typically around 30 μSv.<sup>18</sup> As a reference, the natural background radiation dose is estimated to be 2280 μSv per year.<sup>19</sup>

Conebeam CT is an emerging technology with its main clinical

application to date being dental imaging. Efficient use of the x-ray beam in conebeam CT produces a relatively low x-ray tube power requirement—as modest as 5 mAs in our system—and therefore a low radiation dose.<sup>12,13</sup> A prior study proposed a conebeam CT protocol to image the paranasal sinuses and studied the theoretic, potential radiation-dose savings of such a protocol.<sup>20</sup> Other authors have investigated how often clinically important findings would be missed if conebeam CT were used routinely for sinus imaging by creating a “theoretic conebeam CT” from the original CT images.<sup>21</sup> However, to our knowledge, no previous research has analyzed the diagnostic validity and potential radiation dose savings of dental conebeam CT compared with conventional CT in the evaluation of the paranasal sinuses, in a real clinical scenario.

Imaging of the sinuses involves imaging 3 tissues with considerably different attenuation: air, bone, and soft tissues. The inherent and naturally high contrast among these structures, coupled with CT technologic developments, has favored the use of low-dose CT protocols without losing diagnostic power, pushing the limits of the radiation-dose reduction by a factor of >25 in the past 25 years.<sup>4,10,11,22</sup>

A large number of prior studies have successfully achieved reduction of the CT-related radiation dose by either adjusting the acquisition settings that determine the radiation dose,<sup>1,4,6,8-11</sup> the image reconstruction algorithms,<sup>23</sup> or by using the latest available CT systems.<sup>24</sup> The lowest published effective radiation dose for a sinus CT protocol in the clinical setting was 47  $\mu$ Sv, very low, but more than double that with conebeam CT.<sup>11</sup> A recent study using state-of-the-art CT technology with the lowest possible radiation dose in postmortem heads yielded an absorbed dose of 0.64 mGy for the lens of the eye and 0.085 mGy for the thyroid gland,<sup>19</sup> still 88% and 70% more radiation doses, respectively, than the results obtained with our dental conebeam CT protocol.

Patients with inflammatory disorders of the paranasal sinuses are often pediatric or young adults,<sup>1,6</sup> and in this population, radiation-dose reduction is particularly important,<sup>5</sup> especially considering that for chronic sinonasal disorders, serial scanning is often performed for follow-up; hence, patients are subject to a cumulative radiation exposure.<sup>8</sup>

From an economic perspective, a CT scan of the sinuses has an average cost of \$875; for a dental conebeam CT, it is around \$160–\$275.<sup>25,26</sup>

This study had certain limitations. First, it may have been biased toward dental conebeam CT because the readers were able to identify whether the images they were scoring were acquired either with conebeam CT or with a standard CT system, due to the higher noise and lower soft-tissue definition of the images acquired with conebeam CT. Second, the study was limited to adult patients with sinonasal inflammatory conditions. The generalization of our results to all patients who are referred to a radiology department for a CT scan of the sinuses may be problematic. Additionally, a number of pathologic entities may indeed require a soft-tissue algorithm for diagnostic evaluation (sinonasal and oral cavities and oropharyngeal neoplasms). Dental conebeam CT is not reliable for assessing the soft tissues<sup>13</sup> and should probably only be used to screen for uncomplicated inflammatory mu-

cosal disease. Investigation of patients with noninflammatory diseases was beyond the scope of our article.

Third, the imaging protocol installed as standard on our CT system and the one we used in our investigation are not low-dose protocols. They use a tube current of 120 mAs rather than the sufficient 50 mAs recommended by the literature.<sup>1</sup> If we had used a low-dose protocol, the radiation-dose savings of dental conebeam CT would have been proportionately lower in comparison with standard CT. Despite this possible outcome, the effective and absorbed radiation doses obtained with dental conebeam CT compared very favorably with those in all other previous studies and cannot be achieved with the currently available CT scanners. Using a standard-dose CT protocol also ensures that we compared dental conebeam CT with an optimal criterion standard, because there are no published data about the diagnostic quality of a low-dose protocol acquired with our CT system.

## CONCLUSIONS

Due to its image quality, low radiation dose, and low economic cost, dental conebeam CT is a valid first-line imaging test for the evaluation of patients with suspected inflammatory sinonasal disorders. It allows a reduction in radiation dose by a factor of 25 compared with standard CT without a low-dose protocol implemented. Conebeam CT provides mostly bone information; due to its limited soft-tissue contrast discrimination, it may not be appropriate for imaging patients with suspected complicated sinusitis.

## ACKNOWLEDGMENTS

We thank Carmen Argudo, RN, and all the CT technologists for their enthusiasm and wonderful work and Emilio Casal, PhD, from the Centro Nacional de Dosimetría, for providing the TLD chips and assisting in the radiation-dose calculation.

Disclosures: Max Wintermark—RELATED: Grants/Grants Pending: GE Healthcare and Philips Healthcare.\* \*Money paid to the institution.

## REFERENCES

1. Sohaib SA, Peppercorn PD, Horrocks JA, et al. **The effect of decreasing mAs on image quality and patient dose in sinus CT.** *Br J Radiol* 2001;74:157–61
2. Conference of Radiation Control Program Directors, Department of Health and Human Services (2006). What's NEXT? Nationwide Evaluation of X-ray Trends: 2000 computed tomography. [http://www.crcpd.org/Pubs/NEXT\\_docs/NEXT2000-CT.pdf](http://www.crcpd.org/Pubs/NEXT_docs/NEXT2000-CT.pdf). Accessed May 24, 2014
3. Mettler FA Jr, Wiest PW, Locken JA, et al. **CT scanning: patterns of use and dose.** *J Radiol Prot* 2000;20:353–59
4. Mulkens TH, Broers C, Fieuws S, et al. **Comparison of effective doses for low-dose MDCT and radiographic examination of sinuses in children.** *AJR Am J Roentgenol* 2005;184:1611–18
5. Brenner DJ, Hall EJ. **Computed tomography: an increasing source of radiation exposure.** *N Engl J Med* 2007;357:2277–84
6. Nauer CB, Eichenberger A, Dubach P, et al. **CT radiation dose for computer-assisted endoscopic sinus surgery: dose survey and determination of dose-reduction limits.** *AJNR Am J Neuroradiol* 2009;30:617–22
7. Dammann F, Momino-Traserra E, Remy C, et al. **Radiation exposure during spiral-CT of the paranasal sinuses** [in German]. *Rof* 2000;172:232–37
8. Brem MH, Zamani AA, Riva R, et al. **Multidetector CT of the para-**

- nasal sinus: potential for radiation dose reduction. *Radiology* 2007;243:847–52
9. Kropil P, Cohnen M, Andersen K, et al. **Image quality in multidetector CT of paranasal sinuses: potential of dose reduction using an adaptive post-processing filter** [in German]. *Rofo* 2010;182:973–78
  10. Marmolya G, Wiesen EJ, Yagan R, et al. **Paranasal sinuses: low-dose CT**. *Radiology* 1991;181:689–91
  11. Tack D, Widelec J, De Maertelaer V, et al. **Comparison between low-dose and standard-dose multidetector CT in patients with suspected chronic sinusitis**. *AJR Am J Roentgenol* 2003;181:939–44
  12. Gupta R, Cheung AC, Bartling SH, et al. **Flat-panel volume CT: fundamental principles, technology, and applications**. *Radiographics* 2008;28:2009–22
  13. Miracle AC, Mukherji SK. **Conebeam CT of the head and neck. Part 1. Physical principles**. *AJNR Am J Neuroradiol* 2009;30:1088–95
  14. Hashimoto K, Kawashima S, Araki M, et al. **Comparison of image performance between cone-beam computed tomography for dental use and four-row multidetector helical CT**. *J Oral Sci* 2006;48:27–34
  15. Bongartz G, Golding S, Jurik A, et al. **European guidelines on quality criteria for computed tomography**. 2000; Publication no. EUR 16262 EN. <http://www.dr.dk/guidelines/ct/quality/htmlindex.htm>. Accessed May 24, 2014
  16. Ludlow JB, Davies-Ludlow LE, Brooks SL. **Dosimetry of two extraoral direct digital imaging devices: NewTom conebeam CT and Orthophos Plus DS panoramic unit**. *Dentomaxillofac Radiol* 2003;32:229–34
  17. Ludlow JB, Ivanovic M. **Comparative dosimetry of dental CBCT devices and 64-slice CT for oral and maxillofacial radiology**. *Oral Surg Oral Med Oral Pathol Oral Radiol Endod* 2008;106:106–14
  18. Wall BF, Hart D. **Revised radiation doses for typical X-ray examinations: report on a recent review of doses to patients from medical X-ray examinations in the UK by NRPB—National Radiological Protection Board**. *Br J Radiol* 1997;70:437–39
  19. National Council on Radiation Protection and Measurements. NCRP Report No. 160, Ionizing radiation exposure of the population of the United States. National Council on Radiation Protection and Measurements. [http://www.ncrponline.org/Publications/Press\\_Releases/160press.html](http://www.ncrponline.org/Publications/Press_Releases/160press.html). Accessed August 15, 2013
  20. Güldner C, Ningo A, Voigt J, et al. **Potential of dose reduction in cone-beam-computed tomography (CBCT) for radiological diagnostics of the paranasal sinuses**. *Eur Arch Otorhinolaryngol* 2013;270:1307–15
  21. Fakhran S, Alhilali L, Sreedher G, et al. **Comparison of simulated cone beam computed tomography to conventional helical computed tomography for imaging of rhinosinusitis**. *Laryngoscope* 2014;124:2002–06
  22. Zinreich SJ, Kennedy DW, Rosenbaum AE, et al. **Paranasal sinuses: CT imaging requirements for endoscopic surgery**. *Radiology* 1987;163:769–75
  23. Bulla S, Blanke P, Hassepass F, et al. **Reducing the radiation dose for low-dose CT of the paranasal sinuses using iterative reconstruction: feasibility and image quality**. *Eur J Radiol* 2012;81:2246–50
  24. Schulz B, Potente S, Zangos S, et al. **Ultra-low dose dual-source high-pitch computed tomography of the paranasal sinus: diagnostic sensitivity and radiation dose**. *Acta Radiol* 2012;53:435–40
  25. CT Maxillofacial (Sinus) Procedure and Cost Information. New Choice Health. 2013. [http://www.newchoicehealth.com/Directory/Procedure/4/CT%20Maxillofacial%20\(Sinus\)](http://www.newchoicehealth.com/Directory/Procedure/4/CT%20Maxillofacial%20(Sinus)). Accessed October 25, 2013
  26. Christell H, Birch S, Horner K, et al. **A framework for costing diagnostic methods in oral health care: an application comparing a new imaging technology with the conventional approach for maxillary canines with eruption disturbances**. *Community Dent Oral Epidemiol* 2012;40:351–61

# Memory Part 1: Overview

F.D. Raslau, A.P. Klein, J.L. Ulmer, V. Mathews, and L.P. Mark

A common layman's conception of memory is the simple storage and retrieval of learned information that often evokes comparison to a filing system. Our everyday experience of memory, however, is in fact a complicated multifactorial process that consists of both conscious and unconscious components, and depends on the integration of a variety of information from distinct functional systems, each processing different types of information by different areas of the brain (substrates), while working in a concerted fashion.<sup>1-4</sup> In other words, memory is not a singular process. It represents an integrated network of neurologic tasks and connections. In this light, memory may evoke comparison with an orchestra composed of many different instruments, each making different sounds and responsible for different parts of the score, but when played together in the proper coordinated fashion, making an integrated musical experience that is greater than the simple sum of the individual instruments.

Memory consists of 2 broad categories (Fig 1): short- and long-term memory.<sup>5</sup> Short-term memory is also called working memory. Long-term memory can be further divided into declarative and nondeclarative memory. These are also referred to as explicit/conscious and implicit/unconscious memory, respectively. Declarative or explicit memory consists of episodic (events) and semantic (facts) memory. Nondeclarative or implicit memory consists of priming, skill learning, and conditioning. In everyday experiences (Fig 2), declarative memory refers to things you know that you can tell others, and nondeclarative or procedural memory to things you know that you can show by doing.<sup>6</sup> An example of episodic memory is remembering your first day of school, whereas semantic memory is knowing the capital of Canada. Nondeclarative memory manifests as knowing how to ride a bicycle (skill learning), being more likely to use a word that you recently

## MEMORY IS NOT A UNITARY PHENOMENON

I. **Short term memory** is called **working memory** (seconds or minutes)

II. **Long term memory**

1. **Declarative memory**: explicit or conscious memory.

- a. Episodic memory (events)
- b. Semantic memory (facts)

2. **Nondeclarative memory**: implicit or unconscious memory.

a. Priming

- i. Direct Priming
- ii. Indirect Priming

- a. Semantic priming
- b. Perceptual priming
- c. Conceptual priming

b. Skill Learning

- i. Motor skill
- ii. Perceptual skill
- iii. Cognitive skill

c. Conditioning

FIG 1. Classification of memory.

heard (priming), and salivating when you see a favorite food (conditioning).

The process of memory is dynamic with continual change over time.<sup>5</sup> Memory traces are initially formed as a series of connections between the hippocampus and various cortical areas that are responsible for processing the particular characteristics of an event (Fig 3). Over time, with repetitive conscious retrieval of the memory and/or sleep, connections are formed between the cortical areas relevant for that memory, while the hippocampal connections become less important. Eventually, the hippocampal connections become unnecessary and the cortical connections stand alone as an integrated representation of the memory. This occurs when the memory is consolidated. Figure 4 illustrates a more concrete example of this phenomenon. A particular event (such as a birthday party) with auditory, visual, and spatial information is acquired (encoded). The hippocampus holds a unified representation of the event and the auditory information is distributed to the superior aspect of the temporal lobe, the spatial information is distributed to the parietal lobe (inferior parietal lobule), and the visual information is distributed to the occipital cortex. The memory traces are formed as connections

Received April 9, 2014; accepted after revision April 14.

From the University of Kentucky (F.D.R.), Lexington, Kentucky; and Medical College of Wisconsin (A.P.K., J.L.U., V.M., L.P.M.), Milwaukee, Wisconsin.

Address correspondence to Leighton P. Mark, MD, Froedtert Hospital, Department of Radiology, Neuroradiology Section, 9200 West Wisconsin Ave, Milwaukee, WI 53226; e-mail: lmark@mcw.edu

<http://dx.doi.org/10.3174/ajnr.A4059>

between the hippocampus and these cortical areas. At this point in time, the memory has yet to be consolidated so that retrieval of the memory requires reactivation of the particular connections between the hippocampus and cortical regions. After the memory is consolidated, the cortical-to-cortical connections strengthen and the hippocampal-to-cortical connections weaken or become unnecessary. The memory is then directly accessed from the neocortex, bypassing the hippocampus. A key point is that the early unconsolidated mem-

ory consists of hippocampal-to-cortical connections that are relatively rapid forming but transient, whereas the consolidated memory consists of cortical-to-cortical connections that are slow forming and long-lasting.

Théodule Armand Ribot, a noted French psychologist, first described the concept of memory consolidation in 1882.<sup>7</sup> He noted a temporal gradient to memory loss after brain damage. The tendency for recent memories to be affected to a greater extent than remote memories has become known as Ribot's law. This commonly observed phenomenon among trauma victims underscores the transient and less stable nature of recent memories that have yet to be fully consolidated, especially if the insult occurs early in the memory processing timeframe. Memories in close chronologic proximity to the traumatic event are often lost, whereas memories that are more remote tend to be less affected. The loss of memory for events that happened before an insult/injury to the brain is called retrograde amnesia. The inability to form new memories after brain injury is called anterograde amnesia. When bilateral hippocampal formation injury occurs, the ability to form new memories can be greatly impeded because of the critical

extent than remote memories has become known as Ribot's law. This commonly observed phenomenon among trauma victims underscores the transient and less stable nature of recent memories that have yet to be fully consolidated, especially if the insult occurs early in the memory processing timeframe. Memories in close chronologic proximity to the traumatic event are often lost, whereas memories that are more remote tend to be less affected. The loss of memory for events that happened before an insult/injury to the brain is called retrograde amnesia. The inability to form new memories after brain injury is called anterograde amnesia. When bilateral hippocampal formation injury occurs, the ability to form new memories can be greatly impeded because of the critical

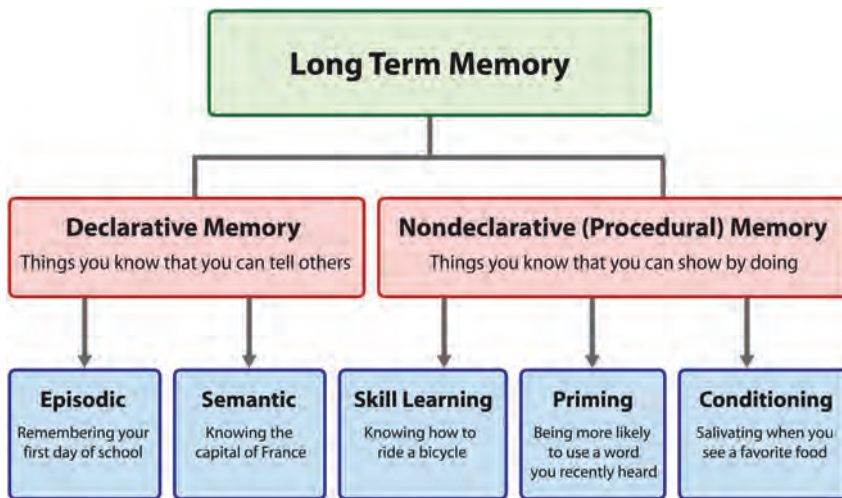


**FIG 2.** The everyday experience of different aspects of memory. Adapted with permission from Breedlove SM, Watson NV, Rosenzweig MR. *Biological Psychology: An Introduction to Behavioral, Cognitive, and Clinical Neuroscience*. 6th ed. Sunderland, Massachusetts: Sinauer Associates; 2010.

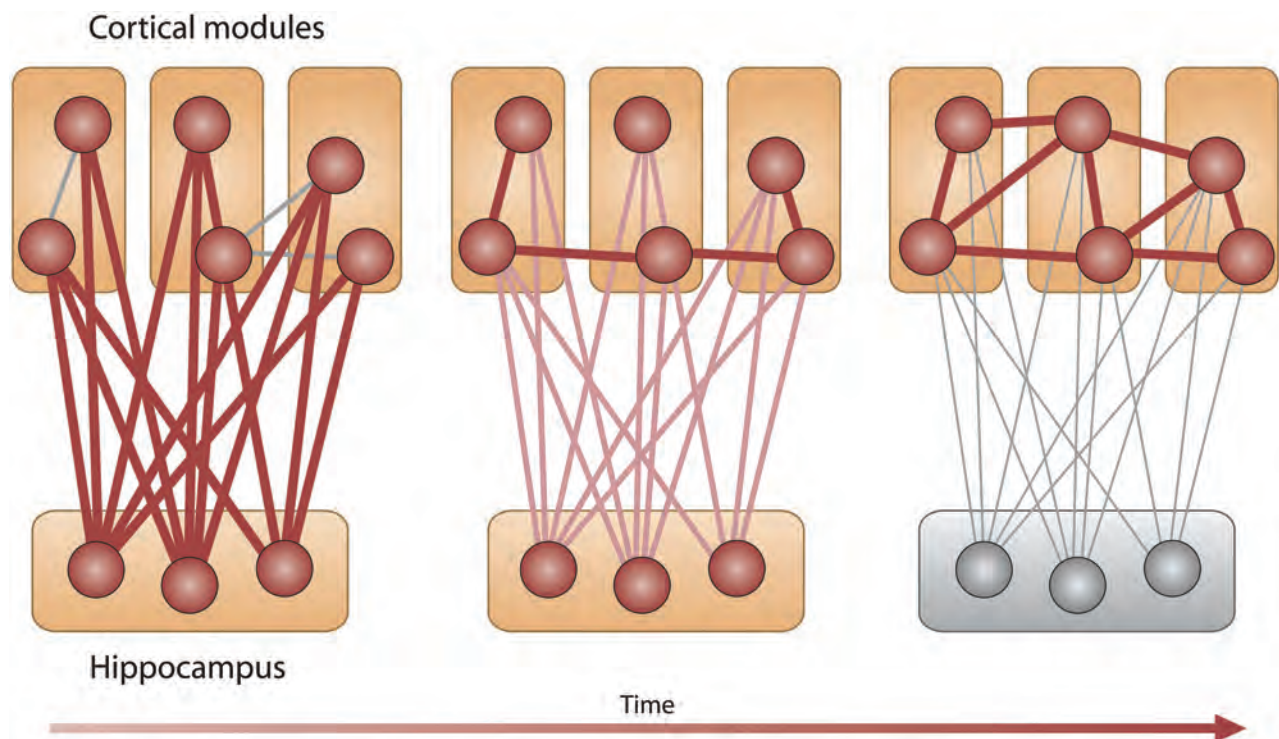


**FIG 3.** Memory consolidation. Connections between the hippocampus and various cortical modules are critical in early memory formation (left). Over time, the cortical modules form connections among themselves and the connections with the hippocampus become less important (center). When the memory is fully consolidated, only the cortical to cortical connections are important and the hippocampus becomes unnecessary (right). Adapted with permission from Frankland PW, Bontempi B. The organization of recent and remote memories. *Nat Rev Neurosci* 2005;6:119–30.

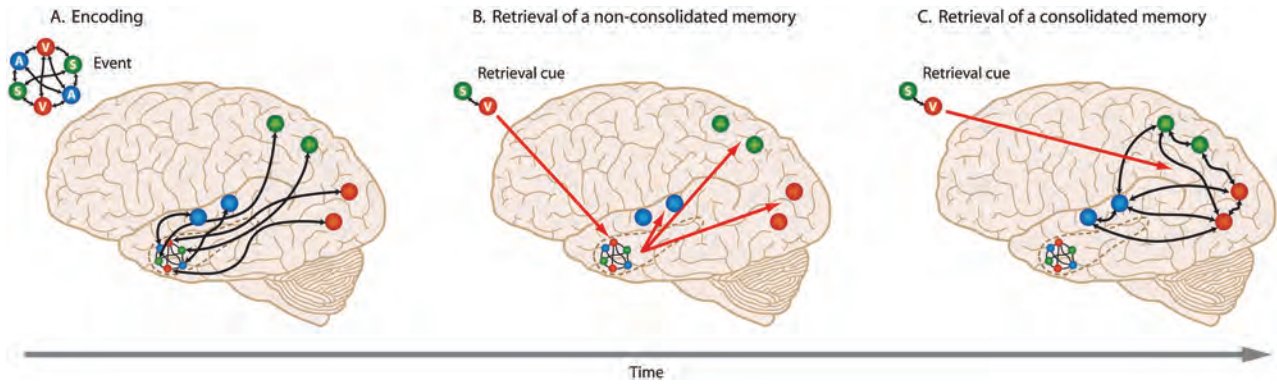


**FIG 4.** Retrieval of nonconsolidated and consolidated memory. A, An event with audio (A), spatial (S), and visual (V) information is encoded. The hippocampus contains a unified representation of the event and forms connections with the relevant cortical areas to process the audio, spatial, and visual information. B, When a retrieval cue containing only spatial and visual information is encountered early in the memory formation process before the memory has been consolidated, the hippocampus plays a critical role by accessing its connections with the pertinent cortical areas for the entire memory. C, After the memory is fully consolidated, the connections with the hippocampus become unnecessary and the retrieval cue accesses the memory directly from the cortical to cortical network of connections that form the unified representation of the memory. Adapted with permission from Purves D, Cabeza R, Huettel SA, et al. *Principles of Cognitive Neuroscience*, 2nd ed. Sunderland, Massachusetts: Sinauer Associates; 2013.

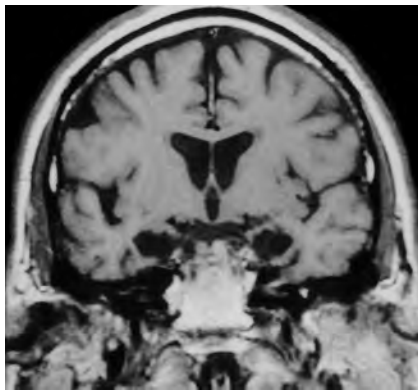


**FIG 5.** Patient H.M. and medial temporal lobe damage. A 1992 coronal T1-weighted image of patient H.M. shows abnormal hippocampal formation hypointense signal after previous bilateral medial temporal lobe resection performed decades earlier for intractable seizures. After the surgery, the patient experienced anterograde amnesia and has been extensively studied for years afterward. Adapted from Corkin S, Amaral DG, González RG, et al. H.M.'s medial temporal lobe lesion: findings from magnetic resonance imaging. *J Neurosci* 1997;17:3964–79.

role the hippocampal formation plays in the early formation of memories. Figure 5 is a coronal T1-weighted image from an MR examination performed in 1992 showing bilateral medial temporal lobe injury to the extensively studied patient, H.M., who in 1953 underwent bilateral resection of the entire piriform-amygdaloid-hippocampal complex for seizures and subsequently experienced severe anterograde amnesia.<sup>8–11</sup>

Many components of the brain (prefrontal cortex, temporal lobe, parietal lobe, occipital lobe, medial diencephalon) are involved in the processes that form memories; however, this review

will focus more on the medial temporal lobe and fornix. These medial temporal lobe components consist of the hippocampal formation, parahippocampal gyrus, parahippocampal cortex, entorhinal cortex, and perirhinal cortex. The contribution of these structures to the function of memory will be the subject of the next article in the Functional Vignettes series.

## REFERENCES

1. Zola-Morgan S, Squire LR. **Neuroanatomy of memory.** *Annu Rev Neurosci* 1993;16:547–63
2. Yancey SW, Phelps EA. **Functional neuroimaging and episodic memory: a perspective.** *J Clin Exp Neuropsychol* 2001;23:32–48
3. Tulving E. **What is episodic memory?** *Curr Dir Psychol Sci* 1993;2: 67–70
4. Squire LR. **Memory systems of the brain: a brief history and current perspective.** *Neurobiol Learn Mem* 2004;82:171–77
5. Frankland PW, Bontempi B. **The organization of recent and remote memories.** *Nat Rev Neurosci* 2005;6:119–30
6. Breedlove SM, Watson NV, Rosenzweig MR. *Biological Psychology: An Introduction to Behavioral, Cognitive, and Clinical Neuroscience.* 6th ed. Sunderland, Massachusetts: Sinauer Associates; 2010
7. Ribot TA. *Diseases of Memory: An Essay in the Positive Psychology.* *The International Scientific Series.* New York: D. Appleton and Co; 1882
8. Corkin S, Amaral DG, González RG, et al. **H.M.'s medial temporal lobe lesion: findings from magnetic resonance imaging.** *J Neurosci* 1997;17:3964–79
9. Salat DH, van der Kouwe AJ, Tuch DS, et al. **Neuroimaging H.M.: 10-year follow-up examination.** *Hippocampus* 2006;16:936–45
10. Schmolck H, Kensinger EA, Corkin S, et al. **Semantic knowledge in patient H.M. and other patients with bilateral medial and lateral temporal lobe lesions.** *Hippocampus* 2002;12:520–33
11. Kensinger EA, Ullman MT, Corkin S. **Bilateral medial temporal lobe damage does not affect lexical or grammatical processing: evidence from amnesic patient H.M.** *Hippocampus* 2001;11:347–60

# Susceptibility-Diffusion Mismatch Predicts Thrombolytic Outcomes: A Retrospective Cohort Study

M. Lou, Z. Chen, J. Wan, H. Hu, X. Cai, Z. Shi, and J. Sun



## ABSTRACT

**BACKGROUND AND PURPOSE:** Asymmetric hypointensity of cerebral veins on susceptibility-weighted imaging has been shown to indirectly reflect tissue hypoxia after cerebral ischemia. We therefore investigated whether patients with prominent asymmetry of the cerebral veins on SWI and a relatively small diffusion-weighted imaging lesion (SWI-DWI mismatch), representing the presence of salvageable tissue, were more likely to benefit from thrombolytic therapy.

**MATERIALS AND METHODS:** We conducted a retrospective study of the anterior circulation of patients with ischemic stroke with SWI/DWI acquired before thrombolysis. The asymmetry index was defined as the ratio of cerebral vein voxel count between the ischemic and normal hemisphere on the SWI phase map. We defined SWI-DWI mismatch as an asymmetry index score of  $\geq 1.75$  with a DWI lesion volume of  $\leq 25$  mL. Favorable outcome was defined as modified Rankin Scale 0–2 at 3 months. Univariate and multivariate logistic regression analyses were used to examine the association between the mismatch profile and favorable outcome.

**RESULTS:** Fifty-four patients undergoing thrombolytic treatment were enrolled in this study. The rate of favorable outcome was significantly higher among patients with baseline SWI-DWI mismatch compared with those without (78% versus 44%; adjusted odds ratio, 6.317; 95% CI, 1.12–35.80;  $P = .037$ ). Patients with SWI-DWI mismatch were also more likely to have a favorable outcome from reperfusion (91% versus 43%,  $P = .033$ ) or recanalization (100% versus 40%,  $P = .013$ ). The accuracy of SWI-DWI mismatch for predicting favorable outcome was higher than that of perfusion-diffusion mismatch (63% versus 48.1%).

**CONCLUSIONS:** The presence of SWI-DWI mismatch may identify patients with ischemia who would benefit from early reperfusion therapy.

**ABBREVIATIONS:** AI = asymmetry index; TIMI = Thrombolysis in Myocardial Infarction; Tmax = time-to-peak of the residue function

Intravenous thrombolysis with recombinant tissue plasminogen activator is a proved treatment for acute ischemic stroke within 4.5 hours of symptom onset.<sup>1</sup> However, increasing evidence indicates that it may be more logical to move from this time-based method to a tissue-based imaging paradigm for patient selection

for thrombolytic therapy because carefully selected patients may still benefit from thrombolytic therapy beyond 4.5 hours.<sup>2</sup> The perfusion-diffusion mismatch model, based on a mismatch between the lesion volume on MR perfusion imaging and diffusion-weighted imaging, has been proposed as a method of selecting patients for reperfusion therapy. Despite theoretic evidence, there is no consensus about the optimal perfusion parameter to accurately define ischemic tissue, and it is uncertain whether perfusion lesion volumes overestimate the penumbra tissue.<sup>3,4</sup> Positron-emission tomography is considered the criterion standard for detection of reversibly damaged tissue. However, its availability is limited to a few centers and restricted by complex logistics.<sup>5</sup> Thus, until now, the optimal method to identify eligible candidates for reperfusion therapy in the acute setting remains elusive.

More recently, susceptibility-weighted imaging, which was originally called blood oxygen level–dependent venographic imaging, has demonstrated advantages over conventional gradient-echo T2\*-weighted imaging in the detection of hemorrhagic events due to its exquisite sensitivity to paramagnetic substances

Received January 17, 2014; accepted after revision March 23.

From the Departments of Neurology (M.L., Z.C., J.W., H.H., X.C., Z.S.) and Radiology (J.S.), the Second Affiliated Hospital of Zhejiang University, School of Medicine, Hangzhou, China.

This work was supported by the Science Technology Department of Zhejiang Province (grant 2013C13G2010032), Zhejiang Provincial Natural Science Foundation of China (grant LR12H09001), and the National Natural Science Foundation of China (grant 81171095).

Please address correspondence to Jianzhong Sun, MB, Department of Neurology, e-mail: hzjszjz@163.com; or Min Lou, MD, PhD, Department of Radiology, the Second Affiliated Hospital of Zhejiang University School of Medicine, 88 Jiefang Rd, Hangzhou, China; e-mail: loumingxc@vip.sina.com

Indicates open access to non-subscribers at www.ajnr.org

Indicates article with supplemental on-line tables.

<http://dx.doi.org/10.3174/ajnr.A4017>

such as deoxyhemoglobin.<sup>6</sup> SWI venography allows clear visualization of cerebral veins.<sup>7</sup> Shortly after arterial occlusion in patients with acute stroke, there is an increase in deoxyhemoglobin and a decrease in oxyhemoglobin within cerebral veins and tissue capillaries, due to an increase in the oxygen extraction fraction.<sup>8-10</sup> This intravascular deoxygenation leads to a signal drop along the course of cerebral veins on SWI venography.<sup>11-14</sup> SWI venography may thus provide the oxygen metabolic information about ischemic brain tissue by the noninvasive estimation of blood oxygen level–dependent levels.

A previous study by using gradient-echo T2\*-weighted imaging demonstrated that abnormal hypointensity of the deep cerebral veins was correlated with a delayed mean transit time and a large perfusion defect.<sup>9</sup> Abnormal hypointensity of superficial cerebral veins also correlates with increased cerebral blood volume.<sup>15</sup> Due to the relatively poor resolution of gradient-echo T2\*-weighted imaging, no previous studies combined the deep and superficial venous systems as a whole when examining the clinical implications of hypointense cerebral veins. The higher resolution of SWI allowed us to evaluate the ischemic state of the whole brain and the level of tissue hypoxia caused by hypoperfusion. We then developed a novel mismatch model, based on prominent hypointense cerebral veins on SWI and a relatively small DWI lesion (SWI-DWI mismatch), and tested whether this model was more likely to benefit from thrombolytic therapy.

## MATERIALS AND METHODS

### Patients

We retrospectively reviewed our prospectively collected data base for consecutive patients with acute ischemic stroke who received intravenous rtPA (alteplase, 0.9 mg/kg, up to a maximum of 90 mg; 10% of the total dosage as a bolus and the rest during 1 hour) within 6 hours after symptom onset from August 2009 to December 2012. Our predefined inclusion criteria for MR imaging–guided intravenous thrombolysis included the following: 1) age older than 18 years; 2) stroke symptoms lasting >1 hour; 3) an NIHSS score of  $\geq 4$  or NIHSS score of <4 but with aphasia or severe dysarthria; 4) the absence of intracranial hemorrhage confirmed by SWI; 5) onset-to-treatment time within 4.5 hours and fulfilling standard clinical criteria, or onset-to-treatment time of 4.5–6 hours with large-vessel occlusion on MR angiography and fulfilling the perfusion-diffusion mismatch criteria: DWI lesion of  $\leq 70$  mL, a perfusion lesion to diffusion lesion volume ratio of  $\geq 1.2$ , and an absolute difference between perfusion and diffusion lesion volume of >10 mL.<sup>16</sup> Standard IV thrombolysis exclusion criteria were applied according to current guidelines.<sup>17</sup> We prospectively obtained baseline demographic and clinical information. All subjects gave written informed consent before the study, and the protocols were approved by the human ethics committee of the hospital. All procedures were conducted according to the principles expressed in the Declaration of Helsinki.

### MR Imaging Protocol

Multimodal MR imaging was performed on a 3T system (Signa Excite HD; GE Healthcare, Milwaukee, Wisconsin) before initiation of thrombolysis. Structural imaging included DWI (TR = 4000 ms, TE = 69.3 ms, b-value = 1000 s/mm<sup>2</sup>, acquisition ma-

trix = 160 × 160, FOV = 240 mm, section thickness = 5 mm, section gap = 1 mm, duration = 32 seconds), a perfusion-weighted sequence (TR/TE = 1500/30 ms, acquisition matrix = 128 × 128, dynamic scans = 50, FOV = 240 mm, section thickness = 5 mm, section gap = 1 mm, gadolinium dose = 15 mL, contrast speed = 4–5 mL/s, duration = 1 minute 15 seconds), time-of-flight MR angiography (TR/TE/flip angle = 20 ms/3.2 ms/15°, acquisition matrix = 320 × 224, section thickness = 1.4 mm, 3 slabs, duration = 3 minutes 46 seconds), and SWI (3D multiecho T2\*-weighted gradient-echo sequence, TR/TE/flip angle = 58 ms/5.0 ms/20°, FOV = 240 mm, acquisition matrix = 384 × 32, section thickness = 2 mm, duration = 3 minutes 27 seconds). The entire duration of the MR imaging protocol was 15 minutes.

### Follow-Up Protocol and Clinical Assessments

All patients experiencing thrombolysis underwent follow-up multimodal MR imaging within 24 hours after treatment. Clinical follow-up assessments included the NIHSS score at 1, 4, and 24 hours, 7 days, and 1 month and modified Rankin Scale scores at 1 and 3 months. Early NIHSS improvement was defined as an increase on the NIHSS of at least 8 points between baseline and 1 week after onset or an NIHSS score = 0 at 1 week.<sup>18</sup> Favorable outcome was defined as mRS 0–2 at 3 months.

### Radiologic Assessment

DWI lesion volumes were measured by using a semiautomated thresholding algorithm that identified the region with intensity higher than that in the contralateral frontal lobe by >3 SDs.<sup>19</sup> Artfactual lesion areas were visually identified by an experienced neuroradiologist (J.S.) and were manually removed. Time-to-peak of the residue function (Tmax) maps were generated by deconvolution of the tissue concentration–time curve by using an arterial input function from the contralateral middle cerebral artery.<sup>19,20</sup> The perfusion lesion was defined as a Tmax delay of >6 seconds.<sup>21</sup> Reperfusion was defined as a  $\geq 50\%$  and  $\geq 10$  mL reduction of PWI lesion volume<sup>22</sup> between baseline and follow-up within 24 hours of MR imaging. PWI lesions of  $\leq 3$  mL were excluded.<sup>23</sup>

The MRA was rated independently by 3 experienced stroke neurologists (M.L., Z.C., and J.S.), who then reached consensus by using the Thrombolysis in Myocardial Infarction (TIMI) grading scale<sup>16,24</sup>: 0 = complete occlusion, which was defined as lack of flow signal of a vascular segment and distal vessels; 1 = severe stenosis, defined as severe or critical stenosis of a vascular segment with significant reduction of flow signal distal to stenosis; 2 = mild-to-moderate stenosis, which was characterized by stenosis with normal distal flow signal; 3 = normal arterial caliber. Recanalization was defined as improvement of TIMI grading by  $\geq 2$  points from baseline to follow-up MRA.

### Definition of the Asymmetry Index

We used a high-pass filter with a central matrix size of 32 × 32 to remove background field inhomogeneities to create the corrected SWI phase images. We used MRIcro software (<http://www.mccauslandcenter.sc.edu/mricro/mricro/mricro.html>) to assess venous structures in 5 consecutive sections around the level of the lateral ventricles (from immediately above the basal ganglia to the highest section including the ventricle) because these sections in-

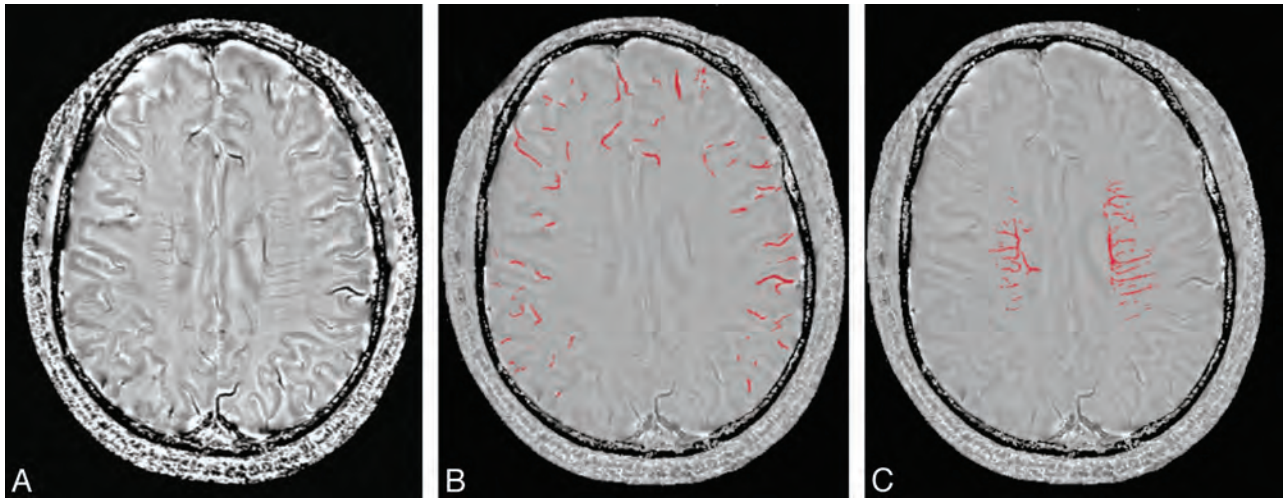


**FIG 1.** Image postprocessing and segmentation of cerebral venous structures based on SWI phase images. The SWI phase image (A) was used to calculate the number of voxels of superficial cerebral veins (B) and deep cerebral veins (C) for quantification after segmentation. The asymmetry index of cerebral veins was set as a ratio of voxel numbers of cerebral veins between the ipsilateral and contralateral side.

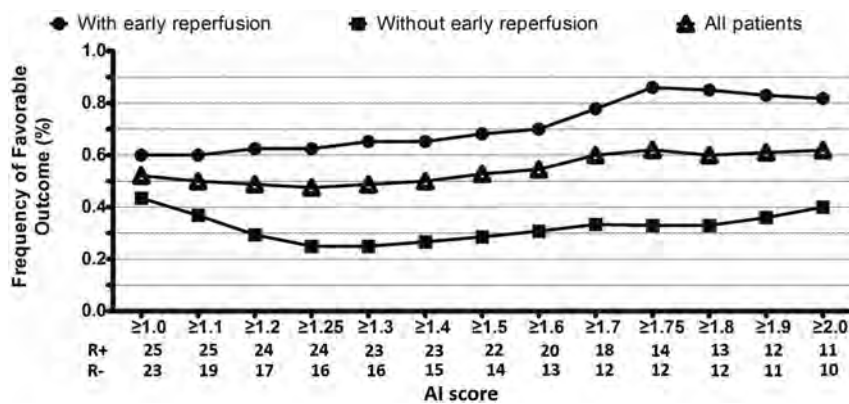


**FIG 2.** The AI score was positively correlated with the frequency of favorable outcome in patients with early reperfusion. The optimal AI score was set as 1.75 based on maximizing the Youden index (sensitivity, 83%; specificity, 67%; Youden index, 53%) for predicting favorable outcome in patients with early reperfusion. R (+) indicates the number of patients with early reperfusion; R (–), the number of patients without early reperfusion.

clude most of the cerebral veins draining the anterior circulation territory. The segmentation threshold for deep and superficial cerebral veins was determined as 2 SDs in voxel intensity below the mean of the fitted distribution of white matter and cortex, respectively (Fig 1). Bilateral venous voxel counts were computed, and an asymmetry index (AI) was defined as the ratio of the venous voxel number between the ischemic and normal hemispheres to eliminate individual bias.<sup>25–27</sup>

### Definition of SWI-DWI Mismatch

The interaction among early reperfusion, AI score, and favorable outcome was assessed (Fig 2), and receiver operating characteristic analysis was used to determine the cutoff value for an optimal AI score when it gave the highest Youden index.<sup>20</sup> We defined SWI-DWI mismatch as an AI score greater than the optimal threshold and a DWI lesion of  $\leq 25$  mL.<sup>28,29</sup> To examine whether patients with SWI-DWI mismatch were more likely to benefit from reperfusion or recanalization after rtPA therapy, we compared the rate of favorable outcome from reperfusion or recanalization between patients with and without SWI-DWI mismatch.

We also compared the accuracy of this novel SWI-DWI mismatch with the perfusion-diffusion mismatch. We used several different perfusion-diffusion mismatch definitions: 1) standard PWI-DWI mismatch: mismatch ratio of  $\geq 1.2$  and absolute mismatch of  $\geq 10$  mL<sup>16</sup>; 2) optimal PWI-DWI mismatch: mismatch ratio of  $\geq 2.6$  and absolute mismatch of  $\geq 10$  mL<sup>20</sup>; 3) target PWI-DWI mismatch: mismatch ratio  $\geq 1.2$ , absolute mismatch  $\geq 10$  mL, Tmax  $\geq 8$  seconds, lesion  $\leq 100$  mL, and DWI  $\leq 100$  mL.<sup>30</sup>

### Statistical Analysis

We divided patients into high and low AI groups, by using the Youden-derived threshold. We also compared variables

between patients with and without SWI-DWI mismatch. We used the Fisher exact test to compare dichotomous variables between groups, the *t* test for normally distributed continuous variables, and the Wilcoxon rank sum test for ordinal variables and non-normally distributed continuous variables. Univariate and multivariate logistic regression analyses were used to investigate whether SWI-DWI mismatch was an independent predictor of favorable outcome. Statistical significance was set at  $P < .05$ . All statistical analyses were performed by using SPSS, Version 19 (IBM, Armonk, New York).

### RESULTS

Eighty consecutive patients had multimodal MR imaging, and 60 had cerebral infarction in the anterior circulation territory. Six patients were excluded before the analysis because of poor-quality SWI due to dental artifacts (1 patient) and motion artifacts (5 patients), which interfered with the assessment of cerebral veins. Thus 54 patients were included in the analysis. The mean age of the patients was  $69 \pm 13$  years, and the median baseline NIHSS

**Table 1: Univariate analysis of the baseline variables according to the asymmetry index of cerebral veins<sup>a</sup>**

Variable	High AI (n = 27)	Low AI (n = 27)	P Value
Mean age (yr)	69 ± 13	69 ± 14	.926
Sex, female (%)	8 (30%)	13 (48%)	.264
Serum glucose (mmol/L)	141 ± 41	159 ± 72	.268
Systolic BP (mm Hg)	156 ± 19	153 ± 24	.653
Time to imaging (min)	175 ± 58	186 ± 68	.514
Time to treatment (min)	222 ± 68	235 ± 60	.448
Baseline NIHSS score	15 (6–18)	9 (5–14)	.096
Stroke risk factors			
Atrial fibrillation (%)	13 (48%)	11 (41%)	.785
Hypertension (%)	20 (74%)	18 (67%)	.766
Diabetes mellitus (%)	7 (26%)	9 (33%)	.766
Hyperlipidemia (%)	11 (41%)	9 (33%)	.779
Current smoking (%)	11 (41%)	4 (15%)	.066
Coronary heart disease (%)	7 (26%)	8 (30%)	1.000
Hyperhomocysteinemia (%)	9 (33%)	7 (26%)	.766
White blood cell/mm <sup>3</sup>	7.1 ± 2.2	8.3 ± 2.4	.052
PT (sec)	12.7 ± 0.9	12.4 ± 1.4	.368
APTT (sec)	27.6 ± 5.6	25.3 ± 3.4	.066
INR	1.06 ± 0.08	1.03 ± 0.12	.325
Fibrinogen level (g/L)	7.7 ± 24.9	2.8 ± 0.9	.313
Serum creatinine level (mg/dL)	0.82 ± 0.14	0.99 ± 0.93	.366
Serum urea nitrogen level (mg/dL)	16.2 ± 5.1	16.1 ± 4.3	.909
TIMI grading	1 (0–1)	2 (0–3)	.002 <sup>b</sup>
Sites of occlusion			.042 <sup>b</sup>
Proximal	22	14	
Distal	5	13	
DWI lesion volume (mL)	37 ± 57	15 ± 33	.091
PWI lesion volume (mL)	120 ± 83	58 ± 67	.004 <sup>b</sup>
24-Hour DWI lesion volume (mL)	66 ± 82	35 ± 69	.131
Hemorrhagic transformation (%)	11 (41%)	7 (26%)	.387
HI	7 (26%)	5 (19%)	.745
PH	4 (15%)	2 (33%)	.669
sICH	1 (4%)	2 (7%)	1.000
Favorable outcome	17 (63%)	13 (48%)	.412

**Note:**—BP indicates blood pressure; PT, prothrombin time; APTT, activated partial thromboplastin time; INR, international normalized ratio; HI, hemorrhagic infarction; PH, parenchymal hematoma; sICH, symptomatic intracerebral hemorrhage.

<sup>a</sup>Table cells express results in mean ± SD for normally distributed continuous variables, *n* (%) for dichotomous variables, and median (interquartile range) for ordinal variables and non-normally distributed continuous variables, respectively.

<sup>b</sup>*P* < .05.

score was 12 (interquartile range, 5–17). Eight patients received thrombolytic therapy beyond 4.5 hours according to the criteria described in “Materials and Methods.” Favorable outcome occurred in 3/3 with SWI-DWI mismatch versus 1/5 (20%) without SWI-DWI mismatch.

#### Optimal AI Score for SWI-DWI Mismatch Analysis

As shown in Fig 2, in the presence of reperfusion, the rate of favorable outcome correlated with increasing AI score. Receiver operating characteristic analysis revealed that the optimal threshold for the AI score was 1.75 (sensitivity, 86%; specificity, 67%; Youden index, 53%) for predicting favorable outcome from early reperfusion.

#### AI Score and Hypoperfusion Lesion Volume

Table 1 summarizes the baseline and 24-hour follow-up variables in patients with high (*n* = 27) versus low AI scores (*n* = 27). Univariate analysis showed that patients with high AI scores had more frequent arterial occlusion (median TIMI 1 [interquartile range, 0–1] versus 2 [interquartile range, 0–3], *P* = .002) and

larger perfusion lesion volume (120 ± 83 mL versus 58 ± 67 mL, *P* = .004) than those with a low AI score. Figure 3 illustrates the relationship among AI score, perfusion lesion volume, and TIMI grading.

#### SWI-DWI Mismatch and Favorable Outcome

SWI-DWI mismatch, defined by a high AI score (AI ≥ 1.75) with a small DWI lesion volume (≤25 mL), was present in 18 of 54 patients (33%). Univariate analysis showed that patients with SWI-DWI mismatch were more likely to have early NIHSS improvement (67% versus 31%, *P* = .019) and favorable outcome (On-line Table 1) compared with those without SWI-DWI mismatch (78% versus 44%, *P* = .024). The rates of reperfusion, recanalization, and hemorrhagic transformation were not significantly different between these 2 groups. Logistic regression analysis revealed that the presence of SWI-DWI mismatch (OR = 6.317; 95% CI, 1.12–35.80; *P* = .037) was independently associated with favorable outcome (On-line Table 2).

#### Favorable Outcome of SWI-DWI Mismatch based on Reperfusion

Table 2 shows that 11 patients (61%) with SWI-DWI mismatch and 14 (39%) patients without it achieved reperfusion. Patients with SWI-DWI mismatch were more likely to obtain favorable outcome from reperfusion than those without SWI-DWI mismatch (91% versus 43%, *P* = .033).

#### Comparison of Accuracy between SWI-DWI Mismatch and PWI-DWI Mismatch

As shown in Table 3, the accuracy of SWI-DWI mismatch (63.0%) was higher than that of PWI-DWI mismatch (37.0% for standard PWI-DWI mismatch, 44.4% for optimal PWI-DWI mismatch, 48.1% for target PWI-DWI mismatch).

#### DISCUSSION

Our study proposes a novel SWI-DWI mismatch paradigm for predicting neurologic outcome after intravenous thrombolysis. Patients with SWI-DWI mismatch had a higher rate of favorable outcome than those without this mismatch (78% versus 44%). The accuracy of SWI-DWI mismatch was higher than that of PWI-DWI mismatch in the current study. Thus, SWI-DWI mismatch may provide an alternative method for selecting patients who are good candidates for thrombolytic therapy.

Deoxyhemoglobin is used as an endogenous contrast agent due to its paramagnetic properties on SWI. Because venous blood volume contains higher concentrations of deoxyhemoglobin, the

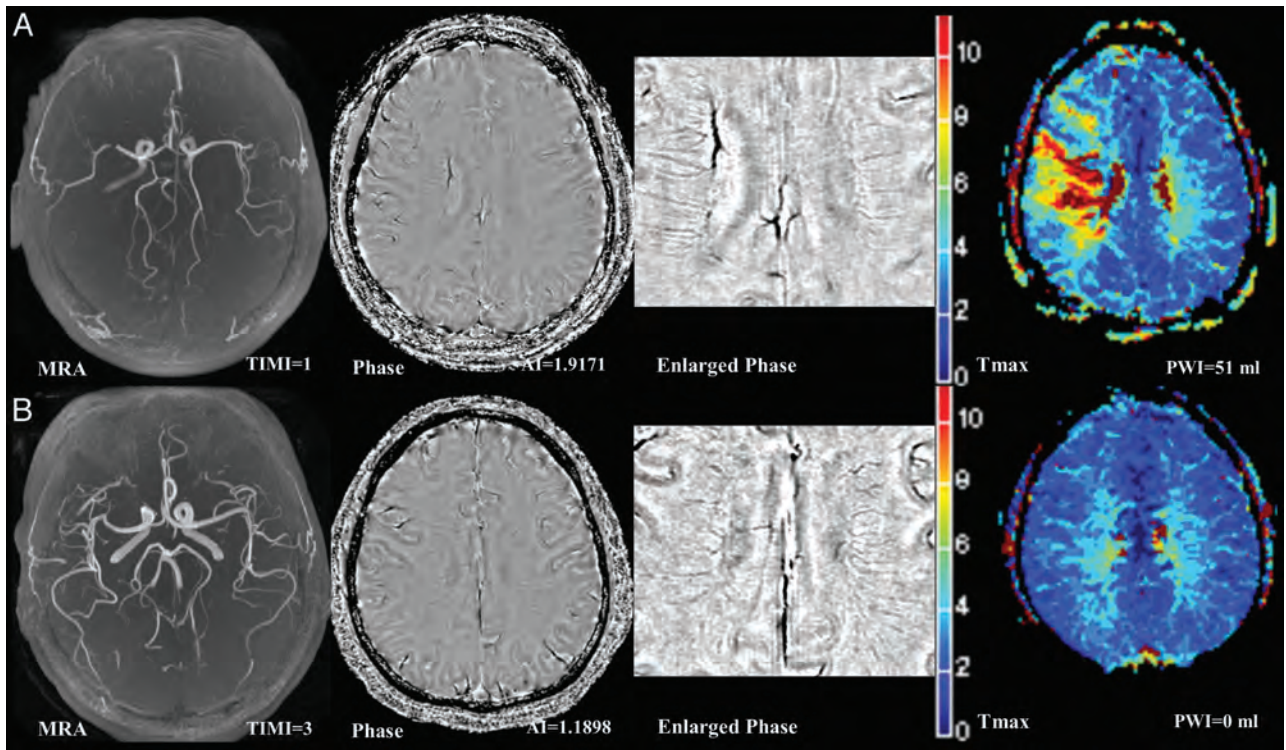


**FIG 3.** Representative pretreatment MR imaging in patients receiving thrombolysis. The first column on the left depicts time-of-flight MR angiography; the second and third columns depict phase images of susceptibility-weighted imaging and an enlarged view focusing on the deep cerebral veins. The right column depicts Tmax maps of perfusion-weighted MR imaging. Patients with a high AI score (A, TIMI = 1, AI score = 1.92, PWI lesion volume = 51 mL) had a lower TIMI score and larger PWI lesion volume than those with low AI scores (B, TIMI = 3, AI score = 1.19, PWI lesion volume = 0 mL).

**Table 2: Different outcomes in patients with or without SWI-DWI mismatch based on reperfusion**

	Reperfusion		No Reperfusion	
	Total	Favorable Outcome	Total	Favorable Outcome
SWI-DWI Mismatch ( <i>n</i> = 18)	11	10 (91%)	7	4 (57%)
Non-SWI-DWI mismatch ( <i>n</i> = 36)	14	6 (43%)	22	10 (45%)
<i>P</i> value		.033		.682

**Table 3: The sensitivity, specificity, and accuracy between SWI-DWI and PWI-DWI mismatches<sup>a</sup>**

	Sensitivity	Specificity	Accuracy	AUC
SWI-DWI mismatch	46.7	55.6	63.0%	0.511
Standard PWI-DWI mismatch	63.3	8.3	37.0%	0.338
Optimal PWI-DWI mismatch	60.0	25.0	44.4%	0.425
Target PWI-DWI mismatch	63.3	38.9	48.1%	0.463

**Note:**—AUC indicates area under the curve.

<sup>a</sup> Accuracy is the proportion of true results (both true-positives and true-negatives) in the population. Standard PWI-DWI mismatch was defined as PWI/DWI  $\geq$  1.2, PWI-DWI  $\geq$  10 mL. Optimal PWI-DWI mismatch was defined as PWI/DWI  $\geq$  2.6 and PWI-DWI  $\geq$  10 mL. Target PWI-DWI mismatch was defined as PWI/DWI  $\geq$  1.2, PWI-DWI  $\geq$  10 mL, PWI (Tmax  $\geq$  8 seconds)  $\leq$  100 mL, and DWI  $\leq$  100 mL.

signal change on SWI is mainly related to venous structures.<sup>11-14</sup> In the setting of acute arterial occlusion, decreased oxygen supply causes an increased tissue oxygen extraction fraction, which leads to the increased level of deoxyhemoglobin and results in signal reduction of ipsilateral cerebral veins in the ischemic tissue on phase maps.<sup>8-10</sup> Thus, as in the previous studies on gradient-echo T2\*-weighted imaging,<sup>25,26</sup> we used asymmetry of cerebral veins

to reflect the change of oxygen extraction fraction in the ischemic hemisphere.

In the current study, we found that patients with a high cerebral vein AI score after ischemic stroke were more likely to have severe arterial occlusion and hypoperfusion. This outcome is consistent with that in a previous study which, by using gradient-echo T2\*-weighted imaging, demonstrated that abnormal prominent deep cerebral veins were correlated with a delayed MTT, a large perfusion defect, and increased CBV.<sup>9</sup> Prominent superficial cerebral veins have also been correlated with an increase in CBV.<sup>15</sup> Recently, an Alberta Stroke Program Early CT Score–based rating of asymmetric prominent vessels on SWI was shown to correlate best with MTT in patients with nonlacunar ischemic stroke within 24 hours after symptom onset.<sup>27</sup> Therefore, extensive hypointense cerebral veins on SWI may be a useful indicator of ipsilateral large-artery occlusion and severe hypoperfusion. Most important, unlike the previous study, which found an association between abnormal visualization of the superficial venous system on gradient-echo T2\*-weighted imaging and smaller DWI lesions,<sup>15</sup> we did not find such an association between the AI score and DWI lesion volume. According to previous literature,<sup>31,32</sup> the superficial cerebral veins and deep cerebral veins differ in anatomic structure and function.<sup>25,33</sup> We, therefore, considered it improper to compare the change of partial draining veins with DWI lesions.

We then tested the SWI-DWI mismatch, which may represent the presence of salvageable tissue based on tissue oxygen metabolism, and found that patients with SWI-DWI mismatch were

more likely to benefit from thrombolytic therapy. One might argue that the relatively small DWI lesion volume in SWI-DWI mismatch may have a critical impact on patient outcome. However, we did not find a significant relationship between posttreatment neurologic outcome and either baseline DWI lesion volume or the AI score alone from logistic regression. Several studies have demonstrated metabolic derangement and evolution of infarction in brain regions with increased oxygen extraction fraction by PET.<sup>34,35</sup> An increased oxygen extraction fraction may be a target for acute therapy to improve compromised cerebral circulation. Our study further revealed that in the presence of reperfusion, patients with SWI-DWI mismatch were more likely to have favorable outcome, compared with patients without it. We speculate that the presence of SWI-DWI mismatch after arterial occlusion in acute stroke may indicate salvageable tissue. The compensatory increase of oxygen uptake by tissue can provide the hypoxic tissue with a chance to revive if there is timely reperfusion. Therefore, we believe this MR imaging profile can identify the subgroup who may benefit from early reperfusion therapy. However, quantitative metabolic parameters that relate directly to the cerebral metabolic rate of oxygen consumption detected by PET are needed to assess this hypothesis.

The main advantage of using the SWI-DWI mismatch is that it provides a new concept to examine the penumbra on the basis of tissue oxygen metabolism. Although the SWI-DWI mismatch is not able to directly measure the cerebral metabolic rate of oxygen consumption, the concept of SWI-DWI mismatch is more closely aligned with the fundamental pathogenesis of neuronal energy disruption in acute ischemia than the perfusion-diffusion mismatch. In the perfusion-diffusion mismatch, identifying a perfusion threshold to reliably differentiate critically hypoperfused tissue<sup>21</sup> from benign oligemia, which will survive regardless of reperfusion,<sup>20,36</sup> is a major challenge. The site of vascular occlusion and the extent of collateral blood flow also affect the complex relationship between perfusion lesions and their final fate. Another potential advantage of SWI over MR perfusion is that it obviates gadolinium contrast, which is contraindicated in patients with severe renal insufficiency or gadolinium allergy.<sup>37</sup> The SWI-DWI mismatch may therefore be a useful alternative method that does not require MR perfusion to select patients who are good candidates for thrombolytic therapy. Moreover, our finding that patients with SWI-DWI mismatch achieved more favorable outcome based on successful reperfusion lends support to its future application in patients treated with an endovascular approach. In the current study, approximately 33% of patients had SWI-DWI mismatch. This was similar to the proportion (36%) with “optimal” mismatch (mismatch ratio of >2.6) in post hoc analysis of the Diffusion and Perfusion Imaging Evaluation for Understanding Stroke Evolution study.<sup>20</sup> These patients may be a suitable “responder” subgroup for randomization between reperfusion therapy and standard therapy.

There are limitations to our study. First, the exploratory nature of this study and the relatively small number of subjects necessitate the validation of the SWI-DWI mismatch model in an external dataset. Our conclusions should be considered hypothesis-generating and require further testing in prospective studies. Second, the asymmetry index of signal reduction along the cere-

bral veins may vary among different MR imaging magnetic field strengths and can be influenced by the presence of microbleeds and a previous large ischemic stroke. Moreover, the segmentation of cerebral veins may be partly affected by cortex and ependymal epithelium signals. Third, the relationship of oxygen consumption and SWI-DWI mismatch needs further validation by PET studies. Fourth, the postprocessing and calculation of the AI index would take an additional 3 minutes, which may delay thrombolysis. Fifth, the definition of reperfusion and recanalization by MR imaging are still not unified. Last, our conclusions were all based on patients receiving tPA, without a control group, though we analyzed the outcome on the basis of reperfusion. Thus, we could not clarify whether withholding thrombolytic therapy in patients without a mismatch would yield better results. A randomized controlled trial would be needed to validate the usefulness of the SWI-DWI mismatch in the selection of patients for reperfusion therapy.

## CONCLUSIONS

A high AI score of cerebral veins may be related to arterial occlusion or severe hypoperfusion. The presence of an SWI-DWI mismatch may predict a favorable outcome after intravenous thrombolysis. Our data provide evidence that SWI venography, related to oxygen metabolism, may provide an alternative for the evaluation of patients with acute ischemic stroke.

## ACKNOWLEDGMENTS

We are grateful for the support from our patients. The authors thank Yi-hong Zhu, MD, from Zhejiang University School of Public Health for the critical verification of statistics, and Bruce Campbell, MD, from the Department of Neurology, Royal Melbourne Hospital, Australia, for the critical reading of the manuscript.

Disclosures: Min Lou—RELATED: grant support: Science Technology Department of Zhejiang Province (grant 2013C13G2010032), Zhejiang Provincial Natural Science Foundation (grant LR12H09001), and the National Natural Science Foundation of China (grant 81171095).\* \*Money paid to the institution.

## REFERENCES

1. Hacke W, Kaste M, Bluhmki E, et al. **Thrombolysis with alteplase 3 to 4.5 hours after acute ischemic stroke.** *N Engl J Med* 2008;359:1317–29
2. Bivard A, Spratt N, Levi CR, et al. **Acute stroke thrombolysis: time to dispense with the clock and move to tissue-based decision making?** *Expert Rev Cardiovasc Ther* 2011;9:451–61
3. Grandin CB, Duprez TP, Smith AM, et al. **Which MR-derived perfusion parameters are the best predictors of infarct growth in hyperacute stroke? Comparative study between relative and quantitative measurements.** *Radiology* 2002;223:361–70
4. Heiss WD. **The ischemic penumbra: correlates in imaging and implications for treatment of ischemic stroke: the Johann Jacob Wepfer award 2011.** *Cerebrovasc Dis* 2011;32:307–20
5. Sobesky J. **Refining the mismatch concept in acute stroke: lessons learned from PET and MRI.** *J Cereb Blood Flow Metab* 2012;32:1416–25
6. Wang M, Dai Y, Han Y, et al. **Susceptibility weighted imaging in detecting hemorrhage in acute cervical spinal cord injury.** *Magn Reson Imaging* 2011;29:365–73
7. Haacke EM, Xu Y, Cheng YC, et al. **Susceptibility weighted imaging (SWI).** *Magn Reson Med* 2004;52:612–18

8. An H, Lin W. **Quantitative measurements of cerebral blood oxygen saturation using magnetic resonance imaging.** *J Cereb Blood Flow Metab* 2000;20:1225–36
9. Hermier M, Nighoghossian N, Derex L, et al. **Hypointense transcerebral veins at T2\*-weighted MRI: a marker of hemorrhagic transformation risk in patients treated with intravenous tissue plasminogen activator.** *J Cereb Blood Flow Metab* 2003;23:1362–70
10. Lee JM, Vo KD, An H, et al. **Magnetic resonance cerebral metabolic rate of oxygen utilization in hyperacute stroke patients.** *Ann Neurol* 2003;53:227–32
11. Heiss WD. **Ischemic penumbra: evidence from functional imaging in man.** *J Cereb Blood Flow Metab* 2000;20:1276–93
12. Powers WJ. **Cerebral hemodynamics in ischemic cerebrovascular disease.** *Ann Neurol* 1991;29:231–40
13. Robertson CA, McCabe C, Gallagher L, et al. **Stroke penumbra defined by an MRI-based oxygen challenge technique. 2. Validation based on the consequences of reperfusion.** *J Cereb Blood Flow Metab* 2011;31:1788–98
14. Santosh C, Brennan D, McCabe C, et al. **Potential use of oxygen as a metabolic biosensor in combination with T2\*-weighted MRI to define the ischemic penumbra.** *J Cereb Blood Flow Metab* 2008;28:1742–53
15. Hermier M, Nighoghossian N, Derex L, et al. **Hypointense leptomeningeal vessels at T2\*-weighted MRI in acute ischemic stroke.** *Neurology* 2005;65:652–53
16. Davis SM, Donnan GA, Parsons MW, et al. **Effects of alteplase beyond 3 h after stroke in the Echoplanar Imaging Thrombolytic Evaluation Trial (EPITHET): a placebo-controlled randomised trial.** *Lancet Neurol* 2008;7:299–309
17. Jauch EC, Saver JL, Adams HP Jr, et al. **Guidelines for the early management of patients with acute ischemic stroke: a guideline for healthcare professionals from the American Heart Association/American Stroke Association.** *Stroke* 2013;44:870–947
18. Cappellari M, Bovi P, Moretto G, et al. **The THRombolysis and STatins (THRaST) study.** *Neurology* 2013;80:655–61
19. Olivot JM, Mlynash M, Thijs VN, et al. **Relationships between cerebral perfusion and reversibility of acute diffusion lesions in DEFUSE: insights from RADAR.** *Stroke* 2009;40:1692–97
20. Kakuda W, Lansberg MG, Thijs VN, et al. **Optimal definition for PWI/DWI mismatch in acute ischemic stroke patients.** *J Cereb Blood Flow Metab* 2008;28:887–91
21. Olivot JM, Mlynash M, Thijs VN, et al. **Optimal Tmax threshold for predicting penumbral tissue in acute stroke.** *Stroke* 2009;40:469–75
22. Lansberg MG, Straka M, Kemp S, et al. **MRI profile and response to endovascular reperfusion after stroke (DEFUSE 2): a prospective cohort study.** *Lancet Neurol* 2012;11:860–67
23. Straka M, Albers GW, Bammer R. **Real-time diffusion-perfusion mismatch analysis in acute stroke.** *J Magn Reson Imaging* 2010;32:1024–37
24. Fiebach JB, Al-Rawi Y, Wintermark M, et al. **Vascular occlusion enables selecting acute ischemic stroke patients for treatment with desmoteplase.** *Stroke* 2012;43:1561–66
25. Jensen-Kondering U, Böhm R. **Asymmetrically hypointense veins on T2\*w imaging and susceptibility-weighted imaging in ischemic stroke.** *World J Radiol* 2013;5:156–65
26. Rosso C, Belleville M, Pires C, et al. **Clinical usefulness of the visibility of the transcerebral veins at 3T on T2\*-weighted sequence in acute stroke patients.** *Eur J Radiol* 2012;81:1282–87
27. Kao HW, Tsai FY, Hasso AN. **Predicting stroke evolution: comparison of susceptibility-weighted MR imaging with MR perfusion.** *Eur Radiol* 2012;22:1397–403
28. Lansberg MG, Thijs VN, Bammer R, et al. **The MRA-DWI mismatch identifies patients with stroke who are likely to benefit from reperfusion.** *Stroke* 2008;39:2491–96
29. Parsons MW, Christensen S, McElduff P, et al. **Pretreatment diffusion- and perfusion-MR lesion volumes have a crucial influence on clinical response to stroke thrombolysis.** *J Cereb Blood Flow Metab* 2010;30:1214–25
30. Albers GW, Thijs VN, Wechsler L, et al. **Magnetic resonance imaging profiles predict clinical response to early reperfusion: the diffusion and perfusion imaging evaluation for understanding stroke evolution (DEFUSE) study.** *Ann Neurol* 2006;60:508–17
31. Sheerin F. **The imaging of the cerebral venous sinuses.** *Semin Ultrasound CT MR* 2009;30:525–58
32. Leach JL, Fortuna RB, Jones BV, et al. **Imaging of cerebral venous thrombosis: current techniques, spectrum of findings, and diagnostic pitfalls.** *Radiographics* 2006;26(suppl 1):S19–41, discussion S42–43
33. Oran I, Memis A, Sener RN, et al. **The so-called transcerebral veins: appearance in three different cases.** *Comput Med Imaging Graph* 1999;23:127–31
34. Hakim AM, Evans AC, Berger L, et al. **The effect of nimodipine on the evolution of human cerebral infarction studied by PET.** *J Cereb Blood Flow Metab* 1989;9:523–34
35. Wise RJ, Bernardi S, Frackowiak RS, et al. **Serial observations on the pathophysiology of acute stroke: the transition from ischaemia to infarction as reflected in regional oxygen extraction.** *Brain* 1983;106(pt 1):197–222
36. Kidwell CS, Alger JR, Saver JL. **Beyond mismatch: evolving paradigms in imaging the ischemic penumbra with multimodal magnetic resonance imaging.** *Stroke* 2003;34:2729–35
37. Marckmann P, Skov L, Rossen K, et al. **Nephrogenic systemic fibrosis: suspected causative role of gadodiamide used for contrast-enhanced magnetic resonance imaging.** *J Am Soc Nephrol* 2006;17:2359–62

## On the Search for the Perfect Mismatch!

The selection of candidates who are likely to benefit from reperfusion therapy has been a focus of research in acute ischemic stroke. This produced a number of paradigms to the conceptual approach and imaging of patients with acute ischemic stroke. These paradigms aim to establish the presence of a sizable salvageable brain tissue that justifies taking the risks of medical interventions to achieve reperfusion. This introduced the concept of mismatch: a clinically important difference between the brain tissue that is already infarcted (the core) and the tissue that is on its way to infarct if complete reperfusion is not rapidly achieved (the penumbra). The identification of mismatch has been a premise of acute stroke imaging either to allow the treatment of those with an onset time that is unknown or outside the conventional time window; or to help select candidates for endovascular therapies after intravenous thrombolysis.

The evidence to support improved functional outcomes with the use of a mismatch paradigm is yet to be shown in randomized clinical trials. Trials of intravenous thrombolysis<sup>1</sup> or endovascular therapies<sup>2</sup> have failed to show a significant difference in clinical outcomes between patients with acute stroke selected based on the detection of mismatch versus those selected based on typical clinical or imaging criteria. An important challenge is the dynamic and heterogeneous nature of ischemic stroke contrary to the static quality of many of the available imaging modalities. This makes the a priori prediction of tissue fate often flawed, especially when rapid reperfusion is increasingly achieved using contemporary endovascular devices. In addition, the distinction between the core versus the penumbra and the penumbra versus areas of benign oligemia may not be as well delineated as what is perceived by viewing the color-coded perfusion maps.<sup>3</sup>

An emerging paradigm that has received special attention in recent years is the assessment of the collateral circulation. These vascular channels are believed to sustain the penumbra for a relatively longer period of time and their extent is thought to be directly proportional to the volume of the penumbra. Patients with good collaterals have fared clinically better after thrombolytic or endovascular therapies compared with patients with poor collaterals even when reperfusion was achieved.<sup>4-6</sup> Traditionally, the collateral status was assessed in the acute stroke setting using

conventional angiography.<sup>7</sup> However, the advancement of non-invasive imaging techniques provided more readily available alternatives. Single-phase CTA assessment of leptomeningeal collaterals produced a number of scores, all of which concluded that better collaterals were associated with smaller infarct volume or better functional outcome than poor collaterals.<sup>8-10</sup> The sensitivity of single-phase CTA to the timing of image acquisition in relation to the bolus led researchers to develop techniques to provide dynamic collateral assessment. This produced time-resolved, CT-based collateral imaging techniques that used partial<sup>11</sup> or complete<sup>12</sup> brain coverage to assess the temporal filling of collaterals beyond an arterial occlusion. These data provided grounds for excluding patients with poor or no collaterals on multiphase CTA<sup>12</sup> from the ongoing Endovascular treatment for Small Core and Anterior circulation Proximal occlusion with Emphasis on minimizing CT to recanalization times (ESCAPE) trial.

The role of MR imaging in collateral assessment relied on few techniques.<sup>13</sup> The presence of distal hyperintense vessels on FLAIR imaging,<sup>14</sup> believed to reflect good collateral status, corresponded to smaller core volume, favorable diffusion-perfusion mismatch, and milder stroke severity. Collateral assessment using arterial spin-labeling has shown good agreement with conventional angiography in patients with cervical or intracranial stenosis in the nonacute setting.<sup>15</sup> Scattered reports described the potential utility of susceptibility-weighted imaging techniques in this context.<sup>13,16</sup> It is hypothesized that the increased brain tissue demand for oxygen downstream from an occlusion leads to a higher concentration of deoxyhemoglobin in the capillaries and venous outflow channels leading to a susceptibility difference that discriminates these vessels from the adjacent brain.<sup>17</sup> The detection of these channels is thought to signify the presence of penumbra.

In this issue of the *American Journal of Neuroradiology*, a mismatch paradigm based on the venous outflow estimation is used to define a susceptibility/diffusion (SWI/DWI) mismatch. This previously described paradigm<sup>18-20</sup> is objectively measured to assess the relationship between clinical outcome and an SWI/DWI mismatch in 54 patients with stroke treated with IV tPA. Automated venous SWI segmented maps were generated and com-

pared with the contralateral side to calculate an asymmetry index. Patients with more than 1.75 asymmetry index and DWI volume of  $\leq 25$  mL achieved over 90% favorable outcome with recanalization. The SWI/DWI mismatch was a better predictor of functional independence than the PWI/DWI mismatch in this study.

Despite a number of limitations, many of which were acknowledged by the investigators, the study findings may have important future applications. Once the method to identify this SWI/DWI mismatch is simplified and accessible, studying this paradigm in past or ongoing large prospective cohorts will help advance the understanding of its significance and define its role in patient selection for reperfusion therapies outside the standard window or via the endovascular approach. Another interesting aspect will be to investigate any regional correlation of these venous outflow channels with penumbral tissue or the presence of robust collaterals. Once its validity is established, this imaging paradigm will face the practical challenges that all MR-based acute stroke techniques need to overcome<sup>21</sup> in addition to the lack of evidence from a randomized trial supporting the improved outcomes of patients selected using penumbral imaging.<sup>2</sup>

Whether it is collateral-, tissue-, or venous outflow-based mismatch, the important question remains: which of these paradigms will be shown to predict improved functional outcomes? To achieve this, it will also need to be readily available, easily interpretable with minimal postprocessing, and able to be efficiently incorporated into the hyperacute stroke workflow to allow timely reperfusion. Finding the “perfect” mismatch is not easy after all!

## REFERENCES

1. Davis SM, Donnan GA, Parsons MW, et al. Effects of alteplase beyond 3 h after stroke in the Echoplanar Imaging Thrombolytic Evaluation Trial (EPITHET): a placebo-controlled randomised trial. *Lancet Neurol* 2008;7:299–309
2. Kidwell CS, Jahan R, Gornbein J, et al. A trial of imaging selection and endovascular treatment for ischemic stroke. *N Engl J Med* 2013;368:914–23
3. Kidwell CS, Alger JR, Saver JL. Beyond mismatch: evolving paradigms in imaging the ischemic penumbra with multimodal magnetic resonance imaging. *Stroke* 2003;34:2729–35
4. Bang OY, Saver JL, Buck BH, et al. Impact of collateral flow on tissue fate in acute ischaemic stroke. *J Neurol Neurosurg Psychiatry* 2008;79:625–29
5. Nambiar V, Sohn SI, Almekhlafi MA, et al. CTA collateral status and response to recanalization in patients with acute ischemic stroke. *AJNR Am J Neuroradiol* 2014;35:884–90
6. Liebeskind DS, Tomsick TA, Foster LD, et al. Collaterals at angiog-

- raphy and outcomes in the Interventional Management of Stroke (IMS) III trial. *Stroke* 2014;45:759–64
7. Bozzao L, Fantozzi LM, Bastianello S, et al. Early collateral blood supply and late parenchymal brain damage in patients with middle cerebral artery occlusion. *Stroke* 1989;20:735–40
  8. Maas MB, Lev MH, Ay H, et al. Collateral vessels on CT angiography predict outcome in acute ischemic stroke. *Stroke* 2009;40:3001–05
  9. Menon BK, O'Brien B, Bivard A, et al. Assessment of leptomeningeal collaterals using dynamic CT angiography in patients with acute ischemic stroke. *J Cereb Blood Flow Metab* 2013;33:365–71
  10. Miteff F, Levi CR, Bateman GA, et al. The independent predictive utility of computed tomography angiographic collateral status in acute ischaemic stroke. *Brain* 2009;132:2231–38
  11. Frolich AM, Wolff SL, Psychogios MN, et al. Time-resolved assessment of collateral flow using 4D CT angiography in large-vessel occlusion stroke. *Eur Radiol* 2014;24:390–96
  12. Goyal M, Menon B. Optimizing acute stroke imaging for maximizing information and minimizing acquisition, post processing and interpretation times: analysis of data from a prospective imaging cohort study. In: *Proceedings of the European Stroke Conference*, London, UK. May 28–31, 2013
  13. McVerry F, Liebeskind DS, Muir KW. Systematic review of methods for assessing leptomeningeal collateral flow. *AJNR Am J Neuroradiol* 2012;33:576–82
  14. Lee KY, Latour LL, Luby M, et al. Distal hyperintense vessels on FLAIR: an MRI marker for collateral circulation in acute stroke? *Neurology* 2009;72:1134–39
  15. Wu B, Wang X, Guo J, et al. Collateral circulation imaging: MR perfusion territory arterial spin-labeling at 3T. *AJNR Am J Neuroradiol* 2008;29:1855–60
  16. Hermier M, Nighoghossian N, Derex L, et al. Hypointense leptomeningeal vessels at T2\*-weighted MRI in acute ischemic stroke. *Neurology* 2005;65:652–53
  17. Hermier M, Nighoghossian N. Contribution of susceptibility-weighted imaging to acute stroke assessment. *Stroke* 2004;35:1989–94
  18. Kao HW, Tsai FY, Hasso AN. Predicting stroke evolution: comparison of susceptibility-weighted MR imaging with MR perfusion. *Eur Radiol* 2012;22:1397–403
  19. Meoded A, Poretti A, Benson JE, et al. Evaluation of the ischemic penumbra focusing on the venous drainage: the role of susceptibility weighted imaging (SWI) in pediatric ischemic cerebral stroke. *J Neuroradiol* 2014;41:108–16
  20. Fujioka M, Okuchi K, Iwamura A, et al. A mismatch between the abnormalities in diffusion- and susceptibility-weighted magnetic resonance imaging may represent an acute ischemic penumbra with misery perfusion. *J Stroke Cerebrovasc Dis* 2013;22:1428–31
  21. Wisco D, Uchino K, Saqur M, et al. Addition of hyperacute MRI aids in patient selection, decreasing the use of endovascular stroke therapy. *Stroke* 2014;45:467–72

M.A. Almekhlafi  
King Abdulaziz University  
Jeddah, Saudi Arabia

<http://dx.doi.org/10.3174/ajnr.A4024>

# Leukoaraiosis Predicts a Poor 90-Day Outcome after Endovascular Stroke Therapy

J. Zhang, A.S. Puri, M.A. Khan, R.P. Goddeau Jr, and N. Henninger



## ABSTRACT

**BACKGROUND AND PURPOSE:** Leukoaraiosis is a common finding among patients with ischemic stroke and has been associated with poor stroke outcomes. Our aim was to ascertain whether the severity of pre-existing leukoaraiosis is associated with outcome in patients with acute ischemic stroke who are treated with endovascular stroke therapy.

**MATERIALS AND METHODS:** We retrospectively analyzed data from 129 consecutive, prospectively enrolled patients with stroke undergoing endovascular stroke therapy at a single tertiary care center between January 2006 and August 2013. Leukoaraiosis was assessed as supratentorial white matter hypoattenuation on admission head CT and graded as 0–2 (absent-to-moderate) versus 3–4 (severe) according to the van Swieten scale. We dichotomized the 90-day mRS into good (0–2 or return to baseline) versus poor (3–6) as the primary study outcome. Incremental multivariable logistic regression analyses were performed to identify independent predictors of a poor 90-day outcome.

**RESULTS:** In all multivariable models, severe leukoaraiosis was independently ( $P < .05$ ) associated with a poor outcome at 90 days (fully adjusted model: OR, 6.37; 95% CI, 1.83–12.18;  $P = .004$ ). The independent association between leukoaraiosis and a poor outcome remained when the analysis was restricted to patients who were alive at discharge ( $n = 87$ ,  $P < .05$ ). Last, among patients who were alive at discharge, those with severe leukoaraiosis had significantly less frequent improvement on the mRS from discharge to 90 days compared with patients with absent-to-moderate leukoaraiosis ( $P = .034$ ).

**CONCLUSIONS:** The severity of pre-existing leukoaraiosis is independently associated with 90-day functional outcome in patients with stroke who underwent endovascular stroke therapy. These results highlight the need to further explore leukoaraiosis as a promising surrogate marker for poor outcome after endovascular stroke therapy to improve risk assessment, patient selection, and early prognostic accuracy.

**ABBREVIATION:** EST = endovascular stroke therapy

Thrombolysis with IV rtPA remains the only proved therapy for acute ischemic stroke.<sup>1</sup> However, its efficacy is limited by several variables, including a narrow treatment time window and reduced efficacy with larger thrombus burden.<sup>1,2</sup> In particular, proximal large intracranial artery occlusion portends a poor

prognosis and poses a substantial therapeutic challenge.<sup>3</sup> Endovascular approaches to recanalization may allow more frequent and rapid recanalization of the target vessel, which is critical for achieving better outcomes.<sup>2,3</sup> However, despite the acceptable safety of endovascular approaches, definitive proof of superiority over IV thrombolysis in achieving good functional outcomes remains to be established.<sup>1,3</sup> Understanding factors that influence outcome in patients undergoing endovascular stroke therapy (EST) is paramount to help improve selection of patients most likely to benefit from this therapy.<sup>2</sup>

While numerous studies have focused on procedural aspects, treatment window, and neuroimaging signatures of acute tissue injury, little is known regarding the potential contribution of pre-existing white matter rarefaction (leukoaraiosis) on outcome.<sup>3–5</sup> Yet, leukoaraiosis is frequently encountered in the elderly<sup>6,7</sup> and is well-known to contribute to worse outcomes after acute ischemic

Received March 27, 2014; accepted after revision May 12.

From the Departments of Neurology (J.Z., N.H., R.P.G.), Radiology (A.S.P.), Neurosurgery (A.S.P.), and Psychiatry (N.H.), University of Massachusetts Medical School, Worcester, Massachusetts; and Department of Neurology (M.A.K.), Warren Alpert Medical School of Brown University, Providence, Rhode Island.

Please address correspondence to Nils Henninger, MD, Departments of Neurology and Psychiatry, University of Massachusetts Medical School, 55 Lake Ave, North, Worcester, MA 01655; e-mail: nils.henninger@umassmed.edu

 Indicates article with supplemental on-line tables.

 Indicates article with supplemental on-line figures.

<http://dx.doi.org/10.3174/ajnr.A4029>

stroke.<sup>7,8</sup> Given the expected tripling of the number of persons aged 60 or older in developed nations by 2050<sup>9</sup> and the increasing prevalence of stroke with advancing age,<sup>10,11</sup> it is expected that an increasing number of patients with pre-existing leukoaraiosis will be treated with EST.<sup>12</sup> Accordingly, it is important to understand the potential contribution of leukoaraiosis to functional outcome after EST.

To address this issue, we tested the hypothesis that the severity of pre-existing leukoaraiosis is associated with outcome as assessed by the 90-day mRS in consecutive patients with acute ischemic stroke treated with EST.

## MATERIALS AND METHODS

### Study Population

This study was reviewed and approved by our institutional review board. We retrospectively analyzed 129 consecutive, prospectively collected patients with acute ischemic stroke who underwent EST at a single academic stroke center from January 2006 to August 2013. Of note, 42 (33%) studied subjects have been included in prior investigations.<sup>8,13</sup> We adhered to the Strengthening the Reporting of Observational Studies in Epidemiology guidelines ([www.strobe-statement.org](http://www.strobe-statement.org)).

All patients underwent head CT and CTA at admission. Demographics, NIHSS scores, laboratory data, comorbidities, pre-admission medications, and stroke etiology (by using the Trial of Org 10172 in Acute Stroke Treatment classification),<sup>8,13</sup> after completion of diagnostic evaluation, were collected on all patients. mRS scores were assessed at the time of presentation (pre-admission mRS), discharge, and at 90 days by a stroke-trained physician or stroke study nurse, certified in mRS.<sup>8</sup> When the mRS was unavailable, the same observers reconstructed the score from the case description, according to the mRS criteria.<sup>8</sup>

### Neuroimaging Protocol

All CT sequences were obtained on a 64-detector row scanner (Brilliance; Philips Healthcare, Best, the Netherlands). CT was performed in a nonhelical mode at 120 kV(peak) and 200 mA, with data reconstruction at 5-mm axial sections. CTA was performed by using 64 × 0.625 mm detector configuration with a pitch of 0.673 from the arch of the aorta to the vertex by using 120 kV(p), 300 mA, and 0.5-second rotation time. Patients received 60–80 mL of iopamidol (Isovue 370; Bracco Diagnostics, Princeton, New Jersey) in the antecubital vein at a rate of 4 mL/s through a power injector followed by 40 mL of saline. 3D orthogonal MIP images were created in 3 planes.

### Digital Subtraction Angiography

All endovascular procedures were performed by senior neurointerventionalists by using a biplane angiography unit with 3D rotational angiography capability (Allura Xper FD20/20; Philips) with patients under conscious sedation or general anesthesia. Endovascular access was obtained by a standard transfemoral approach.

### Image Review and Analysis

CT and CTA were reviewed independently by experienced readers blinded to both clinical data and any follow-up scans. Variable

window width and center-level settings were used for optimal ischemic hypoattenuation detection with CT and CTA.<sup>8,13</sup>

Leukoaraiosis was retrospectively defined by 2 readers (N.H. and J.Z.) as supratentorial white matter hypoattenuation on admission noncontrast head CT according to the Standards for Reporting Vascular changes on neuroimaging criteria,<sup>14</sup> and it was graded on a 5-point van Swieten scale as previously described in detail (On-line Fig 1).<sup>15</sup> Disagreements in readings were resolved by consensus. In the present study, leukoaraiosis was separately assessed in each hemisphere, but only the score from the nonischemic hemisphere was considered after unblinding. Hemorrhagic transformation on follow-up imaging was determined according to the European Cooperative Acute Stroke Study definition.<sup>16</sup>

Angiography-based collateral flow was graded from 0 (no collaterals) to 4 (complete) before EST,<sup>17</sup> and final recanalization was assessed according to the TICI classification as previously defined.<sup>17</sup> The time to recanalization was defined as the time from symptom onset (or last time known well) to the final attempt at recanalization.

To avoid classification bias and to minimize interrater variability,<sup>8</sup> we also dichotomized the degree of leukoaraiosis (van Swieten scale 0–2 [absent-to-moderate] versus 3–4 [severe]), the presence of collaterals (grades 0–2 [poor] versus 3–4 [good]), recanalization (TICI 0–2a [poor] versus 2b–3 [good]), and the presence versus absence of parenchymal hemorrhage (parenchymal hemorrhage 1 and parenchymal hemorrhage 2) for statistical purposes.

Last, to assess the potential association among leukoaraiosis, infarct volume, and outcome, manual lesion assessment<sup>13,15</sup> was conducted in patients who had follow-up imaging within 7 days of stroke onset (MR imaging:  $n = 43$ ; CT:  $n = 25$ ), allowing reliable measurements.

### Statistics

Weighted  $\kappa$  statistics were used to determine the degree of interrater agreement in the van Swieten scale assessment in all 129 included patients and to determine  $\kappa$  values as previously defined.<sup>13</sup> In addition, intrarater agreement was assessed in 65 randomly chosen patients who were graded 5 months apart by an experienced reader (N.H.).

Unless otherwise stated, continuous variables are reported as mean  $\pm$  SD or as median (interquartile range). Categorical variables are reported as proportions. Between-group comparisons for continuous variables were made with the unpaired  $t$  and Mann-Whitney  $U$  tests, as appropriate. Categorical variables were compared by using the  $\chi^2$  or Fisher exact test as appropriate.

**Primary Analysis.** We defined the 90-day mRS dichotomized into good (0–2 or return to baseline) versus poor (3–6) as the primary study outcome. To test the hypothesis that the degree of leukoaraiosis was independently associated with outcome, we created several incremental multivariable logistic regression models as follows: first unadjusted (model 1); then adjusted for admission variables: age, NIHSS, atrial fibrillation, creatinine level, low-density lipoprotein cholesterol, random blood sugar (model 2); then additionally adjusted for endovascular variables: poor recanalization, time to recanalization, poor collateral grade (model 3);

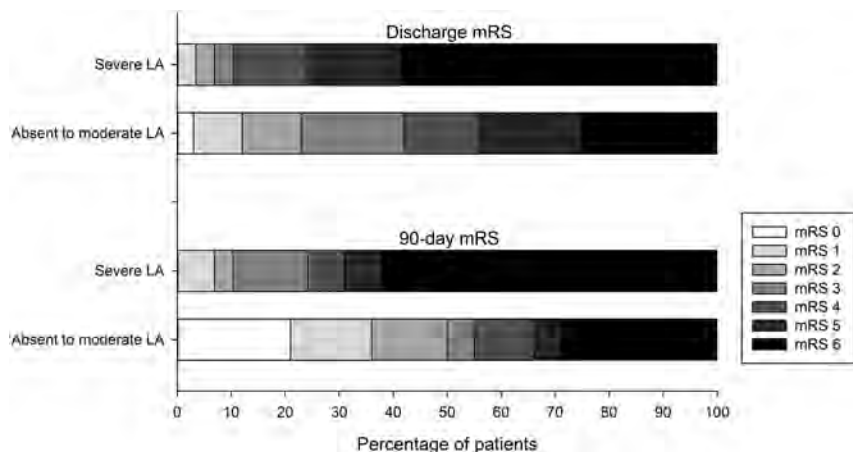


**FIG 1.** Functional outcome at discharge and at 3 months according to leukoaraiosis (LA) severity (unadjusted). Scores of  $\leq 2$  or return to baseline on the mRS are considered a good outcome (darker shades indicate worse outcomes).

and finally additionally adjusted for the presence of parenchymal hemorrhage (model 4). We then repeated all analyses, entering leukoaraiosis severity, collateral grade, and degree of recanalization as ordinal variables.

**Secondary Analyses.** We performed preplanned sensitivity analyses for predictors of a good (0–2 or return to baseline) versus poor (3–6) mRS at 90 days in patients who were alive by the time of discharge ( $n = 87$ ). Furthermore, we compared the frequency of any improvement (defined as an improvement by  $\geq 1$  point on the mRS between discharge and 90 days) in patients with absent-to-moderate versus severe leukoaraiosis who were alive at the time of discharge. Last, we conducted multivariable linear regression analysis with backward elimination of factors independently associated with the final infarct volume. We performed multivariable logistic regression analyses (by using bootstrapping for more stable results, given the limited number) to assess whether leukoaraiosis and infarct volume were independently associated with a poor 90-day outcome.

Collinearity diagnostics were performed for all multivariable logistic and linear regression models. Associations are presented as ORs with corresponding 95% confidence intervals. The Hosmer-Lemeshow goodness-of-fit statistic was used to assess all models for final fit. Two-sided significance tests were used throughout, and a 2-sided  $P < .05$  was considered statistically significant. All statistical analyses were performed by using SPSS Statistics 20.0.0 (IBM, Armonk, New York).

## RESULTS

During the study period, 3057 patients were admitted with a diagnosis of acute ischemic stroke. Of these, 142 patients were treated with EST. Thirteen patients were lost to follow-up. Data were complete for all included patients except for collateral grade, which could not be assessed in 8 patients due to proximal internal carotid artery occlusion and absent contralateral injection before the intervention.

Free marginal  $\kappa$  values for interobserver agreement indicated moderate and almost perfect agreement for graded ( $\kappa = 0.50$ ) and dichotomized leukoaraiosis severity ( $\kappa = 0.91$ ), respectively.<sup>13</sup> Intraobserver agreement was substantial and

almost perfect for graded ( $\kappa = 0.78$ ) and dichotomized leukoaraiosis severity ( $\kappa = 0.89$ ), respectively.

### Factors Associated with Leukoaraiosis Severity (Unadjusted)

Baseline characteristics of the 129 included patients stratified by leukoaraiosis severity and outcome are summarized in On-line Table 1. Severe leukoaraiosis was associated with greater in-hospital mortality ( $P = .001$ ), worse mRS scores at discharge ( $P = .003$ ), and worse 90-day outcome ( $P = .001$ , Fig 1). Furthermore, patients with severe leukoaraiosis were more likely to have experienced a prior stroke or TIA ( $P = .002$ ), atrial fibrillation ( $P = .001$ ), coronary artery disease ( $P = .030$ ), or peripheral vascular disease ( $P =$

$.009$ ), were older ( $P < .001$ ), less frequently underwent mechanical thrombectomy, and had more frequent cardioembolic strokes ( $P = .005$ ) and strokes of other or undetermined pathogenesis ( $P = .039$ ).

There was a weak inverse relation between leukoaraiosis and collateral grade (ie, patients with worse leukoaraiosis had better collaterals; graded:  $r = -.218$ ,  $P = .016$ ; dichotomized:  $r = -.265$ ,  $P = .003$ ). There was no association between the severity of leukoaraiosis and the degree of recanalization (graded:  $r = 0.083$ ,  $P = .351$ ; dichotomized:  $r = 0.029$ ,  $P = .743$ ).

### Factors Associated with a Poor 90-Day Outcome (Unadjusted)

Poor 90-day outcome (On-line Table 2) was associated with older age ( $P < .001$ ) and worse leukoaraiosis (graded:  $P = .005$ ; dichotomized:  $P < .001$ ) and higher admission NIHSS scores ( $P < .001$ ), glucose levels ( $P = .032$ ), creatinine levels ( $P = .02$ ), and low-density lipoprotein levels ( $P = .031$ ), good recanalization ( $P = .023$ ), the presence of atrial fibrillation ( $P = .014$ ), and the presence of parenchymal hemorrhage<sup>16</sup> (parenchymal hemorrhage 1 and parenchymal hemorrhage 2,  $P = .001$ ). The association between leukoaraiosis severity and 90-day outcome was similar across the endovascular modalities used (On-line Fig 2).

### Primary Analysis: Multivariable Analysis of Factors Associated with the 90-Day Outcome

The association between severe leukoaraiosis and poor 90-day outcome remained after adjusting for pertinent covariates (Table). The association of leukoaraiosis with outcome remained when leukoaraiosis severity, degree of recanalization, and collateral grade were entered as ordinal variables in all models ( $P < .01$ , not shown).

### Secondary Analyses

**Association between Leukoaraiosis and Outcome among Patients Alive at Discharge.** By the time of discharge, 33% ( $n = 42$ ) of patients had died (Fig 1, all because of “withdrawal of care”). To

### Multivariable logistic regression analysis of factors independently associated with a poor 90-day outcome

Independent Variable	Model 1 <sup>a</sup>	P Value	Model 2 <sup>b</sup>	P Value	Model 3 <sup>c</sup>	P Value	Model 4 <sup>d</sup>	P Value
Severe leukoaraiosis <sup>e</sup>	6.50 (2.11–20.06)	<.001	4.40 (1.22–15.74)	.023	6.03 (1.80–22.11)	.004	6.37 (1.83–22.18)	.004
Admission NIHSS score	—	—	1.08 (1.00–1.16)	.027	1.09 (1.01–1.17)	.023	1.08 (1.00–1.16)	.041
Age (yr)	—	—	1.03 (0.99–1.07)	.065	1.03 (1.00–1.07)	.028	1.03 (0.99–1.06)	.005
LDL	—	—	0.98 (0.97–1.00)	.057	0.98 (0.97–1.00)	.014	0.99 (0.97–1.00)	.064
Creatinine level	—	—	—	—	3.21 (0.78–13.19)	.105	—	—
Poor recanalization	—	—	—	—	3.72 (1.10–12.53)	.034	2.94 (0.84–10.21)	.089
Parenchymal hemorrhage	—	—	—	—	—	—	3.23 (1.01–10.37)	.049

**Note:** — indicates not applicable; LDL, low-density lipoprotein. Factors that were not included in the final model iteration are omitted from the table. Data are odds ratios with 95% confidence intervals.

<sup>a</sup> Model 1, unadjusted.

<sup>b</sup> Model 2, adjusted for age, admission NIHSS score, atrial fibrillation, creatinine level, LDL, and random blood sugar (Hosmer-Lemeshow statistics:  $\chi^2 = 6.047$ ,  $P = .642$ ).

<sup>c</sup> Model 3, additionally adjusted for collateral grade, degree of recanalization, and time to recanalization (Hosmer-Lemeshow statistics:  $\chi^2 = 9.856$ ,  $P = .275$ ).

<sup>d</sup> Model 4, adjusted for model 3 plus the presence of parenchymal hemorrhagic transformation (Hosmer-Lemeshow statistics:  $\chi^2 = 3.418$ ,  $P = .905$ ).

<sup>e</sup> The association with outcome remained when leukoaraiosis, degree of recanalization, and collateral grade were entered as ordinal variables ( $P < .01$ ).

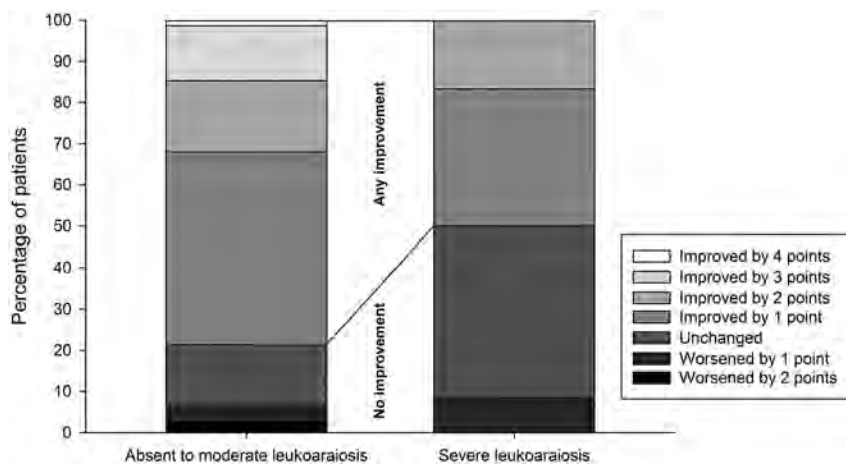


**FIG 2.** Functional improvement of patients who were alive at the time of discharge ( $n = 87$ ) according to leukoaraiosis severity (unadjusted). Compared with patients with absent-to-moderate leukoaraiosis, patients with severe leukoaraiosis are significantly less likely to have any improvement on the mRS from discharge to 90 days (50% versus 79% of surviving patients [21% versus 59% of all patients, respectively];  $P = .034$ ; darker shades indicate less improvement).

gain a better understanding of whether leukoaraiosis can serve as a useful independent prognostic factor for outcome in patients who did not have early withdrawal of care (which may be related to factors independent of measured patient characteristics), we then repeated the logistic regression analyses in patients who were alive by discharge ( $n = 87$ ). These analyses yielded similar results, showing an independent association between severe leukoaraiosis and poor outcome (unadjusted  $P = .001$ ; adjusted  $P < .05$ , not shown).

**Association between Leukoaraiosis and Recovery among Patients Alive at Discharge.** Among patients who were alive at discharge, those with severe leukoaraiosis had significantly less frequent improvement on the mRS from discharge to 90 days compared with patients with absent-to-moderate leukoaraiosis (OR, 3.69; 95% CI, 1.05–12.99;  $P = .034$ ; Fig 2). Given the limited number of subjects in the outcome category, multivariable analysis to adjust for covariates was not attempted.

**Association among Infarct Volume, Leukoaraiosis, and Outcome.** Among patients with follow-up imaging ( $n = 68$ ), those with severe leukoaraiosis ( $n = 11$ ) had significantly larger infarcts compared with patients with absent-to-moderate leukoaraiosis ( $152 \pm 145$  mL versus  $51 \pm 68$  mL,  $P = .044$ ).

Patients with a poor outcome ( $n = 29$ ) had significantly larger infarcts compared with patients with a good outcome ( $131 \pm 111$  mL versus  $20 \pm 16$  mL,  $P < .001$ ). Multivariable linear regression analysis (including age, admission NIHSS, leukoaraiosis, time to recanalization, degree of recanalization, collateral grade, random blood sugar, atrial fibrillation, use of antihypertensive medications, and glycated hemoglobin) indicated that leukoaraiosis ( $P < .001$ ), degree of recanalization ( $P < .001$ ), and age ( $P = .036$ ) were independently associated with the final infarct volume (not shown). Last, multivariable logistic regression (including age, leukoaraiosis, infarct volume, and admission NIHSS score) indicated that severe leukoaraiosis ( $P = .035$ ), infarct volume ( $P = .006$ ), and age ( $P = .004$ ) were independently associated with a poor outcome (not shown).

### DISCUSSION

We demonstrate that pre-existing leukoaraiosis severity is associated with a poor 90-day outcome after EST, independent of established predictors of stroke outcome.

This finding is important because translating favorable angiographic results of endovascular treatment to correspondingly robust clinical outcomes is needed. Because endovascular approaches to acute ischemic stroke treatment are increasingly offered to older patients, despite a higher risk of poor outcome compared with younger patients,<sup>12</sup> appropriate patient selection beyond procedural aspects represents an important goal in this population.

Imaging biomarkers are of particular interest, given that neuroimaging is a prerequisite to patient selection for acute therapy. Leukoaraiosis may represent a viable biomarker because it can be determined by standard neuroimaging and has been consistently shown to predict a higher risk for poor post-stroke outcome.<sup>5-8,15,18</sup>

How leukoaraiosis contributes to worse poststroke outcomes

is incompletely understood. For example, leukoaraiosis has been associated with a greater risk for parenchymal hemorrhage after EST, which is a predictor of poor poststroke outcome.<sup>4</sup> However, in the current study, we did not note a significant association between leukoaraiosis and parenchymal hemorrhage risk, possibly because we included patients treated with newer generation devices, which may have a lower risk for hemorrhagic transformation<sup>19</sup> and our study was likely underpowered to detect a significant association. Although our results are consistent with a retrospective analysis of patients treated with EST,<sup>5</sup> further research is required to elucidate the potential association between leukoaraiosis and the risk for hemorrhagic transformation in this patient population.

An alternate explanation for poor outcomes in patients with leukoaraiosis may be chronic cerebral hypoperfusion that results in reduced cerebral ischemic resilience and thus greater final lesion volumes,<sup>20</sup> which are a known outcome predictor after EST.<sup>21</sup> Indeed, we and others have previously shown that leukoaraiosis severity is associated with a larger ischemic core, mismatch lost, and final infarct volume, supporting this hypothesis.<sup>13,15,22</sup> Indeed, subgroup analyses in patients with available follow-up imaging indicated that worse leukoaraiosis independently predicted larger infarct volumes. However, because infarct volumes could not be measured in all patients, additional studies are required to confirm the association among leukoaraiosis, infarct volume, and outcome. Furthermore, because the impact of leukoaraiosis on poststroke outcome was only partially explained by larger infarct extent in this and prior studies,<sup>18</sup> it appears likely that the loss of compensatory network integrity results in decreased cerebral plasticity. For example, decreased integrity of fiber tracts within the unaffected hemisphere and purported compensatory pathways (such as the corticorubrospinal system) have been shown to impair poststroke recovery.<sup>23,24</sup> Accordingly, global white matter changes such as those caused by leukoaraiosis are expected to adversely affect the potential for poststroke recovery. However, although several studies have linked leukoaraiosis to poor functional outcomes, there is a paucity of data regarding the degree of poststroke recovery, particularly in patients with large-artery occlusion.<sup>25-27</sup>

In this respect, our observation of significantly decreased long-term recovery in patients having undergone EST with severe leukoaraiosis is a novel and important finding, supporting the hypothesis that leukoaraiosis disrupts cerebral connectivity and plasticity. Considering that most patients undergoing EST have early functional deficits,<sup>3</sup> it is critical to understand factors that modulate recovery. Our findings highlight the clinical importance of investigating leukoaraiosis in patients with stroke to better understand its predictive value for functional recovery after stroke.

The strengths of the present study relate to the relatively large sample size, a well-defined patient population, investigation of variables that have been associated with poststroke outcome, and blinded imaging assessment. Our study has limitations related to its retrospective design and should be considered hypothesis-generating. EST was not standardized across patients, and most patients were treated with multiple modalities with or without rtPA. For this reason, it was not feasible to adjust our analysis to

account for the various treatment approaches or perform subgroup analyses. Nevertheless, exploratory analysis indicated a similar association across treatment modalities. This finding is consistent with the presumed pathophysiology and described association with poor poststroke outcomes in numerous studies across heterogeneous patient populations, allowing better generalization of our results.<sup>4,8,18</sup> Misclassification of leukoaraiosis severity is possible given the CT-based grading system. However, although MR imaging has a higher sensitivity and specificity to research leukoaraiosis compared with CT,<sup>14</sup> the latter is more broadly available and routinely used in the hyperacute setting to evaluate patients with stroke. Furthermore, as noted, the classification used in our study is easy to perform, had a high inter- and intraobserver agreement, and does not require extensive postprocessing.<sup>8,13</sup> Last, although our data show a strong association between leukoaraiosis and outcome, a causal relationship remains to be fully established.

## CONCLUSIONS

In summary, with a projected increase in the occurrence of strokes, especially among the elderly,<sup>9-11</sup> clinicians will be increasingly<sup>12</sup> faced with the issue of appropriately selecting elderly patients with severe strokes for EST. Our data provide preliminary evidence that patients with severe pre-existing leukoaraiosis are at high risk for a poor functional outcome after EST. Given absent association with parenchymal hemorrhage and favorable outcome in a small subset of patients, the presence of severe leukoaraiosis currently does not justify exclusion from EST. Nevertheless, these results highlight the need to further explore leukoaraiosis as a promising surrogate marker for poor outcome after EST to improve risk assessment and aid in discussing expectations of different outcome types with family members. Further study is required to confirm our findings and investigate underlying mechanisms.

Disclosures: Muhib A. Khan—UNRELATED: Payment for Development of Educational Presentations: Cyberrounds, for the development of a Continuing Medical Education on atrial fibrillation and newer oral anticoagulants.

## REFERENCES

1. Jauch EC, Saver JL, Adams HP Jr, et al. **Guidelines for the early management of patients with acute ischemic stroke: a guideline for healthcare professionals from the American Heart Association/American Stroke Association.** *Stroke* 2013;44:870-947
2. Nogueira RG, Gupta R, Davalos A. **IMS-III and SYNTHESIS expansion trials of endovascular therapy in acute ischemic stroke: how can we improve?** *Stroke* 2013;44:3272-74
3. Broderick JP, Palesch YY, Demchuk AM, et al. **Endovascular therapy after intravenous t-PA versus t-PA alone for stroke.** *N Engl J Med* 2013;368:893-903
4. Shi ZS, Loh Y, Liebeskind DS, et al. **Leukoaraiosis predicts parenchymal hematoma after mechanical thrombectomy in acute ischemic stroke.** *Stroke* 2012;43:1806-11
5. Jung S, Mono ML, Findling O, et al. **White matter lesions and intra-arterial thrombolysis.** *J Neurol* 2012;259:1331-36
6. Simoni M, Li L, Paul NL, et al. **Age- and sex-specific rates of leukoaraiosis in TIA and stroke patients: population-based study.** *Neurology* 2012;79:1215-22
7. Pantoni L. **Cerebral small vessel disease: from pathogenesis and clinical characteristics to therapeutic challenges.** *Lancet Neurol* 2010;9:689-701

8. Henninger N, Lin E, Baker SP, et al. **Leukoaraiosis predicts poor 90-day outcome after acute large cerebral artery occlusion.** *Cerebrovasc Dis* 2012;33:525–31
9. United Nations Department of Economic and Social Affairs, Population Division. *World Population Prospects. The 2006 Revision, Highlights, Working Paper No. ESA/P/WP. 202.* Published 2007. [http://www.un.org/esa/population/publications/wpp2006/WPP2006\\_Highlights\\_rev.pdf](http://www.un.org/esa/population/publications/wpp2006/WPP2006_Highlights_rev.pdf). Accessed May 12, 2014
10. Lozano R, Naghavi M, Foreman K, et al. **Global and regional mortality from 235 causes of death for 20 age groups in 1990 and 2010: a systematic analysis for the Global Burden of Disease Study 2010.** *Lancet* 2012;380:2095–128
11. Murray CJ, Vos T, Lozano R, et al. **Disability-adjusted life years (DALYs) for 291 diseases and injuries in 21 regions, 1990–2010: a systematic analysis for the Global Burden of Disease Study 2010.** *Lancet* 2012;380:2197–223
12. Duffis EJ, He W, Prestigiacomo CJ, et al. **Endovascular treatment for acute ischemic stroke in octogenarians compared with younger patients: a meta-analysis.** *Int J Stroke* 2014;9:308–12
13. Henninger N, Lin E, Haussen DC, et al. **Leukoaraiosis and sex predict the hyperacute ischemic core volume.** *Stroke* 2013;44:61–67
14. Wardlaw JM, Smith EE, Biessels GJ, et al. **Neuroimaging standards for research into small vessel disease and its contribution to ageing and neurodegeneration.** *Lancet Neurol* 2013;12:822–38
15. Henninger N, Khan MA, Zhang J, et al. **Leukoaraiosis predicts cortical infarct volume after distal middle cerebral artery occlusion.** *Stroke* 2014;45:689–95
16. Hacke W, Kaste M, Fieschi C, et al. **Intravenous thrombolysis with recombinant tissue plasminogen activator for acute hemispheric stroke: the European Cooperative Acute Stroke Study (ECASS).** *JAMA* 1995;274:1017–25
17. Higashida RT, Furlan AJ, Roberts H, et al. **Trial design and reporting standards for intra-arterial cerebral thrombolysis for acute ischemic stroke.** *Stroke* 2003;34:e109–37
18. Arsava EM, Rahman R, Rosand J, et al. **Severity of leukoaraiosis correlates with clinical outcome after ischemic stroke.** *Neurology* 2009;72:1403–10
19. Nogueira RG, Gupta R, Jovin TG, et al. **Predictors and clinical relevance of hemorrhagic transformation after endovascular therapy for anterior circulation large vessel occlusion strokes: a multicenter retrospective analysis of 1122 patients.** *J Neurointerv Surg* 2014 Jan 8. [Epub ahead of print]
20. O’Sullivan M, Lythgoe DJ, Pereira AC, et al. **Patterns of cerebral blood flow reduction in patients with ischemic leukoaraiosis.** *Neurology* 2002;59:321–26
21. Zaidi SF, Aghaebrahim A, Urta X, et al. **Final infarct volume is a stronger predictor of outcome than recanalization in patients with proximal middle cerebral artery occlusion treated with endovascular therapy.** *Stroke* 2012;43:3238–44
22. Ay H, Arsava EM, Rosand J, et al. **Severity of leukoaraiosis and susceptibility to infarct growth in acute stroke.** *Stroke* 2008;39:1409–13
23. Rüber T, Schlaug G, Lindenberg R. **Compensatory role of the cortico-rubro-spinal tract in motor recovery after stroke.** *Neurology* 2012;79:515–22
24. Borich MR, Mang C, Boyd LA. **Both projection and commissural pathways are disrupted in individuals with chronic stroke: investigating microstructural white matter correlates of motor recovery.** *BMC Neurosci* 2012;13:107
25. Held V, Szabo K, Bazner H, et al. **Chronic small vessel disease affects clinical outcome in patients with acute striatocapsular stroke.** *Cerebrovasc Dis* 2012;33:86–91
26. Koton S, Schwammenthal Y, Merzeliak O, et al. **Cerebral leukoaraiosis in patients with stroke or TIA: clinical correlates and 1-year outcome.** *Eur J Neurol* 2009;16:218–25
27. Kang HJ, Stewart R, Park MS, et al. **White matter hyperintensities and functional outcomes at 2 weeks and 1 year after stroke.** *Cerebrovasc Dis* 2013;35:138–45
28. van Swieten JC, Hijdra A, Koudstaal PJ, et al. **Grading white matter lesions on CT and MRI: a simple scale.** *J Neurol Neurosurg Psychiatry* 1990;53:1080–83

# Whole-Brain Diffusion Tensor Imaging in Correlation to Visual-Evoked Potentials in Multiple Sclerosis: A Tract-Based Spatial Statistics Analysis

D. Lobsien, B. Ettrich, K. Sotiriou, J. Classen, F. Then Bergh, and K.-T. Hoffmann



## ABSTRACT

**BACKGROUND AND PURPOSE:** Functional correlates of microstructural damage of the brain affected by MS are incompletely understood. The purpose of this study was to evaluate correlations of visual-evoked potentials with microstructural brain changes as determined by DTI in patients with demyelinating central nervous disease.

**MATERIALS AND METHODS:** Sixty-one patients with clinically isolated syndrome or MS were prospectively recruited. The mean P100 visual-evoked potential latencies of the right and left eyes of each patient were calculated and used for the analysis. For DTI acquisition, a single-shot echo-planar imaging pulse sequence with 80 diffusion directions was performed at 3T. Fractional anisotropy, radial diffusivity, and axial diffusivity were calculated and correlated with mean P100 visual-evoked potentials by tract-based spatial statistics.

**RESULTS:** Significant negative correlations between mean P100 visual-evoked potentials and fractional anisotropy and significant positive correlations between mean P100 visual-evoked potentials and radial diffusivity were found widespread over the whole brain. The highest significance was found in the optic radiation, frontoparietal white matter, and corpus callosum. Significant positive correlations between mean P100 visual-evoked potentials and axial diffusivity were less widespread, notably sparing the optic radiation.

**CONCLUSIONS:** Microstructural changes of the whole brain correlated significantly with mean P100 visual-evoked potentials. The distribution of the correlations showed clear differences among axial diffusivity, fractional anisotropy, and radial diffusivity, notably in the optic radiation. This finding suggests a stronger correlation of mean P100 visual-evoked potentials to demyelination than to axonal damage.

**ABBREVIATIONS:** AD = axial diffusivity; FA = fractional anisotropy; fMRI = Functional MR Imaging of the Brain; mVEP = mean P100 visual-evoked potentials latencies; RD = radial diffusivity; VEP = visual-evoked potentials

MR imaging plays a pivotal role in establishing the diagnosis and follow-up of MS.<sup>1,2</sup> Besides conventional MR imaging, an advanced technique frequently used in MS studies is DTI.<sup>3</sup> By measuring the diffusion directions of water molecules, DTI is capable of detecting microstructural changes not visible on standard MR imaging. Common parameters obtained from DTI to assess these

changes are fractional anisotropy (FA) and mean diffusivity. Recently, mean diffusivity was further analyzed and divided into radial diffusivity (RD) and axial diffusivity (AD), parameters that allow a more specific approach to the underlying microstructural changes.<sup>4,5</sup> AD was shown to be the primary correlate for histologic markers of axonal integrity,<sup>4</sup> while RD was suggested to provide a specific tool to assess demyelination, distinct from axonal damage.<sup>5</sup>

Pattern reversal visual-evoked potentials (VEP) are an established tool for the evaluation of the optic pathway within the diagnostic work-up of MS, especially as a marker of the integrity of the prechiasmatic part.<sup>6-8</sup> However, they failed to provide reliable results in predicting lesions of the retrochiasmatic part.<sup>9,10</sup> Evoked potentials, in general, and combined evoked potential analysis, in particular, seem to correlate well with the long-term disability of patients with MS. Correlations of evoked potentials and MR imaging are reported controversially. While some studies showed no correlations between evoked potentials and MR imaging,<sup>11</sup> other studies reported significant correlations between VEP and T2 lesion load.<sup>12</sup> However, to the best of our knowledge, a correlation of DTI with VEP has not been published.

Received January 14, 2014; accepted after revision May 16.

From the Departments of Neuroradiology (D.L., K.-T.H., K.S.) and Neurology (B.E., F.T.B., K.S., J.C.), University and University Hospital Leipzig, Leipzig, Germany.

D. Lobsien and B. Ettrich contributed equally to this work.

F. Then Bergh and K.-T. Hoffmann contributed equally to this work.

This work was supported by the German Federal Ministry of Education and Research (PtJ-Bio, 0313909, to B.E. and F.T.B.) and the Hellenic Society of Neurology (to K.S.).

Paper previously presented in part as a poster at: Annual Meeting of the American Academy of Neurology, April 21–28, 2012; New Orleans, Louisiana.

Please address correspondence to Donald Lobsien, MD, Department of Neuroradiology, University and University Hospital Leipzig, Liebigstr 20, 04103 Leipzig, Germany; e-mail: Donald.Lobsien@medizin.uni-leipzig.de

Indicates open access to non-subscribers at [www.ajnr.org](http://www.ajnr.org)

<http://dx.doi.org/10.3174/ajnr.A4034>

## Patient characteristics

Characteristics	
Patients (No.)	61 (41 women, 20 men)
Age (yr)	38.4 ± 12.04
Diagnosis:	
RR-MS	49
CIS	10
PP-MS	1
Recurrent optic neuritis	1
Total patients with optic neuritis (No.) (duration before inclusion in the study)	23 (2.7 ± 1.3 yr)
Mean EDSS score	2.46 ± 1.95
Mean visual acuity	0.85 ± 0.24
mVEP (ms)	113.05 ± 14.26

**Note:**—CIS indicates clinically isolated syndrome; RR-MS, relapsing-remitting MS; PP-MS, primary-progressive MS; EDSS, Expanded Disability Status Scale.

The aim of our study was, therefore, to evaluate the correlation of VEP with parameters derived from DTI with the following objectives: 1) to identify potential relations of VEP to microstructural changes, and 2) to analyze whether such changes reflect demyelination or axonal damage.

## MATERIALS AND METHODS

The study was approved by the local ethics committee of the University of Leipzig.

### Patients

Sixty-one patients (41 women, 20 men) with clinically isolated syndrome or MS were prospectively recruited from the Neuroimmunology Clinic of the Department of Neurology. Ten patients were classified as having clinically isolated syndrome, 49 had definite MS with a relapsing-remitting course, 1 had primary-progressive MS, and 1 had recurrent optic neuritis but did not fulfill the criteria for neuromyelitis optica. The mean age was 38.4 ± 12.0 years, and the mean Expanded Disability Status Scale score was 2.46 ± 1.95. All patients underwent a neurologic examination, a standard VEP examination, and brain MR imaging, including DTI at 3T (see below). Clinical data are shown in the Table. All clinical, electrophysiologic, and imaging examinations in each patient were performed within 3 months. Patients were free of an acute relapse as defined by clinical criteria (history and neurologic examination) for at least 6 months before the first examination and during the study period. None of the patients had a gadolinium-enhancing lesion on T1-weighted images after contrast administration.

### Visual-Evoked Potentials

All VEP were recorded by using the same electrophysiologic device (Medelec Synergy; Oxford Instruments, Oxfordshire, United Kingdom). Stimulation was performed according to standard protocols by checkerboard pattern reversal by using a computer screen at a distance of 1.25 m with a check size of 60 minutes of arc. Latencies of N70 and P100 and N70/P100 amplitudes were determined for all recordings with identifiable VEP. Normal mean laboratory values for P100 latency were determined previously in 30 healthy, 20- to 60-year-old controls at 101.0 ± 6.0 ms. The mean P100 VEP latencies (mVEP) of the right and the left eyes of each patient were calculated.

### MR Imaging

DTI scans were acquired on a clinical 3T MR imaging scanner (Magnetom Trio; Siemens, Erlangen, Germany). A single-shot, echo-planar imaging pulse sequence with the following parameters was performed in all patients: TR, 2700 ms; TE, 93 ms; flip angle, 90°; parallel imaging; 80 diffusion-encoding gradient directions; 1 B0 image;  $b=1000$  s/mm<sup>2</sup>; matrix size, 128 × 128; voxel size, 1.8 × 1.8 × 5 mm. Additionally, standard diagnostic MR imaging sequences were applied, including FLAIR and a T1-weighted axial sequence, after the administration of gadolinium contrast at a standard dosage. A 12-channel head coil was used for all sequences.

### DTI Data Analysis

DTI analysis was performed in a standardized, voxel-based, rater-independent manner by applying tract-based spatial statistics, which belongs to the Functional MRI of the Brain Software Library (FMRIB [FSL; <http://www.fmrib.ox.ac.uk/fsl>]).<sup>13</sup>

Images were preprocessed by using eddy\_correct, the Brain Extraction Tool, and DTIFit in FSL to correct motion and eddy current artifacts, extract the brain, and calculate FA, AD, and RD. All subjects' FA data were then aligned to a 1 × 1 × 1 mm standard space (FMRIB58\_FA) and averaged, and the mean FA image was skeletonized. The skeleton was then thresholded at an FA value of 0.2. Following this step, each FA image was projected onto the mean FA skeleton common to all subjects. The same nonlinear transformations derived from the FA maps were applied to the AD and RD maps.

The imaging data were subsequently analyzed by using the Randomise Tool (<http://www.fmrib.ox.ac.uk/fsl/randomise/>). We set up the General Linear Model design with mVEP as a continuous variable of interest and tested for correlations with diffusion parameters (FA, RD, AD), controlled for the effect of age and sex (covariates of noninterest). All the data were mean-centered. Cluster-like structures were enhanced by using the threshold-free cluster enhancement method. Statistics were built over 10,000 permutations with the maximum threshold-free cluster enhancement recorded at each permutation. The 95th percentile of this distribution was used as a threshold-free cluster enhancement threshold, and the significance level was calculated from this distribution. Thus, significant clusters were fully corrected for family-wise error at  $P < .05$ .

Additionally, we calculated the mean FA, RD, and AD in 2 manually selected ROIs of the skeleton. These ROIs correspond to the thalamic radiations (including the optic radiations) according to the ICBM DTI-81 Atlas ([http://www.loni.usc.edu/ICBM/Downloads/Downloads\\_DTI-81.shtml](http://www.loni.usc.edu/ICBM/Downloads/Downloads_DTI-81.shtml)), which is included in the FMRIB Software Library package. The results of each subject (1 value per patient and parameter, ie, the mean of the 2 ROIs) and each DTI-derived parameter were correlated with the mVEP by using the Spearman rank coefficient. The correlation was performed with GraphPad Prism 4 software (GraphPad Software, San Diego, California).

### Lesion Maps

The T2-FLAIR datasets of all patients were coregistered to a 1 × 1 × 1 mm standard space (Montreal Neurological Institute 156)

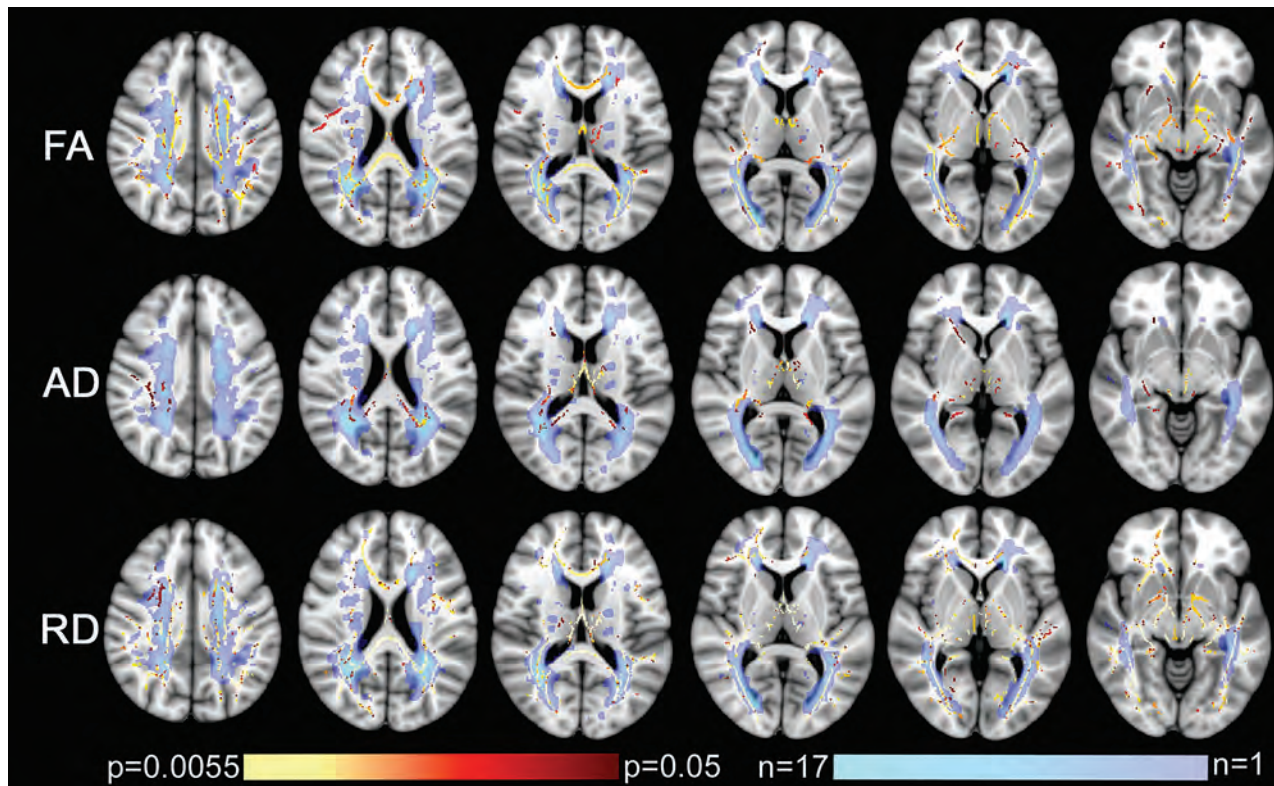


**FIG 1.** Correlations among FA, RD, AD, and mVEP. Shown are the tract-based spatial statistics results of the correlation analysis and the MS lesion distribution. Significant correlations are shown in red to yellow, from  $P = .05$  to  $P = .0055$ . The MS lesion maps (a summation of all patients) are presented in violet to turquoise. Violet indicates an area where only 1 patient had a lesion, while turquoise indicates an area where up to 17 patients had a lesion. The background image is the T1 image of the Montreal Neurological Institute 158 brain. First line (FA): correlation of FA and mVEP. Second line (AD): correlation of AD and mVEP. Third line (RD): correlation of RD and mVEP. Correlations with FA and RD are present in widespread areas, while there are fewer correlations with AD. Highly significant correlations can be identified in the optic radiations among mVEP, FA, and RD, while no correlation could be found between mVEP and AD. Conversely, there are highly significant correlations between mVEP and all measured parameters of DTI within the fornix. T2 lesions are predominantly found along the ventricles. The parieto-occipital region is the location where most patients had lesions.

by using the FMRIB Linear Image Registration Tool to assess white matter lesions. Hyperintense lesions on the T2-FLAIR images of all patients were manually segmented and transformed into binary masks by using FSLView (<http://fsl.fmrib.ox.ac.uk/fsl/fslview/>). Afterward, the masks were summarized with FMRIB's fslmaths and plotted by using a colorized scale to indicate regions with a high or low incidence of lesions among the subjects. The resulting maps were merged with the results of the tract-based spatial statistics analysis to qualitatively identify whether changes were related to normal-appearing white matter or to lesions.

## RESULTS

### Whole-Brain Fractional Anisotropy

Significant negative correlations were found between FA and mVEP (the longer the mVEP, the more decreased was the FA) in widespread regions of the brain. The most significant regions (up to  $P < .0055$ ) were located in the optic radiation, frontoparietal white matter, medial thalamus, fornix bilaterally, and splenium of the corpus callosum. The correlations within the splenium of the corpus callosum and in the fornix included areas of predominantly normal-appearing white matter. Further significant correlations ( $P < .05$ ) were found in multiple locations along the skeleton, including the genu of the corpus callosum, the frontoparietal white matter, and the internal capsule bilaterally. In the

genu of the corpus callosum and the adjacent frontal white matter, a slight asymmetry was detected with a more significant correlation on the right side, while, in the internal capsule, the correlations were a little more significant on the left side. Results are shown in Fig 1.

### Whole-Brain Radial Diffusivity

Multiple significant correlations were found between RD and mVEP (the longer the mVEP the more increased was the RD) along the skeleton. Correlations with the highest significance (up to  $P < .0055$ ) were found in the corpus callosum and bilaterally in the frontoparietal white matter, thalamus, fornix, internal capsule, and optic radiation. In the corpus callosum and the right frontal white matter and the left frontotemporal white matter, these correlations were located in normal-appearing white matter. Voxels of lower significance could be found as well in all these areas. There was a slight asymmetry with more significant correlations in the right frontal white matter. Results are shown in Fig 1.

### Whole-Brain Axial Diffusivity

Compared with the widespread regions in which FA and RD correlated to mVEP, much more restricted areas showed a positive correlation between AD and mVEP. Correlations with the highest

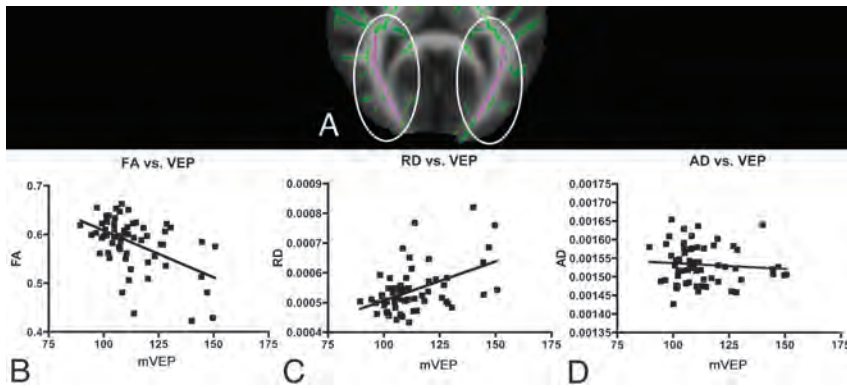


**FIG 2.** Correlations among mean FA, RD, and AD with mVEP in the optic radiation. *A*, The 2 manually selected ROIs of the skeleton corresponding to thalamic radiations (including the optic radiations) according to the ICBM DTI-81 Atlas in the FMRIB Software Library package are shown in purple on the green skeleton. The results of each subject (1 value per patient and parameter, ie, the mean of the 2 ROIs) and each DTI-derived parameter were correlated with the mVEP. *B*, The highly significant negative correlation of the mVEP with the mean FA derived from these particular ROIs is shown (Spearman  $r = -0.432$ ,  $P$  [2-tailed] = .0005). *C*, The highly significant positive correlation of the mean VEP with the mean RD measured in the ROIs is shown (Spearman  $r = 0.398$ ,  $P$  [2-tailed] = .0015). *D*, The missing correlation of the mean AD derived from the ROIs and the mean VEP is shown (Spearman  $r = -0.097$ ,  $P$  [2-tailed] = .458).

significance ( $P < .0055$ ) were found only in the fornix and thalamus bilaterally. Correlations of lower significance were found bilaterally in the splenium of the corpus callosum, the periventricular parietal white matter, the frontoparietal white matter, the right frontal white matter, and the anterior limb of the right internal capsule. There were no correlations in the optic radiations. Results are shown in Fig 1.

#### Optic Radiation Region-of-Interest Analysis

There was a highly significant correlation in the ROIs along the skeleton corresponding to the optic radiation between mean RD and mVEP, a highly negative correlation between mean FA and mVEP, and no correlation between mean AD and mVEP. The results are shown in Fig 2.

## DISCUSSION

We analyzed the relationship between VEP latencies and cerebral microstructure as measured by different parameters of DTI in 61 subjects with demyelinating diseases. A strong positive correlation was found between mVEP and RD, and a strong negative correlation, between mVEP and FA in various areas of the brain, whereas very few positive correlations were found between AD and mVEP.

#### Analysis of Whole-Brain Correlation Patterns

We found far more correlations of the mVEP with RD and FA than with AD. Similar patterns of RD, AD, and FA were reported previously, despite different study designs or correlations with different clinical parameters.

For example, in a study by Liu et al,<sup>14</sup> the degree of disability of patients with MS correlated strongly with RD and FA but not with AD in disseminated areas of the brain, including the thalamus and optic radiation. Additionally, they found correlations among RD, FA, and disease duration, which, in turn, correlated poorly with AD. Sbardella et al<sup>15</sup> reported a strong correlation between multiple sclerosis functional composite subscales and FA in various

areas of the brain regarding almost the whole skeleton, while Onu et al<sup>16</sup> found significant correlations between clinical motor scores and both FA and RD but not AD.

The widespread correlations of mVEP in our study can be considered an *in vivo* equivalent to the observations in a post-mortem study by Klawiter et al,<sup>17</sup> in which RD was predominantly associated with demyelination and, to a much lesser degree, with axonal loss; hence, RD was postulated as a marker of overall tissue integrity within MS lesions. AD, conversely, seemed to be a less sensitive marker because it showed a poor correlation with axonal loss in the same study. Furthermore, postmortem studies suggested that RD and FA could be considered surrogates of cerebral myelin content in patients with MS.<sup>18</sup> In mice, RD was identified as a demyelination marker, and AD

was identified as an axonal damage marker.<sup>5</sup>

In accordance with the literature, our results seem to support the hypothesis that RD could possibly serve as an overall marker for tissue damage caused by MS that correlates not only with clinical parameters of cognitive and motor impairment but also with results of electrophysiologic examinations of the visual system. The prolonged VEP latency might be caused mainly by demyelination, which seems reasonable, because myelination is a main determinant in the speed of action-potential propagation along the axon.

#### Analysis of the Visual Tract

We found a strong correlation between mVEP and RD as well as FA, but not with AD, when focusing on the optic radiation, similar to whole-brain analysis. In the literature, similar patterns of RD, AD, and FA have been reported, despite different study designs and correlations with different clinical parameters.

Liu et al<sup>19</sup> found significant differences between patients and controls in the optic radiation that were present bilaterally in RD and mean diffusivity but only unilaterally in the AD analysis. In another study, they also found significant differences in the optic radiation between patients and controls for RD and FA but not for AD.<sup>14</sup> Rueda Lopes et al<sup>20</sup> also found significant differences within the optic radiation for RD and FA but not for AD in their study of patients with neuromyelitis optica. Roosen daal et al<sup>21</sup> found a significantly lower FA within the optic radiation, including areas with MS lesions and normal-appearing white matter in patients with MS in comparison with healthy controls. Onu et al<sup>16</sup> found a significant difference between patients with MS and controls for RD and FA in the optic radiation. However, in a recent study, Kolbe et al<sup>22</sup> found no correlation of visual acuity in optic neuritis with DTI parameters within the optic radiation but did find a correlation within prefrontal and temporal brain regions.

Optic pathway involvement is common in MS, in the acute phase and in chronic stages.<sup>23</sup> VEP show a correlation with measures of visual acuity and disease severity, though there are con-

troveries regarding the correlation with the clinical course of the disease.<sup>8</sup> If we take these aspects into account, the relation between the electrophysiologic function (mVEP) and the microstructural damage (DTI) we found seems very reasonable.

### **Analysis of Normal-Appearing White Matter and Deep Gray Matter of the Fornix and Thalamus**

In contrast to most other areas that showed correlations to mVEP, we found a highly significant correlation of mVEP with both an AD and RD increase and with an FA decrease in the fornix bilaterally and in the medial aspects of the thalamus, all being areas of normal-appearing white or deep gray matter, respectively.

Concerning changes of the fornix in MS, the literature is limited. Kern et al<sup>24</sup> found significantly reduced FA in patients with MS compared with healthy controls in the fornix in a study of verbal memory function. Higher FA values correlated with a better performance in verbal memory tests in patients. The authors concluded that successful functional compensation of hippocampal involvement might be limited in part by damage to the fornix, consistent with the critical role of this pathway in the clinical expression of memory impairment in MS. This limitation could be a direct consequence of demyelination and an indirect result of primary hippocampal damage.<sup>25</sup>

Roosendaal et al<sup>21</sup> found clearly reduced FA in both fornices by using a tract-based spatial statistics–based analysis, mainly focusing on normal-appearing white matter. Similar to Kern et al,<sup>24</sup> they assumed at least 2 reasons for this: 1) secondary degeneration caused by disseminated focal demyelination of the hippocampus, and 2) direct demyelination of the fornix, both of which had been demonstrated in postmortem studies of patients with MS. Experimental studies in rats identified important functions of hippocampal projections for spatial-visual perception, and animals with fornix lesions performed substantially worse than healthy ones in visual shape recognition.<sup>25,26</sup>

It is unclear why in our study, mVEP correlated so significantly with all 3 DTI metrics in this specific white matter tract that is not directly associated with visual function. A hypothesis is that secondary and primary pathologic changes might play a role in this structure; therefore, both demyelination and axonal damage are present. This hypothesis could explain the significant correlation with AD, RD, and FA in the fornix in contrast to the correlation patterns in most other brain structures.

Regarding the thalamus in MS, there is very little literature dealing specifically with DTI. Extensive, confluent, subependymal thalamic demyelination is relatively common as is diffuse microglial activation in normal-appearing thalami, indicating direct and secondary tissue damage.<sup>27</sup> This finding seems to support ours of rather mixed changes with a correlation pattern pointing to various causes of thalamic tissue alterations in demyelinating disease (ie, both primarily and secondarily induced damage).

### **Limitations**

There are some limitations of our study. The patient sample was not homogeneous in terms of sex. Although reflecting the normal sex distribution of MS, an implication on the results is possible because sex-specific differences in various aspects of DTI analyses were found in other studies.<sup>28</sup> Therefore, we corrected for sex as a

covariate of noninterest. However, because our major aim was to analyze the correlation between mVEP and DTI and not to evaluate sex differences, we did not perform subgroup analyses.

Concerning technical aspects, the DTI sequence used has a relatively low resolution on the z-axis. This could bias the detection of correlations, especially in small structures, to an unknown extent. However, the technique used is in line with recent literature referring to this topic, which is relatively heterogeneous. For example, in the literature, section thickness ranges from approximately 2–5 mm; some studies use gaps between sections and varying field strengths, and various numbers of diffusion gradients (among other parameters) are applied.<sup>16,19,21</sup> Finally, the exact histopathologic processes responsible for changes detected by DTI are understood only in part; therefore, conclusions must be interpreted with caution.

### **CONCLUSIONS**

Our results show that widespread microstructural changes of the whole brain in MS correlate significantly with VEP. Clear differences among AD, FA, and RD, notably in the optic radiation, suggest a stronger correlation of mVEP with demyelination than with axonal damage. In conjunction with the literature, our results support the hypothesis that the parameters FA, RD, and AD could serve potentially as relevant imaging markers for demyelinating disease staging and burden quantification beyond the application in clinical studies.

### **ACKNOWLEDGMENTS**

We thank Alfred Anwander, MD, for helpful technical hints with DTI data analysis.

Disclosures: Barbara Ettrich—*RELATED: Grant:* Federal Ministry of Education and Research, through the Translational Centre for Regenerative Medicine.\* Konstantinos Sotiriou—*RELATED: Grant:* Hellenic Neurological Society, *Comments:* I received a grant from the Hellenic (Greek) Neurological society, for my fellowship in the Neuroradiology Department of the University Hospital in Leipzig, Germany. Florian Then Bergh—*RELATED: Grant:* Federal Ministry of Education and Research through the Translational Centre for Regenerative Medicine.\* *UNRELATED: Board Membership:* I received personal compensation for activities with Bayer, Biogen Idec, Novartis, Merck-Serono, and Sanofi-Aventis Pharmaceuticals as a speaker and/or member on an advisory board, *Grants/Grants Pending:* I received research support from Bayer Pharmaceuticals Corporation\* and Teva Neuroscience.\* *Payment for Lectures (including service on Speakers Bureaus):* I received personal compensation for activities with Bayer, Biogen Idec, Novartis, Merck-Serono, and Sanofi-Aventis Pharmaceuticals as a speaker and/or member on an advisory board. \*Money paid to the institution.

### **REFERENCES**

1. Ciccarelli O, Toosy AT, Hickman SJ, et al. **Optic radiation changes after optic neuritis detected by tractography-based group mapping.** *Hum Brain Mapp* 2005;25:308–16
2. Vigeveno RM, Wiebenga OT, Wattjes MP, et al. **Shifting imaging targets in multiple sclerosis: from inflammation to neurodegeneration.** *J Magn Reson Imaging* 2012;36:1–19
3. Filippi M, Rocca MA, De Stefano N, et al. **Magnetic resonance techniques in multiple sclerosis: the present and the future.** *Arch Neurol* 2011;68:1514–20
4. Budde MD, Xie M, Cross AH, et al. **Axial diffusivity is the primary correlate of axonal injury in the experimental autoimmune encephalomyelitis spinal cord: a quantitative pixelwise analysis.** *J Neurosci* 2009;29:2805–13
5. Song SK, Yoshino J, Le TQ, et al. **Demyelination increases radial diffusivity in corpus callosum of mouse brain.** *Neuroimage* 2005;26:132–40

6. Halliday AM, McDonald WI, Mushin J. **Visual evoked response in diagnosis of multiple sclerosis.** *Br Med J* 1973;4:661–64
7. Lascano AM, Brodbeck V, Lalive PH, et al. **Increasing the diagnostic value of evoked potentials in multiple sclerosis by quantitative topographic analysis of multichannel recordings.** *J Clin Neurophysiol* 2009;26:316–25
8. Weinstock-Guttman B, Baier M, Stockton R, et al. **Pattern reversal visual evoked potentials as a measure of visual pathway pathology in multiple sclerosis.** *Mult Scler* 2003;9:529–34
9. Benbadis SR, Lancman ME, Wolgamuth BR, et al. **Value of full-field visual evoked potentials for retrochiasmal lesions.** *J Clin Neurophysiol* 1996;13:507–10
10. Plant GT, Kermode AG, Turano G, et al. **Symptomatic retrochiasmal lesions in multiple sclerosis: clinical features, visual evoked potentials, and magnetic resonance imaging.** *Neurology* 1992;42:68–76
11. Schlaeger R, D'Souza M, Schindler C, et al. **Combined evoked potentials as markers and predictors of disability in early multiple sclerosis.** *Clin Neurophysiol* 2012;123:406–10
12. Kantorová E, Ziak P, Kurca E, et al. **Visual evoked potential and magnetic resonance imaging are more effective markers of multiple sclerosis progression than laser polarimetry with variable corneal compensation.** *Front Hum Neurosci* 2014;8:10
13. Smith SM, Jenkinson M, Johansen-Berg H, et al. **Tract-based spatial statistics: voxelwise analysis of multi-subject diffusion data.** *Neuroimage* 2006;31:1487–505
14. Liu Y, Duan Y, He Y, et al. **Whole brain white matter changes revealed by multiple diffusion metrics in multiple sclerosis: a TBSS study.** *Eur J Radiol* 2012;81:2826–32
15. Sbardella E, Petsas N, Tona F, et al. **Assessing the correlation between grey and white matter damage with motor and cognitive impairment in multiple sclerosis patients.** *PLoS One* 2013;8:e63250
16. Onu M, Roceanu A, Sbotto-Frankensten U, et al. **Diffusion abnormality maps in demyelinating disease: correlations with clinical scores.** *Eur J Radiol* 2012;81:e386–91
17. Klawiter EC, Schmidt RE, Trinkaus K, et al. **Radial diffusivity predicts demyelination in ex vivo multiple sclerosis spinal cords.** *Neuroimage* 2011;55:1454–60
18. Schmierer K, Wheeler-Kingshott CA, Boulby PA, et al. **Diffusion tensor imaging of post mortem multiple sclerosis brain.** *Neuroimage* 2007;35:467–77
19. Liu Y, Duan Y, He Y, et al. **A tract-based diffusion study of cerebral white matter in neuromyelitis optica reveals widespread pathological alterations.** *Mult Scler* 2012;18:1013–21
20. Rueda Lopes FC, Doring T, Martins C, et al. **The role of demyelination in neuromyelitis optica damage: diffusion-tensor MR imaging study.** *Radiology* 2012;263:235–42
21. Roosendaal SD, Geurts JJ, Vrenken H, et al. **Regional DTI differences in multiple sclerosis patients.** *Neuroimage* 2009;44:1397–403
22. Kolbe SC, Marriott M, Walt Av, et al. **Diffusion tensor imaging correlates of visual impairment in multiple sclerosis and chronic optic neuritis.** *Invest Ophthalmol Vis Sci* 2012;53:825–32
23. Jasse L, Vukusic S, Durand-Dubief F, et al. **Persistent visual impairment in multiple sclerosis: prevalence, mechanisms and resulting disability.** *Mult Scler* 2013;19:1618–26
24. Kern KC, Ekstrom AD, Suthana NA, et al. **Fornix damage limits verbal memory functional compensation in multiple sclerosis.** *Neuroimage* 2012;59:2932–40
25. Gaffan EA, Bannerman DM, Warburton EC, et al. **Rats' processing of visual scenes: effects of lesions to fornix, anterior thalamus, mammillary nuclei or the retrohippocampal region.** *Behav Brain Res* 2001;121:103–17
26. Thomas AG, Koumellis P, Dineen RA. **The fornix in health and disease: an imaging review.** *Radiographics* 2011;31:1107–21
27. Minagar A, Barnett MH, Benedict RH, et al. **The thalamus and multiple sclerosis: modern views on pathologic, imaging, and clinical aspects.** *Neurology* 2013;80:210–19
28. Schoonheim MM, Vigeveno RM, Rueda Lopes FC, et al. **Sex-specific extent and severity of white matter damage in multiple sclerosis: implications for cognitive decline.** *Hum Brain Mapp* 2014;35:2348–58

# Utility of Intravoxel Incoherent Motion MR Imaging for Distinguishing Recurrent Metastatic Tumor from Treatment Effect following Gamma Knife Radiosurgery: Initial Experience

D.Y. Kim, H.S. Kim, M.J. Goh, C.G. Choi, and S.J. Kim



## ABSTRACT

**BACKGROUND AND PURPOSE:** Intravoxel incoherent motion MR imaging can simultaneously measure the diffusion and perfusion characteristics of brain tumors. Our aim was to determine the utility of intravoxel incoherent motion–derived perfusion and diffusion parameters for assessing the treatment response of metastatic brain tumor following gamma knife radiosurgery.

**MATERIALS AND METHODS:** Ninety-one consecutive patients with metastatic brain tumor treated with gamma knife radiosurgery were assessed by using intravoxel incoherent motion imaging. Two readers independently calculated the 90th percentile and the 10th percentile histogram cutoffs for perfusion, normalized CBV, diffusion, and ADC. Areas under the receiver operating characteristic curve and interreader agreement were assessed.

**RESULTS:** With the combination of the 90th percentile histogram cutoff for perfusion and the 10th percentile histogram cutoff for diffusion, the sensitivity and specificity for differentiating recurrent tumor and treatment were 79.5% and 92.3% for reader 1 and 84.6% and 94.2% for reader 2, respectively. With the combination of the 90th percentile histogram cutoff for normalized CBV and the 10th percentile histogram cutoff for ADC, the sensitivity and specificity for differentiating recurrent tumor and treatment were 69.2% and 100.0% for reader 1 and 74.3% and 100.0% for reader 2, respectively. Compared with the combination of 90th percentile histogram cutoff for normalized CBV and the 10th percentile histogram cutoff for ADC, adding intravoxel incoherent motion to 90th percentile histogram cutoff for normalized CBV substantially improved the diagnostic accuracy for differentiating recurrent tumor and treatment from 86.8% to 92.3% for reader 1 and from 89.0% to 93.4% for reader 2, respectively. The intraclass correlation coefficients between readers were higher for perfusion parameters (intraclass correlation coefficient range, 0.84–0.89) than for diffusion parameters (intraclass correlation coefficient range, 0.68–0.79).

**CONCLUSIONS:** Following gamma knife radiosurgery, intravoxel incoherent motion MR imaging can be used as a noninvasive imaging biomarker for differentiating recurrent tumor from treatment effect in patients with metastatic brain tumor.

**ABBREVIATIONS:** ADC10 = 10th percentile histogram cutoff for ADC; D = diffusion; D\* = pseudodiffusion coefficient; D10 = 10th percentile histogram cutoff for D; f = perfusion; f90 = 90th percentile histogram cutoff for f; GKRS = gamma knife radiosurgery; ICC = intraclass correlation coefficient; IVIM = intravoxel incoherent motion; nCBV = normalized CBV; nCBV90 = 90th percentile histogram cutoff for nCBV

Perfusion MR imaging techniques have significantly advanced and can now provide information regarding tumor physiology. There are several reports suggesting the usefulness of dy-

namic susceptibility contrast-enhanced perfusion MR imaging for differentiating recurrent metastatic brain tumor from stereotactic radiosurgery–induced radiation necrosis.<sup>1–3</sup> However, quantitative brain perfusion measurement remains a challenge for currently available MR perfusion methods. DSC and dynamic contrast-enhanced MR imaging are inhibited by their signal non-linearity, and arterial spin-labeling exhibits, in addition to a low signal-to-noise ratio, a strong dependence on the transit time.

Le Bihan et al<sup>4</sup> defined intravoxel incoherent motion (IVIM) as the microscopic translational motion occurring in each image voxel in MR imaging. In biologic tissue, this incoherent motion includes molecular diffusion of water and microcirculation of blood in the capillary network, referred to as “perfusion.” These 2 phenomena account for the biexponential decay of the signal in-

Received February 8, 2014; accepted after revision April 3.

From the Department of Radiology and Research Institute of Radiology, University of Ulsan College of Medicine, Asan Medical Center, Seoul, Korea.

This research was supported by Basic Science Research Program through the National Research Foundation of Korea funded by the Ministry of Education, Science and Technology (grant 2011-0002629).

Please address correspondence to Ho Sung Kim, MD, PhD, Department of Radiology and Research Institute of Radiology, University of Ulsan College of Medicine, Asan Medical Center, 86 Asanbyeongwon-Gil, Songpa-Gu, Seoul 138–736, Korea; e-mail: radhskim@gmail.com

Indicates open access to non-subscribers at [www.ajnr.org](http://www.ajnr.org)

<http://dx.doi.org/10.3174/ajnr.A3995>

tensity on DWI when different diffusion b-values are applied. With the IVIM theory, both true molecular diffusion and water molecule motion in the capillary network can be estimated by using a single diffusion imaging-acquisition technique. As opposed to DSC, dynamic contrast-enhanced imaging, and arterial spin-labeling, IVIM has a unique capillary dependence that is not sensitive to the coherent laminar flow of arteries and veins. The measurement of IVIM is intrinsically local (ie, the encoding and readout are performed at the same location).<sup>5</sup>

In our clinical experience, the major advantage of IVIM MR imaging is that because it allows the simultaneous acquisition of diffusion and perfusion parameters, it can provide both measures within corresponding solid lesions without the requirement for a further coregistration processing step. In the current study, we attempted to validate the IVIM-derived perfusion and diffusion parameters by using the clinicoradiologic correlation in patients with post-gamma knife radiosurgery (GKRS) metastatic brain tumor. We also assessed the diagnostic accuracy and added value of the IVIM method for differentiating recurrent tumor from treatment effect, compared with the combination of DSC perfusion MR imaging and DWI, which has commonly been used as a parameter for brain tumor imaging.

Our hypothesis was that the difference in vascularity between recurrent tumor and the treatment effect can be assessed by using an IVIM-derived perfusion fraction (*f*); and the combination of *f* and the true diffusion parameter (*D*) would show diagnostic performance comparable with the combination of normalized CBV (*nCBV*) and the ADC. The purpose of this study was to determine the utility of IVIM-derived perfusion and diffusion parameters for assessing the treatment response of metastatic brain tumor following GKRS.

## MATERIALS AND METHODS

### Study Population

A retrospective review of the data base of our medical institution identified 571 consecutive patients treated with GKRS between May 2010 and January 2014. Among these patients, 138 met the following inclusion criteria: 1) They had pathologically confirmed primary systemic cancer, 2) had a metastatic intra-axial tumor seen on brain MR imaging, 3) demonstrated enlarged regions of contrast enhancement based on  $\geq 2$  consecutive MR images within the radiation field suggestive of recurrent tumor or treatment effect, 4) underwent conventional MR imaging by using both IVIM and DSC perfusion MR imaging to evaluate the enlarged contrast-enhancing lesion, 5) were on zero steroid dose at the time of IVIM and DSC perfusion MR imaging, 6) had adequate image acquisition and quality without patient motion and significant susceptibility artifacts, and 7) underwent adequate clinicoradiologic follow-up to definitively determine their diagnosis. Eight patients were initially excluded from this study because they underwent gross total resection of the contrast-enhancing mass for a presumptive diagnosis of glioblastoma.

The remaining 130 who did not undergo surgical resection for presumed metastatic brain tumor before GKRS were subsequently followed by using both a clinical examination and an MR imaging study every 3 months. According to the protocol of our institution, the decision-making for treatment change or salvage

radiation therapy was based on both the clinical symptoms and the findings of noninvasive advanced imaging studies by consensus of a neuro-oncologist and a neuroradiologist. Therefore, stereotactic biopsy only for the pathologic diagnosis of an enlarged contrast-enhancing lesion has been rarely performed and was not included in this study. A surgical resection was indicated only for decompression to relieve significant patient symptoms. In this study, we determined the final diagnosis between recurrent tumor and treatment effect on the basis of adequate clinicoradiologic follow-up. The diagnosis of treatment effect was made if an enlarged contrast-enhancing lesion showed complete response, partial response, or stable disease depending on the Response Evaluation Criteria in Solid Tumor method on  $>2$  subsequent follow-up MR imaging studies for a minimum of 3 months. Complete and partial responses were defined as the disappearance of lesions or a decrease in tumor volume of  $>50\%$  on MR imaging. Recurrent metastatic tumor was also clinicoradiologically diagnosed if the contrast-enhancing lesion presented with a volume increase on  $>2$  subsequent follow-up MR imaging studies for a minimum of 3 months, accompanied by neurologic deterioration. Thirty-nine patients with equivocal clinical and image findings that did not meet the above final diagnostic criteria, such as prolonged asymptomatic increases of a contrast-enhancing lesion, were excluded from this study. Finally, 91 patients were enrolled. The most common primary tumor was lung cancer (69 of 91 patients, 76%), followed by breast cancer (21 of 91 patients, 23%) and colon cancer (1 of 91 patients, 1%). According to our inclusion criteria, hemorrhagic metastatic tumors, which can affect the results of IVIM and DSC perfusion MR imaging, were excluded from this study.

For contrast-enhancing lesion volume measurement, the maximal diameter of the lesion was measured in 3 orthogonal planes. Lesion volume was calculated according to the following formula: volume = length  $\times$  width  $\times$  height / 2.17. Each contrast-enhancing lesion volume on follow-up MR imaging was then compared with that on a prior MR imaging study.<sup>2</sup>

### Imaging Protocol

MR imaging was performed by using a 3T system (Achieva; Philips Healthcare, Best, the Netherlands) with an 8-channel sensitivity-encoding head coil. We acquired 16 different b-values (0, 10, 20, 40, 60, 80, 100, 120, 140, 160, 180, 200, 300, 500, 700, and 900 s/mm<sup>2</sup>) in 3 orthogonal directions, and the corresponding trace was calculated before contrast injection. We used a large number of lower b-values in our study to improve the accuracy of the perfusion fraction. The images were oriented axially with a section thickness of 5 mm, FOV of 240 mm, matrix of 136  $\times$  138, and TR/TE of 3000/72 ms. A correction of eddy current-induced distortions was enabled by using gradient pre-emphasis. Parallel imaging was done with an acceleration factor of 2, and the total acquisition time was 4 minutes 21 seconds.

DSC MR perfusion imaging was performed by using a gradient-echo, echo-planar sequence during the administration of contrast material (gadoterate meglumine, Dotarem; Guerbet, Aulnay-sous-Bois, France) at a rate of 4 mL/s by using an MR imaging-compatible power injector (Spectris MR injector; MedRad, Indianola, Pennsylvania). The bolus of contrast mate-

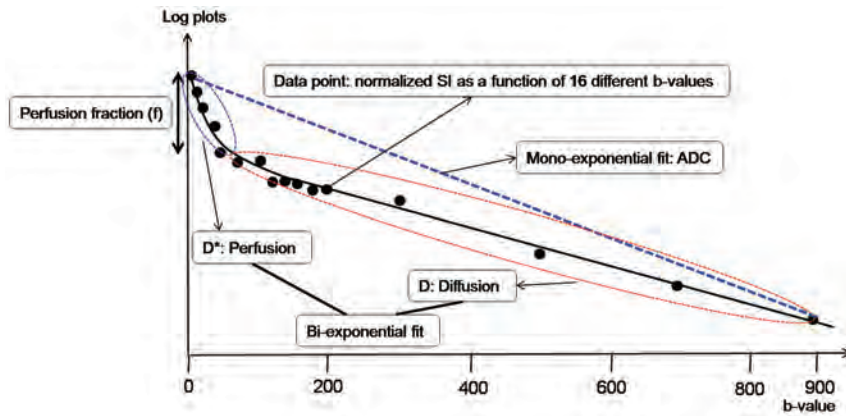


**FIG 1.** Illustration for biexponential signal decay as a function of the 16 different diffusion b-values in a given voxel of a recurrent tumor. The bold, solid line is the IVIM nonlinear regression fit providing D, D\*, and f. The biexponential fit provides the fast decay associated with perfusion (blue dotted circle), and the red dotted circle represents the slow decay of the biexponential fit, thus indicating true diffusion. The blue dotted line shows the monoexponential fit providing the ADC.

rial was followed by a 20-mL bolus of saline administered at the same injection rate. The image dataset was obtained during the first pass of the contrast agent until 59 time points were obtained, with a temporal resolution of 1.4 seconds and 5 baseline time points. The detailed imaging parameters for the DSC study were as follows: TR/TE, 1407/40 ms; flip angle, 35°; FOV, 24 cm; matrix, 128 × 128; and number of sections, 20. The total DSC MR imaging acquisition time was 1 minute 30 seconds.

### IVIM Fitting

The relationship between signal variation and b factors in an IVIM-type sequence can be expressed by the following equation<sup>5</sup>:

$$1) \quad \frac{S(b)}{S_0} = (1 - f)e^{-bD} + fe^{-bD^*}$$

where S is the mean signal intensity; S<sub>0</sub> is the signal intensity without diffusion; a pseudodiffusion coefficient D\* can be defined, which describes macroscopically the incoherent movement of blood in the microvasculature compartment; a perfusion fraction, f, describes the fraction of incoherent signal that arises from the vascular compartment in each voxel over the total incoherent signal; and D is the diffusion parameter representing true molecular diffusion (the slow component of diffusion) (Fig 1).

The IVIM signal equation was fitted on a voxel-by-voxel basis by using an in-house program with Matlab2010b (MathWorks, Natick, Massachusetts). Two different approaches were implemented to generate IVIM parametric images (D, D\*, and f): first, full biexponential fit, and second, initial estimation of D by using a reduced set of b-values of >200 s/mm<sup>2</sup>. In the second method, because D\* contribution can be neglected at high b-values (b ≥ 200 s/mm<sup>2</sup>), D was extracted by using high b-values and a monoexponential fit. Subsequently, with the resulting D as a fix parameter, the curve was fitted for f and D\* with a nonlinear regression.<sup>5,6</sup> Previous reports found that the second approach delivered the most robust and signal-to-noise-enhanced results; therefore, IVIM parameters were calculated by using the second approach in all patients.<sup>7,8</sup> In addition, an ADC measurement was

calculated by using b=0 and 900 s/mm<sup>2</sup> and a simple monoexponential fit to compare the ADC with the IVIM-derived D.

### Image Processing

All imaging data were transferred from the MR imaging scanner to an independent personal computer for quantitative IVIM and DSC MR perfusion analyses. Contrast-enhancing lesion volumes were segmented on 3D postcontrast T1-weighted images by using a semiautomated adaptive thresholding technique so that all the pixels above the threshold value were selected. Therefore, significant regions of macroscopic necrosis, cystic areas, and CSF-filled ventricles and sulci were excluded. The resulting entire enhancing tumor volumes were verified by 2 experienced neuroradiologists (H.S.K.,

with 9 years of clinical experience in neuro-oncologic imaging, and M.J.G., with 2 years of clinical experience in neuro-oncologic imaging) who were blinded to pathologic and other imaging findings. A rigid coregistration between IVIM and anatomic MR images was performed. Each parametric value was calculated on a voxel-by-voxel basis for the segmented contrast-enhancing volume and was used for the histogram analysis (Fig 2).

The DSC perfusion parametric map was obtained by using a commercial software package (nordicICE; NordicNeuroLab, Bergen, Norway). For DSC MR perfusion imaging, after eliminating recirculation of the contrast agent by using  $\gamma$ -variate curve fitting and contrast agent leakage correction, the relative CBV was computed by using numeric integration of the curve. On a pixel-by-pixel basis, the nCBV maps were calculated by dividing each relative CBV value by an unaffected, white-matter relative CBV value defined by 2 readers (H.S.K. and M.J.G.).

### Imaging Analysis

For the cumulative histogram parameters, the 90th percentile for f (f<sub>90</sub>) and nCBV (nCBV<sub>90</sub>) and the 10th percentile for D (D<sub>10</sub>) and ADC (ADC<sub>10</sub>) were derived (the *n*th percentile is the point at which *n*% of the voxel values that form the histogram are found to the left). This choice was made because the 10th percentile parameter is analogous to and statistically more reliable than the minimum value that has been commonly used with the “hot-spot” method. The 90th percentile cutoffs are analogous to and statistically more reliable than the maximum value, which has commonly been used with the hot-spot method. Moreover, this type of histogram parameter is more effective than the mean value for identifying areas where tumorous lesions intermix with treatment-related change, and it is less influenced by random statistical fluctuations than are the maximum and mean values.

### Statistical Analysis

The Student *t* test was used to identify significant differences in the independent variables between the 2 groups. Receiver operat-

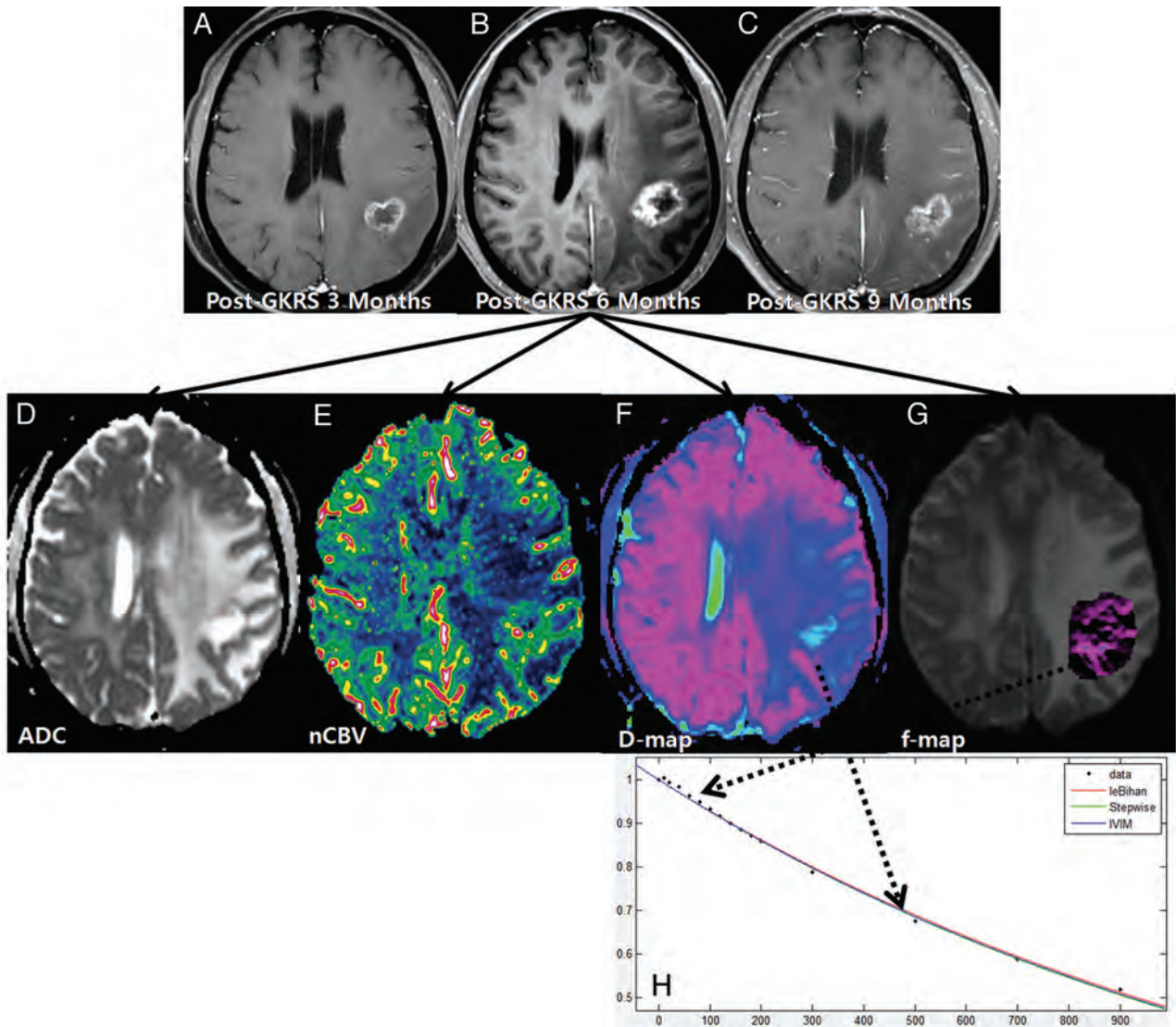


**FIG 2.** A 61-year-old woman with treatment effect following GKRS. Axial contrast-enhanced T1-weighted images, obtained 3 (A) and 6 months (B) after GKRS, show a progressively enlarging necrotic contrast-enhancing lesion in the left parietal lobe. C, The necrotic contrast-enhancing lesion is stabilized on a subsequent follow-up image obtained 9 months after GKRS, thus indicating treatment effect. The ADC (D) and nCBV (E) maps show no visual decrease of the ADC and no visual increase of the nCBV in the corresponding area of the contrast-enhancing lesion in B, respectively. The D (F) and f (G) maps show no visual decrease of the D value and no visual increase of the f value in the corresponding area of the contrast-enhancing lesion in B, respectively. H, The signal decay curve, plotted as a function of the diffusion b-values, is monoexponential.

ing characteristic curve analysis was performed to assess the optimum cutoff of the independent variables for differentiating recurrent tumor-versus-treatment effect.

A leave-one-out cross-validation was used to evaluate the performance of the independent variables (f90, nCBV90, D10, and ADC10). In each round of the leave-one-out validation, 1 participant was selected as a testing sample. The remaining participants were used as training samples to construct the classifier. The testing sample was then classified with the trained classifier. Such a procedure was repeated until each participant was tested 1 time.

Interreader agreement was assessed by using the ICC with 95% confidence intervals and applying a 2-way ICC with random raters' assumption reproducibility. A  $P$  value  $< .05$  was considered a significant difference. Statistical analyses were

performed by using the Statistical Package for the Social Sciences software (Version 19.0; IBM, Armonk, New York).

## RESULTS

Of the 91 study patients, 39 (42.9%) were subsequently classified as having recurrent tumors, and 52 (57.1%), as having treatment effects. Descriptive statistics regarding the demographic data obtained in both the recurrent tumor and the treatment effect patients are summarized in Table 1.

### Visual Analysis of Imaging Parameters

Among the 91 study patients, analysis of all of the patients with recurrent tumor and 9 patients with treatment effect showed that the signal decay curve, plotted as a function of the diffusion b-val-

ues, was biexponential and ranged from 0 to 900 s/mm<sup>2</sup>. The recurrent tumor group showed more rapid signal decay than the treatment effect group in the range of lower b-values ( $b < 200$  s/mm<sup>2</sup>) (Fig 3). In the remaining 43 patients with treatment effect, the signal decay curve was similar to the monoexponential pattern (Fig 2). The f, nCBV, D, and ADC maps of representative

cases of recurrent tumor and treatment effect are shown in Figs 2 and 3.

### Diagnostic Accuracy of Imaging Parameters

The mean  $\pm$  SD of f90, D10, nCBV90, and ADC10 in both the recurrent tumor and treatment effect groups are shown in Table 2. The mean f90 showed statistically significant differences between recurrent tumor and treatment effect, with the recurrent tumor group showing a higher f90 (mean of 0.079 versus 0.048 for reader 1 and 0.081 versus 0.046 for reader 2;  $P < .001$  for each). The mean D10 was significantly lower in the recurrent tumor group (mean of 0.970 [ $10^{-3}$  mm<sup>2</sup>s<sup>-1</sup>] and 0.967 for readers 1 and 2, respectively) than in the treatment effect group (mean

**Table 1: Comparison of study patient demographic data**

Variables	Recurrent Tumor	Treatment Effect	P Value
No. of male patients	19 (53.3%)	27 (61.9%)	.272
No. of female patients	20 (46.7%)	25 (38.1%)	
Age (yr) <sup>a</sup>	47.4 $\pm$ 6.7	51.5 $\pm$ 8.5	.395
Mean gamma knife dose (Gy) <sup>a</sup>	17.5 $\pm$ 0.7	17.3 $\pm$ 0.5	.872
Target volume (mL) <sup>a</sup>	6.52 $\pm$ 7.01	5.97 $\pm$ 5.19	.312
Time interval between GKRS and detection of a new or enlarging, contrast-enhancing lesion (wk) <sup>a</sup>	34.7 $\pm$ 15.4	37.9 $\pm$ 17.3	.159
Time interval between GKRS and the last follow-up (wk) <sup>a</sup>	85.1 $\pm$ 22.1	89.2 $\pm$ 27.2	.576

<sup>a</sup>Data are means.

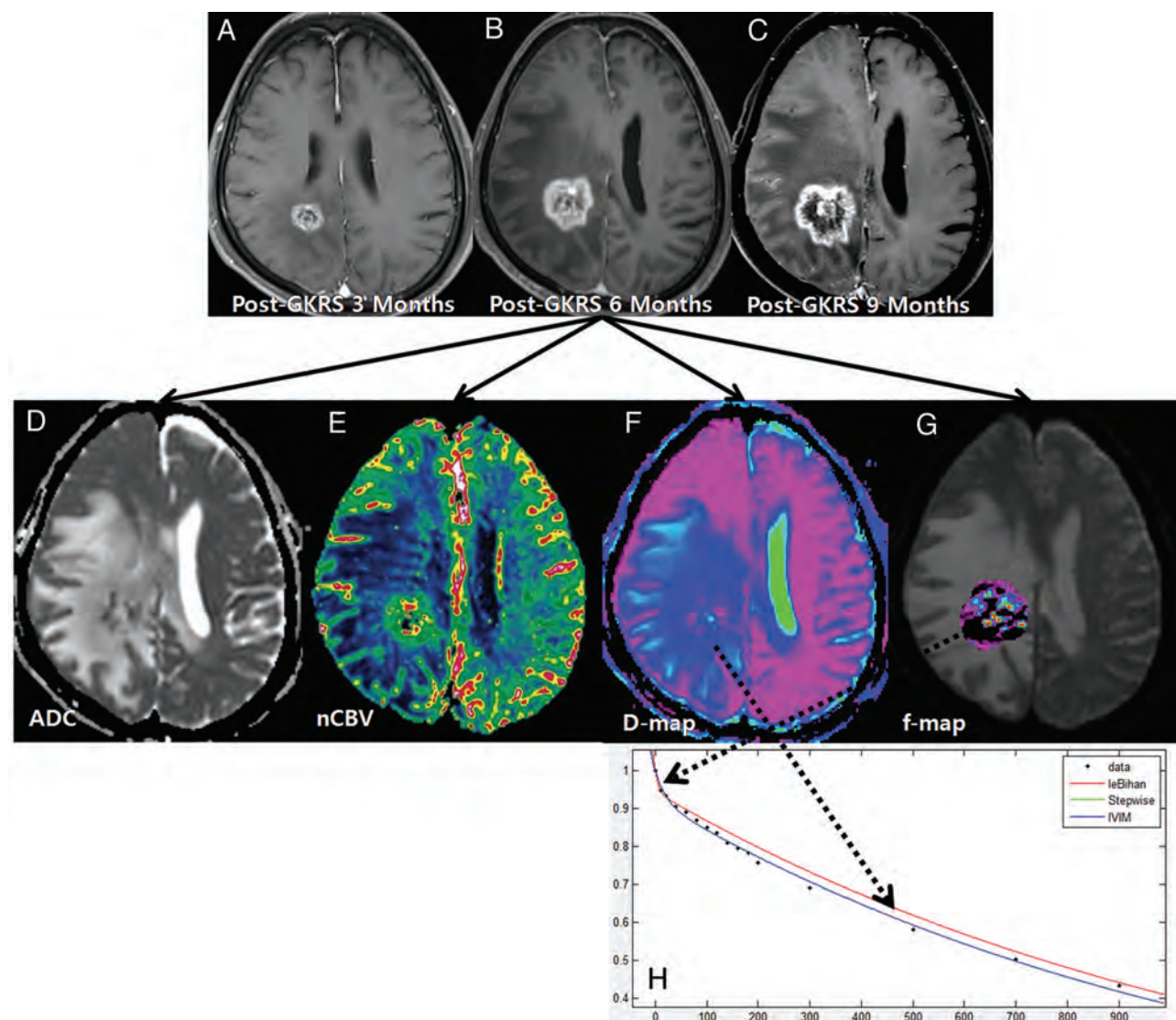


**FIG 3.** A 54-year-old man with recurrent tumor following GKRS. Axial contrast-enhanced T1-weighted images, obtained 3 (A), 6 (B), and 9 months (C) after GKRS, show a progressively enlarging necrotic contrast-enhancing lesion in the right parietal lobe. The ADC (D) and nCBV (E) maps show a visual decrease of the ADC and a visual increase of the nCBV in the corresponding area of the contrast-enhancing lesion in B, respectively. The D (F) and f (G) maps show a visual decrease of the D value and a visual increase of the f value in the corresponding area of the contrast-enhancing lesion in B, respectively. H, The signal-decay curve, plotted as a function of the diffusion b-values, is biexponential.

**Table 2: Differences in the imaging parameters in patients with recurrent tumor and those with treatment effect**

Parameters	Reader 1			Reader 2		
	Recurrent Tumor	Treatment Effect	P Value	Recurrent Tumor	Treatment Effect	P Value
f90 <sup>a</sup>	0.079 ± 0.019	0.048 ± 0.009	<.001	0.081 ± 0.017	0.046 ± 0.012	<.001
D*90 <sup>a</sup> (10 <sup>-3</sup> mm <sup>2</sup> s <sup>-1</sup> )	39.1 ± 21.2	16.4 ± 12.6	.009	32.4 ± 22.5	19.5 ± 11.6	.024
D10 <sup>a</sup> (10 <sup>-3</sup> mm <sup>2</sup> s <sup>-1</sup> )	0.970 ± 0.082	1.043 ± 0.062	<.001	0.967 ± 0.071	1.045 ± 0.055	<.001
nCBV90 <sup>a</sup>	4.457 ± 1.301	2.674 ± 0.348	<.001	4.782 ± 1.122	2.551 ± 0.416	<.001
ADC10 <sup>a</sup> (10 <sup>-3</sup> mm <sup>2</sup> s <sup>-1</sup> )	0.986 ± 0.079	1.052 ± 0.059	<.001	0.991 ± 0.092	1.055 ± 0.072	<.001

Note:—D\*90 indicates the 90th percentile histogram cutoff of D\*.

<sup>a</sup>Data are means.

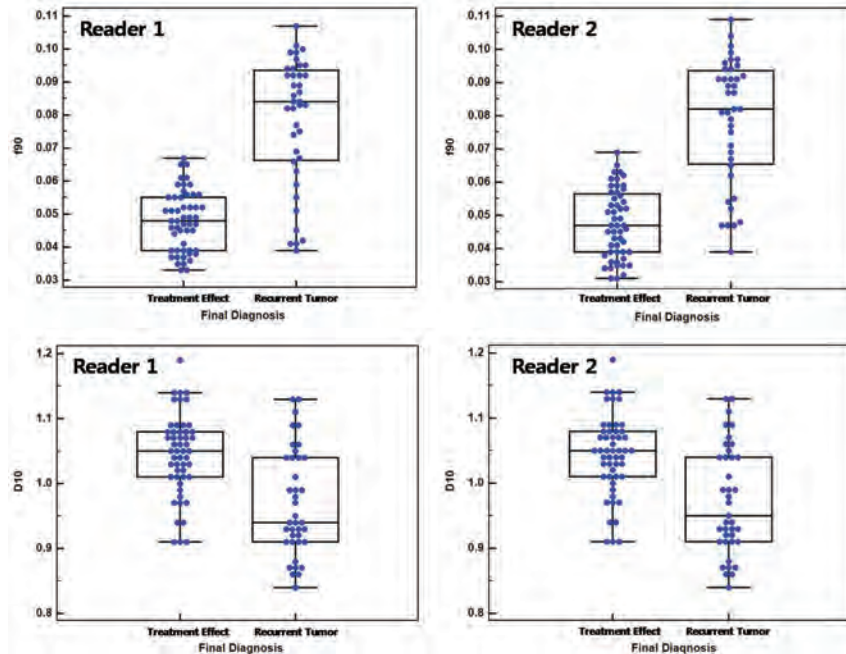


**FIG 4.** Box-and-whisker plots for the IVIM-derived f and D values between recurrent tumor and treatment effect for both readers.

**Table 3: ROC analysis of MR imaging methods and their combination**

MR Imaging Method and Comparison	Reader 1			Reader 2		
	AUC	95% CI	P Value	AUC	95% CI	P Value
MR imaging method						
IVIM	0.939	0.868–0.978		0.947	0.879–0.983	
DSC + DWI	0.911	0.832–0.960		0.933	0.861–0.975	
DSC + IVIM	0.982	0.928–0.998		0.987	0.938–1.000	
Comparison						
IVIM vs DSC + DWI			.3762			.5897
IVIM vs DSC + IVIM			.0471			.0951
DSC + DWI vs DSC + IVIM			.0312			.0455

Note:—ROC indicates receiver operating characteristic analysis; AUC, area under the ROC curve.

of 1.043 and 1.045 for readers 1 and 2, respectively) ( $P < .001$  for each). Figure 4 shows a number of patients in the recurrent tumor group within an overlap zone where misclassifications can occur (10 of 39 patients for reader 1; 12 of 39 patients for reader 2).

The combination of DSC perfusion MR imaging with IVIM showed a significantly larger area under the receiver operating characteristic curve than the combination of DSC perfusion MR imaging with DWI (area under the receiver operating characteristic curve of 0.911 versus 0.982 for reader 1,  $P = .0312$ ; area under the receiver operating characteristic curve of 0.933 versus 0.987 for reader 2,  $P = .0455$ ) (Table 3 and Fig 5). Table 4 shows the sensitivities and specificities of the imaging parameters for distin-

guishing recurrent tumor from treatment effect when all 91 patients were regarded as a training set. With the combination of f90 and D10 used as a discriminative index, the sensitivity and specificity for differentiation were 79.5% and 92.3% for reader 1 and 84.6% and 94.2% for reader 2, respectively. With the combination of nCBV90 and ADC10 used as a discriminative index, the sensitivity and specificity were 69.2% and 100.0% for reader 1 and 74.3% and 100.0% for reader 2, respectively. Compared with the combination of DSC perfusion MR imaging and DWI, adding IVIM to DSC perfusion MR imaging improved the diagnostic accuracy from 86.8% to 92.3% for reader 1 and from 89.0% to 93.4% for reader 2, respectively (Table 4).

### Interreader Agreement

Table 5 summarizes the interreader agreement by using the corresponding ICCs. Interreader agreement was highest for measurement of f90 (ICC, 0.89) and was lowest for measurement of the 90th percentile histogram cutoff of D\* (ICC, 0.42). The ICCs between readers were higher for calculations of the perfusion parameters including f90 and nCBV90 (ICC range, 0.84–0.89) than for calculations of the diffusion parameters including D10 and ADC10 (ICC range, 0.68–0.79).

### DISCUSSION

Our study findings demonstrate that IVIM-derived perfusion and diffusion parameters can be used to distinguish recurrent tumor from treatment effect in patients with post-GKRS metastatic tumor. We found that the combination of f90 and D10, compared with the combination of nCBV90 and ADC10, provided better diagnostic performance of the MR imaging protocol for differentiating recurrent tumor versus treatment effect. Furthermore, the diagnostic model that added IVIM-derived parameters to DSC perfusion MR imaging performed better than the DSC perfusion MR imaging before the IVIM-derived parameters were added. We found that the highest interreader agreement in the detection of recurrent tumor after GKRS was achieved with f90 measurement. However, the D\*

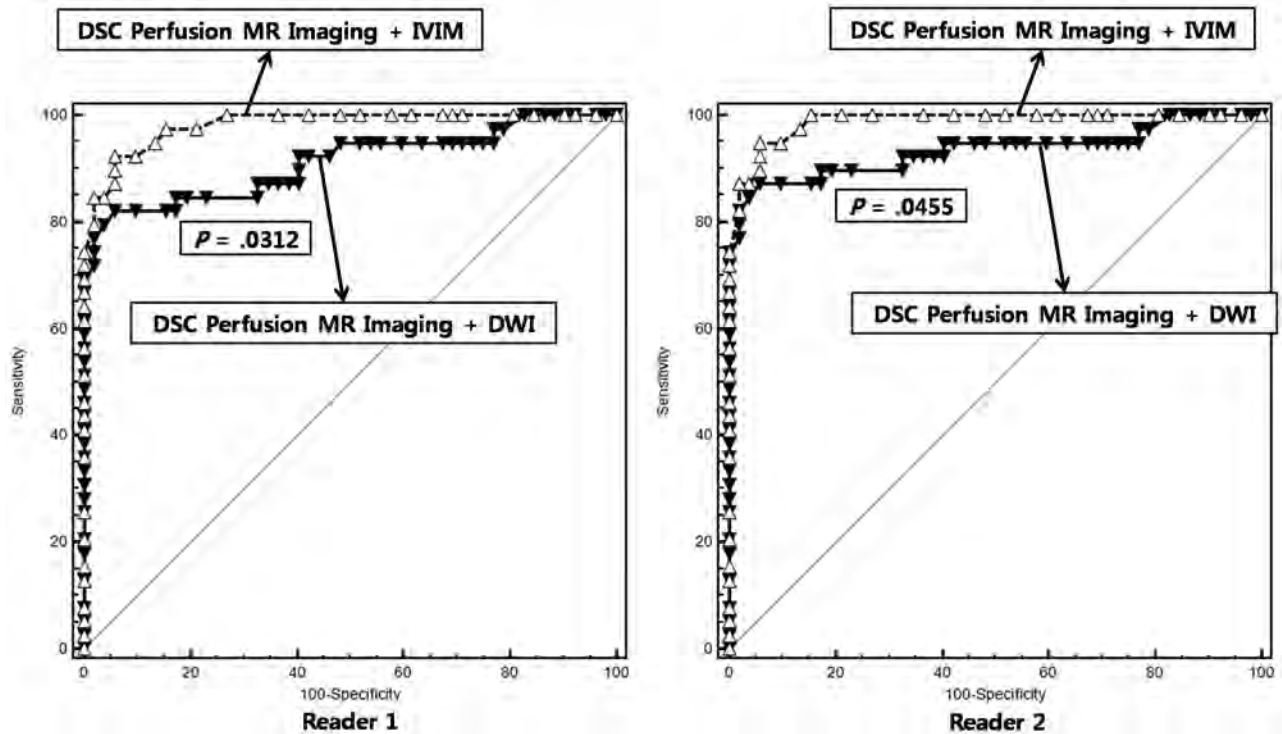


**FIG 5.** The graph shows the comparison between the receiver operating characteristic curve for the combination of DSC MR imaging and IVIM and for the combination of DSC MR imaging and DWI. The combination of DSC MR imaging and IVIM resulted in a significantly higher area under the receiver operating characteristic curve than the combination of DSC MR imaging and DWI for both readers, thus indicating improved diagnostic performance.

**Table 4: Diagnostic performance of MR imaging methods and their combination**

Reader and MR Imaging Method	Sensitivity	Specificity	Accuracy
Reader 1			
IVIM	79.5%	92.3%	86.8%
DSC + DWI	69.2%	100.0%	86.8%
DSC + IVIM	89.7%	94.2%	92.3%
Reader 2			
IVIM	84.6%	94.2%	90.1%
DSC + DWI	74.3%	100.0%	89.0%
DSC + IVIM	92.3%	94.2%	93.4%

**Table 5: Interreader ICC for measurements of imaging parameters**

Parameters	Interreader ICC <sup>a</sup>
f90	0.89 (0.81–0.94)
D*90	0.42 (0.25–0.54)
D10	0.79 (0.67–0.89)
nCBV90	0.84 (0.73–0.91)
ADC10	0.68 (0.52–0.82)

**Note:**—D\*90 indicates 90th percentile histogram cutoff of D\*.

<sup>a</sup>Numbers in parentheses are the 95% confidence intervals.

value was poorly reproducible, presumably due to its high sensitivity to capillary blood flow and any partial volume effect with CSF-filled or necrotic spaces. This finding is consistent with the results of a previous study.<sup>9</sup> Therefore, we did not use the D\* in the evaluation of the diagnostic performance of IVIM.

Previously published reports have suggested that DSC perfusion MR imaging based on the measurement of the first-pass T2\* effect of a bolus of paramagnetic exogenous contrast material has

the potential to distinguish tumor recurrence from treatment effect by using relative CBV maps.<sup>10,11</sup> IVIM has a unique capillary dependence, which is not sensitive to the coherent laminar flow of arteries and veins. The measurement of IVIM is intrinsically local (ie, the encoding and readout are done at the same location).<sup>4</sup> Although the IVIM parameters estimated from the biexponential model could be sensitive to noise and to the initial values used for data fitting, IVIM MR imaging using spin-echo-based DWI can be less sensitive to the T2\* susceptibility artifacts than DSC MR imaging. Moreover, in our clinical experience, IVIM MR imaging allowed both diffusion and perfusion measures within corresponding solid lesions. The significant difference in f90 between the recurrent tumor and the treatment effect groups is consistent with previous reports in which tumor recurrence had a higher relative CBV than treatment-related effect.<sup>1,10</sup> Remarkably, in our study, we identified the better diagnostic performance of IVIM-derived perfusion and diffusion parameters for differentiating recurrent tumor from treatment effect, compared with the combination of DSC perfusion MR imaging with DWI.

Le Bihan et al<sup>5</sup> suggested that the f-value measures the fractional volume of capillary blood flowing in each voxel. Recurrent tumors are usually higher grade tumors with increased neoangiogenesis, which leads to increased microvascular attenuation and increased permeability surface area product. In our study, we did not find any visual discordance between the nCBVs and IVIM-derived perfusion parameters for differentiating recurrent tumor from treatment effect. However, these 2 perfusion parameters represent different aspects of tumor vessels. CBV primarily measures microvascular attenuation, and f measures microscopic translational motion associated with microcirculation of the

blood. Moreover, spin-echo-based IVIM imaging has a substantially different vessel-size sensitivity profile from that of gradient-echo-based DSC MR imaging. The relation between the IVIM-derived perfusion parameters and the contrast-enhanced perfusion parameters has been studied theoretically,<sup>12</sup> but clinical validation is still lacking. Although our prior study indicated that f90 showed a significant correlation with the nCBV90 in patients with posttreatment glioblastomas,<sup>13</sup> further studies that correlate the IVIM-derived perfusion fraction with various MR perfusion parameters, including cerebral blood flow and the permeability parameter, will be needed to understand the exact meaning of the IVIM-derived perfusion parameter.

The ADC has shown the potential to distinguish tumor regrowth from radiation injury. Several previous studies have shown that the ADC value derived from a monoexponential model can help differentiate tumor recurrence from treatment-related change.<sup>14,15</sup> Most interesting, our study showed that D10 differed more significantly between the recurrent tumor and the treatment effect groups than did ADC10. Although the exact pathophysiologic mechanism for determining the difference between the ADC10 and D10 results is unclear, the significant perfusion difference between the recurrent tumor and the treatment effect groups may contribute to the ADC-D difference. Similarly, Yamada et al<sup>16</sup> reported lower IVIM-derived D values compared with ADC seen in enhancing lesions of the liver, thus confirming that the ADC is contaminated by perfusion.

Our study has several limitations. The primary limitation of this initial-experience study was the bias introduced by only including patients clinically suspected of having recurrent tumor or treatment effect. Therefore, some patients with equivocal clinical and image findings that did not meet our clinicoradiologic diagnostic criteria, such as prolonged asymptomatic increases of a contrast-enhancing lesion, were excluded from this study. This exclusion did not allow us to accurately assess sensitivities and specificities for random, consecutive patients. However, this group of patients was the most clinically relevant for accurate noninvasive assessment of post-GKRS metastatic tumors, to minimize unnecessary, additional diagnostic procedures. Second, the number of study patients was relatively small; this size can reduce the statistical power for the superiority of IVIM imaging over other MR imaging techniques. Further prospective analyses with a larger number of patients will be needed to validate our results. Third, because there was no case with histopathologically diagnosed recurrent tumor or radiation necrosis in this study, we would caution against overinterpretation of our study results. A direct image-guided histopathologic correlation for recurrent tumor and radiation necrosis is needed for further validation of IVIM-derived parameters. Such a study may confirm the efficacy of the techniques described in this article.

Fourth, the set of b-values used in our study was not optimized. The number of b-values may affect a robust curve fitting for diffusion signal decay, especially in the lower range of b-values. Moreover, the b-values might be further optimized in a separate study as a function of the available IVIM parameter values in the brain, to achieve a shorter examination time without sacrificing the precision of the techniques. Fifth, the quantitative assessment of IVIM-parameters in the brain is even more complicated due to its anisotropic diffusion. The deconvolution of multiexpo-

ponential processes like water diffusion in living tissue is a strongly ill-posed problem, and a large number of signal points and signal-to-noise ratio are necessary for a reliable separation of >1 exponential time constant.<sup>17</sup> The evaluation of current fitting modalities for IVIM data and investigation of their limitations in relation to SNR and the number of b-values are, therefore, prudent.

Last, if the IVIM techniques merely “diagnose” tumor response or progression, one labor-intensive analysis by using IVIM is more accurate than another labor-intensive analysis by using DSC perfusion MR imaging; however, conventional MR imaging studies are the reference standard for diagnosis. Nevertheless, the rationale for our study can be summarized as follows: First, new advanced MR imaging techniques are more accurate and could avoid a stereotactic biopsy for histologic assessment, the only reliable but invasive method; second, in this field, the results of advanced imaging studies suggest encouraging results, but comparative studies are needed to investigate the relationship, diagnostic performance, and complementary character of advanced MR imaging techniques. Last, an increased size of contrast-enhancing lesions on follow-up MR imaging study not only creates management dilemmas but is also anxiety-provoking for patients and clinicians.

## CONCLUSIONS

IVIM imaging may be helpful in making a more accurate diagnosis of recurrent tumor and can be used as a potential, noninvasive imaging biomarker for monitoring the treatment response in patients with post-GKRS metastatic tumor. Moreover, adding IVIM imaging to an MR imaging protocol improves the diagnosis of recurrent tumor beyond that achieved by using the combination of DSC perfusion MR imaging and DWI.

## REFERENCES

1. Barajas RF, Chang JS, Sneed PK, et al. **Distinguishing recurrent intra-axial metastatic tumor from radiation necrosis following gamma knife radiosurgery using dynamic susceptibility-weighted contrast-enhanced perfusion MR imaging.** *AJNR Am J Neuroradiol* 2009;30:367–72
2. Essig M, Waschki M, Wenz F, et al. **Assessment of brain metastases with dynamic susceptibility-weighted contrast-enhanced MR imaging: initial results.** *Radiology* 2003;228:193–99
3. Gasparetto EL, Pawlak MA, Patel SH, et al. **Posttreatment recurrence of malignant brain neoplasm: accuracy of relative cerebral blood volume fraction in discriminating low from high malignant histologic volume fraction.** *Radiology* 2009;250:887–96
4. Le Bihan D, Breton E, Lallemand D, et al. **Separation of diffusion and perfusion in intravoxel incoherent motion MR imaging.** *Radiology* 1988;168:497–505
5. Le Bihan D, Turner R, MacFall JR. **Effects of intravoxel incoherent motions (IVIM) in steady-state free precession (SSFP) imaging: application to molecular diffusion imaging.** *Magn Reson Med* 1989; 10:324–37
6. Luciani A, Vignaud A, Cavet M, et al. **Liver cirrhosis: intravoxel incoherent motion MR imaging—pilot study.** *Radiology* 2008; 249:891–99
7. Federau C, Maeder P, O’Brien K, et al. **Quantitative measurement of brain perfusion with intravoxel incoherent motion MR imaging.** *Radiology* 2012;265:874–81
8. Bisdas S, Koh TS, Roder C, et al. **Intravoxel incoherent motion diffusion-weighted MR imaging of gliomas: feasibility of the method and initial results.** *Neuroradiology* 2013;55:1189–96
9. Andreou A, Koh DM, Collins DJ, et al. **Measurement reproducibility**

- of perfusion fraction and pseudodiffusion coefficient derived by intravoxel incoherent motion diffusion-weighted MR imaging in normal liver and metastases. *Eur Radiol* 2013;23:428–34
10. Fatterpekar GM, Galheigo D, Narayana A, et al. **Treatment-related change versus tumor recurrence in high-grade gliomas: a diagnostic conundrum—use of dynamic susceptibility contrast-enhanced (DSC) perfusion MRI.** *AJR Am J Roentgenol* 2012;198:19–26
  11. Sugahara T, Korogi Y, Tomiguchi S, et al. **Posttherapeutic intraaxial brain tumor: the value of perfusion-sensitive contrast-enhanced MR imaging for differentiating tumor recurrence from nonneoplastic contrast-enhancing tissue.** *AJNR Am J Neuroradiol* 2000; 21:901–09
  12. Lemke A, Stieltjes B, Schad LR, et al. **Toward an optimal distribution of b values for intravoxel incoherent motion imaging.** *Magn Reson Imaging* 2011;29:766–76
  13. Kim HS, Suh CH, Kim N, et al. **Histogram analysis of intravoxel incoherent motion for differentiating recurrent tumor from treatment effect in patients with glioblastoma: initial clinical experience.** *AJNR Am J Neuroradiol* 2014;35:490–97
  14. Al Sayyari A, Buckley R, McHenry C, et al. **Distinguishing recurrent primary brain tumor from radiation injury: a preliminary study using a susceptibility-weighted MR imaging-guided apparent diffusion coefficient analysis strategy.** *AJNR Am J Neuroradiol* 2010;31:1049–54
  15. Provenzale JM, Mukundan S, Barboriak DP. **Diffusion-weighted and perfusion MR imaging for brain tumor characterization and assessment of treatment response.** *Radiology* 2006;239:632–49
  16. Yamada I, Aung W, Himeno Y, et al. **Diffusion coefficients in abdominal organs and hepatic lesions: evaluation with intravoxel incoherent motion echo-planar MR imaging.** *Radiology* 1999;210: 617–23
  17. Bennett KM, Schmainda KM, Bennett RT, et al. **Characterization of continuously distributed cortical water diffusion rates with a stretched-exponential model.** *Magn Reson Med* 2003;50:727–34

# Comparison of Multiple Parameters Obtained on 3T Pulsed Arterial Spin-Labeling, Diffusion Tensor Imaging, and MRS and the Ki-67 Labeling Index in Evaluating Glioma Grading

H. Fudaba, T. Shimomura, T. Abe, H. Matsuta, Y. Momii, K. Sugita, H. Ooba, T. Kamida, T. Hikawa, and M. Fujiki



## ABSTRACT

**BACKGROUND AND PURPOSE:** Pulsed arterial spin-labeling, DTI, and MR spectroscopy provide useful data for tumor evaluation. We evaluated multiple parameters by using these pulse sequences and the Ki-67 labeling index in newly diagnosed supratentorial gliomas.

**MATERIALS AND METHODS:** All 32 patients, with grade II (3 each of diffuse astrocytoma, oligodendroglioma, and oligoastrocytoma), grade III (3 anaplastic astrocytomas, 4 anaplastic oligodendrogliomas, and 1 anaplastic oligoastrocytoma), and grade IV (14 glioblastomas and 1 glioblastoma with an oligodendroglioma component) cases underwent pulsed arterial spin-labeling, DTI, and MR spectroscopy studies by using 3T MR imaging. The following variables were used to compare the tumors: relative cerebral blood flow, fractional anisotropy; ADC tumor/normal ratios; and the Cho/Cr, NAA/Cho, NAA/Cr, and lactate/Cr ratios. A logistic regression and receiver operating characteristic analysis were used to assess parameters with a high sensitivity and specificity to identify the threshold values for separate grading. We compared the Ki-67 index with various MR imaging parameters in tumor specimens.

**RESULTS:** Significant correlations were observed between the Ki-67 index and the mean, maximum, and minimum ADC, Cho/Cr, and lactate/Cr ratios. The receiver operating characteristic analysis showed that the combination of the minimum ADC and Cho/Cr ratios could differentiate low-grade and high-grade gliomas, with a sensitivity and specificity of 87.0% and 88.9%, respectively. The mean and maximum relative cerebral blood flow ratios were used to classify glioblastomas from other-grade astrocytomas, with a sensitivity and specificity of 92.9% and 83.3%, respectively.

**CONCLUSIONS:** Our findings indicate that pulsed arterial spin-labeling, DTI, and MR spectroscopy are useful for predicting glioma grade. Additionally, the parameters obtained on DTI and MR spectroscopy closely correlated with the proliferative potential of gliomas.

**ABBREVIATIONS:** ASL = arterial spin-labeling; C1 error = average observed sensitivity and specificity; C2 error = observed number of instances of tumor-grade misclassification; FA = fractional anisotropy; Lac = lactate; NPV = negative predictive value; PASL = pulsed arterial spin-labeling; PPV = positive predictive value; rCBF = relative cerebral blood flow; ROC = receiver operating characteristic

Grading gliomas is necessary to determine the appropriate treatment strategy and assess prognosis. Classifying lesions into 4 grades based on histologic analyses requires tumor specimens obtained via biopsy or surgical resection.<sup>1</sup>

On conventional MR imaging with gadolinium contrast, the presence of FLAIR abnormalities or gadolinium enhancement re-

veals the appearance of new lesions. Advanced MR imaging, pulsed arterial spin-labeling (PASL), DTI, and MR spectroscopy provide useful data for evaluating tumors preoperatively. The PASL technique allows cerebral blood flow to be measured noninvasively without exogenous contrast agents. The usefulness of perfusion MR imaging with arterial spin-labeling (ASL) for assessing brain tumor angiogenesis and grading gliomas has been evaluated.<sup>2-7</sup> DTI provides information on anisotropy, including fractional anisotropy (FA), and ADC. A recent study investigating DTI of gliomas showed that the FA and ADC tumor/normal tissue ratios are possible indicators of glioma proliferation and/or grading.<sup>8-10</sup> MR spectroscopy is also a noninvasive method that allows the measurement of various metabolites in vivo, such as Cho, Cr, NAA, and the pathologic levels of lactate (Lac), and has been reported useful for investigating gliomas.<sup>11-13</sup> The use of a combination of these noninvasive parameters has been reported to increase the diagnostic accuracy of glioma grading.<sup>7,9,11,12,14-18</sup>

Received February 20, 2014; accepted after revision April 25.

From the Department of Neurosurgery, Oita University Faculty of Medicine, Oita, Japan.

This work was supported by a grant from the Japan Science and Technology Agency and the Ministry of Education, Culture, Sports, Science and Technology.

Please address correspondence to Hirotsuka Fudaba, MD, Department of Neurosurgery, Oita University Faculty of Medicine, Oita, 879-5593 Japan; e-mail: fudaba@oita-u.ac.jp

Indicates open access to non-subscribers at [www.ajnr.org](http://www.ajnr.org)

Indicates article with supplemental on-line table.

<http://dx.doi.org/10.3174/ajnr.A4018>

Very few reports describe comparisons of multiple parameters, including the relative cerebral blood flow (rCBF)-measured PASL sequence on 3T MR imaging, and glioma grading. Immunohistologically, the Ki-67 labeling index on histologic examinations is known to correlate with malignancy, and it also functions as a marker of proliferation in gliomas.<sup>19</sup> According to the previous literature, this index is correlated with various advanced MR imaging parameters.<sup>8,20,21</sup>

In this study, we performed a comparative review of multiple parameters obtained with pulse sequences evaluated by using 3T MR imaging and glioma grading in newly diagnosed patients with glioma. Our purpose was to evaluate whether the parameters provide useful, complementary information and whether this combination of parameters shows the best performance for grading cerebral gliomas. The results of the present study are clinically valuable for evaluating sensitivity, specificity, positive predictive value (PPV), and negative predictive value (NPV) and determining the threshold values by analyzing receiver operating characteristic (ROC) curves. Under the same conditions, we evaluated the correlations between various MR imaging parameters and the proliferation marker, the Ki-67 labeling index.

## MATERIALS AND METHODS

### Patients

Thirty-two patients ranging in age from 16 to 82 years with newly diagnosed supratentorial glioma, to avoid confounding findings related to posttherapeutic effects, were entered into this study. All patients underwent PASL, DTI, and MR spectroscopy studies by using 3T MR imaging. We reviewed all PASL, FA, ADC, and MR spectroscopy studies of supratentorial cerebral gliomas performed between March 2010 and October 2012. No patients had a clinical history of previous surgery, chemotherapy, or radiation therapy.

The histologic analysis was performed, according to the World Health Organization brain tumor classification revised in 2007, of tissue samples obtained at the time of either surgical resection or image-guided biopsies.<sup>1</sup>

All patients provided their informed consent to participate in this study, which was conducted in accordance with the ethical principles of the Declaration of Helsinki. The study protocol was approved by the Ethics Committee of the Oita University Faculty of Medicine.

### MR Imaging Protocol

Conventional MR imaging included T1-weighted spin-echo, T2-weighted fast spin-echo, fluid-attenuated inversion recovery, and contrast-enhanced T1-weighted axial imaging (0.1-mmol/kg meglumine gadoterate, Magnescape; Guerbet Japan, Tokyo, Japan) performed at a field strength of 1.5T. After 2–5 days, we performed the advanced MR imaging examination. All participating patients underwent an advanced MR imaging protocol that included PASL, DTI, MR spectroscopy, and SWI by using a superconducting magnet at a field strength of 3T (Magnetom Verio; Siemens, Erlangen, Germany). T1-weighted structural images were acquired with a 3D MPRAGE device in the sagittal plane. The imaging parameters were as follows: TR/TE = 1900/2.53 ms,

TI = 900 ms, flip angle = 9°, FOV = 21.0 cm, section thickness = 1 mm, section gap = 0.5 mm, number of sections collected = 176, matrix = 192 × 192 × 256. An SWI sequence was performed to detect calcification and hemorrhagic areas. On the basis of advanced MR imaging, rCBF, FA, ADC, and MR spectra were calculated by the MR imaging console software program (syngo MR B17; Siemens).

### Pulsed Arterial Spin-Labeling

We performed pulsed arterial spin-labeling perfusion MR imaging by using QUIPSS II with thin-slice T1 periodic saturation (Q2TIPS).<sup>22</sup> The Q2TIPS technique is a pulsed arterial spin-labeling method that enables the acquisition of multiple sections. The inversion and saturation pulse parameters of Q2TIPS were set as follows: TI1 = 700 ms, TI1S = 1600 ms, and TI2 = 1800 ms. The other imaging parameters were as follows: TR/TE = 2800/13 ms, flip angle = 90°, FOV = 25.6 cm, section thickness = 8 mm, voxel size = 4 × 4 × 8 mm, section number = 9. Crusher gradients were not used. The total acquisition time was 4 minutes 19 seconds. Motion correction was interpolated according to the 3D *k*-space method, with a spatial filter setting of 2.0.

### Diffusion Tensor Imaging

Axial DTI was performed by using single-shot spin-echo echo-planar imaging sequences. The parameters were as follows: TR/TE = 9200/96 ms, FOV = 23.0 cm, matrix = 128 × 128, *b* = 0 s/mm<sup>2</sup> as reference imaging and *b* = 1000 s/mm<sup>2</sup>, diffusion-sensitive dimensions = 12, average = 3, scanning time = 6 minutes 28 seconds.

### PASL and Diffusion Tensor Images

After reconstruction, the PASL, FA, and ADC images were converted into the DICOM format and inserted into the data base. To minimize confounding factors in the analysis, we kept the size of the ROIs in the lesion and contralateral normal brain constant (diameter = 8.0 mm) on both the PASL and diffusion tensor images. Two observers placed 5 ROIs each within the solid tumor component and 1 region of interest each in the contralateral normal brain.<sup>6</sup> Whenever possible, the ROIs were placed in mirrored white matter regions; when this placement was not possible, the ROIs were positioned in representative normal white matter in the same transaxial plane.<sup>14</sup> Care was taken to ensure that the ROIs were entirely within the solid part of the lesion to avoid contamination of the region of interest from normal tissue, areas of necrosis, cysts, hemorrhage, or intratumoral mineralization. We placed the ROIs at the site of the enhanced lesions on the contrast-enhanced T1-weighted MR images. In patients with nonenhancing tumors, the tumor parenchyma was identified as the area of hyperintensity on T2-weighted and FLAIR images. The ROIs were evaluated for eligibility independently by 2 authors (H.F. and T.S.), and any disagreements were resolved by consensus.

The rCBF, FA, and ADC ratios were calculated as follows: rCBF (FA or ADC) ratio = rCBF (FA or ADC) [tumor] / rCBF (FA or ADC) [contralateral normal tissue]. The average values of the minimum, maximum, and mean of the rCBF, FA, and ADC ratios were then selected for the analysis.

### MR Spectroscopy

A single-voxel water-suppressed point-resolved spectroscopy sequence and multivoxel chemical shift imaging were performed. The single-voxel water-suppressed point-resolved spectroscopy sequence was performed by using the following parameters: TR/TE = 2000/270 ms, flip angle = 90°, voxel size = 20 × 20 × 20 mm (normal-sized lesion) or 15 × 15 × 15 mm (small lesion: lesions measuring less than approximately 20 mm in diameter), acquisition average = 192 (normal-sized lesion) or 256 (small lesion). The total acquisition time was 6 minutes 32 seconds (normal-sized lesion) or 8 minutes 40 seconds (small lesion). Multivoxel chemical shift imaging was performed by using the following parameters: TR/TE = 1700/270 ms, flip angle = 90°, FOV = 16.0 cm, section thickness = 8 mm, voxel size = 10 × 10 × 8 mm, acquisition average = 5. The total acquisition time was 9 minutes 26 seconds. The single-voxel water-suppressed point-resolved spectroscopy sequence was primarily performed; however, multivoxel chemical shift imaging was performed in cases of deep and centrally located tumors measuring >3 cm in diameter because for some temporal lobe and inferior frontal lobe tumors, adequate shimming can be problematic, while for intraventricular tumors and/or very peripheral tumors, CSF or scalp fat contamination may adversely affect MR spectroscopy acquisition. We selected the region of interest of the multivoxel area in the center region to prevent the influence of magnetic susceptibility and to optimize the shimming procedure. To the extent possible, we selected the multivoxel technique because the previous literature suggests that multivoxel MR spectroscopy is more useful for distinguishing glioma recurrence from posttreatment effects than single-voxel MR spectroscopy.<sup>23</sup>

The spectra were automatically analyzed for the relative signal intensity (area under the fitted peaks in the time domain) of the following metabolites: Cho, Cr, NAA, and Lac. The ratios of Cho/Cr, NAA/Cho, NAA/Cr, and Lac/Cr at TE 270 ms were calculated. The postprocessing steps, including the frequency shift, baseline correction, phase correction, and peak fitting/analysis, were performed first automatically and then manually. All spectral analyses were conducted within a window from 0.50 to 4.30 ppm (by using the standard method of assigning a shift value of 4.7 ppm to the measured unsuppressed water peak). The metabolite peak areas were assigned as follows: Cho, 3.20 ppm; Cr, 3.02 ppm; NAA, 2.00 ppm; Lac, 1.29 ppm. To avoid contamination of the voxel from normal tissue or areas of necrosis or cysts based on conventional MR imaging, we obtained the metabolite ratios within the solid portion of the lesion by consensus without knowledge of the final histologic tumor diagnosis.

### Immunohistologic Assay

For Ki-67 immunostaining, the specimens were sliced from formalin-fixed, paraffin-embedded tissues. We stained the sections with a mouse anti-Ki-67 monoclonal antibody (MIB-1; Dako Cytomation, Carpinteria, California; 1:50 dilution). The Ki-67 labeling index, defined as the number of positive tumor cells / the total number of tumor cells × 100%, was calculated for at least 10 fields selected at random under a magnification ×400.

### Statistical Analysis

We compared the MR imaging parameters and the Ki-67 labeling index in each of 3 groups (grade II versus grade III versus grade IV) by using the Tukey-Kramer test. The sensitivity, specificity, PPV, and NPV were calculated by using an ROC analysis to correctly identify high-grade gliomas (grade III and IV) and glioblastomas (grade IV), to differentiate the 2 groups, such as patients with high- and low-grade gliomas and those with glioblastomas and other-grade gliomas (grade II and III). Because oligodendroglial tumors tend to demonstrate hyperperfusion relative to astrocytic tumors, we also analyzed the CBF data only for purely astrocytic tumors that did not contain oligodendroglial regions, such as diffuse astrocytomas, anaplastic astrocytomas, and glioblastomas. The optimal threshold values were those that did the following: 1) minimized the observed number of instances of tumor-grade misclassification (C2 error = fraction of misclassified tumors), and 2) maximized the average observed sensitivity and specificity (C1 error) resulting in  $C1 = 1 - (\text{sensitivity} + \text{specificity}) / 2$ . To determine the combination of the most discriminative parameters, we used a stepwise multiple logistic backwards regression. The logistic regression was selected by using a cutoff level of .05 for significance. The correlations between the MR imaging parameters and the Ki-67 labeling index were analyzed statistically by using a Spearman correlation coefficient analysis.

### RESULTS

Among 32 patients, 9 tumors were grade II (3 each of diffuse astrocytoma, oligodendroglioma, and oligoastrocytoma), 8 tumors grade III (3 anaplastic astrocytomas, 4 anaplastic oligodendrogliomas, and 1 anaplastic oligoastrocytoma), and 15 tumors grade IV (14 glioblastomas and 1 glioblastoma with an oligodendroglioma component). The patients included 13 men and 19 women, with a mean age of  $59.8 \pm 16.8$  years. The conventional MR imaging characteristics of the tumors are shown in the Online Table. Patient 27 was unable to undergo an examination by using contrast agent due to her current treatment with dialysis. We performed multivoxel MR spectroscopy in 9 cases and single-voxel MR spectroscopy in 23 cases. Examples of low-grade and high-grade glial neoplasms are provided in Figs 1 and 2, respectively.

Both the mean ADC ratio ( $r = -0.455, P = .0113$ ) and maximum ADC ratio ( $r = -0.352, P = .0497$ ) exhibited a negative correlation with the Ki-67 index. In particular, there was a significant negative correlation between the minimum ADC ratio and the Ki-67 index ( $r = -0.470, P = .0089$ ). A positive correlation was also observed between the Cho/Cr ratio and the Ki-67 index ( $r = 0.461, P = .0103$ ) and between the Lac/Cr ratio and the Ki-67 index ( $r = 0.418, P = .0199$ ). In contrast, no significant correlations were noted between the other parameters and the Ki-67 index.

The maximum rCBF ratio of the grade IV gliomas was higher than that of the grade III gliomas, while the Ki-67 labeling index of the grade II gliomas was lower than that of the grade III and grade IV gliomas ( $P < .05$ ). The maximum FA ratio associated with grade II gliomas was lower than that associated with the grade IV gliomas, while the mean and minimum ADC ratios of grade II gliomas were higher than those of grade IV gliomas ( $P < .05$ ).

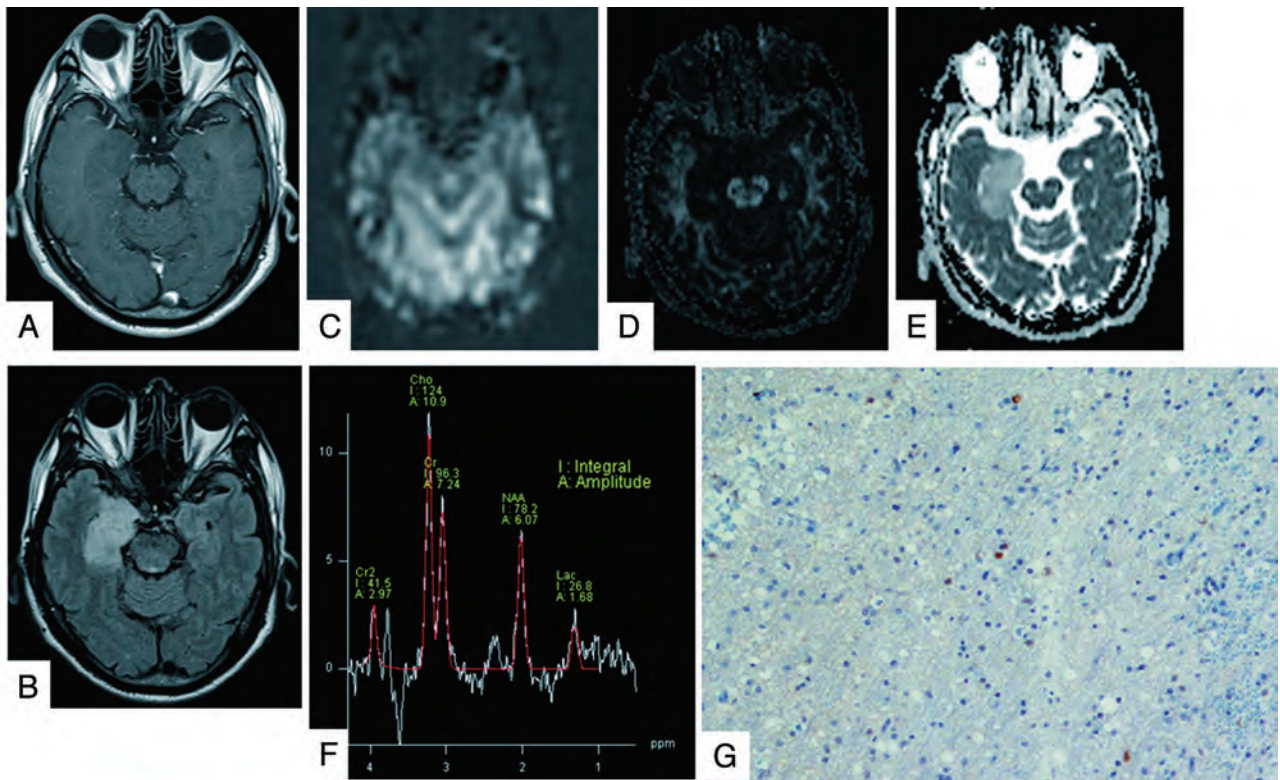


**FIG 1.** A 62-year-old man with a grade II oligoastrocytoma. The contrast-enhanced T1-weighted image shows a nonenhancing mass in the right hippocampus (A). The lesions presented high-intensity signals on FLAIR images (B). The rCBF map on PASL shows no areas of hyperperfusion (C). The FA map shows low FA values (D). The ADC map shows increased tumor diffusion values (E). The tumor MR spectrum shows decreased NAA and slightly increased Cho and Lac (F). The Ki-67 labeling index is 5.0% (original magnification  $\times 400$ ) (G).

Other comparisons did not reveal any statistically significant differences.

Regarding the parameters calculated from PASL, DTI, and MR spectroscopy, the threshold values were obtained separately for the minimum C1 and C2 errors, as shown in Tables 1 and 2. With respect to individual parameters for separating high-grade from low-grade gliomas, a threshold value of 1.789 for the Lac/Cr ratio, which exhibited the best performance for a minimum C1 error, provided sensitivity, specificity, PPV, and NPV of 73.9%, 100.0%, 100.0%, and 60.0%, respectively. Meanwhile, a threshold value of 1.789 for the Cho/Cr ratio, which exhibited the best performance for a minimum C2 error, provided sensitivity, specificity, PPV, and NPV of 91.3%, 77.8%, 91.3%, and 77.8%, respectively. Regarding individual parameters for separating glioblastomas from other-grade gliomas, a threshold value of 2.845 for the maximum rCBF ratio, which exhibited the best performance for minimum C1 and C2 errors, provided sensitivity, specificity, PPV, and NPV of 86.7%, 82.4%, 81.3%, and 87.5%, respectively. In particular, for evaluating purely astrocytic tumors, both the mean and maximum rCBF ratios demonstrated sensitivity, specificity, PPV, and NPV of 92.9%, 83.3%, 92.8%, and 83.4%, respectively.

According to multivariate logistic regression analysis, the combinations of parameters for differentiating high- and low-grade gliomas included the minimum ADC and Cho/Cr ratios, while those for differentiating glioblastomas and other-grade gliomas included the maximum rCBF and mean ADC ratios. The results of the ROC analyses by using these combinations are shown in Tables 3 and 4. The combination of the minimum ADC

ratio and the Cho/Cr ratio provided sensitivity, specificity, PPV, and NPV of 87.0%, 88.9%, 95.2%, and 72.7%, respectively, for minimum C1 and C2 errors for differentiating high- and low-grade gliomas. Meanwhile, the combination of the maximum rCBF ratio and the mean ADC ratio provided sensitivity, specificity, PPV, and NPV of 73.3%, 94.1%, 91.7%, and 80.0%, respectively, for minimum C1 and C2 errors for differentiating glioblastomas and other-grade gliomas. This combination appears to be inferior compared with the minimum C1 and C2 errors of the maximum rCBF ratio; however, its accuracy was 84.4%, which is as high as that observed for the maximum rCBF ratio.

## DISCUSSION

Cerebral gliomas are important and the most common primary brain tumors. MR imaging plays a critical role in the preoperative assessment and grading of gliomas. The classification and grading of gliomas on conventional MR imaging are sometimes unreliable. The sensitivity, specificity, PPV, and NPV for identifying high-grade gliomas on conventional MR imaging are 72.5%, 65.0%, 86.1%, and 44.1%, respectively.<sup>15</sup> The current study demonstrated contrast enhancement in 66.7%, 75.0%, and 100% of grade II, III, and IV gliomas, respectively, which suggests that it is difficult to perform glioma grading by only using structural gadolinium-enhanced MR imaging.<sup>17</sup> Physicians must perform a biopsy or surgical resection to make a pathologic diagnosis and evaluate the need for postoperative chemoradiotherapy. However, lesions for which the risks of biopsy are high cannot be accurately diagnosed and graded. The noninvasive evaluation of

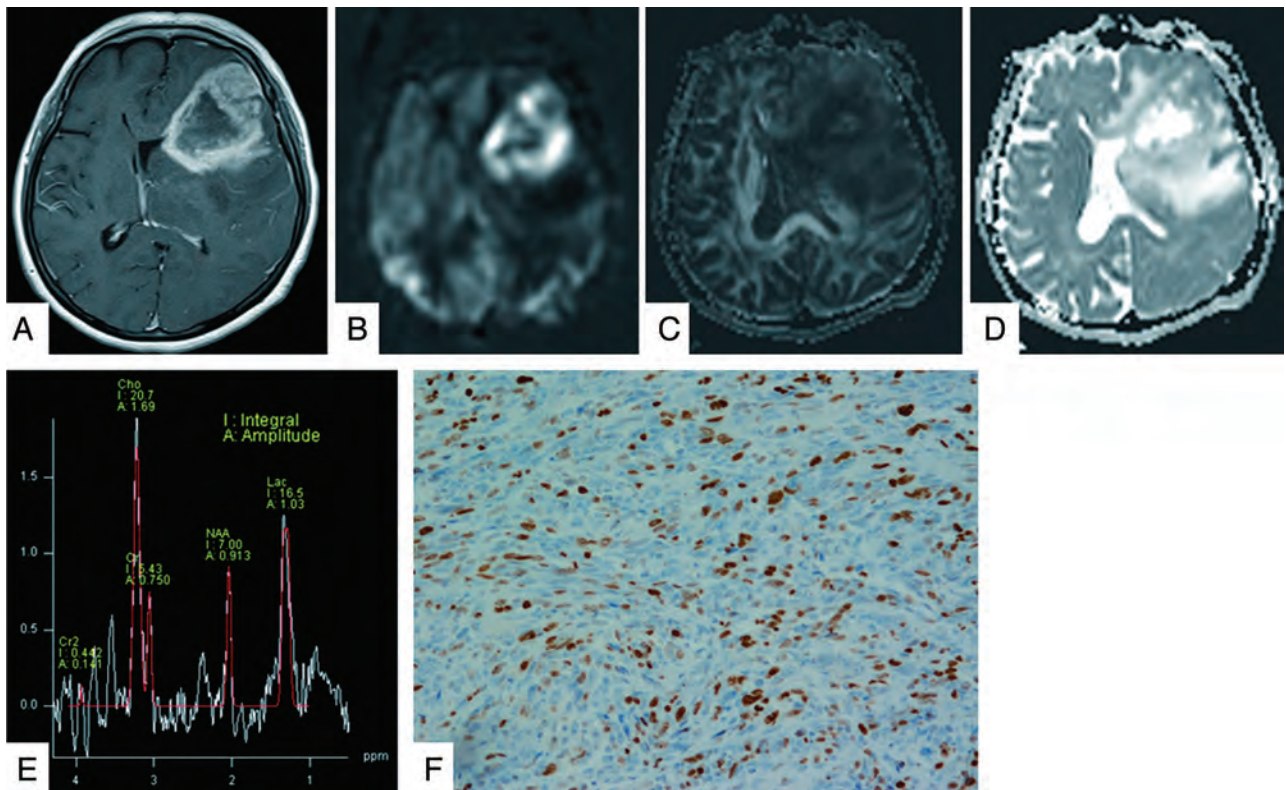


**FIG 2.** A 60-year-old woman with a grade IV glioblastoma. The lesion on the left frontotemporal lobe exhibits strong enhancement on gadolinium T1-weighted image (A). The neoplasm is clearly hyperperfused compared with the healthy parenchyma on the PASL image (B). The FA map shows slightly low FA values (C). The ADC map shows heterogeneous tumor diffusion values (D). The tumor MR spectrum shows decreased NAA with a marked increase in Cho and Lac (E). The Ki-67 labeling index is 27.0% (original magnification  $\times 400$ ) (F).

**Table 1: Threshold values for multiple parameters for differentiating high- and low-grade gliomas**

Parameters	Based on Minimum C1 Error					Errors		Based on Minimum C2 Error					Errors	
	Threshold	Sensitivity	Specificity	PPV	NPV	C1	C2	Threshold	Sensitivity	Specificity	PPV	NPV	C1	C2
rCBF ratio mean	2.562	0.652	0.778	0.882	0.467	0.285	0.170	2.562	0.652	0.778	0.882	0.467	0.285	0.170
rCBF ratio max	2.845	0.609	0.778	0.875	0.438	0.307	0.202	2.845	0.609	0.778	0.875	0.438	0.307	0.202
rCBF ratio min	2.017	0.739	0.667	0.850	0.500	0.297	0.179	2.017	0.739	0.667	0.850	0.500	0.297	0.179
rCBF ratio mean <sup>a</sup>	1.800	0.824	0.667	0.933	0.401	0.255	0.142	1.800	0.824	0.667	0.933	0.401	0.255	0.142
rCBF ratio max <sup>a</sup>	2.258	0.765	0.667	0.929	0.334	0.284	0.166	2.258	0.765	0.667	0.929	0.334	0.284	0.166
rCBF ratio min <sup>a</sup>	1.254	0.882	0.667	0.938	0.499	0.226	0.125	1.254	0.882	0.667	0.938	0.499	0.226	0.125
FA ratio mean	0.236	0.870	0.556	0.834	0.626	0.287	0.214	0.267	0.739	0.667	0.850	0.500	0.297	0.179
FA ratio max	0.288	0.870	0.667	0.870	0.668	0.232	0.128	0.288	0.870	0.667	0.870	0.668	0.232	0.128
FA ratio min	0.279	0.565	0.667	0.813	0.375	0.384	0.300	0.279	0.565	0.667	0.813	0.375	0.384	0.300
ADC ratio mean	1.659	0.913	0.667	0.875	0.750	0.210	0.118	1.659	0.913	0.667	0.875	0.750	0.210	0.118
ADC ratio max	1.538	0.826	0.556	0.826	0.556	0.309	0.227	1.538	0.826	0.556	0.826	0.556	0.309	0.227
ADC ratio min	1.564	0.913	0.667	0.875	0.750	0.210	0.118	1.564	0.913	0.667	0.875	0.750	0.210	0.118
Cho/Cr	1.789	0.913	0.778	0.913	0.778	0.155	0.057	1.789	0.913	0.778	0.913	0.778	0.155	0.057
NAA/Cho	0.349	0.696	0.778	0.889	0.500	0.263	0.142	0.349	0.696	0.778	0.889	0.500	0.263	0.142
NAA/Cr	1.289	0.304	1.000	1.000	0.360	0.348	0.484	0.478	0.778	0.846	0.368	0.372	0.322	0.322
Lac/Cr	1.789	0.739	1.000	1.000	0.600	0.131	0.068	1.789	0.739	1.000	1.000	0.600	0.131	0.068

**Note:**—min indicates minimum; max, maximum.

<sup>a</sup>rCBF ratios derived from purely astrocytomas.

gliomas results in a more precise assessment for selecting the surgical approach or chemoradiotherapy.

In the present study, the combination of the minimum ADC ratio and the Cho/Cr ratio exhibited a high sensitivity and specificity for distinguishing high- and low-grade gliomas. The mean ADC and minimal ADC values have been reported to be correlated with the tumor cell attenuation and thus used to grade astrocytomas.<sup>10,14</sup> In addition, the ADC ratio has been reported to be useful for grading gliomas.<sup>18</sup> Past studies have revealed that the Cho/Cr ratio tends to increase as glioma malignancy progresses.<sup>13,18</sup> Furthermore, Server et al<sup>18</sup> reported a minimum

ADC ratio threshold value of 1.41 and a Cho/Cr threshold value of 1.35 for dividing high- and low-grade gliomas, similar to the results of our analysis. Published data regarding intracranial tumors indicate that a high ADC is attributable to a low level of cellularity, necrosis, or cysts, while a lower ADC is attributable to the presence of an attenuated, highly cellular tumor. The typical spectrum corresponding to a tumor shows an increased Cho peak, which corresponds to increased cell attenuation and membrane turnover in neoplastic tissue. With respect to glioma grading, our results consistently reflect the mitotic activity and presence of microvascular proliferation.

**Table 2: Threshold values for multiple parameters for differentiating glioblastomas and other-grade gliomas**

Parameters	Based on Minimum C1 Error					Errors		Based on Minimum C2 Error					Errors	
	Threshold	Sensitivity	Specificity	PPV	NPV	C1	C2	Threshold	Sensitivity	Specificity	PPV	NPV	C1	C2
rCBF ratio mean	2.562	0.867	0.765	0.765	0.867	0.184	0.073	2.562	0.867	0.765	0.765	0.867	0.184	0.073
rCBF ratio max	2.845	0.867	0.824	0.813	0.875	0.155	0.049	2.845	0.867	0.824	0.813	0.875	0.155	0.049
rCBF ratio min	2.017	0.867	0.588	0.650	0.834	0.273	0.187	2.164	0.800	0.647	0.667	0.786	0.277	0.165
rCBF ratio mean <sup>a</sup>	1.857	0.929	0.833	0.928	0.834	0.119	0.033	1.857	0.929	0.833	0.928	0.834	0.119	0.033
rCBF ratio max <sup>a</sup>	2.258	0.929	0.833	0.928	0.834	0.119	0.033	2.258	0.929	0.833	0.928	0.834	0.119	0.033
rCBF ratio min <sup>a</sup>	2.164	0.786	0.833	0.917	0.625	0.191	0.074	2.164	0.786	0.833	0.917	0.625	0.191	0.074
FA ratio mean	0.380	0.733	0.765	0.733	0.765	0.251	0.127	0.380	0.733	0.765	0.733	0.765	0.251	0.127
FA ratio max	0.371	0.800	0.588	0.631	0.769	0.306	0.210	0.418	0.667	0.706	0.667	0.706	0.314	0.197
FA ratio min	0.333	0.600	0.647	0.600	0.647	0.377	0.285	0.333	0.600	0.647	0.600	0.647	0.377	0.285
ADC ratio mean	1.305	0.800	0.765	0.750	0.813	0.218	0.095	1.305	0.800	0.765	0.750	0.813	0.218	0.095
ADC ratio max	1.494	0.933	0.529	0.636	0.899	0.269	0.226	1.494	0.933	0.529	0.636	0.899	0.269	0.226
ADC ratio min	1.449	0.933	0.647	0.700	0.916	0.210	0.129	1.148	0.733	0.824	0.786	0.778	0.222	0.102
Cho/Cr	1.789	0.933	0.471	0.609	0.888	0.298	0.284	2.813	0.733	0.647	0.647	0.733	0.310	0.196
NAA/Cho	0.338	0.733	0.647	0.647	0.733	0.310	0.196	0.338	0.733	0.647	0.647	0.733	0.310	0.196
NAA/Cr	1.922	0.200	1.000	1.000	0.586	0.400	0.640	0.725	0.600	0.412	0.474	0.539	0.494	0.506
Lac/Cr	2.778	0.667	0.882	0.833	0.750	0.226	0.125	2.778	0.667	0.882	0.833	0.750	0.226	0.125

<sup>a</sup>rCBF ratio derived from purely astrocytomas.

**Table 3: Combination of the minimum ADC ratio and Cho/Cr for differentiating high- and low-grade gliomas**

Based on Minimum C1 Error				Errors		Based on Minimum C2 Error				Errors	
Sensitivity	Specificity	PPV	NPV	C1	C2	Sensitivity	Specificity	PPV	NPV	C1	C2
0.870	0.889	0.952	0.727	0.121	0.029	0.870	0.889	0.952	0.727	0.121	0.029

**Table 4: Combination of the maximum rCBF ratio and mean ADC ratio for differentiating glioblastomas and other-grade gliomas**

Based on Minimum C1 Error				Errors		Based on Minimum C2 Error				Errors	
Sensitivity	Specificity	PPV	NPV	C1	C2	Sensitivity	Specificity	PPV	NPV	C1	C2
0.733	0.941	0.917	0.800	0.163	0.075	0.733	0.941	0.917	0.800	0.163	0.075

On the other hand, the maximum rCBF ratio, in addition to being helpful in combination with the mean ADC ratio, is most useful for differentiating glioblastomas and other-grade gliomas. The minimum ADC ratio was excluded in the logistic analysis, though the minimum ADC ratio of the glioblastomas was significantly lower than that of the other-grade lesions ( $P < .05$ ). Perhaps, this is due to the inclusion of oligodendroglial tumors and astrocytic tumors in the assessment. It is surprising that the parameters obtained on MR spectroscopy did not demonstrate a high utility in differentiating glioblastomas from the remaining tumors. In particular, we did not expect that the sensitivity and specificity of the NAA/Cho ratio would be so low because prior studies have suggested that a prominent elevation of the Cho/NAA ratio is a hallmark of glioblastomas.<sup>13,24</sup> In the present study, we only evaluated astrocytomas, except for oligodendroglial tumors, and found that the maximum and mean rCBF ratios can be used to discriminate glioblastomas and other lesions, with C1 and C2 errors of 11.9% and 3.3%, respectively. Perfusion MR imaging is one of the most effective noninvasive methods for quantifying the grade of neoplastic neovascularization.<sup>5,25-29</sup> Furthermore, neovascularization is one of the most important criteria of malignancy for glioma grading. There has been extensive perfusion research related to predicting the glioma grade, much of it by using the DSC MR imaging technique.<sup>27,28</sup> On the other hand, ASL is a promising tool for assessing tumor angiogenesis and glioma grading.<sup>2-7,26,29</sup> ASL has several advantages, including being a nonionizing and completely noninvasive MR imaging technique that uses magnetically labeled arterial blood water protons as an endogenous tracer. For this reason, ASL is very suitable for diagnosing individuals with renal insufficiency and providing repeat follow-up.

Histologically, glioblastomas statistically have a larger microvessel attenuation than grade III lesions.<sup>30</sup> Previous studies have reported a positive correlation between rCBF-derived continuous ASL and vascular attenuation in gliomas.<sup>3,5</sup> Weber et al<sup>16</sup> attempted to elucidate the relationships between the rCBF on PASL and histopathologic findings, including the cell proliferation index and vessel attenuation, as defined by the number of microvessels. Our results indicated a high level of vascularity in glioblastomas and suggest that rCBF is a potential indicator of malignancy in gliomas based on vascular attenuation.

A multiparametric MR imaging approach has been attempted in past reports. Roy et al<sup>17</sup> studied 56 patients by using conventional MR imaging, DTI, dynamic contrast-enhanced perfusion imaging, and volumetric whole-brain MR spectroscopy and concluded that relative cerebral blood volume can be used to individually classify gliomas as low- or high-grade, with a sensitivity and specificity of 100% and 88%, respectively. On combining this parameter with the maximum relative cerebral blood volume, FA, ADC, and minimal NAA + Cr, classification was achieved with a 2% error and a sensitivity and specificity of 100% and 96%, respectively.<sup>17</sup> Unfortunately, the findings of the present study do not reach these levels of sensitivity and specificity; however, we used the ASL technique, which can measure the rCBF without a contrast agent. Weber et al<sup>16</sup> investigated the functional MR imaging methods DSC and PASL, dynamic contrast-enhanced MR imaging, and MR spectroscopy at 1.5T and suggested that the rCBF derived by using the PASL technique offers superior diagnostic performance in predicting the grade of gliomas. In another study of 1.5T, the combination of PASL and ADC significantly improved the sensitivity and predictive value of the preoperative

grading of gliomas compared with conventional imaging.<sup>4</sup> Only 1 study of the multiparametric MR imaging technique in combination with the ASL perfusion technique at 3T has been reported. Chawla et al<sup>7</sup> showed that the rCBF evaluated by using continuous ASL cannot be used to differentiate low-grade from high-grade gliomas, though the rCBF-guided voxel assessed by using a voxel analysis of multivoxel MR spectroscopy is useful for grading such tumors.

Histologically, we examined the Ki-67 labeling index as a marker of proliferation. Previous studies have shown that a higher rate of Ki-67-positive cells corresponds to greater malignancy and a worse survival rate in patients with gliomas.<sup>19</sup> Our studies demonstrated that the Ki-67 labeling index is correlated with MR imaging parameters, such as the ADC ratio, Cho/Cr ratio, and Lac/Cr ratio, consistent with the findings of previous literature.<sup>20,21,31</sup> These noninvasive imaging modalities can be used to reliably assess the potential for proliferation among brain tumors without a surgical procedure.

This study has several limitations. For example, the design included a relatively small population. In addition, when using diagnostic methods based on histologic biopsies, sampling bias should be considered. Although we used the same size region of interest for the multiple parameters of PASL, FA, and ADC, the region-of-interest diameter was relatively larger than that used in past reports and the effects of tumoral heterogeneity and regional differences were difficult to assess. Our method is based on the findings of an article by Hirai et al<sup>6</sup>; however, the placement of 5 ROIs on the ipsilesional side with only 1 region of interest on the contralateral side appears to be problematic for determining the ideal ratio. Regarding the limitation of the PASL sequence, a section thickness of 8 mm is relatively thick compared with that used in previous literature. We carefully placed the region of interest and minimized the potential for such errors. In the present study, we evaluated the data obtained by using both single-voxel and multivoxel techniques to secure the patients, though there may be a potential weaknesses in analyzing the combined single- and multivoxel MR spectroscopy data. Furthermore, the same TE conditions were used in each MR spectroscopy study to reduce the potential for error.

## CONCLUSIONS

Our findings indicate that PASL, DTI, and MR spectroscopy provide useful parameters for predicting malignant grades of cerebral gliomas. In particular, the rCBF ratio calculated by using PASL at a high field strength is useful for distinguishing glioblastomas from grade II or III gliomas. The ADC, Cho/Cr, and Lac/Cr ratios have the potential to predict glioma proliferation.

## REFERENCES

1. Louis DN, Ohgaki H, Wiestler OD, et al. **The 2007 WHO classification of tumours of the central nervous system.** *Acta Neuropathol* 2007;114:97–109
2. Warmuth C, Gunther M, Zimmer C. **Quantification of blood flow in brain tumors: comparison of arterial spin labeling and dynamic susceptibility weighted contrast-enhanced MR imaging.** *Radiology* 2003;228:523–32
3. Kimura H, Takeuchi H, Koshimoto Y, et al. **Perfusion imaging of meningioma by using continuous arterial spin-labeling: comparison with dynamic susceptibility-weighted contrast-enhanced MR images and histopathologic features.** *AJNR Am J Neuroradiol* 2006;27:85–93
4. Kim HS, Kim SY. **A prospective study on the added value of pulsed arterial spin-labeling and apparent diffusion coefficients in the grading of gliomas.** *AJNR Am J Neuroradiol* 2007;28:1693–99
5. Noguchi T, Yoshiura T, Hiwatashi A, et al. **Perfusion imaging of brain tumors using arterial spin-labeling: correlation with histopathologic vascular density.** *AJNR Am J Neuroradiol* 2008;29:688–93
6. Hirai T, Kitajima M, Nakamura H, et al. **Quantitative blood flow measurements in gliomas using arterial spin-labeling at 3T: inter-modality agreement and inter- and intraobserver reproducibility study.** *AJNR Am J Neuroradiol* 2011;32:2073–79
7. Chawla S, Wang S, Wolf RL, et al. **Arterial spin-labeling and MR spectroscopy in the differentiation of gliomas.** *AJNR Am J Neuroradiol* 2007;28:1683–89
8. Zikou AK, Alexiou GA, Kosta P, et al. **Diffusion tensor and dynamic susceptibility contrast MRI in glioblastoma.** *Clin Neurol Neurosurg* 2012;114:607–12
9. Liu X, Tian W, Kolar B, et al. **MR diffusion tensor and perfusion-weighted imaging in preoperative grading of supratentorial nonenhancing gliomas.** *Neuro Oncol* 2011;13:447–55
10. Lee EJ, Lee SK, Agid R, et al. **Preoperative grading of presumptive low-grade astrocytomas on MR imaging: diagnostic value of minimum apparent diffusion coefficient.** *AJNR Am J Neuroradiol* 2008;29:1872–77
11. Yang D, Korogi Y, Sugahara T, et al. **Cerebral gliomas: prospective comparison of multivoxel 2D chemical-shift imaging proton MR spectroscopy, echoplanar perfusion and diffusion-weighted MRI.** *Neuroradiology* 2002;44:656–66
12. Zou QG, Xu HB, Liu F, et al. **In the assessment of supratentorial glioma grade: the combined role of multivoxel proton MR spectroscopy and diffusion tensor imaging.** *Clin Radiol* 2011;66:953–60
13. Li X, Lu Y, Pirzkall A, et al. **Analysis of the spatial characteristics of metabolic abnormalities in newly diagnosed glioma patients.** *J Magn Reson Imaging* 2002;16:229–37
14. Di Costanzo A, Scarabino T, Trojsi F, et al. **Multiparametric 3T MR approach to the assessment of cerebral gliomas: tumor extent and malignancy.** *Neuroradiology* 2006;48:622–31
15. Law M, Yang S, Wang H, et al. **Glioma grading: sensitivity, specificity, and predictive values of perfusion MR imaging and proton MR spectroscopic imaging compared with conventional MR imaging.** *AJNR Am J Neuroradiol* 2003;24:1989–98
16. Weber MA, Zoubaa S, Schlieter M, et al. **Diagnostic performance of spectroscopic and perfusion MRI for distinction of brain tumors.** *Neurology* 2006;66:1899–906
17. Roy B, Gupta RK, Maudsley AA, et al. **Utility of multiparametric 3-T MRI for glioma characterization.** *Neuroradiology* 2013;55:603–13
18. Server A, Kulle B, Gadmar ØB, et al. **Measurements of diagnostic examination performance using quantitative apparent diffusion coefficient and proton MR spectroscopic imaging in the preoperative evaluation of tumor grade in cerebral gliomas.** *Eur J Radiol* 2011;80:462–70
19. Johannessen AL, Torp SH. **The clinical value of Ki-67/MIB-1 labeling index in human astrocytomas.** *Pathol Oncol Res* 2006;12:143–47
20. Guillemin R, Menuel C, Duffau H, et al. **Proton magnetic resonance spectroscopy predicts proliferative activity in diffuse low-grade gliomas.** *J Neurooncol* 2008;87:181–87
21. Yin Y, Tong D, Liu X, et al. **Correlation of apparent diffusion coefficient with Ki-67 in the diagnosis of gliomas.** *Zhongguo Yi Xue Ke Xue Yuan Xue Bao* 2012;34:503–08
22. Luh WM, Wong EC, Bandettini PA, et al. **QUIPSS II with thin-slice T11 periodic saturation: a method for improving accuracy of quantitative perfusion imaging using pulsed arterial spin labeling.** *Magn Reson Med* 1999;41:1246–54
23. Fink JR, Carr RB, Matusue E, et al. **Comparison of 3 Tesla proton MR spectroscopy, MR perfusion and MR diffusion for distinguish-**

- ing glioma recurrence from posttreatment effects. *J Magn Reson Imaging* 2012;35:56–63
24. Magalhaes A, Godfrey W, Shen Y, et al. **Proton magnetic resonance spectroscopy of brain tumors correlated with pathology.** *Acad Radiol* 2005;12:51–57
25. Cha S, Knopp EA, Johnson G, et al. **Intracranial mass lesions: dynamic contrast-enhanced susceptibility-weighted echo-planar perfusion MR imaging.** *Radiology* 2002;223:11–29
26. Järnum H, Steffensen EG, Knutsson L, et al. **Perfusion MRI of brain tumours: a comparative study of pseudo-continuous arterial spin labelling and dynamic susceptibility contrast imaging.** *Neuroradiology* 2010;52:307–17
27. Aronen HJ, Gazit IE, Louis DN, et al. **Cerebral blood volume maps of gliomas: comparison with tumor grade and histologic findings.** *Radiology* 1994;191:41–51
28. Knopp EA, Cha S, Johnson G, et al. **Glial neoplasms: dynamic contrast-enhanced T2\*-weighted MR imaging.** *Radiology* 1999;211:791–98
29. Kim MJ, Kim HS, Kim JH, et al. **Diagnostic accuracy and interobserver variability of pulsed arterial spin labeling for glioma grading.** *Acta Radiol* 2008;49:450–57
30. Sharma S, Sharma MC, Gupta DK, et al. **Angiogenic patterns and their quantitation in high grade astrocytic tumors.** *J Neurooncol* 2006;79:19–30
31. Calvar JA, Meli FJ, Romero C, et al. **Characterization of brain tumors by MRS, DWI and Ki-67 labeling index.** *J Neurooncol* 2005;72:273–80

# Evaluation of Normal Changes in Pons Metabolites due to Aging Using Turbo Spectroscopic Imaging

A. Yang, X.h. Xiao, and Z.l. Wang

## ABSTRACT

**BACKGROUND AND PURPOSE:** To date, MRS study of both normal and pathologic brains have focused mainly on the supratentorial regions; few studies have investigated the infratentorial regions. However, the pons, an important structure of the brain, is associated with many neurodegenerative diseases and is often damaged by brain trauma. For MRS study of pontine disease, one must obtain MRS reference data on normal metabolite levels in the pons, including data on how these levels vary with age. The aim of this study was to analyze normal, age-related, metabolic changes in the pons by using turbo spectroscopic imaging.

**MATERIALS AND METHODS:** Seventy-eight healthy subjects with ages ranging from 5 days to 78 years were included in this study. NAA/Cr, Cho/Cr, and Cho/NAA ratios were measured by using turbo spectroscopic imaging. The 78 cases were divided into 4 groups by age: 0–5, 6–20, 21–50, and older than 50 years. The metabolite levels were compared with observed age-related changes among the groups.

**RESULTS:** The normal mean pontine metabolite ratios obtained for the combined age groups were NAA/Cr,  $2.44 \pm 0.45$  (mean); Cho/Cr,  $1.93 \pm 0.25$ ; and Cho/NAA,  $0.83 \pm 0.28$ . Statistically significant differences were found in the NAA/Cr between the 0- to 5- and 6- to 20-year-old groups, and among the 6- to 20-, 21- to 50-, and older than 50-year-old groups. A statistically significant difference was found in Cho/Cr between the 0- to 5- and 6- to 20-year-old subjects; however, no differences were found among the 6- to 20-, 21- to 50-, and older than 50-year-old groups. Statistically significant differences in Cho/NAA were also found among the 4 age groups. The NAA/Cr at birth was low, it rose rapidly at 0–5 years, reaching a peak at approximately 10–20 years, and then gradually decreased. The Cho/Cr decreased rapidly at 0–5 years, then continued to decline, and was stable after 20 years of age.

**CONCLUSIONS:** Turbo spectroscopic imaging is a good method for analyzing normal changes in the pons metabolites during growth, maturation, and aging.

**ABBREVIATION:** TSI = turbo spectroscopic imaging

Proton MR spectroscopy of the human brain is being increasingly used for both research and clinical applications.<sup>1</sup> To date, most spectroscopic studies of both normal and pathologic brains have focused mainly on the supratentorial brain regions.<sup>2–10</sup> In contrast, few studies have investigated the infratentorial regions and brain stem.<sup>11–13</sup>

The pons is part of the brain stem and is an important structure of the human brain. It contains various motor and sensory nuclei and bundles. The upper pons and midbrain tegmentum are

the main components of the ascending reticular activating system. Many neurodegenerative diseases, such as Parkinson disease and olivopontocerebellar atrophy, are associated with the pons. In addition, as a central axis structure, the pons can be easily damaged by brain trauma.<sup>13–16</sup>

Different brain structures have varying metabolite levels, which change with age.<sup>6–8</sup> To study pontine diseases, one must obtain MR spectroscopy reference data on normal metabolite levels in the pons, including data on how these levels vary with age. MR spectroscopy studies of the pons have been challenging because the structure is relatively small and surrounded by bones; this anatomy makes it difficult to acquire a homogeneous magnetic field.

Chemical shift imaging is a multivoxel MR spectroscopy technique that can be used to subdivide the spectral frequency information from a large MR spectroscopy volume into smaller MR

Received April 20, 2014; accepted after revision May 11.

From the Medical Imaging Center, Affiliated Zhongshan City Hospital of Sun Yat-sen University, Zhongshan City, Guangdong Province, China.

Please address correspondence to Ang Yang, MD, Medical Imaging Center, Affiliated Zhongshan City Hospital of Sun Yat-sen University, Sun Wendong Rd No. 2, Zhongshan City, Guangdong Province, China; e-mail: yang19781230@gmail.com

<http://dx.doi.org/10.3174/ajnr.A4031>

spectroscopy volumes within the volume of interest and to obtain the average spectral frequency information within the VOI. A spectroscopic imaging technique called turbo spectroscopic imaging (TSI) applies fast spin-echo imaging to obtain chemical shift imaging data rapidly without the loss of spatial resolution, and it is less sensitive to susceptibility effects.<sup>9,10,17</sup> In this study, we aimed to develop a proton MR spectroscopic data base of normal pons metabolite levels in vivo that could be used to study pontine lesions in the future. We applied TSI to measure metabolite levels in normal pontine tissues and to examine the variations of these levels with age.

## MATERIALS AND METHODS

### Subjects

Seventy-eight healthy subjects, ranging from 5 days to 78 years of age, underwent TSI. Among these subjects, there were 45 males and 33 females. The subjects were divided into 4 groups by age: 0–5 (20 cases), 6–20 (15 cases), 21–50 (21 cases), and older than 50 years (22 cases). For statistical reasons, for subjects younger than 1 year of age, the age in months was divided by 12 and rounded. The inclusion criteria were subjects with no history of neurologic abnormalities and no abnormal findings on routine scans. Permission was granted by the institutional review board of Affiliated Zhongshan City Hospital of Sun Yat-sen University, and informed consent of all subjects or their parents was obtained.

### MR Imaging and Data-Processing Methods

All subjects were scanned in a quiet state and were observed for any movement during the localizing and routine scans. A 1.5T MR imaging scanner (Intera; Philips Healthcare, Best, the Netherlands) equipped with a standard 8-channel head coil was used. Conventional transversal and sagittal T2-weighted images were obtained. The scan parameters for TSI were as follows: FOV, 230 × 180 mm; spatial resolution, 1 × 1 × 15 mm; sample, 256; reconstruction matrix, 24 × 24; sensitivity encoding acceleration factor, 2; TSI acceleration factor, 3; TR, 1600 ms; TE, 288 ms. The total TSI scan time was approximately 1 minute 20 seconds. For the scanning positioning methods, the conventional transversal and sagittal T2WI was used as the reference, and the TSI was positioned parallel to the frontal cranial fossa. The collected spectral data were transferred to a postprocessing workstation equipped with Achieva software, Version 2.6.3.5 (Philips Healthcare). The SpectroView software package was used for data processing, which involved selecting LongTeBrain\_csi, laying out the VOI in the pons with its manual outlining function, and then selecting the “display average.” The average metabolite ratio value for each of the voxels in the VOI was then accessed (Fig 1).

### Statistical Analysis

Data are presented as the mean ± SD for normal data and as the median/quarter for skewed data. For normally distributed data, 1-way analysis of variance was conducted among groups. For skewed data, the nonparametric rank sum test for 2 independent samples was applied. A difference with a *P* value < .05 was considered statistically significant. Scatterplots were graphed to observe changes in metabolite levels with age.

## RESULTS

For the 78 cases, the mean pontine NAA/Cr was  $2.44 \pm 0.45$ . The mean choline-containing compounds/Cr in the pons was  $1.93 \pm 0.25$ , and the mean Cho/NAA was  $0.83 \pm 0.28$ . Figure 2 shows the pons MR spectroscopy results for the different age groups.

Curve fitting was performed on the NAA/Cr, Cho/Cr, and Cho/NAA scatterplots (Fig 3). The NAA/Cr at birth was low, it rose rapidly at 0–5 years, reaching a peak at approximately 10–20 years, and then it gradually decreased (Fig 3). The Cho/Cr decreased rapidly at 0–5 years, then continued to decline, and was stable after 20 years of age. The Cho/NAA decreased rapidly at 0–5 years, then continued to decline, and finally rose after 20 years of age.

The pontine NAA/Cr ratios were compared among the groups of 0–5, 6–20, 21–50, and older than 50 years as shown in Table 1. There was no statistically significant difference between the 0- to 5- and older than 50-year-old subjects. In contrast, there were statistically significant differences among the other age groups. Compared with the 0- to 5-year-old subjects, the NAA/Cr was higher in the 6- to 20-year-old subjects. In addition, the NAA/Cr of the older than 50-year group was lower than that in the 21- to 50-year group.

The Cho/Cr ratios of the groups were also compared as shown in Table 2. There were no statistically significant differences among the groups of 6–20, 21–50, and older than 50 years. There were statistically significant differences between the 0- to 5-year-old group and the other 3 age groups. Compared with the 0- to 5-year-old group, the Cho/Cr was lower in the groups 6–20, 21–50, and the older than 50 years. The Cho/Cr ratios were >1 in all groups.

The Cho/NAA ratios of the groups were compared as shown in Table 3. There were statistically significant differences among all the groups. Compared with the 0- to 5-year-old group, there was a decline in Cho/NAA in the 6- to 20-year-old group. There was a slow rise in Cho/NAA from 21–50 years to older than 50 years.

## DISCUSSION

To develop a proton MR spectroscopic data base of in vivo changes in pons metabolite levels during aging, we used the TSI technique to analyze 78 healthy subjects. These data on normal pontine metabolite levels may be applied in future studies of pontine lesions. The results showed that a short TSI scan time could be used to produce good reconstructed spectra for clinical analysis. Our results indicate that the NAA/Cr in the pons rose rapidly in the 0- to 5-year-old group, reached a peak in the 10- to 20-year-old group, and then gradually decreased. The Cho/Cr decreased rapidly in the 0- to 5-year-old group, then continued to decrease, and remained stable after 20 years of age. The Cho/NAA decreased rapidly in the 0- to 5-year-old group, followed by a decline in the 6- to 20-year-old group, then the ratio slowly rose after 20 years of age.

Currently, MR spectroscopy analysis of normal brain tissue has focused on the frontal, temporal, and occipital lobes, and there are few relevant data for the pons.<sup>6</sup> This lack of data is due to obstacles to using MR spectroscopy on the pons. The posterior fossa is surrounded by skull base bones, and the pons itself is a relatively small organ. These anatomic features are disadvantages

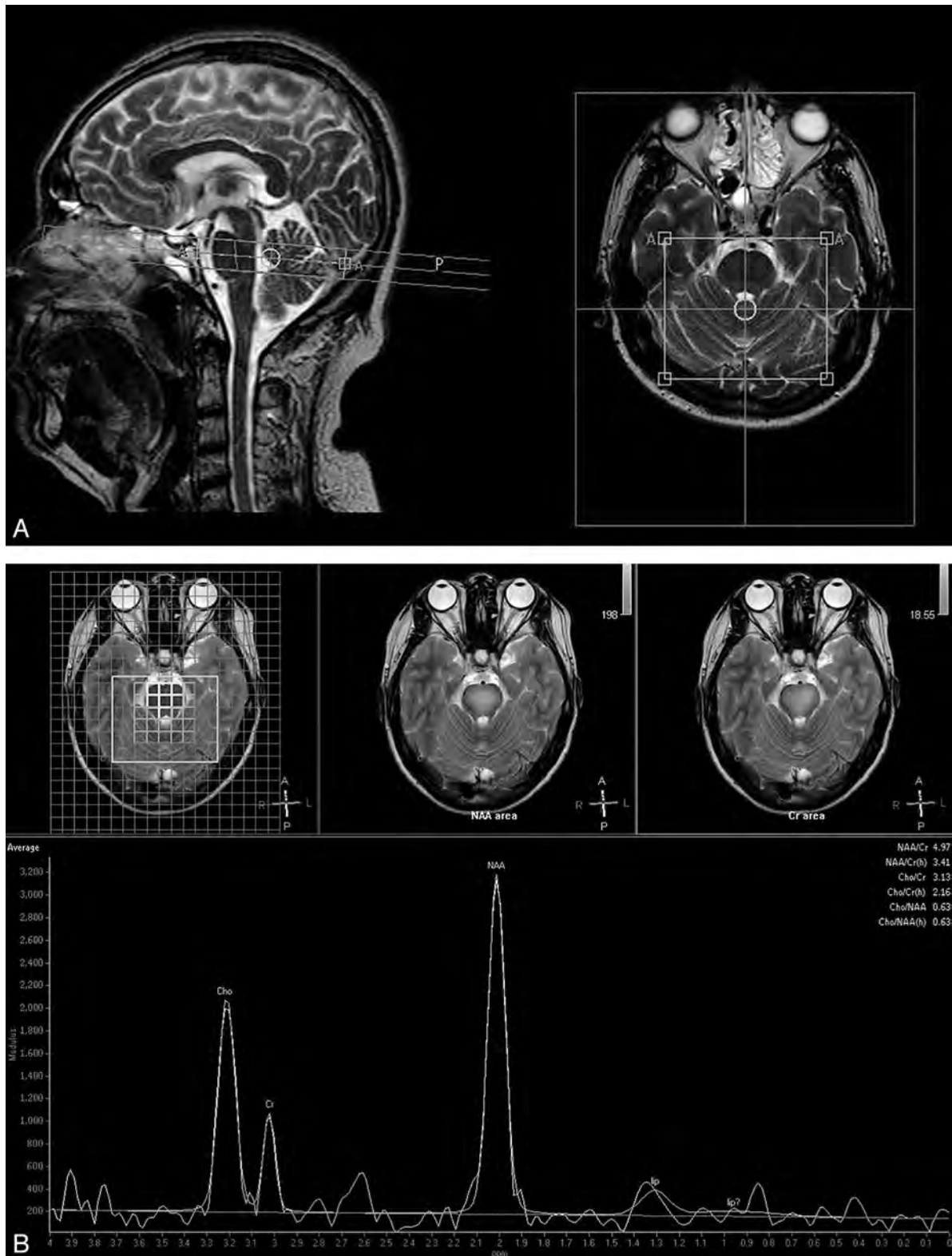


**FIG 1.** Positioning of the pons TSI scan and spectrum data processing. *A*, T2-weighted images show the placement of volumes of interest in the pons. The left side is sagittal, and the right side is transversal. The TSI was positioned parallel to the frontal cranial fossa. Note that the box is the signal-generating area. *B*, The upper row of images shows the region-of-interest selection area, and the lower image shows the reconstructed average metabolite ratios of the region of interest.

for MR spectroscopy because it requires a uniform magnetic field. The TSI technique used in this study provides a solution to the above problems. Unlike ordinary MR imaging techniques that

use frequency and 1 phase direction for spatial encoding, chemical shift imaging usually uses 2 phase directions for spatial coding, which leads to a relatively longer acquisition time;

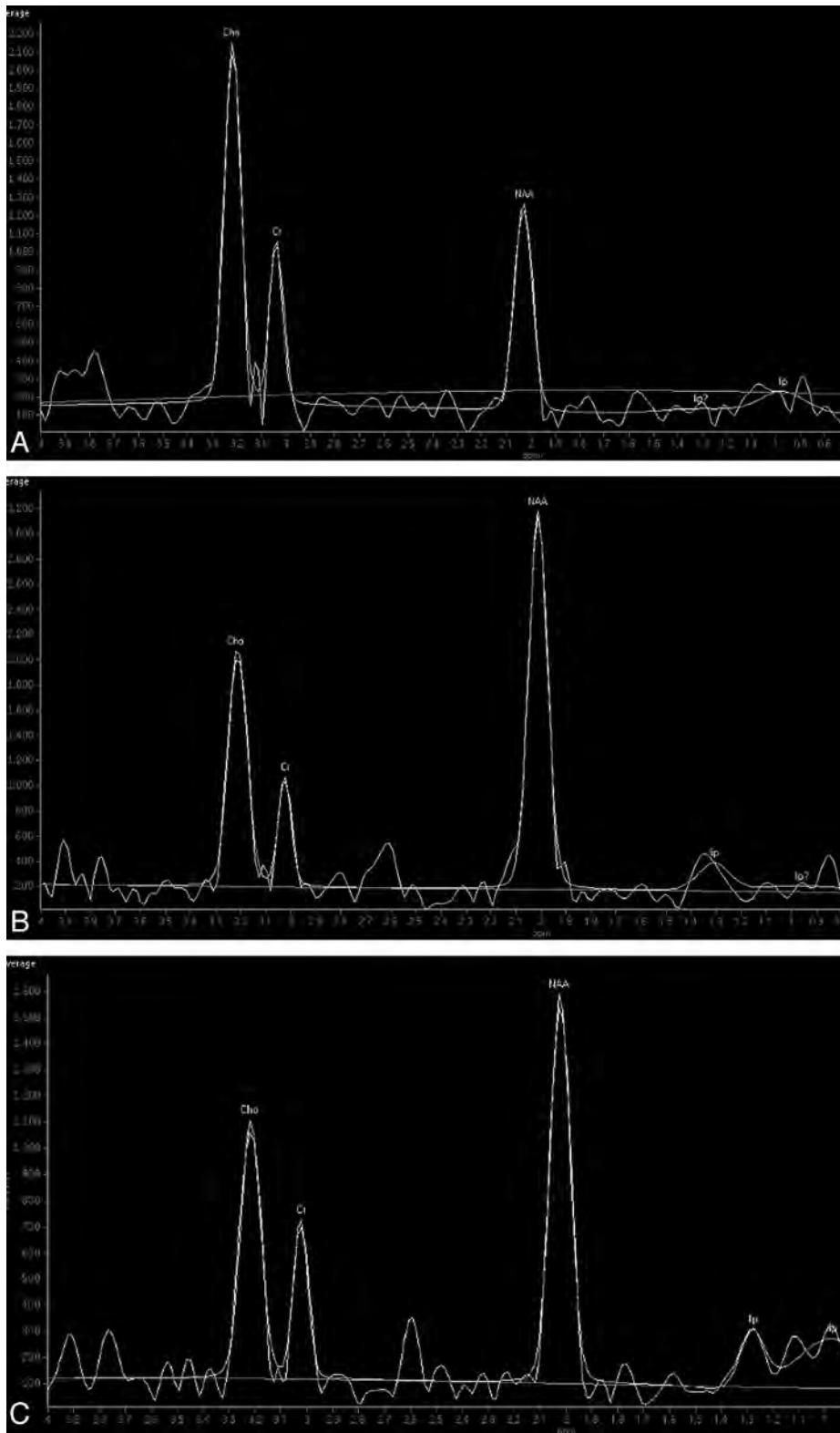


**FIG 2.** Proton MR spectrum of the pons in subjects of different ages. *A*, Spectrum of a 1-month-old baby's pons. *B*, Spectrum of a 5-year-old boy's pons. *C*, Spectrum of a 63-year-old man's pons. Note the relatively high Cho and low NAA levels in the baby. There is a higher NAA level and a lower Cho level in the 5-year-old child compared with the baby. The Cho level is lower in the 63-year-old man compared with the 5-year-old child.

faster acquisitions typically require the sacrifice of spatial resolution.<sup>10</sup>

Compared with a standard 2D point-resolved spectroscopic

sequence, TSI uses an additional 180° pulse (like fast spin-echo) to obtain an additional phase-encoding data-acquisition window, thus reducing the acquisition time. Also like the FSE sequence,

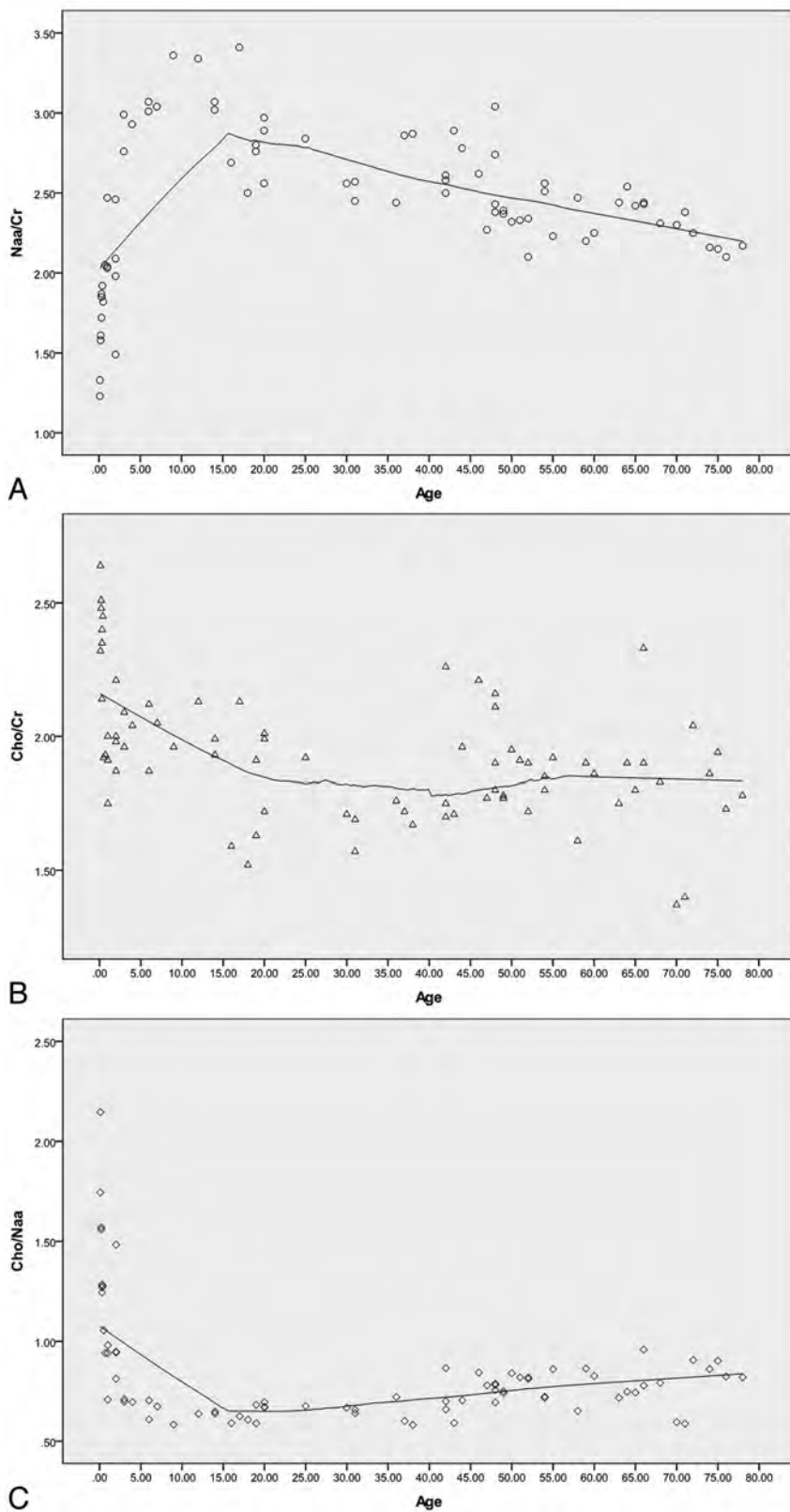


**FIG 3.** Scatterplot showing the metabolite changes in the pons with age. *A*, The scatterplot shows that NAA/Cr was low at birth, rose rapidly at 0–5 years, reaching a peak at approximately 10–20 years, and then gradually decreased. *B*, The Cho/Cr decreased rapidly at 0–5 years, then continued to decline, and was stable after 20 years of age. *C*, The Cho/NAA decreased rapidly at 0–5 years, then continued to decline, and finally rose after 20 years of age. Note that the curve-fitting model used is locally weighted scatterplot smoothing (LOESS), and the percentage of fitting points is 50%.

with its multiecho technique, TSI is less sensitive to B0 inhomogeneity. Moreover, TSI can be combined with sensitivity encoding to further shorten the scan time and be more insensitive to susceptibility effects.<sup>10,17</sup> The major disadvantage of TSI is that it sacrifices spectral resolution because there is insufficient time between the 2 successive refocusing pulses to read the signal. However, by using TSI, 4.4-Hz spectral resolution can be obtained on a 1.5T system, which is sufficient to resolve NAA, Cr, Cho, and lactate spectra. However, for short TE metabolites such as glutamate and glutamine and myo-inositol, the signal rapidly decays with increasing TE, rendering the long echo spacing (at least 100 ms) of TSI impractical for their detection.<sup>9,10</sup> In this study, the TSI scan time was reduced to approximately 1 minute 20 seconds, the baseline of the reconstructed spectrum was flat, the metabolite peaks were sharp, and the NAA, Cho, Cr spectra were well-resolved.

The levels of various metabolites in the pons vary with age as the human brain undergoes a maturation process. In a neonate's brain, the Cho level is at its highest, and the NAA level is at its minimum. NAA mainly exists in mature neuronal cells, and its levels rise with the development of the brain. Cho is the precursor to phosphatidylcholine, which is the main component of cell membranes. During brain development, the maturation of myelin and the synthesis of cell membranes cause rapid consumption of Cho, and its level declines.<sup>11,18,19</sup> The decline of the Cho/Cr may also be related to the increase of Cr after birth, but Cr is mainly stable after the first year of life and can be used as an internal reference.<sup>18</sup> In this study, the NAA levels increased rapidly in the 0- to 5-year-old group and the Cho levels declined rapidly, in support of the above viewpoint. The Cho/Cr value in the pons is relatively high (>1). The pons is characterized by a high attenuation of white matter because it contains many astrocytes and oligodendrocytes, which have a higher Cho content than neurons. This condition is similar to the higher Cho levels observed in the centrum semiovale compared with the cortex.<sup>12,20,21</sup>

A previous MR spectroscopy study on a healthy population of subjects 4–88 years of age showed that the NAA/Cho of

**Table 1: Comparison of NAA/Cr among different age groups**

Age Groups (yr)	Mean	No.	P Value
0–5	2.14 ± 0.25	20	.001, <sup>a</sup> <.001 <sup>b</sup>
6–20	1.90 ± 0.20	15	.468, <sup>c</sup> .261 <sup>d</sup>
21–50	1.85 ± 0.19	21	.665 <sup>e</sup>
Older than 50	1.82 ± 0.20	22	<.001 <sup>f</sup>

<sup>a</sup> Comparison between 0 to 5- and 6 to 20-year-old subjects.

<sup>b</sup> Comparison between 0 to 5- and 21 to 50-year-old subjects.

<sup>c</sup> Comparison between 6 to 20- and 21 to 50-year-old subjects.

<sup>d</sup> Comparison between 6 to 20- and older than 50-year-old subjects.

<sup>e</sup> Comparison between 21 to 50- and older than 50-year-old subjects.

<sup>f</sup> Comparison between 0 to 5- and older than 50-year-old subjects.

**Table 2: Comparison of Cho/Cr among different age groups**

Age Groups (yr)	Mean	No.	P Value
0–5	2.14 ± 0.25	20	0.001, <sup>a</sup> <.001 <sup>b</sup>
6–20	1.90 ± 0.20	15	0.468, <sup>c</sup> .261 <sup>d</sup>
21–50	1.85 ± 0.19	21	.665 <sup>e</sup>
Older than 50	1.82 ± 0.20	22	<.001 <sup>f</sup>

<sup>a</sup> Comparison between 0 to 5- and 6 to 20-year-old subjects.

<sup>b</sup> Comparison between 0 to 5- and 21 to 50-year-old subjects.

<sup>c</sup> Comparison between 6 to 20- and 21 to 50-year-old subjects.

<sup>d</sup> Comparison between 6 to 20- and older than 50-year-old subjects.

<sup>e</sup> Comparison between 21 to 50- and older than 50-year-old subjects.

<sup>f</sup> Comparison between 0 to 5- and older than 50-year-old subjects.

**Table 3: Comparison of Cho/NAA among different age groups**

Age Groups (yr)	Median/Quartile	No.	P Value
0–5	1.01/0.84–1.43	20	<.001, <sup>a</sup> <.001 <sup>b</sup>
6–20	0.63/0.60–0.67	15	.005, <sup>c</sup> <.001 <sup>d</sup>
21–50	0.70/0.65–0.78	21	.015 <sup>e</sup>
Older than 50	0.81/0.72–0.86	22	.001 <sup>f</sup>

<sup>a</sup> Comparison between 0 to 5- and 6 to 20-year-old subjects.

<sup>b</sup> Comparison between 0 to 5- and 21 to 50-year-old subjects.

<sup>c</sup> Comparison between 6 to 20- and 21 to 50-year-old subjects.

<sup>d</sup> Comparison between 6 to 20- and older than 50-year-old subjects.

<sup>e</sup> Comparison between 21 to 50- and older than 50-year-old subjects.

<sup>f</sup> Comparison between 0 to 5- and older than 50-year-old subjects.

the white matter in the centrum semiovale increased rapidly in the first decade of life, reached a maximum by the second-to-third decades of life, and then declined steadily.<sup>11</sup> Although most maturation events in the human brain occur within the first few years of life, the brain is still establishing functional neuronal interconnections until puberty, and this maturation process is associated with significant alterations in the biochemical composition of the brain. As an example, the increase in the number of neuronal cells in the centrum semiovale reaches its peak by approximately 6 months after birth, but maturational changes continue to occur after infancy, with significant increases in the number and size of axonal and dendritic fluctuations.<sup>8,11</sup> In this study, the NAA and Cho levels in the pons reached a relatively stable phase by 10–20 years of age, which may correspond to the full maturation of the pons. NAA/Cr continued to decline in the 21- to 50- and the older than 50-year-old groups. This change implies that NAA decreases gradually after puberty. There were few changes in the Cho/Cr among the groups of 6–20, 21–50, and older than 50 years, implying that Cho is relatively stable after puberty. This result is similar to that reported previously by Moreno-Torres et al.<sup>13</sup> The reduction in the level of NAA may be due to diminished neuronal attenuation and/or neuronal loss in the aged brain and also a

diminished concentration of NAA in neurons.<sup>21</sup> With the exception of neurons, Cho is widely present in various types of cells, particularly glial cells, which undergo less dramatic changes with aging than neurons. The minimal changes in Cho levels after puberty may also be explained by the release of Cho compounds related to membrane breakdown during the aging process.<sup>13,21</sup>

There are some limitations of this study. First, the population sample enrolled in this study was relatively small, and more data should be collected in future studies to correct possible bias. However, the age range examined in this study was wide, with subjects from 0 to 78 years of age. In particular, we examined subjects during the first 5 years of life, which is a critical period for the developing brain, despite the difficulty in collecting data from children without sedation. Second, the regions of interest in TSI do not cover the whole pons. We attempted using 3D MR spectroscopy but the time required was not acceptable and the larger coverage to include the lower parts of the pons caused more difficulty in shimming. Therefore, we chose the region of interest covering as much of the pons as possible.

## CONCLUSIONS

Our findings indicate that TSI is an appropriate method for detecting changes in metabolites in the pons. We observed significant alterations in NAA/Cr and Cho/Cr in the pons in the 0- to 5-year-old group and noted that these ratios reached a plateau by 20 years of age, which may correspond to the maturation of the pons. After 20 years of age, the NAA/Cr decreased slowly and the Cho/Cr was relatively stable. These data may serve as a basis for studies of normal human neurochemistry and studies of metabolic alterations in diseases of the pons.

## REFERENCES

- Soares DP, Law M. **Magnetic resonance spectroscopy of the brain: review of metabolites and clinical applications.** *Clin Radiol* 2009; 64:12–21
- Tedeschi G, Bertolino A, Massaquoi SG, et al. **Proton magnetic resonance spectroscopic imaging in patients with cerebellar degeneration.** *Ann Neurol* 1996;39:71–78
- Pouwels PJ, Frahm J. **Regional metabolite concentrations in human brain as determined by quantitative localized proton MRS.** *Magn Reson Med* 1998;39:53–60
- Hetherington HP, Pan JW, Mason GF, et al. **Quantitative 1H spectroscopic imaging of human brain at 4.1 T using image segmentation.** *Magn Reson Med* 1996;36:21–29
- Michaelis T, Merboldt KD, Bruhn H, et al. **Absolute concentrations of metabolites in the adult human brain in vivo: quantification of localized proton MR spectra.** *Radiology* 1993;187:219–27
- Haga KK, Khor YP, Farrall A, et al. **A systematic review of brain metabolite changes, measured with 1H magnetic resonance spectroscopy, in healthy aging.** *Neurobiol Aging* 2009;30:353–63
- Chang L, Ernst T, Poland RE, et al. **In vivo proton magnetic resonance spectroscopy of the normal aging human brain.** *Life Sci* 1996;58:2049–56
- Saunders DE, Howe FA, van den Boogaart A, et al. **Aging of the adult human brain: in vivo quantitation of metabolic content with proton magnetic resonance spectroscopy.** *J Magn Reson Imaging* 1999;9:711–16
- Yahya A, Fallone BG. **Detection of glutamate and glutamine (Glx) by turbo spectroscopic imaging.** *J Magn Reson* 2009;196:170–77
- Martin AJ, Liu H, Hall WA, et al. **Preliminary assessment of turbo spectroscopic imaging for targeting in brain biopsy.** *AJNR Am J Neuroradiol* 2001;22:959–68

11. Kadota T, Horinouchi T, Kuroda C. **Development and aging of the cerebrum: assessment with proton MR spectroscopy.** *AJNR Am J Neuroradiol* 2001;22:128–35
12. Jacobs MA, Horská A, van Zijl PC, et al. **Quantitative proton MR spectroscopic imaging of normal human cerebellum and brain stem.** *Magn Reson Med* 2001;46:699–705
13. Moreno-Torres A, Pujol J, Soriano-Mas C, et al. **Age-related metabolic changes in the upper brainstem tegmentum by MR spectroscopy.** *Neurobiol Aging* 2005;26:1051–59
14. Carpentier A, Galanaud D, Puybasset L, et al. **Early morphologic and spectroscopic magnetic resonance in severe traumatic brain injuries can detect “invisible brain stem damage” and predict “vegetative states.”** *J Neurotrauma* 2006;23:674–85
15. Paus T. **Functional anatomy of arousal and attention systems in the human brain.** *Prog Brain Res* 2000;126:65–77
16. Young GB, Pigott SE. **Neurobiological basis of consciousness.** *Arch Neurol* 1999;56:153–57
17. Duyn JH, Moonen CT. **Fast proton spectroscopic imaging of human brain using multiple spin-echoes.** *Magn Reson Med* 1993;30:409–14
18. Dezortova M, Hajek M. **1H MR spectroscopy in pediatrics.** *Eur J Radiol* 2008;67:240–49
19. Urenjak J, Williams SR, Gadian DG, et al. **Specific expression of N-acetylaspartate in neurons, oligodendrocyte-type-2 astrocyte progenitors, and immature oligodendrocytes in vitro.** *J Neurochem* 1992;59:55–61
20. Brandão LA, ed. *MR Spectroscopy of the Brain.* Philadelphia: Lippincott Williams & Wilkins; 2003:10
21. Angélie E, Bonmartin A, Boudraa A, et al. **Regional differences and metabolic changes in normal aging of the human brain: proton MR spectroscopic imaging study.** *AJNR Am J Neuroradiol* 2001;22:119–27

# WEB Intrasaccular Flow Disruptor—Prospective, Multicenter Experience in 83 Patients with 85 Aneurysms

C. Papagiannaki, L. Spelle, A.-C. Januel, A. Benaissa, J.-Y. Gauvrit, V. Costalat, H. Desal, F. Turjman, S. Velasco, X. Barreau, P. Courtheoux, C. Cognard, D. Herbreteau, J. Moret, and L. Pierot

EBM  
2

## ABSTRACT

**BACKGROUND AND PURPOSE:** The safety and efficacy of WEB flow disruption have been analyzed in small, retrospective series. The object of this study was to evaluate the safety and efficacy of WEB flow disruption in a large, multicenter, prospectively collected population.

**MATERIALS AND METHODS:** Data from all patients treated with the WEB-DL device between June 2011 and October 2013 in 11 French neurointerventional centers were prospectively collected and retrospectively analyzed. Complications occurring during and after treatment were analyzed as well as morbidity and mortality at 1 month. Aneurysm occlusion status at the last follow-up was analyzed.

**RESULTS:** Eighty-three patients with 85 aneurysms were included in this series. Technical success was achieved in 77 patients with 79 aneurysms (92.9%). Periprocedural complications were observed in 9 patients (10.8%), leading to permanent neurologic deficits in 3 (3.9%). Morbidity and mortality at 1 month were 1.3% and 0.0%, respectively. Angiographic follow-up was performed for 65/79 aneurysms (82.3%) 3–24 months after treatment (mean, 5.3 months). Complete aneurysm occlusion was observed in 37/65 aneurysms (56.9%); neck remnant, in 23/65 (35.4%); and aneurysm remnant, in 5/65 (7.7%).

**CONCLUSIONS:** In this large prospective series of patients, WEB flow disruption was a safe and efficient technique.

**ABBREVIATIONS:** AcomA = anterior communicating artery; ATENA = Analysis of Treatment by Endovascular Approach of Nonruptured Aneurysms; CLARITY = Clinical and Anatomic Results in the Treatment of Ruptured Intracranial Aneurysms; DL = Dual Layer; WEB = Woven Endoluminal Bridge

Endovascular treatment is now the first therapeutic option for ruptured aneurysms and is important in the treatment of unruptured aneurysms.<sup>1–3</sup> Aneurysms with a complex anatomy (fusiform, wide-neck, large, or giant) are in some cases untreatable or difficult to treat with standard coiling. For these cases, endovascular techniques such as balloon-assisted coiling, stent-assisted coiling, or flow diversion have been used with good results.<sup>4–9</sup>

The Woven Endoluminal Bridge–Dual Layer (WEB-DL; Se-

quent Medical, Aliso Viejo, California) is an intra-aneurysmal flow-disruption device, developed to modify the blood flow at the aneurysm neck. Preliminary clinical experience with the WEB has shown the clinical utility of this treatment in wide-neck bifurcation aneurysms. Several preliminary, small, retrospective series have shown good feasibility of the treatment, with a limited number of complications, low morbidity, and no mortality.<sup>10–13</sup> However, because these series were small and conducted in highly specialized centers with a careful selection of cases, there was a need for a safety analysis in a larger series of patients treated in several neurointerventional units.

Regarding the efficacy of the method, these preliminary series have also shown good anatomic results but with a relatively high percentage of neck remnants (33.3%–56.7%).<sup>10,12</sup> Further analysis demonstrated that some of the neck remnants were, in fact, due to the opacification of the proximal recess of the WEB device.<sup>13</sup> This proximal recess opacification has proved stable at midterm follow-up in a recent retrospective series that has also demonstrated good anatomic results and stability of aneurysm obliteration at midterm follow-up.<sup>13</sup>

The first patient treated with the WEB-DL device in France was in June 2011. Since this initial case, all further consecutive

Received March 3, 2014; accepted after revision April 21.

From the Department of Neuroradiology (C.P., D.H.), Centre Hospitalier Universitaire (CHU) Tours, Tours, France; Department of Neuroradiology (L.S., J.M.), Hôpital Beaujon, Assistance Publique-Hôpitaux de Paris, Clichy, France; Department of Neuroradiology (A.-C.J., C.C.), CHU Toulouse, Toulouse, France; Department of Neuroradiology (A.B., L.P.), CHU Reims, Reims, France; Department of Neuroradiology (J.-Y.G.), CHU Rennes, Rennes, France; Department of Neuroradiology (V.C.), CHU Montpellier, Montpellier, France; Department of Neuroradiology (H.D.), CHU Nantes, Nantes, France; Department of Neuroradiology (F.T.), CHU Lyon, Lyon, France; Department of Neuroradiology (S.V.), CHU Poitiers, Poitiers, France; Department of Neuroradiology (X.B.), CHU Bordeaux, Bordeaux, France; and Department of Neuroradiology (P.C.), CHU Caen, Caen, France.

Please address correspondence to Laurent Pierot, MD, Service de Radiologie, Hôpital Maison-Blanche, 45 Rue Cognacq-Jay, 51092 Reims cedex, France; e-mail: lpierot@gmail.com

EBM  
2 Evidence-Based Medicine Level 2.

<http://dx.doi.org/10.3174/ajnr.A4028>

cases were prospectively included in a data base. The retrospective analysis of the patients treated between June 2011 and October 2013 is presented in this article.

## MATERIALS AND METHODS

The study received institutional review board approval, and according to the study design, informed consent was waived.

### Study Design

Patients treated consecutively with the WEB-DL between June 2011 and October 2013 in 11 French neurointerventional centers were prospectively included in the study.

The indication for treatment and the technique chosen (surgery or endovascular) were decided for both ruptured and unruptured aneurysms by a multidisciplinary team consisting of neurosurgeons, interventional neuroradiologists, and neuroanesthesiologists in each center. The selection of the aneurysms for treatment with a WEB device was made by the interventional neuroradiology team of each center according to the aneurysm characteristics (location, size, and neck size).

### WEB Device

There are now several WEB devices available in Europe, including the WEB Dual Layer, the WEB Single Layer (WEB-SL), and the WEB-Single Layer Spherical. In the present series, all patients and all aneurysms were treated with the WEB-DL. All WEB devices received European Conformity Mark for unruptured and ruptured aneurysms.

The WEB-DL is a self-expanding, oblate, braided, nitinol mesh. The device is composed of inner and outer braids held together by proximal, middle, and distal radiopaque markers creating 2 compartments: 1 distal and 1 proximal. Blood flow into a WEB-embolized aneurysm initially encounters 2 layers comprising 216 or 288 wires with the largest interwire distance ranging from 106 to 181  $\mu\text{m}$ , respectively, depending on the device size. The WEB implant is deployed—or retrieved before detachment—similar to deployment in endovascular coil systems, through microcatheters with an internal diameter of  $\geq 0.027$  inches. The detachment system is electrothermal and instantaneous.<sup>5,7</sup>

### Data Collection

Information regarding sex, age, aneurysm characteristics (location, rupture status, size, neck size), initial modified Rankin Scale score, endovascular procedure technique, and immediate outcome was registered as well as all peri- and postprocedural complications. All patients had a clinical examination or telephonic interview 1 month after the procedure with evaluation by the mRS score. Aneurysm occlusion was evaluated by using DSA, MRA, or CTA according to the protocol of each center.

### Data Analysis

Population characteristics, feasibility of the treatment, peri- and postprocedural complications, morbidity (defined as mRS  $>1$ ), and mortality at 1 month were analyzed. Last follow-up imaging (DSA or MRA) results were used to evaluate the quality of aneu-

rysm occlusion by using the 3-grade Montreal scale (total occlusion, neck remnant, aneurysm remnant).

## RESULTS

### Population

Eighty-three patients (57 women and 26 men) with 85 aneurysms, 34–75 years of age (mean,  $56.0 \pm 8.8$  years), were included. Twenty-two and 24 of the patients in these series also participated in the Woven Endoluminal Bridge Clinical Assessment of intraSaccular aneurysmal Therapy (WEBCAST) study and the French Observatory study, respectively.

Seventy-five aneurysms were unruptured (88.2%), 4 were ruptured (4.7%), and 6 (7.1%) were recanalized.

Forty-eight aneurysms were located on the MCA (56.5%), 18 on the basilar artery (21.2%), 11 on the anterior communicating artery (AcomA) (12.9%), and 8 on the supraclinoid ICA (9.4%). Aneurysm size varied from 4.6 to 13.8 mm (mean,  $7.4 \pm 1.4$  mm). Size was  $<5$  mm in 4 aneurysms (4.7%), between 5 and 10 mm in 73 aneurysms (85.9%), and  $>10$  mm in 8 aneurysms (9.4%). Neck size was between 2.6 and 9.5 mm (mean,  $5.6 \pm 1.5$  mm). Neck size was  $<4$  mm in 12 aneurysms (14.1%) and  $>4$  mm in 73 aneurysms (85.9%).

All procedures were performed with the patient under systemic heparinization. After femoral puncture, a bolus of intravenous weight-adjusted heparin (50 IU/kg) was given, followed by a continuous IV administration of 30 IU/kg/h. Heparin administration was then adjusted with activated clotting time aiming for 2–3 times. Fifteen of 83 patients (18.1%) did not have any antiplatelet treatment during or after treatment, 44 (53.0%) had 1 antiplatelet agent continued for 1 month after treatment, and 24 (28.9%) received double antiplatelet treatment also continued after treatment. Of these 24 patients, 4 had adjunctive stent placement for the treatment of their aneurysm.

### Treatment Feasibility

Technical success (deployment of the WEB in the target aneurysm) was achieved in 77 patients (92.8%) with 79 aneurysms (92.9%) (Figs 1 and 2). The remaining 6 patients (7.2%) with 6 unruptured aneurysms were successfully treated with coiling alone (1 patient), balloon-assisted coiling (3 patients), and stent-assisted coiling (2 patients), uneventfully (Fig 3). The reasons for deployment failure were the following: difficulty in navigating the WEB delivery microcatheter in tortuous anatomy (3 patients with AcomA aneurysms) and inadequate visualization of the device, leading to the inability to verify the patency of the bifurcation branches arising from the aneurysm neck (3 patients with 2 MCA aneurysms and 1 basilar tip aneurysm). Most of these cases were the first ones in the centers.

### Additional Treatment

Nine of 79 aneurysms successfully treated with the WEB (11.4%) received additional endovascular treatment after the WEB deployment. All were unruptured aneurysms, and the additional treatment was standard coiling in 6 aneurysms, balloon-assisted coiling in 1 aneurysm, and stent-assisted coiling in 2 aneurysms. The reasons for additional treatment after the WEB deployment were the following: 1) persisting aneurysm filling of complex-shaped aneurysms for which the operator decided to perform a

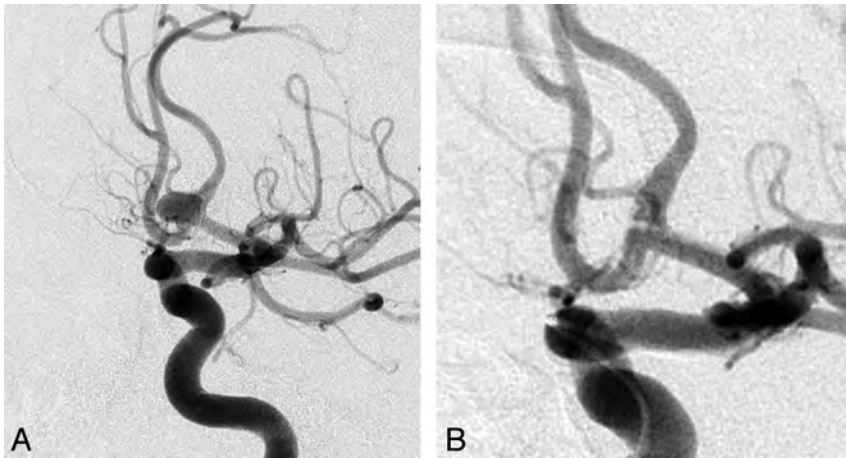


**FIG 1.** Anterior communicating artery unruptured aneurysm with a wide neck, before (A) and immediately after (B) WEB deployment.

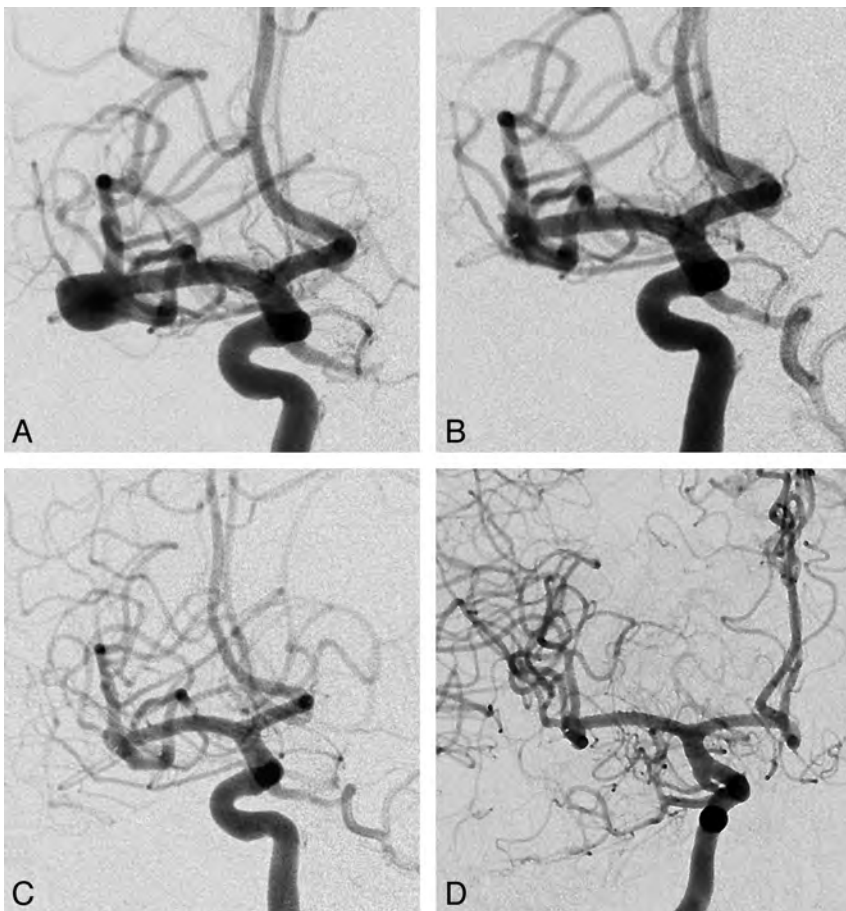


**FIG 2.** Middle cerebral bifurcation wide-neck unruptured aneurysm before (A) and immediately after (B) WEB deployment. Eight-month follow-up DSA, working projection (C) and frontal projection (D).

complete neck occlusion to ensure aneurysm occlusion or 2) programmed staged embolization in which the WEB was used to remodel a large complex-shaped aneurysm so that it would then be better suited for classic endovascular procedures.

### Complications

Perioperative complications occurred in 10/77 patients (13.0%) during the treatment of 11 aneurysms (Table). One inadvertent

device detachment was observed, without clinical worsening (1/77 patients, 1.3%). Intraoperative rupture occurred in 1/77 patients (1.3%). This patient presented with massive SAH (Fisher grade IV) and multiple aneurysms with 2 treated with the WEB. An intraoperative rupture occurred during the placement of the WEB in a ruptured AcomA aneurysm (Hunt and Hess scale 3), and a thromboembolic complication occurred during the treatment, at the same session, of an unruptured MCA aneurysm. Thromboembolic events occurred in 9/77 patients (11.7%) during treatment (including the patient presenting with 2 complications). One patient was treated for a ruptured MCA aneurysm, and the remaining 8 patients were treated for unruptured or recanalized aneurysms (6 MCA aneurysms, 1 AcomA aneurysm, and 1 basilar artery aneurysm). Three patients (3.9%) presented with a transient neurologic deficit, and 3, with a permanent deficit (3.9%). The remaining 3 patients (3.9%) did not have any neurologic symptoms.

There were no postoperative complications such as a thromboembolic event, delayed rupture, or delayed intraparenchymal hematoma observed.

### One-Month Clinical Follow-Up

From the 77 patients who were eventually treated with a WEB, 2 were lost to follow-up (2.6%). The remaining 75 patients (77 aneurysms) underwent a clinical control 1 month after embolization.

Seventy-one of 75 patients (94.7%) had mRS 0. Three patients (4.0%) presented with mRS 1. Two were treated for unruptured aneurysms and had intraoperative thromboembolic events (1 basilar tip and 1 AcomA), and the third was treated for recanalization of a previously ruptured MCA aneurysm and was already mRS 1 before retreatment with the WEB. One patient treated at the acute phase of subarachnoid hemorrhage (World Federation of Neurosurgical

Societies III) had both intraoperative rupture (of an initially ruptured AcomA aneurysm) and a thromboembolic event (during the simultaneous treatment of an unruptured MCA aneurysm [see above]). This patient had mRS 3 at 1 month (1.3%).

In total, a good outcome (mRS 0–1) was observed in 96.1% of patients. Morbidity and mortality at 1 month were 1.3% and 0.0%, respectively. Considering the 2 patients lost to follow-up as

an unfavorable outcome, the total rate of unfavorable outcomes was 3.9% (3/77 patients).

### Short-Term Anatomic Results

Of the 77 patients with 79 aneurysms that were eventually treated with a WEB, 63 patients (81.8%) with 65 aneurysms (82.3%) had an imaging control 3–24 months after treatment (mean,  $5.3 \pm 2.9$  months), 52 by DSA, 10 by MRA, and 1 by CTA (dual-energy CT). Limited artifacts were observed with MRA and CTA.

Of the 65 aneurysms, 37 (56.9%) presented with complete occlusion at follow-up; 23 (35.4%), with a neck remnant; and 5 (7.7%), with an aneurysm remnant. Adequate aneurysm occlusion (total occlusion or neck remnant) was observed in 60/65 (92.3%) of the aneurysms that had an imaging control.

For the 9 patients treated with a WEB who had an additional

treatment, the aneurysm occlusion rate at follow-up was complete occlusion in 3, neck remnant in 4, and aneurysm remnant in 1 patient (1 patient had not been followed up).

At the present time, none of the patients presenting with neck remnants or aneurysm remnants at follow-up have been retreated.

### DISCUSSION

The present, large, multicenter series confirms the results of the preliminary, small, retrospective series dealing with WEB aneurysm treatment.<sup>10–12</sup> The treatment is highly feasible (92.9%) with a low complication rate (11.7%), low permanent morbidity (1.3%), and no mortality. At short-term follow-up, adequate occlusion (complete occlusion or neck remnant) was observed in 92.3% of aneurysms.

Intrasaccular flow disruption is an innovative endovascular treatment that aims to create thrombosis of the aneurysmal sac by disrupting the blood flow in the aneurysm by covering its neck with an intrasaccular device. According to series presented in the literature, this approach applies mainly to complex wide-neck bifurcation aneurysms (MCA, basilar artery, AcomA, ICA).<sup>10–13</sup> Most aneurysms in our series are unruptured (88.2%), but treatment is also feasible for ruptured aneurysms (4.7%). Because no antiplatelet medication is needed for aneurysm treatment with the WEB, a rapid thrombosis of at least of the distal compartment and aneurysm dome is usually observed, which makes the device suitable for ruptured aneurysm treatment in the acute phase of a subarachnoid hemorrhage. The main reason for the low percentage of ruptured aneurysms treated in the present series is logistic organization, with no permanent material supply in most of the participating centers. Due to the small number of patients with ruptured aneurysms treated in this series, it is not possible to conduct a meaningful analysis of this subgroup. Retreatment of previously embolized, recanalized aneurysms is also feasible with the WEB (7.1%).

WEB treatment failures were encountered in 6/83 patients (7.1%) due to navigation difficulties (3 patients) or inadequate visualization of the device (3 patients). The microcatheters used for the WEB deployment are relatively larger compared with those used for simple coiling; this difference makes it more difficult to navigate in tortuous anatomy, which mainly applies to AcomA aneurysms. After deployment, the WEB position is sometimes difficult to verify completely, due to poor visualization of the device, especially when it is superimposed on bony structures of the skull base. Improvement of its radiopacity will potentially im-

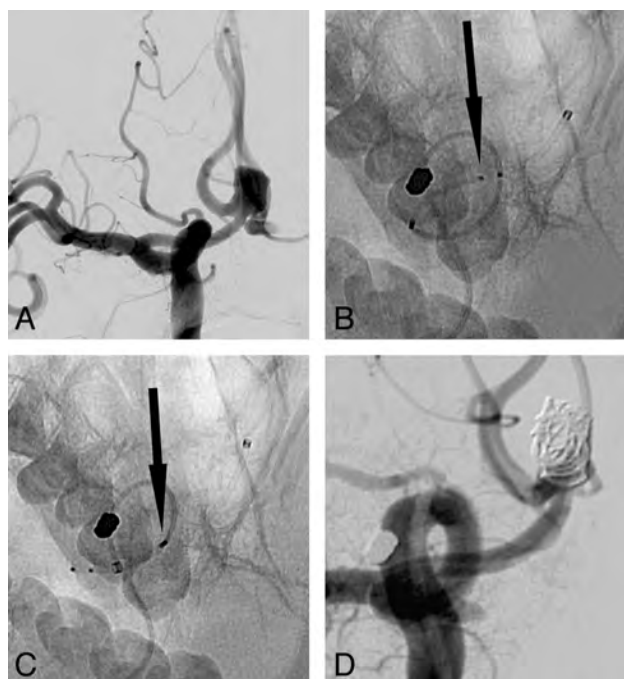


**FIG 3.** Failure to deploy the WEB due to the tortuous vessel anatomy. *A*, Unruptured AcomA aneurysm. *B*, WEB-DL (arrow on the second of 3 marker bands) could not be advanced through a tortuous turn by using only the delivery catheter. *C*, WEB-DL could not be advanced through the tortuous turn with intermediate catheter support of the delivery catheter (arrow shows the proximal marker of the WEB). *D*, Final result after balloon-assisted coiling of the aneurysm.

### Characteristics of patients and aneurysms in patients presenting with complications

Patient	Age (yr)	Sex	Aneurysm Location	Aneurysm Size (mm)	Status	Complication	Outcome (1-Month mRS)
1 <sup>a</sup>	50	F	AcomA	5.6	Ruptured	IOR	3
			MCA	6.0	Unruptured	TE	
2	66	F	MCA	6.5	Rec	TE	0
3	45	F	MCA	7.2	Unruptured	TE	0
4	69	F	BA	7.0	Unruptured	TE	1
5	66	M	MCA	9.3	Unruptured	TE	0
6	46	M	MCA	8.5	Unruptured	TE	0
7	63	F	MCA	5.6	Unruptured	TE	0
8	53	F	MCA	9.5	Ruptured	TE	0
9	56	M	AcomA	8.0	Unruptured	TE	1
10	49	F	BA	8.0	Unruptured	ID	0

**Note:**—BA indicates basilar artery; Rec, recanalization; IOR, intraoperative rupture; ID, inadvertent detachment; TE, thromboembolic events.

<sup>a</sup> Patient 1 had 2 aneurysms treated in the same session and 2 complications.

prove the feasibility of the treatment. In fact, the failure rate is not higher compared with that observed with standard coiling if one takes into account the complexity of aneurysms treated with the WEB and the learning curve in each center (this series includes the first cases treated in each center). In the Gallas et al<sup>14</sup> series, dealing with the treatment of 321 unruptured aneurysms with Guglielmi detachable coils (Stryker, Kalamazoo, Michigan), the failure rate was 6.0%. In the Analysis of Treatment by Endovascular Approach of Nonruptured Aneurysms (ATENA) and Clinical and Anatomic Results in the Treatment of Ruptured Intracranial Aneurysms (CLARITY) studies,<sup>2,3</sup> the failure rate was, respectively, 6.0% and 0.7%, given that the percentage of wide-neck aneurysms was 30.9% in ATENA and 9.1% in CLARITY compared with 85.9% in the present series.

The rate of adverse events reported in this series (13.0%) is similar to that observed in ATENA (13.4%) or CLARITY (17.0%).<sup>2,3</sup> The rate of intraoperative rupture (1.3%) was slightly lower compared with those in ATENA (2.6%) and CLARITY (3.7%). In addition, the rate of thromboembolic events (11.7%) was very similar to those reported in ATENA (7.1%) and CLARITY (13.3%). In Naggara et al,<sup>15</sup> a review of the endovascular treatment of unruptured aneurysms, thromboembolic events occurred at a rate of 7.6%, leading to an unfavorable outcome in 4.8% of patients and death in 1.9%. Treatment morbidity and mortality with the WEB (1.3% and 0.0%) are consistent with those reported in ATENA (respectively, 1.7 and 1.4%) and CLARITY (respectively, 3.7% and 1.5%).<sup>2,3</sup>

In our series, aneurysm occlusion was evaluated at short-term follow-up in a high percentage of aneurysms (82.3%). Adequate aneurysm occlusion (total occlusion or neck remnant) was observed in a high percentage of aneurysms (92.3%). The results reported in the CLARITY series are slightly worse, with an adequate occlusion rate of 81.2%, but the results are, in fact, not really comparable because most aneurysms in the present series were unruptured (CLARITY was dealing exclusively with ruptured aneurysms) and the follow-up was shorter in the present series compared with CLARITY.<sup>16</sup> However, the percentage of wide-neck aneurysms was clearly higher in the present series compared with CLARITY (respectively, 85.9% and 9.1%), and this is a well-known factor for aneurysm recanalization.<sup>17</sup> Neck remnants observed in our series were relatively high (35.4%). As outlined in a recent article, what is classified as a “neck remnant” after WEB treatment is not always a true neck remnant but is often an opacification of the proximal recess of the WEB device, which will be stable for a long time and has, in fact, been classified as complete occlusion.<sup>13</sup>

Our series has several limitations. Patients were prospectively included, but data were retrospectively collected and analyzed. In addition, the clinical and anatomic results were evaluated by the neurointerventional teams that performed the procedures, without an independent core lab. All patients were treated with the WEB-DL device, and further studies are necessary to analyze the safety and efficacy of the WEB-Single Layer and WEB-Single Layer Spherical devices.

## CONCLUSIONS

In this large multicenter series, the WEB device seems to be a promising tool for the treatment of complex wide-neck bifurca-

tion aneurysms with equal safety and efficacy compared with other endovascular treatments. Of course, due to the small number of patients, subgroup analysis that could draw conclusions according to aneurysm size and location is not feasible and further studies are needed to establish the extent of indications for this kind of treatment.

Disclosures: Anne-Christine Januel—RELATED: Travel/Accommodations/Meeting Expenses Related to Activities Listed: Sequent Medical (World Live Neurovascular Conference 2013 in Istanbul) and proctoring for Sequent Medical. Laurent Spelle—RELATED: proctoring for Sequent Medical, Travel/Accommodations/Meeting Expenses Related to Activities Listed: Sequent Medical, UNRELATED: Consultancy: Covidien/ev3 and Stryker. Jean-Yves Gauthier—UNRELATED: Other: a core lab agreement for a European WEB series from Sequent. Vincent Costalat—UNRELATED: Consultancy: Covidien, Stryker, Codman, Balt, and Sequent, Payment for Lectures (including service on Speakers Bureaus): for the development of educational presentations from Covidien, Stryker, and MicroVention. He also discloses a limited research agreement with Sequent. Francis Turjman—RELATED: Fees for Participation in Review Activities (such as data monitoring boards, statistical analysis, endpoint committees, and the like): Sequent Medical, UNRELATED: Consultancy: Covidien, Balt, and Codman, Grants or Grants Pending: Covidien, Payment for Lectures (including service on Speakers Bureaus): Covidien and Codman, Payment for the Development of Educational Presentations: Covidien, Travel, Accommodations, or Meeting Expenses: Covidien and Codman. Xavier Barreau—RELATED: Consulting Fees or Honoraria: Sequent Medical, UNRELATED: Consultancy: MicroVention, Codman, and Covidien, Payment for Lectures (including service on Speakers Bureaus): Codman, Travel, Accommodations, or Meeting Expenses: Covidien and Codman.\* Christophe Cognard—RELATED: Consulting Fees or Honoraria: Sequent Medical for proctoring, Support for Travel to Meetings for the Study or Other Purposes: Subsequent. UNRELATED: Consultancy: Stryker, MicroVention, Sequent, Codman, and Covidien. Denis Herbreteau—UNRELATED: Consultancy: Sequent and Covidien. Jacques Moret—UNRELATED: Consultancy: Covidien and MicroVention. Laurent Pierot—RELATED: Proctoring and Consultancy: Sequent Medical, Principal Investigator for WEBCAST and French Observatory, RELATED: Consulting Fees or Honoraria: Sequent Medical, UNRELATED: Consultancy: Covidien/ev3, MicroVention, and Penumbra.\*Money paid to the institution.

## REFERENCES

- Molyneux A, Kerr R, Stratton I, et al, for the International Subarachnoid Aneurysm Trial (ISAT) Collaborative Group. **International Subarachnoid Aneurysm Trial (ISAT) of neurosurgical clipping versus endovascular coiling in 2143 patients with ruptured intracranial aneurysms: a randomised trial.** *Lancet* 2002;360:1267–74
- Cognard C, Pierot L, Anxionnat R, et al, for the Clarity Study group. **Results of embolization used as the first treatment choice in a consecutive nonselected population of ruptured aneurysms: clinical results of the Clarity GDC study.** *Neurosurgery* 2011;69:837–41
- Pierot L, Spelle L, Vitry F, for the ATENA Investigators. **Immediate clinical outcome of patients harbouring unruptured intracranial aneurysms treated by endovascular approach: results of the ATENA trial.** *Stroke* 2008;39:2497–504
- Pierot L, Cognard C, Spelle L, et al. **Safety and efficacy of balloon remodeling technique during endovascular treatment of intracranial aneurysms: critical review of the literature.** *AJNR Am J Neuroradiol* 2012;33:12–15
- Pierot L, Spelle L, Leclerc C, et al. **Endovascular treatment of unruptured intracranial aneurysms: comparison of safety of remodeling technique and standard treatment with coils.** *Radiology* 2009;251:846–55
- Pierot L, Cognard C, Anxionnat R, et al, for the CLARITY Investigators. **Remodeling technique for endovascular treatment of ruptured intracranial aneurysms had a higher rate of adequate postoperative occlusion than did conventional coil embolization with comparable safety.** *Radiology* 2011;258:546–53
- Shapiro M, Becske T, Sahlein, et al. **Stent-supported aneurysm coiling: a literature survey of treatment and follow-up.** *AJNR Am J Neuroradiol* 2012;33:159–63
- Pierot L. **Flow diverter stents in the treatment of intracranial aneurysms: where are we?** *J Neuroradiol* 2011;38:40–46

9. Berge J, Biondi A, Machi P, et al. **Flow-diverter Silk stent for the treatment of intracranial aneurysms: 1-year follow-up in a multicenter study.** *AJNR Am J Neuroradiol* 2012;33:1150–55
10. Pierot L, Liebig T, Sychra V, et al. **Intrasaccular flow disruption: a new endovascular approach for the treatment of intracranial aneurysms—results of a preliminary clinical evaluation in a multicenter series.** *AJNR Am J Neuroradiol* 2012;33:1232–38
11. Lubicz B, Mine B, Collignon L, et al. **WEB device for endovascular treatment of wide-necked bifurcation aneurysms.** *AJNR Am J Neuroradiol* 2013;34:1209–14
12. Pierot L, Klisch J, Cognard C, et al. **Endovascular WEB flow disruption in middle cerebral artery aneurysms: preliminary feasibility, clinical, and anatomical results in a multicenter study.** *Neurosurgery* 2013;73:27–34, discussion 34–35
13. Lubicz B, Klisch J, Gauvrit JY, et al. **WEB-DL endovascular treatment of wide-neck bifurcation aneurysms: short- and midterm results in a European study.** *AJNR Am J Neuroradiol* 2014;35:432–38
14. Gallas S, Drouineau J, Gabrillargues J, et al. **Feasibility, procedural morbidity and mortality, and long-term follow-up of endovascular treatment of 321 unruptured aneurysms.** *AJNR Am J Neuroradiol* 2008;29:63–68
15. Naggara ON, White PM, Guilbert F, et al. **Endovascular treatment of intracranial unruptured aneurysms: systematic review and meta-analysis of the literature on safety and efficacy.** *Radiology* 2010;256:887–97
16. Pierot L, Cognard C, Ricolfi F, et al, for the CLARITY investigators. **Mid-term anatomic results after endovascular treatment of ruptured intracranial aneurysms with Guglielmi detachable coils and Matrix coils: analysis of the CLARITY series.** *AJNR Am J Neuroradiol* 2012;33:469–73
17. Pierot L, Cognard C, Anxionnat R, et al, for the CLARITY investigators. **Endovascular treatment of ruptured intracranial aneurysms: factors affecting midterm quality anatomic results: analysis in a prospective, multicenter series of patients (CLARITY).** *AJNR Am J Neuroradiol* 2012;33:1475–80

# Contrast-Enhanced Time-Resolved MRA for Follow-Up of Intracranial Aneurysms Treated with the Pipeline Embolization Device

S.R. Boddu, F.C. Tong, S. Dehkharghani, J.E. Dion, and A.M. Saindane

## ABSTRACT

**BACKGROUND AND PURPOSE:** Endovascular reconstruction and flow diversion by using the Pipeline Embolization Device is an effective treatment for complex cerebral aneurysms. Accurate noninvasive alternatives to DSA for follow-up after Pipeline Embolization Device treatment are desirable. This study evaluated the accuracy of contrast-enhanced time-resolved MRA for this purpose, hypothesizing that contrast-enhanced time-resolved MRA will be comparable with DSA and superior to 3D-TOF MRA.

**MATERIALS AND METHODS:** During a 24-month period, 37 Pipeline Embolization Device–treated intracranial aneurysms in 26 patients underwent initial follow-up by using 3D-TOF MRA, contrast-enhanced time-resolved MRA, and DSA. MRA was performed on a 1.5T unit by using 3D-TOF and time-resolved imaging of contrast kinetics. All patients underwent DSA a median of 0 days (range, 0–68) after MRA. Studies were evaluated for aneurysm occlusion, quality of visualization of the reconstructed artery, and measurable luminal diameter of the Pipeline Embolization Device, with DSA used as the reference standard.

**RESULTS:** The sensitivity, specificity, and positive and negative predictive values of contrast-enhanced time-resolved MRA relative to DSA for posttreatment aneurysm occlusion were 96%, 85%, 92%, and 92%. Contrast-enhanced time-resolved MRA demonstrated superior quality of visualization ( $P = .0001$ ) and a higher measurable luminal diameter ( $P = .0001$ ) of the reconstructed artery compared with 3D-TOF MRA but no significant difference compared with DSA. Contrast-enhanced time-resolved MRA underestimated the luminal diameter of the reconstructed artery by  $0.965 \pm 0.497$  mm ( $27\% \pm 13\%$ ) relative to DSA.

**CONCLUSIONS:** Contrast-enhanced time-resolved MRA is a reliable noninvasive method for monitoring intracranial aneurysms following flow diversion and vessel reconstruction by using the Pipeline Embolization Device.

**ABBREVIATIONS:** CE-TR = contrast-enhanced time-resolved; PED = Pipeline Embolization Device; TR-MRA = time-resolved MRA

Surgical clipping or endovascular coil embolization is generally the preferred treatment for intracranial aneurysms.<sup>1</sup> The Pipeline Embolization Device (PED; Covidien, Irvine, California) is an endovascular device that has redefined the scope of treatment for large, giant, wide-neck, or fusiform aneurysms or aneurysms having failed coil embolization, by reconstructing the parent artery and restoring its natural course.<sup>2</sup> The PED is designed

for 85% reduction of blood flow within an aneurysm, which induces thrombosis<sup>2</sup> while keeping perforators and/or side branch vessels patent.<sup>3</sup> Results from a multicenter prospective trial for treatment of uncoilable or failed large and giant ICA aneurysms with the PED demonstrated 99% technical success and 74% complete occlusion with 6% major ipsilateral stroke or death.<sup>4</sup> Flow diversion with the PED has also been reported in the treatment of HIV vasculopathy, with fusiform cerebral aneurysms precluding parent vessel sacrifice or surgical bypass.<sup>5</sup>

Digital subtraction angiography is the reference standard for the evaluation of aneurysms after endovascular treatment due to its unsurpassed spatial resolution; however, DSA is invasive and not without risks of puncture site and neurologic complications.<sup>6</sup> Posttreatment follow-up of intracranial aneurysms after coil embolization with MRA by using 3D-TOF or contrast-enhanced techniques is a potential noninvasive alternative to DSA for the evaluation of PED-treated aneurysms without the use of ionizing radiation.<sup>7</sup> Contrast-enhanced time-resolved MRA (CE-TR

Received January 6, 2014; accepted after revision March 31.

From the Departments of Radiology and Imaging Sciences (S.R.B., F.C.T., S.D., J.E.D., A.M.S.) and Neurological Surgery (F.C.T., J.E.D.), Emory University School of Medicine, Atlanta, Georgia.

Paper previously presented as a poster at: Annual Meeting of the American Society of Neuroradiology, May 18–23, 2013; San Diego, California; and as an oral presentation at: 25th International Workshop on Magnetic Resonance Angiography, August 20–23, 2013; New York, New York.

Please address correspondence to Srikanth R. Boddu, MSc, FRCR, Department of Radiology and Imaging Sciences, Division of Neuroradiology, Emory University Hospital, 1364 Clifton Rd NE, BG22, Atlanta, GA, 30322; e-mail: sboddu6@gmail.com

<http://dx.doi.org/10.3174/ajnr.A4008>

MRA) uses acquisition schemes aimed at accelerated data collection, primarily using parallel imaging algorithms and novel *k*-space trajectories to achieve high temporal resolution for multiphase MRA examinations. This technique provides consistent, technologist-independent, optimal arterial enhancement for contrast-enhanced MRA and provides information on temporal contrast kinetics.<sup>8,9</sup> Use of CE-TR MRA has been reported in the evaluation of intracranial lesions such as arteriovenous malformations and dural arteriovenous fistulas and for assessment of stenosis of the extracranial carotid artery, and it seems to be a promising technique for evaluating aneurysms after stent-assisted coil embolization.<sup>9-11</sup>

We hypothesized that TR-CE MRA could provide information comparable with DSA and would be superior to 3D-TOF MRA in the evaluation of intracranial aneurysms and the parent artery following flow diversion and parent vessel reconstruction with the PED.

## **MATERIALS AND METHODS**

### **Patient and Aneurysm Characteristics**

Approval for this study was obtained from the institutional review board. Since the use of PED at our institution was instituted in April 2011, 27 patients had follow-up evaluation with 3D-TOF MRA, CE-TR MRA, and DSA following PED treatment, allowing direct comparison. One patient with a PED-treated supraclinoid ICA aneurysm was excluded from this study due to extensive susceptibility artifacts on MRA related to a previously clipped contralateral MCA aneurysm, rendering the study nondiagnostic. Of the remaining 26 patients, there were 4 men and 22 women with a median age of 58 years (range, 41–84 years) with 36 aneurysms. The distribution of aneurysms is as follows: cavernous ICA ( $n = 10$ ), supraclinoid ICA ( $n = 8$ ), ophthalmic artery ( $n = 7$ ), posterior communicating artery ( $n = 5$ ), superior hypophyseal artery ( $n = 2$ ), anterior choroidal artery ( $n = 2$ ), anterior temporal artery ( $n = 1$ ), intracranial vertebral artery ( $n = 1$ ), and carotid terminus ( $n = 1$ ). Eight patients had 2 aneurysms each, and 1 patient had 3 aneurysms. Eighteen patients had a single PED placed, 5 patients had 2 PEDs placed, and 3 patients had 3 PEDs placed. The mean maximal diameter of the aneurysms was  $11 \pm 7.4$  mm (range, 1.2–28 mm). The median MRA follow-up was 149 days after PED placement (range, 49–184 days). The median time from CE-TR MRA to DSA for follow-up was 0 days (range, 0–68 days) because 19/26 patients had both CE-TR MRA and DSA on the same day.

### **MRA Technique**

MRA was performed on a 1.5T MR imaging system (Signa HDx; GE Healthcare, Milwaukee, Wisconsin) with an 8-channel head coil. 3D-TOF MRA was first performed by using a gradient-echo sequence (spoiled gradient-recalled-echo) with parallel imaging and scan parameters of TE, 6.9 ms; TR, 38 ms; flip angle, 20°; total acquisition time, 6:09 minutes; number of sections, 110; section thickness, 0.7 mm; FOV, 220 mm; rectangular FOV, 70%; acquisition matrix, 320; reconstruction matrix, 512; reconstructed voxel size,  $0.43 \times 0.43 \times 0.7$  mm.

The CE-TR MRA method used in this study is a commercially available sequence (time-resolved imaging of contrast kinetics or

TRICKS; GE Healthcare). Imaging parameters were as follows: TR/TE, 4.5/1.97 ms; flip angle, 35°; FOV, 170 mm; section thickness, 1.2 mm interpolated to 0.6 mm; reconstructed voxel size,  $0.48 \times 0.48 \times 0.7$  mm; matrix,  $256 \times 160$  zero-filled and interpolated to  $512 \times 512$ ; averages, 0.75; bandwidth, 62.5 KHz; array spatial sensitivity encoding technique acceleration factor, 2, yielding 10 or 12 dynamic, temporally discrete postcontrast phases at an approximately 4.0-second temporal update. Time-resolved MRA (TR-MRA) in all patients was performed after the injection of either a low protein-bound gadobenate dimeglumine (MultiHance; Bracco Diagnostics, Princeton, New Jersey), prescribed at 0.1-mmol/kg and 2-mL/s injection rates, or the blood pool agent gadofosveset trisodium (Ablavar; Lantheus Medical Imaging, North Billerica, Massachusetts) at 0.03-mmol/kg and 1.5-mL/s injection rates. Bolus infusion in both protocols was followed immediately by 25- to 30-mL normal saline flush at 2 mL/s. Postinjection delay and sequence triggering were prescribed in an automated fashion, without user input. The dynamic data generated by the time-resolved imaging of contrast kinetics sequence are presented in numbered temporal datasets. The scan baseline reflects the simultaneous initiation of the sequence and initiation of contrast injection, both occurring under fully automated parameters prescribed by the scanner/sequence manufacturer without user input. Before contrast/sequence triggering, a noncontrast mask is acquired for subtraction. Background subtraction of the precontrast imaging volume was performed in-line during acquisition, allowing production of both background-subtracted and unsubtracted TR-MRA volumes.

### **DSA Technique**

All DSA was performed transfemorally with 5F catheters by using a DSA unit (Integris Allura; Philips Healthcare, Best, the Netherlands) with an image-intensifier matrix of  $1024 \times 1024$  pixels. DSA was performed with bilateral selective internal carotid artery injections and either unilateral or bilateral vertebral artery injections, as necessary. Ten milliliters of nonionic contrast medium (270 mg of iodine per milliliter of iodixanol, Visipaque 270; GE Healthcare) was used for each hand injection. Rotational 3D angiography was performed for additional confirmation of findings. Standard anteroposterior and lateral projections were routinely acquired for carotid and vertebral injections. Additional selected oblique projections were obtained to clarify aneurysm anatomy at the discretion of the angiographer. All acquired DSA images were converted to internationally compatible DICOM files, and then the converted files were transferred to our server through a PACS.

### **Image Analysis**

All imaging studies were evaluated for occlusion of the treated aneurysm, reconstruction of the parent artery (quality of visualization and measurable luminal diameter), and stent-related complications such as stent migration or in-stent stenosis. Studies from all patients for each imaging technique were placed into an anonymized folder on the PACS (ie, 3D-TOF MRA, CE-TR MRA, and DSA studies from all patient populations formed 3 anonymized folders). The entire original acquired data, including both source images (mask, subtracted, and unsubtracted images) and standard reformats (MIP and MPR) for each technique, were made available for review when evaluating that technique. Addi-

**Table 1: Quality of visualization of the reconstructed parent artery with the PED using 3D-TOF MRA and CE-TR MRA<sup>a</sup>**

Technique	Mean	SD	95% CI of Mean	Comparison with DSA (P Value)	Comparison with TR-MRA (P Value)
3D-TOF MRA	2.62	0.898	2.243–2.936	.0001	.0001
CE-TR MRA	3.81	0.694	3.464–4.162	.344	NA

Note:—NA indicates not applicable.

<sup>a</sup> Five-point grading scale from 0–4 (0, very poor; 1, poor; 2, fair; 3, good; 4, excellent). DSA is considered the reference standard with a score of 4.

**Table 2: Measured luminal diameter of the reconstructed parent artery with the PED using 3D-TOF MRA and CE-TR MRA**

Technique	Mean (mm)	SD	95% CI of Mean	Comparison with DSA (P Value)	Comparison with TR-MRA (P Value)
3D-TOF MRA	2.108	0.964	1.718–2.497	.0001	.0001
CE-TR MRA	3.137	0.546	2.910–3.351	.661	NA
DSA	4.096	0.687	3.819–4.374	NA	.661

Note:—NA indicates not applicable.

**Table 3: Overestimation of luminal stenosis of the reconstructed parent artery with the PED**

Technique	Mean (mm) (%)	SD (%)	95% CI of Mean
3D-TOF MRA versus DSA	1.992 (71.8)	0.998 (52.7)	0.036–3.948 (31.6%–175%)
CE-TR MRA versus DSA	0.965 (26.6)	0.497 (12.7)	0.01–1.941 (1.7%–51.5%)
3D-TOF MRA versus CE-TR MRA	1.027 (50.1)	0.776 (58.8)	0.495–2.55 (65.1%–165%)

tional reformats in challenging cases were created by the authors as needed by using the subtracted dataset. Images were reviewed by an experienced Certificate of Added Qualification–certified neuroradiologist (A.M.S.) in consensus with a neuroradiology fellow (S.R.B.). The various imaging techniques were reviewed separately to minimize the bias from knowledge of the results of the other imaging technique.

Images were evaluated for aneurysm occlusion following PED as a primary outcome of treatment. MR imaging demonstrating complete aneurysm occlusion in concordance with DSA was considered a true-positive. Angiographic quality of the reconstructed artery was assessed with respect to vessel visualization and susceptibility-mediated degradation compared with the adjacent native artery; the quality of visualization of the reconstructed artery by MRA was graded by using a 5-point scale from 0 to 4 as follows: 0, extremely limited; 1, poor; 2, fair; 3, good; 4, excellent. The apparent luminal stenosis of the reconstructed artery was evaluated by measuring the maximal luminal diameter on both 3D-TOF MRA and CE-TR MRA. These findings were correlated with the quality of visualization and lumen diameter of the reconstructed artery on DSA as the reference standard. An experienced interventional neuroradiologist determined the clinical significance of discrepant findings between MRA techniques and DSA in the context of the particular patient study.

### Statistical Analysis

Statistical analysis was performed by using SPSS software, Version 20 (IBM, Armonk, New York). The sensitivity, specificity, and positive and negative predictive values of 3D-TOF MRA and CE-TR MRA were measured. The quality of visualization of the reconstructed artery was compared between techniques with the Wilcoxon signed rank test. The correlation between the number of PEDs versus the quality of visualization was evaluated by using the Spearman correlation. Correlation between types of contrast

versus intensity of visualization was assessed by using  $\chi^2$  analysis. Bland-Altman analysis was used to measure the numeric and percentage variation in the measurable luminal diameter. The significance of variation in the measurable luminal diameter between techniques was evaluated by using  $\chi^2$  analysis. Correlation between the number of PEDs versus the measured lumen diameter was evaluated by using the Spearman correlation.

### RESULTS

The sensitivity, specificity, and positive and negative predictive values of the 3D-TOF MRA relative to DSA for confirmation of posttreatment aneurysm occlusion were 74%, 85%, 65%, and 90%, respectively. For CE-TR MRA relative to DSA, sensitivity, specificity, and positive and negative predictive values were 96%, 85%, 92%, and 92%.

The mean quality of visualization in the arterial segment, reconstructed with a PED, on 3D-TOF MRA was  $2.62 \pm 0.898$  and  $3.81 \pm 0.694$  for CE-TR MRA (Table 1). The quality of visualization of the arterial segment reconstructed with a PED was superior on CE-TR MRA compared with 3D-TOF MRA ( $P = .0001$ ). Compared with the quality of visualization on DSA, both MRA techniques had inferior quality, with a significant difference for 3D-TOF MRA ( $P = .0001$ ) but not for CE-TR MRA ( $P = .344$ ).

The mean measurable luminal diameter of the arterial segment, reconstructed with the PED, on 3D-TOF MRA was  $2.108 \pm 0.964$  and  $3.137 \pm 0.546$  on CE-TR MRA (Table 2). The measurable luminal diameter of the reconstructed artery on CE-TR MRA was higher compared with 3D-TOF MRA ( $P = .0001$ ). Compared with the luminal measurement on DSA, both MRA techniques overestimated the luminal stenosis within the PED, with a significant difference for 3D-TOF MRA ( $P = .0001$ ) but not for CE-TR MRA ( $P = .661$ ) (Table 3).

Both 3D-TOF MRA and CE-TR MRA techniques showed a negative correlation between the number of PEDs used versus the intensity of visualization ( $r = -0.8$  and  $-0.3$ , respectively) and the number of PEDs used versus the measurable luminal diameter ( $r = -0.9$  and  $-0.6$ , respectively) of the reconstructed artery. The type of contrast material caused no significant variation in the intensity of visualization of the reconstructed artery on CE-TR MRA ( $P = .684$ ).

### DISCUSSION

The PED provides flow diversion by an attenuated braided construction of a bimetallic design of 75% cobalt chromium and 25% platinum tungsten. The device has a 30%–35% metal surface area when fully deployed, which is substantially greater than the 6.5%–9% metal surface area coverage provided by the commercially available self-expanding intracranial microstents.<sup>2</sup> The

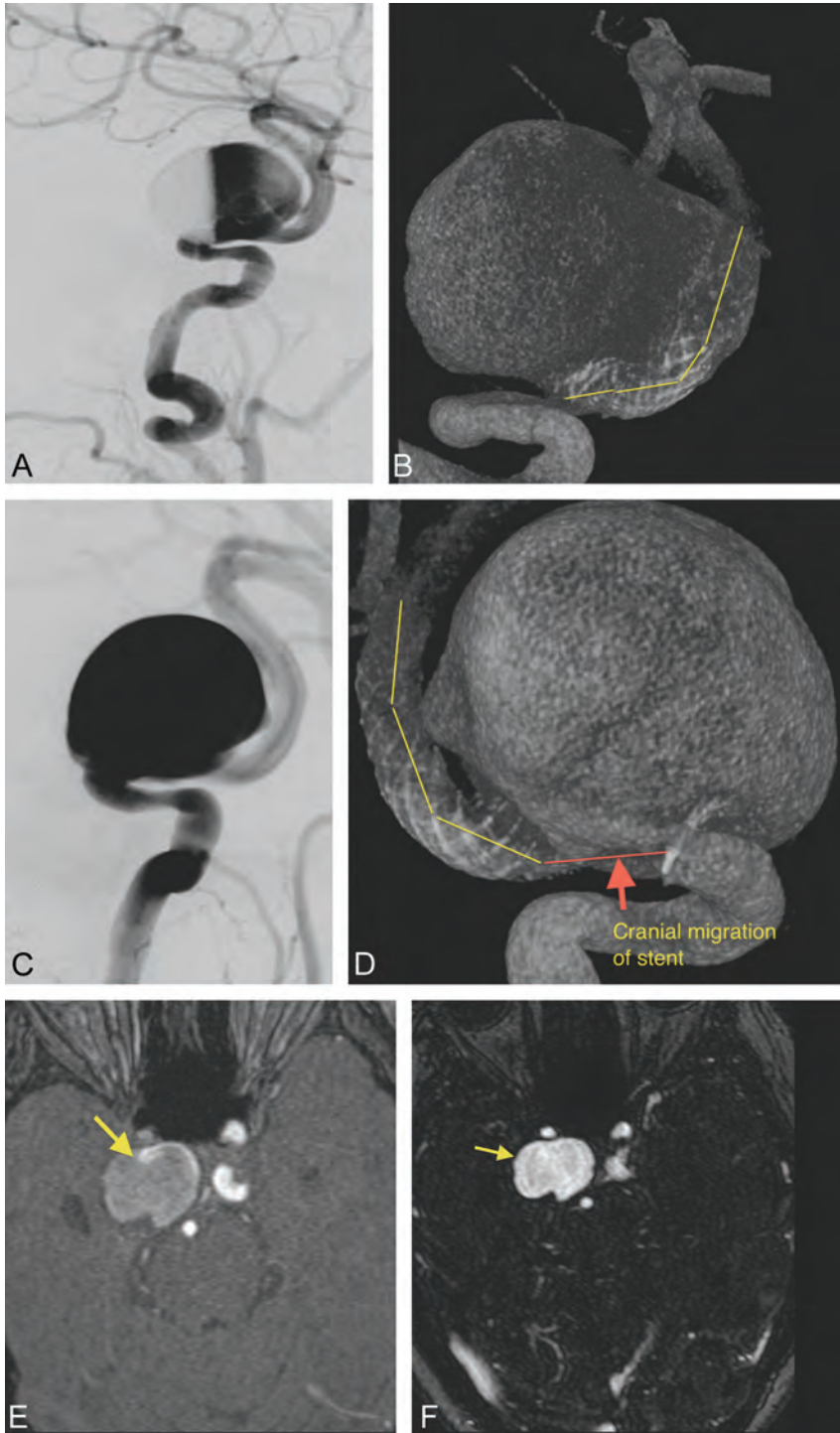


**FIG 1.** Stent migration with concordance between CE-TR MRA and DSA. A 56-year-old woman with a right cavernous carotid aneurysm. *A*, Immediate post-PED of the right cavernous ICA aneurysm with stasis. *B*, DSA shows the actual position of the PED after embolization (yellow line along stent course). *C*, Complete opacification of the aneurysm at 6-month DSA with no stasis or thrombus. *D*, DSA confirms distal migration (yellow line along stent course) resulting in reopening of the aneurysm neck (red line with red arrow). Superior demonstration of complete aneurysm opacification (yellow arrow) on CE-TR MRA (*F*) over 3D-TOF MRA (*E*) at 6-month follow-up. The hyperintensity in the aneurysm sac on TOF MRA (*E*) may represent either thrombus from intact PED or aneurysm refilling from PED migration (yellow arrow).

pooled sensitivity and specificity for evaluating complete aneurysm occlusion after coil embolization was 83% and 91% by using TOF-MRA and 87% and 92% with CE-MRA.<sup>12</sup> CE-MRA was

cavernous ICA and carotid terminus. Tortuosity and redundancy among these segments may expose such vulnerabilities in 3D-TOF MRA and likely account, in part, for the observed results.

contributory in only 6% of the patients with treated intracranial aneurysms by using coil embolization.<sup>7</sup> The results of MRA follow-up for coil-embolized aneurysms should not be directly applied to patients treated with the PED. In contradistinction to platinum coils, the larger bimetallic surface area coverage and radiofrequency shielding by the PED can result in a marked local signal void.<sup>13,14</sup>

Aneurysm residua, recurrence due to recanalization, in-stent stenosis due to intimal hyperplasia, stent occlusion from an organized thrombus, and stent migration must be evaluated by follow-up imaging in patients with parent vessel reconstruction.<sup>15,16</sup> Shorter angiographic follow-up has been shown to be a negative predictor of aneurysm obliteration following PED.<sup>17</sup> This finding highlights the importance of the immediate and long-term posttreatment follow-up in patients after PED.

Our results showed that the quality of visualization and measured luminal diameter of the reconstructed arterial segment on 3D-TOF MRA were significantly less than those on CE-TR MRA and DSA. These parameters were further adversely affected by the increased number of PEDs used for reconstruction. The inherent spatial resolution of 3D-TOF MRA in our imaging protocol is superior, with voxel reconstruction of  $0.43 \times 0.43 \times 0.7$  mm compared with CE-TR MRA with a larger interpolated voxel size of  $0.48 \times 0.48 \times 0.7$  mm. We believe our findings on 3D-TOF MRA, despite its better spatial resolution, are due to the signal loss from a combination of the inherent high metallic surface area of the PED and the predominant use in the proximal anterior intracranial circulation. Turbulent flow with intravoxel dephasing and/or slow flow with subsequent spin saturation can result in marked signal loss and can limit TOF MRA in tortuous vascular segments such as the cavernous or supraclinoid ICA.<sup>13,14,18,19</sup> Among the patients constituting our study population, all except 2 subjects (1 with an anterior temporal artery aneurysm and 1 with a PICA aneurysm) underwent treatment of intracranial ICA aneurysms distributed between the intradural

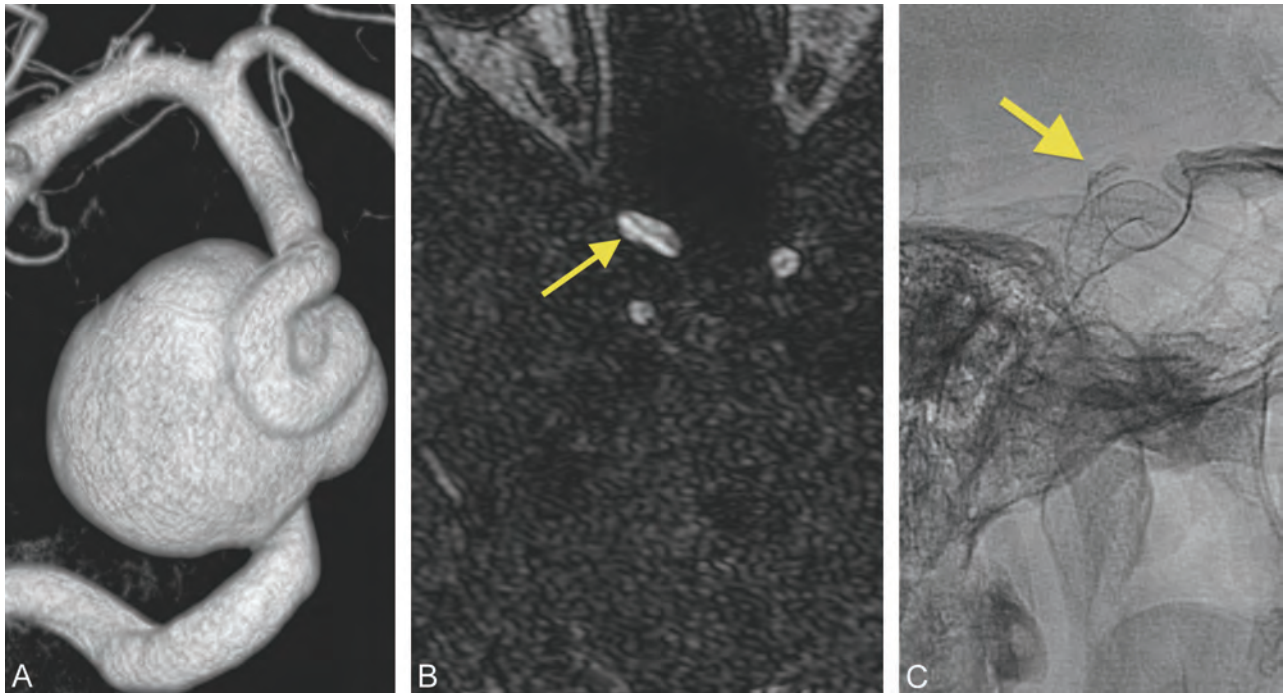


**FIG 2.** Discordance between CE-TR MRA and DSA. A 68-year-old woman with a right paraophthalmic aneurysm. *A*, Post-Pipeline embolization right paraophthalmic aneurysm. *B*, No residual neck is demonstrated (*yellow arrow*) on the 6-month follow-up CE-TR MRA. *C*, A thin crescentic residual neck measuring 1 mm deep (*yellow arrow*) is seen on the subsequent DSA.

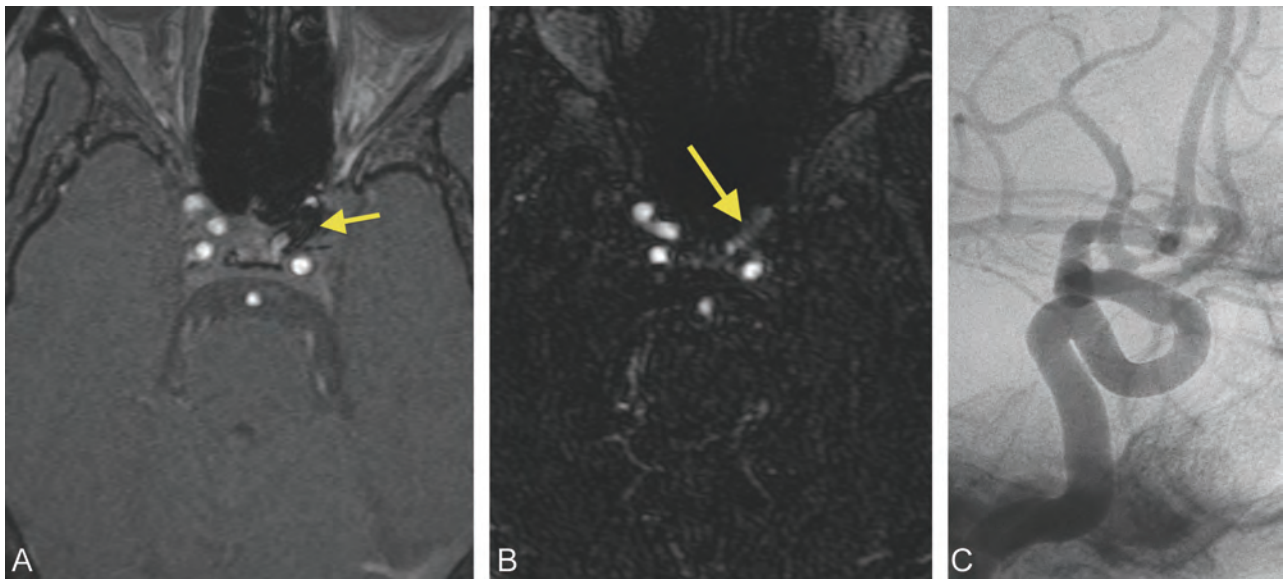


**FIG 3.** Overestimation of in-stent stenosis on MRA techniques. A 63-year-old woman with a left ophthalmic artery aneurysm. *A*, 3D-TOF MRA shows complete loss of flow-related enhancement in the PED (*yellow arrow*), suggestive of occlusion. *B*, Preserved enhancement within the PED with a narrowed lumen (*yellow arrow*) suggestive of in-stent stenosis. *C*, DSA demonstrates a normal-caliber ICA with no in-stent stenosis or occlusion.

3D-TOF MRA is further limited in its ability to differentiate thrombus from residual flow in treated aneurysms, both of which may exhibit intrinsic T1-weighted hyperintensity. Because the PED is designed for 85% reduction of blood circulation within the aneurysm, which induces thrombosis,<sup>20</sup> this limitation decreases the diagnostic accuracy of 3D-TOF MRA compared with CE-TR MRA.

CE-TR MRA showed significantly superior quality of visualization and higher measurable luminal diameter of the recon-

structed arterial segment compared with 3D-TOF MRA, a better reflection of DSA findings. CE-TR MRA uses precontrast mask images to subtract the background signal before contrast injection, so high signal intensity due to the T1 shortening effect of a thrombosed aneurysm is effectively eliminated. Signal loss related to turbulent flow or susceptibility artifacts may be partially overcome with conventional non-time-resolved CE-MRA; however, the limitations with this technique are venous contamination and enhancement of the aneurysm wall, potentially leading to false-

positive results.<sup>11</sup> While high-temporal-resolution and multiphase MRA examinations are not critical for evaluation of the PED, they effectively prevent mistiming of the contrast bolus. Of note, none of the CE-TR MRA examinations were technical failures due to inadequate contrast-bolus timing. CE-TR MRA also would have potential benefit for cases with postprocedural rupture of cavernous segment aneurysms with arteriovenous fistula formation, though none were present in this study population. A single distal stent migration in 1 patient with refilling of the entire aneurysm was diagnosed on CE-TR MRA and was confirmed on DSA (Fig 1).

Small residual lumen and suboptimal projections on DSA were independently associated with discordance between intrarterial DSA and MR angiography.<sup>7</sup> In our study group, 3 patients were nonconcordant between the CE-TR MRA and DSA. Two of 3 patients had false-positives, with erroneous diagnosis of complete aneurysm occlusion following PED. Subsequent DSA confirmed a thin crescentic filling in the aneurysm neck measuring 1 mm in depth (Fig 2). Findings in 1 of 3 patients were false-negative with minimal interstitial filling with an intra-aneurysmal coil pack on CE-TR MRA, which was demonstrated to be complete occlusion on the DSA performed on the same day. The superior spatial resolution of DSA compared with CE-TR MRA can explain the discordance between the techniques. DSA has a superior spatial resolution of  $0.2 \times 0.2 \times 0.2$  mm isotropic voxel size,<sup>21</sup> compared with the  $0.48 \times 0.48 \times 0.7$  mm voxel size of CE-TR MRA, which increases the sensitivity for small 1-mm residual filling in the treated aneurysms. In each of these cases, the results did not affect immediate patient outcome in terms of repeat endovascular treatment or anticoagulation. Patients undergo the standard follow-up procedure of our institution: 6 months, 2 years, and 5 years' posttreatment with the PED.

Overestimation of in-stent stenosis was well-reported in the literature in both in vitro and in vivo studies by using 3D-TOF MRA techniques<sup>22,23</sup> and on CE-TR MRA.<sup>11</sup> Our study results are in agreement with the literature findings (Fig 3). 3D-TOF MRA overestimated the measurable lumen diameter of the PED by 72% in comparison with DSA or by 50% in comparison with CE-TR MRA. CE-TR MRA overestimated the measurable lumen diameter of the PED by only 27% in comparison with DSA. This overestimation is a definite limitation of both MRA techniques, because even small degrees of intimal hyperplasia and luminal narrowing, which are much more effectively evaluated by DSA (due to lack of artifactual apparent narrowing), can impact patient management. Indeed, the intrinsic spatial and temporal resolution of DSA is superior to MRA techniques. Incorporation of MRA techniques in the follow-up algorithm of PED to exclude a tiny residual/recurrent aneurysm filling or in-stent stenosis should be evaluated in light of clinical context, as this may affect the patient management on individual basis.

We acknowledge the limitations of this study. First, the retrospective nature of this study incorporates a learning curve in both the performance of the technique by technologists and the experience of the readers. The relatively small number of cases is also a limitation, and clinically significant discrepancies between the CE-TR MRA and DSA could emerge as a larger number of procedures are performed. In some cases, DSA was performed with

knowledge of the MRA results, potentially influencing detection. Finally, while follow-up MRA and DSA were performed on the same day for most patients, in a few cases there was a time interval between the 2 examinations, which could result in disappearance or new emergence of contrast filling within an aneurysm that would introduce discrepancies between techniques not present if the studies had been performed on the same day.

## CONCLUSIONS

CE-TR MRA can be used to noninvasively monitor intracranial aneurysms following flow diversion and parent vessel reconstruction with the PED. CE-TR MRA is superior to conventional 3D-TOF MRA and has excellent concordance with DSA for detection of aneurysm occlusion and visualization of the reconstructed artery. Both MRA techniques evaluated overestimated apparent in-stent stenosis, which was worse on 3D-TOF MRA compared with CE-TR MRA.

## REFERENCES

1. Molyneux AJ, Kerr RSC, Birks J, et al. Risk of recurrent subarachnoid haemorrhage, death, or dependence and standardised mortality ratios after clipping or coiling of an intracranial aneurysm in the International Subarachnoid Aneurysm Trial (ISAT): long-term follow-up. *Lancet Neurol* 2009;8:427–33
2. Fiorella D, Kelly ME, Turner R, et al. Endovascular treatment of cerebral aneurysms: current devices, emerging therapies and future technology for the management of cerebral aneurysms. *Endovasc Today* 2008;7:53–65
3. Kallmes DF, Ding YH, Dai D, et al. A second-generation, endoluminal, flow-disrupting device for treatment of saccular aneurysms. *AJNR Am J Neuroradiol* 2009;30:1153–58
4. Becske T, Kallmes DF, Saatci I, et al. Pipeline for uncoilable or failed aneurysms: results from a multicenter clinical trial. *Radiology* 2013;267:858–68
5. Delgado Almandoz JE, Crandall BM, Fease JL, et al. Successful endovascular treatment of three fusiform cerebral aneurysms with the Pipeline embolization device in a patient with dilating HIV vasculopathy. *J Neurointerv Surg* 2014;6:e12
6. Kaufmann TJ, Huston J 3rd, Mandrekar JN, et al. Complications of diagnostic cerebral angiography: evaluation of 19,826 consecutive patients. *Radiology* 2007;243:812–19
7. Schaafsma JD, Velthuis BK, Majoie CB, et al. Intracranial aneurysms treated with coil placement: test characteristics of follow-up MR angiography—multicenter study. *Radiology* 2010;256:209–18
8. Blackham KA, Passalacqua MA, Sandhu GS, et al. Applications of time-resolved MR angiography. *AJR Am J Roentgenol* 2011;196:W613–20
9. Cashen TA, Carr JC, Shin W, et al. Intracranial time-resolved contrast-enhanced MR angiography at 3T. *AJNR Am J Neuroradiol* 2006;27:822–29
10. Farb RI, Agid R, Willinsky RA, et al. Cranial dural arteriovenous fistula: diagnosis and classification with time-resolved MR angiography at 3T. *AJNR Am J Neuroradiol* 2009;30:1546–51
11. Choi JW, Roh HG, Moon W-J, et al. Time-resolved 3D contrast-enhanced MRA on 3.0T: a non-invasive follow-up technique after stent-assisted coil embolization of the intracranial aneurysm. *Korean J Radiol* 2011;12:662–70
12. Kwee TC, Kwee RM. MR angiography in the follow-up of intracranial aneurysms treated with Guglielmi detachable coils: systematic review and meta-analysis. *Neuroradiology* 2007;49:703–13
13. Wall A, Kugel H, Bachman R, et al. 3.0 T vs. 1.5 T MR angiography: in vitro comparison of intravascular stent artifacts. *J Magn Reson Imaging* 2005;22:772–79
14. Wang Y, Truong TN, Yen C, et al. Quantitative evaluation of suscep-

- tibility and shielding effects of nitinol, platinum, cobalt-alloy, and stainless steel stents.** *Magn Reson Med* 2003;49:972–76
15. Fiorella D, Albuquerque FC, Deshmukh VR, et al. **Usefulness of the Neuroform stent for the treatment of cerebral aneurysms: results at initial (3–6-mo) follow-up.** *Neurosurgery* 2005;56:1191–201, discussion 1201–02
  16. Siddiqui MA, Bhattacharya J, Lindsay KW, et al. **Horizontal stent-assisted coil embolisation of wide-necked intracranial aneurysms with the Enterprise stent: a case series with early angiographic follow-up.** *Neuroradiology* 2009;51:411–18
  17. Jabbour P, Chalouhi N, Tjoumakaris S, et al. **The Pipeline embolization device: learning curve and predictors of complications and aneurysm obliteration.** *Neurosurgery* 2013;73:113–20, discussion 120
  18. Majoie CB, Sprengers ME, van Rooij WJ, et al. **MR angiography at 3T versus digital subtraction angiography in the follow-up of intracranial aneurysms treated with detachable coils.** *AJNR Am J Neuroradiol* 2005;26:1349–56
  19. Wallace RC, Karis JP, Partovi S, et al. **Noninvasive imaging of treated cerebral aneurysms. Part I. MR angiographic follow-up of coiled aneurysms.** *AJNR Am J Neuroradiol* 2007;28:1001–08
  20. Byrne J, Szikora I. **Flow diverters in the management of intracranial aneurysms: a review.** *EJMINT* 2012:1225000057. <http://www.ejmint.org/original-article/1225000057>. Accessed March 19, 2014
  21. Kaufmann TJ, Kallmes DF. **Diagnostic cerebral angiography: archaic and complication-prone or here to stay for another 80 years?** *AJR Am J Roentgenol* 2008;190:1435–37
  22. Blum MB, Schmook M, Scherthaner R, et al. **Quantification and detectability of in-stent stenosis with CT angiography and MR angiography in arterial stents in vitro.** *AJR Am J Roentgenol* 2007;189:1238–42
  23. Lettau M, Sauer A, Heiland S, et al. **Carotid artery stents: in vitro comparison of different stent designs and sizes using CT angiography and contrast-enhanced MR angiography at 1.5T and 3T.** *AJNR Am J Neuroradiol* 2009;30:1993–97

# The Success of Flow Diversion in Large and Giant Sidewall Aneurysms May Depend on the Size of the Defect in the Parent Artery

J.C. Gentric, T.E. Darsaut, A. Makoyeva, I. Salazkin, and J. Raymond

## ABSTRACT

**BACKGROUND AND PURPOSE:** Flow diverters are designed to occlude aneurysms while preserving flow to jailed arterial branches. We postulated that treatment success depended on the size of the aneurysm ostium or defect in the parent artery.

**MATERIALS AND METHODS:** Flow diverter expansion and deformation were studied in silicone tubes with wall apertures of various sizes. Large and giant canine sidewall aneurysms, featuring a branch located immediately opposite the aneurysm, and a smaller 6- to 8-mm (group A,  $n = 6$ ) or a larger 10- to 16-mm (group B,  $n = 6$ ) ostium were created to study the effects of ostium size on aneurysm or branch occlusion by flow diverters. Angiographic results after deployment and at 3 months were scored by using an ordinal scale. The amount of neointima formation on the segment of the device overlying the aneurysm or the branch ostia was determined by specimen photography.

**RESULTS:** The fusiform deformation of flow diverters was maximal with larger defects in silicone tubes. At 3 months, group B aneurysms showed worse angiographic results than group A aneurysms, with larger residual aneurysm volumes ( $P = .002$ ). Neointimal coverage of the aneurysm ostia was more complete in group A compared with group B ( $P = .002$ ).

**CONCLUSIONS:** The effects of flow diversion may vary with the size of the aneurysm ostium.

**ABBREVIATIONS:** FD = flow diverter; FSS = free segment of the stent

Flow diverters are increasingly used to treat large, giant, and, more recently, bifurcation aneurysms.<sup>1-8</sup> Successful treatment of the aneurysm with a flow diverter (FD) requires protecting the patient from rupture by reducing aneurysm flow, promoting thrombosis, and perhaps even repairing the defect in the parent artery, without occluding arterial branches covered by the device. The optimal device porosity and pore density to successfully occlude aneurysms while sparing jailed branches remain unknown and most likely differ from case to case. While FDs have been introduced in the market as if 1 porosity would be appropriate for

all cases, previous studies, in a modular carotid aneurysm model, have shown that some FDs are capable of occluding straight sidewall aneurysms but fail when implanted across curved sidewall, bifurcation, or giant fusiform aneurysms with multiple side branches.<sup>9-12</sup>

The capacity for a particular FD to occlude an aneurysm may correlate with the size of the defect in the parent vessel or ostium of the aneurysm. In the present investigation, we explored how flow diverters become deformed in silicone tubes in which wall defects of variable sizes have been created. Deformation of the device may change its capacity to divert flow. In vivo, we used a straight sidewall aneurysm model, a configuration previously shown to be favorable to flow diversion,<sup>9</sup> but modified to obtain large or giant aneurysms with variable-sized ostia (small or wide), to study how the size of the defect of the parent artery could influence device expansion, deformation, shortening, and angulation and how it could affect the efficacy of aneurysm occlusion at 3 months.

## MATERIALS AND METHODS

The 3.75 × 32 mm FDs used were stent-in-stent constructions made of 1 outer high-porosity braided stent (similar to the LVIS; MicroVention, Tustin, California) and 1 inner low-porosity FD (a stent-in-stent construction similar to the FRED; MicroVention).

Received February 19, 2014; accepted after revision April 21.

From the Department of Radiology (J.C.G., J.R.), Centre Hospitalier de l'Université de Montréal, Notre-Dame Hospital, Montreal, Quebec, Canada; Groupe d'étude de la Thrombose en Bretagne Occidentale (J.C.G.), Université de Bretagne Occidentale, Brest, France; Division of Neurosurgery (T.E.D.), Department of Surgery, University of Alberta Hospital, Mackenzie Health Sciences Centre, Edmonton, Alberta, Canada; and Laboratory of Interventional Neuroradiology (A.M., I.S., J.R.), Centre Hospitalier de l'Université de Montréal, Notre-Dame Hospital Research Centre, Montreal, Quebec, Canada.

This work was supported by a grant from the Heart and Stroke Foundation of Alberta to Tim E. Darsaut.

Please address correspondence to Jean Raymond, MD, Centre Hospitalier de l'Université de Montréal, Notre-Dame Hospital, Interventional Neuroradiology, 1560 Sherbrooke East, Pavillon Simard, Room Z12909, Montreal, Quebec, Canada H2L 4M1; e-mail: jean.raymond@umontreal.ca

<http://dx.doi.org/10.3174/ajnr.A4010>

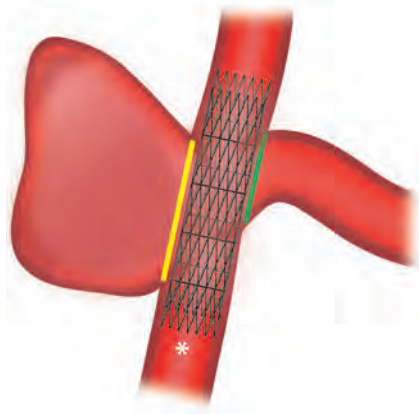


**FIG 1.** Description of the model. Schematic showing the branch opposite the constructed lateral wall aneurysm, with the proximal portion of the flow diverter denoted by an asterisk. Aneurysm-FSS is shown in yellow, and the branch-FSS is shown in green.

Benchtop experiments were performed by using FDs with inner stents of 36, 48, and 64 wires. All in vivo experiments were performed with devices characterized by a very low-porosity inner stent made of 64 braided wires. All devices were gifts from MicroVention.

### Benchtop Studies

Experiments were performed by using silicone tubes of various diameters (2.0, 2.5, 3.5, 4.0 mm), simulating the parent carotid arteries of the animal model. We cut elliptic holes of various lengths (5, 10, 15 mm) from the tubes, removing a varied proportion of the tube circumference (approximately 25%, 50%, or 75%) for 9 different apertures. FDs were deployed within the silicone tubes by using standard deployment techniques. Microphotographs, scaled by including a ruler in the experimental setup, were taken for each condition with a stereomicroscope and were analyzed with image-processing software (ImageJ software; National Institutes of Health, Bethesda, Maryland).<sup>13</sup> Given a sufficiently large opening, flow diverters progressively adopted a characteristic fusiform deformation,<sup>3,13</sup> with 2 transition zones on each side of a compaction zone. Porosities of the transition zones were measured by calculating 1-metallic surface of the device.

### In Vivo Studies

**Surgical Construction of Aneurysms.** All procedures were performed in 7- to 10-kg beagles under general anesthesia, in accordance with the guidelines of the Canadian Council on Animal Care. The model used is a modification of the one previously described (Fig 1).<sup>9</sup>

Briefly, through a linear midline incision, a segment (>30 mm) of the external jugular vein was harvested; then the pretracheal fascia was incised to expose and gain access to both carotid arteries. Under flow arrest, we ligated the left carotid artery proximally and tunneled the distal end behind the esophagus, anastomosing the left carotid to the right carotid artery in an end-to-side configuration. To create giant aneurysms, we anastomosed the venous segment to the right carotid artery side-to-side on the arterial wall.<sup>9</sup> The arteriotomy on the right carotid artery was short (between 6 and 8 mm, group A;  $n = 6$ ) or long (between 10

and 16 mm, group B;  $n = 6$ ) to receive the side-to-side venous graft and produce ostia of various sizes. All incisions were closed in multiple layers (Fig 1).

**Endovascular Treatment and Angiography.** Four days before endovascular treatment, animals were premedicated with acetylsalicylic acid, 81 mg daily, along with a loading dose of 150 mg of clopidogrel, followed by 37.5 mg daily. Endovascular treatment was performed 4–6 weeks after surgical aneurysm construction, through a coaxial microcatheter system introduced by a percutaneous transfemoral approach. All aneurysms were treated with a single 64-wire FD, deployed to leave a minimum of approximately 10-mm landing zones on each side. Clopidogrel therapy was discontinued 10 days post-stent implantation, while acetylsalicylic acid, 81 mg per day, was continued until euthanasia. Transfemoral angiography was performed in all animals immediately before and following FD deployment, at 2 weeks, and immediately before euthanasia at 3 months. To prevent femoral hematomas on dual antiplatelet therapy, all punctured femoral arteries were surgically exposed through a small linear incision and ligated. Angiographic results were scored by 2 experienced observers (T.E.D. and J.R.) by using a previously published system modified from Kamran et al.<sup>1</sup> A score of 0 indicated no change in aneurysm volume with treatment; 1, residual contrast filling >50% of the pretreatment aneurysm volume; 2, residual contrast filling <50% of the pretreatment aneurysm volume; 3, residual filling confined to the neck region; and 4, no residual filling (complete occlusion). The length and width of residual aneurysms at 3 months were also measured by using the distal tip of the angiographic catheter as a fiducial marker to calibrate measurements. The fusiform deformation of the device was measured by the ratio of the diameter of the device at the level of the midpoint of the ostium divided by the mean diameter of the device measured proximal and distal to the ostial opening of aneurysms. The angle between the proximal and distal carotid artery segments of the devices was also measured in the coronal plane defined by the 2 anastomoses, by drawing lines in the center of the lumen of the carotid arteries. The patency of the parent arteries and arterial branches was also assessed, and stenoses, if present, were calculated by using  $1 - N / D$ , where  $N$  indicates the diameter at the level of the more severe stenosis and  $D$ , the diameter of the distal normal artery.

**Euthanasia and Pathology.** Euthanasia by barbiturate overdose was performed at 3 months. After fixation in 10% formalin, the carotid artery aneurysm construct was opened longitudinally. We studied the portion of the stent that was visible over the aneurysm ostium. This free segment of the stent (FSS) or aneurysm-FSS,<sup>14</sup> was photographed by using a computerized imaging system (Vision PE; Clemex Technologies, Longueuil, Quebec, Canada). We also attempted to separately assess the branch-FSS, the segment of the FD covering the ostium of the left carotid artery (Fig 1). For each ex vivo aneurysm and branch, we attempted to determine the final porosity (the surface area through which blood could flow after neointima formation on the FSS), which was calculated by taking 1 minus the surface area of the biologic material plus the area of the metal struts, divided by the ostial surface area, as described by Bing et al.<sup>12</sup> Neointimal coverage was graded by 2 ex-

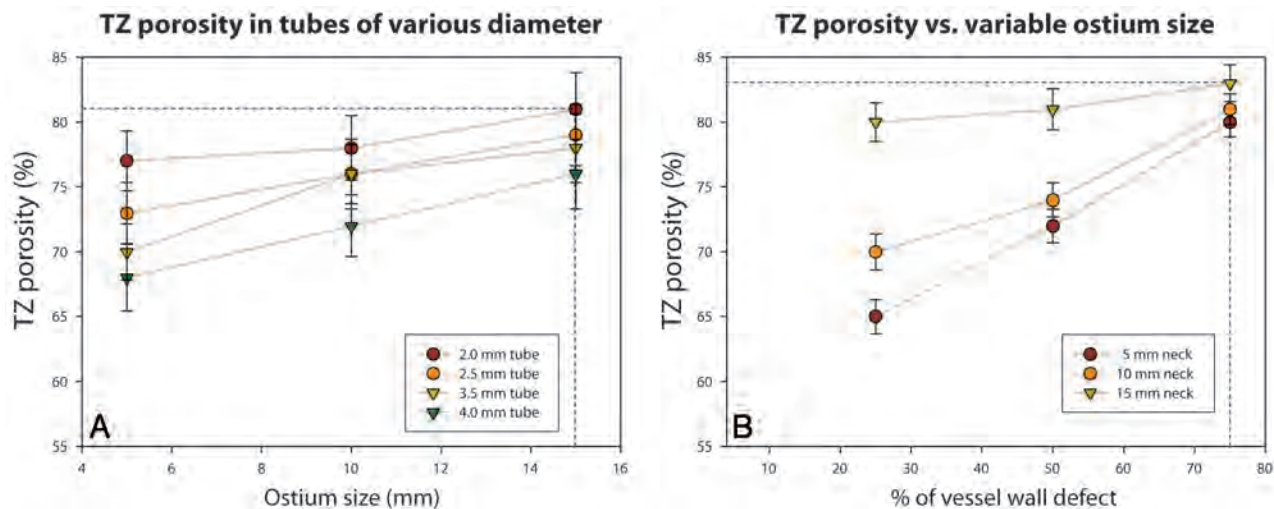


**FIG 2.** Result of benchtop studies. The porosity of the transition zones (TZs) is shown to increase when FDs are constrained in tubes of smaller diameters (A), when the size of the defect is increased in length (A), or when the opening takes a greater proportion of the silicone tube circumference (B).

### Aneurysm characteristics and evolution with treatment

Animal	Initial Aneurysm Dimensions		Final Aneurysm Dimensions (L × W) (mm)	Neointima Formation on FD (%)		Arterial Stenoses (%)		Angiographic Score	Device Geometry	
	Ostium (mm)	Fundus (L × W) (mm)		Aneurysm FSS	Branch FSS	Stented Artery	Jailed Artery		Ratio of Fusiform Dilatation	Angle
Group A										
1	8	30 × 10	16 × 5	90	20	50	0	2	1.8	6°
2	7	15 × 10	9 × 4	80	90	40	20	2	1.6	9°
3	8	35 × 10	13 × 10	80	80	20	0	2	1.8	5°
4	8	26 × 10	9 × 16	90	80	20	50	2	2.5	4°
5	8	17 × 7	17 × 9	70	80	50	0	2	1.4	-6°
6	6	17 × 7	4 × 3	100	80	50	0	3	1.5	-6°
Group B										
7	16	34 × 10	42 × 12	10	0	10	0	0	1.3	30°
8	14	28 × 8	39 × 8	50	60	10	80	0	1.5	26°
9	15	35 × 8	39 × 8	50	80	50	0	0	2.5	26°
10	14	32 × 7	35 × 11	50	50	50	30	0	2.2	25°
11	10	24 × 7	35 × 11	60	90	40	0	0	1.5	16°
12	11	30 × 10	39 × 11	50	90	20	0	0	1.7	16°

**Note:**—L × W indicates length × width.

perienced observers (I.S. and J.R.), and disagreements were resolved during a consensus session. Selected samples of tissue coverage over areas of interest were biopsied under a microscope. Biopsy specimens were stained with hematoxylin-eosin and Movat Pentachrome, followed by immunohistochemistry with smooth-muscle cell  $\alpha$ -actin and endothelial Factor VIII.

### Statistics

Comparisons between groups were made by using the Mann-Whitney test for nonparametric data. For paired data, the Wilcoxon signed rank test was used instead. Correlations between nonparametric data were explored with Spearman rank correlation coefficient  $\rho$ . All analyses were carried out with SPSS, Version 20 (IBM, Armonk, New York).

## RESULTS

### Benchtop Studies

When constrained within silicone tubes smaller than their diameter, all types of FDs tend to expand through the defect in the wall

of the tube, provided the defect is sufficiently large. This expansion causes a fusiform deformation, associated with a characteristic pattern of changing porosities, with a middle compaction zone between 2 transition zones. The transition zones are more porous than the compaction zone, and the porosity of the transition zone increases as the defect in the parent vessel increases in length (Fig 2A), as the defect takes a larger proportion of the wall circumference (Fig 2B), and with a larger discrepancy between tube diameter and the diameter of the stent (Fig 2A). The porosity of the transition zone is maximal, with a combination of the smallest parent vessel diameter with the longest and largest circumferential wall defect (Fig 2B).

### In Vivo Results

The aneurysm characteristics and evolution with treatment are summarized in the Table and illustrated in Fig 3.

Group B aneurysms had significantly wider ostia (mean,  $13 \pm 2$  mm) than group A aneurysms ( $8 \pm 1$  mm;  $P = .002$ ), but other

aneurysm dimensions and volumes were similar before treatment ( $P = .7$ ).

At 3 months, wider ostium aneurysms had significantly worse angiographic outcomes (median Kamran score of 0) than smaller ostium aneurysms (median score of 2;  $P = .002$ ).

Aneurysm volumes were also significantly different at 3 months (mean,  $16,915 \pm 5724 \text{ mm}^3$  compared with  $2500 \pm 2468 \text{ mm}^3$ ;  $P = .002$ ); while smaller ostium aneurysms had substantially decreased in size (mean,  $-6063 \pm 4949 \text{ mm}^3$ ), wider ostium aneurysms had increased in size at 3 months (mean,  $+7717 \pm 4826 \text{ mm}^3$ ;  $P = .004$ ).

Neointimal coverage of the aneurysm-FSS was more complete in the smaller ostium (mean,  $85 \pm 10\%$ ) compared with the wider ostium aneurysms (mean,  $45 \pm 18\%$ ;  $P = .002$ ). There was no significant difference between neointimal coverage of the aneurysm or branch-FSS ( $P = .57$ ) and no difference in branch-FSS neointimal coverage between groups ( $P = .82$ ).

A fusiform deformation of devices was observed at the level of the aneurysm ostium in most cases but was of similar extent in both groups (mean ratio of diameters,  $1.8 \pm 0.5$ ;  $P = .82$ ). The angle between the proximal and distal halves of the device within the parent artery was significantly different in wider ostium ( $23 \pm 6^\circ$ ) compared with smaller ostium aneurysms ( $2 \pm 6^\circ$ ;  $P = .002$ ).

There was no significant difference in the degree of parent artery or branch stenosis between groups.

The most significant correlation was found between neointimal coverage of the aneurysm-FSS and angiographic evolution of aneurysms ( $\rho = -0.757$ ,  $P = .004$ ). There was also a significant correlation between the angiographic evolution of lesions at 3 months and the size of the ostium ( $\rho = 0.620$ ,  $P = .03$ ). Angiographic evolution nearly significantly correlated with parent vessel angle ( $\rho = 0.573$ ,  $P = .05$ ), but no significant correlation was found with the extent of fusiform deformation of the device ( $\rho = -0.424$ ,  $P = .17$ ).

Pathologically, the smaller ostium aneurysms that decreased in size were partially filled with thrombus in various stages of organization combined with vascularized connective tissue, while wider ostium aneurysms were mostly empty and thick-walled. The portion of the device covering the aneurysm ostium (the aneurysm-FSS) was most often covered with thick mature neointima on both the aneurysm and parent artery surfaces, leaving visible holes within the metal struts, which were occasionally partially covered with unorganized thrombus where leaks presumably occurred. Sometimes the aneurysm was fed mainly by a major leak in the distal transition zone of the aneurysm-FSS, while the branch was fed mainly by a leak in the proximal transition zone of the branch-FSS (Fig 4). In some other cases, leaks could be detected at the distal margin of the inner stent, barely bridging the aneurysm ostium and not incorporated into the neointima that covered the landing zone of the outer stent (Fig 5). There was no difference in the appearance of the neointima covering the aneurysm or branch-FSS (Fig 3). Many branches appeared almost completely occluded by neointima at pathology, while no stenosis was perceptible by angiography performed immediately before euthanasia.

## DISCUSSION

The main finding of this work is that the size of the arterial defect (or aneurysm ostium) was an important determinant of the evolution of aneurysms after flow diversion of large or giant sidewall aneurysms. The size of the defect can impact the fusiform deformation of the device and the porosity of the transition zones, at least in benchtop studies. While it is tempting to suggest that worse angiographic outcomes may be the result of the more extensive fusiform deformation seen with the in vitro studies that occurs when the aneurysm ostium is larger, there are other plausible variables to consider. The size of the ostium was also related to device protrusion and angulation, 2 factors that may impact flow diversion. Smaller ostium aneurysms had better neointimal coverage of the FSS and better angiographic evolution, compared with wider ostium large or giant aneurysms. Finally, branches that were bridged by the device were always patent, but substantial neointimal occlusion could also be found at the level of the branch-FSS.

While the sidewall aneurysm model was previously shown to be curable by flow diversion when the neck of aneurysms was small (approximately 5 mm),<sup>9</sup> flow diversion can fail, even in this sidewall configuration, when the defect of the parent artery is large and the aneurysm is large or giant. Many potential mechanisms may contribute to the failure of flow diversion in this wide-ostium aneurysm model. The benchtop studies we performed showed that flow diverters cannot display the characteristic fusiform deformation they adopt when they are free to expand, unless the aperture in the parent vessel is long enough and takes up a sufficient enough proportion of the tube circumference to allow expansion and protrusion of the device through the ostium.<sup>12,13</sup> In vivo, devices adopted the characteristic fusiform deformation as they crossed the level of the aneurysm ostium, but the deformation, when measured as a ratio of diameters, was not shown to be more substantial with wider aneurysm ostia, probably because even the smaller ostium aneurysms already had ostia sufficiently large for the deformation to be equally present in both groups (Table). The evolution of aneurysm size at follow-up correlated with neointimal coverage of the aneurysm-FSS, shown to be less complete in wide-ostium aneurysms.

Residual aneurysms were associated with leaks through the gaps in the neointima that tended to occur at the more porous transition zones. Asymmetric device protrusion through the ostium, with the development of an angle between the proximal and distal segments of the device, was constantly observed in the wider ostium aneurysms, and the angle correlated with angiographic evolution, with  $\rho = 0.573$  and  $P = .05$ . This angle was shown in other studies to influence flow after stent placement and flow diversion in computational fluid dynamics studies and in vitro.<sup>2</sup> We speculate that this angle could perhaps have favored residual flow through the distal transition zone, which was always lacking neointimal coverage when aneurysms persisted at 3 months. Microscopically, leaks were found not only at the level of gaps in the neointima that covered the FSS but also beyond the distal margin of the inner stent, which shortened with expansion at the level of wider ostium aneurysms and may no longer have assured complete neointimal closure of the distal ostium (Fig 5). This phenomenon occurred despite the outer stent, the most visible por-

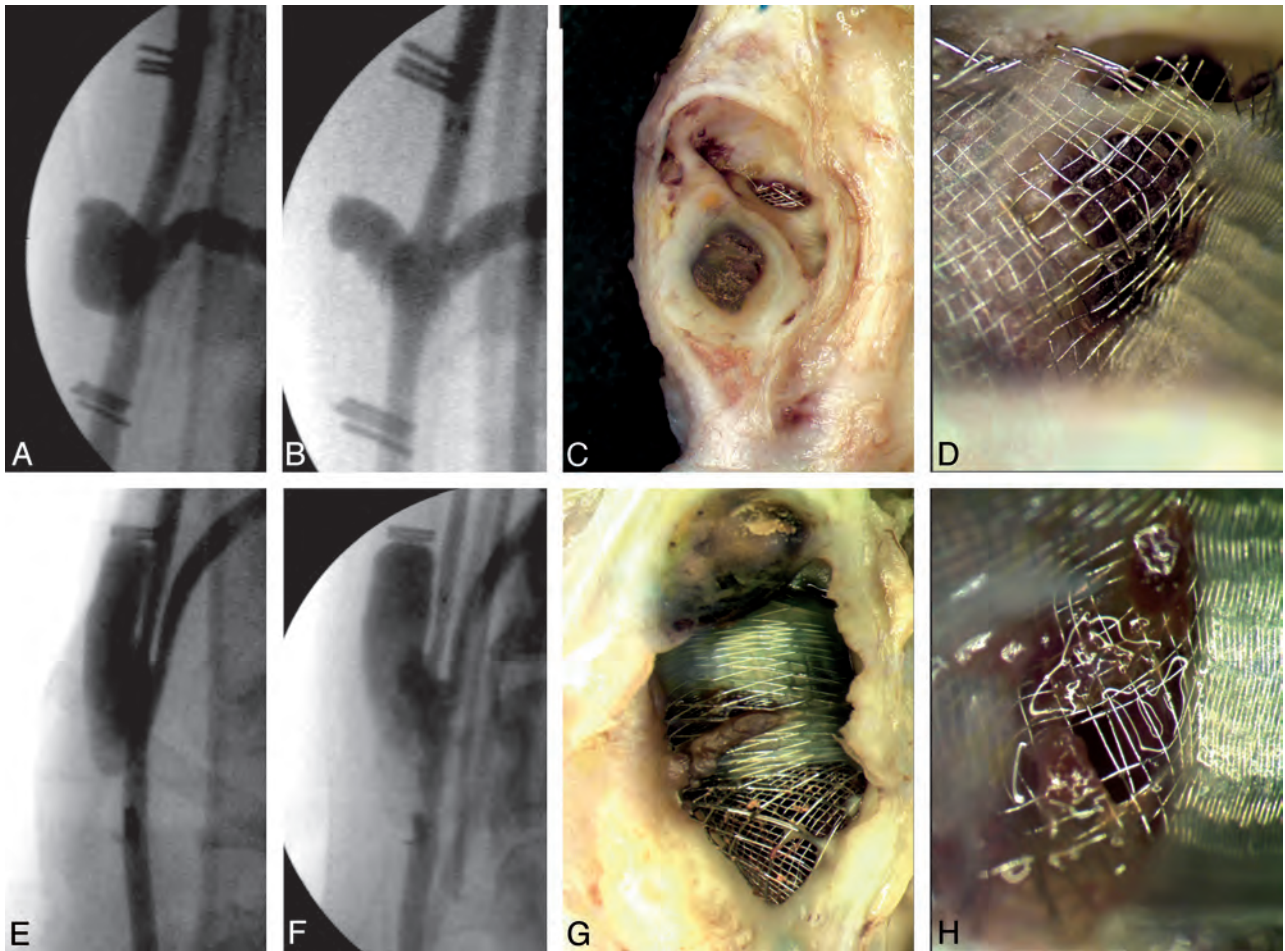


**FIG 3.** Results of in vivo studies. Initial preimplantation angiography (A and E), angiographic results at 3 months (B and F), and photographs of neointimal formation over the device at the level of the aneurysm- (C and G) or branch-FSS (D and H). Panels show how giant aneurysms with smaller ostia (A–D) are more completely occluded at 3 months, with more complete neointimal coverage of the aneurysm-FSS, than aneurysms with a wider ostium (E–H). Note how leaks are related to the more porous transition zones. Neointima formation over the branches is also substantial (D and H).

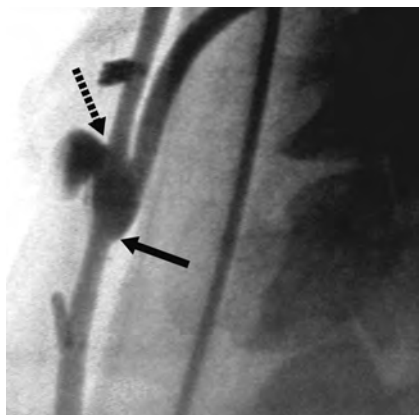


**FIG 4.** Transition zones and flows. Angiographic results 3 months after flow diversion show how the aneurysm fills from persistent flow through the distal transition zone (*dotted arrow*), while the branch is fed by the proximal transition zone (*arrow*).

tion of the device, being satisfactorily deployed with comfortable landing zones.

We speculate that device deformation, expansion, shortening, and angulation, responsible for treatment failures in this wide-



**FIG 5.** Distal ostial leaks. With device expansion in front of wider ostium aneurysms, there is deformation and shortening of the inner stent, which may no longer fully cover the distal edge of the aneurysm ostium (*arrows*).

ostium animal model, could theoretically be minimized by coiling the aneurysm sac or by stent placement before flow diversion. Because the devices we used were already stent-in-stent constructions, more rigid or stronger high-porosity stents would perhaps be necessary for this strategy to succeed.

The 64-wire devices we used for this study were of much lower porosity than the 36-wire devices that were shown to successfully treat sidewall aneurysms with even smaller ( $\approx 5$  mm) necks.<sup>9</sup> They are also less porous than clinically available 48-wire flow diverters. Therefore, we question whether the problems described here

could be completely solved by using devices of even lower porosities without jeopardizing the patency of branches or perforators or even of the parent vessel.

When this canine model was developed, we had postulated that neointima formation on the free segment of stent overlying the aneurysm ostium (or aneurysm-FSS) could meaningfully be compared with neointima formation overlying the branch ostium (the branch-FSS). Quantification of neointimal coverage of the aneurysm or branch-FSS, the segments of the device directly en face the aneurysm or branch ostium, did not turn out to be simple, and the meaning of the proportion of the segment of the device that was covered with neointima may not be as clear as hoped; sometimes large residual aneurysms persisted with only a small hole in the neointimal layer. When we carefully studied and correlated angiographic and pathologic specimens, we realized that blood flow can escape the flow diverter proximally, at the level of the proximal transition zone for example, and contribute to feeding the arterial branch. Thus, thick neointima formation at the level of the branch or aneurysm-FSS may be related to blood flowing inside and outside the lumen of the flow diverter, and neointimal gaps shown directly in front of the branch or aneurysm ostium may not represent all of the flow contributions to the branch or aneurysm.<sup>9,14</sup>

Furthermore, the neointimal gaps we observed were not always in the center of the transition zone, which might have suggested, if neointima formation is centripetal, that the worse outcomes observed in the larger ostium aneurysms could have been related to the amount of time it takes for neointima to cover an implanted device. Because the neointimal gaps were observed to be heterogeneously distributed, we do not think that the failures occurred simply due to an insufficient length of time for the larger aneurysm ostia to be covered.

### Limitations

The construction of large aneurysms with small ostia may result in smaller-sized aneurysms at the time of device implantation compared with aneurysms with larger ostia, as suggested by the seminal work of German and Black,<sup>15</sup> though differences in initial aneurysm dimensions were not significant in the present work ( $P = .7$ ). Whether the canine aneurysm models we have used can help predict the clinical efficacy of flow diverters in patients remains to be validated. The number of animals studied in this work is small, and long-term follow-up angiography beyond 3 months was not performed. We have previously shown, however, that failures at 3 months were not followed by improvement at 6 months.<sup>10</sup> Experimental aneurysms were surgical constructions, with venous pouches anastomosed to cervical carotid arteries; hence, results may differ significantly from spontaneous intracranial aneurysms. Canine biology certainly differs from human biology, and any extrapolation of findings to clinical cases should remain cautious. Although the experimental canine model used here yields different results from those reported in clinical series, we, nonetheless, find them useful because more can be learned from failures than from success.

Finally, the FDs used in this work were prototypes, and substantial modifications of device construction and characteristics have since been made. The results we obtained may not apply to

devices currently available. The device deformations shown in benchtop studies have, however, been reproduced with the Pipeline Embolization Device (Covidien, Irvine, California).<sup>3</sup>

### CONCLUSIONS

Flow diverters may fail to occlude large or giant sidewall aneurysms when the arterial defect or aneurysm ostium is too large. This failure may be related to device deformation and protrusion through the ostial opening and incomplete neointimal closure of the aneurysm ostium.

Disclosures: Tim E. Darsaut—*RELATED*: grant funding in direct support of the current work,\* from the Heart and Stroke Foundation of Alberta (Protocol 678/01/13/D, funding agency/sponsor: Heart and Stroke Foundation, Research Service Office Project RES0011612). Tim E. Darsaut and Jean Raymond—*UNRELATED*: Canadian Institutes of Health Research operating grant unrelated (MOP-119554: for the Canadian Unruptured Endovascular versus Surgery (CURES) Trial [randomized controlled trial]).\*  
\*Money paid to the institution.

### REFERENCES

1. Kamran M, Yarnold J, Grunwald IQ, et al. **Assessment of angiographic outcomes after flow diversion treatment of intracranial aneurysms: a new grading schema.** *Neuroradiology* 2011;53:501–08
2. D'Urso PI, Lanzino G, Cloft HJ, et al. **Flow diversion for intracranial aneurysms: a review.** *Stroke* 2011;42:2363–68
3. Shapiro M, Raz E, Becske T, et al. **Variable porosity of the Pipeline embolization device in straight and curved vessels: a guide for optimal deployment strategy.** *AJNR Am J Neuroradiol* 2014;35:727–33
4. Pistocchi S, Blanc R, Bartolini B, et al. **Flow diverters at and beyond the level of the Willis for the treatment of intracranial aneurysms.** *Stroke* 2012;43:1032–38
5. Becske T, Kallmes DF, Saatci I, et al. **Pipeline for uncoilable or failed aneurysms: results from a multicenter clinical trial.** *Radiology* 2013;267:858–68
6. Szikora I, Berentei Z, Kulcsar Z, et al. **Treatment of intracranial aneurysms by functional reconstruction of the parent artery: the Budapest experience with the Pipeline embolization device.** *AJNR Am J Neuroradiol* 2010;31:1139–47
7. Byrne J V, Beltechi R, Yarnold JA, et al. **Early experience in the treatment of intra-cranial aneurysms by endovascular flow diversion: a multicentre prospective study.** *PLoS One* 2010;5:9:1–8
8. Piano M, Valvassori L, Quilici L, et al. **Midterm and long-term follow-up of cerebral aneurysms treated with flow diverter devices: a single-center experience.** *J Neurosurg* 2013;118:408–16
9. Darsaut TE, Bing F, Salazkin I, et al. **Flow diverters can occlude aneurysms and preserve arterial branches: a new experimental model.** *AJNR Am J Neuroradiol* 2012;33:2004–09
10. Darsaut TE, Bing F, Salazkin I, et al. **Flow diverters failing to occlude experimental bifurcation or curved sidewall aneurysms: an in vivo study in canines.** *J Neurosurg* 2012;117:37–44
11. Darsaut TE, Bing F, Salazkin I, et al. **Testing flow diverters in giant fusiform aneurysms: a new experimental model can show leaks responsible for failures.** *AJNR Am J Neuroradiol* 2011;32:2175–79
12. Bing F, Darsaut TE, Salazkin I, et al. **Stents and flow diverters in the treatment of aneurysms: device deformation in vivo may alter porosity and impact efficacy.** *Neuroradiology* 2013;55:85–92
13. Makoyeva A, Bing F, Darsaut TE, et al. **The varying porosity of braided self-expanding stents and flow diverters: an experimental study.** *AJNR Am J Neuroradiol* 2013;34:596–602
14. Darsaut TE, Bing F, Makoyeva A, et al. **Flow diversion to treat aneurysms: the free segment of stent.** *J Neurointerv Surg* 2013; 5:452–57
15. German WJ, Black SP. **Experimental production of carotid aneurysms.** *N Engl J Med* 1954;250:104–06

# Modifying Flow in the ICA Bifurcation: Pipeline Deployment from the Supraclinoid ICA Extending into the M1 Segment—Clinical and Anatomic Results

E. Nossek, D.J. Chalif, S. Chakraborty, and A. Setton



## ABSTRACT

**BACKGROUND AND PURPOSE:** Utility of the Pipeline Embolization Device extending to the M1 and its clinical and flow consequences at the ICA bifurcation have not been characterized. We analyzed flow modification in cases where a single Pipeline Embolization Device was deployed from the M1 to the distal supraclinoid ICA, covering the A1, for aneurysm treatment.

**MATERIALS AND METHODS:** A1 flow modifications and size regression in postprocedure and follow-up angiography were analyzed. Vessel diameters and ratios of the proximal A1 and M1 segments and the distal ICA were assessed. Relationships between Pipeline Embolization Device nominal diameter and the vessel diameters at landing zones were obtained. Clinical assessments after flow modification were documented.

**RESULTS:** Six of 7 patients demonstrated no change of flow in the anterior cerebral artery/anterior communicating artery complex at immediate postembolization angiography. All patients who underwent follow-up angiography demonstrated size regression of the ipsilateral A1. Midterm follow-up angiography revealed complete reversal of flow in the ipsilateral A1 in 4 of 5 patients. One patient did not demonstrate flow modification. This patient had a dominant ipsilateral A1. Vessel ratios in this case demonstrated a unique configuration in favor of maintaining patency of the ipsilateral A1. There were no clinical or radiographic signs of ischemia. One patient experienced asymptomatic angiographic in-stent stenosis at the M1.

**CONCLUSIONS:** We found that deployment of a Pipeline Embolization Device from the distal supraclinoid ICA to the M1 may result in reversal of flow in the anterior cerebral artery/anterior communicating artery complex and regression of the ipsilateral A1. Preoperative anatomic quantitation and sizing of the Pipeline Embolization Device may predict flow modification results.

**ABBREVIATIONS:** ACA = anterior cerebral artery; AchoA = anterior choroidal artery; AcomA = anterior communicating artery; FD = flow diverter; ICAb = internal carotid artery bifurcation; OphA = ophthalmic artery; PED = Pipeline Embolization Device

Flow-diverter (FD) devices were originally reported to modify and redirect flow as a treatment option for wide-neck aneurysms.<sup>1,2</sup> Recently, extended use for FDs for more distal and small aneurysms has also been described.<sup>3–6</sup> The Pipeline Embolization Device (PED; Covidien, Irvine, California) has been approved specifically to treat wide-neck proximal ICA aneurysms at the cavernous and ophthalmic segments.<sup>2</sup> There are cases, however, where the PED may be used to treat wide-neck aneurysms that are located distal to the ophthalmic segment, at the level of the pos-

terior communicating artery or the anterior choroidal artery (AchoA) segments, as well as those located at the ICA bifurcation (ICAb).

The minimal PED landing length that is recommended to achieve both good anchoring of the stent and efficient flow diversion is approximately 5 mm proximal and 5 mm distal to the aneurysmal neck. In cases where the length of the ICA from the distal neck of the aneurysm to the ICA bifurcation is shorter than 5 mm, or alternately, if the treated aneurysm is an ICAb aneurysm, the distal PED should land and be anchored in the proximal M1 segment. Descriptions of PED deployment that cover the A1 segment origin are rare<sup>6</sup>; in addition, flow modification at the level of the ICAb is challenging to predict. In our review of the current literature, we did not find any descriptions of the hemodynamic effects or clinical efficacy of PED deployment in the ICAb extending to the M1 segment.

We described our experience with cases of PED deployment extending into the M1 segment and focused on the anatomic flow

Received March 25, 2014; accepted after revision April 21.

From the Department of Neurosurgery, Hofstra North Shore–Long Island Jewish School of Medicine and North Shore–Long Island Jewish Health System, Manhasset, New York.

Please address correspondence to Avi Setton, MD, Department of Neurosurgery, North Shore–Long Island Jewish Health System, North Shore University Hospital, 300 Community Dr, 9 Tower, Manhasset, NY 11030; e-mail: asetton@nshs.edu

Indicates article with supplemental on-line table.

<http://dx.doi.org/10.3174/ajnr.A4013>



**FIG 1.** A, A DSA 3D reconstruction of a superior hypophyseal wide-neck aneurysm (1 small additional aneurysm is seen at the AchoA level). B, The aneurysm was treated with coil embolization and 1 PED, covering the right A1 segment. Postembolization injection demonstrates filling of a large A1 segment through the PED.

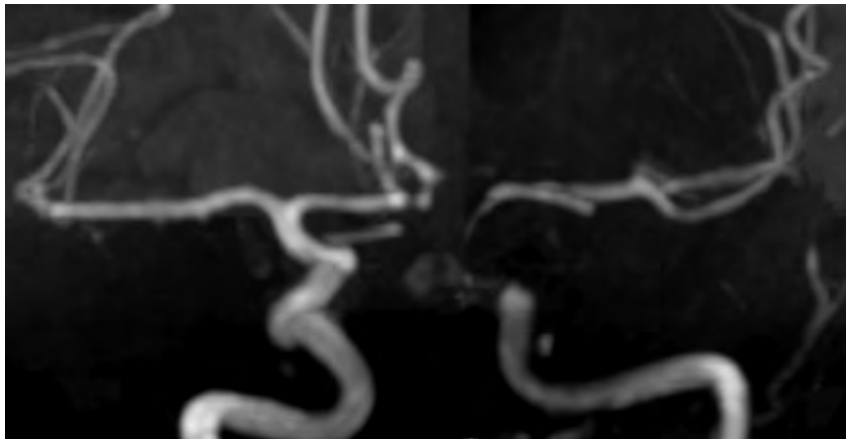


**FIG 2.** Follow-up TOF MRA at 3 months postprocedure demonstrates regression of the ipsilateral A1 segment and complete occlusion of the aneurysms.

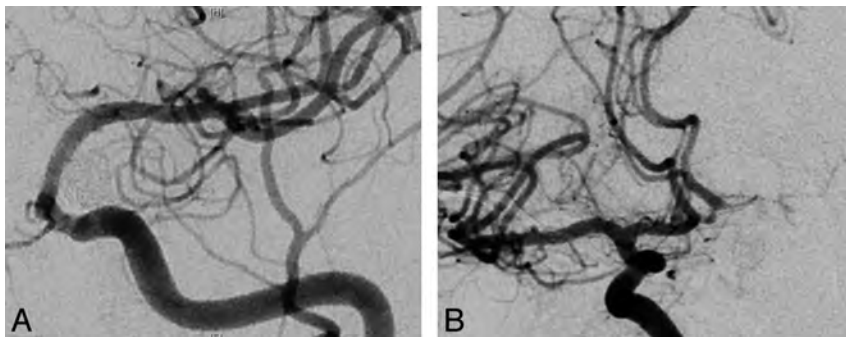


**FIG 3.** A, Seven-month follow-up angiography demonstrates complete aneurysmal occlusion with no antegrade filling of the ipsilateral A1 segment through the flow diverter. B, Contralateral ICA injection demonstrates complete reversal of flow and filling of the ipsilateral A1 segment perforators.

modifications achieved at the ICAB. We have analyzed this technique quantitatively in respect to comparative preoperative anterior circle of Willis angioarchitecture and vessel diameters, and in respect to the specific PED dimensions used.

## MATERIALS AND METHODS

This is a retrospective review of patients who were treated for supraclinoid ICA aneurysms between 2012 and 2013 at our institution (Institutional Review Board approval number 13-303). In this cohort, PEDs were deployed from the proximal M1 segment to the distal supraclinoid ICA. Flow assessments were performed before the

procedure to predict the competence of the collateral circulation (contralateral ICA, bilateral A1 segments, and the anterior communicating artery [AcomA]) to supply both anterior cerebral arteries (ACAs). In all cases, a single PED was deployed, covering the ipsilateral A1 segment (Fig 1). In cases where a second PED was used (either for additional aneurysmal neck coverage or for proximal anchoring of the first PED due to lack of proper wall apposition), there was specifically no additional duplicated PED coverage over the origin of the ipsilateral A1 segment or over the AchoA.

Absolute anatomic vessel diameters and ratios between the sizes of the proximal aspects of the A1 segments, M1 segments, and the distal supraclinoid ICA were assessed in calibrated DSA images. Ratios between the PED nominal diameter and the diameters of the proximal M1 segment and ICA at the stent landing zones were obtained. All measurements were evaluated in respect to immediate and long-term flow modifications and size regressions (Fig 2) of the ipsilateral A1 segment documented by MRA (without and with contrast) at 3 months postembolization, and by formal angiography at 6-month follow-up. We describe the flow modification in the ipsilateral A1 segment as follows: 1) no change of flow, 2) antegrade flow retardation, and 3) complete reversal of flow (Fig 3).

Immediate and midterm clinical assessments were also obtained and reviewed.

## Preoperative Preparation and Procedure

All patients were started on dual antiplatelet therapy before procedures. A P2Y12 assay (VerifyNow; Accumetrics, San Diego, California) was obtained in all patients to evaluate and confirm the level of platelet inhibition obtained by the dual antiplatelet regimen.

A 4-vessel diagnostic angiogram was performed, inclusive of 3D reconstructed images. A thorough angiographic assessment of flow dynamics in the anterior circle of Willis, with emphasis on the bilateral ACAs and the AcomA complex was performed. We evaluated the collateral flow from the contralateral A1 segment through the AcomA into both proximal A2 segments, and the retrograde flow, across the midline, into the ipsilateral A1 segment. In cases where the standard angiographic assessment was not conclusive, we used cross-compression of the ipsilateral common carotid artery with concomitant contralateral ICA injection. This allowed preliminary assessment of reversal of flow in the A1 segment/AcomA complex.

### Ratios of vessel diameters in the anterior circle of Willis

Patient	A1 Segment/ M1 Segment	A1 Segment/ ICA	M1 Segment/ ICA	PED/ M1 Segment	Ipsilateral A1 Segment/ Contralateral A1 Segment
1	0.29	0.28	0.88	1.34	0.38
2	1.12	0.66	0.59	1.72	1.42
3	0.5	0.38	0.76	1.3	0.79
4	0.66	0.45	0.68	1.45	0.75
5	0.72	0.46	0.64	1.59	0.98
6	0.76	0.55	0.73	1.36	1.44
7	0.57	0.53	0.93	1.09	0.79

All embolization procedures were performed via standard transfemoral approach under full heparinization using the combination of platinum and hydrogel coils. The dimensions of the Pipeline Embolization Device were chosen for each case after quantitation of the size of the aneurysmal neck, the landing zones length, and both the M1 segment and the ICA diameters. We attempted to match the size of the nominal PED diameter relative to the proximal landing zone in the ICA. Accordingly, the PED was oversized in most cases in respect to the distal landing zone in the M1 segment.

#### Measurements of the Vessel Diameters

All vessel measurements were obtained on the original calibrated DSA images. Vessel diameters of the ipsilateral M1 segment and the ICA were obtained from injections before PED deployment at the region of the expected landing sites of the proximal and distal ends of the PED. Measurements of the PED landing length in the M1 segment were defined as the distance from the orifice of the M1 segment at the ICAb to the distal end of the PED. Measurements of the ipsilateral A1 segment and the contralateral A1 segment, the M1 segment, and the supraclinoid ICA were evaluated at a distance of 5 mm from the ICAb.

## RESULTS

### Clinical Results

We treated 7 patients where a single PED was deployed from the mid- and proximal M1 segment into the supraclinoid ICA (Online Table). In the cohort, 5 patients were women. Median age was 62 years (range 35–72). Four patients were treated for multiple aneurysms. The following aneurysms were treated: 3 posterior communicating artery aneurysms, 3 AcoA artery aneurysms, 4 ICAb aneurysms, and 1 A1 segment aneurysm. Clinically, all patients were stable in the immediate postprocedural period and all had no new neurologic deficits. All patients maintained their baseline clinical status. There were no radiographic signs of ischemia. One patient demonstrated asymptomatic angiographic in-stent stenosis at the M1 segment at 6-month follow-up angiography without neurologic sequelae. All aneurysms, with the exception of 1 fusiform ICAb aneurysm, were completely occluded on follow-up imaging.

The ICAb aneurysm that was not completely occluded on 3-month postprocedure MRA follow-up was a fusiform aneurysm. This patient also had a posterior communicating artery aneurysm that had recanalized after coiling in the acute hemorrhage. The PED was deployed from the M1 segment to the ICA to simultaneously cover and treat both aneurysms. The posterior commu-

nicating artery aneurysm, which was re-coiled during the current procedure, demonstrated complete occlusion on 3-month follow-up MRA. The ICAb aneurysm demonstrated marked size reduction, but did not demonstrate complete occlusion. This patient is pending mid-term formal angiographic follow-up.

### Flow Modification Results

Immediate antegrade flow retardation in the ipsilateral A1 segment, post-PED deployment, was noticed in 1 patient. All other patients did not demonstrate any change of flow in ACA/AcoA complex during immediate postembolization angiography. Six of the 7 patients subsequently demonstrated significant delayed flow modification. All 5 patients who underwent short term (3–4 month) MRA follow-up demonstrated size regression of the ipsilateral A1 segment. Five patients underwent midterm follow-up angiography (5.5–12 months). Complete reversal of flow in the ipsilateral A1 segment was noted in 4 of 5 patients. One patient did not demonstrate any flow modification. Two patients are awaiting angiographic follow-up.

### Baseline Anatomic Configuration and Flow Modification

All patients who demonstrated regression of the A1 segment or reversal of flow in the AcoA complex manifested an A1 segment/M1 segment average ratio of 0.58 (range 0.29–0.76) and an A1 segment/ICA average ratio of 0.44 (range 0.28–0.55) (Table). The M1 segment/ICA average ratio in this group was 0.77 (range 0.64–0.93). The entirety of the group, except for 2 patients, demonstrated either equal A1 segments or a dominant contralateral A1 segment (ipsilateral A1 segment/contralateral A1 segment, average ratio 0.74 [range 0.38–0.98]).

The only patient who did not demonstrate flow modification, immediately or in follow-up MRA imaging and formal angiography, had a dominant ipsilateral A1 segment (ipsilateral A1 segment/contralateral A1 segment ratio of 1.42). The ratios of the A1 segment/M1 segment (1.12) and the A1 segment/ICA (0.66) were higher in this patient relative to the rest of the patients. Interestingly, the ratio between M1 segment/ICA (0.59) in this patient was the lowest among this group.

### Anatomic Configuration in Respect to PED Deployed

Among the 6 patients who demonstrated flow modification, the partial PED distance extending into the M1 segment from the ICAb measured an average of 7.63 mm (range 4.95–16.3 mm) (Table). The mean nominal PED/M1 segment ratio was found to be oversized at 1.36 (range 1.3–1.59). The patient who did not demonstrate any flow modification had a short length (0.97 mm) of PED in the M1 segment. In addition, in this case we had the highest oversized PED in respect to the M1 segment diameter at the landing zone (ratio 1.72).

## DISCUSSION

Modification of flow in the ACA-AcoA complex by the technique we propose highlights an important hemodynamic concept that has been previously described in other territories—branch

vessel and perforator patency is intimately related to flow demand and potential collateralization.<sup>3,6-8</sup>

Flow modification and persistence of flow in adjacent branch vessels using a FD, distinct from the parent vessel itself, have been previously described both in animal model laboratory studies, as well as in clinical case series studies.<sup>6,8-11</sup> The patency of the ophthalmic artery (OphA) covered by FDs was examined.<sup>8</sup> In this study, 21% of the OphAs were occluded, all without visual changes or clinical symptoms. Only 2 patients who demonstrated OphA occlusion demonstrated collateral retrograde flow into the OphA. The flow and vascular contribution of these more distal collateral vessels might be the reason for proximal occlusion of branch vessels such as the OphA when using FDs. Importantly, when there is a positive flow/pressure gradient (or persistent “demand”), critical perforators and end-arteries will remain patent, even if covered by a FD. Conversely, when the demand is not present, flow regression and/or vessel occlusion is predicted.<sup>3,8</sup>

Based on these concepts, the placement of a PED was described recently for the treatment of distal MCA aneurysms.<sup>4,6,7</sup> Among a series of 26 patients, there were 12 patients who all remained asymptomatic, with reduced flow or occlusion of an MCA branch vessel. Similar to flow modification seen at the OphA region, this phenomenon is most likely dependent on the effectiveness and competency of the regional pial collaterals.<sup>6</sup> An additional report describes the deployment of a PED in an MCA trunk that did not harbor the aneurysm (“competitive” vessel), thus covering the vessel harboring the aneurysm. In long-term follow-up studies, the parent vessel and aneurysm were occluded with reconstitution of the distal territory by pial leptomeningeal collaterals.<sup>7</sup> Again, adequate collateralization was noted in tandem with flow reduction or vessel occlusion related to PED placement.

In our study, we observed size regression of the ipsilateral A1 segment compared with the immediate postprocedure angiographic studies, and significant flow modification at the level of the ICab. A reversal of flow was documented, characterized by retrograde filling of the ipsilateral A1 segment from the contralateral A1 segment through the AcomA, which was consistent with quantitated anatomic configurations (A1 segment/M1 segment average ratio of 0.58, an A1 segment/ICA average ratio of 0.44, and ipsilateral A1 segment/contralateral A1 segment average ratio 0.74). Medial lenticulostriate arteries on the ipsilateral A1 segment maintained persistent patent flow dependent on the contralateral A1 segment flow through the AcomA. We noted that in cases where there was reduced demand on the ipsilateral A1 segment with concurrent robust collateral flow from the contralateral A1 segment, the ipsilateral vessel demonstrated early regression. This parallels the observations seen with the OphA and MCA aneurysms and further supports the relationship of vascular “demand” and potential flow regression.<sup>3,6-8</sup> Our experience with 7 patients demonstrated that ipsilateral A1 regression was not associated with any clinical symptomatology or ischemic lesions manifest on imaging, as the A1 segment perforators will “demand” the flow from the adequate collateralization from the contralateral A1 segment.

We believe that in cases where the contralateral A1 segment or the AcomA are hypoplastic, there is a high demand on the ipsilat-

eral A1. Thus, this ipsilateral A1 segment will not regress and will maintain antegrade filling, resembling a perforator with no collateralization covered by a PED. Accordingly, in our cohort, the 1 case that maintained antegrade filling without size regression had an anatomic configuration suggestive of high demand on the ipsilateral A1 segment. Here we noted a dominant ipsilateral A1 segment (ipsilateral A1 segment/contralateral A1 segment ratio of 1.42), and high ratios of the A1 segment/M1 segment and the A1 segment/ICA (1.12 and 0.66, respectively). Several other factors, however, may have played a role in the persistent flow in this scenario. Only a minimal length of PED was deployed in the M1 segment, and therefore the PED might have provided only a limited flow diversion at the level of the ICab. A second factor that might have impacted on flow diversion at the ICab is the sizing of the PED in respect to the vessel diameter at the M1 segment’s landing zone. In the same patient, we had markedly oversized the PED in respect to the M1 segment diameter, to match the supraclinoid ICA diameter. This differential might have created a higher PED porosity that impacted the flow diversion effect.<sup>12</sup>

In a series recently published of MCA aneurysms treated by FDs, 1 patient had a PED deployment that covered the A1 segment. This patient’s course was complicated by a TIA with demonstration of flow attenuation in the A1 segment. Of note, this patient was treated with 2 PEDs and had discontinued antiplatelet therapy. Questionable patency of the ipsilateral A1 segment or impingement on the patency of M1 perforators may have been associated with the clinical course in this setting. Thus, we do not cover the A1 segment origin with more than 1 PED to allow for potential adequate flow as per its demand.

### Study Limitations

Our series is limited in size, composed of 7 cases that were treated by the same technique. We presented midterm clinical and angiographic follow-up of the flow modification observed in the ACA-AcomA complex. We have attempted to correlate the vessel diameter ratios with the prediction of future modification of flow; this quantitation, however, is a preliminary assessment that will need to be verified by a larger series of patients and longer periods of clinical and imaging follow-up.

### CONCLUSIONS

We found that the deployment of a single PED extending from the supraclinoid ICA to the M1 segment may result in flow modification marked by retrograde filling as well as regression of the ipsilateral A1 segment. Flow modification is usually predictable according to quantifiable anatomic configurations. Deployment of a single PED, when deemed necessary, may be used safely in the treatment of selected aneurysms located in the distal supraclinoid ICA, ICab, and the A1 and M1 segments.

### REFERENCES

1. Briganti F, Napoli M, Tortora F, et al. **Italian multicenter experience with flow-diverter devices for intracranial unruptured aneurysm treatment with periprocedural complications—a retrospective data analysis.** *Neuroradiology* 2012;54:1145–52
2. Becske T, Kallmes DF, Saatci I, et al. **Pipeline for uncoilable or failed aneurysms: results from a multicenter clinical trial.** *Radiology* 2013;267:858–68

3. Saatci I, Yavuz K, Ozer C, et al. **Treatment of intracranial aneurysms using the Pipeline flow-diverter embolization device: a single-center experience with long-term follow-up results.** *AJNR Am J Neuroradiol* 2012;33:1436–46
4. Zanaty M, Chalouhi N, Tjoumakaris SI, et al. **Flow diversion for complex middle cerebral artery aneurysms.** *Neuroradiology* 2014; 56:381–87
5. Chalouhi N, Starke RM, Yang S, et al. **Extending the indications of flow diversion to small, unruptured, saccular aneurysms of the anterior circulation.** *Stroke* 2014;45:54–58
6. Yavuz K, Geyik S, Saatci I, et al. **Endovascular treatment of middle cerebral artery aneurysms with flow modification with the use of the Pipeline embolization device.** *AJNR Am J Neuroradiol* 2014;35:529–35
7. Wajnberg E, Silva TS, Johnson AK, et al. **Progressive deconstruction: a novel aneurysm treatment using the Pipeline embolization device for competitive flow diversion: case report.** *Neurosurgery* 2014; 10(suppl 1):E161–66
8. Puffer RC, Kallmes DF, Cloft HJ, et al. **Patency of the ophthalmic artery after flow diversion treatment of paraclinoid aneurysms.** *J Neurosurg* 2012;116:892–96
9. Darsaut TE, Bing F, Salazkin I, et al. **Flow diverters can occlude aneurysms and preserve arterial branches: a new experimental model.** *AJNR Am J Neuroradiol* 2012;33:2004–09
10. Kallmes DF, Ding YH, Dai D, et al. **A new endoluminal, flow-disrupting device for treatment of saccular aneurysms.** *Stroke* 2007; 38:2346–52
11. Fiorella D, Woo HH, Albuquerque FC, et al. **Definitive reconstruction of circumferential, fusiform intracranial aneurysms with the Pipeline embolization device.** *Neurosurgery* 2008;62:1115–20; discussion 1120–21
12. Shapiro M, Raz E, Becske T, et al. **Variable porosity of the Pipeline embolization device in straight and curved vessels: a guide for optimal deployment strategy.** *AJNR Am J Neuroradiol* 2014;35: 727–33

# Morphologic and Hemodynamic Risk Factors in Ruptured Aneurysms Imaged before and after Rupture

A. Chien and J. Sayre



## ABSTRACT

**BACKGROUND AND PURPOSE:** Due to limited information about aneurysm natural history, choosing the appropriate management strategy for an unruptured aneurysm is challenging. By comparing unruptured and ruptured cases, studies have identified a variety of aneurysm morphologic and hemodynamic properties as risk factors for rupture. In this study, we investigated changes in 4 ruptured aneurysms before and after rupture and tested whether previously published risk factors identified a risk before rupture.

**MATERIALS AND METHODS:** A retrospective review of ruptured aneurysms based on the inclusion criteria of documenting angiographic images before and after rupture was performed. Such cases are extremely rare. To minimize hemodynamic influence due to location, we selected 4 cases at the posterior communicating artery. 3D morphologic and hemodynamic analyses were applied to examine qualitative and quantitative risk factors in aneurysms before and after rupture.

**RESULTS:** When we compared aneurysms before and after rupture, all increased in size. Volume, surface area, and morphology changed in both high and low wall shear stress areas. Aneurysm surface ratio, nonsphericity index, and pulsatility index were the only risk factors to consistently identify risk before and after aneurysm rupture for all aneurysms.

**CONCLUSIONS:** Although changes in shape and flow properties were found before and after aneurysm rupture, in this small study, we found that some risk factors were evident as early as 2 years before rupture.

**ABBREVIATIONS:** AASA = aneurysm surface area to sphere surface area ratio; AVSV = aneurysm volume to sphere volume ratio; NSI = nonsphericity index; PI = pulsatility index; SR = size ratio; WSS = wall shear stress

Due to limited information about aneurysm natural history, one of the biggest challenges in clinical aneurysm management is determining the risk of rupture for incidentally found aneurysms. Currently, size guidelines identified by the International Study of Unruptured Intracranial Aneurysms are the dominant criteria guiding treatment decisions.<sup>1</sup> Studies have suggested that the mechanisms underlying aneurysm rupture are multifactorial, and they have likewise identified different types of

risk factors. For example, researchers have found that certain aneurysm shapes are risk factors that may associate aneurysm morphology with rupture.<sup>2-4</sup> By analyzing blood flow properties in groups of ruptured and unruptured aneurysms, reports have also shown that certain hemodynamic factors may play an important role in aneurysm rupture.<sup>5-9</sup> However, the morphologic and hemodynamic risk factors analyzed in these studies have generally been identified by analyzing ruptured aneurysms after rupture. Because clinical reports also suggest that aneurysms change due to rupture, how well these risk factors can actually help predict rupture has been controversial.<sup>10-12</sup>

In general, it is expected that the predictive ability of any aneurysm rupture risk factor will be higher as an aneurysm is closer to rupture. The fundamental rationale in aneurysm risk analysis based on comparing ruptured and unruptured aneurysm groups is that aneurysms that rupture have the same risk characteristics in the unruptured and ruptured states.<sup>5-9,13</sup> In that case, the results obtained by comparing ruptured with unruptured aneurysms can help assess the risk of rupture in as-yet-unruptured aneurysms. However, there are limited studies testing this hypothesis.

Received December 4, 2013; accepted after revision April 16, 2014.

From the Division of Interventional Neuroradiology (A.C.), David Geffen School of Medicine, and Department of Biostatistics (J.S.), School of Public Health, University of California, Los Angeles, Los Angeles, California.

This work was supported, in part, by a UCLA radiology exploratory research grant.

Paper previously presented in part at: Annual Meeting of the American Society of Neuroradiology, May 18–23, 2013; San Diego, California.

Please address correspondence to Aichi Chien, PhD, Division of Interventional Neuroradiology, David Geffen School of Medicine at UCLA, 10833 LeConte Ave, Box 951721, Los Angeles, CA 90095; e-mail: aichi@ucla.edu

Indicates open access to non-subscribers at [www.ajnr.org](http://www.ajnr.org)

Indicates article with supplemental on-line table

<http://dx.doi.org/10.3174/ajnr.A4016>

In this study, we re-examined morphologic and hemodynamic risk factors that have been reported in the literature by using a unique dataset of aneurysms imaged in both their unruptured and ruptured states.<sup>4,6-8,14-17</sup> Our objective was to investigate morphology and flow properties of aneurysms before and after rupture and find whether previously identified risk factors were present in aneurysms before rupture. We sought to identify risk factors that consistently existed in ruptured aneurysms in both unruptured and ruptured states to guide early determination of aneurysm rupture risk.

## MATERIALS AND METHODS

The study was approved by the institutional review board of the University of California, Los Angeles. A retrospective review of ruptured aneurysms with 3D images before and after rupture collected from the aneurysm database in the University of California, Los Angeles Medical Center was performed. Four aneurysms were included in this study. These cases were selected from the 729 ruptured aneurysms that were treated in our center from 1998 to 2012. The details of our case-selection method follow, to highlight the rarity of aneurysms with images before and after rupture. Among the ruptured aneurysms, anterior communicating artery, posterior communicating artery, and basilar artery with 203 (28%), 136 (19%), and 117 (16%) cases, respectively, were the 3 most common locations. Because aneurysm hemodynamic properties are affected by location, posterior communicating artery aneurysms (which had the most cases with before and after rupture images) were selected.<sup>18</sup> Six ruptured posterior communicating artery aneurysms had clinical images documenting aneurysms before and after rupture. The aneurysms were not treated because of advanced patient age. Only the 4 cases that had 3D images (either digital subtraction angiography or CT angiography) for both unruptured and ruptured states were included in this study. The 3D images recording the aneurysms before rupture were acquired in a range of 4 to 24 months prior to rupture. 3D images recording rupture were acquired within 24 hours of the rupture event.

The aneurysm 3D morphology before and after rupture was studied qualitatively and quantitatively on the basis of morphology risk factors previously found to correlate with rupture. Therefore, qualitative analysis was based on aneurysm lobulation (unilobular or multilobular).<sup>16,17</sup> Quantitative 3D morphology risk factors included aspect ratio, size ratio (SR), nonsphericity index (NSI), aneurysm volume ratio (AVSV), and aneurysm surface ratio (AASA) and were collected by using a previously developed automatic aneurysm geometry analysis tool.<sup>4,19,20</sup> Aspect ratio was defined as the ratio between aneurysm height and aneurysm neck (equation 1) proposed by Ujiie et al.<sup>21</sup> SR was defined as the ratio between aneurysm height and average parent artery diameter (equation 2),<sup>15</sup> and NSI was computed on the basis of the ratio of aneurysm volume and aneurysm surface area (equation 3) proposed by Raghavan et al.<sup>3</sup> AVSV was computed as the ratio of the aneurysm volume to the volume of a bounding sphere, defined by the longest distance between 2 points on the aneurysm (equation 4), as proposed by Chien et al.<sup>4</sup> AASA was calculated by comparing surface area in the same manner (equation 5). Previously reported

thresholds for predicting rupture were used for each parameter<sup>4,15,21</sup>:

- 1) *Aneurysm aspect ratio* =  $\frac{(\text{aneurysm height})}{(\text{aneurysm neck})}$
- 2) *Aneurysm size ratio* = SR  
=  $\frac{(\text{maximum aneurysm height})}{(\text{average parent artery diameter})}$
- 3) *Aneurysm nonsphericity index* = NSI  
=  $1 - (18\pi)^{1/3} \frac{(\text{aneurysm volume})^{2/3}}{(\text{aneurysm surface area})}$
- 4) *Aneurysm volume ratio* = AVSV  
=  $\frac{(\text{aneurysm volume})}{(\text{bounding sphere volume})}$
- 5) *Aneurysm surface ratio* = AASA  
=  $\frac{(\text{aneurysm surface area})}{(\text{bounding sphere surface area})}$

Because several studies have found distinct hemodynamic properties in ruptured aneurysms, qualitative and quantitative hemodynamic risk factors previously reported as significant were re-examined for all aneurysms before and after rupture. A previously developed patient-specific hemodynamic simulation was applied to study aneurysmal flow before and after rupture. For all cases, a standard ICA flow profile acquired from a healthy subject with phase-contrast MR imaging was applied.<sup>5,6,18,22</sup> The qualitative hemodynamic risk factors analyzed included aneurysm inflow jet size, flow impingement size, and aneurysmal flow pattern, as proposed by Cebal et al.<sup>5</sup> Quantitative hemodynamic risk factors, including normalized wall shear stress (WSS), maximum aneurysm wall shear stress, and pulsatility index were analyzed.<sup>8,15,22</sup> On the basis of the indices proposed by Xiang et al,<sup>15</sup> normalized aneurysm wall shear stress was obtained by averaging wall shear stress over a cardiac cycle (equation 6), and maximum aneurysm wall shear stress was defined as maximum intra-aneurysmal WSS normalized by the average parent artery WSS (equation 7).<sup>15</sup> Pulsatility index (PI) is an index to analyze pulsatile flow changes at a specific region of an aneurysm. Using the flow rate collected at the aneurysm neck as proposed by Patti et al,<sup>8</sup> we calculated PI by finding the differences between the maximum and minimum flow rates divided by the mean flow rate in a cardiac cycle (equation 8). As with morphology parameters, reported risk values for distinguishing rupture and nonrupture with each index were used<sup>8,15</sup>:

- 6) *Normalized wall shear stress*  
=  $\frac{1}{T} \int_0^1 \left| \frac{\text{aneurysm WSS}}{\text{parent artery WSS}} \right| dt$

where  $T$  is the duration of the cardiac cycle.

### Summary of PcomA aneurysm cases before and after rupture

Case No.	Sex	Age (yr)	Side	Symptomatic/ Asymptomatic	Unruptured Size (mm)	Ruptured Size (mm)	Last Image before Rupture (mo)
1	F	75	Left	Asymptomatic	5.4	6.9	4
2	F	66	Left	Asymptomatic	11.6	11.9	12
3	F	72	Right	Asymptomatic	10.5	12.0	20
4	F	76	Left	Symptomatic	6.7	11.0	24

**Note:**—PcomA indicates posterior communicating artery.

#### 7) Maximum wall shear stress

$$= \frac{\text{maximum aneurysm WSS}}{\text{average parent artery WSS}}$$

#### 8) Pulsatility index = PI

$$= \frac{(\text{maximum flow rate}) - (\text{minimum flow rate})}{(\text{average flow rate})}$$

### Statistical Analysis

To compare our results with other researchers' findings, descriptive statistics, including means, SDs, and confidence intervals, were calculated by using SPSS Statistics for Windows, Version 20.0. (IBM, Armonk, New York). Regression and correlation analysis, Mann-Whitney tests, and Student *t* tests with significance at the 5% level were used to compare risk factors in aneurysms before and after rupture.

### RESULTS

Details of ruptured aneurysms included in this study are shown in the Table. Patients were all women, and the average age was  $72.3 \pm 4.5$  years. Three of the aneurysms were incidentally detected, and 1 aneurysm was found due to mass effect. The On-line Table summarizes the results of morphologic and hemodynamic risk factors in aneurysms before and after rupture. With the exception of case 2, qualitative risk factors generally did not correctly identify high rupture risk before aneurysm rupture. All of the aneurysms exhibited morphology and size changes between the unruptured and ruptured time points (average growth,  $1.90 \pm 1.67$  mm). 3D reconstructions of aneurysms before and after rupture based on 3D angiography are shown in Fig 1. Detailed analysis of 3D aneurysm curvature showed clearly that curvature changed between the unruptured and ruptured states (Fig 1C, -D, respectively). Aneurysm blebs were found in all aneurysms after rupture; however, only 2 cases (case 1 and case 2) had blebs present in the unruptured state.

3D quantitative comparison of aneurysm volume before and after rupture showed volume increases averaging  $59.9 \pm 25.7\%$  and surface area increases averaging  $31.8 \pm 16.9\%$ . Aspect ratio was, on the average,  $1.69 \pm 0.44$  before aneurysm rupture and  $1.96 \pm 0.68$  after rupture. SR was, on average,  $2.68 \pm 1.07$  before and  $3.27 \pm 0.96$  after rupture. Thus, a trend of increasing SR was found when comparing aneurysms before and after rupture. Seventy-five percent of aneurysms had SRs indicating rupture risk before rupture. NSI was, on average,  $0.37 \pm 0.09$  and  $0.30 \pm 0.04$  before and after rupture, respectively. All aneurysms were found to be at risk for rupture from assessment of NSI at both the unruptured and ruptured states. AVSV was, on average,  $0.41 \pm 0.10$  and  $0.46 \pm 0.08$  before and after rupture, respectively, showing a

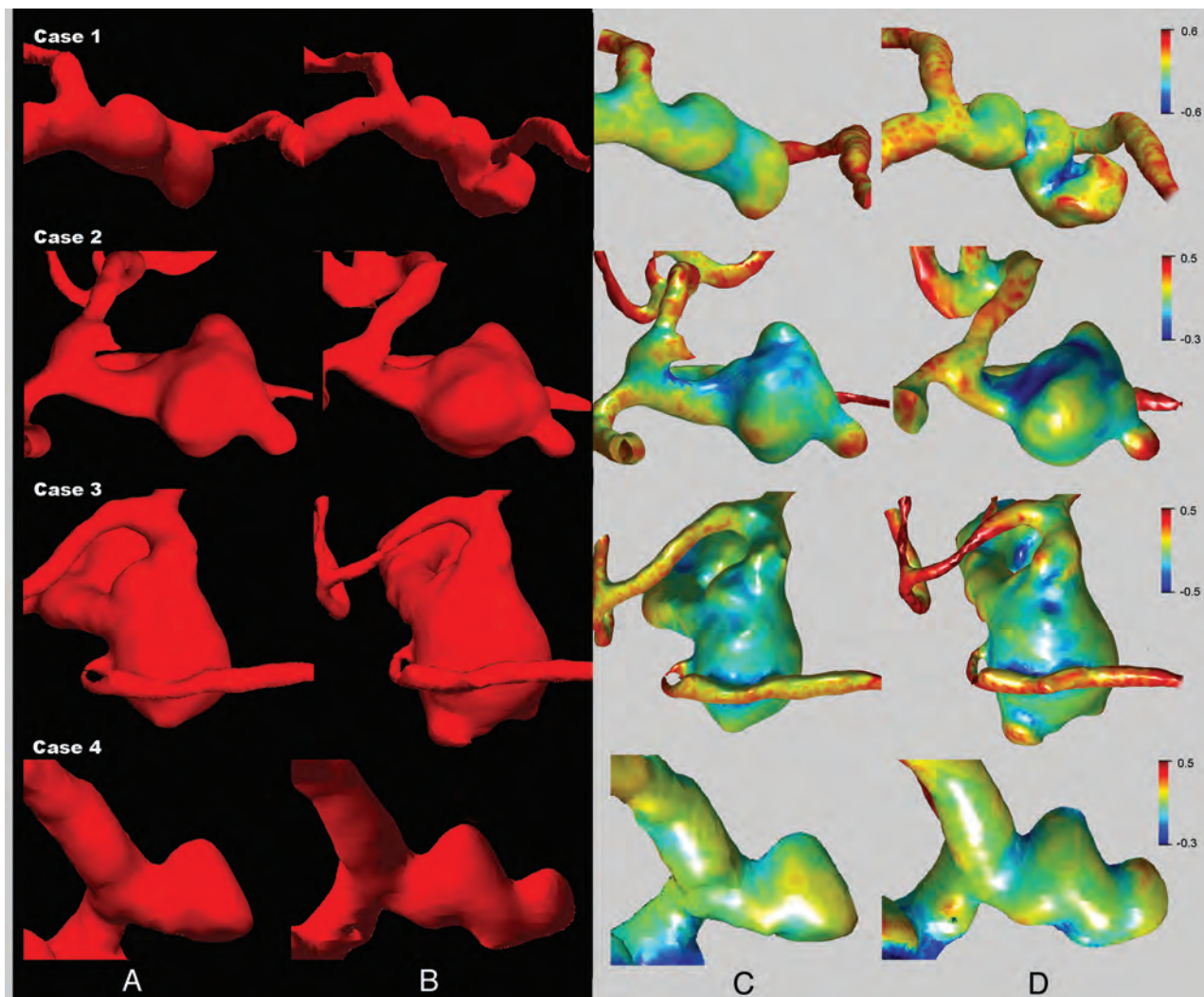
trend of AVSV increasing toward the risk threshold. AASA was, on average,  $0.69 \pm 0.07$  and  $0.67 \pm 0.04$  before and after rupture, respectively. All aneurysms were found to be at risk for rupture when assessing AASA at both the unruptured and ruptured states. There were no significant changes before and after rupture in aspect ratio, SR, NSI, AVSV, and AASA.

Figure 2 presents the results of hemodynamic analysis showing the WSS distributions and flow patterns in aneurysms before and after rupture at the end of systole. Using quantitative analysis, we found that normalized aneurysm wall shear stress was  $1.85 \pm 0.53$  before rupture and  $1.73 \pm 0.26$  after rupture, and in all of the cases, both before and after rupture, it did not indicate rupture risk. Maximum aneurysm wall shear stress was  $2.35 \pm 0.43$  before rupture and  $2.65 \pm 0.48$  after rupture. Maximum aneurysm wall shear stress indicated rupture risk both before and after rupture for only case 4. PI was, on average,  $2.63 \pm 0.63$  before rupture and  $2.57 \pm 0.63$  after rupture. Because in the previously published study of PI, risk was not identified on the basis of a particular numeric threshold but as trend, a residual analysis of regression by using previously reported trends by Patti et al<sup>8</sup> for PI was applied. For all cases, PI identified significant rupture risk before and after rupture. When we compared indices of normalized aneurysm wall shear stress, maximum aneurysm wall shear stress, and PI before and after rupture, none showed significant changes.

### DISCUSSION

Previous studies of aneurysm rupture risk have analyzed ruptured aneurysms after rupture has occurred, primarily because image data for ruptured aneurysms before rupture are extremely rare. Whether we can use the knowledge gained by studying groups of ruptured and unruptured aneurysms to assess the risk of rupture remains an important question.

In this study, we found that NSI and AASA consistently indicated risk before rupture. Both NSI and AASA assess the irregularity of aneurysm morphology on the basis of the aneurysm 3D surface. NSI analyzes the ratio of volume and surface area in the aneurysm itself. AASA is computed solely on the basis of the surface area, comparing aneurysm surface area with the surface area of a minimal bounding sphere. Other morphologic indices, aspect ratio, SR, and AVSV, are not directly related to surface area and did not indicate rupture risk in the cases studied. Aspect ratio compares aneurysm height and neck, and SR compares aneurysm height and artery diameter. AVSV analyzes shape irregularity on the basis of volume ratio. We would expect similar results for indices similar to AVSV, such as undulation index, which is based on the volume ratio of the minimal convex volume around the aneurysm.<sup>3</sup> Although currently there is no defined biologic or pathophysiologic basis for these variables, our findings suggest



**FIG 1.** 3D reconstruction of aneurysm morphology before (A) and after (B) rupture. Quantitative morphology analysis of aneurysm curvature before (C) and after (D) rupture. High-curvature convex areas, such as blebs, are shown in red, with high-curvature concave areas shown in blue. Clear aneurysm morphology and curvature changes before and after rupture were found for all cases.

that surface-related indices such as NSI and AASA may be important morphologic bases to identify risk before rupture.

Our results showed that the WSS distribution changes before and after rupture in aneurysms (Fig 2A, -B). In the past, research analyzing unruptured aneurysms found that aneurysm growth was likely to occur at low WSS areas.<sup>23</sup> Our data showed that changes in aneurysm shape are not restricted to low WSS regions. As previously reported by Kono et al<sup>24</sup> in a study of a single posterior communicating artery aneurysm, we also found WSS changes before and after rupture. The present study of 4 ruptured aneurysms provides the first comparative data in individual aneurysms before and after rupture showing that WSS may change. As a result, while it appears that WSS, as the shear force on the aneurysm wall surface, may play an important role in eliciting a cellular response,<sup>25,26</sup> its value as a predictor of future aneurysm rupture was not supported by this study. Further studies with more cases are needed to understand the mechanism of WSS in the event of rupture and provide results with higher statistical power.

The other quantitative hemodynamic factor considered, the aneurysm pulsatility index, is a dynamic flow factor that examines the pulsatile flow properties within the aneurysm. As previously reported

by Chien et al<sup>6</sup> and Baek et al,<sup>27</sup> aneurysm and vascular shape affect pulsatile flow properties at the aneurysm site. These effects are made especially clear when a single, standard flow profile is used for hemodynamic analysis of all cases, as is the standard method and was done in this research. We found that all cases in the present study, both before and after rupture, had high-risk PIs.<sup>8</sup> These results showed that before aneurysm rupture, all of these aneurysms already had pulsatile flow properties similar to those in previously studied ruptured aneurysms. Because PI is not correlated with morphologic parameters such as NSI or AASA, PI is an independent factor with potential value when combined to help assess rupture risk in unruptured aneurysms. Further study of the sensitivity of PI to different waveforms and heart rates is needed to better understand the relationship of PI to aneurysm rupture.

#### Limitations

Due to the risk of rupture, unruptured aneurysms are often treated before the rupture event occurs. In the present study, these aneurysms were followed to monitor changes and were not treated due to patient age.<sup>1,28</sup> Although we present only 4 cases, this is, to our

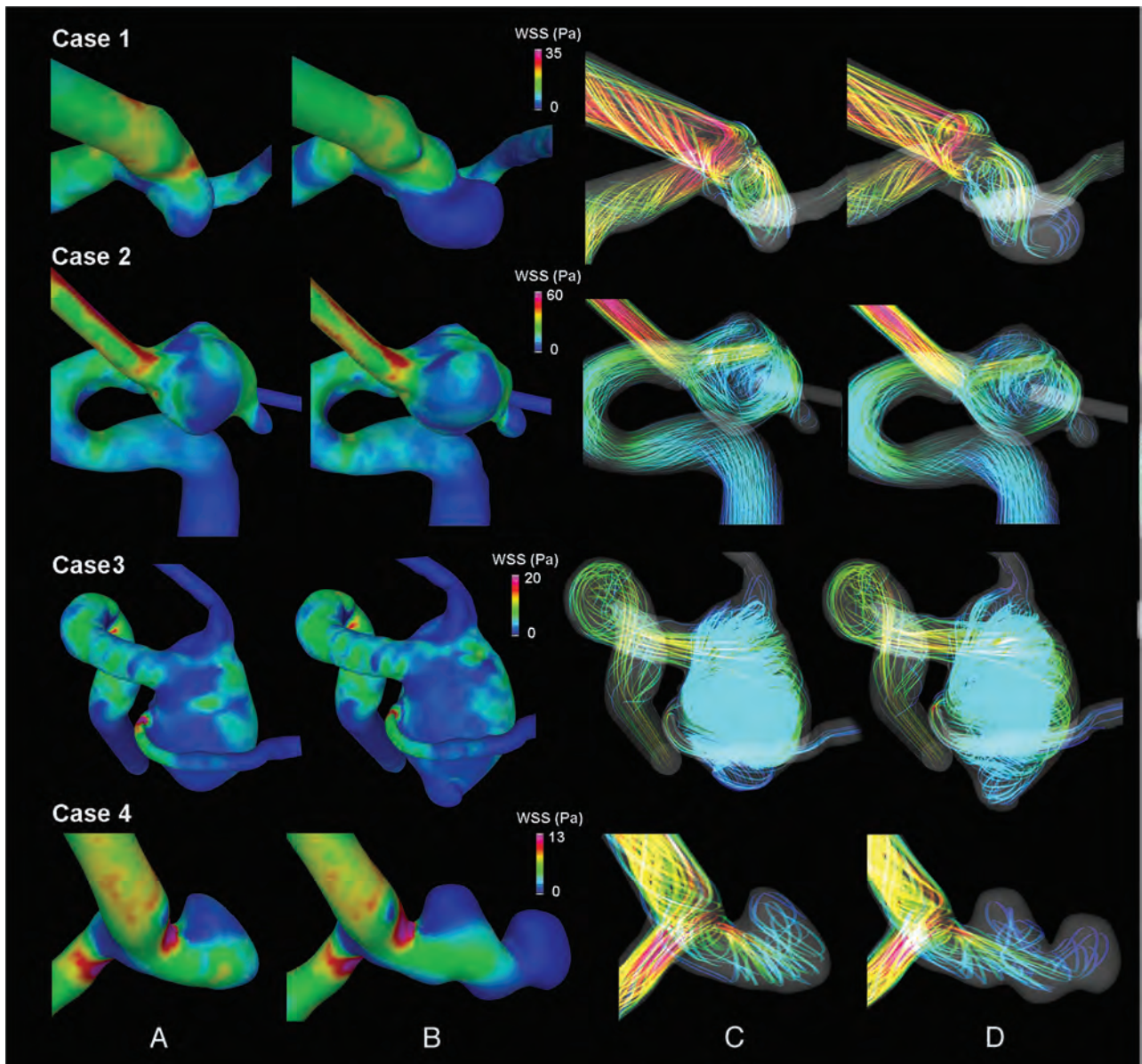


**FIG 2.** Results of hemodynamic analysis of systolic wall shear stress of ruptured aneurysms showed changes before (A) and after (B) rupture. The aneurysm flow pattern also changed before (C) and after (D) rupture.

knowledge, the largest number of cases analyzing morphology and hemodynamics before and after aneurysm rupture.<sup>29</sup> Because of software limitations, a few indices could not be included.<sup>3,15</sup> However, those analyzed represent most hemodynamic and morphologic indices previously associated with aneurysm rupture, and most excluded indices provide equivalent information to those included. To perform hemodynamic simulation, numeric models were made for aneurysms and arteries. These reconstruction procedures affected the outflow vessel geometry. Further improved algorithms to help reconstruct accurate vascular geometry for hemodynamic simulation are important to improve aneurysm risk analysis.

The main purpose of this study was to identify indices, among those previously found to relate to rupture, that do not change due to rupture. This study cannot distinguish imminent risk and permanent danger. How early aneurysms develop risk before rupture remains unclear. The statistical tests performed in this study were to

allow comparisons with other research findings reported previously. The primary goal of statistical tests is not to provide information immediately applicable to clinical practice but to begin to evaluate the many computational indices developed during the past decade. While cases in which imaging was performed before and after rupture are likely to remain rare, larger longitudinal studies of growing aneurysms may provide insight into how various risk factors change during the growth process and allow more powerful statistical analysis. Additional work using follow-up data of unruptured aneurysms with matching size and location is needed to further understand whether the aneurysm changes associated with rupture may be distinct from changes associated with growth.

## CONCLUSIONS

Changes in shape and flow properties were found by analyzing aneurysms before and after rupture. Through quantitative study

of morphologic and hemodynamic factors, this study indicates that while certain risk factors may primarily be evident after rupture (blebs, complex flow pattern, small inflow jet), other indicators of high aneurysm rupture risk may be found a considerable time before rupture. Specifically, the aneurysm surface ratio, non-sphericity index, and pulsatility index were consistent predictive risk factors. On the basis of the earliest available data for ruptured aneurysms before rupture, we found that by using these predictive risk factors, rupture risk could be detected as early as 2 years before rupture.

## ACKNOWLEDGMENTS

The authors gratefully acknowledge Dr Fernando Viñuela in the UCLA Medical Center for providing the clinical ruptured aneurysm data base.

## REFERENCES

1. Wiebers DO, Whisnant JP, Huston J 3rd, et al. **Unruptured intracranial aneurysms: natural history, clinical outcome, and risks of surgical and endovascular treatment.** *Lancet* 2003;362:103–10
2. Ujiie H, Tamano Y, Sasaki K, et al. **Is the aspect ratio a reliable index for predicting the rupture of a saccular aneurysm?** *Neurosurgery* 2001;48:495–502, discussion 502–03
3. Raghavan ML, Ma B, Harbaugh RE. **Quantified aneurysm shape and rupture risk.** *J Neurosurg* 2005;102:355–62
4. Chien A, Sayre J, Viñuela F. **Comparative morphological analysis of the geometry of ruptured and unruptured aneurysms.** *Neurosurgery* 2011;69:349–56
5. Cebral JR, Castro MA, Burgess JE, et al. **Characterization of cerebral aneurysms for assessing risk of rupture by using patient-specific computational hemodynamics models.** *AJNR Am J Neuroradiol* 2005;26:2550–59
6. Chien A, Sayre J, Viñuela F. **Quantitative comparison of the dynamic flow waveform changes in 12 ruptured and 29 unruptured ICA-ophthalmic artery aneurysms.** *Neuroradiology* 2013;55:313–20
7. Chien A, Tateshima S, Sayre J, et al. **Patient-specific hemodynamic analysis of small internal carotid artery-ophthalmic artery aneurysms.** *Surg Neurol* 2009;72:444–50, discussion 450
8. Patti J, Viñuela F, Chien A. **Distinct trends of pulsatility found at the necks of ruptured and unruptured aneurysms.** *J Neurointerv Surg* 2014;6:103–07
9. Shojima M, Oshima M, Takagi K, et al. **Magnitude and role of wall shear stress on cerebral aneurysm: computational fluid dynamic study of 20 middle cerebral artery aneurysms.** *Stroke* 2004;35:2500–05
10. Rahman M, Ogilvy CS, Zipfel GJ, et al. **Unruptured cerebral aneurysms do not shrink when they rupture: multicenter collaborative aneurysm study group.** *Neurosurgery* 2011;68:155–60, discussion 160–61
11. Wiebers DO, Whisnant JP, Sundt TM Jr, et al. **The significance of unruptured intracranial saccular aneurysms.** *J Neurosurg* 1987;66:23–29
12. Fargen KM, Mocco J. **Comment on: comparative morphological analysis of the geometry of ruptured and unruptured aneurysms.** *Neurosurgery* 2011;69:356
13. Takao H, Murayama Y, Otsuka S, et al. **Hemodynamic differences between unruptured and ruptured intracranial aneurysms during observation.** *Stroke* 2012;43:1436–39
14. Cebral JR, Mut F, Weir J, et al. **Association of hemodynamic characteristics and cerebral aneurysm rupture.** *AJNR Am J Neuroradiol* 2011;32:264–70
15. Xiang J, Natarajan SK, Tremmel M, et al. **Hemodynamic-morphologic discriminants for intracranial aneurysm rupture.** *Stroke* 2011;42:144–52
16. Hademenos GJ, Massoud TF, Turjman F, et al. **Anatomical and morphological factors correlating with rupture of intracranial aneurysms in patients referred for endovascular treatment.** *Neuroradiology* 1998;40:755–60
17. Beck J, Rohde S, el Beltagy M, et al. **Difference in configuration of ruptured and unruptured intracranial aneurysms determined by biplanar digital subtraction angiography.** *Acta Neurochir (Wien)* 2003;145:861–65, discussion 865
18. Chien A, Castro MA, Tateshima S, et al. **Quantitative hemodynamic analysis of brain aneurysms at different locations.** *AJNR Am J Neuroradiol* 2009;30:1507–12
19. Lederman C, Vese L, Chien A. **Registration for 3D morphological comparison of brain aneurysm growth.** In: *Advances in Visual Computing: Lecture Notes in Computer Science. Proceedings of the 7th International Symposium on Visual Computing, Las Vegas, Nevada, September 2011*;6938:396–403
20. Buades A, Chien A, Morel JM, et al. **Topology preserving linear filtering applied to medical imaging.** *SIAM Journal on Imaging Sciences* 2008;1:26–50
21. Ujiie H, Tachibana H, Hiramatsu O, et al. **Effects of size and shape (aspect ratio) on the hemodynamics of saccular aneurysms: a possible index for surgical treatment of intracranial aneurysms.** *Neurosurgery* 1999;45:119–29, discussion 129–30
22. Chien A, Tateshima S, Castro M, et al. **Patient-specific flow analysis of brain aneurysms at a single location: comparison of hemodynamic characteristics in small aneurysms.** *Med Biol Eng Comput* 2008;46:1113–20
23. Bousset L, Rayz V, McCulloch C, et al. **Aneurysm growth occurs at region of low wall shear stress: patient-specific correlation of hemodynamics and growth in a longitudinal study.** *Stroke* 2008;39:2997–3002
24. Kono K, Tomura N, Yoshimura R, et al. **Changes in wall shear stress magnitude after aneurysm rupture.** *Acta Neurochir (Wien)* 2013;155:1559–63
25. Malek AM, Alper SL, Izumo S. **Hemodynamic shear stress and its role in atherosclerosis.** *JAMA* 1999;282:2035–42
26. Reneman RS, Arts T, Hoeks AP. **Wall shear stress—an important determinant of endothelial cell function and structure—in the arterial system in vivo: discrepancies with theory.** *J Vasc Res* 2006;43:251–69
27. Baek H, Jayaraman MV, Karniadakis GE. **Wall shear stress and pressure distribution on aneurysms and infundibulae in the posterior communicating artery bifurcation.** *Ann Biomed Eng* 2009;37:2469–87
28. Bederson JB, Awad IA, Wiebers DO, et al. **Recommendations for the management of patients with unruptured intracranial aneurysms: a statement for healthcare professionals from the Stroke Council of the American Heart Association.** *Circulation* 2000;102:2300–08
29. Sforza DM, Putman CM, Scrivano E, et al. **Blood-flow characteristics in a terminal basilar tip aneurysm prior to its fatal rupture.** *AJNR Am J Neuroradiol* 2010;31:1127–31

# Risk Factors for Early Hemorrhagic Complications after Endovascular Coiling of Ruptured Intracranial Aneurysms

T. Ohta, K. Murao, K. Miyake, K. Takemoto, and K. Nakazawa



## ABSTRACT

**BACKGROUND AND PURPOSE:** The risk factors of early hemorrhagic complications after endovascular coiling are not well-known. We identified the factors affecting early hemorrhagic complications, defined as any expansion or appearance of hemorrhage shown by head CT in the initial 48 hours after coiling.

**MATERIALS AND METHODS:** We retrospectively reviewed a series of 93 patients who underwent coiling for a ruptured saccular aneurysm between 2006 and 2012 at our hospital.

**RESULTS:** Five patients showed early hemorrhagic complications, and all involved an expansion of the existing intracerebral hematoma immediately after coiling. The associated risk factors were accompanying intracerebral hemorrhage at onset ( $P < .001$ ), postoperative antiplatelet therapy ( $P < .001$ ), and thromboembolic complications ( $P = .044$ ). In the accompanying intracerebral hemorrhage group, the associated risk factors were postoperative antiplatelet therapy ( $P = .044$ ) and earlier initiation of coiling ( $9.8 \pm 6.5$  versus  $28.1 \pm 24.0$  hours,  $P = .023$ ). Early hemorrhagic complications were significant risk factors for worse clinical outcome (modified Rankin Scale,  $2.02 \pm 2.21$  versus  $4.4 \pm 2.30$ ,  $P = .022$ ). None of the 93 patients showed further hemorrhage after the initial 48 hours after coiling.

**CONCLUSIONS:** The accompanying intracerebral hemorrhage at onset, thromboembolic complications, postoperative antiplatelet therapy, and earlier initiation of coiling were the risk factors for early hemorrhagic complications.

**ABBREVIATION:** ICH = intracerebral hematoma

A recent guideline stated that endovascular coiling should be considered if ruptured aneurysms were judged to be technically amenable to both endovascular coiling and neurosurgical clipping.<sup>1</sup> Consequently, the use of coiling for ruptured saccular cerebral aneurysms has been increasing. One problem is that the incidence of periprocedural hemorrhagic complications within 30 days was reportedly high in the endovascular arm of a study,<sup>2</sup> and they were reported to be associated with high mortality and morbidity.<sup>3</sup> The risk factors for such early hemorrhagic complications are not well-known. Although the word “rebleeding” is often used for perioperative hemorrhagic complications, it is also unclear whether “rebleeding” is really caused by a rerupture of the aneurysm or is due to other mechanisms. Therefore, we analyzed cases of coiling for ruptured saccular aneurysms in which early

hemorrhagic complications had occurred within 48 hours after coiling, to identify factors affecting these complications.

## MATERIALS AND METHODS

We retrospectively reviewed a series of 93 patients who underwent coiling for a ruptured saccular aneurysm between September 2006 and March 2012 at our hospital. Only patients for whom coiling was performed within 3 days of diagnosis were included. We generally recommend early treatment for subarachnoid hemorrhage; however, 7 patients had unstable circulatory conditions that inhibited early interventions; 6 patients were first admitted to another hospital and then were referred to our hospital 1 or 2 days after onset. All patients presented with SAH confirmed by CT. Patients with accompanying intracerebral hematoma (ICH) other than SAH on preprocedural head CT were defined as having “accompanying ICH.” The ruptured aneurysms were identified by CT angiography or digital subtraction angiography. The choice of clipping or coiling was determined by discussion with the neurosurgeons. If the patient had a large ICH with a widespread effect such as ICH with a poor World Federation of Neurosurgical Societies grade<sup>4</sup> of IV and V, clipping with evac-

Received March 9, 2014; accepted after revision May 19.

From the Department of Neuroendovascular Treatment, Shiroshima Hospital, Osaka, Japan.

Please address correspondence to Tsuyoshi Ohta, MD, Department of Neuroendovascular Treatment, Shiroshima Hospital, 2-8-1 Habikino, Habikino City, Osaka 583-0872, Japan; e-mail: tsuyoshi@ya2.so-net.ne.jp

<http://dx.doi.org/10.3174/ajnr.A4033>

**Table 1: Characteristics and surgical outcome of the patients with early hemorrhagic complications**

Age (yr)/Sex	WFNS	ICH	Intraoperative Perforation	Intraoperative Thrombus Formation	Postoperative Antiplatelet Therapy	mRS
31/F	IV	Yes	No	Yes	Yes	1
81/F	II	Yes	No	Yes	Yes	6
57/F	I	Yes	Yes	No	No	3
49/F	II	Yes	No	No	No	6
62/M	V	Yes	No	Yes	Yes	6

**Note:**—WFNS indicates World Federation Neurological Societies grade.

uation of the ICH was selected. If the patient had a small ICH with a minimal effect such as ICH with a good World Federation of Neurosurgical Societies grade, coiling was selected when technically feasible.

Coiling was started as soon as the operator, anesthesiologist, and the patient's medical condition were ready for the treatment. All treatments were performed with the patient under general anesthesia and having been given systemic heparinization with an activated clotting time of approximately 200–250 seconds. In cases with multiple aneurysms, the ruptured one was estimated by the distribution of the subarachnoid hemorrhage. Blood pressures were maintained within normal range. Coiling was performed simply or with an adjunctive technique such as balloon assist. No stents were applied. The strategy of coiling was to employ packing sufficient for hemostasis. Antiplatelet therapy was initiated when intraoperative thrombus formation was found. At the end of treatment, heparin was not reversed but was discontinued because the last activated clotting time was usually <200 seconds. Heparin was reversed with protamine if bleeding events occurred. General anesthesia was continued until the day after the procedure to avoid perioperative elevated intracranial pressure, which is associated with a patient's clinical outcome.<sup>5</sup>

The clinical condition before coiling was assessed according to the World Federation of Neurosurgical Societies grade. Early hemorrhagic complications were defined as an occurrence of new bleeding or enlargement of the pre-existing ICH within 48 hours after coiling. Early rebleeding from the treated aneurysm was assumed if postoperative CT showed an extravasation of contrast or the new hemorrhage was found only in the subarachnoid space. If the postoperative CT did not show any leakage of contrast and the new hemorrhage was added to ICH, we defined the new hemorrhage as an expansion of the accompanying ICH. Diagnostic confirmation was accepted when CT showed an augmentation of any hemorrhage, including SAH, intraventricular hematoma, or intracerebral hemorrhage, compared with that shown on the preprocedural CT, as judged by 2 physicians (T.O. and K.M.). Clinical outcomes were assessed according to the modified Rankin Scale on postoperative day 30.<sup>6</sup> The degree of aneurysmal occlusion was assessed by packing density calculated from the volume of the inserted coil divided by the preprocedural 3D aneurysmal volume, except for the intraoperative perforated cases because coil volume outside the aneurysm could not be evaluated in these cases.

### Statistical Analysis

The Fisher exact test or Student *t* test, as appropriate, was used to compare factors such as accompanying ICH, aneurysmal location, postoperative antiplatelet therapy, intraoperative perforation, and symptomatic thromboembolic complications, which were detected on postoperative head MR imaging; packing density (when calcu-

lated); and time to coil in each group. *P* values < .05 were considered statistically significant. The *P* value was expressed to 2 significant figures; if the value was < .001, it was expressed as *P* < .001.

### RESULTS

Coiling was performed in 93 patients, including 26 men and 67 women, 65.1 ± 15.0 years of age. During the same period, clipping was performed in 136 patients.

Multiple aneurysms were observed in 5 patients. The World Federation of Neurosurgical Societies grade was 2.80 ± 1.54, and the location of the aneurysms was supratentorial in 75 patients (80.6%). The aneurysms were located in the anterior communicating artery (29 cases), internal carotid artery (17 cases), internal carotid–posterior communicating artery (15 cases), basilar tip and basilar–superior cerebellar artery (12 cases), middle cerebral artery (7 cases), vertebral artery–posterior inferior cerebellar artery and vertebrobasilar junction (4 cases), and other locations (9 cases). The maximum diameter of the aneurysms was 6.89 ± 3.1 mm. Eighteen patients (19.4%) had accompanying ICH with SAH at the first head CT (accompanying ICH group). Significantly more patients with poor neurological status, as shown by World Federation of Neurosurgical Societies grades IV and V (66.7% versus 29.3%, respectively; *P* = .006) and poor clinical outcome, as shown by modified Rankin Scale grades 4 and 5 (66.7% versus 24%, respectively; *P* = .001), were included in the accompanying ICH group than in the nonaccompanying ICH group.

Five patients had early hemorrhagic complications (5.4%). All of the early hemorrhagic complications occurred within 24 hours. No patient had early hemorrhagic complications defined as SAH even in the 4 cases of intraoperative perforations. Hemorrhagic transformation of cerebral infarction was not observed. All early hemorrhagic complications involved the expansion of the accompanying ICH. Characteristics of the 5 patients, radiologic findings, and surgical outcomes are summarized in Table 1. Comparisons between the early hemorrhagic complications group and the nonhemorrhagic group are shown in Table 2. Accompanying ICH (*P* < .001), postoperative antiplatelet therapy (*P* < .001), and thromboembolic complications (*P* = .044) were associated with early hemorrhagic complications. In 1 patient (case 3), endoscopic hematoma evacuation of the enlarged accompanying ICH was performed. Other cases were treated conservatively. Because all the early hemorrhagic complications presented as the expansion of the accompanying ICH, a comparison within the accompanying ICH group was performed to analyze the risk factors for expansion. The associated risk factors for the enlargement of a pre-existing ICH were postoperative antiplatelet therapy (*P* = .044) and earlier initiation of coiling (9.8 ± 5.8 versus 28.1 ± 23.1 hours, *P* = .023) (Table 3).

### Representative Case

A 31-year-old woman presented with severe headache and disturbance of consciousness (World Federation of Neurosurgical Societies grade IV). Cerebral angiography revealed a left internal carotid–anterior choroidal artery bifurcation aneurysm with a maximum diameter of 4.5 mm (Fig 1A). With the patient under

**Table 2: Comparison of patient factors between the early hemorrhagic complications and no complications groups**

Factors	Early Hemorrhagic Group (5 Patients)	Nonhemorrhagic Group (88 Patients)	P Value
Accompanying intracerebral hematoma	5 (100%)	13 (14.8%)	<.001 <sup>a</sup>
Supratentorial location	5 (100%)	70 (79.5%)	.58
Postoperative antiplatelet therapy	3 (60%)	1 (1.14%)	<.001 <sup>a</sup>
Intraoperative perforation	1 (20%)	4 (4.55%)	.25
Thromboembolic complications	2 (40%)	5 (5.68%)	.044 <sup>a</sup>
Packing attenuation (when calculated)	26.6 ± 3.7 (3 cases)	29.4 ± 8.2 (83 cases)	.57

<sup>a</sup>Significant.

**Table 3: Risk factors for early hemorrhagic complications in the accompanying intracerebral hemorrhage group**

Factors	Early Hemorrhagic Group (5 Patients)	Nonhemorrhagic Group (13 Patients)	P Value
Supratentorial location	5	12	.72
Postoperative antiplatelet therapy	3	1	.044 <sup>a</sup>
Intraoperative perforation	1	0	.28
Time to coiling (hr)	9.8 ± 5.8	28.1 ± 23.1	.023 <sup>a</sup>

<sup>a</sup>Significant.

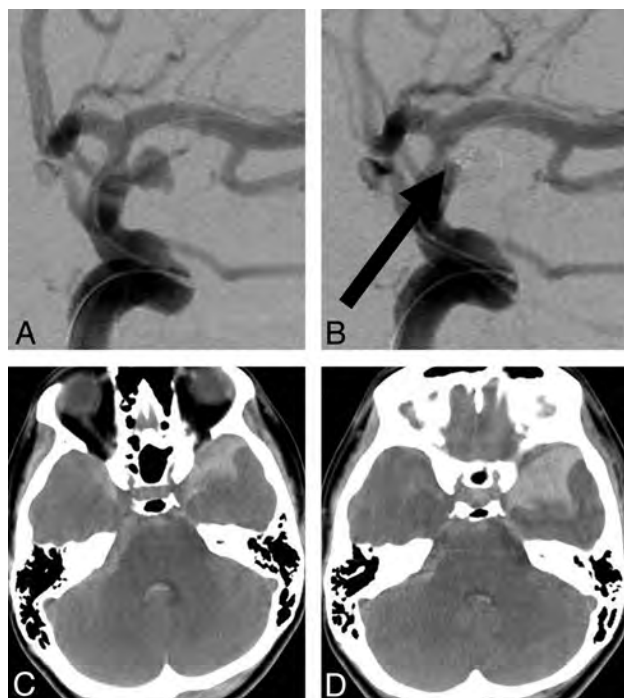


**FIG 1.** Representative case. Cerebral angiography reveals a left internal carotid–anterior choroidal artery bifurcation aneurysm (A) and a small thrombus, indicated by the arrow after placement of coils (B). Head CT on admission shows a subarachnoid hemorrhage with lobar hemorrhage (C). Head CT after the procedure does not show any leakage of contrast, but enlargement of the existing parenchymal temporal lobar hemorrhage is observed (D).

systemic heparinization with injection of 4000 U of heparin, coil embolization was performed by using the balloon-assist technique. After the placement of 4 bare platinum coils, we found a small thrombus (Fig 1B); after the administration of 100 mg of aspirin and the addition of 1000 U of heparin, the thrombus disappeared and 3 additional coils were added to achieve complete occlusion. Her preoperative head CT showed massive subarachnoid hemorrhage with lobar hemorrhage of the left temporal tip (Fig 1C). Postprocedural head CT showed enlargement of the existing left temporal lobar hemorrhage compared with the pre-

operative CT (Fig 1D). Fortunately, she fully recovered with minor sequelae and resumed her previous activities (modified Rankin Scale 1).

## DISCUSSION

The greatest risk of hemorrhagic complications associated with endovascular coil treatment of aneurysms is during the initial 48 hours.<sup>7</sup> Reducing early hemorrhagic complications may produce better clinical outcomes following coiling.

In our study, no patient showed early hemorrhagic complications defined as SAH even in the case of intraoperative perforations. All complications involved the expansion of the pre-existing hematomas. Some reports have stated that early hemorrhagic complications are possible

even when the treatment of a patient appears to be successful on angiography.<sup>8</sup> We speculated that early hemorrhagic complications may be caused by mechanisms other than arterial bleeding from the coiled ruptured aneurysm. The term “acute rebleeding” may limit the situations involving the rerupture of the aneurysm. Therefore, we referred to these cases as those involving “early hemorrhagic complications.”

In our study, the presence of ICH and postoperative antiplatelet therapy were identified as risk factors. Jartti et al<sup>9</sup> evaluated 194 patients with SAH and found that early rehemorrhage appeared as an enlargement of the initial ICH in all these patients. Dmytriw et al<sup>10</sup> reported a series of 137 cases with ruptured aneurysms that underwent endovascular treatment and 2 cases with early hemorrhagic complications (1.4%) for which one received recombinant tissue plasminogen activator and both received acetylsalicylic acid. Egashira et al<sup>11</sup> reported the results in the endovascular treatment of 101 consecutive cases with SAH and found that 14 (13.9%) had hematoma growth unrelated to aneurysmal rebleeding. The other reported risk factors for early hemorrhagic complications after coiling are an occurrence of a residual aneurysm at the end of a coiling procedure,<sup>12</sup> an intra-arterial infusion of abciximab or tirofiban,<sup>3</sup> and maintenance of anticoagulation after the procedure.<sup>3</sup> Antiplatelet therapy may inhibit the hemostasis process of the existing ICH. The presence of intraoperative thrombus formation was also a risk factor, which may be because of subsequent antiplatelet therapy. The incidence of early hemorrhagic complications has been reported as 1%, even after angiographically successful coiling.<sup>8</sup> In our study, there was no significant difference in packing density between the groups.

The presence of ICH is a predictor of unfavorable outcome of SAH,<sup>13</sup> especially hematoma growth without aneurysmal rebleeding.<sup>11</sup> As reported previously,<sup>11</sup> ultra-early embolization performed within 6 hours of onset was a risk factor for early hemorrhagic complications. An earlier intervention led to an earlier initiation of anticoagulation therapy and may have promoted expansion of the existing ICH. Intentional delay in performing coiling may be considered, but because early aneurysmal rebleeding is associated with very poor outcomes, urgent prevention is recommended.<sup>1</sup> Therefore, if treatment can be initiated earlier than 24

hours in cases with accompanying ICH, clipping and evacuation of the hematoma may be a better approach. If coiling is selected, it should be performed without antiplatelet therapy, and clot evacuation should be performed subsequently to prevent the risk of early hemorrhagic complications. Endoscopic aspiration of hematomas was reported to improve outcomes<sup>14,15</sup> and may be preferred over craniotomy, as in our single case.

Some researchers reported that intraprocedural perforations have appeared to be associated with relatively high rates of morbidity and mortality.<sup>16,17</sup> Other researchers have reported that new neurologic deficits directly associated with aneurysm perforation were found in only 20% of cases with leakage of contrast.<sup>18</sup> In our study, 4 intraoperative perforations occurred, but these were not a significant risk factor for either early hemorrhagic complications or worse clinical outcomes. If we found intraoperative perforation, we quickly reversed heparin and lowered the blood pressure. We never pulled back the protruded coil or microcatheter. We rapidly coiled from that point, and the perforated portion was closed in a few minutes. With this method, fortunately, we saw no increase in the incidence of SAH. Aneurysm perforation may not necessarily be associated with worse clinical outcome.

Thromboembolic complications and postoperative antiplatelet therapy were identified as risk factors for early hemorrhagic complications. From a technical point of view, it is better to avoid overly aggressive coiling, which may lead to these complications. Antiplatelet agents and anticoagulants have been suggested as risk factors for the early expansion of spontaneous ICH.<sup>19,20</sup> Even if apparent thromboembolic complications followed, postoperative antiplatelet therapy may be more hazardous in cases with accompanying ICH.

A limitation of this study was its retrospective nature, which made it impossible to determine whether the factors affecting early hemorrhagic complications were causes of or simply results associated with early complications after coiling. In addition, because we avoided coiling in patients with large ICHs with widespread effects, over- or underestimation of the importance of ICH as it relates to the risk of postcoiling hemorrhage may have occurred. However, our results may be helpful in determining the clinical steps that should be taken for patients who undergo coiling for ruptured aneurysms, particularly those with accompanying ICH.

## CONCLUSIONS

We analyzed early hemorrhagic complications after coiling to treat ruptured cerebral aneurysms. Accompanying ICH, thromboembolic complications, postoperative antiplatelet therapy, and earlier initiation of coiling were identified as risk factors. In patients for whom there is a high probability of early hemorrhagic complications, clipping and/or clot evacuation may be selected.

Disclosures: Tsuyoshi Ohta—UNRELATED: Payment for Lectures (including service on Speakers Bureaus); Kaneka, Stryker, Comments: paid for lectures on device training.

## REFERENCES

- Connolly E Jr, Rabinstein AA, Carhuapoma JR, et al. **Guidelines for the management of aneurysmal subarachnoid hemorrhage: a guideline for healthcare professionals from the American Heart Association/American Stroke Association.** *Stroke* 2012;43:1711–37
- Molyneux A, Kerr R, Stratton I, et al. **International Subarachnoid Aneurysm Trial (ISAT) of neurosurgical clipping versus endovascular coiling in 2143 patients with ruptured intracranial aneurysms: a randomised trial.** *Lancet* 2002;360:1267–74
- Cho YD, Lee JY, Seo JH, et al. **Early recurrent hemorrhage after coil embolization in ruptured intracranial aneurysms.** *Neuroradiology* 2012;54:719–26
- Report of World Federation of Neurological Surgeons Committee on a Universal Subarachnoid Hemorrhage Grading Scale.** *J Neurosurg* 1988;68:985–86
- Heuer GG, Smith MJ, Elliott JP, et al. **Relationship between intracranial pressure and other clinical variables in patients with aneurysmal subarachnoid hemorrhage.** *J Neurosurg* 2004;101:408–16
- Farrell B, Godwin J, Richards S, et al. **The United Kingdom transient ischaemic attack (UK-TIA) aspirin trial: final results.** *J Neurol Neurosurg Psychiatry* 1991;54:1044–54
- Willinsky RA, Peltz J, da Costa L, et al. **Clinical and angiographic follow-up of ruptured intracranial aneurysms treated with endovascular embolization.** *AJNR Am J Neuroradiol* 2009;30:1035–40
- Kang DH, Kim YS, Baik SK, et al. **Acute serious rebleeding after angiographically successful coil embolization of ruptured cerebral aneurysms.** *Acta Neurochir* 2010;152:771–81
- Jartti P, Isokangas JM, Karttunen A, et al. **Early rebleeding after coiling of ruptured intracranial aneurysms.** *Acta Radiol* 2010;51:1043–49
- Dmytriw AA, Pickett GE, Shankar JJ. **Rupture of aneurysms in the immediate post-coiling period.** *J Neurointerv Surg* 2014;6:16–18
- Egashira Y, Yoshimura S, Enomoto Y, et al. **Ultra-early endovascular embolization of ruptured cerebral aneurysm and the increased risk of hematoma growth unrelated to aneurysmal rebleeding.** *J Neurosurg* 2013;118:1003–08
- Klompshouwer EG, Dings JT, van Oostenbrugge RJ, et al. **Single-center experience of surgical and endovascular treatment of ruptured intracranial aneurysms.** *AJNR Am J Neuroradiol* 2011;32:570–75
- Güresir E, Beck J, Vatter H, et al. **Subarachnoid hemorrhage and intracerebral hematoma: incidence, prognostic factors, and outcome.** *Neurosurgery* 2008;63:1088–93, discussion 1093–94
- Nagasaka T, Tsugeno M, Ikeda H, et al. **Early recovery and better evacuation rate in neuroendoscopic surgery for spontaneous intracerebral hemorrhage using a multifunctional cannula: preliminary study in comparison with craniotomy.** *J Stroke Cerebrovasc Dis* 2011;20:208–13
- Y Nieves MC, Toktamis S, Haas E, et al. **Benefits of adapting minimal invasive techniques to selected patients with spontaneous supratentorial intracerebral hematomas.** *Neurol Res* 2005;27:755–61
- Ryu CW, Lee CY, Koh JS, et al. **Vascular perforation during coil embolization of an intracranial aneurysm: the incidence, mechanism, and clinical outcome.** *Neurointervention* 2011;6:17–22
- Zang P, Liang C, Shi Q, et al. **Intraprocedural cerebral aneurysm rupture during endovascular coiling.** *Neurol India* 2011;59:369–72
- Kwon BJ, Chang HW, Youn SW, et al. **Intracranial aneurysm perforation during endosaccular coiling: impact on clinical outcome, initial occlusion, and recanalization rates.** *Neurosurgery* 2008;63:676–82, discussion 682–83
- Naidech AM, Jovanovic B, Liebling S, et al. **Reduced platelet activity is associated with early clot growth and worse 3-month outcome after intracerebral hemorrhage.** *Stroke* 2009;40:2398–401
- Flibotte JJ, Hagan N, O'Donnell J, et al. **Warfarin, hematoma expansion, and outcome of intracerebral hemorrhage.** *Neurology* 2004;63:1059–64

# Vision Outcomes and Major Complications after Endovascular Coil Embolization of Ophthalmic Segment Aneurysms

C.R. Durst, R.M. Starke, J. Gaughen, Q. Nguyen, J. Patrie, M.E. Jensen, and A.J. Evans

## ABSTRACT

**BACKGROUND AND PURPOSE:** As aneurysms arising from the ophthalmic segment of the internal carotid artery increase in size, they can compress the optic nerve, prompting patients to present with visual disturbances. The purpose of this article is to describe the clinical and angiographic results with an emphasis on visual outcomes following the endovascular treatment of ophthalmic segment ICA aneurysms.

**MATERIALS AND METHODS:** The records of 1254 patients who presented for endovascular treatment of a cerebral aneurysm were retrospectively reviewed to identify 65 consecutive patients who underwent coil embolization of an ophthalmic segment ICA aneurysm. The clinical records, treatment reports, and imaging were reviewed with a focus on visual outcomes.

**RESULTS:** Twenty-two of the 65 patients (34%) who presented for treatment of an ophthalmic aneurysm reported a visual disturbance at presentation. Fifteen of the 22 patients (68%) experienced an improvement in their symptoms after treatment. Overall, patients with visual symptoms were significantly more likely to benefit from treatment than to have a decline in vision ( $P = .03$ ). The overall morbidity was 4%, and mortality was 0%. The retreatment rate was high at 30%, though this was disproportionately weighted by an 86% retreatment rate in patients with ruptured aneurysms.

**CONCLUSIONS:** Patients with visual symptoms attributable to ophthalmic segment ICA aneurysms undergoing endovascular coil embolization were statistically more likely to experience an improvement in their vision than to have worsening or unchanged vision. Coiling was associated with a low morbidity rate, though an elevated retreatment rate.

Aneurysms arising from the ophthalmic segment of the internal carotid artery account for approximately 5% of all intracranial aneurysms.<sup>1,2</sup> As these aneurysms increase in size, they can compress the optic nerve, prompting the patient to present with visual disturbances, often involving the inferior and/or nasal fields first.<sup>2,3</sup> Both surgical and endovascular treatment of these aneurysms have shown the potential to improve visual disturbances if occurring early.<sup>2,4-11</sup> However, treatment of these aneurysms is not without its own set of inherent risks. Retinal artery

occlusion or delayed optic ischemia may occur after either surgical or endovascular repair.<sup>12-14</sup> A review of recent surgical literature suggests a permanent morbidity ranging from 3% to 38% following treatment of an ophthalmic segment ICA aneurysm.<sup>3,5,6,10,15-18</sup> This morbidity includes a risk of new or worsened visual disturbance in 2%–30% of surgically treated patients and 3%–8% of endovascularly treated patients.<sup>3,5,6,15,16</sup>

This article assesses the angiographic and clinical outcomes of 65 consecutive patients who presented for initial treatment of an ophthalmic segment ICA aneurysm via an endovascular approach. Our goal is to describe the clinical and angiographic outcomes with an emphasis on visual outcomes following the endovascular treatment of ophthalmic segment aneurysms.

## MATERIALS AND METHODS

### Study Design

Under the auspices of the institutional review board, the records of 1254 patients who presented for treatment of a cerebral aneurysm between October 2001 and April 2009 were retrospectively reviewed. For the purposes of this article, only ophthalmic segment aneurysms arising from the dorsal internal carotid artery at or immediately adjacent to the origin of the ophthalmic artery

Received February 19, 2014; accepted after revision April 28.

From the Departments of Radiology and Medical Imaging (C.R.D., J.G., M.E.J., A.J.E.), Neurosurgery (R.M.S.), and Public Health Services (J.P.), University of Virginia, Charlottesville, Virginia; and Department of Radiology (Q.N.), Beth Israel Deaconess Medical Center, Boston, Massachusetts.

This work was funded in its entirety by the University of Virginia Department of Radiology.

Paper previously presented at: Annual Meeting of the American Society of Neuroradiology, May 18–23, 2013; San Diego, California.

Please address correspondence to Christopher Durst, MD, University of Virginia Health Systems, Department of Radiology, Neuroradiology Division, PO Box 800170 (FedEx:1215 Lee St-New Hospital), Charlottesville, VA 22908; e-mail: cdurst@virginia.edu

<http://dx.doi.org/10.3174/ajnr.A4032>



**FIG 1.** Endovascular coil embolization of an ophthalmic segment aneurysm.

were included, in keeping with the definition by Day.<sup>2</sup> From our cohort, we identified 65 consecutive patients (5.2%) who presented for initial endovascular treatment of an ophthalmic segment aneurysm. Medical and radiographic records were independently reviewed by a member of the research team who did not participate in the treatment of any of the included patients. Demographics, details of treatments, effects of treatments, results of follow-up procedures, and complications were recorded.

### **Interventional Procedures**

All procedures were performed under the care of 1 of 3 neurointerventional surgeons. Endovascular intervention was performed by using a biplane flat panel digital subtraction unit with the patient under general anesthesia. All patients were treated with a bolus of heparin at the beginning of the procedure to reach an activated clotting time of 250–300 seconds. In standard fashion, a guiding catheter was placed in the internal carotid artery, and diagnostic cerebral angiography was performed. Working projections were obtained, the aneurysm was measured, and under roadmap guidance, a microcatheter was placed into the aneurysm sac (Fig 1). Adjunct treatment measures, such as stent-assistance, dual-catheter technique, or balloon remodeling, were performed at the operator's discretion, as noted in the "Results" section. Immediate postprocedural DSA confirmed the occlusion status of the aneurysm and allowed evaluation of parent vessel patency and thromboembolic procedural complications.

### **Imaging Assessment**

Imaging outcomes were recorded for each case. Immediate treatment outcomes were documented in all cases via digital subtraction angiography in 2 planes. At discharge, patients were scheduled for 6- and 12-month angiographic follow-up with the intent to image via CTA, MRA, or additional DSA studies at 24 months. Long-term follow-up imaging analysis was limited to those patients with at least 12 months' follow-up. The follow-up imaging was evaluated for stability, recurrence, or progressive/delayed occlusion of the aneurysm. In cases of recurrent or residual aneurysms, the remnant was classified according to the Raymond classification scale.<sup>19</sup>

### **Clinical Assessment**

Through a review of the medical records, the clinical presentation and outcomes were recorded for each patient. Complete neurological examinations were available for each patient. Visual assess-

ment was performed by a neuro-ophthalmologist, neurologist, neurosurgeon, or neurointerventional surgeon. In patients with visual disturbances believed likely to be related to their ophthalmic segment ICA aneurysms, the preprocedural visual disturbance was recorded and compared with their postprocedural evaluation to assess stability, improvement, or deterioration. Major complications were classified as any hemorrhage, clinically significant infarction, or dissection that was directly related to the procedure, as determined by consensus between the neurointerventionalist and the neurosurgeon or neurologist who provided concurrent care to the patient.

### **Statistical Analysis**

Data are presented as mean and range for continuous variables and as frequency for categorical variables. Statistical analyses of categorical variables were performed by using the  $\chi^2$  and Fisher exact tests and the Mantel-Haenszel test for linear association, and comparison of means was performed by using the Student *t* test and Wilcoxon rank sum test as appropriate. Univariate analysis was used to test covariates predictive of the following dependent variables: treatment-related complications, retreatment, and unfavorable visual outcome (decreased visual function or increased visual pain). Additionally, stable or worse visual outcome was defined as those patients with increased visual pain or decreased neurologic function or no improvement in baseline visual pain or neurologic dysfunction. Only 1 patient had improvement in visual dysfunction but increased visual pain and was categorized as an unfavorable visual outcome. No patients had decreased visual pain but decreased visual function. Interaction and confounding were assessed through stratification and relevant expansion covariates. Independent factors predictive of the 5 dependent variables in univariate analysis ( $P < .20$ ) were entered into 5 separate multivariate logistic regression analyses. *P* values  $\leq .05$  were considered statistically significant.<sup>20</sup> Statistical analysis was performed with STATA 10.0 (StataCorp, College Station, Texas).

## **RESULTS**

### **Patient Demographics and Aneurysm Characteristics**

Of the 65 patients included in this study, 57 (87.7%) were women (Table 1). The average age was 56 years. Twenty-two of the 65 patients presented with a visual disturbance (Table 2). Eleven patients presented after rupture of the aneurysm. Almost half of the patients were hypertensive ( $n = 31$ ).

The average diameter of the aneurysms was 8.4 mm, with the difference between ruptured aneurysm diameter (10.6 mm) and unruptured aneurysm diameter (7.9 mm) approaching significance ( $P = .086$ ). Aneurysms causing a visual disturbance (9.1 mm) tended to be larger than those that did not (8.1 mm), though this was not statistically significant ( $P = .18$ ).

Most patients ( $n = 52$ , 80%) were treated by coil embolization alone. Four patients (6%) were treated by using balloon assistance. Nine (14%) underwent stent-assisted coil embolization.

### **Visual Outcomes**

Twenty-two of the 53 patients (42%) who presented for elective treatment of an unruptured ophthalmic segment ICA aneurysm

**Table 1: Patient demographics and aneurysm characteristics with breakdown of the characteristics according to the presence/absence of a visual disturbance at presentation**

Variable	Total	Visual Disturbance	No Visual Disturbance	P Value
Total	65	22 (34)	43 (66)	
Demographics				
Age (yr) (average) (range)	56 ± 11.4 (26–78)	55 ± 14 (26–70)	56.5 ± 10.1 (38–78)	.656
Sex				
Female (No.) (%)	57 (88)	19 (86)	38 (88)	1.000
Male (No.) (%)	8 (12)	3 (14)	5 (12)	
Presentation (patient may be included in multiple categories)				
Visual disturbance (No.) (%)	22 (20)	22 (100)	0 (0)	
Headache (without SAH) (No.) (%)	24 (37)	9 (41)	15 (35)	
Incidental (No.) (%)	15 (23)	0 (0)	13 (30)	
Hemorrhage (No.) (%)	12 (18)	1 (5)	10 (23)	
Other neurologic sequelae (No.) (%)	11 (17)	2 (10)	9 (21)	
Hypertension				
Yes (No.) (%)	31 (48)	11 (50)	20 (47)	.800
No (No.) (%)	34 (52)	11 (50)	23 (53)	
Aneurysm characteristics				
Diameter (mm) (average) (range)	8.4 ± 4.6 (2–20)	9.1 ± 5.5 (2–20)	8.1 ± 4.1 (2.2–19)	.476
Volume (mm <sup>3</sup> ) (average) (range)	417 ± 681 (3–2724)	565 ± 850 (3.7–2724)	341 ± 573 (3–2544)	.273
Neck width (mm) (average) (range)	3.9 ± 1.5 (1.3–8)	3.9 ± 1.9 (1.5–7.4)	3.9 ± 1.3 (1.3–8)	.905
Dome-to-neck ratio (average) (range)	2.1 ± 0.8 (1–6)	2.3 ± 1 (1.2–6)	2.1 ± 0.7 (1–3.8)	.320
Sidedness				
Left (No.) (%)	39 (60)	14 (64)	25 (58)	.791
Right (No.) (%)	26 (40)	8 (36)	18 (42)	

**Table 2: Visual disturbances prompting 22 patients to present for evaluation<sup>a</sup>**

Presenting Symptom	No. of Patients (%)
Change in visual acuity	16 (73)
Visual field defect	5 (23)
Ophthalmoplegia	4 (18)
Diplopia	2 (9)

<sup>a</sup> Patients may have presented with >1 symptom.

were found to have a visual disturbance at presentation. A change in visual acuity was the most common symptom (Table 1). Seven of the 22 patients (32%) were evaluated by an ophthalmologist. The average magnification requirement for patients seen by an ophthalmologist was 10.6 ± 6.1. Four of the 7 patients (57%) had a visual field deficit, 2 with a central deficit, 1 with a nasal field deficit, and 1 with a left superior homonymous deficit. Three of the 7 patients (43%) had evidence of optic nerve atrophy. Patients with visual disturbances were more likely to have a larger aneurysm diameter, though this was not statistically significant (Table 1).

Following treatment, patients in this study were much more likely to have an improvement in their visual symptoms than to develop a new or worsening visual disturbance ( $P = .03$ ). Fifteen of the 22 patients (68%) experienced an improvement in their ophthalmologic examinations as measured by a combination of confrontational testing and a Snellen chart. Five patients (23%) had no change in their visual symptoms. Three of these 5 patients (60%) had documented optic nerve atrophy on their ophthalmologic examination. Two patients (9%) experienced a decline in their visual acuity. One patient (2%) developed a new decline in visual acuity after treatment.

Patients whose visual disturbance improved following endovascular coiling of their ophthalmic segment aneurysm tended to

**Table 3: Aneurysm characteristics among patients who either presented with a visual disturbance or developed one after treatment<sup>a</sup>**

Variable	Not		P Value
	Improved (n = 15)	Improved or Worse (n = 8)	
Aneurysm size	7.7 ± 5.2	11.9 ± 5.1	.082
Neck diameter	3.2 ± 1.5	5.3 ± 1.6	.009
Dome-to-neck ratio	2.09 ± 1.1	2.2 ± 0.7	.738
Packing attenuation	28.6 ± 13.7	27.1 ± 10.1	.773
Requiring retreatment	2 (13%)	4 (50%)	.131

<sup>a</sup> There are 23 total patients because 1 patient developed a new visual disturbance after treatment.

have smaller aneurysms with a smaller neck than those who remained stable or whose vision deteriorated (Table 3).

### Complications

Sixteen patients required ≥1 retreatment, resulting in 91 total treatments of the 65 unique aneurysms (Table 4). The overall morbidity from the 91 treatments was 4% (4 cases). There were no deaths. Three of the complications occurred in the 81 treatments of unruptured aneurysms (3%). In 1 of these cases, the patient developed hydrocephalus despite the lack of hemorrhage, requiring a shunt. Two patients presented with an acute infarction >7 days after treatment. Of the 12 treatments of ruptured aneurysms, there was 1 complication (8%). In this case, the patient experienced a postprocedural infarction due to hypoperfusion.

Univariate predictors of treatment-related complications ( $P < .20$ ) included the presence of subarachnoid hemorrhage ( $P = .105$ ), no visual disturbance on presentation ( $P = .102$ ), a history of hypertension ( $P = .037$ ), packing attenuation of <22% ( $P = .158$ ), the presence of a stent ( $P = .171$ ), the use of clopidogrel (0.146), and the presence of residual filling of the aneurysm at the end of the procedure ( $P = .049$ ). A multivariate analysis showed that patients with

ruptured aneurysms were 5.8 times more likely to experience a major complication (95% CI, 1.02–33.03;  $P = .047$ ). In addition, those patients with hypertension were 5.2 times more likely to experience a complication (95% CI, 1.08–24.93;  $P = .039$ ).

### Imaging Outcomes

Of the 65 aneurysms, 35 (55%) were completely occluded at the end of the procedure. Thirty of the 53 unruptured aneurysms (58%) and 5 of the 12 (42%) ruptured aneurysms were completely occluded at the end of the case (Table 4). At 12 months' follow-up, 2 of the 26 (8%) patients who had some residual filling at the end of the procedure demonstrated delayed occlusion of the aneurysm.

Long-term outcomes ( $\geq 12$  months) were available for 53 (82%) patients. Overall, 16 (30%) of the patients with at least 12 months' follow-up required retreatment, including 10 of 46 (22%) patients treated electively and 6 of 7 (86%) patients treated after a subarachnoid hemorrhage. Univariate predictors of retreatment ( $P < .20$ ) included ruptured aneurysm ( $P = .002$ ), increasing Hunt and Hess scale score ( $P = .013$ ), family history of

aneurysms ( $P = .144$ ), aneurysms on the left ( $P = .039$ ), increasing maximum aneurysm diameter ( $P < .001$ ), increasing maximum neck diameter ( $P = .008$ ), increasing neck-to-dome ratio ( $P = .090$ ), decreasing packing attenuation ( $P = .034$ ), and packing attenuation of  $< 22\%$  ( $P = .003$ ). The multivariate analysis demonstrated that those with a ruptured aneurysm were 44.2 times more likely to have a recurrence (95% CI, 3.80–514.04;  $P = .002$ ). In addition, the diameter of the aneurysm was predictive of recurrence (OR = 1.36; 95% CI, 1.10–1.69;  $P = .005$ ). In particular, aneurysms of  $> 10$  mm were at greater risk of recurrence (OR = 12.64; 95% CI, 2.05–78.06;  $P = .022$ ). Finally, aneurysms with a packing attenuation of  $\geq 22\%$  were 84% less likely to recur (OR = 0.16; 95% CI, 0.03–0.96;  $P = .045$ ).

### DISCUSSION

Patients who present with a visual disturbance attributable to an ophthalmic segment ICA aneurysm can expect further deterioration of their vision if the aneurysm is left untreated.<sup>7,21</sup> Once treated, either endovascularly or surgically, a patient's vision would be expected to improve. Suction decompression during surgery relieves the direct mass effect of the aneurysm on the optic apparatus. The means by which endovascular treatment improves visual outcomes is not well-understood. One possibility is that thrombosis after coil embolization may relieve the pulsatile pressure on the optic nerve.<sup>22</sup> A review of prior literature suggests that 49% of patients treated endovascularly<sup>3-6,12,23</sup> and 63% of patients treated surgically<sup>2,5,8-11,23-25</sup> could be expected to experience improvement in their visual symptoms (Tables 5 and 6). Treatment, of course, is not without risk. If one looked broadly at the literature and combined data that included ruptured and unruptured ophthalmic segment ICA aneurysms, approximately 6% of patients treated endovascularly<sup>3-5,15,16,18,23</sup> and 9% of patients treated surgically<sup>2,3,5,6,9-11,15,17,18,23-25</sup> may develop a new visual disturbance or experience worsening of their visual symptoms. In

**Table 4: Clinical and imaging outcomes according to the presence/absence of a subarachnoid hemorrhage at presentation**

Variable	Total (No.) (%)	Unruptured (No.) (%)	Ruptured (No.) (%)	P Value
<b>Clinical outcomes</b>				
Total treatments	93	81 (87)	12 (13)	
Mortality	0	0 (0)	0 (0)	1.000
Morbidity	4 (4)	3 (3)	1 (8)	.430
Infarction	3 (3)	2 (2)	1 (8)	.343
Hydrocephalus	1 (1)	1 (1)	0 (0)	1.000
<b>Visual outcomes</b>				
Total patients	65	54 (83)	11 (17)	
Visual disturbance at presentation	22 (34)	21 (39)	1 (9)	.082
Visual disturbance after treatment				.03
Improved	15 (68)	15 (71)	0 (0)	
Unchanged	5 (22)	4 (27)	1 (100)	
Worse	2 (9)	2 (9)	0 (0)	
New (% of all patients)	1 (2)	0 (0)	1 (9)	
<b>Imaging outcomes</b>				
Aneurysms	65	53 (82)	12 (18)	
Primary occlusion	35 (55)	30 (58)	5 (42)	.523
Aneurysms with $> 12$ months' follow-up	53	45	8	.211
Retreatment	16 (30)	10 (22)	6 (75)	.0007 <sup>a</sup>
Progressive occlusion	2 (4)	2 (4)	0 (0)	
Unchanged	34 (64)	33 (73)	2 (25)	

<sup>a</sup>Retreatment-versus-progressive occlusion/unchanged.

**Table 5: Visual outcomes after endovascular treatment of aneurysms affecting the visual pathway**

Reference	Preoperative Visual Disturbance (No.)	Postoperative Improvement (No.)	Visual Improvement (%)	Total Aneurysms (No.)	New or Worsening Visual Disturbance (%)	Visual Decline (%)
Our data	22	15	68	65	3	5
Andaluz et al, 2005 <sup>15</sup>				17	1	6
Heran et al, 2007 <sup>4</sup>	16	6	38	16	6	38
Hoh et al, 2001 <sup>5</sup>	4	3	75	57	2	4
Iihara et al, 2003 <sup>16</sup>				77	2	3
Kanagalingam et al, 2012 <sup>3</sup>				22	1	5
Schuss et al, 2011 <sup>23</sup>	8	3	38	8	2	25
Sherif et al, 2009 <sup>18</sup>				38	2	5
Vargas et al, 1994 <sup>7</sup>	19	7	37	19	1	5
Yadla et al, 2011 <sup>6</sup>	10	5	50			
Total	79	39	49	319	20	6

**Table 6: Visual outcomes after surgical treatment of aneurysms affecting the visual pathway**

Reference	Preoperative Visual Disturbance (No.)	Postoperative Improvement (No.)	Visual Improvement (%)	Total Aneurysms (No.)	New or Worsening Visual Disturbance (%)	Visual Decline (%)
Andaluz et al, 2005 <sup>15</sup>				65	4	6
Date et al, 1998 <sup>8</sup>	6	4	67			
Day, 1990 <sup>2</sup>	23	17	74	54	6	11
Drake et al, 1968 <sup>9</sup>	32	15	47	100	5	5
Ferguson et al, 1981 <sup>11</sup>	29	15	52	29	5	17
Fulkerson et al, 2009 <sup>17</sup>				118	7	6
Hoh et al, 2001 <sup>5</sup>	12	8	67	187	5	3
Kanagalingam et al, 2012 <sup>3</sup>				69	21	30
Mattingly et al, 2013 <sup>24</sup>	14	11	79	18	4	22
Nanda and Javalkar, 2011 <sup>10</sup>	15	10	67	80	7	9
Park et al, 2009 <sup>30</sup>	10	8	80	10	0	0
Schuss et al, 2011 <sup>23</sup>	12	9	75	12	2	17
Sherif et al, 2009 <sup>18</sup>				23	1	4
Yadla et al, 2011 <sup>6</sup>				23	2	9
Total	153	97	63	788	69	9

our series, 68% of patients treated endovascularly experienced an improvement in their visual symptoms. Two of 53 (4%) patients treated electively and 1 of 12 (8%) treated after a rupture developed a new or worse visual disturbance. Of note, 2 of the 3 patients who developed a new or worse visual disturbance were found to have a recurrence of their aneurysm, which may have contributed to their worsening symptoms.<sup>14</sup> This information can help neurointerventional surgeons better inform patients about the risks and benefits of the endovascular treatment of ophthalmic segment aneurysms.

A potential benefit in treating ophthalmic segment ICA aneurysms via endovascular coil embolization is a relative reduction in overall morbidity compared with open surgery. Three of 79 elective treatments (4%) in this study resulted in permanent morbidity. Two of the patients experienced an infarction, 1 of which was clearly related to the procedure and the other most likely not because emboli were found in multiple vascular territories. The third patient developed hydrocephalus after treatment. Overall, the 4% rate of complications reported here is within the range of 0.8%–18%, with an average of 4% reported for 691 endovascularly treated ophthalmic segment ICA aneurysms in the literature.<sup>3-7,15,16,18,19,23,25-28</sup> This complication rate is considerably less than those reported for the open treatment of ophthalmic segment aneurysms. Even with the development of microsurgical techniques, the reported morbidity in the literature during the past 5 years ranged from 9% to 39%, with an average of 21% for 381 patients.<sup>3,6,10,17,18,23,29</sup> Although this study does not directly compare endovascular and open surgical techniques, the studies that have made this comparison have demonstrated an endovascular complication rate ranging from 0% to 18%, with an average of 4.5% for 358 aneurysms, while the surgical complication rate ranged from 3.7% to 27.5% with an average of 11.2% for 402 aneurysms.<sup>3,5,15,16</sup>

Of the 65 unruptured aneurysms, 55% were occluded primarily. This finding is similar to the 47% primary occlusion rate of 523 cumulative aneurysms treated endovascularly reported in the literature.<sup>3-6,25-27,28</sup> In the 30 patients who presented for at least 12 months of follow-up, 2 aneurysms (7%) that were not completely occluded at initial coiling progressed to complete occlusion

at their follow-up examinations. The appearance of 64% of the aneurysms at follow-up was unchanged.

Overall, 30% of the aneurysms reported in this study required retreatment. This retreatment rate is skewed by the 86% retreatment rate in ruptured aneurysms compared with the 22% retreatment rate in unruptured aneurysms ( $P = .002$ ). At our institution, our intent when treating ruptured aneurysms is to first protect the dome and any suspicious components of the aneurysm that may represent a point of rupture, such as a bleb or pseudoaneurysm. A broad review of the literature suggests a 20% recurrence rate with a range of 9%–53% in 503 aneurysms.<sup>3-6,18,25-27,28</sup> As expected, the retreatment rate after open clipping is significantly less than that after endovascular coil embolization. In a direct comparison of endovascular and open treatment of ophthalmic segment aneurysms, Sherif et al<sup>18</sup> and Yadla et al<sup>6</sup> reported a combined 4% retreatment rate after open clipping.

This study is limited by the retrospective nature and all of the biases imparted therein. Formal neuro-ophthalmologic evaluation was not available for all patients. In each of these cases, a visual assessment was available from a neurologist, neurosurgeon, or the interventional neuroradiologist. In cases of opposition testing, small defects may have been missed by either the patient or the physician. Given the retrospective nature of the study, the quality of the data is dependent on the clinical skill and reporting practices of multiple physicians. Thus, interpretation of improvement or worsening in visual symptoms at follow-up in patients not seen by an ophthalmologist is essentially subjective and dependent on the thoroughness of the documentation.

## CONCLUSIONS

Patients with visual symptoms attributable to ophthalmic segment ICA aneurysms having undergone endovascular coil embolization were statistically more likely to experience an improvement in their vision than to have worsening or unchanged vision. Coiling was associated with a low morbidity rate (4%). However, the retreatment rate following coiling was elevated (30%).

Disclosures: John Gaughen—UNRELATED: Consultancy: Covidien, MicroVention, Stryker. Mary E. Jensen—UNRELATED: Payment for Lectures (including service on Speakers Bureaus): Speakers Bureau for Stryker Neurovascular; training lectures for Covidien. Avery J. Evans—UNRELATED: Consultancy: Stryker, Covidien, Grants/

## REFERENCES

1. Locksley HB. Natural history of subarachnoid hemorrhage, intracranial aneurysms and arteriovenous malformations: based on 6368 cases in the cooperative study. *J Neurosurg* 1966;25:219–39
2. Day AL. Aneurysms of the ophthalmic segment: a clinical and anatomical analysis. *J Neurosurg* 1990;72:677–91
3. Kanagalingam S, Gailloud P, Tamargo RJ, et al. Visual sequelae after consensus-based treatment of ophthalmic artery segment aneurysms: the Johns Hopkins experience. *J Neuroophthalmol* 2012;32:27–32
4. Heran NS, Song JK, Kupersmith MJ, et al. Large ophthalmic segment aneurysms with anterior optic pathway compression: assessment of anatomical and visual outcomes after endosaccular coil therapy. *J Neurosurg* 2007;106:968–75
5. Hoh BL, Carter BS, Budzik RF, et al. Results after surgical and endovascular treatment of paraclinoid aneurysms by a combined neurovascular team. *Neurosurgery* 2001;48:78–89, discussion 89–90
6. Yadla S, Campbell PG, Grobelny B, et al. Open and endovascular treatment of unruptured carotid-ophthalmic aneurysms: clinical and radiographic outcomes. *Neurosurgery* 2011;68:1434–43, discussion 1443
7. Vargas ME, Kupersmith MJ, Setton A, et al. Endovascular treatment of giant aneurysms which cause visual loss. *Ophthalmology* 1994;101:1091–98
8. Date I, Asari S, Ohmoto T. Cerebral aneurysms causing visual symptoms: their features and surgical outcome. *Clin Neurol Neurosurg* 1998;100:259–67
9. Drake CG, Vanderlinden RG, Amacher AL. Carotid-ophthalmic aneurysms. *J Neurosurg* 1968;29:24–31
10. Nanda A, Javalkar V. Microneurosurgical management of ophthalmic segment of the internal carotid artery aneurysms: single-surgeon operative experience from Louisiana State University, Shreveport. *Neurosurgery* 2011;68:355–70, discussion 370–71
11. Ferguson GG, Drake CG. Carotid-ophthalmic aneurysms: visual abnormalities in 32 patients and the results of treatment. *Surg Neurol* 1981;16:1–8
12. Turner RD, Byrne JV, Kelly ME, et al. Delayed visual deficits and monocular blindness after endovascular treatment of large and giant paraophthalmic aneurysms. *Neurosurgery* 2008;63:469–74, discussion 474–75
13. Castillo B Jr, De Alba F, Thornton J, et al. Retinal artery occlusion following coil embolization of carotid-ophthalmic aneurysms. *Arch Ophthalmol* 2000;118:851–52
14. Schmidt GW, Oster SF, Golnik KC, et al. Isolated progressive visual loss after coiling of paraclinoid aneurysms. *AJNR Am J Neuroradiol* 2007;28:1882–89
15. Andaluz N, Beretta F, Keller JT, et al. Aneurysms of the ophthalmic (C6) segment of the internal carotid artery: clinical experience, treatment options, and strategies (Part 2). *Neurosurg Q* 2005;15:91–102
16. Iihara K, Murao K, Sakai N, et al. Unruptured paraclinoid aneurysms: a management strategy. *J Neurosurg* 2003;99:241–47
17. Fulkerson DH, Horner TG, Payner TD, et al. Endovascular retrograde suction decompression as an adjunct to surgical treatment of ophthalmic aneurysms: analysis of risks and clinical outcomes. *Neurosurgery* 2009;64:ons107–111, discussion ons111–12
18. Sherif C, Gruber A, Dorfer C, et al. Ruptured carotid artery aneurysms of the ophthalmic (C6) segment: clinical and angiographic long term follow-up of a multidisciplinary management strategy. *J Neurol Neurosurg Psychiatry* 2009;80:1261–67
19. Roy D, Raymond J, Bouthillier A, et al. Endovascular treatment of ophthalmic segment aneurysms with Guglielmi detachable coils. *AJNR Am J Neuroradiol* 1997;18:1207–15
20. Altman DG. *Practical Statistics for Medical Research*. Boca Raton: Chapman & Hall/CRC; 1999
21. Peiris JB, Ross Russell RW. Giant aneurysms of the carotid system presenting as visual field defect. *J Neurol Neurosurg Psychiatry* 1980;43:1053–64
22. Kazekawa K, Tsutsumi M, Aikawa H, et al. Internal carotid aneurysms presenting with mass effect symptoms of cranial nerve dysfunction: efficacy and imitations of endosaccular embolization with GDC. *Radiat Med* 2003;21:80–85
23. Schuss P, Guresir E, Berkefeld J, et al. Influence of surgical or endovascular treatment on visual symptoms caused by intracranial aneurysms: single-center series and systematic review. *J Neurosurg* 2011;115:694–99
24. Mattingly T, Kole MK, Nicolle D, et al. Visual outcomes for surgical treatment of large and giant carotid ophthalmic segment aneurysms: a case series utilizing retrograde suction decompression (the “Dallas technique”). *J Neurosurg* 2013;118:937–46
25. Park HK, Horowitz M, Jungreis C, et al. Endovascular treatment of paraclinoid aneurysms: experience with 73 patients. *Neurosurgery* 2003;53:14–23, discussion 24
26. Boet R, Wong GK, Poon WS, et al. Aneurysm recurrence after treatment of paraclinoid/ophthalmic segment aneurysms: a treatment-modality assessment. *Acta Neurochir (Wien)* 2005;147:611–16, discussion 616
27. D’Urso PI, Karadeli HH, Kallmes DF, et al. Coiling for paraclinoid aneurysms: time to make way for flow diverters? *AJNR Am J Neuroradiol* 2012;33:1470–74
28. Jin SC, Kwon do H, Ahn JS, et al. Clinical and radiological outcomes of endovascular detachable coil embolization in paraclinoid aneurysms: a 10-year experience. *J Korean Neurosurg Soc* 2009;45:5–10
29. Sharma BS, Kasliwal MK, Suri A, et al. Outcome following surgery for ophthalmic segment aneurysms. *J Clin Neurosci* 2010;17:38–42
30. Park JH, Park SK, Kim TH, et al. Anterior communicating artery aneurysm related to visual symptoms. *J Korean Neurosurg Soc* 2009;46:232–38

# Endovascular Treatment of Ophthalmic Artery Aneurysms: Assessing Balloon Test Occlusion and Preservation of Vision in Coil Embolization

J.H. Ahn, Y.D. Cho, H.-S. Kang, J.E. Kim, W.-S. Cho, S.C. Jung, C.H. Kim, and M.H. Han



## ABSTRACT

**BACKGROUND AND PURPOSE:** ICA–ophthalmic artery aneurysms have unique configurations corresponding to relative risks of ophthalmologic morbidities. Presented herein are clinical and radiologic outcomes of coil embolization in ophthalmic artery aneurysms.

**MATERIALS AND METHODS:** From January 2003 to September 2013, endovascular coiling was performed in 43 consecutive patients with ophthalmic artery aneurysms, each classified by the degree to which the ophthalmic artery was incorporated by the aneurysm and the contiguity between the ophthalmic artery entry and parent ICA. Clinical and radiologic outcomes of this approach were investigated, including the technical aspects of treatment and the efficacy of balloon test occlusion.

**RESULTS:** Among 14 patients (32.6%, all ophthalmic artery types) undergoing balloon test occlusion before endovascular coiling, patent collaterals between the external carotid artery and ophthalmic artery were demonstrated in 12 (85.7%) and complete compromise of the ophthalmic artery (without affecting vision) occurred in 4 patients during coiling. Steam-shaped S-configured (67.9%) or straight microcatheters (17.8%) facilitated aneurysm selection in most of the superiorly directed ophthalmic artery aneurysms ( $n = 28$ ), and steam-shaped pigtail microcatheters (85.7%) were useful in medially directed aneurysms ( $n = 14$ ). Balloon protection ( $n = 22$ ) was generally used to facilitate coiling, or a stent ( $n = 9$ ) was alternatively deployed. Satisfactory aneurysmal occlusion was achieved through coil embolization in 37 lesions (86.1%). During follow-up of 35 patients (mean interval,  $12.9 \pm 9.4$  months), only 1 instance (2.9%) of major recanalization was observed.

**CONCLUSIONS:** If one tailors technical strategies, ophthalmic artery aneurysms are amenable to safe and effective endovascular coil embolization, which tends to be stable in follow-up. Balloon test occlusion may be helpful in devising treatment strategies to preserve vision when coiling ophthalmic artery aneurysms (especially those incorporating an ophthalmic artery origin) is done.

**ABBREVIATIONS:** BTO = balloon test occlusion; ECA = external carotid artery; OA = ophthalmic artery

Despite considerable progress in microsurgical techniques, surgical treatment of ICA–ophthalmic artery aneurysms (OAs) is challenging, given their proximity to the optic apparatus, anterior clinoid process, and cavernous sinus. The recently devel-

oped neurointerventional arm enables an endovascular approach in this setting as an alternative to surgical clipping and the relatively high morbidity it entails. Nevertheless, the risk of impaired vision due to unexpected thromboembolism or occlusion of the OA after coiling is still a major concern.<sup>1-3</sup> Earlier investigations of endovascular treatment generally have considered OA lesions a subset of paraclinoid aneurysms.<sup>4-7</sup> Furthermore, such reviews have not fully addressed vision as an outcome, including angiographic assessment of collateral circulation before treatment. In this study, only aneurysms originating at the orifice of the OA are presented; we focused on angiographic and clinical aspects of vision as a measure of therapeutic outcome.

## MATERIALS AND METHODS

### Study Population

Between January 2003 and September 2013, a total of 2654 patients with 3163 intracranial aneurysms were treated by endovascular methods at our institution. Among them, we identified 43

Received January 17, 2014; accepted after revision March 31.

From the Department of Neurosurgery (J.H.A.), Hallym University Sacred Heart Hospital, Hallym University College of Medicine, Anyang, Korea; Departments of Radiology (Y.D.C., M.H.H.) and Neurosurgery (H.-S.K., J.E.K., W.-S.C., M.H.H.), Seoul National University Hospital, Seoul National University College of Medicine, Seoul, Korea; Department of Radiology (S.C.J.), Asan Medical Center, Ulsan University College of Medicine, Seoul, Korea; and Department of Neurology (C.H.K.), Stroke Center, Myongji Hospital, Goyang, Korea.

This study was supported by a grant from the Korea Healthcare Technology R&D Project, Ministry for Health, Welfare and Family Affairs, Republic of Korea (A111101).

Please address correspondence to Young Dae Cho, MD, Department of Radiology, Seoul National University Hospital, Seoul National University College of Medicine, 101 Daehak-ro, Jongno-gu, Seoul 110-744, Korea; e-mail: aronnn@naver.com

Indicates open access to non-subscribers at [www.ajnr.org](http://www.ajnr.org)

<http://dx.doi.org/10.3174/ajnr.A3999>

patients with 43 OA aneurysms from the prospectively recorded data base. Paraclinoid ICA aneurysms apart from an OA origin and pure OA aneurysms without continuity with the ICA were excluded. All lesions were further classified by the degree to which the OA was incorporated by the aneurysm and the contiguity between the OA entry and the parent ICA. Aneurysms incorporating an OA origin were designated “OA type,” whereas those adjacent to the OA but originating from the ICA were termed “ICA type” (Fig 1). Arterial branches associated with these aneu-

rysms were confirmed by digital subtraction angiography and 3D imaging. Therapeutic decisions were reached through multidisciplinary deliberation of both neurosurgeons and nonsurgical neurointerventionalists, and informed consent was obtained from all patients. The study protocol was approved by our institutional review board.

### Endovascular Procedures

Most of the endovascular procedures were performed with the patient under general anesthesia; the remaining 8 patients had local anesthesia, which was limited to the patients with favorable arterial architecture and aneurysmal configuration for coil embolization and good cooperation. All patients underwent cerebral angiography and rotational angiography with 3D image reconstruction with Integris V (Philips Healthcare, Best, the Netherlands) or Innova IGS 630 scanners (GE Healthcare, Milwaukee, Wisconsin) to evaluate aneurysmal configuration and arterial vasculature. All patients were managed with an antiplatelet agent before coiling

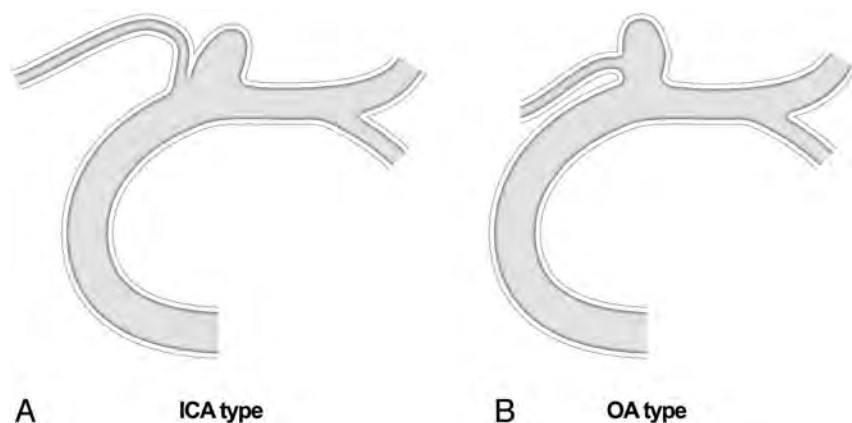


**FIG 1.** Classification of OA aneurysms (ICA type versus OA type).

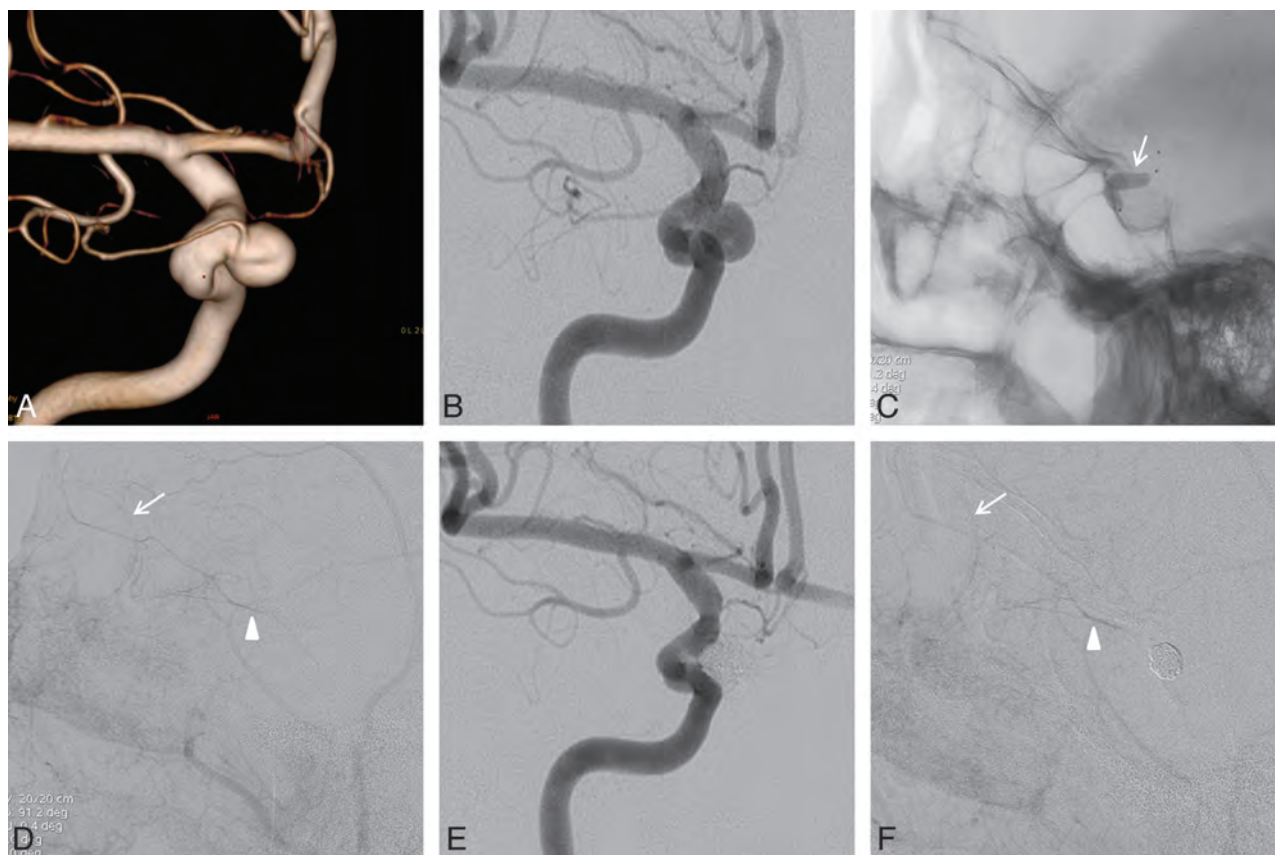


**FIG 2.** A and B, Conventional angiography and 3D imaging of a medially directed OA aneurysm (OA originating from the aneurysmal neck and an aneurysm incorporating most of the OA entry). C, Balloon test occlusion performed after planned sacrifice of the OA orifice during coil embolization; the balloon catheter was placed at the ophthalmic segment (*arrow*) and inflated. D, With the balloon inflated, angiographic image of the common carotid artery reveals choroidal blush (*arrow*) and contrast filling (*arrowhead*) of the OA through the middle meningeal artery. E, Final angiographic view of the occluded aneurysm and OA orifice. F, Angiography of the external carotid artery confirms a patent choroidal blush (*arrow*) and contrast filling of the OA (*arrowhead*) after coiling.

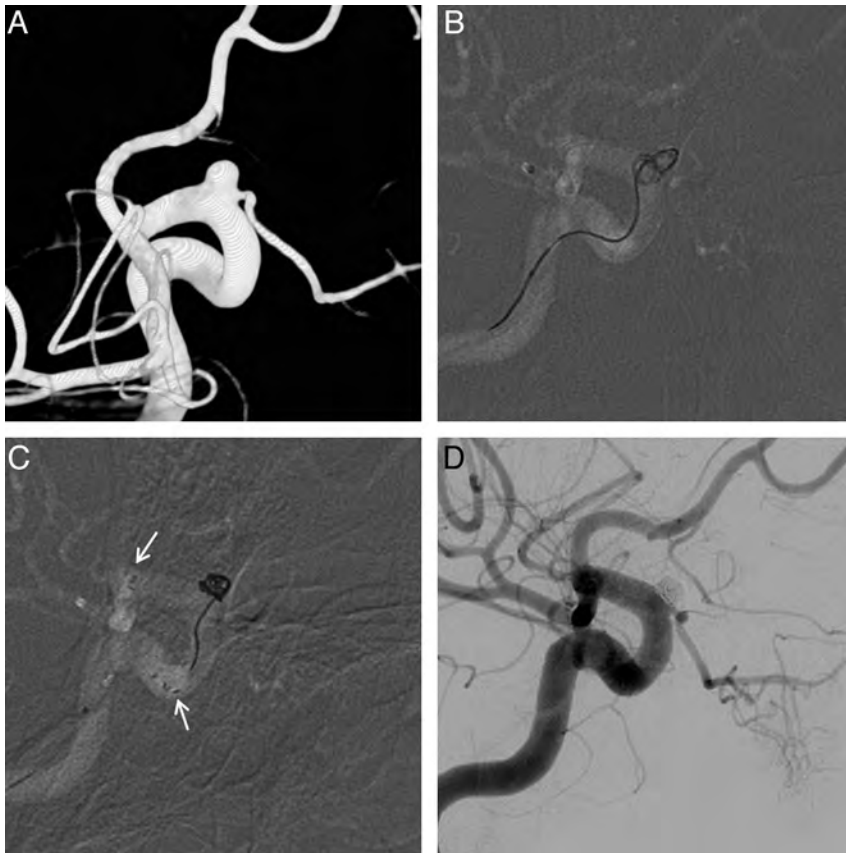


**FIG 3.** A, 3D imaging of a superiorly directed OA aneurysm; balloon test occlusion was not performed due to the aneurysm type (ICA) and a relatively well-demarcated margin between the OA orifice and the aneurysmal neck in the working projection. B, Simple technique via a steam-shaped S-configured microcatheter results in persistent herniation of coils into the parent artery. C, A Neuroform stent (arrows, stent markers) stabilizes the coil mass and secures the OA orifice. D, Completion angiography of successfully occluded aneurysm, with the OA preserved.

in a relatively consistent scheme at our institution.<sup>8</sup> In all patients with unruptured aneurysms, a 300-mg loading dose of clopidogrel was given the day before the procedure, and an additional 75 mg of clopidogrel was given the morning of the procedure. In patients with poor response to clopidogrel, based on the VerifyNow P2Y12 assay (Accumetrics, San Diego, California) (ie, P2Y12 reactivity unit of >285), a 300-mg loading dose of aspirin was added. Dual-agent antiplatelet therapy was administered if stent protection was anticipated. In patients showing poor response to clopidogrel, cilostazol (200 mg) was added. After femoral sheath placement, systemic heparinization was started with a loading dose of 3000 IU and was maintained with a dose of 1000 IU hourly. In a patient with an acutely ruptured aneurysm, antiplatelet medication was not administered before the procedure. In these cases, systemic heparinization was initiated shortly after adequate protection of the aneurysm. After the procedure, antiplatelet medications were not routinely prescribed for maintenance except in case of stent protection, coil protrusion, and procedural thromboembolism.

#### Assessment of Balloon Test Occlusion

Baseline neurologic examinations were performed, with visual acuity assessed before and after each coiling procedure. After detailed analysis of the aneurysmal configuration and arterial

course, the most appropriate therapeutic strategies were planned. Balloon test occlusion (BTO) was performed selectively and before endovascular treatment for the following reasons: 1) anticipated compromise of the OA entry during coiling, or 2) compromise of the OA unavoidable during coil embolization (ie, aneurysms incorporating much of the OA orifice or the OA originating from the aneurysmal dome) (Fig 2). If OA preservation was likely, based on aneurysm/OA properties favorable for endovascular coiling, BTO was not performed (Fig 3). The treatment algorithm for this cohort is depicted in a schematic (Fig 4).

BTO involved the following steps: 1) a guiding catheter placed in the common carotid artery; 2) a balloon catheter, HyperGlide (Covidien, Irvine, California) and Scepter C (MicroVention, Tustin, California) (4 × 15 mm or 20 mm), placed at the ophthalmic segment of the ICA, including OA origin; 3) careful inflation of a balloon with saline-diluted contrast media under fluoroscopic observation; and 4) contrast instilled (on ICA occlusion) through the common carotid artery to evaluate collateral flow between the external carotid artery (ECA) and the OA. A positive result with BTO was defined as retrograde filling of the OA main trunk via ECA

branches and demonstration of retinobulbar blush (Fig 2). In BTO-positive patients, occlusion of the aneurysm and compromise of the OA orifice were attempted in combination. Once coiling was complete, collateral flow was re-affirmed by ECA angiography. With negative BTO results, we elected one of the following options on the basis of aneurysmal configuration and size: 1) coil embolization by using various protective devices to preserve OA flow (intentional partial protective embolization on occasion), 2) no treatment and follow-up, or 3) surgical clipping.

#### Angiographic Outcome and Follow-Up

Immediate angiographic results after coil embolization were classified according to a 3-point Raymond scale: complete obliteration (no residual filling of contrast medium in the aneurysms), residual neck (the persistence of any portion of the original defect of the arterial wall), and residual aneurysm (any opacification of the sac).<sup>9</sup>

Clinical outcomes were evaluated with the Glasgow Outcome Scale, which was applied throughout hospitalization and at the last available clinical follow-up. In patients with unruptured aneurysms, MR angiography with 3D reconstruction was recommended 6, 12, 24, and 36 months after coil embolization. Additionally, plain radiography was recommended at 1 and 3 months

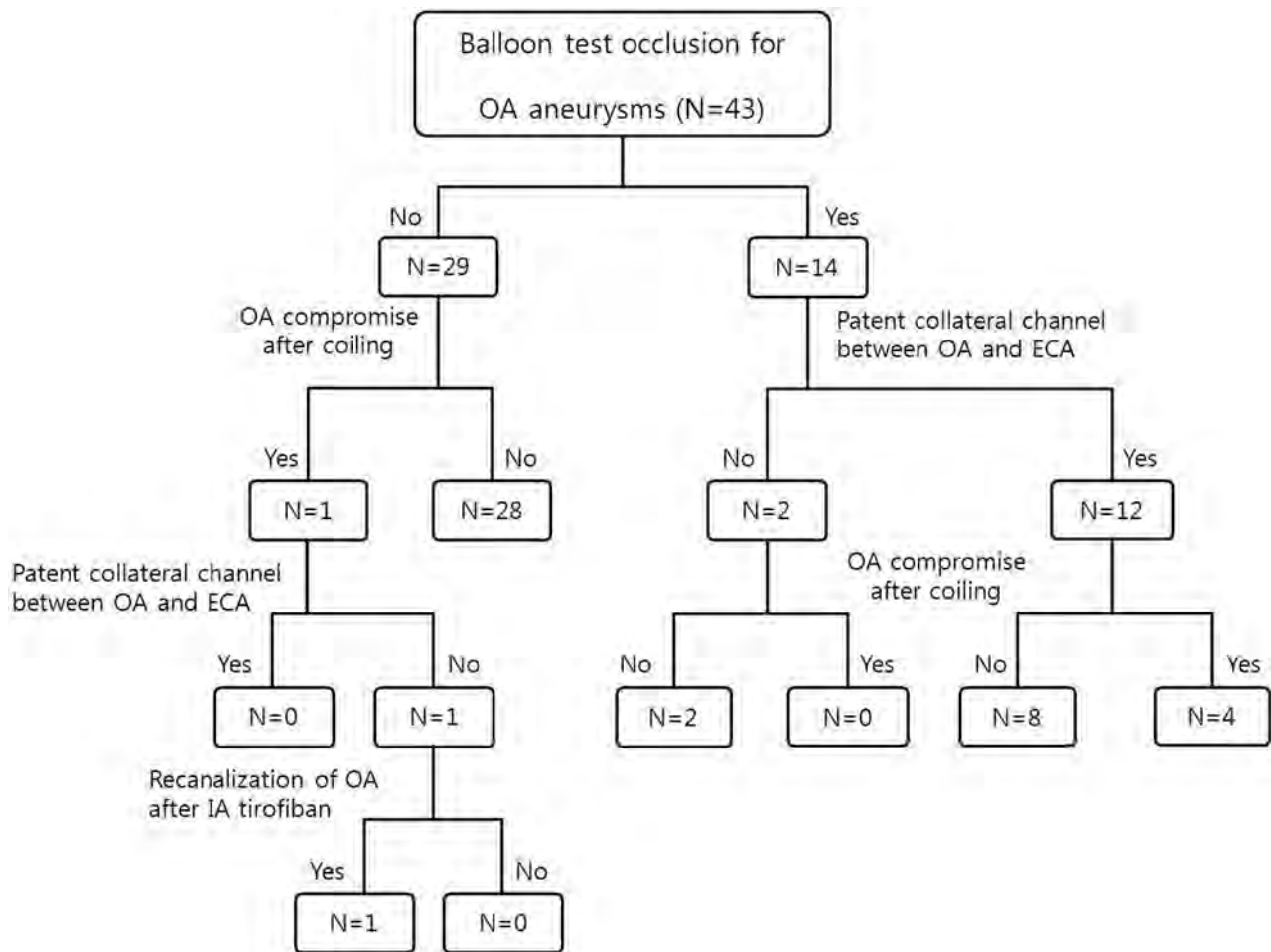


**FIG 4.** Schematic depicting the treatment algorithm in the study population.

postembolization in patients with ruptured aneurysms. Two experienced neurointerventionalists (M.H.H., H.-S.K.) who were blinded to the immediate postembolization angiogram independently reviewed anatomic follow-up results and categorized them as follows: stable occlusion (no interval change since the procedure or progressive thrombosis within the aneurysm), minor recanalization (progressive filling limited to the neck of the aneurysm), and major recanalization (aneurysmal sac filling). Conventional angiography and repeat embolization were recommended for patients showing major recanalization.

## RESULTS

### Population and Aneurysmal Characteristics

General characteristics of the study population ( $n = 43$ ) undergoing endovascular coil embolization for OA aneurysms are summarized in Table 1. The mean patient age at the time of the procedure was  $53.3 \pm 10.4$  years (range, 30–74 years), with a male/female ratio of 1:3.3. Nearly all OA aneurysms (97.6%) were discovered incidentally, with 1 exception in which the patient presented with subarachnoid hemorrhage.

Maximal diameters of aneurysms treated ranged from 2.7 to 15.7 mm (mean,  $5.6 \pm 2.7$  mm), and 53.5% of all lesions were  $< 5$  mm. There were 19 aneurysms of the ICA type and 24 of the OA type. Additional aneurysms existed in 18 patients (41.9%). Most lesions were wide-neck (38/43, 88.4%), with depth-to-neck ratios

$< 1.5$ . The aneurysms occupied either the superior wall of the ICA (28/43, 65.1%), the medial wall (14/43, 32.6%), or the inferior wall (1/43, 2.3%).

### Technical Aspects of Endovascular Treatment and Anatomic Outcomes

Treatment techniques applied to this series of OA aneurysms are shown in Table 2. The microcatheters used to select the aneurysms differed, depending on the aneurysm location and direction and parent artery course. In aneurysms of the superior wall, steam-shaped S-configured microcatheters (19/28, 67.9%) (Fig 3) or straight microcatheters (5/28, 17.9%) were used in most patients. In lesions of the medial wall, primarily steam-shaped pigtail microcatheters (12/14, 85.7%) were used (Fig 2).

Regarding other technical aspects, balloon remodeling was most frequently used (22/43, 51.3%), followed by stent protection (9/43, 20.9%) and either a multiple-microcatheter or single-microcatheter technique (6/43, 13.9%, each). All implanted stents were Neuroform devices (Stryker Neurovascular, Fremont, California) with open cells (Fig 3). Immediate angiographic assessment revealed occlusion in 14 aneurysms (32.6%), residual neck in 23 (53.5%), and residual aneurysm in 6 (13.9%).

Although an asymptomatic thrombus did occur in 1 patient, no other procedure-related adverse events were encountered. All

**Table 1: OA aneurysms: general characteristics and outcomes of endovascular coiling**

Characteristics	
No. of aneurysms and patients	43 aneurysms, 43 patients
Age (yr) (mean)	53.3 ± 10.4
Female/male	33:10
Presentation	
Incidental	42
Visual disturbance	0
Ruptured	1
Aneurysm direction	
Superior	28 (65.1%)
Medial	14 (32.6%)
Inferior	1 (2.3%)
Aneurysm type	
ICA type	19 (44.2%)
OA type	24 (55.8%)
Aneurysm size	
≤5 mm	23 (53.5%)
5~10 mm	18 (41.8%)
≥10 mm	2 (4.7%)
No. of aneurysms of other locations	
OA aneurysm only	25 (58.1%)
Multiple aneurysm	18 (41.9%)
Depth-to-neck ratio	
≤1	22 (51.2%)
1.0~1.5	16 (37.2%)
≥1.5	5 (11.6%)
Direction of aneurysm	
Superior	27 (62.8%)
Medial	14 (32.5%)
Other	2 (4.7%)
Initial occlusion result	
Complete occlusion	14 (32.6%)
Residual neck	23 (53.5%)
Residual aneurysm	6 (13.9%)
Follow-up result	
Stable occlusion	30 (85.7%)
Minor recanalization	4 (11.4%)
Major recanalization	1 (2.9%)

**Table 2: Technical strategies and directional shaping of microcatheters**

	Superior (n = 28)	Medial (n = 14)	Inferior (n = 1)
Technique			
Single microcatheter	5	1	0
Multiple microcatheter	4	2	0
Balloon remodeling	15	7	0
Stent protection	4	4	1
Microcatheter shape			
Steam-shaped S	19	2	0
Straight	5	0	0
Steam-shaped pigtail	3	10	1
Preshaped 45° or 90°	1	2	0

patients were neurologically intact (Glasgow Outcome Scale score 5) at the time of discharge.

### Balloon Test Occlusion and Clinical Outcomes

In approximately one-third (14/43, 32.6%) of the cohort (all OA type aneurysms, representing 58.3% [14/24] of patients with OA type aneurysms), BTO was performed without complications before the coiling procedure, confirming patent collateral channels between the ECA and OA in 12 patients (85.7%). Complete com-

promise of the OA (without a decline in vision) occurred in 4 of these 12 patients (Fig 2) because of endovascular coiling. The other 8 patients with favorable collaterals by BTO showed persistent antegrade filling of the OA with contrast and choroidal blush, despite protrusion of the coil into the OA entry. All patients received antiplatelet medication for at least 1 month.

Among the 29 patients not undergoing BTO, unexpected compromise of flow to the OA occurred in 1 patient during endovascular coiling. ECA angiography was performed immediately, and there was no filling of the OA through the ECA. Intra-arterial tirofiban (0.75 mg) then was infused to resolve the thrombus, and flow was restored (Fig 5). After the coiling procedure, an intravenous infusion of tirofiban was maintained for 12 hours and antiplatelet medication was administered for 1 month. The patient had no symptoms related to vision.

### Follow-Up Results

Follow-up radiologic imaging at least 6 months after coil embolization was performed in 35 aneurysms (mean interval, 12.9 ± 9.4 months), with the exception of 3 recently treated aneurysms (<6 months). Thus, the follow-up rate was 87.5% (35/40). On the basis of follow-up imaging, stable occlusion was observed in 30 aneurysms (87.5%); minor recanalization, in 4 (11.4%); and major recanalization, in 1 (2.9%). One patient with major recanalization underwent repeat endovascular coiling. Follow-up angiography performed 12 months after re-embolization showed stable occlusion. During the follow-up period, none of the patients had delayed cerebral infarction.

### DISCUSSION

A number of terms are used to describe aneurysms of the ICA segment between the OA and posterior communicating artery, namely paraophthalmic, paraclinoid, and ophthalmic segment aneurysms. Such lesions represent approximately 1.5%–8.0% of all intracranial aneurysms<sup>5,10,11</sup> and show a marked female preponderance (in most series) and a strong association with multiple aneurysms.<sup>5,6,11</sup> These demographics, including a propensity for multiple lesions, were shared by our patients, all of whom had aneurysms originating at the orifice of the OA. The tendency to rupture was also relatively low. Only 1 of our subjects presented with subarachnoid hemorrhage.

BTO of the ICA has become an established means of evaluating the adequacy of collateral flow in patients with large/giant aneurysms or head and neck tumors involving the carotid artery, in which arterial sacrifice or prolonged transient occlusion is expected during surgical or endovascular therapy.<sup>12</sup> However, research aimed at estimating the adequacy of collateral flow from the ECA to the OA or correlating vision outcomes with pretreatment angiographic studies of collateral circulation to the OA is scarce. Shaibani et al<sup>13</sup> performed BTO in 2 patients, each with an aneurysm incorporating the OA into its neck. They gauged the adequacy of collateral flow by deterioration of vision, rather than by confirming collateral circulation as we did through angiography. Both patients exhibited deteriorating vision within 6 minutes after balloon inflation that resolved on deflation, thus signifying insufficient collateral blood flow and an indication for surgical clipping. However, this method carries some potential limitations

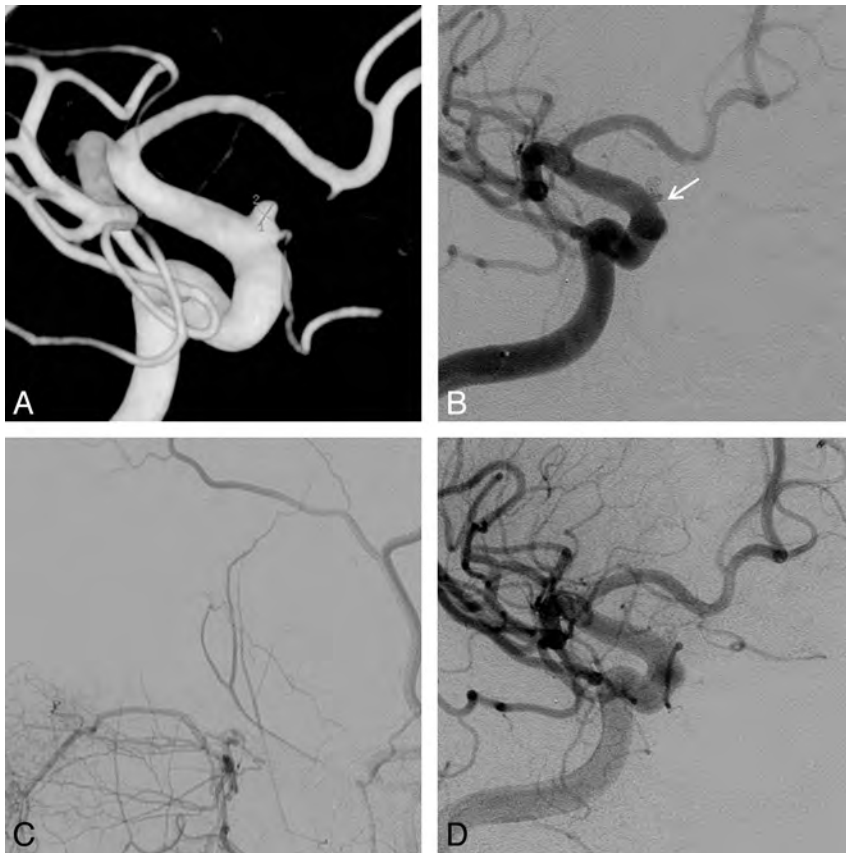


**FIG 5.** A, 3D imaging of a superiorly directed OA aneurysm; balloon test occlusion was not performed due to the aneurysm type (ICA) and relatively well-demarcated margin, B, Completion angiography of a successfully occluded aneurysm with OA compromise (arrow). C, Angiography of the external carotid artery confirms no patent contrast filling of the OA. D, Restoration of OA flow after intra-arterial tirofiban infusion (0.75 mg).

and risks, despite its apparent utility. The authors were concerned that perhaps duration of BTO was critical for accurate assessment. In other words, collateral flow from the ECA may have been evident with longer occlusion. Mathis et al<sup>12</sup> similarly performed continuous neurologic monitoring of 500 patients throughout 15-minute periods of test occlusion. Here, 16 patients (3.2%) had complications during BTO, including dissection, thromboembolism, and pseudoaneurysm.

No patients had complications of BTO in our hands, compared with the above study, which may attest to the merits of highly compliant balloons, less procedural time, and a simple procedure for confirming collateral flow from the ECA to the OA. Likewise, none of our patients experienced visual complications after complete OA compromise, gauged by our angiographic criteria (ie, OA flow determination and retinochoroidal blush by ECA-OA collaterals). Our study illustrates that the use of BTO to confirm collateral flow is seemingly innocuous and may provide a reliable index of postprocedural vision integrity, despite the limited sampling of patients involved. Because OA filling via the ECA does not precisely reflect the perfusion status of the central retinal artery and retinochoroidal blush also stems from the posterior ciliary artery, both criteria are important guides. None of our BTO-negative patients had OA compromise, so outcomes in terms of vision were not compared by positive and negative BTO-based subsets. Still, this study does show that vision is preserved

after OA compromise in BTO-positive patients. Concomitant monitoring with electroretinography or visual evoked potentials may also be helpful in predicting retinal ischemia or delayed thromboembolic events.

Collateral channels between the ECA and OA prevent permanent blindness after occlusion of the OA in 90% of patients.<sup>14,15</sup> In our study, the rate of patent collateral channels between the OA and ECA (84.6%), confirmed by BTO, was similar to that in previous reports. However, thrombotic occlusion at the OA orifice is a major concern during the coil embolization procedure itself and in the follow-up period. Should a thrombus unexpectedly form during coil embolization in patients who have not been evaluated by BTO, ECA angiography should be performed immediately in search of collateral channels between the ECA and OA. Although the probability of patent collaterals is high, the potential risk of ocular ischemia after coiling cannot be ignored. In this study, 1 instance of unexpected thrombus did occur in which there was no demonstrable filling of the OA through the ECA. Intra-arterial tirofiban infusion subsequently restored flow to the OA, but ocular ischemia may result from thromboembolism and

not from loss of OA perfusion alone. Ischemia from hypoperfusion ostensibly is avoidable by confirming collateral flow through BTO. In 8 patients with positive BTO results, initially slated for OA sacrifice, antegrade flow through the OA persisted, despite intentional OA compromise. We worried that incomplete compromise of the OA, with coil protrusion into the OA entry, might be a source of thromboembolism. Therefore, these patients were advised to continue anticoagulation and antiplatelet medication after the procedures.

Unfavorable aneurysmal configurations, including wide-neck lesions and those in which OA entry is incorporated into the aneurysmal neck, constitute a persistent challenge for endovascular treatment. Coil embolization with OA preservation is especially difficult in OA type aneurysms. The shape of the microcatheter used to select the aneurysm depends on aneurysm direction and the parent artery course. OA aneurysms are uniformly situated at the distal carotid siphon with sharp curves, so the direction of the microcatheter is inescapably affected by the curve of the carotid siphon. In superiorly directed aneurysms, steamed-shaped S-configured and straight microcatheters were generally used, whereas straight microcatheters were particularly helpful in aneurysms more proximally situated at the carotid siphon. In aneurysms directed medially, steam-shaped pigtail microcatheters were beneficial. Steamed-S and steamed-pigtail microcatheters tend to offer less resistance to kick-back during coil insertion. Thus, balloon protection or stent assistance was often required, not only for

neck protection but also for bolstering the microcatheter. In all instances in which stents were deployed, Neuroform devices were used exclusively. We wanted the struts of this open-cell stent to herniate into the aneurysmal neck and preserve the OA entry (Fig 3).

Relative to other locations, occlusion immediately following coil embolization seemed more difficult to achieve in the OA aneurysms of this series, possibly due to incorporation of the OA into these aneurysms and their proximity to the carotid siphon. In any event, anatomic outcomes were excellent at follow-up, possibly influenced by aneurysmal configurations (ie, sidewall aneurysms) and hemodynamic buffering by the carotid siphon.

## CONCLUSIONS

Because of their unique configurations and related ophthalmologic morbidities, OA aneurysms are considered a challenge for endovascular coiling. Balloon test occlusion seems helpful in planning treatment strategies for coiling of OA aneurysms that preserve vision. Through tailored techniques for shaping and insertion of microcatheters, excellent clinical and radiologic outcomes in OA aneurysms are possible by this method.

## ACKNOWLEDGMENTS

We thank Yoon-Kyung Choi for preparation of the illustrations.

Disclosures: Moon Hee Han—RELATED: Consultancy: MicroVention Inc.

## REFERENCES

1. Castillo B Jr, De Alba F, Thornton J, et al. **Retinal artery occlusion following coil embolization of carotid-ophthalmic aneurysms.** *Arch Ophthalmol* 2000;118:851–52
2. Ferrell AS, Lessne ML, Alexander MJ, et al. **Visual complications after stent-assisted endovascular embolization of paraophthalmic and suprasellar variant superior hypophyseal aneurysms: the Duke Cerebrovascular Center experience in 57 patients.** *World Neurosurg* 2012;78:289–94
3. Sherif C, Gruber A, Dorfer C, et al. **Ruptured carotid artery aneurysms of the ophthalmic (C6) segment: clinical and angiographic long term follow-up of a multidisciplinary management strategy.** *J Neurol Neurosurg Psychiatry* 2009;80:1261–67
4. Heran NS, Song JK, Kupersmith MJ, et al. **Large ophthalmic segment aneurysms with anterior optic pathway compression: assessment of anatomical and visual outcomes after endosaccular coil therapy.** *J Neurosurg* 2007;106:968–75
5. Roy D, Raymond J, Bouthillier A, et al. **Endovascular treatment of ophthalmic segment aneurysms with Guglielmi detachable coils.** *AJNR Am J Neuroradiol* 1997;18:1207–15
6. Sengupta RP, Gryspeerdt GL, Hankinson J. **Carotid-ophthalmic aneurysms.** *J Neurol Neurosurg Psychiatry* 1976; 39:837–53
7. Yadla S, Campbell PG, Grobelny B, et al. **Open and endovascular treatment of unruptured carotid-ophthalmic aneurysms: clinical and radiographic outcomes.** *Neurosurgery* 2011;68:1434–43
8. Cho YD, Lee WJ, Kim KM, et al. **Endovascular coil embolization of middle cerebral artery aneurysms of the proximal (M1) segment.** *Neuroradiology* 2013;55:1097–102
9. Roy D, Milot G, Raymond J. **Endovascular treatment of unruptured aneurysms.** *Stroke* 2001;32:1998–2004
10. Almeida GM, Shibata MK, Bianco E. **Carotid-ophthalmic aneurysms.** *Surg Neurol* 1976;5:41–45
11. Drake CG, Vanderlinden RG, Amacher AL. **Carotid-ophthalmic aneurysms.** *J Neurosurg* 1968;29:24–31
12. Mathis JM, Barr JD, Jungreis CA, et al. **Temporary balloon test occlusion of the internal carotid artery: experience in 500 cases.** *AJNR Am J Neuroradiol* 1995;16:749–54
13. Shaibani A, Khawar S, Bendok B, et al. **Temporary balloon occlusion to test adequacy of collateral flow to the retina and tolerance for endovascular aneurysmal coiling.** *AJNR Am J Neuroradiol* 2004;25: 1384–86
14. Johnson HC, Walker AE. **The angiographic diagnosis of spontaneous thrombosis of the internal and common carotid arteries.** *J Neurosurg* 1951;8:631–59
15. Dehdashti AR, Safran AB, Martin JB, et al. **Intraorbital ophthalmic artery aneurysm associated with basilar tip saccular aneurysm.** *Neuroradiology* 2002;44:600–03

# “Y” and “X” Stent-Assisted Coiling of Complex and Wide-Neck Intracranial Bifurcation Aneurysms

B. Bartolini, R. Blanc, S. Pistocchi, H. Redjem, and M. Piotin



## ABSTRACT

**BACKGROUND AND PURPOSE:** Stent-assisted coiling with two stents has been described in some series for the treatment of complex and wide-neck bifurcation aneurysms. Our aim was to report our experience of a stent-assisted coiling technique with double stents in “Y” and “X” configurations, with emphasis on safety, feasibility, and efficacy.

**MATERIALS AND METHODS:** Clinical and angiographic outcomes of patients for whom the strategic therapeutic option was the stent-assisted coiling technique in a Y or X configuration for neck scaffolding from June 2006 to June 2013 were retrospectively analyzed.

**RESULTS:** One hundred five aneurysms in 97 patients were treated during 100 consecutive procedures. There were 54.2% (57/105) MCA, 28.6% (30/105) anterior communicating artery, 16.2% (17/105) basilar tip, and 1.0% (1/105) ICA termination aneurysms. A Y stent placement was used to treat 87 aneurysms in 85 procedures; an X stent placement was used to treat 7 aneurysms in 6 procedures, while 9 procedures failed for 11 aneurysms. There were 10.0% (10/100) procedure-related permanent neurologic deficits and 1.0% (1/100) death. The immediate angiographic controls showed a complete occlusion in 47.6% (50/105) of the aneurysms and a partial (neck or sac remnant) occlusion in 52.4% (55/105). To date, 81.0% (85/105) of the aneurysms have been followed up (mean, 17 months) with angiography, disclosing a recanalization in 5.9% (5/85) and an improvement in 42.4% (36/85). At discharge and follow-up, the mRS score was 0 in 83.5% (81/97) of patients, 1 in 4.1% (4/97), 2 in 3.1% (3/97), 3 in 4.1% (4/97), 4 in 3.1% (3/97), and 6 in 2.1% (2/97).

**CONCLUSIONS:** Y and X stent-assisted coiling of complex and wide-neck intracranial bifurcation aneurysms is an effective technique.

**ABBREVIATION:** AcomA = anterior communicating artery

In the past decade, endovascular treatment of intracranial aneurysms became a valid alternative to neurosurgery<sup>1</sup> and is now performed as a first option in many centers. Recently, the treatment of wide-neck intracranial aneurysms with self-expandable intracranial stents has also been reported to be feasible and effective in many clinical series<sup>2-6</sup> at bifurcation sites,<sup>7-9</sup> at the price of an increased risk of thromboembolic and ischemic complications compared with coiling.<sup>10</sup> Unfortunately, endovascular treatment of complex or wide-neck bifurcation aneurysms still remains a challenge for the endovascular surgeon. Different techniques have been proposed, such as balloon and double-balloon remodel-

ing,<sup>11,12</sup> neck bridge,<sup>13</sup> linear stent placement,<sup>14</sup> and waffle-cone<sup>15</sup> techniques. Small series and case reports have described novel stent placement techniques such as “X” and “Y” stent placement to treat complex and wide-neck bifurcation aneurysms, with promising results.<sup>16-23</sup> Recently, the efficacy, feasibility, and long-term durability were described in a large retrospective series.<sup>24</sup> Although several concerns remain regarding stent combinations and the rate of neurologic complications, in our institution since 2006, we have been using this technique with different stent combinations to treat complex and wide-neck bifurcation intracranial aneurysms. Our purpose is to present our experience with double stents in X and Y configurations, with an emphasis on safety, feasibility, and efficacy.

## MATERIALS AND METHODS

### Patient Selection

From June 2006 to June 2013, clinical and angiographic outcomes of consecutive patients treated in a single center with double stents in a Y or X configuration for bifurcation aneurysms were prospectively collected. Patients for whom the preprocedural

Received February 7, 2014; accepted after revision May 4.

From the Department of Interventional and Functional Neuroradiology, Fondation Rothschild Hospital, Paris, France.

Please address correspondence to Bruno Bartolini, MD, Service de Neuroradiologie Interventionnelle et Fonctionnelle, Fondation Ophtalmologique Adolphe de Rothschild, 25-29 rue Manin, 75019, Paris, France; e-mail: bbartolini@fo-rothschild.fr

Indicates article with supplemental on-line table.

<http://dx.doi.org/10.3174/ajnr.A4060>

strategy was to use a stent-assisted coiling technique in a Y or X configuration but which ultimately failed were also included (intention to treat). The wide-neck aneurysms were defined as having a large neck (>4 mm) and/or a fundus-to-neck ratio of <2. The complex aneurysms were defined as having the origin in a branch from the sac or being located at a vascular trifurcation or being multiple at the same bifurcation.

### Endovascular Procedures

Endovascular procedures were performed with the patient under general anesthesia and full anticoagulation with heparin. In addition, all patients with no history of recent subarachnoid hemorrhage were given dual antiplatelet therapy (aspirin, 250 mg, and clopidogrel, 75–150 mg) 2 weeks before the treatment. Patients were kept under dual antiplatelet therapy for 3 months, followed by aspirin daily for 3 months. Platelet-aggregation inhibition has been tested in all patients (VerifyNow P2Y12 assay; Accumetrics, San Diego, California) since 2008. In case of bailout stent placement, an intravenous bolus of 0.25 mg/kg of abciximab (ReoPro) was administered and a continuous intravenous perfusion of 0.125 µg/kg per minute for 12 hours was started immediately after the procedure. Aspirin and clopidogrel were started the day after the treatment. Distal and proximal vessel diameters were taken into consideration in the choice of stent dimension and type. After the deployment of the stents, a flat panel CT (XperCT, Allura series; Philips Healthcare, Best, the Netherlands) was performed. The proximal landing zone of the first stent was chosen at least 10 mm away from the bifurcation, to navigate the second stent with a margin of error. Coiling was performed before and after stent delivery, with or without a jailed catheter. Angiographic images were acquired in anteroposterior, lateral, and working projections before and immediately after the treatment. There were no strict exclusion criteria, but a massive SAH requiring drainage and a low (0%–20%) response to clopidogrel were thought to be contraindications to stent placement.

### Clinical Events

Any clinical events appearing in the postoperative course up to 42 months were noted. A neurologic assessment was performed before the treatment, at discharge (Glasgow Outcome Score and mRS), and at follow-up (mRS).

### Follow-Up Protocol

The standard angiographic follow-up protocol consisted of a first angiographic follow-up performed at 6–12 months after endovascular treatment and a second angiographic follow-up performed 1 year after the first follow-up. A third angiographic follow-up was performed 2 years after the second one.

### Data Collection and Statistical Analysis

Patient age and sex; aneurysm location, size, and rupture status at presentation; degree of aneurysm occlusion; stent type (open-versus closed-cell) and configuration (Y versus X stent placement); and technical and clinical complications in successful and attempted stent placement were noted. A single reader evaluated all the angiograms. Aneurysm occlusion was classified as described by Roy et al.<sup>25</sup>

**Table 1: Summary of demographics and clinical data**

Demographics	No.	%
Sex		
Male	35	36.1
Female	62	63.9
Aneurysm location		
MCA	57	54.2
AcomA	30	28.6
Basilar tip	17	16.2
Carotid termination	1	1.0
Clinical finding		
Incidental discovery	79	75.2
Recurrence	20	19.0
SAH	5	4.8
Compression	1	1.0
Aneurysm size		
Small: 0–10 mm	90	85.7
Large: 10–25 mm	13	12.4
Giant: >25 mm	2	1.9

**Table 2: Summary of aneurysm characteristics**

Aneurysm Size (No.) (%)	Mean ± σ (mm)	Ruptured (No.) (%)	Complex (No.) (%)
Small: 90 (85.7)		5 (5.5)	27 (30.0)
Largest diameter	6.5 ± 2.1		
Neck	5.0 ± 1.3		
Dome/neck	1.1 ± 0.3		
Large: 13 (12.4)		0 (0)	7 (54.0)
Largest diameter	12.7 ± 2.6		
Neck	6.8 ± 2.0		
Dome/neck	1.6 ± 0.7		
Giant: 2 (1.9)		0 (0)	0 (0)
Largest diameter	28.3 ± 3.9		
Neck	5.5 ± 1.1		
Dome/neck	2.3 ± 1.7		

## RESULTS

### Population

One hundred five aneurysms were treated in 97 patients (age, 28–86 years; mean, 54 years) during 100 procedures. MCA bifurcation aneurysms were 54.2% (57/105), anterior communicating artery (AcomA) aneurysms were 28.6% (30/105), basilar tip aneurysms were 16.2% (17/105), and carotid termination aneurysm was 1.0% (1/105). Clinical presentations were the following: incidental discovery in 75.2% (79/105), compression in 1.0% (1/105), angiographic recurrences of previously coiled aneurysms in 19.0% (20/105), and SAH in 4.8% (5/105). A Y stent placement was used to treat 87 aneurysms in 85 procedures; an X stent placement was used to treat 7 aneurysms in 6 procedures, while 9 procedures failed for 11 aneurysms. Of 91 successful procedures, stents were delivered after coiling in 5.5% (5/91), including a subgroup of 2 bailout stent placements to prevent parent vessel occlusion, and before coiling in 93.4% (85/91). In 1.1% (1/91), no coils were delivered. Demographics and clinical data are detailed in Table 1. Aneurysm characteristics are detailed in Table 2. Stent types and configurations are detailed in Table 3.

### Attempted Stent Placement

We failed to perform a stent-assisted procedure in Y or X fashion in 9 cases as described in Table 4.

## Stent-Related Technical Complications in Successful

### Stent Placement

We encountered 5 asymptomatic technical complications. In 1 procedure, we broke the proximal module of the first stent. In 2 cases, we partially dislocated the proximal end of the first stent with the microcatheter; and in another procedure, we partially unraveled the last coil and secured it with an Enterprise stent (Codman & Shurtleff, Raynham, Massachusetts) in the second segment of the vertebral artery. In the last case, after deployment of the 2 stents, a coil protruded between the stent and the parent artery wall with a reduction of distal outflow. The flow was re-established with a balloon angioplasty inside the stent.

### Clinical Complications

There were 19 procedure-related neurologic complications; 84.2% (16/19) were perioperative (within 30 days), while 15.8% (3/19) were delayed (after 30 days). Complications associated with transitory (<24 hours) or reversible (<7 days) neurologic deficits were encountered in 8.0% (8/100) of the procedures, while permanent neurologic deficits were noted in 10.0% (10/100) of the procedures. The mortality rate was 1.0% (1/100), a Y stent-assisted coiling of an unruptured AcomA aneurysm; this patient had a hyper-response to clopidogrel (81%), was discharged at day 5 asymptomatic, and was re-admitted at day 12 with a mild left hemiparesis. Brain CT found a frontal intraparenchymal hematoma. Aspirin was stopped, but he presented with hemiplegia at day 20 secondary to an increase of the hematoma and an intraventricular hemorrhage. The level of consciousness

deteriorated; therefore, the patient was sedated and intubated and an external ventricular drain was placed. The patient died at day 28; brain CT showed a larger hematoma with a severe midline shift. Neurologic complications are detailed in the On-line Table.

### Bailout Stent Placement

In 2 cases, stents were delivered after thromboembolic events related to coil protrusion. The first patient presented with a ruptured basilar tip aneurysm, treated primarily with double-balloon remodeling. The second patient presented with an unruptured right MCA aneurysm treated with simple coiling.

### Immediate Angiographic Results

The immediate angiographic controls showed a complete occlusion in 47.6% (50/105) of the aneurysms, a neck remnant in 17.1% (18/105), and a sac remnant in 35.2% (37/105).

### Angiographic Follow-Up

To date, 81.0% (85/105) of the aneurysms have been followed up (mean, 17 months) with angiography. Of 50 initially occluded aneurysms, so far we have controlled 41 (82.0%) aneurysms, disclosing a neck recurrence in 1 case. Of 18 aneurysms with neck remnants, so far we have controlled 13 (72.2%) aneurysms, disclosing, in 10 cases, complete occlusions; in 1 case, a neck remnant; and in 2 cases, sac recurrences. Of 37 aneurysms with sac remnants, we have controlled, so far, 31 (83.8%) aneurysms, disclosing a complete occlusion in 23 aneurysms, a neck remnant in 4, and a sac remnant in 4. Overall, in 81.0% (85/105) of aneurysms controlled, follow-up disclosed complete occlusion in 85.8% (73/85), neck remnant in 7.1% (6/85), and sac remnant in 7.1% (6/85). We performed 2 retreatments. No aneurysm bled or rebled during the follow-up period. We observed 1 asymptomatic occlusion of the 2 stents in a Y configuration at the first follow-up and 4 cases of asymptomatic in-stent stenosis at the first follow-up. In 1 case, in a partially thrombosed aneurysm, the neck was excluded but there was late contrast enhancement of the aneurysmal wall.

### Clinical Follow-Up

On clinical follow-up, the modified Rankin Scale score was 0 in 83.5% (81/97) of the patients; 1 in 4.1% (4/97); 2 in 3.1% (3/97); 3 in 4.1% (4/97); 4 in 3.1% (3/97); and 6 in 2.1% (2/97).

**Table 3: Summary of stent types and configurations in successful treatments**

	Y	X
Neuroform <sup>a</sup> + Neuroform	47	3
Neuroform + Enterprise <sup>b</sup>	27	2
Enterprise + Enterprise	4	1
Neuroform + Solitaire AB <sup>c</sup>	2	–
LVIS <sup>d</sup> + LVIS	1	–
LVIS Jr <sup>d</sup> + LVIS Jr	3	–
Neuroform + Baby LEO <sup>e</sup>	1	–

<sup>a</sup> Stryker Neurovascular, Fremont, California.

<sup>b</sup> Cordis Neurovascular, Miami, Florida.

<sup>c</sup> Covidien, Irvine, California.

<sup>d</sup> MicroVention, Tustin, California.

<sup>e</sup> Balt Extrusion, Montmorency, France.

**Table 4: Summary of attempted stenting**

Age (yr), Sex	Aneurysm Location	Aneurysms Treated during the Procedure	Stents	Event	Final Result	F/U	mRS Score
50, F	MCA	1	0	Sac perforation with the guidewire	C	–	0
62, F	MCA	1	0	Sac perforation with the microdelivery stent system and exchange guidewire	A	–	4
70, F	MCA	2	1	First stent was delivered too distally, with the proximal end covering the neck; impossible to navigate the microcatheter in the second branch	C, C	B, B	0
38, M	AcomA	1	1	Guidewire tip broke in the parent vessel and a single stent was delivered due to the impossibility of navigating the microcatheter in the second branch	C	A	0
48, F	MCA	1	2	First stent was delivered too distally, no overlapping	C	C	0
30, F	AcomA	1	2	First stent was delivered too distally, no overlapping	B	A	0
86, F	BA	1	2	First stent fell into aneurysmal sac, no overlapping	C	C	2
51, F	CT	1	2	First stent fell into aneurysmal sac, no overlapping	C	–	0
58, F	AcomA	2	2	Second stent was deployed inside the first one (coaxial)	C, C	C, C	0

**Note:**—F/U indicates follow-up; BA, basilar artery; CT, carotid termination; A, complete occlusion; B, neck remnant; C, sac remnant.

## DISCUSSION

Complex and wide-neck bifurcation aneurysms that incorporate  $\geq 2$  parent vessels are rarely treated with a single stent, due to the risk of coil prolapse and parent vessel occlusion. Different techniques have been proposed to obviate this problem. Balloon remodeling and double-balloon remodeling were the first endovascular techniques used to treat wide-neck aneurysms.<sup>11,12</sup> Safety and efficacy are similar to those in standard coiling,<sup>26</sup> and the immediate occlusion rate in ruptured aneurysms is higher than that in standard coiling.<sup>27</sup> These techniques are effective for the treatment of aneurysms in the setting of SAH, to minimize the risk of early rebleeding even if total aneurysm occlusion is not obtained. Unfortunately, this technique does not provide an arterial reconstruction, and long-term follow-up showed a recurrence rate similar to that in standard coiling, in particular for wide-neck and large aneurysms.<sup>2</sup>

Crossover stent placement for basilar tip and AcomA aneurysms has been illustrated in few publications. Kelly et al<sup>28</sup> described this technique in bifurcation aneurysms with unfavorable distal limb configuration. For the authors, this technique, compared with Y stent placement, offered a better coverage of the aneurysmal neck and limited the use of multiple stents, decreasing the risk of thrombogenicity. Nevertheless, this technique cannot be used with MCA aneurysms and in AcomA and basilar tip aneurysms when the circle of Willis is incomplete.

The waffle-cone technique has been described in small series<sup>15,29</sup> as a valid alternative to Y and X stent placement when the latter cannot be performed due to an unfavorable distal limb configuration. In this case, the distal part of the stent is placed inside the aneurysmal sac and the blood flow is direct into the aneurysmal sac. This technique is technically easier than Y stent placement but probably presents a higher risk of coil protrusion due to the incomplete neck coverage. The major drawback is the risk of recurrence due to the redirection of the flow inside the aneurysm.

In our single-center retrospective series, all cases of unruptured aneurysms were previously discussed during our interventional meetings. We treated most small aneurysms (85.7%) that we considered suitable for Y or X stent-assisted coiling. We could have treated some with single stent-assisted coiling for wide-neck aneurysms or with a flow diverter for complex aneurysms, but during the discussion, we finally decided to perform Y or X stent-assisted coiling. Concerning the indication to treat this subgroup of aneurysms, 17/90 (18.9%) were recurrences and 33/90 (36.7%) were in patients with multiple intracranial aneurysms with or without a previous history of SAH.

In our series, stent placement was performed before coiling in most cases, to scaffold the aneurysmal neck and reduce the risk of coil protrusion. We used different stent combinations, always overlapping. In most of our cases, an open-cell stent was deployed as a first stent in the smaller and more acute vascular branch. This stent, compared with closed-cell-design stents, presented 2 advantages, a better vessel conformability in acute curvature and an outward prolapse of the struts at the convexity.<sup>30</sup> A better conformability reduces the risk of thromboembolic events<sup>31</sup>; the outward prolapse improves neck coverage and should reduce friction during the deployment of the second stent. The second stent, open- or closed-cell, was delivered in the larger and less angulated

vascular branch. We used flat panel CT to evaluate stent apposition. Recently, Cho et al,<sup>32</sup> described a nonoverlapping Y stent placement technique in wide-neck basilar tip aneurysms with the Enterprise stent, advising that this technique presents the advantages of both open and closed stents together. Cekirge et al<sup>21</sup> described an overlapping Y stent placement technique by using 2 closed-cell-design stents without endosaccular coiling; they preferred this combination of stents because it is easier to deliver and deploy but also seems more likely to provide superior modification on aneurysm hemodynamic parameters. However, 2 closed stents in overlapping configuration, in particular in an acute curvature, may lead to inappropriate vessel wall apposition and to higher thrombogenicity. Furthermore, there is a high risk of kinking of the second stent and, therefore, minor scaffolding at the neck.

Technical problems were previously encountered, but in our series the friction between the stents was not a major matter. Our major problem was the navigation of the microcatheter in the most angulated branch. To obviate this matter, we always used a triaxial access to improve proximal support, and in few cases, we turned the microguidewire inside the aneurysmal sac with a higher risk of perforation. Another difficulty was to achieve a correct proximal position of the first stent to avoid its displacement during the navigation of the microcatheter in the second branch. A proper length selection of the first stent of at least 20 mm is necessary to cover the neck completely and to stabilize the stent, in particular in MCA and AcomA aneurysms. However in these locations, the proximal part of the first stent must not land in the terminal carotid artery; otherwise catheterization of the second branch becomes more difficult to achieve.

In our series, including successful and attempted stent placements, we observed a relatively high rate of complications, with a mortality rate of 1.0% and permanent neurologic morbidity of 10.0%. The comparison of complications across reported series is difficult due to the limited number of procedures performed with Y and X stent placement in other series. Recently, a larger retrospective multicenter series,<sup>23</sup> with ruptured and unruptured aneurysms, reported a good outcome (mRS 0–2) in 93% of the patients. In this series, most were basilar tip aneurysms (87%), a location where the navigation and the deployment of stents are easier due to favorable distal limb configuration. In a large retrospective series<sup>24</sup> consisting of 193 bifurcation aneurysms, by using mostly closed-cell stents, the authors reported a low rate of permanent morbidity (1.1%) and mortality (0.5%). Although we also applied a strict antiaggregation protocol and checked 1 week before the procedure, our hemorrhagic and ischemic complications led to a higher rate of permanent morbidity.

Our immediate angiographic complete occlusion rate was quite low, as previously reported<sup>2,3,6,33</sup> in stent-assisted coiling. The procedure was performed with the patient under heparin, clopidogrel, and aspirin; therefore, thrombus formation was slow and achieving attenuated packing, in particular at the neck, was quite difficult due to the immobility of the microcatheter. Nevertheless, Chalouhi et al<sup>34</sup> suggested that a moderate packing attenuation seems to be effective in stent-assisted coiling to achieve complete occlusion. At angiographic follow-up, we observed an improvement in 42.4% (36/85) of the aneurysms. This progres-

sive thrombosis was reported in many stent-assisted coiling series,<sup>2,6,33</sup> probably due to antiplatelet discontinuity and “intimal overgrowth” at the neck. Cekirge et al<sup>21</sup> also described a “flow remodeling effect” in aneurysms treated by Y closed-cell stent placement, which showed promising results in their retrospective series consisting of 193 bifurcation aneurysms, with a recanalization rate of 2.2%.<sup>24</sup>

## CONCLUSIONS

Y and X stent-assisted coiling of complex and wide-neck intracranial bifurcation aneurysms is an effective technique, leading to long-term stability of aneurysm occlusion. Nevertheless, we encountered a higher rate of technical failures and clinical complications compared with those of other endovascular techniques, such as single stent-assisted coiling or balloon-assisted coiling. Our results concerning safety and feasibility show the limits of this technique, in particular for AcomA and MCA aneurysms. We learned from our experience to apply more rigorous criteria for the selection of suitable patients. Advances in stent design and newer antiplatelet drugs may improve the feasibility and the safety in the future.

Disclosures: Bruno Bartolini—RELATED: Support for Travel to Meetings for the Study or Other Purposes: MicroVention,\* Comments, flight, Paris to San Diego (round-trip), International Stroke Conference 2014; UNRELATED: Consultancy: ev3/Covidien,\* Stryker,\* MicroVention.\* Raphael Blanc—UNRELATED: Consultancy: Balt,\* Covidien,\* Stryker,\* MicroVention,\* Penumbra.\* Silvia Pistocchi—UNRELATED: Consultancy: Covidien/ev3,\* Stryker,\* MicroVention.\* Michel Piotin—UNRELATED: Consultancy: Stryker,\* MicroVention,\* Covidien,\* Balt\*; Payment for Development of Educational Presentations: Stryker, MicroVention, Covidien, Balt. \*Money paid to the institution.

## REFERENCES

- Molyneux A. International Subarachnoid Aneurysm Trial (ISAT) of neurosurgical clipping versus endovascular coiling in 2143 patients with ruptured intracranial aneurysms: a randomised trial. *Lancet* 2002;360:1267–74
- Piotin M, Blanc R, Spelle L, et al. Stent-assisted coiling of intracranial aneurysms: clinical and angiographic results in 216 consecutive aneurysms. *Stroke* 2010;41:110–15
- Biondi A, Janardhan V, Katz JM, et al. Neuroform stent-assisted coil embolization of wide-neck intracranial aneurysms: strategies in stent deployment and midterm follow-up. *Neurosurgery* 2007;61:460–68, discussion 468–69
- Akpek S, Arat A, Morsi H, et al. Self-expandable stent-assisted coiling of wide-necked intracranial aneurysms: a single-center experience. *AJNR Am J Neuroradiol* 2005;26:1223–31
- Higashida RT, Halbach VV, Dowd CF, et al. Initial clinical experience with a new self-expanding nitinol stent for the treatment of intracranial cerebral aneurysms: the Cordis Enterprise stent. *AJNR Am J Neuroradiol* 2005;26:1751–56
- Fiorella D, Albuquerque FC, Deshmukh VR, et al. Usefulness of the Neuroform stent for the treatment of cerebral aneurysms: results at initial (3–6 mo) follow-up. *Neurosurgery* 2005;56:1191–201, discussion 1201–02
- Vendrell JF, Costalat V, Brunel H, et al. Stent-assisted coiling of complex middle cerebral artery aneurysms: initial and midterm results. *AJNR Am J Neuroradiol* 2011;32:259–63
- Yang P, Liu J, Huang Q, et al. Endovascular treatment of wide-neck middle cerebral artery aneurysms with stents: a review of 16 cases. *AJNR Am J Neuroradiol* 2010;31:940–46
- Huang Q, Xu Y, Hong B, et al. Stent-assisted embolization of wide-neck anterior communicating artery aneurysms: review of 21 consecutive cases. *AJNR Am J Neuroradiol* 2009;30:1502–06

- Shapiro M, Becske T, Sahlein D, et al. Stent-supported aneurysm coiling: a literature survey of treatment and follow-up. *AJNR Am J Neuroradiol* 2012;33:159–63
- Moret J, Cognard C, Weill A, et al. Reconstruction technic in the treatment of wide-neck intracranial aneurysms: long-term angiographic and clinical results—apropos of 56 cases [in French]. *J Neuroradiol* 1997;24:30–44
- Takahashi A. Letter to the editor: neck plastic intra-aneurysmal GDC embolisation with double protective balloons—method of multiple guiding catheter introduction. *Interv Neuroradiol* 1998;4:177–79
- Raymond J, Guilbert F, Roy D. Neck-bridge device for endovascular treatment of wide-neck bifurcation aneurysms: initial experience. *Radiology* 2001;221:318–26
- Lubicz B. Linear stent-assisted coiling: another way to treat very wide-necked intracranial aneurysms. *Neuroradiology* 2011;53:457–59
- Horowitz M, Levy E, Sauvageau E, et al. Intra/extra-aneurysmal stent placement for management of complex and wide-necked-bifurcation aneurysms: eight cases using the waffle cone technique. *Neurosurgery* 2006;58:ONS-258–62, discussion ONS-262
- Chow MM, Woo HH, Masaryk TJ, et al. A novel endovascular treatment of a wide-necked basilar apex aneurysm by using a Y-configuration, double-stent technique. *AJNR Am J Neuroradiol* 2004;25:509–12
- Sani S, Lopes DK. Treatment of a middle cerebral artery bifurcation aneurysm using a double Neuroform stent “Y” configuration and coil embolization: technical case report. *Neurosurgery* 2005;57:E209
- Thorell WE, Chow MM, Woo HH, et al. Y-configured dual intracranial stent-assisted coil embolization for the treatment of wide-necked basilar tip aneurysms. *Neurosurgery* 2005;56:1035–40, discussion 1035–40
- Lozen A, Manjila S, Rhiew R, et al. Y-stent-assisted coil embolization for the management of unruptured cerebral aneurysms: report of six cases. *Acta Neurochir (Wien)* 2009;151:1663–72
- Rohde S, Bendszus M, Hartmann M, et al. Treatment of a wide-necked aneurysm of the anterior cerebral artery using two Enterprise stents in “Y” configuration stenting technique and coil embolization: a technical note. *Neuroradiology* 2010;52:231–35
- Cekirge HS, Yavuz K, Geyik S, et al. A novel “Y” stent flow diversion technique for the endovascular treatment of bifurcation aneurysms without endosaccular coiling. *AJNR Am J Neuroradiol* 2011;32:1262–68
- Zhao KJ, Yang PF, Huang QH, et al. Y-configuration stent placement (crossing and kissing) for endovascular treatment of wide-neck cerebral aneurysms located at 4 different bifurcation sites. *AJNR Am J Neuroradiol* 2012;33:1310–16
- Fargen KM, Mocco J, Neal D, et al. A multicenter study of stent-assisted coiling of cerebral aneurysms using a Y configuration. *Neurosurgery* 2013;73:466–72
- Yavuz K, Geyik S, Cekirge S, et al. Double stent-assisted coil embolization treatment for bifurcation aneurysms: immediate treatment results and long-term angiographic outcome. *AJNR Am J Neuroradiol* 2013;34:1778–84
- Roy D, Milot G, Raymond J. Endovascular treatment of unruptured aneurysms. *Stroke* 2001;32:1998–2004
- Pierot L, Cognard C, Spelle L, et al. Safety and efficacy of balloon remodeling technique during endovascular treatment of intracranial aneurysms: critical review of the literature. *AJNR Am J Neuroradiol* 2012;33:12–15
- Pierot L, Cognard C, Anxionnat R, et al. Remodeling technique for endovascular treatment of ruptured intracranial aneurysms had a higher rate of adequate postoperative occlusion than did conventional coil embolization with comparable safety. *Radiology* 2011;258:546–53
- Kelly ME, Turner R, Gonugunta V, et al. Stent reconstruction of wide-necked aneurysms across the circle of Willis. *Neurosurgery* 2007;61:249–54, discussion 254–55
- Sychra V, Klisch J, Werner M, et al. Waffle-cone technique with

- Solitaire AB remodeling device: endovascular treatment of highly selected complex cerebral aneurysms.** *Neuroradiology* 2011;53:961–72
30. Ebrahimi N, Claus B, Lee CY, et al. **Stent conformity in curved vascular models with simulated aneurysm necks using flat-panel CT: an in vitro study.** *AJNR Am J Neuroradiol* 2007;28:823–29
31. Heller RS, Miele WR, Do-Dai DD, et al. **Crescent sign on magnetic resonance angiography revealing incomplete stent apposition: correlation with diffusion-weighted changes in stent-mediated coil embolization of aneurysms.** *J Neurosurg* 2011;115:624–32
32. Cho YD, Park SW, Lee JY, et al. **Nonoverlapping Y-configuration stenting technique with dual closed-cell stents in wide-neck basilar tip aneurysms.** *Neurosurgery* 2012;70:244–49
33. Maldonado IL, Machi P, Costalat V, et al. **Neuroform stent-assisted coiling of unruptured intracranial aneurysms: short- and midterm results from a single-center experience with 68 patients.** *AJNR Am J Neuroradiol* 2011;32:131–36
34. Chalouhi N, Dumont AS, Hasan D, et al. **Is packing density important in stent-assisted coiling?** *Neurosurgery* 2012;71:381–86, discussion 386–87

# Cerebral Aneurysm Pulsation: Do Iterative Reconstruction Methods Improve Measurement Accuracy In Vivo?

T. Illies, D. Säring, M. Kinoshita, T. Fujinaka, M. Bester, J. Fiehler, N. Tomiyama, and Y. Watanabe

## ABSTRACT

**BACKGROUND AND PURPOSE:** Electrocardiogram-gated 4D-CTA is a promising technique allowing new insight into aneurysm pathophysiology and possibly improving risk prediction of cerebral aneurysms. Due to the extremely small pulsational excursions (<0.1 mm in diameter), exact segmentation of the aneurysms is of critical importance. In vitro examinations have shown improvement of the accuracy of vessel delineation by iterative reconstruction methods. We hypothesized that this improvement shows a measurable effect on aneurysm pulsations in vivo.

**MATERIALS AND METHODS:** Ten patients with cerebral aneurysms underwent 4D-CTA. Images were reconstructed with filtered back-projection and iterative reconstruction. The following parameters were compared between both groups: image noise, absolute aneurysm volumes, pulsatility, and sharpness of aneurysm edges.

**RESULTS:** In iterative reconstruction images, noise was significantly reduced (mean,  $9.8 \pm 4.0$  Hounsfield units versus  $8.0 \pm 2.5$  Hounsfield units;  $P = .04$ ), but the sharpness of aneurysm edges just missed statistical significance (mean,  $3.50 \pm 0.49$  mm versus  $3.42 \pm 0.49$  mm;  $P = .06$ ). Absolute volumes (mean,  $456.1 \pm 775.2$  mm<sup>3</sup> versus  $461.7 \pm 789.9$  mm<sup>3</sup>;  $P = .31$ ) and pulsatility (mean,  $1.099 \pm 0.088$  mm<sup>3</sup> versus  $1.095 \pm 0.082$  mm<sup>3</sup>;  $P = .62$ ) did not show a significant difference between iterative reconstruction and filtered back-projection images.

**CONCLUSIONS:** CT images reconstructed with iterative reconstruction methods show a tendency toward shorter vessel edges but do not affect absolute aneurysm volumes or pulsatility measurements in vivo.

**ABBREVIATIONS:** AIDR = adaptive iterative dose reduction; IR = iterative reconstruction; FBP = filtered back-projection; HU = Hounsfield units

Electrocardiogram-gated 4D-CT angiography has been used to analyze the pulsation of cerebral aneurysms.<sup>1-7</sup> Insight into aneurysm pathophysiology and improvement of risk prediction of incidental cerebral aneurysms can be expected. The technique is limited by the small pulsational excursions of cerebral aneurysms. If one considers a volume change of 5% within the cardiac cycle, the change in diameter of a spherical aneurysm of 5 mm diameter is on the order of 0.1 mm,<sup>1,2</sup> which is below the resolution of CTA. Exact segmentation of the aneurysm is, therefore, critical and of the utmost importance for the correct analysis of pulsations.

In vitro experiments with vascular models have shown that vessel delineation depends on various factors, including intraluminal contrast attenuation, vascular wall thickness, post-processing, and reconstruction methods.<sup>8</sup> Iterative reconstruction (IR) algorithms have gained importance in clinical routine CT because the radiation dose can be reduced significantly while image quality is maintained compared with filtered back-projection (FBP) reconstruction. At a constant radiation dose, IR reduces image blur, enhances edges, and increases image resolution.<sup>8-10</sup> Depiction of vessels in the posterior fossa and the spinal canal<sup>11,12</sup> is improved in vivo. Moreover, in vitro studies reveal improvement of the accuracy of quantitative measurement of vessel diameters.<sup>8</sup>

These findings and its overall characteristics make IR an interesting tool for improving the accuracy of pulsation measurements of cerebral aneurysms. To our knowledge, the influence of IR on vessel-volume measurement, especially in 4D-CTA, has not been examined in vivo. We hypothesized that IR methods have a measurable effect on the accuracy of quantification of cerebral aneurysm pulsation in vivo.

Received January 21, 2014; accepted after revision April 14.

From the Departments of Diagnostic and Interventional Neuroradiology (T.I., M.B., J.F.) and Medical Informatics (D.S.), University Medical Center Hamburg-Eppendorf, Hamburg, Germany; and Departments of Neurosurgery (M.K., T.F.) and Radiology (N.T., Y.W.), Osaka University Graduate School of Medicine, Osaka, Japan.

This work was supported by a grant of the Japanese German Radiology Affiliation.

Please address correspondence to Till Illies, MD, Department of Diagnostic and Interventional Neuroradiology, University Medical Center Hamburg-Eppendorf, Martinistr 52, 20355 Hamburg, Germany; e-mail: tillies@uke.de

<http://dx.doi.org/10.3174/ajnr.A4000>

## MATERIALS AND METHODS

### Patients

Ten patients with unruptured cerebral aneurysms underwent 4D-CTA. Four aneurysms were located at the internal carotid artery; 4, at the middle cerebral artery; 1, at the anterior communicating artery; and 1, at the anterior cerebral artery. The local ethics committee approved the use of the clinical data for research and waived the requirement for written informed consent from patients. Patient data are listed in the Table.

### 4D-CTA Acquisition

Retrospectively electrocardiogram-gated CTA was performed on a 320-detector row Aquilion ONE CT scanner (Toshiba Medical Systems, Tokyo, Japan). We used the following parameters: 120-kV tube voltage, 270-mA tube current, 350-ms gantry rotation time, 140-mm z-coverage. Contrast medium (ioversol, Optiray 320 mg I/mL; Covidien Japan, Tokyo, Japan) was injected at 5 mL/s. Timing for the image acquisition was determined with a test injection of 15 mL of contrast medium. For CTA, 50 mL of contrast medium was injected followed by a saline flush. 4D-CTAs were reconstructed with half reconstruction by using FBP and a kernel optimized for intracranial vessel imaging and IR

algorithm (adaptive iterative dose reduction [AIDR] 3D) with 10 steps of each 10% of the R-R interval,  $512 \times 512$  image matrix, 0.5-mm section thickness, and  $0.39 \times 0.39$  mm in-plane resolution.

### Postprocessing

We used an in-house-developed software as well as ImageJ software (National Institutes of Health, Bethesda, Maryland) and MeVisLab (MeVis Medical Solutions, Bremen, Germany) for volume measurement, and R (<http://www.r-project.org/>) and R Studio 0.97 (<http://rstudio.org/download/desktop>) for statistical analysis.

### Noise

Mean and SDs were calculated from circular ROIs in air ( $400 \text{ mm}^2$ ), brain tissue ( $200 \text{ mm}^2$ ), and the aneurysm on transversal sections in all phases in FBP and AIDR images. The SDs of the densities within the ROIs were averaged over all timeframes, and their means and SDs were compared between the FBP and AIDR images with *t* tests as a measure of objective image noise.

### Edge Sharpness

For each aneurysm, 1 attenuation profile along a line passing through its center was acquired on axial images. Measurement points were interpolated by using cubic splines. The width of the edge response of the aneurysm wall was defined as the distance between points corresponding to 10% and 90% of the maximum intra-aneurysmal attenuation on the border of the aneurysms. A shorter edge response corresponds to a sharper edge representation. Edge responses were compared between FBP and IR groups (Fig 1).

### Absolute Volumes and Pulsatility

Datasets were loaded into an in-house-developed postprocessing software. Perivascular tissue was removed with a thresholded segmentation (160–

### Patient characteristics

Patient No.	Age (yr)	Location (Artery)	Volume (mm <sup>3</sup> ) <sup>a</sup>		Diameter (mm) <sup>b</sup>
			AIDR	FBP	
1	53	MCA	2336.4	2386.0	16.7
2	66	AcomA	95.1	95.7	6.1
3	55	ICA	69.1	72.9	5.7
4	70	MCA	15.3	15.4	3.9
5	50	ICA	1352.5	1361.7	15.1
6	69	ACA	67.4	67.3	4.3
7	61	ICA	76.7	77.2	5.9
8	76	MCA	58.6	59.2	5.7
9	50	ICA	408.8	407.1	10.7
10	68	MCA	82.2	74.4	7.1

**Note:**—AcomA indicates anterior communicating artery; ACA, anterior cerebral artery.

<sup>a</sup> For volume measurement, a 3D model of the vasculature was created and the aneurysms were interactively segmented (see “Material and Methods” section).

<sup>b</sup> The aneurysm diameter is the maximum value of the axial, coronal, or sagittal aneurysm diameter.

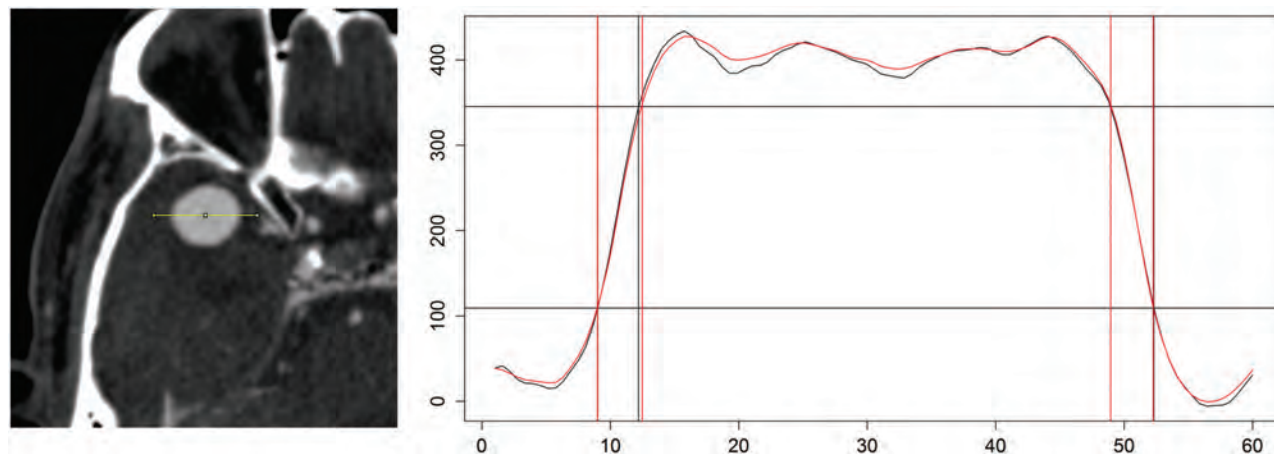


**FIG 1.** Creation of a line profile across the aneurysms for calculations of edge lengths. The left side shows a right middle cerebral artery aneurysm. A linear region of interest is positioned through the center of the aneurysm. The right side shows a cubic spline function fitted to the measurements for FBP (black) and AIDR (red). Edges are defined as the distance between the 10% and 90% interval of the maximum intra-aneurysmal attenuation (*horizontal black lines*).

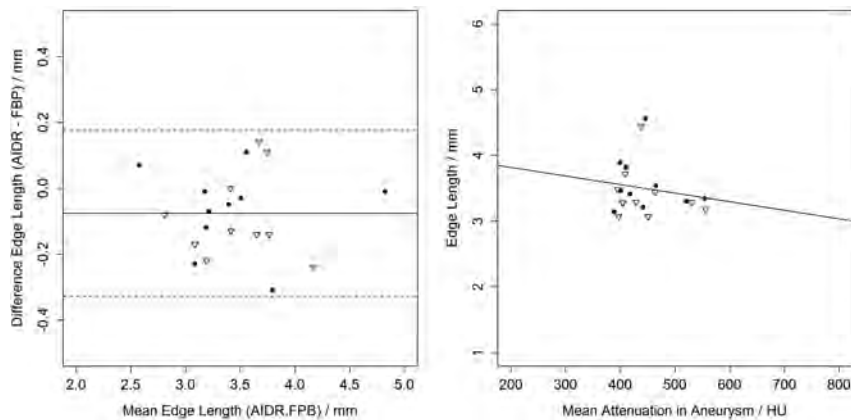


**FIG 2.** Edge lengths compared between AIDR and FBP and edge length compared with intra-aneurysmal attenuation (*triangles*, left side; *dots*, right side). On the left side, a Bland-Altman plot shows a small bias of shorter edges in AIDR images. The right side shows the plot and regression line of edge length and intra-aneurysmal attenuation ( $P = .45$ ).

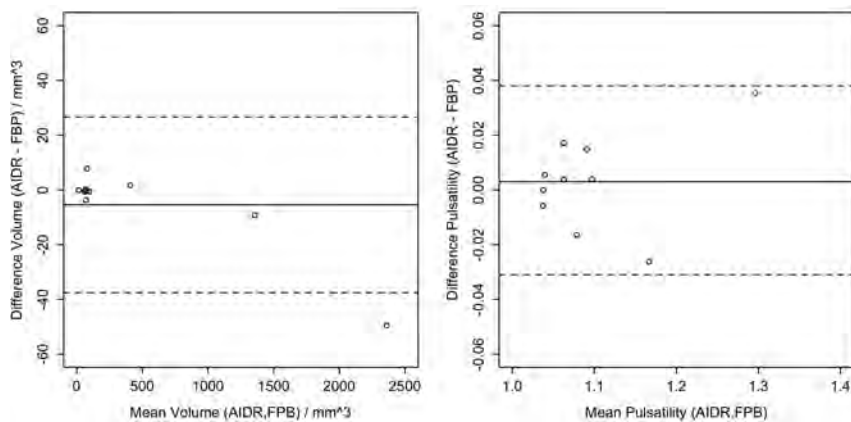


**FIG 3.** Bland-Altman plots of absolute volumes and pulsatility. Left side shows a small bias, with a tendency toward smaller absolute volumes in AIDR images. On the right side, there are no differences in pulsatility between the aneurysms in AIDR and FBP images.

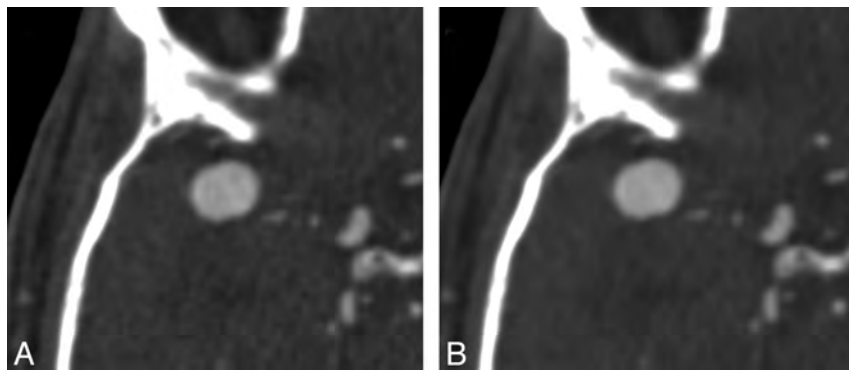


**FIG 4.** Aneurysm of the right middle cerebral artery in a 53-year-old patient (patient 1). CT angiography of the 2 reconstruction methods; acquisition parameters are the same. A, Filtered back-projection. B, Image reconstruction with adaptive iterative dose reduction. Note the smoother appearance of the image, consistent with reduced image noise.

890 Hounsfield units [HU]). On the basis of the segmentation of the aneurysm and the attached vessel system, a single surface model was generated by using the marching cube algorithm. To separate the aneurysm structure from the vessels, the observer manually selected a number of points representing the cutting line at the

time point zero. This initial cutting line was transferred automatically to all other time points by using an iterative closest-point approach, to reduce interaction time. Now, the surface model of the aneurysm for each time point was generated on the basis of the transferred cutting lines. For analysis, the absolute volumes and maximum and minimum volumes of the aneurysm surface model within the cardiac cycle were calculated and compared between both groups. Pulsatility was calculated as the ratio of maximum and minimum volumes and was compared between both groups.

## RESULTS

### Noise

In ROIs placed in the air, mean intensity values were  $-1040.2 \pm 22.2$  HU versus  $-1040.6 \pm 22.1$  HU ( $P = .97$ ) and SDs were  $9.8 \pm 4.0$  HU versus  $8.0 \pm 2.5$  HU ( $P = .04$ ) (FBP versus AIDR). In brain parenchyma, the means were  $53.7 \pm 5.0$  HU versus  $53.9 \pm 4.8$  HU ( $P = .91$ ) and the SDs were  $15.0 \pm 3.5$  HU versus  $11.9 \pm 1.9$  HU ( $P = .03$ ) (FBP versus AIDR); and in aneurysms, the means were  $433.0 \pm 136.1$  HU versus  $427.0 \pm 132.6$  HU ( $P = .89$ ) and the SDs were  $20.3 \pm 7.4$  HU versus  $14.6 \pm 5.2$  HU ( $P < .001$ ) (FBP versus AIDR).

### Edge Sharpness

Mean edge length was  $3.50 \pm 0.49$  mm versus  $3.42 \pm 0.49$  mm (FBP versus AIDR). Bland-Altman analysis revealed a bias of  $-0.08$  mm (AIDR-FBP,  $P = .06$ , paired  $t$  test) and limits of agreement between  $-0.32$  and  $0.19$  mm. Edge sharpness did not correlate significantly with intraluminal attenuation ( $P = .45$ ,  $r^2 = 0.032$ ) (Fig 2).

### Absolute Volumes

Mean aneurysm size was  $461.7 \pm 789.9$  mm<sup>3</sup> versus  $456.1 \pm 775.2$  mm<sup>3</sup> (FBP versus AIDR). Bland-Altman analysis revealed a bias of  $-5.6$  mm<sup>3</sup> (AIDR-FBP,  $P = .31$ , paired  $t$  test) and limits of agreement of  $-37.6$  and  $26.6$  mm<sup>3</sup> for mean volumes (Fig 3).

### Pulsatility

Mean pulsatility was  $1.095 \pm 0.082$  mm<sup>3</sup> versus  $1.099 \pm 0.088$  mm<sup>3</sup> (FBP versus AIDR), and Bland-Altman analysis revealed a bias of  $0.003$  (AIDR-FBP,  $P = .62$ , paired  $t$  test), with limits of agreement between  $-0.03$  and  $0.04$  (Fig 4).

## DISCUSSION

Analysis of the pulsations of cerebral aneurysms could improve the understanding of mechanisms involved in their enlargement and rupture and increase the accuracy of risk prediction of unruptured aneurysms. Previous studies found volume changes of cerebral aneurysms within the cardiac cycle of approximately 5%.<sup>1</sup> These pulsations did not differ significantly from those of normal cerebral arteries but showed a tendency toward larger values. Due to the small excursions of the aneurysm wall, pulsation analysis is technically challenging and improving its accuracy is demanding. IR methods have been shown to improve measurement precision of vessel diameter in a phantom study, a finding from which aneurysm pulsation analysis could benefit. We compared pulsations of 10 cerebral aneurysms from FBP and AIDR reconstructed datasets to analyze the effect size in vivo. No significant changes were observed in absolute aneurysm volumes and pulsations between images reconstructed with IR and AIDR. However, vessel sharpness, one of AIDR's characteristics for improving measurement accuracy, was increased, a finding that just missed statistical significance.

The aforementioned phantom study investigated the influence of wall thickness, intraluminal attenuation, and the reconstruction method on diameter measurement. In our study, the wall thicknesses of aneurysms were essentially unknown but could be estimated by the results of previous reports. In a pathologically based study, the wall thickness was found to be 0.25 mm for 10-mm<sup>13</sup> aneurysms, and an MR imaging-based study found a wall size of 0.6 mm.<sup>14</sup> Mean intra-aneurysmal attenuation was 430 HU, ranging from 223 to 555 HU for the aneurysms, due to the capture of the bolus in first-pass 4D-CTA. Of the 9 groups in the phantom study, for the one comparable to our samples with respect to wall thickness (0.5 mm) and intraluminal attenuation (396 HU), a difference in diameter measurement between FBP and IR images could not be proved. While vessel diameters were overestimated with both reconstruction methods, IR reduced measurement errors significantly in larger-diameter vessels and with higher intraluminal attenuation. Our findings in humans reflect these results by showing smaller volumes in all aneurysms in the AIDR group. However, this finding did not reach a statistically significant level. For a small effect size as found in our study, a much larger sample size is needed to achieve sufficient statistical power.

The effect of IR on vessel delineation is attributed to its ability to improve resolution, reduce image noise, and enhance edges.<sup>15</sup> The examination of image resolution with respect to the reconstruction method is beyond the scope of this article and has been shown in previous examinations.<sup>16</sup> AIDR-reconstructed images expectedly showed reduced overall noise levels, and intra-aneurysmal noise was decreased by 28% (Fig 4). The ability of IR to reduce noise and enhance edges at the same time distinguishes it from FBP reconstruction, which compromises between these as it uses a filter kernel. A quantitative measure for edge sharpness is the length of the attenuation profile at the vessel border, ranging from 10% to 90% of the maximum intraluminal attenuation. The previously described phantom study also examined the influence of wall thickness, intraluminal attenuation, and reconstruction methods on this edge sharpness. IR images showed shorter edges throughout all groups. Edge lengths in our study just missed a

statistically significant level but showed a tendency toward shorter values in AIDR-reconstructed images as seen in the phantom study (Fig 2). There, vessels with 0.5-mm walls did not show an edge profile corresponding to the actual vessel wall as was seen in the thicker-walled vessels. The lack of depiction of the wall in thin-walled vessels was attributed to reconstruction blur and might be the major source of the lack of improvement of accuracy in measuring vessel diameters in this group. With an estimated wall thickness of 0.25 mm in aneurysms in vivo, this effect is even more pronounced.

Due to the small sample size, our study lacks the statistical power to draw further conclusions. Hence, the absence of a significantly different absolute volume or pulsation fraction does not translate into a lack of improvement of accuracy by IR in pulsation analysis. The effect size is small, necessitating large study groups. However, further effort should be made because our results show the applicability of the findings of a well-controlled in vitro study that proved the superiority of IR methods in the diameter measurement of vessels. Furthermore, IR methods from different vendors may have variable effects on edge enhancement and could show a larger improvement of accuracy for this specific application.

## CONCLUSIONS

IR methods do not increase the accuracy of pulsation measurements of cerebral artery aneurysms in vivo. This finding might be mainly due to their small wall size.

Disclosures: Till Illies—RELATED: Support for Travel to Meetings for the Study or Other Purposes: Japanese German Radiology Affiliation, Comments: for an exchange to Osaka, Japan. Jens Fiehler—UNRELATED: Consultancy: Codman, Stryker, MicroVention; Grants/Grants Pending: Covidien, Stryker, MicroVention\*; Payment for Lectures Including Service on Speakers Bureaus: Codman, Covidien, Stryker, MicroVention, Penumbra; Travel/Accommodations/Meeting Expenses Unrelated to Activities Listed: Covidien. Yoshiyuki Watanabe—RELATED: Grant: Toshiba Medical.\* Comments: research fund about radiation dose reduction using 320-detector row CT. \*Money paid to the institution.

## REFERENCES

1. Kuroda J, Kinoshita M, Tanaka H, et al. **Cardiac cycle-related volume change in unruptured cerebral aneurysms: a detailed volume quantification study using 4-dimensional CT angiography.** *Stroke* 2012;43:61–66
2. Umeda Y, Ishida F, Hamada K, et al. **Novel dynamic four-dimensional CT angiography revealing 2-type motions of cerebral arteries.** *Stroke* 2011;42:815–18
3. Yaghmai V, Rohany M, Shaibani A, et al. **Pulsatility imaging of saccular aneurysm model by 64-slice CT with dynamic multiscan technique.** *J Vasc Interv Radiol* 2007;18:785–88
4. Matsumoto M, Sasaki T, Suzuki K, et al. **Visualizing the dynamics of cerebral aneurysms with four-dimensional computed tomographic angiography.** *Neurosurgery* 2006;58:E1003, author reply E1003
5. Kato Y, Hayakawa M, Sano H, et al. **Prediction of impending rupture in aneurysms using 4D-CTA: histopathological verification of a real-time minimally invasive tool in unruptured aneurysms.** *Minim Invasive Neurosurg* 2004;47:131–35
6. Ishida F, Ogawa H, Simizu T, et al. **Visualizing the dynamics of cerebral aneurysms with four-dimensional computed tomographic angiography.** *Neurosurgery* 2005;57:460–71, discussion 460–71
7. Hayakawa M, Katada K, Anno H, et al. **CT angiography with electrocardiographically gated reconstruction for visualizing pulsation of intracranial aneurysms: identification of aneurysmal protuberance presumably associated with wall thinning.** *AJNR Am J Neuroradiol* 2005;26:1366–69

8. Suzuki S, Machida H, Tanaka I, et al. **Vascular diameter measurement in CT angiography: comparison of model-based iterative reconstruction and standard filtered back projection algorithms in vitro.** *AJR Am J Roentgenol* 2013;200:652–57
9. Ziegler A, Köhler T, Proksa R. **Noise and resolution in images reconstructed with FBP and OSC algorithms for CT.** *Med Phys* 2007;34:585–98
10. Sprawls P. **AAPM tutorial: CT image detail and noise.** *Radiographics* 1992;12:1041–46
11. Machida H, Takeuchi H, Tanaka I, et al. **Improved delineation of arteries in the posterior fossa of the brain by model-based iterative reconstruction in volume-rendered 3D CT angiography.** *AJNR Am J Neuroradiol* 2013;34:971–75
12. Machida H, Tanaka I, Fukui R, et al. **Improved delineation of the anterior spinal artery with model-based iterative reconstruction in CT angiography: a clinical pilot study.** *AJR Am J Roentgenol* 2013;200:442–46
13. Steiger HJ, Aaslid R, Keller S, et al. **Strength, elasticity and viscoelastic properties of cerebral aneurysms.** *Heart Vessels* 1989;5:41–46
14. Park JK, Lee CS, Sim KB, et al. **Imaging of the walls of saccular cerebral aneurysms with double inversion recovery black-blood sequence.** *J Magn Reson Imaging* 2009;30:1179–83
15. Beister M, Kolditz D, Kalender WA. **Iterative reconstruction methods in X-ray CT.** *Phys Med* 2012;28:94–108
16. Suzuki S, Machida H, Tanaka I, et al. **Measurement of vascular wall attenuation: comparison of CT angiography using model-based iterative reconstruction with standard filtered back-projection algorithm CT in vitro.** *Eur J Radiol* 2012;81:3348–53

# Evaluation of a Metal Artifacts Reduction Algorithm Applied to Postinterventional Flat Panel Detector CT Imaging

D.A. Stidd, H. Theessen, Y. Deng, Y. Li, B. Scholz, C. Rohkohl, M.D. Jhaveri, R. Moftakhar, M. Chen, and D.K. Lopes

## ABSTRACT

**BACKGROUND AND PURPOSE:** Flat panel detector CT images are degraded by streak artifacts caused by radiodense implanted materials such as coils or clips. A new metal artifacts reduction prototype algorithm has been used to minimize these artifacts. The application of this new metal artifacts reduction algorithm was evaluated for flat panel detector CT imaging performed in a routine clinical setting.

**MATERIALS AND METHODS:** Flat panel detector CT images were obtained from 59 patients immediately following cerebral endovascular procedures or as surveillance imaging for cerebral endovascular or surgical procedures previously performed. The images were independently evaluated by 7 physicians for metal artifacts reduction on a 3-point scale at 2 locations: immediately adjacent to the metallic implant and 3 cm away from it. The number of visible vessels before and after metal artifacts reduction correction was also evaluated within a 3-cm radius around the metallic implant.

**RESULTS:** The metal artifacts reduction algorithm was applied to the 59 flat panel detector CT datasets without complications. The metal artifacts in the reduction-corrected flat panel detector CT images were significantly reduced in the area immediately adjacent to the implanted metal object ( $P = .05$ ) and in the area 3 cm away from the metal object ( $P = .03$ ). The average number of visible vessel segments increased from 4.07 to 5.29 ( $P = .1235$ ) after application of the metal artifacts reduction algorithm to the flat panel detector CT images.

**CONCLUSIONS:** Metal artifacts reduction is an effective method to improve flat panel detector CT images degraded by metal artifacts. Metal artifacts are significantly decreased by the metal artifacts reduction algorithm, and there was a trend toward increased vessel-segment visualization.

**ABBREVIATIONS:** FDCT = flat panel detector CT; MAR = metal artifacts reduction

With continued technologic developments, both diagnostic and interventional neuroendovascular applications of flat panel detector CT (FDCT) have increasingly expanded. FDCT offers higher spatial resolution relative to multidetector row CT and improved visualization of clipped aneurysms and endovascular stents.<sup>1</sup> Imaging performed in the endovascular suite also offers rapid visualization of periprocedural complications, thus allowing faster management.<sup>2</sup> The acquired FDCT images, however, are degraded by artifacts created by radiodense cerebral endovascular and surgical implants including coils, stents, and clips, limiting the use of FDCT as a postprocedural imaging technique.

Metal artifacts reduction (MAR) in CT images has been attempted by both interpolation and algebraic methods. Interpolation methods have been quite successful and, most important, require less computational power relative to algebraic methods, resulting in less computing time. One of the first interpolation-based MAR algorithms used a 1D linear interpolation for single-row CT data, which is inadequate for FDCT data.<sup>3</sup> The MAR algorithm investigated in this work, developed by Siemens Healthcare Sector, is a modification and extension of a recently published MAR procedure by Prell et al.<sup>4</sup> We present validation of the FDCT MAR prototype algorithm by using a phantom study and an objective critique by 7 clinicians.

## MATERIALS AND METHODS

### Image Acquisition

During standard clinical care, FDCT images were acquired on a biplane Axiom Artis zee angiography system (Siemens, Erlangen, Germany) by using a 20-second scan protocol with the following parameters: 70 kV, 200° rotation, 496 projections, 1.2  $\mu$ Gy/frame. The average patient radiation dose was 2.9

Received November 1, 2013; accepted after revision March 20, 2014.

From the Departments of Neurosurgery (D.A.S., R.M., M.C., D.K.L.), Internal Medicine (Y.D., Y.L.), and Radiology (M.D.J.), Rush University Medical Center, Chicago, Illinois; and Siemens Healthcare Sector (B.S., C.R., H.T.), Erlangen, Germany.

Please address correspondence to Demetrius K. Lopes, MD, Rush University Medical Center, 1725 W. Harrison St, Suite 855, Chicago, Illinois 60612; e-mail: brainaneurysm@mac.com; @Cure4Stroke

<http://dx.doi.org/10.3174/ajnr.A4079>

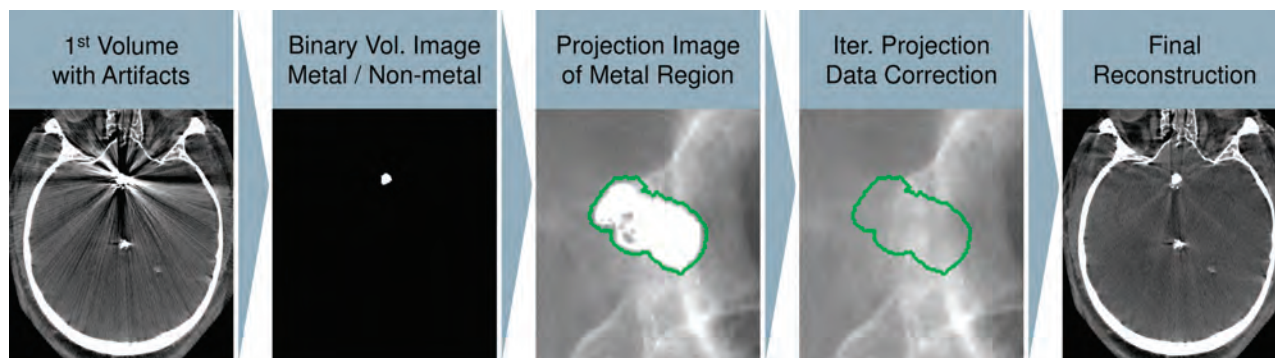


**FIG 1.** A graphic depiction of the metal artifacts prototype algorithm used for the flat panel detector CT images. An initial volume is reconstructed from the raw data containing metal artifacts. The metallic implant is then segmented, creating a binary volume of the implant, which is forward-projected onto the first reconstruction to identify data corrupted by artifacts. The corrupted data are replaced by a nonlinear interpolation procedure by using the data along the metal region boundaries (depicted in green). A new MAR-corrected volume is reconstructed. The segmented metallic implant is overlaid back onto the dataset for the final reconstruction.

mSv, based on prior measurement data. Twenty-eight datasets were acquired without contrast injection. Of the 31 datasets acquired with contrast, 14 patients received intravenous contrast and 17 patients received intra-arterial contrast. For patients who received IV contrast, 80 mL was injected at 4 mL/s, and image acquisition was started after a 14-second delay. For patients receiving intra-arterial contrast, 40 mL of 20% contrast diluted with saline was injected through an intra-arterial catheter at 2 mL/s. Initial image reconstruction for each case was performed on syngo X Workplace software, Version VB15 or VB21 (Siemens). The parameters used to reconstruct the FDCT images were the following: section thickness, 0.46 mm; “normal” reconstruction kernel; full FOV; 512 × 512 matrix, resulting in an isotropic voxel size of 0.3 mm<sup>3</sup>.

### **Metal Artifacts Reduction Algorithm**

The MAR prototype algorithm (Fig 1) investigated is a modification and extension of the procedure first published by Prell et al.<sup>4</sup> The MAR reconstructions were performed on an off-line prototype research workstation (Siemens). The algorithm consists of several steps. Initially, an uncorrected volume image is reconstructed from the acquired imaging data. A binary metal volume image is obtained by segmenting the metallic objects in this volume. In this step, the metallic objects are manually segmented. For each projection, this binary volume is forward-projected to yield a binary projection image of metal regions on the detector in each respective position. The projection data contained in these metal regions are generated by rays through metal objects; thus, these data are responsible for the artifacts. The data along the metal region boundaries are used to replace these data by a nonlinear interpolation procedure. This initial corrected volume is then used for a second normalized MAR correction step.<sup>5</sup> This step includes additional iterative improvements of the metal region boundaries to enhance the consistency of the corrected data as a whole. Finally, a procedure minimizing the total variation is applied to reduce residual streaks.

### **Phantom Aneurysm Model**

A phantom aneurysm model was created to demonstrate the reliability and accuracy of the metal artifacts reduction algorithm. The model was created with 10-mm-diameter silicone elastomer

tubing with a 12 × 12 mm simulated aneurysm. The model was filled with 20% diluted iopamidol (Isovue 250; Bracco Diagnostics, Princeton, New Jersey) to simulate a patient-like injection protocol and was submerged in a basin of water. A Neuroform EZ Stent (Stryker Neurovascular, Kalamazoo, Michigan) was deployed into the parent vessel of the model, and the aneurysm was filled with 4 Target Detachable Coils (Stryker Neurovascular). A piece of water-soluble polyurethane (Stryker Neurovascular) representative of a clot was placed inside the stent (Fig 2A). Two sets of FDCT images of the model were obtained in 2 different orthogonal positions relative to the C-arm, by using a 20-second scan protocol and 109 kV. Uncorrected and MAR-corrected volumes were reconstructed as described above (Figs 2B–E).

### **Patients**

FDCT scans obtained as routine imaging from 59 patients (62.7% women; mean age, 55.9 years; age range, 21–85 years) between January 2012 and May 2013 were retrospectively included as common neuroendovascular images (Figs 3 and 4). Images were selected to be representative of various metal objects in the head and neck region displaying a large amount of metal artifact (Table 1). Images were de-identified, and the MAR algorithm was applied after the conclusion of patient care. This study and imaging protocol were reviewed and approved by the university institutional review board.

### **Image Evaluation**

The uncorrected and MAR-corrected datasets were independently evaluated by 7 physicians. Two evaluators were dual-trained neurosurgeons practicing both open and neuroendovascular interventions for cerebral vascular disease. One evaluator was a neurologist trained as a neuroendovascular interventionist. Another evaluator was a practicing neuroradiologist. The 3 remaining evaluators were a neurosurgeon training as a fellow in neuroendovascular surgery and 2 radiologists training as fellows in neuroradiology.

The uncorrected datasets of the 59 paired image sets were randomized and evaluated for the amount of metal artifacts present by using a 3-point scale (Table 2) at 2 different locations on the images. The first location was the area immediately surrounding the metallic object, and the second location was an area approx-

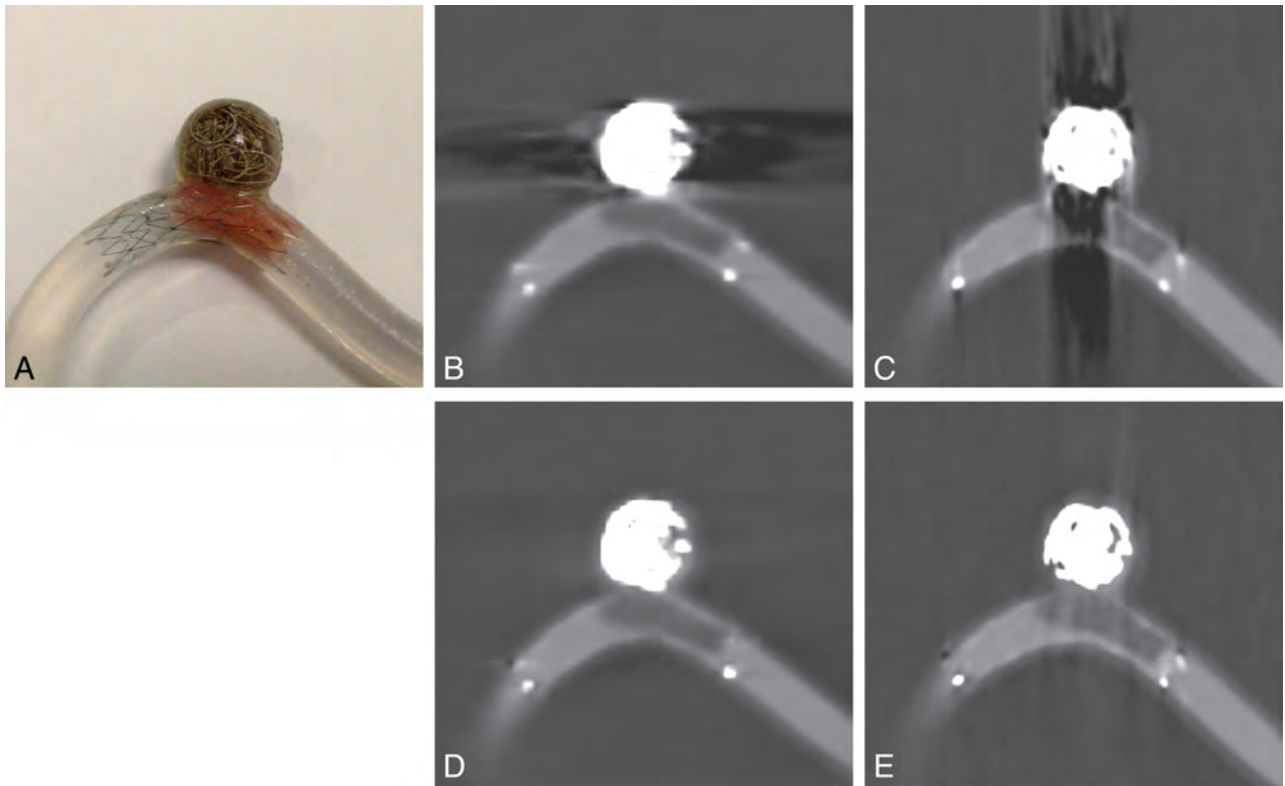


**FIG 2.** A, A phantom aneurysm model constructed of silicone elastomer tubing used to test the MAR algorithm prototype. Platinum coils were deployed in the aneurysm, and a small piece of polyurethane was placed inside a stent deployed across the aneurysm neck to model a clot. B and C, Uncorrected FDCT images acquired of the model constructed with stent, coils, and the simulated clot show streak artifacts created by the metal alloys of the stent and coils. D and E, Corresponding MAR-corrected FDCT images show reduced artifacts.

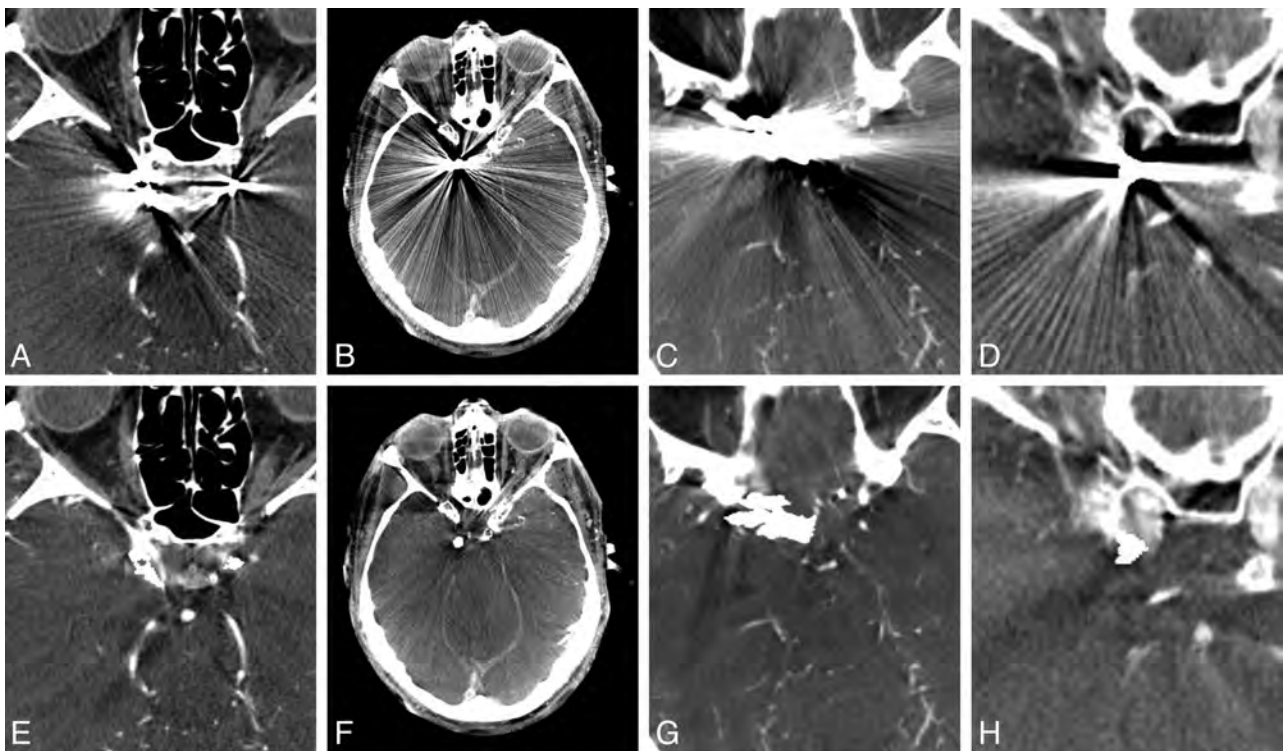


**FIG 3.** Flat panel detector CT uncorrected (A–D) and corresponding MAR-corrected (E–H) images depicting reduction of streak artifacts caused by coils deployed to treat intracranial aneurysms. The images were independently scored for the amount of metal artifacts and the number of visualized vessel segments within a 3-cm radius surrounding the metal objects.

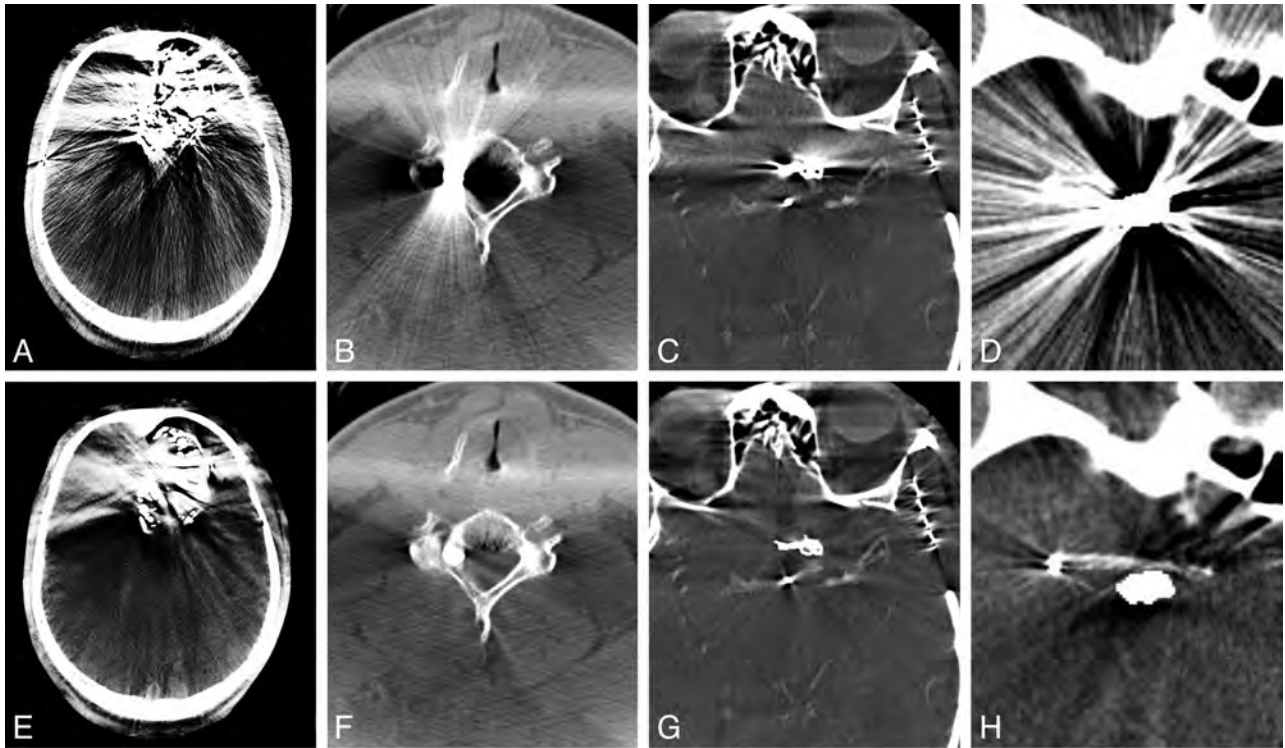


**FIG 4.** Sample FDCT images of various metallic objects causing streak artifacts and the application of the MAR algorithm. *A* and *E*, Onyx embolization of an intracranial AVM. The MAR algorithm was less effective at reducing the artifacts caused by Onyx. *B* and *F*, A bullet lodged within the cervical spine. *C* and *G*, A vascular clip used to treat an intracranial aneurysm. *D* and *H*, Stent-assisted coil embolization of an intracranial aneurysm. This example is similar to the phantom model created to evaluate the MAR algorithm. The stent is completely obscured by the metal artifacts but is visible after the application of the MAR algorithm.

**Table 1: Datasets included for MAR evaluation**

Metal Objects	No. of Datasets
Coils only	19
Clips	10
Stent	3
Onyx	3
Stent and coils	21
Other (bullet, spinal screws, mandibular fixtures)	3

**Table 2: Score used to quantify the amount of metal artifacts**

Score	Definition
0	No metal artifacts; relevant surrounding anatomy well-visualized
1	Moderate metal artifacts; relevant anatomy visible but affected by artifacts
2	Severe artifacts; relevant anatomy not visible

imately 3 cm away from the metallic object that was affected the most by streak artifacts. The 59 MAR-corrected datasets were evaluated in a similar manner. The scores assigned by the evaluators were recorded for analysis later. All images were evaluated at an imaging workstation with a medical-grade monitor (Siemens). Each evaluator had the ability to adjust image contrast and brightness levels and scroll through the topography sections as needed.

Of the 31 datasets acquired with contrast, 25 image sets were selected as representative acquisitions of cerebral vasculature. A single section through the metallic object most degraded by arti-

facts was selected for each uncorrected dataset, and the corresponding section of the MAR-corrected dataset was selected. These 50 images were randomized and loaded onto a viewer. A circle centered on the metallic object defining an area with a radius of 3 cm was overlaid onto each image. The 7 evaluators then independently counted the number of visible vessel segments within the defined areas without the ability to adjust contrast or brightness levels. The number of vessels counted for each image was recorded for analysis later. Bias was minimized by randomizing the 25 pairs of prepared images, creating 50 separate images presented in random order.

### Statistical Analysis

The amount of metal artifacts rated on a 3-point scale for the images were reported as relative frequencies. Nonparametric paired Wilcoxon signed rank tests were used to test for statistically significant differences among the distributions of scored artifact values. The results of the vessel-count analysis were reported as means  $\pm$  standard error of the mean, and paired *t* tests were used for statistically significant differences between the uncorrected and corrected groups. *P* values were calculated as 2-tailed; *P* < .05 was considered statistically significant. Interobserver agreement was measured for the metal artifacts scoring by calculating the  $\kappa$  statistic and interpreting the results as suggested by Landis and Koch.<sup>6</sup> A 1-way absolute-agreement intraclass correlation coefficient was used to assess the interobserver agreement for the vessel-count analysis. All statistical analyses were conducted by using the STATA 11 statistical software package (StataCorp, College Sta-

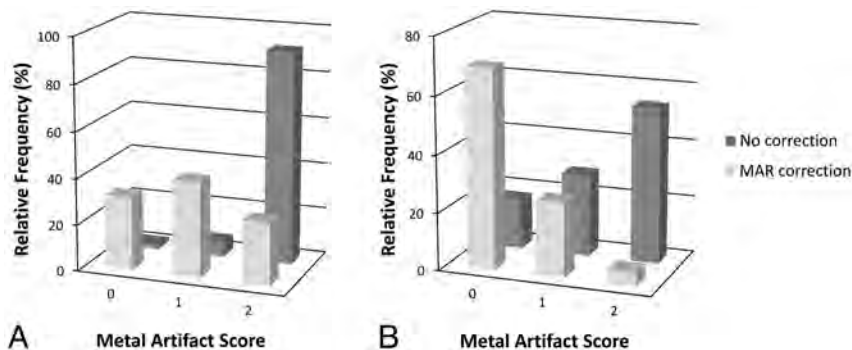


**FIG 5.** Relative frequencies of metal artifacts scores assigned to FDCT scans for areas immediately adjacent to the implanted metal object (A) or 3 cm away from the implanted metal object (B). The median  $P$  value for the uncorrected and MAR-corrected image pairs adjacent to the metal object was  $P = .05$ , and the median  $P$  value for the image pairs 3 cm away was  $P = .03$ . The uncorrected and MAR-corrected images were independently evaluated by 7 clinicians on a 3-point scale ( $n = 59$ ).

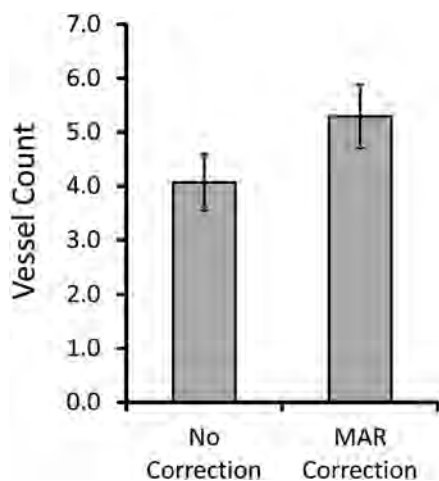


**FIG 6.** The mean number of visualized vessel segments within a 30-cm radius of the implanted metal object before and after MAR correction. The images were independently evaluated by 7 clinicians. The error bars represent the standard error of the mean ( $n = 25$ ).

tion, Texas) or the package “irr” of R, Version 0.84 (<http://www.r-project.org/>).

## RESULTS

Metal streak artifacts were noted on the acquired FDCT images of the phantom aneurysm model (Fig 2B, -C). The artifacts were caused by the metal alloys contained within the stent and coils, and the artifacts were directed in-line to the radiation beam. Application of the MAR algorithm qualitatively reduced the amount of streak artifacts without corresponding image degradation (Fig 2D, -E). The simulated polyurethane clot within the model filled with 20% contrast was visible as a hypoattenuation at the level of the stent. The visibility of the clot remained qualitatively unchanged after the application of the MAR algorithm. The space not occupied by coils within the aneurysm was notably more defined.

The MAR algorithm was applied to the 59 acquired patient FDCT scans with metallic implants without difficulty, and the uncorrected and MAR-corrected datasets were evaluated for metal artifacts (Fig 5). A 3-point scale was used to quantify the amount of metal artifacts (Table 2). The relative frequencies of the

quantified amount of metal artifacts adjacent to the metallic implants scored as not present, moderate, or severe were, respectively, 1.9%, 6.3%, and 91.8% for the uncorrected images and 31.7%, 41.2%, and 27.1% for the MAR-corrected images (median  $P = .05$ ). In an area 3 cm away from the metallic implants, the relative frequencies of the quantified metal artifacts scored as not present, moderate, or severe were, respectively, 17.4%, 28.6%, and 54% for the uncorrected images and 69.2%, 25.9%, and 4.8% for the MAR-corrected images (median  $P = .03$ ). There was moderate interobserver agreement among the 7 evaluators ( $\kappa = 0.44$ ). The MAR algorithm subjectively was not as

effective in the 3 datasets involving Onyx (Covidien, Irvine, California). When analyzed separately, the relative frequencies of the quantified amount of metal artifacts adjacent to the Onyx cast scored as not present, moderate, or severe were respectively 0%, 4.8%, and 95.2% for the uncorrected images and 0%, 52.4%, and 47.6% for the MAR-corrected images (median  $P = .13$ ). At 3 cm away from the Onyx cast, the relative frequencies of the amount of artifacts scored as not present, moderate, or severe were, respectively, 23.8%, 19.0%, and 57.1% for the uncorrected images and 52.4%, 19.0%, and 28.6% for the MAR-corrected images (median  $P = 1.00$ ).

Twenty-five pairs of uncorrected and MAR-corrected image sets were evaluated for the number of visible vessel segments within a 3-cm radius of the metallic implant (Fig 6). The average number of visible vessel segments increased from  $4.07 \pm 0.52$  to  $5.29 \pm 0.58$  ( $P = .124$ ) after the MAR algorithm was applied to the images. There was moderate interobserver agreement for the vessel count analysis (intraclass correlation coefficient = 0.55).

## DISCUSSION

Late detection and management of complications occurring after neuroendovascular procedures have an adverse impact on patient outcome.<sup>7-9</sup> Transporting a patient to a conventional multidetector CT scan after a complication delays critical decision-making and time to intervention. Technical advances in both image acquisition and postprocessing have improved FDCT imaging quality. Relative to multidetector CT imaging, FDCT imaging has better spatial resolution,<sup>1,10</sup> making it better suited to visualize the fine geometric details of the metal stents and coils used in neuroendovascular interventional procedures<sup>11</sup> and fine cerebral vascular anatomy.<sup>12</sup> The metal alloys within the implants, however, degrade the image quality of FDCT imaging, limiting its use as a routine postprocedural technique. An effective means of reducing the metal artifacts caused by metal implants would make FDCT imaging an ideal postprocedural technique to visualize complications such as intracranial hemorrhage, residual filling of aneurysms, or thrombus within newly deployed stents.

Several strategies have been proposed to reduce the metal artifacts for conventional multidetector row CT,<sup>13</sup> but these strate-

gies cannot be directly applied to images acquired with a flat panel detector. The first FDCT-adequate MAR algorithm proposed by Prell et al<sup>2</sup> used a nonlinear interpolation procedure to restore corrupted data and has subsequently been shown to decrease metal artifacts of FDCT images obtained for neuroendovascular procedures.<sup>13,14</sup> This finding correlates with the results of the current study in which we show that the MAR algorithm described above significantly lowered the amount of metal artifacts hindering visualization of the intracranial tissues. Another strategy used to successfully reduce metal artifacts in FDCT imaging is to subtract a volume reconstructed from data corrupted by artifacts from an initial uncorrected volume reconstruction without a nonlinear interpolation process to replace the corrupted data.<sup>15</sup>

The mean number of visualized vessel segments within a 3-cm radius centered on the metallic foreign body was increased after the MAR algorithm was applied, though this was not a significant increase. This lack of significance is likely due to the decreased interobserver agreement. In this study, 7 independent evaluators were used from 3 different subspecialties, hence reflecting a variety of training styles and backgrounds.

As demonstrated in Fig 4A, -E, the MAR algorithm prototype was not as effective at reducing the metal streak artifacts caused by the tantalum within the Onyx in datasets of liquid embolization. Onyx casts are very inhomogeneous structures with various densities; therefore, it becomes difficult to determine all boundaries precisely. This imprecise boundary definition manifests as a non-optimal interpolation result, which likely induces residual streaks in the newly reconstructed volume. The MAR prototype algorithm will need further improvement to minimize streak artifacts caused by Onyx.

The MAR algorithm used for this study did reduce the amount of metal artifacts in all datasets, but the corrected images with reduced streak artifacts may not have improved diagnostic information. The corrupted data replaced by the nonlinear interpolation process may contain new subtle artifacts that might obscure data in the original acquisition. Also, data that are completely degraded by severe artifacts, including motion artifacts or conebeam artifacts at the skull base, for example, cannot be recovered by the MAR algorithm.<sup>13</sup> Despite these limitations, the MAR algorithm represents a significant improvement of the FDCT image quality, increasing the value of FDCT as a post-neurointerventional procedure imaging technique.

## CONCLUSIONS

The evaluated MAR algorithm is effective in improving FDCT images degraded by streak artifacts caused by metallic implants used for cerebral endovascular and open interventions. Metal artifacts are significantly decreased by the MAR algorithm, with a trend toward increased vessel-segment visualization. These decreased metal artifacts increase the chance for visualizing complications associated with cerebrovascular interventions such as

acute hemorrhage surrounding a coiled aneurysm and increase the value of FDCT as a source of postprocedural imaging.

## ACKNOWLEDGMENTS

We recognize Drs Arthur Maydell and Sumeet G. Dua for their contribution to this project.

Disclosures: Heike Theessen, Bernhard Scholz, and Christopher Rohkohl—RELATED: full-time employees of Siemens Healthcare Sector. Miral D. Jhaveri—UNRELATED: Royalties: Amirsys. Demetrius K. Lopes—UNRELATED: Consultancy: Covidien, Stryker, Penumbra, Siemens\*; Grants/Grants Pending: Siemens\*; Payment for Development of Educational Presentations: Covidien, Penumbra; Stock/Stock Options: Penumbra, VasSol, Blockade Medical; Travel/Accommodations/Meeting Expenses Unrelated to Activities Listed: Siemens.\* \*Money paid to the institution.

## REFERENCES

1. Gupta R, Cheung AC, Bartling SH, et al. **Flat-panel volume CT: fundamental principles, technology, and applications.** *Radiographics* 2008;28:2009–22
2. Prell D, Kyriakou Y, Struffert T, et al. **Metal artifact reduction for clipping and coiling in interventional C-arm CT.** *AJNR Am J Neuroradiol* 2010;31:634–39
3. Kalender WA, Hebel R, Ebersberger J. **Reduction of CT artifacts caused by metallic implants.** *Radiology* 1987;164:576–77
4. Prell D, Kyriakou Y, Beister M, et al. **A novel forward projection-based metal artifact reduction method for flat-detector computed tomography.** *Phys Med Biol* 2009;54:6575–91
5. Meyer E, Raupach R, Lell M, et al. **Normalized metal artifact reduction (NMAR) in computed tomography.** *Med Phys* 2010;37:5482–93
6. Landis JR, Koch GG. **The measurement of observer agreement for categorical data.** *Biometrics* 1977;33:159–74
7. Horowitz MB, Crammond D, Balzer J, et al. **Aneurysm rupture during endovascular coiling: effects on cerebral transit time and neurophysiologic monitoring and the benefits of early ventriculostomy: case report.** *Minim Invasive Neurosurg* 2003;46:300–05
8. Levy E, Koebbe CJ, Horowitz MB, et al. **Rupture of intracranial aneurysms during endovascular coiling: management and outcomes.** *Neurosurgery* 2001;49:807–11, discussion 811–13
9. Cloft HJ, Kallmes DF. **Cerebral aneurysm perforations complicating therapy with Guglielmi detachable coils: a meta-analysis.** *AJNR Am J Neuroradiol* 2002;23:1706–09
10. Heran NS, Song JK, Namba K, et al. **The utility of DynaCT in neuroendovascular procedures.** *AJNR Am J Neuroradiol* 2006;27:330–32
11. Ionescu M, Metcalfe RW, Cody D, et al. **Spatial resolution limits of multislice computed tomography (MS-CT), C-arm-CT, and flat panel-CT (FP-CT) compared to MicroCT for visualization of a small metallic stent.** *Acad Radiol* 2011;18:866–75
12. Saake M, Goelitz P, Struffert T, et al. **Comparison of conventional CTA and volume perfusion CTA in evaluation of cerebral arterial vasculature in acute stroke.** *AJNR Am J Neuroradiol* 2012;33:2068–73
13. van der Bom IM, Hou SY, Puri AS, et al. **Reduction of coil mass artifacts in high-resolution flat detector conebeam CT of cerebral stent-assisted coiling.** *AJNR Am J Neuroradiol* 2013;34:2163–70
14. Psychogios MN, Scholz B, Rohkohl C, et al. **Impact of a new metal artefact reduction algorithm in the noninvasive follow-up of intracranial clips, coils, and stents with flat-panel angiographic CTA: initial results.** *Neuroradiology* 2013;55:813–18
15. Buhk JH, Groth M, Sehner S, et al. **Application of a novel metal artifact correction algorithm in flat-panel CT after coil embolization of brain aneurysms: intraindividual comparison.** *Rofa* 2013; 185:824–29

# Treatment of Supratentorial Spontaneous Intracerebral Hemorrhage Using Image-Guided Minimally Invasive Surgery: Initial Experiences of a Flat Detector CT–Based Puncture Planning and Navigation System in the Angiographic Suite

Z. Yang, B. Hong, Z. Jia, J. Chen, J. Ge, J. Han, J. Beilner, Y. Zhang, Y. Fang, and J. Liu

## ABSTRACT

**BACKGROUND AND PURPOSE:** The intracerebral hemorrhage drainage through minimally invasive approach is emerging as an alternative for traditional craniotomy, due to its improved survival rate and reduced complication rate. In this study, we investigated the feasibility and safety of a flat detector CT–based puncture planning and navigation system for minimally invasive hematoma drainage on patients with intracerebral hemorrhage.

**MATERIALS AND METHODS:** The minimally invasive hematoma drainage was performed on 21 hypertensive patients with intracerebral hemorrhage in the angiographic suite with the guidance of a flat detector CT–based puncture planning and navigation system. This system is integrated in the angiographic machine, and was used for 1) planning the needle path based on a preprocedural flat detector CT scan, 2) advancing the catheter with real-time fluoroscopic guidance, and 3) confirming the procedure outcome based on an immediate postprocedural flat detector CT. The surgery efficiency, accuracy, and the treatment outcome were measured and compared with the published data.

**RESULTS:** All procedures were successfully completed with the catheter placed  $4 \pm 1$  mm from the planned position. The average surgery time was  $40 \pm 7$  minutes. The volume of the hematoma was reduced to  $28 \pm 4\%$  of the original volume. The Glasgow Coma Scale score was significantly improved from  $10 \pm 1$  at the admission to  $14 \pm 1$  at the discharge. The Extended Glasgow Coma Scale score also improved from  $5 \pm 1$  at the discharge to  $6 \pm 1$  at the 6-month follow-up. No major complication, rebleeding, and mortality were observed in this study.

**CONCLUSIONS:** This flat detector CT–based needle guidance system provided a feasible, convenient, and safe way to perform the puncture and drainage of brain hematoma in the angiographic suite.

**ABBREVIATIONS:** FDCT = flat detector CT; ICH = intracerebral hemorrhage; GCS = Glasgow Coma Scale; GOSE = Extended Glasgow Coma Scale

Spontaneous intracerebral hemorrhage (ICH) affects more than 2 million people each year around the world.<sup>1</sup> Timely medical intervention is critical for ICH, as it is a medical emergency with a mortality rate range from 35% to 52% within 1 month.<sup>2</sup> However, the current treatments for patients with ICH continue to be controversial, with several large-scale randomized trials reporting no significant benefit of early surgery, primarily craniotomy, over conservative treatment.<sup>3–5</sup> In recent years, the surgical removal of hematoma through burr-holes is emerging as a minimally invasive alternative for conventional craniotomy because of its improved complication rate and survival rate.<sup>6</sup> These new techniques usually involve stereo-

tactic positioning and intraprocedural image guidance, such as endoscopic, traditional CT, intraoperative CT, and sonography-guided aspiration.<sup>6–8</sup> These techniques have not yet been widely used because of expensive clinical costs such as the demand for specialized equipment, difficulties scheduling procedures on the diagnostic machines (eg, CT scan suite), and a lack of confirmed clinical benefit from large-scale clinical trials. Until now, the implementation of minimally invasive surgery for treating intracranial hemorrhage remains investigational, with only 2 ongoing large-scale randomized trials (Minimally Invasive Surgery and Thrombolytic Evacuation in ICH [MISTIE] and Clot Lysis Evaluating Accelerated Resolution III [CLEAR III]).<sup>9,10</sup> MISTIE and CLEAR III are currently phase III trials aimed at comparing minimally invasive surgery combined with a thrombolysis agent with the best critical management alone for treating ICH, and with minimally invasive surgery combined with placebo for treating intraventricular hemorrhage, respectively. Both of their early results indicated that the catheter location is one of the most important criteria for good surgery outcome, and careful planning and accurate execution is necessary for optimal catheter placement.<sup>10</sup>

Received January 27, 2014; accepted after revision April 1.

From the Department of Neurosurgery (Z.Y., B.H., Z.J., J.C., Y.Z., Y.F., J.L.), Changhai Hospital, Second Military Medical University, Shanghai, China; and Siemens Ltd. China (J.G., J.H., J.B.), Healthcare Sector, Angiography & Interventional X-Ray Systems, Shanghai, China.

Z. Yang and B. Hong contributed equally to this work as co-first authors.

Please address correspondence to Jianmin Liu, MD, Department of Neurosurgery, 168 Changhai Rd, Shanghai 200433, China; e-mail: renzhuang@hotmail.com

<http://dx.doi.org/10.3174/ajnr.A4009>

In this study, we attempted an affordable clinical solution for image-guided hematoma drainage that could be performed in the traditional angiographic suite without the need for specialized equipment. We implemented an innovative puncture planning and navigation system that is integrated into the angiographic machine for hematoma evacuation. This guided evacuation procedure based on an intraprocedural flat detector CT (FDCT), in which a 3D CT-like image was reconstructed from a rotational scan<sup>11</sup> using a C-arm angiographic machine. Commercial software (syngo iGuide needle guidance; Siemens, Erlangen, Germany) then facilitates the needle path planning that allows physicians to choose optimum entry and target points of the puncture, and automatically overlays the path onto the fluoroscopic images during the procedure for real-time guidance.

The feasibilities of this puncture planning and guidance system had been previously demonstrated in selective cervical nerve root block,<sup>12</sup> percutaneous kidney puncture,<sup>13</sup> and hepatic tumor ablation<sup>13</sup> based on ex vivo animal models and real patients. Its application in the brain was only recently demonstrated on 6 patients with cerebrovascular ischemia for external ventricular drainage.<sup>14</sup> In this study, we further expanded this technique on a more complicated brain procedure, intracranial hemorrhage evacuation in 21 hypertensive patients with ICH. Unlike the external ventricular drainage, the location of hemorrhage in pa-

tients with ICH could vary from patient to patient, and could not be performed freehand without any image guidance. Moreover, we assessed the feasibility and the safety of this technique in terms of procedure length, puncture accuracy, drainage volume, and treatment outcome at the discharge and 6-month follow-up. This is also the first attempt to evaluate the short-term treatment outcome of FDCT-guided hemorrhage drainage using Glasgow Coma Scale (GCS) and Extended Glasgow Coma Scale (GOSE) scores.

## MATERIALS AND METHODS

### Patients

Between February 2011 and May 2011, 21 consecutive supratentorial hypertensive patients with ICH (15 men and 6 women, age 49 to 80 years, mean  $59.3 \pm 7.9$  years) were included in this study. The inclusion criteria were 1) definite hematoma associated neurologic symptoms and signs; 2) no signs of brain herniation and acute rising intracranial pressure; 3) hematoma was deeply located, craniotomy operation of hematoma evacuation was difficult, or might cause more iatrogenic injury; 4) the hemorrhagic vascular diseases such as aneurysms or vascular malformations were definitely treated; and 5) informed patient consent. All patients had a history of hypertension. On admission, GCS score of the cohort was  $9.5 \pm 0.9$  with details listed in Table 1. Among them, 13 patients experienced various degrees of aphasia and 16 patients had contralateral limb muscle strength grades worse than 3. CT examination identified that 6 cases had hematoma in the left putamen, 10 cases in the right putamen, and 5 cases in the thalamus. There were also 2 patients whose hematoma had spread into

**Table 1: The GCS score of all 21 patients measured at admission and discharge**

GCS Score	7–9	10–12	13–15	Average
At admission (no. of patients)	11 (52%)	10 (48%)	0	$9.5 \pm 0.9$
At discharge (no. of patients)	0	0	21 (100%)	$14.1 \pm 0.6$



**FIG 1.** The generation of burr-hole for hematoma drainage. A, The burr-hole position is preselected by the surgeon before the puncture planning procedures, and marked on the patient's forehead as the blue cross. The surgeon then uses the hand drill, B, to manually drill a hole at the selected position. The drainage catheter, C, is then inserted into the burr-hole with the FDCT-based real-time guidance.

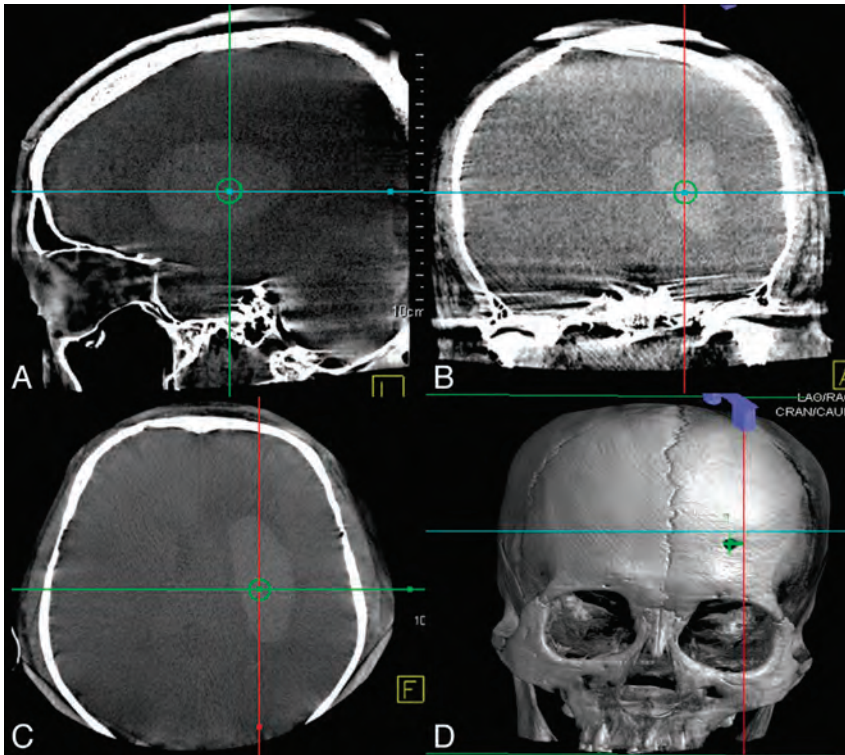


**FIG 2.** The selection of the entry point and the target point is based on 3D FDCT images acquired immediately before the surgery in the angiographic suite. The planned target point is placed within the hematoma based on the preference of the surgeon. Its position is indicated by the center of the cross hair in sagittal (A), coronal (B), and axial (C) axes. In our practice, the burr-hole is generated before the presurgery FDCT, hence we could directly place the entry point at the center of the burr-hole (small green cross in D).

the ventricle. The time spans from the onset of the hemorrhage to surgery ranged from 12 hours to 7 days, with an average of  $3.5 \pm 1.5$  days.

### Anesthesia

Fifteen patients were under local anesthesia with certain degrees of sedation, the other 6 patients who were too dysphoric to be cooperative were under general anesthesia.

### Needle Planning and Path Guidance

All procedures were performed in an angiographic suite that conformed to ISO 7 (Class of 10,000) standards with average of air flow velocity of 10–15 feet/minute. During the procedure, all patients lay on the angiographic table in supine position. The puncture was generally performed at the location of 3 cm superior to the supraorbital ridge and 2.5 cm lateral to midline using a manual twist drill (Fig 1). After the establishment of a burr-hole, 1 FDCT acquisition was performed on a C-arm angiographic system (Artis zee Biplane, Siemens) with the following parameters: 20-second acquisition protocol,  $0.4^\circ$  increment,  $512 \times 512$  matrix,  $200^\circ$  total angle, and 496 projections. The cross-sectional images were then reconstructed on a commercially available workstation (syngo X-Workplace; Siemens) with section thickness of 5 mm. After identification of the hemorrhage in the reconstructed image, the integrated puncture planning and guidance system (syngo iGuide needle guidance) was initiated. The syngo iGuide enabled preprocedural needle path planning,

intraoperative live guidance during needle progress, and postprocedural verification. During the needle path planning, the entry point and target point could be chosen based on reconstructed 3D FDCT images. In our cases, we slightly modified the workflow by generating the burr-hole before the acquisition of FDCT, hence the entry point was chosen by identifying the center of the burr-hole in the 3D FDCT scan (Fig 2D). The target point was chosen by selecting a point within the hemorrhage and 1 cm away from the posterior boundary of the hemorrhage (Fig 2A–C). The needle guidance software then automatically calculates the puncture depth and corresponding C-arm working angles in bull's eye view (Fig 3A, -B) and 2 progression views (Fig 3C, -D). After manual confirmation of the puncture path, we started the image-guided puncture by overlaying the planned path onto the real-time fluoroscopic images. After the puncture and the initial drainage, a postprocedural FDCT was performed immediately to confirm the location of the drainage tube.

### Postprocedural Patient Care

The liquefied hematoma was partially drained out immediately after the successful placement of the drainage tube. The disposable drainage system (Gred; ShanDong Gredmedic, Dalian, China) used in the procedure has a built-in U-shape tube that could prevent reversed flow of hematoma from drainage bag back to patient (as shown in Fig 1C). For 5 patients with large hematoma volume, a 20-mL syringe with 1 to 2 mL negative pressure was used for gentle suction. Starting from the second day after the surgery, all patients received diluted saline urokinase (2 million units in 2 mL) treatment 1 time per day. Dehydration was performed according to the results of intracranial pressure monitor.

### Surgery Evaluation

The feasibility and safety of this image-guided hematoma drainage was evaluated based on the surgery efficiency and accuracy, and the treatment outcome. The efficiency of the surgery was represented by the total surgery time excluding anesthesia time, and the number of puncture attempts per surgery. The accuracy of the surgery was represented by the deviation between the planned and actual location of the needle tip. This distance was manually measured on the postprocedural FDCT as it has an automatic overlay of the planned puncture path.

The immediate treatment outcome was evaluated based on the hematoma drainage volume and the GCS score at the time of admission and discharge. The short-term outcome was evaluated based on the GOSE score at the time of the discharge and 6-month

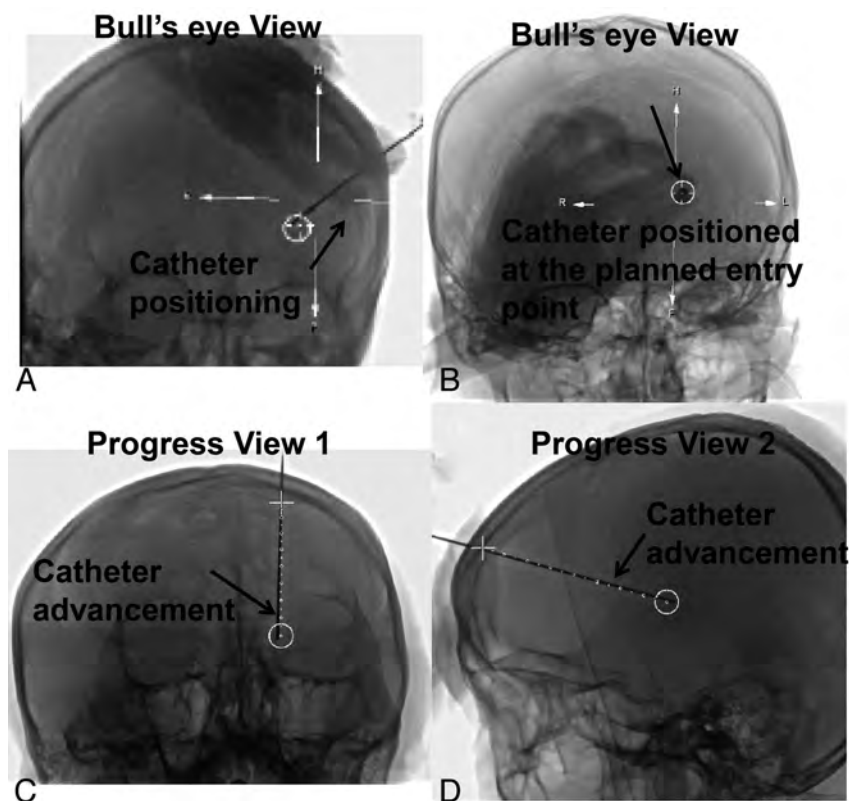


**FIG 3.** The catheter placement is guided by real-time fluoroscopic images with overlaid planned needle path (white dotted line in A–D). Under the bull's eye view (A and B), the surgeon adjusts the direction of the catheter until the catheter is in-line with the beam angle, and its tip overlaps with the planned entry point (white circle) (C and D). The surgeon then slowly advances the catheter while watching the real-time fluoroscopy acquired perpendicular to the planned needle path.

follow-up. The volumes of the hematoma were measured based on presurgery and postsurgery CT scan using the Tada formula.

#### Statistical Analysis

The results were analyzed with SPSS 13.0 edition (IBM, Armonk, New York). A *t* test was performed to compare 1) the change of hematoma volume pre- and postsurgery, 2) the GCS score at the time of admission and discharge, and 3) the GOSE score at the time of discharge and 6-month follow-up.

#### RESULTS

The image-guided operation time ranged from 25 to 55 minutes, with mean length of  $40 \pm 7$  minutes. All punctures succeeded in 1 attempt. The deviation between planned and actual needle point location ranged from 2 to 7 mm, with mean deviation of  $4 \pm 1$  mm. The average drainage volume was  $24 \pm 7$  mL, with average hematoma volume of  $33 \pm 9$  mL at the admission, and  $9 \pm 2$  mL at the discharge. The volume of hematoma was significantly reduced ( $P < .001$ ) and the drainage ratio ranged from 67% to 80%, and averaged at  $72 \pm 4\%$ . An exemplary patient hematoma shrinkage after this image-guided surgery was clearly shown on a series of CT scans in Fig 4. The GCS score was significantly improved from  $10 \pm 1$  at the admission to  $14 \pm 1$  at the discharge ( $P < .001$ ), with the details of the GCS score listed in Table 1. The GOSE score also significantly improved from  $5 \pm 1$  at the discharge to  $6 \pm 1$  at the 6-month follow-up ( $P < .001$ ), as listed in Table 2. All patients survived the procedure without major com-

plications; however, 1 patient suffered from pneumonia due to nosocomial infection. Postoperative hospital stay was 5–8 days. Among 13 cases of aphasia, 3 patients could speak simple words, and 4 could voice. Among 16 cases of hemiplegia, 12 patients improved their muscle strength more than 1 level.

#### DISCUSSION

The prolonged operation time is one of the limitations for removing clot using craniotomy. In our experience with this FDCT-based puncture planning and navigation method, we were able to complete the procedure in around 40 minutes. This procedure time was significantly shorter than that of the conventional craniotomy treatment, which usually takes around 3 hours in our institute. It was also slightly faster than other reported image-guided surgery times, such as 89 minutes using intraoperative CT<sup>14</sup> and 85 minutes using endoscopic navigation.<sup>7</sup> The shortened workflow was mainly a benefit from the convenience of performing intraprocedural FDCT within the angiographic suite. FDCT, in general, has lower resolution than that of volumetric CT, but it is sufficient for the application of intracranial hematoma evacuation.

First, the attenuation difference of the skull, the hemorrhage, and the normal brain tissue within the brain is large enough to be easily differentiated in a reconstructed 3D FDCT image (as shown in Fig 2). Second, the respiratory motion and the cardiac rhythm only minimally affect the brain tissue; hence its immobility could further enhance the image quality.

The key factor for hemorrhage evacuation through burr-holes is the precise positioning of the drainage catheter. The maximum deviation between planned and actual position of the drainage catheter was found to be less than 7 mm in our study. Moreover, postprocedural FDCT indicated that the catheter tips arrived at the center of the hemorrhage in all cases. The accurate placement of the catheter in our study was mainly due to the real-time guidance of the fluoroscopic image with overlaid planned needle path. The surgeon could make a slight adjustment to the trajectory path simultaneously as the catheter advanced to the planned location while watching the real-time fluoroscopy with overlaid planning needle path. By doing this, we could avoid the multiple punctures that tend to have a much higher chance of brain tissue damage than a single attempt. We also noticed that the small deviation still existed in some cases, and that could be due to the lack of bilateral guidance during catheter advancement. This should be taken into consideration in the future version of the needle guidance tool.

Theoretically, the accurate placement of the evacuation catheter could lead to better treatment outcome. The treatment outcome evaluation based on our patients' condition at discharge

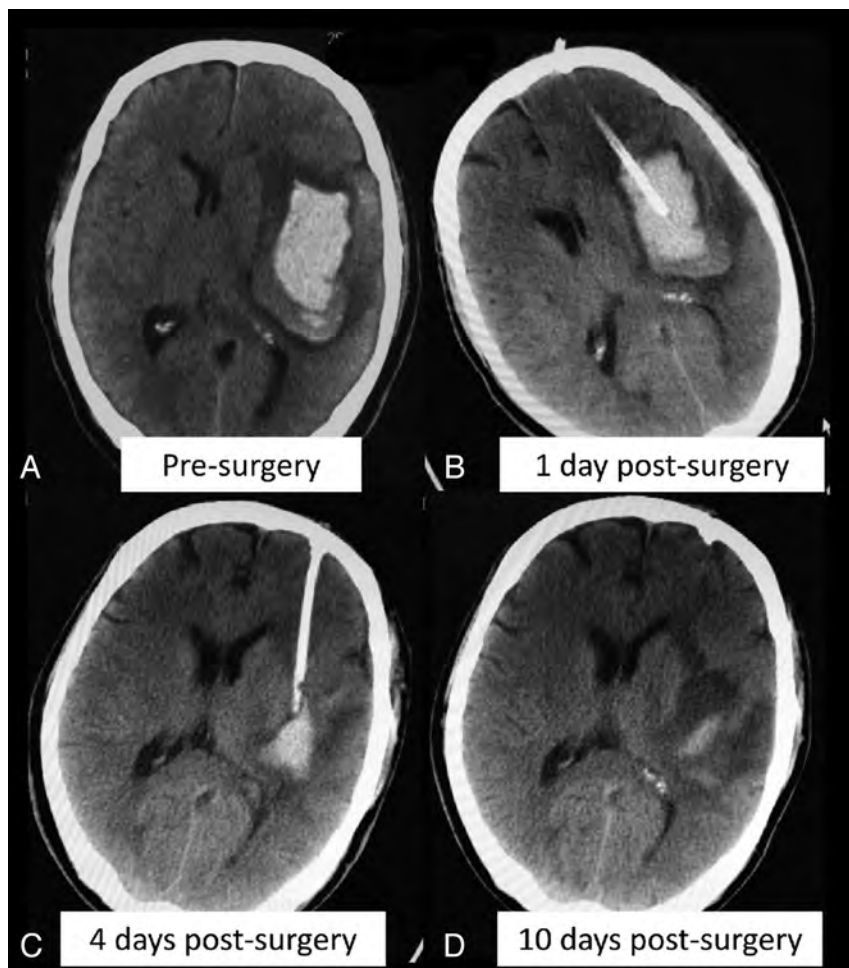


**FIG 4.** An exemplary patient case that was treated using this image-guided hemorrhage drainage procedure. The significantly reduced hematoma volume could be observed in a series of pre- and postsurgery CT scans.

**Table 2: The GOSE score of all 21 patients measured at discharge and 6-month check-up**

GOSE Score	3	4	5	6	7	Average
At discharge (no. of patients)	2 (10%)	7 (33%)	10 (48%)	1 (5%)	1 (5%)	4.6 ± 0.9
At 6-month check-up (no. of patients)	0	1 (5%)	8 (38%)	8 (38%)	4 (19%)	5.7 ± 0.6

and 6-month follow-up supported this assumption. In our study, no patient showed recurrent bleeding or technique-related post-surgery complication, whereas the reported studies have shown that the complication rate of the stereotactic aspiration treatment was 17.9%–37.3%, and the rebleeding incidence was 5%–13.3%.<sup>6,15–19</sup>

For the FDCT/fluoro-assisted hematoma evacuation in the angiographic suite, our experiences in 21 hypertensive patients with ICH were concluded as follows: 1) Puncture site selection: The frontal approach was preferred over the temporal approach because of the consideration that there is relatively less neurologic and vascular traffic in the frontal lobe area. In addition, puncturing and advancing the catheter from the forehead was convenient for operators because the bull's eye view and progression views in the C-arm were nearly vertical and horizontal in direction, with minimal interference on operations and anesthesia. 2) Operation procedures: We suggested generating the burr-hole before the acquisition of planning FDCT for this specific application on a

human head. In this way, the impact of the twist drill on the scalp and head shift will be excluded from the puncture planning; 3) Surgery timing: At least 24 hours after the onset of the hemorrhage. Although there were extensive reports of the benefit of ultra-early and early removal of the hematoma in the literature, the surgery timing is still controversial due to a lack of evidence-based support. In our opinion, the hematoma drainage could be easier and the risk of rebleeding could be lower when we allow at least 1 day for hematoma to liquefy.

One of the important benefits of this demonstrated FDCT/fluoro-assisted minimally invasive surgery was the low cost of the procedure, as it can be performed in the traditional angiographic suite, without adding extra cost to patients for specialized devices. The shortened operation time compared with craniotomy also significantly reduced the clinical cost of this procedure. This is especially useful for underdeveloped countries that experience high patient volume but have limited medical resources. In this way, more low-income patients will have the chance to receive timely treatment. Moreover, given the low cost and high performance of the procedure, this could potentially encourage more eligible patients to be recruited into a future prospective study.

One limitation of this study is that only patients with indications for surgery were included in this retrospective study. Although we attempted to compare the treatment outcome with published meta-

analysis results from large-scale clinical trials, the comparison was not based on the same patient baseline. Retrospectively matching the surgery group with patients receiving medical treatment only, however, could bring uncertainties such as different medical treatment strategies and varied treatment timings into comparison because patient treatments were originally conducted without clear guidelines. Hence, though the feasibility of this FDCT/fluoro-guided ICH evacuation was demonstrated, one of our immediate future works is to initiate a multicenter, prospective trial that compares the immediate and long-term treatment outcome of combined FDCT/fluoro-assisted minimally invasive surgery and urokinase treatment with conventional medical therapy only for patients with ICH.

## CONCLUSIONS

We demonstrated the feasibility of performing intracranial hemorrhage evacuation in an angiographic suite, with the assistance of puncture planning and guidance software that uses intraprocedural FDCT and fluoroscopy. According to our clinical outcomes,

intraprocedural FDCT and integrated needle guidance software provided a feasible, convenient, and safe solution for hemorrhage evacuation. In the future, the benefit of this demonstrated image-guided ICH evacuation should be further investigated in a large-scale prospective and randomized trial.

Disclosures: Jijia Ge is employed by Siemens Healthcare. Siemens Healthcare supports some of the scientific activities on which this manuscript is based. Jingfeng Han is employed by Siemens Limited China. Janina Beilner is working for Siemens Limited China; Siemens equipment was used for this study.

## REFERENCES

1. Qureshi AI, Mendelow AD, Hanley DF. **Intracerebral haemorrhage.** *Lancet* 2009;373:1632–44
2. Broderick J, Connolly S, Feldmann E, et al. **Guidelines for the management of spontaneous intracerebral hemorrhage in adults: 2007 update: a guideline from the American Heart Association/American Stroke Association Stroke Council, High Blood Pressure Research Council, and the Quality of Care and Outcomes in Research Interdisciplinary Working Group.** *Stroke* 2007;38:2001–23
3. Elliott J, Smith M. **The acute management of intracerebral hemorrhage: a clinical review.** *Anesth Analg* 2010;110:1419–27
4. Mendelow AD, Gregson BA, Fernandes HM, et al. **Early surgery versus initial conservative treatment in patients with spontaneous supratentorial intracerebral haematomas in the International Surgical Trial in Intracerebral Haemorrhage (STICH): a randomised trial.** *Lancet* 2005;365:387–97
5. Sykora M, Diedler J, Juttler E, et al. **Intensive care management of acute stroke: surgical treatment.** *Int J Stroke* 2010;5:170–77
6. Zhou H, Zhang Y, Liu L, et al. **A prospective controlled study: minimally invasive stereotactic puncture therapy versus conventional craniotomy in the treatment of acute intracerebral hemorrhage.** *BMC Neurol* 2011;11:76
7. Kuo LT, Chen CM, Li CH, et al. **Early endoscope-assisted hematoma evacuation in patients with supratentorial intracerebral hemorrhage: case selection, surgical technique, and long-term results.** *Neurosurg Focus* 2011;30:E9
8. Barlas O, Karadereler S, Bahar S, et al. **Image-guided keyhole evacuation of spontaneous supratentorial intracerebral hemorrhage.** *Minim Invasive Neurosurg* 2009;52:62–68
9. Morgan T, Zuccarello M, Narayan R, et al. **Preliminary findings of the minimally-invasive surgery plus rtPA for intracerebral hemorrhage evacuation (MISTIE) clinical trial.** *Acta Neurochir Suppl* 2008;105:147–51
10. Dey M, Stadnik A, Awad IA. **Spontaneous intracerebral and intraventricular hemorrhage: advances in minimally invasive surgery and thrombolytic evacuation, and lessons learned in recent trials.** *Neurosurgery* 2014;74(suppl 1):S142–50
11. Kyriakou Y, Struffert T, Dorfler A, et al. **Basic principles of flat detector computed tomography (FD-CT).** *Der Radiologe* 2009;49:811–19
12. Freundt MI, Ritter M, Al-Zghloul M, et al. **Laser-guided cervical selective nerve root block with the Dyna-CT: initial experience of three-dimensional puncture planning with an ex-vivo model.** *PloS One* 2013;8:e69311
13. Ritter M, Rassweiler MC, Hacker A, et al. **Laser-guided percutaneous kidney access with the Uro Dyna-CT: first experience of three-dimensional puncture planning with an ex vivo model.** *World J Urol* 2013;31:1147–51
14. Fujisawa M, Yamashita S, Katagi R. **Usefulness of intraoperative computed tomography for the evacuation of lobar hemorrhage.** *Acta Neurochir Suppl* 2013;118:175–79
15. Bhattathiri PS, Gregson B, Prasad KS, et al. **Intraventricular hemorrhage and hydrocephalus after spontaneous intracerebral hemorrhage: results from the STICH trial.** *Acta Neurochir Suppl* 2006;96:65–68
16. Hanley DF. **Intraventricular hemorrhage: severity factor and treatment target in spontaneous intracerebral hemorrhage.** *Stroke* 2009;40:1533–38
17. Rossitti S. **Spontaneous intracerebral and intraventricular hemorrhage. Hemostasis by transarterial glue embolization.** *Clin Neuro-radiol* 2010;20:131–34
18. Marquardt G, Wolff R, Janzen RW, et al. **Basal ganglia haematomas in non-comatose patients: subacute stereotactic aspiration improves long-term outcome in comparison to purely medical treatment.** *Neurosurg Rev* 2005;28:64–69
19. Tang ZP, Shi YH, Yin XP, et al. **Modifying the details of aspiration operation may contribute to the improvement of prognosis of patients with ICH.** *Turk Neurosurg* 2012;22:13–20

# Imaging-Detected Incidental Thyroid Nodules that Undergo Surgery: A Single-Center Experience Over 1 Year

M. Bahl, J.A. Sosa, R.C. Nelson, and J.K. Hoang



## ABSTRACT

**BACKGROUND AND PURPOSE:** Incidental thyroid nodules are commonly seen on imaging, and their work-up can ultimately lead to surgery. We describe characteristics and pathology results of imaging-detected incidental thyroid nodules that underwent surgery.

**MATERIALS AND METHODS:** A retrospective review was performed of 303 patients who underwent thyroid surgery over a 1-year period to identify patients who presented with incidental thyroid nodules on imaging. Medical records were reviewed for the types of imaging studies that led to detection, nodule characteristics, and surgical pathology.

**RESULTS:** Of 303 patients, 208 patients (69%) had surgery for thyroid nodules. Forty-seven of 208 patients (23%) had incidental thyroid nodules detected on imaging. The most common technique leading to detection was CT (47%). All patients underwent biopsy before surgery. The cytology results were nondiagnostic (6%), benign (4%), atypia of undetermined significance or follicular neoplasm of undetermined significance (23%), follicular neoplasm or suspicious for follicular neoplasm (19%), suspicious for malignancy (17%), and diagnostic of malignancy (30%). Surgical pathology was benign in 24 of 47 (51%) cases of incidental thyroid nodules. In the 23 incidental cancers, the most common histologic type was papillary (87%), the mean size was 1.4 cm, and nodal metastases were present in 7 of 23 cases (30%). No incidental cancers on imaging had distant metastases.

**CONCLUSIONS:** Imaging-detected incidental thyroid nodules led to nearly one-fourth of surgeries for thyroid nodules, and almost half were initially detected on CT. Despite indeterminate or suspicious cytology results that lead to surgery, more than half were benign on final pathology. Guidelines for work-up of incidental thyroid nodules detected on CT could help reduce unnecessary investigations and surgery.

**ABBREVIATIONS:** FNAB = fine needle aspiration biopsy; ITN = incidental thyroid nodule

Incidental thyroid nodules (ITNs) are commonly encountered on imaging studies, being seen in 50% of ultrasonographic studies and 16%–18% of CT and MR imaging studies that include the thyroid gland.<sup>1–3</sup> While ITNs are associated with a low rate of malignancy, and subclinical thyroid cancers have an excellent prognosis,<sup>2–6</sup> ITNs pose a management dilemma for radiologists and other clinicians whose concern for missing malignancies may lead to further evaluation for small nonspecific thyroid nodules.

The reporting practice of ITNs seen on imaging is highly variable among radiologists.<sup>7</sup> Radiologists must exercise their judgment when reporting and issuing recommendations regarding incidental thyroid nodules. The reporting of ITN on imaging can lead to further investigation, such as follow-up sonography examinations, fine needle aspiration biopsy (FNAB), or, in some cases, diagnostic thyroid lobectomy or thyroidectomy.<sup>8,9</sup> Of patients who undergo FNAB, 22%–51% proceed to surgery.<sup>10–12</sup> These surgical patients represent an important group to study because they have higher costs and morbidity associated with the work-up of their ITNs. Thus, it is important to consider the costs and benefits of work-up in patients with ITN who fall into this surgical group.

A substantial number of patients who undergo surgery do not have cancer.<sup>10</sup> When the preoperative cytology result from FNAB is malignant, the sensitivity of cytology is high (99%).<sup>13</sup> However, it is recommended that patients with cytology of “follicular neoplasm,” “suspicion for follicular neoplasm,” and “suspicion for malignancy” also proceed to surgery. With these other categories, the false-positive rate of cytology can be as high as 44%.<sup>13</sup> In

Received March 5, 2014; accepted after revision April 16.

From the Departments of Radiology (M.B., R.C.N., J.K.H.), Radiation Oncology (J.K.H.), and Surgery, Duke Cancer Institute and Duke Clinical Research Institute (J.A.S.), Duke University Medical Center, Durham, North Carolina.

Paper previously presented at: Annual Meeting of the American Society of Head and Neck Radiology, September 25–39, 2013; Milwaukee, Wisconsin.

M. Bahl was the recipient of the ASHNR Radiologist-in-Training Award for 2013.

Please address correspondence to Jenny K. Hoang, MBBS, Duke University Medical Center, Department of Radiology, Box 3808, Erwin Rd, Durham, NC 27710; e-mail: jennykh@gmail.com

<http://dx.doi.org/10.3174/ajnr.A4004>

addition, thyroid surgery can result in such complications as recurrent laryngeal nerve injury, hypoparathyroidism, and bleeding. Therefore, radiologists should understand the downstream sequelae of a clinical pathway that begins with an imaging-detected ITN and ends with surgery.

The purpose of this study was to describe characteristics and pathology results of ITNs that undergo surgery. We hypothesize that imaging-detected ITN comprise a substantial proportion of surgeries for thyroid nodules, and that many thyroid nodules are in the end benign on final surgical pathology.

## MATERIALS AND METHODS

### Study Subjects

We performed a retrospective study of 303 consecutive patients who underwent thyroidectomy or lobectomy between January 1, 2012, and December 31, 2012, at a single large academic institution to identify patients who presented with an ITN on imaging. Patients were identified by Current Procedural Terminology codes for thyroid lobectomy and thyroidectomy (60210, 60212, 60220, 60240, 60252, 60254, 60255, 60260, 60270, and 60271). Medical records were reviewed for the presentation of the thyroid nodule and identification of thyroid cancer. This study was approved by the Institutional Review Board and was compliant with the Health Insurance Portability and Accountability Act.

An ITN on imaging was defined as a nodule originally detected on an imaging study performed for other reasons in a patient with no clinical symptoms, examination findings, or suspicion for thyroid cancer. Patients were excluded if they had a palpable nodule or mass (representing primary or nodal disease) or had thyroid nodules detected on sonography performed for abnormal thyroid function test results without a palpable nodule or mass. The decision to biopsy an ITN is made by the referring clinician. Many clinicians follow the American Thyroid Association guidelines for sonography criteria, but this may not be uniform practice.<sup>14</sup>

Patients with ITN generally proceed to surgery if the cytologic results obtained by FNAB demonstrate follicular neoplasm or suspicion for follicular neoplasm, suspicion for malignancy, or malignancy (Bethesda classes IV, V, and VI).<sup>15</sup> Patients could also proceed to surgery if cytology demonstrates atypia of undetermined significance or follicular lesion of undetermined significance (Bethesda class III) if they do not want to undergo surveillance or rebiopsy or have worrisome characteristics on sonography. Medical records were also reviewed for demographic information, including patient age and sex, clinical features, including the risk factors for thyroid cancer such as a family history of glandular abnormalities or exposure to external beam radiation, and nodule characteristics on imaging.

### Outcome Measures and Statistical Analysis

The primary outcomes of interest were the cytology and final surgical pathology results. These results were interpreted by board-certified pathologists. We also described the pattern of work-up, including imaging studies leading to detection, subsequent steps in work-up, and timing of surgery after detection of the nodule. The imaging-detected incidental cancers were reviewed for cancer characteristics, histology, and tumor stage according to the American Joint Committee on Cancer.<sup>16</sup> Patient

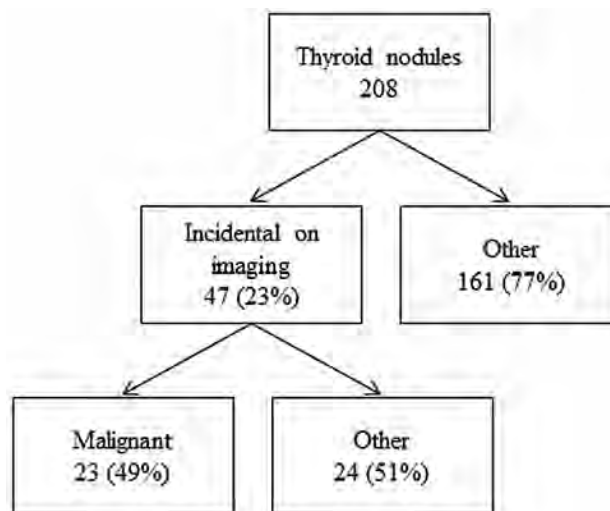


FIG 1. Flowchart of study subjects.

demographic data, nodule size, imaging modalities, and FNAB cytology were compared for the benign and malignant imaging-detected ITNs with the unpaired *t*-test for continuous data and the  $\chi^2$  test or Fisher exact test for categorical data. The Fisher exact test was used when expected cell frequencies were less than 5. Specifically, for categorical variables with independent groups, *P* values were calculated for CT versus other imaging modalities and for cytology diagnostic categories I, II, and III versus IV, V, and VI. *P* < .05 was considered to indicate a statistically significant difference. Data were entered into a spreadsheet for analysis and generation of the descriptive statistics (Excel; Microsoft, Redmond, Washington). Statistical analyses were performed using SAS Enterprise software (version 4.2; SAS Institute, Cary, North Carolina).

## RESULTS

Over a 1-year period, 303 patients (236 females and 67 males, mean age 51 years, age range of 8–87, and with 5 patients younger than 16 years of age) underwent thyroid surgery for symptomatic and asymptomatic thyroid disease. Of the 303 patients who underwent surgery, 208 (69%) patients underwent surgery for thyroid nodules and 95 (31%) were for symptomatic multinodular goiter or hyperthyroidism refractory to medical treatment (Fig 1).

Of the 208 patients who presented with thyroid nodules, 47 (23%) had ITNs detected on imaging (Table 1). The most common imaging studies leading to detection were CT (22 of 47, 47%), followed by PET/CT (10 of 47, 21%), sonography (9 of 47, 19%), MR imaging (4 of 47, 9%), chest radiograph (1 of 47, 2%), and echocardiogram (1 of 47, 2%). Of note, 6 of the sonography studies were performed for evaluation of the carotid arteries, and 3 were performed for purposes of parathyroid adenoma localization in patients with primary hyperparathyroidism. All 47 patients with imaging-detected ITN underwent FNAB within a median of 34 days (interquartile range 18–82 days). In 4 (9%) patients, the decision to biopsy was based on the initial imaging, and full diagnostic sonography was not performed.

The FNAB cytology results for the 47 patients with imaging-detected ITN were nondiagnostic (*n* = 3, 6%), benign (*n* = 2, 4%), atypia of undetermined significance or follicular neoplasm of undetermined significance (*n* = 11, 23%), follicular neoplasm

**Table 1: Characteristics of benign and malignant ITNs that undergo surgery**

	Benign ITN	Malignant ITN	All ITN	P Value
Age <sup>a</sup>	58 ± 14	54 ± 13	56 ± 14	.3
Sex				
Female	16 (67)	19 (83)	35 (74)	.3 <sup>b</sup>
Male	8 (33)	4 (17)	12 (26)	
Nodule size (in mm)				
Imaging <sup>a</sup>	22 ± 13	17 ± 7	20 ± 11	.2
Pathology	NA	14 ± 8	NA	
Imaging modality on which ITN was detected				.2 <sup>b,c</sup>
CT	9 (38)	13 (57)	22 (47)	
PET/CT	4 (17)	6 (26)	10 (21)	
Ultrasound	7 (29)	2 (9)	9 (19)	
MRI	3 (13)	1 (4)	4 (9)	
Chest radiograph	1 (4)	0	1 (2)	
Echocardiogram	0	1 (4)	1 (2)	
Cytology				<.001 <sup>b,d</sup>
I—Nondiagnostic or unsatisfactory	2 (8)	1 (4)	3 (6)	
II—Benign	2 (8)	0	2 (4)	
III—Atypia of undetermined significance/ follicular lesion of undetermined significance	10 (42)	1 (4)	11 (23)	
IV—Follicular neoplasm/suspicious for follicular neoplasm	8 (33)	1 (4)	9 (19)	
V—Suspicious for malignancy	2 (8)	6 (26)	8 (17)	
VI—Malignant	0	14 (61)	14 (30)	
Total	24	23	47	

**Note:**—Unless otherwise specified, data are numbers of patients, with percentages in parentheses. Percentages may not add up to 100% due to rounding.

<sup>a</sup> Data reported as mean ± standard deviation.

<sup>b</sup> Calculated with Fisher exact test.

<sup>c</sup> For CT versus other imaging modalities.

<sup>d</sup> For diagnostic categories I, II, and III versus IV, V, and VI.

or suspicious for follicular neoplasm ( $n = 9$ , 19%), suspicious for malignancy ( $n = 8$ , 17%), and diagnostic of malignancy ( $n = 14$ , 30%). Note that the 2 patients with benign cytologies underwent thyroid lobectomy at the same time as parathyroidectomy for primary hyperparathyroidism.

The median time between the FNAB and thyroid surgery was 46 days (interquartile range 28–77 days). Despite the cytology results, the final surgical pathology was benign in 24 of 47 (51%). In the 23 incidental cancers, the histologic types were 20 papillary (87%), 2 follicular (9%), and 1 medullary (4%) thyroid cancer. The mean and median size of imaging-detected tumors was 1.4 cm (SD 0.8 cm) and 1.2 cm (interquartile range 1.0–1.6 cm), respectively. Nodal metastases were present in 7 of 23 (30%), 4 of which were present in the central neck compartment (N1a) and 3 of which were present in the lateral neck compartment (N1b). No incidental cancers on imaging had distant (extra-cervical) metastases.

## DISCUSSION

Outcomes of imaging-detected ITN have been reported, but this study is the first to focus on ITN in patients who underwent surgery. This group represents only a fraction of all ITNs encountered in a radiology practice, but it is a group that is more likely to harbor malignancy and to have higher costs associated with work-up. We found that imaging-detected ITNs comprise nearly one-fourth of surgeries for thyroid nodules. Despite cytology results that lead to surgery, more than half of ITNs are ultimately benign on final surgical pathology.

The malignancy rate in ITNs undergoing surgery varies widely in the existing literature. Kroeker et al<sup>11</sup> studied 133 imaging-detected ITNs referred to a single surgeon and found that 41% were managed surgically, of which 86% were malignant. Hobbs et al<sup>10</sup> also evaluated 114 imaging-detected ITNs in patients who underwent FNAB under sonography guidance. They found that 25% of patients proceeded to surgery after FNAB, and only 24% of these patients were diagnosed with thyroid cancer. The marked difference in malignancy rate is likely related to differences in the study cohorts. Patients referred to a single surgeon in Kroeker et al's<sup>11</sup> study were more likely to have malignancy because they were referred for concerning features that warrant surgery. Hobbs et al's<sup>10</sup> study cohort was more likely to have benign pathology results because it represents indeterminate ITNs that a radiologist was asked to biopsy under sonography, and many of these nodules were small. Our study had a malignancy rate of 49%, which lies between these 2 studies. All 3 studies highlight that FNAB is a minimally invasive and critical diagnostic tool, but it is important to select nodules carefully for biopsy.

After FNAB, a significant portion of patients with imaging-detected ITN proceed to surgery because of suspicious or indeterminate cytology results and many may be for benign disease. New strategies, such as sonography elastography and molecular testing, may reduce unnecessary surgery in those patients with inconclusive FNAB.<sup>17</sup> Another strategy may be to apply stricter guidelines to reduce FNAB or to observe thyroid nodules with serial ultrasounds rather than performing FNAB.<sup>14,18</sup>

Another reason for studying a group of surgical ITNs is to understand the contribution of imaging-detected ITN to a surgical cohort. In our study, 23% of thyroid nodules that proceeded to surgery were imaging-detected ITNs. The rate of ITN is similar to the study by Hobbs et al<sup>10</sup> whose cohort were patients undergoing sonography-guided FNAB; they found that 29% (114 of 390) of these patients presented with imaging-detected ITN. Other studies that focus on thyroid cancers report that 15%–39% are incidental cancers detected on imaging.<sup>19,20</sup> It is possible that many of the incidental cases in our study would not have been diagnosed in the patient's lifetime if not for imaging. If we consider the scenario in which they were not diagnosed, the impact would be 23 undiagnosed cancers and 24 patients who would not have undergone work-up and surgery for benign disease in 1 year at our institution. While missing 23 cancers in 1 year may alarm some radiologists, it is important to recognize that most of the cancers were localized small papillary thyroid cancers, which have excellent prognosis with treatment. Although it is controversial, many believe the prognosis is excellent even without treatment, especially for older patients ( $\geq 60$  years).<sup>21,22</sup> The disadvantage of

**Table 2: The Duke 3-tiered system for CT, MRI, or PET-detected thyroid nodules**

Category	Criteria for Categories	Recommendations
Risk category 1: Highly suspicious for malignancy	PET avid thyroid nodule Suspicious lymphadenopathy <sup>a</sup> Extrathyroid spread with or without signs of vocal cord palsy on side of nodule Lung metastases	Strongly consider work-up with ultrasound for any size nodule
Risk category 2: Indeterminate with risk factor of young age	Age <35 years	Consider work-up with ultrasound if ≥1 cm in adults Consider work-up with ultrasound for any size in pediatric patients
Risk category 3: Indeterminate without risk factors	Age ≥35 years	Consider work-up with ultrasound if ≥1.5 cm

**Note:**—Intended for management of incidental thyroid nodules in low-risk patients.

<sup>a</sup>Suspicious lymph nodes are defined as nodes >10 mm in short axis (with the exception of jugulodigastric lymph nodes, which were permitted to be up to 15 mm in short axis), or nodes that contained either calcifications, cystic components, or irregular margins.

work-up is that these 47 patients represent just a small fraction of the patients who underwent work-up for ITN with sonography and FNAB. The health care costs attributed to work-up of thyroid nodules is significant because 1 in 2 Americans have thyroid nodules greater than 5 mm.<sup>6</sup>

An unexpected finding in this study was that CT accounted for almost half of ITNs that went to surgery. Sonography has higher resolution than CT and has been commonly proposed as the primary technique responsible for the over-diagnosis of thyroid cancer.<sup>2,3</sup> Our study draws attention to CT as a large source of ITNs. This finding may also be explained, in part, by the fact that CT utilization has increased rapidly in the United States, at a rate greater than sonography, and utilization of CT scanning exceeds sonography.<sup>24,25</sup> Hoang et al<sup>24</sup> reported a strong linear relationship between new cases of subcentimeter thyroid cancer and the number of CT scans per year, suggesting that the increase in CT scans may account for increased detection of incidental thyroid cancers. The fact that nearly half of ITNs that proceed to surgery are detected on CT underscores the need for guidelines to reduce the potentially unnecessary work-up of CT-detected ITN. The Duke three-tiered system (Table 2), for example, addresses ITN on CT, MR imaging, and PET/CT and has been shown to reduce the number of benign biopsies by more than one-third without missing clinically significant malignancies.<sup>3,10,26</sup>

There were several limitations to this study. First, this study was retrospective in nature and was performed at a single academic radiology practice, which may differ from other institutions with regard to the reporting and work-up of incidental thyroid nodules, the diagnostic yield of FNAB, and the accuracy of cytopathology. Second, the criteria we used to define incidental cancers on imaging may underestimate the incidental cancer rate compared with criteria used in other studies. If we had included nonpalpable cancers in patients with abnormal thyroid function test results, the prevalence of incidental thyroid cancers would be higher. We chose to exclude these groups to estimate the impact of work-up of nodules that radiologists encounter when imaging is performed for reasons truly unrelated to the thyroid gland.

## CONCLUSIONS

Imaging-detected ITNs comprise nearly one-fourth of surgeries for thyroid nodules at our institution, and CT scans are the source of almost half of the ITNs identified in this series. Despite indeterminate or suspicious cytology that leads to surgery, more than half are benign on final pathology. Most incidental thyroid can-

cers on imaging are small papillary cancers without nodal and distant metastases. Future guidelines that address reporting and work-up of ITNs seen on CT imaging may better tailor work-up and reduce unnecessary surgery.

**Disclosures:** Julie Sosa—UNRELATED: participated in one-time advisory committee meeting sponsored by Bayer; received one-time honorarium from Exelixis for a speech about surgery. Rendon Nelson—UNRELATED: Consultancy: GE Healthcare; Expert Testimony: settled case *Woessner v. Toledo Hospital*; Grants/Grants Pending: Bracco Diagnostics for research support\*; Payment for Lectures Including Service on Speakers Bureaus: Applied Radiology; Patents Issued: GE Healthcare. Comments: using the scout radiograph on CT to determine the contrast media dose (no payment or money for this); Royalties: Lippincott Williams and Wilkins. \*Money paid to the institution.

## REFERENCES

- Acar T, Ozbek SS, Acar S. Incidentally discovered thyroid nodules: frequency in an adult population during Doppler ultrasonographic evaluation of cervical vessels. *Endocrine* 2014;45:73–78
- Yousem DM, Huang T, Loevner LA, et al. Clinical and economic impact of incidental thyroid lesions found with CT and MR. *AJNR Am J Neuroradiol* 1997;18:1423–28
- Nguyen XV, Choudhury KR, Eastwood JD, et al. Incidental thyroid nodules on CT: evaluation of 2 risk-categorization methods for work-up of nodules. *AJNR Am J Neuroradiol* 2013;34:1812–17
- Yoon DY, Chang SK, Choi CS, et al. The prevalence and significance of incidental thyroid nodules identified on computed tomography. *J Comput Assist Tomogr* 2008;32:810–15
- National Cancer Institute Surveillance, Epidemiology, and End Results, Data 1983 to 2009. <http://seer.cancer.gov/>. Accessed December 15, 2012
- Smith-Bindman R, Lebda P, Feldstein VA, et al. Risk of thyroid cancer based on thyroid ultrasound imaging characteristics: results of a population-based study. *JAMA Intern Med* 2013;173:1788–96
- Hoang JK, Riofrio A, Bashir MR, et al. High variability in radiologists' reporting practices for incidental thyroid nodules detected on CT and MRI. *AJNR Am J Neuroradiol* 2014;35:1190–94
- Centers for Medicare and Medicaid Services. Physician Fee Schedule Search. <http://www.cms.gov/apps/physician-fee-schedule/>. Accessed December 4, 2012
- Bahl M, Sosa JA, Nelson RC, et al. Thyroid cancers incidentally detected at imaging in a 10-year period: how many cancers would be missed with use of the recommendations from the Society of Radiologists in Ultrasound? *Radiology* 2014;271:888–94
- Hobbs HA, Bahl M, Nelson RC, et al. JOURNAL CLUB: Incidental thyroid nodules detected at imaging: can diagnostic workup be reduced by use of the Society of Radiologists in Ultrasound recommendations and the three-tiered system? *AJR Am J Roentgenol* 2014;202:18–24
- Kroeker TR, le Nobel G, Merdad M, et al. Outcomes of incidentally

- discovered thyroid nodules referred to a high-volume head and neck surgeon. *Head Neck* 2014;36:126–29
12. Shrestha M, Crothers BA, Burch HB. **The impact of thyroid nodule size on the risk of malignancy and accuracy of fine-needle aspiration: a 10-year study from a single institution.** *Thyroid* 2012;22:1251–56
  13. Bongiovanni M, Spitale A, Faquin WC, et al. **The Bethesda system for reporting thyroid cytopathology: a meta-analysis.** *Acta Cytol* 2012;56:333–39
  14. American Thyroid Association (ATA) Guidelines Taskforce on Thyroid Nodules and Differentiated Thyroid Cancer, Cooper DS, Doherty GM, et al. **Revised American Thyroid Association management guidelines for patients with thyroid nodules and differentiated thyroid cancer.** *Thyroid* 2009;19:1167–214
  15. Cibas ES, Ali SZ. **NCI Thyroid FNA. State of the Science Conference. The Bethesda system for reporting thyroid cytopathology.** *Am J Clin Pathol* 2009;132:658–65
  16. National Cancer Institute. Stage Information for Thyroid Cancer. <http://www.cancer.gov/cancertopics/pdq/treatment/thyroid/HealthProfessional/page3>. Accessed December 6, 2012
  17. Tonacchera M, Pinchera A, Vitti P. **Assessment of nodular goitre.** *Best Pract Res Clin Endocrinol Metab* 2010;24:51–61
  18. Frates MC, Benson CB, Charboneau JW, et al. **Management of thyroid nodules detected at US: Society of Radiologists in Ultrasound consensus conference statement.** *Radiology* 2005;237:794–800
  19. Bahl M, Sosa JA, Nelson RC, et al. **Trends in incidentally identified thyroid cancers over a decade: a retrospective analysis of 2,090 surgical patients.** *World J Surg* 2014;38:1312–17
  20. Malone MK, Zagzag J, Ogilvie JB, et al. **Thyroid cancers detected by imaging are not necessarily small or early stage.** *Thyroid* 2014;24:314–18
  21. Ito Y, Miyauchi A, Inoue H, et al. **An observational trial for papillary thyroid microcarcinoma in Japanese patients.** *World J Surg* 2010;34:28–35
  22. Ito Y, Miyauchi A, Kihara M, et al. **Patient age is significantly related to the progression of papillary microcarcinoma of the thyroid under observation.** *Thyroid* 2014;24:27–34
  23. Davies L, Welch HG. **Increasing incidence of thyroid cancer in the United States, 1973–2002.** *JAMA* 2006;295:2164–67
  24. Hoang JK, Choudhury KR, Eastwood JD, et al. **An exponential growth in incidence of thyroid cancer: trends and impact of CT imaging.** *AJNR Am J Neuroradiol* 2014;35:778–83
  25. Davies L, Welch HG. **Current thyroid cancer trends in the United States.** *JAMA Otolaryngol Head Neck Surg* 2014;140:317–22
  26. Hoang JK, Raduazo P, Yousem DM, et al. **What to do with incidental thyroid nodules on imaging? An approach for the radiologist.** *Semin Ultrasound CT MR* 2012;33:150–57

# The “Boomerang” Malleus-Incus Complex in Congenital Aural Atresia

S. Mukherjee, B.W. Kesser, and P. Raghavan

## ABSTRACT

**SUMMARY:** “Boomerang” malleus-incus fusion deformity is identified on axial high-resolution CT in a subset of patients with congenital aural atresia, and it is associated with an absent incudostapedial joint and stapes capitulum and attachment of the incus to the tympanic segment of the facial nerve canal. Twelve patients with this deformity were identified on a retrospective review of imaging from a cohort of 673 patients with congenital aural atresia, with surgical confirmation in 9 of these patients. Eight of 9 patients underwent partial ossicular replacement prosthesis reconstruction with improvement in hearing outcome. We hypothesize that the boomerang anomaly represents a more severe ossicular anomaly than is normally seen in congenital aural atresia, arising from an arrest earlier in the embryonic development of the first and second branchial arch. This has potentially important implications for surgical planning because hearing outcomes with placement of prosthesis may not be as good as with conventional atresia surgery, in which reconstruction is performed with the patient’s native ossicular chain.

**ABBREVIATIONS:** CAA = congenital aural atresia; HRCT = high-resolution CT; PORP = partial ossicular replacement prosthesis

Congenital aural atresia (CAA) is a rare disorder of the temporal bone with an estimated incidence of 1 in 10–20,000 live births.<sup>1</sup> CAA refers to a spectrum of predominantly external and middle ear abnormalities resulting from incomplete or arrested development of the first and sometimes second branchial arches. The anomaly includes a failure of canalization of the external auditory canal with varying degrees of atresia, or underdevelopment, of the middle ear and ossicles. Depending on the timing of the arrest in development, the ear canal can be completely absent or mildly stenotic, with a wide range of ossicular malformations most commonly involving the malleus and incus.<sup>2</sup>

While patients with CAA have a wide variety of ossicular malformations and configurations seen on high-resolution CT (HRCT), we present a series of 12 patients with a characteristic “boomerang”-shaped fusion abnormality of the malleus and incus on axial sections through the epitympanum. In this anomaly, the malleus is hypoplastic, with an absent neck, manu-

brium, and umbo. The incus is the dominant ossicle and is fused to a rudimentary, hypoplastic malleus head to form the boomerang. This abnormality is accompanied by absence/hypoplasia of the stapes capitulum and ossicular discontinuity, with a fibrous attachment of the dysplastic incus to the tympanic segment of the facial nerve canal (Fig 1).

Recognition of this characteristic imaging finding can alert the radiologist and otologic surgeon to the presence of the associated findings. Because the incus is not attached to the stapes, this deformity will most often require a partial ossicular replacement prosthesis (PORP) reconstruction; hence, this finding should be communicated to the referring surgeon for optimal clinical decision-making, surgical planning, and patient counseling.

## MATERIALS AND METHODS

### Patients

This study was approved by the institutional review board of the University of Virginia, which waived consent for the study (IRB-HSR 16763). Data were collected retrospectively from a chart and radiographic review, obviating individual patient consent. All data were de-identified in compliance with the institutional review board and Health Insurance Portability and Accountability Act regulations.

The cohort of 12 patients was collected through a retrospective search of electronic medical records of all patients diagnosed with CAA at our institution from 2001 to 2012, which was cross-referenced with the University of Virginia PACS imaging data base.

Received January 23, 2014; accepted after revision May 3.

From the Departments of Radiology and Medical Imaging (S.M.) and Otolaryngology-Head and Neck Surgery (B.W.K.), University of Virginia Health System, Charlottesville, Virginia; and Department of Diagnostic Radiology and Nuclear Medicine (P.R.), University of Maryland School of Medicine, Baltimore, Maryland.

Drs Mukherjee and Kesser are co-first authors.

Please address correspondence to Sugoto Mukherjee, MD, Department of Radiology and Medical Imaging, Division of Neuroradiology, University of Virginia Health System, PO Box 800170, Charlottesville, VA 22908-0170; e-mail: Sm5qd@virginia.edu

<http://dx.doi.org/10.3174/ajnr.A4022>

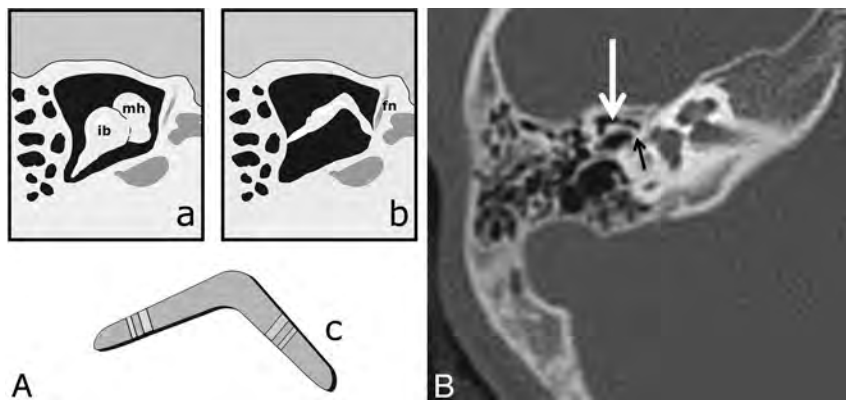


**FIG 1.** Schematic drawing (A) showing the normal appearance (a) of the malleus head (mh) and incus body (ib) and the abnormal fused dysplastic malleus-incus complex, appearing as a boomerang (b) as seen on axial CT images. Note the similarity to the appearance of a real boomerang (c). Axial HRCT scan (B) in patient 4 demonstrates the fused boomerang-shaped malleus head and incus body in the epitympanum (white arrow) and the attachment of the malleus-incus complex to the tympanic segment of the facial nerve canal (black arrow), rather than the stapes suprastructure. Also note the lateral attachment of the boomerang to the atretic plate. Findings were confirmed at surgery. fn indicates the location of tympanic segment of the facial nerve canal.

The search revealed 673 patients (770 ears) with CAA. Inclusion criteria were a diagnosis of CAA, an accessible HRCT on PACS (all outside films were loaded into the PACS system of the University of Virginia), and an identified boomerang malleus-incus complex either at surgery or, if the patient did not have surgery, through the author's (B.W.K.) CAA data base (UVA IRB 11484). Exclusion criteria included poor image quality secondary to motion artifacts and section width of  $>1.25$  mm. All imaging studies were performed with the same protocol (see below), established by the surgeon to optimize evaluation for surgical candidacy. Because several of the studies were from multiple outside institutions, exposure parameters and radiation dosages were not collected. No patient had a named syndrome.

The neuroimaging was reviewed by all authors together (who, by the nature of the finding, were not blinded to the presence of this anatomic abnormality), and the findings were reached by consensus and tabulated. All authors (2 attending neuroradiologists and 1 otologic surgeon) had a minimum of 10 years' experience reviewing temporal bone images. All imaging studies were performed for assessing the patient's suitability for canaloplasty surgery. Demographic data, Jahrsdoerfer grade, and clinical, radiographic, and surgical findings (in 9 of 12 patients) were gathered. Three patients elected not to have surgery, so the radiographic anatomy could not be surgically confirmed.

### CT Technique

All subjects in our institution had imaging performed on a 16-section LightSpeed Pro multidetector scanner (GE Healthcare, Milwaukee, Wisconsin). The raw data were acquired helically with 0.625-mm collimation at 300 mAs and 120 kV(peak), with coverage from the arcuate eminence through to the mastoid tip. The raw data from each ear were separated and reconstructed into 0.6- (section thickness) to 0.2-mm (reconstruction interval) axial images in bone algorithms.

All outside HRCT studies were acquired helically on multidetector CT scanners by using 0.625- to 1.0-mm section thickness and 0.3-mm interval reconstructions in bone

algorithms. Coronal and sagittal ( $1.5 \times 1$  mm thickness) reconstructions were obtained as per the outside protocol.

### Image Analysis

The HRCT images were interpreted in consensus by 3 experienced authors (S.M., P.R., and B.W.K.). The images were initially analyzed in the axial plane for the presence of the characteristic boomerang-shaped fusion abnormality of the malleus-incus complex in the epitympanum and any other associated abnormalities in the rest of the middle ear. The findings were then confirmed on multiplanar reformats. The Jahrsdoerfer grading scale was used to determine surgical candidacy and served as a template for the radiologic review,<sup>1</sup> with particular attention paid to the oval window, incudostapedial joint, stapes bone, and course of the facial nerve.

Imaging characteristics were correlated with ossicular and middle ear anatomy seen at the time of surgery for those patients undergoing surgical repair.

### Audiometric Outcomes

Pure tone average (defined as the average of the air-conduction thresholds at 500, 1000, 2000, and 4000 Hz), speech reception thresholds (minimum intensity of sound [threshold] at which a patient is able to repeat 50% of a spondee word list), and air-bone gap (difference between the air-conduction pure tone average and the bone-conduction pure tone average) were collected and compared between the preoperative and postoperative values.

### RESULTS

We identified 12 patients with CAA (10 males and 2 females) of 673 patients (770 ears) with the fused malleus-incus complex resembling a boomerang shape for a prevalence rate of 1.6 per 100 atretic ears. The ages of the patients ranged from 3 to 23 years. We obtained clinical and imaging data in all patients. Surgical confirmation was obtained in 9 of the 12 patients; 3 patients elected not to have surgery. All patients had grade III microtia, and all patients had complete atresia of the external auditory canal. Ten patients had unilateral CAA, with 2 patients having bilateral CAA. The boomerang deformity was unilateral in all patients. Demographic, clinical, and imaging findings are summarized in Table 1.

The characteristic fused boomerang malleus-incus complex was identified in all 12 patients on axial sections in the epitympanum (Fig 1). In this anomaly, the malleus is hypoplastic, with an absent neck, manubrium, and umbo. The incus is the dominant ossicle and is fused to a rudimentary, hypoplastic malleus head forming the boomerang. The boomerang complex also showed attachment laterally to the atretic tympanic plate in 9 patients and medially to the tympanic segment of the bony facial nerve canal in all patients (Figs 1 and 2). Coronal imaging shows mostly the incus with a hypoplastic malleus head and the absence of the incudostapedial joint at its expected location adjacent to the oval

**Table 1: Imaging and clinical findings in patients with boomerang malleus-incus complex in patients with CAA**

Pt	Age		Side	Boomerang Malleus-Incus Complex	Attachment to Tympanic Segment of Facial Canal	Absent/Dysmorphic Stapes Capitulum	Oval Window Stenosis/Atresia	Attachment to Atretic Plate	Jahrsdoerfer Score	Intraoperative Reconstruction
	(yr)	Sex								
1	8	M	R	Y	Y	Y	N	Y	7	Y-PORP
2	9	M	L	Y	Y	Y	N	Y	8	Y-No PORP <sup>a</sup>
3	9	F	R	Y	Y	Y	N	Y	7.5	Y-PORP
4	4	M	R	Y	Y	Y	N	Y	7	Y-PORP
5	3	M	R	Y	Y	Y	N	Y	6	Y-PORP
6	6	M	L	Y	Y	Y	N	N	6	Y-PORP
7	11	M	R	Y	Y	Y	N	N	7.5	Y-PORP
8	6	M	R	Y	Y	Y	N	Y	7.5	Y-PORP
9	23	M	L	Y	Y	Y	N	Y	6	Y-PORP
10	5	M	R	Y	Y	Y	N	N	7	No surgery
11	8	F	R	Y	Y	Y	N	Y	6.5	No surgery
12	11	F	R	Y	Y	Y	N	Y	6.5	No surgery

**Note:**—Pt indicates patient; L, left; R, right; Y, yes; N, no.

<sup>a</sup>No PORP was placed because the incudostapedial joint was intact.

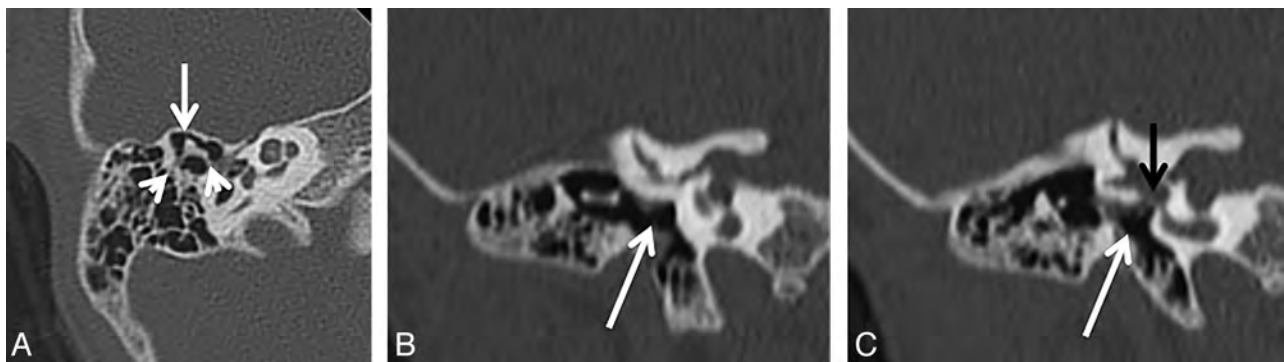


**FIG 2.** Axial (A) and coronal HRCT (B and C) images in patient 5 demonstrate the boomerang deformity (white arrow in A) and the attachment of the medial and lateral ends of this boomerang complex to the tympanic segment of the facial nerve canal medially and the atretic plate laterally (white arrowheads in A). Two sequential coronal images (B and C) show the absence of the incudostapedial articulation in its expected location (white arrow in B and C) adjacent to the oval window. The oval window appears patent (black arrow in C). The findings were confirmed at surgery. Additional findings of an absent stapes capitulum with the presence of the rest of the stapes suprastructure were also noted at surgery.

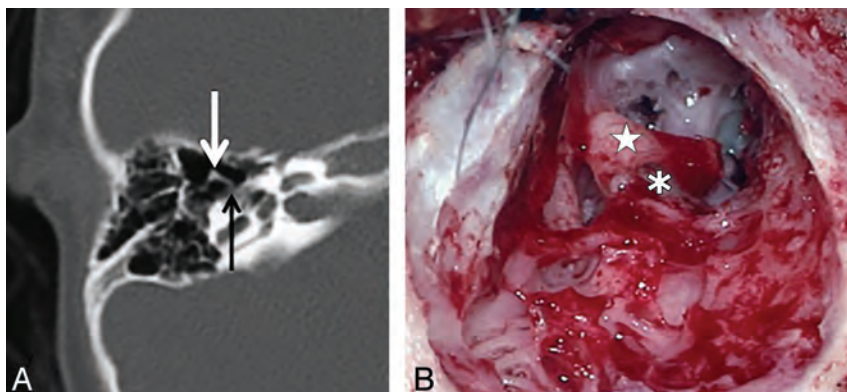


**FIG 3.** Axial HRCT (A) and intraoperative (B) images in patient 8 showing the fused malleus-incus complex in the right ear. Note the characteristic shape on both axial HRCT (arrow in A) and intraoperative (white star in B) images. This intraoperative image also shows a fibrous band extending medially from the complex toward the tympanic segment of the facial nerve canal (black arrow in A, white asterisk in B).

window. Moreover, the stapes capitulum was radiographically absent in all cases, and this finding was confirmed in 9 patients undergoing surgery. The remainder of the stapes suprastructure was intact. The oval window was patent in all patients (Fig 2), and the facial nerve took a somewhat anterior course in the second genu and mastoid segments. No inner ear abnormalities were identified.

At surgery, the dysmorphic malleus-incus complex was as described—a dominant incus with its body fused to a hypoplastic malleus head with absence of the neck, manubrium, and umbo (Figs 3 and 4). The long arm of the incus was attached to the bony tympanic facial nerve canal by a fibrous band; and the absent stapes suprastructure was confirmed in all 9 patients (Fig 3). The anterior position of the facial nerve at the second genu and early mastoid segment was confirmed at surgery in all patients, and the genu seemed to take a more acute angle than normal, but this was not measured. The ossicular deformity required removal of the boomerang malleus-incus complex with partial ossicular replacement prosthesis reconstruction in 8 of 9 patients. The PORP was not placed in 1 patient due to a fibrous attachment between the incus and stapes that was thought to be sufficient for sound transmission. No surgical complications, including sensorineural hearing loss, facial nerve injury, or labyrinthine injury, were noted.

With a mean follow-up of 28 months after surgery, patients

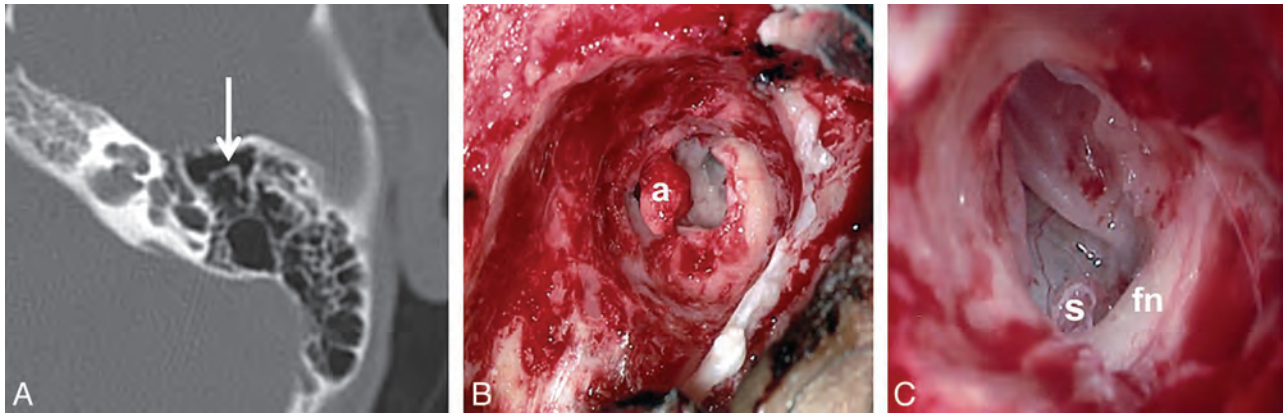


**FIG 4.** Axial HRCT images (A) in patient 9 show the boomerang complex in the left atretic ear. Intraoperative images (B and C) demonstrate the boomerang complex (a) and a dysmorphic stapes capitulum (S) after removal of the boomerang complex in C. fn represents the tympanic segment of the facial nerve.

**Table 2: Audiometric data for patients with a boomerang malleus-incus**

	Preop PTA	Preop SRT	Preop ABG	Postop PTA	Postop SRT	Postop ABG	Follow-Up (mo)
Patient No.							
1	72	65	69	32	25	30	24
2	57	50	55	32	25	22	58
3	72	65	59	33	35	25	36
4	57	50	42	18	10	16	43
5	65	60	60	42	40	37	33
6	77	70	74	20	15	7	4
7	65	40	50	43	35	23	1
8	67	65	59	27	25	24	53
9	73	65	48	28	25	8	1
Average	67.2	58.9	57.3	30.5	26.1	21.3	28.1

**Note:**—Preop indicates preoperative; Postop, postoperative; PTA, pure tone average; SRT, speech reception threshold; ABG, air-bone gap.

enjoyed significant improvement in hearing after surgery, with pure tone average improving 36.7 dB, speech reception thresholds improving 32.8 dB, and the air-bone gap improving 36 dB (Table 2). Average postoperative air-conduction pure tone average, speech reception thresholds, and air-bone gap were 30.5, 26.1, and 21.3, respectively.

## DISCUSSION

Surgical repair of congenital aural atresia is a challenging operation, which relies ultimately on choosing appropriate candidates for surgery. Not all patients with congenital aural atresia are candidates for surgery to open the ear canal to improve hearing. Patients must have normal inner function as demonstrated by bone-conduction audiometry, and the anatomy of the middle ear and its structures must be favorable to support the operation. HRCT is critical in the anatomic and surgical evaluation of patients with congenital aural atresia.<sup>1</sup>

Most patients, including those in this study, with CAA have normal inner ear function because of the different embryologic derivation of the inner ear (otocyst) from the middle and outer ear (branchial apparatus). Some children with CAA in the setting of a named syndrome do have inner ear abnormalities.<sup>3</sup> The children in this study were nonsyndromic, with normal inner ear morphology on CT and normal inner ear function as evidenced by normal bone-conduction thresholds on audiometry. CAA may stem from an arrest in the embryologic development of the first and possibly second branchial arches. The most common middle ear configuration seen is a malleus-incus complex fused to the

atretic plate/lateral middle ear wall, with a normal incudostapedial joint, stapes bone, and oval window. The facial nerve often takes a more acute turn at the second genu and is more anterior. The nerve can also course more laterally in the shortened mastoid segment.

The anatomic appearance of the middle ear and its structures on HRCT offers the surgeon an opportunity to anticipate the patient's middle ear anatomy and to prognosticate to the patient and family the chances of hearing improvement with surgery. To determine surgical candidacy, Jahrsdoerfer developed a 10-point grading scale more than 2 decades ago by using the CT imaging appearance of the middle ear structures and the outer ear.<sup>4</sup> A point is awarded on the basis of the appearance of each anatomic structure, with 2 points awarded for the stapes bone. The Jahrsdoerfer grading scale does have prognostic significance for hearing outcomes—scores 7/10 or higher have a very favorable outcome with normal or near-normal hearing in 85%–90% of these patients.<sup>5</sup> In the current patient population, 6 of 9 patients scored  $\geq 7$  on the scale, indicating a favorable outcome.

Here we describe an unusual configuration of the malleus-incus complex, in which the malleus and incus, fused in all patients with aural atresia, have a boomerang appearance and the incus has a fibrous attachment to the fallopian canal and is not attached to the stapes bone. In addition, the stapes capitulum is absent and the suprastructure is small. The boomerang corresponds anatomically to the short process, body, and long process of the incus, the dominant ossicle, with no cleavage plane or joint

space between the body of the incus and the very hypoplastic malleus head. There is no malleus neck, manubrium, or umbo. These findings were corroborated at the time of surgery.

The boomerang configuration most likely represents a more severely hypoplastic malleus bone, possibly from an arrest earlier in the embryologic development of the first branchial arch than is normally seen in patients with aural atresia. This characteristic finding certainly has implications for surgical repair.

When this anatomic anomaly is recognized, the surgeon can anticipate possibly needing to use a partial ossicular replacement prosthesis placed over a rudimentary stapes bone. Hearing results may not be as good as those of conventional atresia surgery compared with when the patient's native ossicular chain is used.<sup>2</sup> However, hearing results in the current study are comparable with those of other reports, with the postoperative pure tone average in the mild hearing loss range and speech reception thresholds in the borderline normal range.<sup>2,4-8</sup>

In addition, the PORP reconstruction in which the prosthesis is placed on the mobile stapes crural arch appears to be more stable and reliable than the PORP reconstruction in which the prosthesis is placed through the obturator foramen down onto the stapes footplate.<sup>5</sup> Other studies have reported comparable results between intact native ossicular chain reconstruction and ossicular replacement prostheses.<sup>6</sup> The method of reconstruction is dictated by the anatomy at surgery, but if the stapes suprastructure is intact and mobile, the author has found superior results from placing the prosthesis on the suprastructure.<sup>2</sup>

One limitation of this study is the lack of long-term data (mean follow-up hearing data are 28 months after surgery; range, 1–58 months). Patients come to the University of Virginia for surgery from around the country. Obtaining long-term hearing outcome data has been a challenge in this population.

This data is important when counseling patients and their families on the possibility of successful hearing gain with canaloplasty surgery. While early short-term hearing results appear favorable with this reconstruction in this anomaly, long-term stability of hearing remains to be demonstrated.

## CONCLUSIONS

Recognizing the boomerang sign in the middle ear in patients with congenital aural atresia carries implications for the otologic surgeon and for potential hearing outcomes after surgery. This anomaly is almost always associated with other abnormalities of the middle ear, including an absent or dysmorphic stapes capitulum and ossicular discontinuity, with a fibrous attachment between the long process of the incus and the fallopian canal. The boomerang malleus-incus is commonly associated with an abnormal capitulum, but due to the presence and mobility of the remainder of the stapes, patients with this anomaly may undergo successful PORP placement. Preoperative identification by the radiologist with communication to the referring otologist helps in optimal clinical decision-making, surgical planning, and patient counseling.

Disclosures: Bradley W. Kesser—*RELATED: Patents: Royalties:* less than \$200 per year for an ear simulator that he and his colleagues patented and licensed to Nasco Inc for educational purposes.

## REFERENCES

1. Gassner EM, Mallouhi A, Jaschke WR. **Preoperative evaluation of external auditory canal atresia on high-resolution CT.** *AJR Am J Roentgenol* 2004;182:1305–12
2. Dobratz EJ, Rastogi A, Jahrsdoerfer RA, et al. **To POP or not: ossiculoplasty in congenital aural atresia surgery.** *Laryngoscope* 2008;118:1452–57
3. Vrabec JT, Lin JW. **Inner ear anomalies in congenital aural atresia.** *Otol Neurotol* 2010;31:1421–26
4. Jahrsdoerfer RA, Yeakley JW, Aguilar EA, et al. **Grading system for the selection of patients with congenital aural atresia.** *Am J Otol* 1992;13:6–12
5. Shonka DC, Jahrsdoerfer RA, Kesser BW. **The Jahrsdoerfer grading scale in surgery for congenital aural atresia.** *Arch Otolaryngol Head Neck Surg* 2008;134:873–77
6. Chang H, Song JJ, Choi BY, et al. **Partial ossicular replacement versus type II tympanoplasty in congenital aural atresia surgery: a matched group study.** *Otol Neurotol* 2009;30:609–13
7. Lambert PR. **Congenital aural atresia: stability of surgical results.** *Laryngoscope* 1998;108:1801–05
8. De la Cruz A, Teufert KB. **Congenital aural atresia surgery: long term results.** *Otolaryngol Head Neck Surg* 2003;129:121–27

# Incidental Radiologic Findings in the 22q11.2 Deletion Syndrome

J.E. Schmitt, J.J. Yi, D.R. Roalf, L.A. Loevner, K. Ruparel, D. Whinna, M.C. Souders, D.M. McDonald-McGinn, E. Yodh, S. Vandekar, E.H. Zackai, R.C. Gur, B.S. Emanuel, and R.E. Gur



## ABSTRACT

**BACKGROUND AND PURPOSE:** The 22q11.2 deletion syndrome is a common genetic microdeletion syndrome that results in cognitive delays and an increased risk of several psychiatric disorders, particularly schizophrenia. The current study investigates the prevalence of incidental neuroradiologic findings within this population and their relationships with psychiatric conditions.

**MATERIALS AND METHODS:** Brain MR imaging from 58 individuals with 22q11.2 deletion syndrome was reviewed by board-certified radiologists by using standard clinical procedures. Intracranial incidental findings were classified into 8 categories and compared with a large typically developing cohort.

**RESULTS:** The rate of incidental findings was significantly higher ( $P < .0001$ ) in 22q11.2 deletion syndrome compared with typically developing individuals, driven by a high prevalence of cavum septum pellucidum (19.0%) and white matter abnormalities (10.3%). Both of these findings were associated with psychosis in 22q11.2 deletion syndrome.

**CONCLUSIONS:** Cavum septum pellucidum and white matter hyperintensities are significantly more prevalent in patients with the 22q11.2 deletion syndrome and may represent biomarkers for psychosis.

**ABBREVIATIONS:** CSP = cavum septum pellucidum; PNC = Philadelphia Neurodevelopmental Cohort; 22q11DS = 22q11.2 deletion syndrome; TD = typically developing

The 22q11.2 deletion syndrome (22q11DS, also known as DiGeorge syndrome, velocardiofacial syndrome, and CATCH-22) is an uncommon genetic disorder occurring in approximately 1:2000–1:4000 live births.<sup>1</sup> It is typically caused by a sporadic uneven recombination event resulting in hemizygous deletion of approximately 3 megabases on the long arm of chromosome 22.<sup>2–4</sup> In addition to craniofacial and vascular abnormalities, this deletion of approximately 50 genes results in cognitive delays and

increased risk of several psychiatric diseases, including anxiety, mood disorders, attention deficit, and autistic features.<sup>5–8</sup> However, perhaps the most striking effect of the 22q deletion is an approximately 30-fold increased risk of schizophrenia relative to the general population.<sup>9,10</sup>

Neuroimaging studies demonstrate consistent anatomic differences between individuals with 22q11DS and typically developing (TD) individuals. Findings include globally decreased cerebral brain volumes, volumetric reductions in the parietal lobe, reduction of cortical thickness in the parietal lobes and orbitofrontal cortex, reduction in the cerebellar vermis hemisphere size, abnormalities in gyral complexity, and white matter hyperintensities.<sup>11–16</sup> Additionally, prior neuroimaging studies report an increased prevalence of cavum septum pellucidum (CSP) and cavum vergae in 22q11DS,<sup>15,17,18</sup> an observation also noted in individuals with schizophrenia.<sup>19,20</sup>

Observations such as CSP and white matter hyperintensities are often considered incidental findings, usually of questionable clinical significance. In the TD adult population, the reported rate of incidental findings on neuroanatomic scans is widely variable, ranging from 3% to 85%.<sup>21–24</sup> In a recent prospective investigation of incidental findings, our group estimated the rate of incidental findings to be approximately 10% in a pediatric and young

Received February 10, 2014; accepted after revision March 26.

From the Department of Radiology (J.E.S., L.A.L.), Hospital of the University of Pennsylvania, Philadelphia, Pennsylvania; Brain Behavior Laboratory (J.E.S., J.J.Y., D.R.R., K.R., D.W., E.Y., S.V., R.C.G., R.E.G.), Department of Psychiatry, University of Pennsylvania, Philadelphia, Pennsylvania; Department of Psychiatry (J.J.Y.) and Division of Human Genetics (M.C.S., D.M.M.-M., E.H.Z., B.S.E.), Children's Hospital of Philadelphia, Philadelphia, Pennsylvania; Department of Pediatrics (D.M.M.-M., E.H.Z., B.S.E.), University of Pennsylvania School of Medicine, Philadelphia, Pennsylvania; and Department of Pediatrics (D.M.M.-M., E.H.Z., B.S.E.), Perelman School of Medicine, University of Pennsylvania, Philadelphia, Pennsylvania.

This study was supported by National Institutes of Health grants MH087626, MH087636, and T32 and grants MH019112 (J.J.Y.) and EB004311 (J.E.S.).

Please address correspondence to Raquel E. Gur, MD, Brain Behavior Laboratory, 10th Floor, Gates Building, Hospital of the University of Pennsylvania, Philadelphia, PA 19104; e-mail address: raquel@mail.med.upenn.edu

Indicates open access to non-subscribers at www.ajnr.org

<http://dx.doi.org/10.3174/ajnr.A4003>

adult TD population.<sup>25</sup> That study also found an association between psychosis-related symptoms and CSP.

The purpose of the present study was to investigate the rate of incidental findings in a large sample of pediatric and young adult subjects with 22q11DS by using methods similar to those in our prior study in a TD group. To our knowledge, the present study represents the first systematic review of incidental findings in 22q11DS by board-certified neuroradiologists on scans acquired at 3T. Given evidence of CSP as a potential biomarker for schizophrenia and psychosis, we were particularly interested in this finding in subjects with an established genetic predisposition for the disease. Additionally, because of the association between 22q11DS and cardiovascular disease, we also hypothesized that the prevalence of vascular findings would be increased in our sample.

## MATERIALS AND METHODS

### Subjects

The sample was drawn from a prospective study, *Brain-Behavior and Genetic Studies of the 22q11DS*, at the University of Pennsylvania and Children's Hospital of Philadelphia. Individuals with the diagnosis of 22q11DS and 8 years of age or older were eligible for the study and were recruited from the 22q and You Center at the Children's Hospital and through social media. Inclusion criteria were the following: 8 years of age or older, English proficiency, stable medical status, and estimated intelligence quotient of >70 by the Wide Range Achievement Test IV.<sup>26</sup> Exclusion criteria were the following: pervasive developmental disorder or intelligence quotient of <70 and medical disorders that may affect brain function (eg, uncontrolled seizures, head trauma, CNS tumor, and infection) or visual performance (eg, blindness). Participants with an intelligence quotient of <70 were excluded to increase the reliability of the clinical data that focus on neuropsychiatric presentation and neurocognition. Furthermore, to enable comparison with participants without deletions with psychosis spectrum features, we excluded potential participants with significant intellectual disability.

As previously described,<sup>27</sup> all participants underwent clinical assessment with semistructured interviews. Additionally, participants 12 years of age or older and without conditions interfering with MR imaging (eg, metallic inserts, orthopedic circumstances, poor vision, and pregnancy) underwent neuroimaging. Fifty-eight participants were scanned. Deletion status was confirmed by using multiplex ligation-dependent probe amplification.<sup>28</sup> Fifty-three patients had the typical 3 megabase and 4 had a 1.5 megabase deletion. For 1 subject, the deletion size could not be determined due to sample quality, though the presence of a deletion was identified by using fluorescence in situ hybridization. All procedures were approved by the institutional review boards of the University of Pennsylvania and the Children's Hospital of Philadelphia. Informed consent/assent was obtained from each participant and accompanying parent for those younger than 18 years at the time of initial evaluation.

### Image Acquisition and Analyses

For each subject, high-resolution axial T1-weighted magnetization-prepared rapid acquisition of gradient echo imaging was ac-

quired, with the following parameters: TR/TE, 1810/3.51 ms; TI, 1100 ms; FOV, 180 × 240 mm; effective resolution, 1 mm<sup>3</sup>. All subjects were scanned on the same 3T MR imaging scanner (Tim Trio; Siemens, Erlangen, Germany) by using a 32-channel head coil. A board-certified technologist in the Department of Radiology at the Hospital of the University of Pennsylvania performed all scans.

All images were reviewed by board-certified neuroradiologists by using standard clinical procedures, and findings were communicated via standard reports within the medical record. Clinical reports were categorized as the following: 1) normal without incidental findings, 2) incidental findings not requiring follow-up, and 3) incidental findings requiring follow-up.

As in prior studies,<sup>25</sup> incidental findings were categorized as the following: 1) pineal cysts, 2) other cysts (eg, arachnoid cysts), 3) cavum septum pellucidum/cavum vergae, 4) other ventricular abnormalities (ventricular asymmetries or prominence), 5) vascular abnormalities (absent flow voids, aneurysms, developmental venous anomalies, and so forth), and 6) cerebellar abnormalities (eg, hypoplasia, Chiari 1, cerebellar cysts). Two additional categories were added on the basis of prior 22q11DS studies: 7) white matter abnormalities, and 8) subcortical abnormalities. Extracranial findings were not included in the analyses.

### Statistical Analysis

All analyses were performed in the R statistical environment (<http://www.r-project.org/>).<sup>29</sup> Prevalence rates were calculated for individual incidental finding categories and for the aggregate prevalence of all incidental findings within the 22q11DS population. Demographic differences were tested by using ANOVA for age and the Fisher exact test for proportions (sex, race). An  $\alpha$  of .05 was set as the threshold for statistical significance. Additionally, logistic regression was performed to test whether demographic variables or their interactions predicted incidental findings (generalized linear model function in R). Linear and nonlinear effects of age, sex, race, and interaction terms were included in the full model. All models were evaluated for goodness of fit by using the Hosmer-Lemeshow test.<sup>30</sup> Best fit submodels were determined via combined stepwise regression by using Akaike information criteria as the test statistic.<sup>31</sup>

The 22q11DS dataset was then compared with data on incidental findings from the Philadelphia Neurodevelopmental Cohort (PNC), a TD sample of children and young adults 8–21 years of age comprising 1445 individuals. Details on this sample are described elsewhere.<sup>32</sup> Logistic regression models were performed to test whether group (PNC versus 22q11DS) predicted the presence of incidental findings. These models included linear and nonlinear effects of age, sex, and race to control for these potential confounds. Because our original report on the PNC did not explicitly include categories for WM and subcortical abnormalities, the original PNC reports were re-reviewed to identify any potential under-reported findings in these categories.

Finally, we tested the associations of incidental findings and the prevalence of psychiatric disease. On the basis of our a priori hypothesis that CSP and psychosis were related, we tested the hypothesis that CSP is associated with psychotic features. Specifically, logistic regression was used to predict whether subjects who

**Table 1: Demographic differences in 22q11DS with and without incidental findings**

	No Incidentals	Incidentals	P Value
No.	31 (53%)	27 (47%)	
Age (mean years ± SD)	22.8 (8.1)	22.4 (7.1)	.8512
Sex			.5990
Male	17 (55%)	12 (44%)	
Female	14 (45%)	15 (56%)	
Race			.9999
White	27 (87%)	19 (88%)	
African American	3 (10%)	2 (7%)	
Other	1 (3%)	1 (4%)	

**Table 2: Frequency of incidental findings in 21q11DS**

Finding	Count	Prevalence
Pineal cyst	2	2.58%
Other cysts	0	0%
Cavum septum pellucidum	11	19.0%
Ventricular abnormalities	5	8.62%
Other CSF abnormalities	1	1.72%
Vascular abnormalities	5	8.62%
Cerebellar abnormalities	0	0%
White matter abnormalities	6	10.34%
Subcortical	2	3.45%
All subjects with incidental findings	27	46.6%

carry psychiatric diagnoses with severe psychotic features (schizophrenia, schizoaffective disorder, or major depression with psychotic features) have increased rates of CSP. This analysis was repeated for WM abnormalities. We then tested the predictive ability of incidental findings for categories of other psychiatric diagnoses (attention deficit/hyperactivity disorder, anxiety disorders, prodromal psychosis, and severe psychosis) via multivariate generalized linear models in R.

## RESULTS

Of the 58 subjects with 22q11DS imaged, 27 had incidental findings (47%). There were no statistically significant differences in age, sex, or race between subjects with and without incidentals (Table 1). CSP and WM abnormalities were the most common incidental findings (Table 2). Secondary review of the 11 individuals with CSP demonstrated that CSP et vergae was present in all reported cases (Fig 1). Representative examples of other common incidental findings are provided in Fig 2. Five individuals in the sample presented with multiple incidental findings: 1) CSP and ventricular prominence, 2) white matter hyperintensities and a 12-mm pineal cyst, 3) multiple white matter hyperintensities and a nonspecific hypointensity in the left thalamus, 4) CSP and absent left ICA flow, and 5) ventricular asymmetry and a nonspecific white matter hyperintensity.

Compared with the TD population, the overall rate of incidental findings was >4 times greater in the 22q11DS population ( $P < .0001$ ). Similar to prior studies, these differences were largely driven by an increased rate of CSP and white matter abnormalities (Table 3). Ventricular abnormalities also were more common in the 22q11DS population. In our sample, differences in infratentorial abnormalities were not statistically significant; no clinical abnormalities were reported in the cerebellum in our 22q11DS sample.

Figure 3 summarizes the relative prevalence of incidental find-

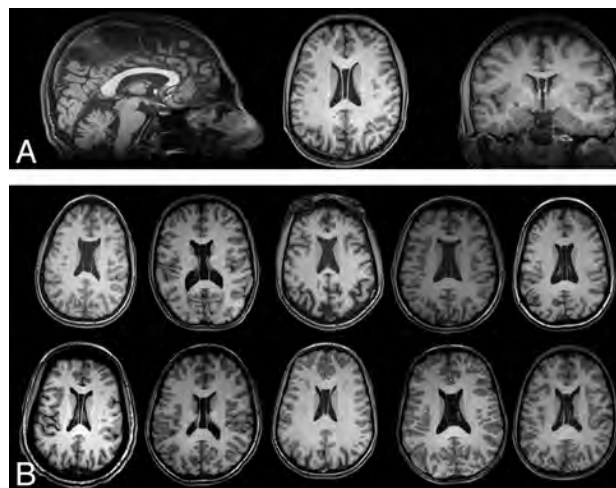


**FIG 1.** High prevalence of cavum septum pellucidum et vergae in 22q11DS. A, Triplanar view centered on the lateral ventricles in a subject with CSP et vergae. B, Single representative axial sections from 10 other subjects with this finding.

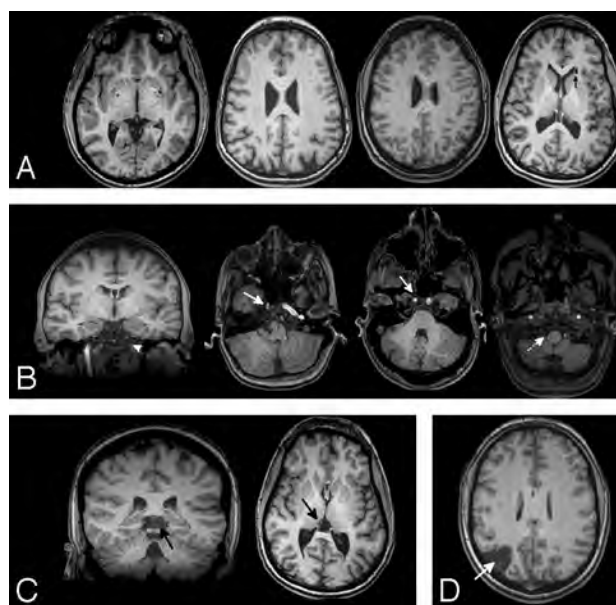


**FIG 2.** Incidental findings in 11 representative individuals with 22q11DS. Other than CSP, white matter abnormalities (A) were the most common finding. Scattered WM hypointensities were most frequent, with 1 subject having a nonspecific cyst in the periventricular WM (arrow). Vascular abnormalities (B) were seen in 8.6% of the population and included an absent left ICA flow void (arrowhead) with a CSP also noted, asymmetries in the ICA (solid arrows), and absence of a right vertebral flow void (dotted arrow). Pineal cysts (C) were also seen. A single subject had a known right posterior infarct (D).

ings in 22q11DS by psychiatric diagnosis. Of the 11 subjects with CSP (19%), 3 carried a diagnosis of schizophrenia, psychotic depression, or schizoaffective disorder (27%). In contrast, these diagnoses were seen in only 3 of the remaining 53 subjects (6%); this finding was statistically significant ( $P = .04$ ). Similarly, of the 6 individuals with incidental white matter abnormalities, 3 had diagnoses with psychotic features (50%), significantly greater than those without these abnormalities (6%,  $P$  value = .01). Notably, there was no comorbidity between CSP and WM abnormalities in our sample, but all subjects with psychosis had either CSP or WM

abnormalities. There were no statistically significant associations between other psychiatric diagnoses and incidental findings as determined by post hoc multivariate logistic regression.

## DISCUSSION

To our knowledge, the current study represents the first neuro-radiologic evaluation of incidental findings at a high field strength in 22q11DS. We found a higher rate of incidental findings within this population relative to a control population when analyzed by using similar methods. The increased rate of incidental findings was driven by a higher prevalence of cavum septum pellucidum, white matter hyperintensities, and vascular abnormalities, findings that have been noted in prior samples with 22q11DS. We also observed an increased rate of psychiatric diagnoses with psychotic features in subjects with 22q11DS with either CSP or WM abnormalities.

Cavum septum pellucidum were first described in 1671 by Franciscus Sylvius.<sup>33</sup> In prenatal life, a CSP is a normal anatomic structure. Identification of a CSP is considered part of a standard evaluation during fetal sonography, and its absence is associated with several abnormalities including septo-optic dysplasia, abnormalities of the corpus callosum, and hydrocephalus.<sup>34</sup> During typical development, the CSP slowly closes following birth; the septal leaflets fuse in approximately 15% of the population within 1 month following birth and in 85% by 6 months.<sup>35</sup> The reported prevalence of a persistent CSP in late childhood and adulthood is

highly variable, ranging from 2% to nearly 60%.<sup>36,37</sup> The high variability in reported prevalence is at least in part due to disagreement on whether persistent CSP represents a true radiographic abnormality. For example, many of the largest studies on incidental neuroimaging findings do not mention the CSP at all<sup>23,24</sup> or explicitly exclude the CSP from analysis.<sup>22</sup>

The precise developmental trigger that results in fusion of the cavum remains uncertain. It is hypothesized that growth of midline structures such as the corpus callosum, fornix, and hippocampus result in increased pressure on the leaflets of the septum, ultimately resulting in fusion.<sup>38,39</sup> Thus, a persistent CSP may be a proxy for aberrant development of midline structures or possibly for abnormal global cerebral growth. CSP has been associated with several disorders including schizophrenia, Sotos syndrome, Apert syndrome, fetal alcohol syndrome, and chronic head trauma.<sup>40-42</sup> In a recent meta-analysis of the extant literature on schizophrenia and CSP, Trzesniak et al<sup>20</sup> found that a large CSP was associated with an increased risk of schizophrenia spectrum disorders. Schizophrenia has also been associated with decreased size of several midline structures such as the hippocampus and corpus callosum, again suggesting that CSP may be related to abnormalities in midline development in this condition.<sup>20</sup>

In the 22q11DS population specifically, several prior studies noted an increased incidence of CSP.<sup>15,18,38,43</sup> For example, van Amelsvoort et al<sup>15</sup> estimated a 40% prevalence of CSP in a sample of 10 subjects with 22q11DS, compared with 9% in TD controls, though this finding did not reach statistical significance. In a multisite study of 45 children with 22q11DS, a prevalence of 84% was reported.<sup>18</sup> Beaton et al<sup>18</sup> measured CSP volume and length differences between 45 individuals with 22q11DS and matched TD controls, finding quantitative increases in both measures within the 22q11DS population. There also is some evidence that CSP and psychosis are associated in patients with 22q11DS: Chow et al<sup>17</sup> noted CSP in 5/11 subjects with either a diagnosis of schizophrenia or schizoaffective disorder, though the lack of a control group prevented tests of statistical significance. Our data provide statistical evidence that there is an association between CSP and psychosis within this population.

We also observed increased rates of vascular abnormalities in 22q11DS, predominantly due to absent intracranial flow voids. Extracranial cardiovascular abnormalities are common in this condition, with 70% of individuals having congenital heart disease.<sup>1</sup> Abnormal placement of the extracranial internal carotid arteries<sup>44</sup> and kinked or tortuous vertebral arteries<sup>45</sup> have also been reported, occasionally complicating the pharyngeal surgeries that are common in this condition. The available data are more limited within the calvaria, but several abnormalities in intracranial vascularity have been reported, including hypoplasia of the circle of Willis and other major intracranial vessels.<sup>46</sup> These vascular abnormalities

**Table 3: Comparison in incidental findings between subjects with 22q11DS and typically developing (PNC) sample**

	22q11DS	PNC	P Value
Pineal cyst	2.58%	2.43%	.6213
Other cyst	0%	1.36%	.9855
Cavum septum pellucidum	18.96%	1.14%	<.0001
Vascular abnormalities	8.62%	2.57%	.0173
White matter	11.53%	0.56%	<.0001
Subcortical	3.45%	0.06%	.0960
Cerebellar	0%	2.36%	.9860
All incidental	46.55%	10.72% <sup>a</sup>	<.0001

**Note:**—VCFS indicates velocardiocardial syndrome.

<sup>a</sup> Previously reported as 10.57%, with WM and subcortical abnormalities included in the current analyses.

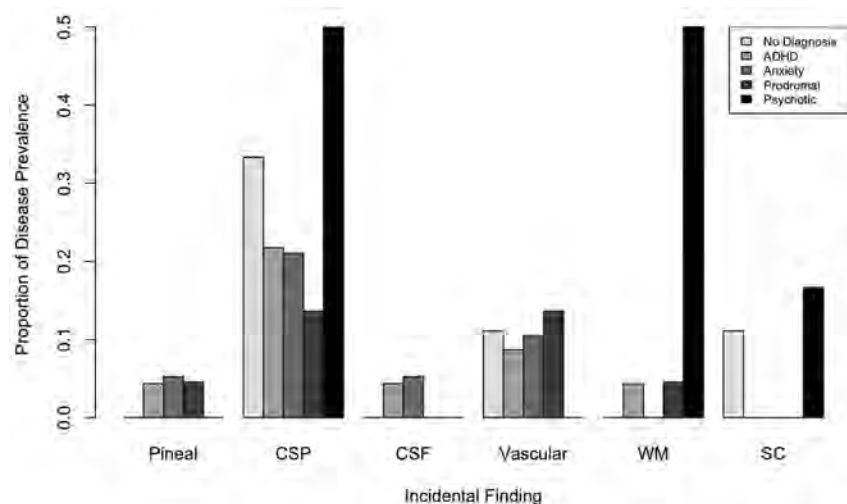


**FIG 3.** Proportion of incidental findings in 22q11DS split by psychiatric diagnosis.

may be in part responsible for downstream neuroanatomic abnormalities that have been previously described in 22q11DS such as volume loss and white matter hyperintensities.<sup>47</sup> Further research into this potential link between intracranial vascular anomalies and brain abnormalities, such as with noninvasive MR angiography and perfusion MR imaging, may be of value.

Additionally, there was an increased incidence of WM abnormalities in 22q11DS. Several prior studies have noted this finding in smaller samples or case reports.<sup>15,48,49</sup> For example, van Amelsvoort et al<sup>15</sup> noted a rate of hyperintensities at approximately twice that in their control population, though the finding did not reach statistical significance. Chow et al<sup>17</sup> observed WM hyperintensities in 9/10 subjects with schizophrenia or schizoaffective disorder. The pathophysiology of white matter hyperintensities is incompletely understood at present, but pathologic correlation in the general population has suggested that they occur in regions of gliosis, axonal loss, and demyelination, likely secondary to perivascular damage.<sup>50</sup> In the TD population, the prevalence of focal white matter abnormalities increases with age, and increased WM burden is associated with an increased risk of dementia, cerebrovascular disease, mood disorders, and death.<sup>51,52</sup> Because subjects with 22q11DS have an increased risk of vascular abnormalities, it is tempting to conclude that focal white matter abnormalities in this population may also represent premature perivascular damage due to a genetic predisposition. However, this hypothesis has not been tested directly because there are no large studies providing radiologic-pathologic correlation within the 22q11DS population specifically.

Although the current study supports several prior findings in the literature in a relatively large sample, there are some limitations. First, our estimates of a few incidental findings are lower than those reported elsewhere. These differences may be related to subject ascertainment procedures. Specifically, our study selected for higher functioning subjects and therefore may have underestimated the true prevalence of any incidentals with direct impact on brain function. The lack of cerebellar findings, in particular, was unexpected, given prior reports of vermian and cerebellar hemispheric abnormalities.<sup>13,16,53</sup> Second, our comparisons between the 22q11DS and PNC samples controlled for demographic variables by using statistical methods rather than by directly matching for age, sex, and race. The higher mean age of the 22q11DS group (22.6 versus 14.8 years) could potentially contribute to the increased rate of white matter abnormalities in this group, though the natural history of these findings within the TD population makes this less likely because they generally develop after 40 years of age.<sup>52</sup> In contrast, incomplete control of group age differences would be expected to underestimate the relative rate of CSP in the 22q11DS on the basis of its natural history of decreasing size with age.<sup>35</sup>

## CONCLUSIONS

The current study confirms an increased rate of incidental brain MR imaging findings within the 22q11DS population in a large sample. In concordance with prior literature, cavum septum pellucidum and white matter hyperintensities drive the increases in

the prevalence of incidental findings. Both cavum septum pellucidum and white matter abnormalities are found with increased prevalence in 22q11DS with psychosis and may represent potential biomarkers for schizophrenia and psychosis in 22q11DS. Future longitudinal studies within this sample could help further refine our understanding of these putative risk factors.

Disclosures: James E. Schmitt—RELATED: T32 Training Grant from the National Institutes of Health (EB004311, to Mitch Schnall),\* UNRELATED: a Fellow Grant submission to the Radiological Society of North America (Imaging Genomic Analysis of the 22q11DS Syndrome). James Yi—RELATED: National Institute of Mental Health grant (T32 MH019112),\* David Roalf—RELATED: a postdoctoral fellow during part of this work, supported by National Institute of Mental Health grant T32 MH019112 (Principal Investigator: Raquel E. Gur),\* Margaret C. Souders—RELATED: National Institutes of Health grant support,\* Ruben C. Gur—RELATED: grant support from the National Institute of Mental Health,\* UNRELATED: medicolegal services for death penalty defense. Beverly S. Emanuel—These studies were supported in part by an National Institutes of Health/National Institute of Mental Health U01 Grant MH 87636.\* Raquel E. Gur—RELATED and UNRELATED: grants from the National Institutes of Health.\* \*Money paid to the Institution.

## REFERENCES

1. Shprintzen RJ. **Velo-cardio-facial syndrome: 30 years of study.** *Dev Disabil Res Rev* 2008;14:3–10
2. Driscoll D, Salvin J, Sellinger B, et al. **Prevalence of 22q11 microdeletions in DiGeorge and velocardiofacial syndromes: implications for genetic counselling and prenatal diagnosis.** *J Med Genet* 1993;30:813–17
3. Edelmann L, Pandita RK, Morrow BE. **Low-copy repeats mediate the common 3-Mb deletion in patients with velo-cardio-facial syndrome.** *Am J Hum Genet* 1999;64:1076–86
4. Shaikh TH, Kurahashi H, Saitta SC, et al. **Chromosome 22-specific low copy repeats and the 22q11.2 deletion syndrome: genomic organization and deletion endpoint analysis.** *Hum Mol Genet* 2000;9:489–501
5. Eisenberg DP, Jabbi M, Berman KF. **Bridging the gene-behavior divide through neuroimaging deletion syndromes: velocardiofacial (22q11.2 deletion) and Williams (7q11.23 deletion) syndromes.** *Neuroimage* 2010;53:857–69
6. Gothelf D, Furfaro JA, Penniman LC, et al. **The contribution of novel brain imaging techniques to understanding the neurobiology of mental retardation and developmental disabilities.** *Ment Retard Dev Disabil Res Rev* 2005;11:331–39
7. Gothelf D, Lombroso PJ. **Genetics of childhood disorders. XXV. Velocardiofacial syndrome.** *J Am Acad Child Adolesc Psychiatry* 2001;40:489–91
8. Baker KD, Skuse DH. **Adolescents and young adults with 22q11 deletion syndrome: psychopathology in an at-risk group.** *Br J Psychiatry* 2005;18:115–20
9. Murphy KC, Jones LA, Owen MJ. **High rates of schizophrenia in adults with velo-cardio-facial syndrome.** *Arch Gen Psychiatry* 1999;56:940–45
10. Bassett A, Chow E. **22Q11 deletion syndrome: a genetic subtype of schizophrenia.** *Biol Psychiatry* 1999;46:882–91
11. Gothelf D, Schaer M, Eliez S. **Genes, brain development and psychiatric phenotypes in velo-cardio-facial syndrome.** *Dev Disabil Res Rev* 2008;14:59–68
12. Schaer M, Schmitt JE, Glaser B, et al. **Abnormal patterns of cortical gyrification in velo-cardio-facial syndrome (deletion 22q11.2): an MRI study.** *Psychiatry Res* 2006;146:1–11
13. Eliez S, Schmitt JE, White CD, et al. **Children and adolescents with velocardiofacial syndrome: a volumetric MRI study.** *Am J Psychiatry* 2000;157:409–15
14. Bearden CE, van Erp TG, Dutton RA, et al. **Mapping cortical thickness in children with 22q11.2 deletions.** *Cerebral Cortex* 2007;17:1889–98
15. van Amelsvoort T, Daly E, Robertson D, et al. **Structural brain abnormalities associated with deletion at chromosome 22q11: quan-**

- titative neuroimaging study of adults with velo-cardio-facial syndrome.** *Br J Psychiatry* 2001;178:412–19
16. Eliez S, Schmitt JE, White CD, et al. **A quantitative MRI study of posterior fossa development in velocardiofacial syndrome.** *Biol Psychiatry* 2001;49:540–46
  17. Chow EW, Mikulis DJ, Zipursky RB, et al. **Qualitative MRI findings in adults with 22q11 deletion syndrome and schizophrenia.** *Biol Psychiatry* 1999;46:1436–42
  18. Beaton EA, Qin Y, Nguyen V, et al. **Increased incidence and size of cavum septum pellucidum in children with chromosome 22q11.2 deletion syndrome.** *Psychiatry Res* 2010;181:108–13
  19. Galarza M, Merlo AB, Ingratta A, et al. **Cavum septum pellucidum and its increased prevalence in schizophrenia: a neuroembryological classification.** *J Neuropsychiatry Clin Neurosci* 2004;16:41–46
  20. Trzesniak C, Oliveira IR, Kempton MJ, et al. **Are cavum septum pellucidum abnormalities more common in schizophrenia spectrum disorders? A systematic review and meta-analysis.** *Schizophr Res* 2011;125:1–12
  21. Seki A, Uchiyama H, Fukushi T, et al. **Incidental findings of brain magnetic resonance imaging study in a pediatric cohort in Japan and recommendation for a model management protocol.** *J Epidemiol* 2010;20(supplement 2):S498–504
  22. Morris Z, Whiteley W, Longstreth WT Jr, et al. **Incidental findings on brain magnetic resonance imaging: systematic review and meta-analysis.** *BMJ* 2009;33:b3016
  23. Vernooij MW, Ikram MA, Tanghe HL, et al. **Incidental findings on brain MRI in the general population.** *N Engl J Med* 2007;357:1821–28
  24. Katzman GL, Dagher AP, Patronas NJ. **Incidental findings on brain from 1000 asymptomatic volunteers.** *JAMA* 1999;282:36–39
  25. Gur R, Kaltman D, Melhem E, et al. **Incidental findings in youths volunteering for brain MRI research.** *AJNR Am J Neuroradiol* 2013;34:2021–25
  26. Wilkinson G, Robertson G. *Wide Range Achievement Test*. 4th ed. Lutz: Psychological Assessment Resources; 2006
  27. Tang SX, Yi JJ, Calkins ME, et al. **Psychiatric disorders in 22q11.2 deletion syndrome are prevalent but undertreated.** *Psychol Med* 2013;1–11
  28. Jalali GR, Vorstman JA, Errami A, et al. **Detailed analysis of 22q11.2 with a high density MLPA probe set.** *Human Mutat* 2008;29:433–40
  29. R Core Team. *R: A Language and Environment for Statistical Computing*. Vienna, Austria: R Foundation for Statistical Computing; 2014. <http://www.R-project.org>. Accessed January 24, 2014
  30. Lemeshow S, Hosmer D. **A review of goodness of fit statistics for use in the development of logistic regression models.** *Am J Epidemiol* 1982;115:92–106
  31. Akaike H. **Factor analysis and AIC.** *Psychometrika* 1987;52:317–32
  32. Satterthwaite TD, Elliott MA, Ruparel K, et al. **Neuroimaging of the Philadelphia neurodevelopmental cohort.** *Neuroimage* 2014;86:544–53
  33. Sylvius F. *Opera Medica, Tam Hactenus Inedita, Quam Variis Locis et Formis Edita*. Amsterdam: Aput Danielem Elsevirium et Abrahamum Wolfgang; 1679
  34. Winter TC, Kennedy AM, Byrne J, et al. **The cavum septi pellucidi: why is it important?** *J Ultrasound Med* 2010;29:427–44
  35. Saba L, Anzidei M, Raz E, et al. **MR and CT of brain's cava.** *J Neuroimaging* 2013;23:326–35
  36. Aldur MM, Gürçan F, Başar R, et al. **Frequency of septum pellucidum anomalies in non-psychotic population: a magnetic resonance imaging study.** *Surg Radiol Anat* 1999;21:119–23
  37. Born CM, Meisenzahl EM, Frodl T, et al. **The septum pellucidum and its variants: an MRI study.** *Eur Arch Psychiatry Clin Neurosci* 2004;254:295–302
  38. Shashi V, Muddasani S, Santos CC, et al. **Abnormalities of the corpus callosum in nonpsychotic children with chromosome 22q11 deletion syndrome.** *Neuroimage* 2004;21:1399–406
  39. Bodensteiner JB, Schaefer GB. **Wide cavum septum pellucidum: a marker of disturbed brain development.** *Pediatr Neurol* 1990;6:391–94
  40. May FS, Chen QC, Gilbertson MW, et al. **Cavum septum pellucidum in monozygotic twins discordant for combat exposure: relationship to posttraumatic stress disorder.** *Biol Psychiatry* 2004;55:656–58
  41. Schaefer GB, Bodensteiner JB, Buehler B a, et al. **The neuroimaging findings in Sotos syndrome.** *Am J Med Genet* 1997;68:462–65
  42. Johnson VP, Swayze VW II, Sato Y, et al. **Fetal alcohol syndrome: craniofacial and central nervous system manifestations.** *Am J Med Genet* 1996;61:329–39
  43. Campbell LE, Daly E, Toal F, et al. **Brain and behaviour in children with 22q11.2 deletion syndrome: a volumetric and voxel-based morphometry MRI study.** *Brain* 2006;129(pt 5):1218–28
  44. MacKenzie-Stepner K, Witzel M, Stringer D, et al. **Abnormal carotid arteries in the velocardiofacial syndrome: a report of three cases.** *Plas Reconstr Surg* 1987;80:347–51
  45. Mitnick R, Bello J, Golding-Kushner KJ, et al. **The use of magnetic resonance angiography prior to pharyngeal flap surgery in patients with velocardiofacial syndrome.** *Plas Reconstr Surg* 1996;97:908–19
  46. Shprintzen RJ. **Velo-cardio-facial syndrome: a distinctive behavioral phenotype.** *Ment Retard Dev Disabil Res Rev* 2000;6:142–47
  47. Tan GM, Arnone D, McIntosh AM, et al. **Meta-analysis of magnetic resonance imaging studies in chromosome 22q11.2 deletion syndrome (velocardiofacial syndrome).** *Schizophr Res* 2009;115:173–81
  48. Altman DH, Altman NR, Mitnick RJ, et al. **Further delineation of brain anomalies in velo-cardio-facial syndrome.** *Am J Med Genet* 1995;60:174–75
  49. Kates WR, Burnette CP, Jabs EW, et al. **Regional cortical white matter reductions in velocardiofacial syndrome: a volumetric MRI analysis.** *Biol Psychiatry* 2001;49:677–84
  50. Fazekas F, Kleinert R, Offenbacher H, et al. **Pathologic correlates of incidental MRI white matter signal hyperintensities.** *Neurology* 1993;43:1683–89
  51. Dupont RM, Butters N, Schafer K, et al. **Diagnostic specificity of focal white matter abnormalities in bipolar and unipolar mood disorder.** *Bio Psychiatry* 1995;38:482–86
  52. Dobbie S, Markus H. **The clinical importance of white matter hyperintensities on brain magnetic resonance imaging: systematic review and meta-analysis.** *BMJ* 2010;341
  53. Mitnick RJ, Bello JA, Shprintzen RJ. **Brain anomalies in velo-cardio-facial syndrome.** *Am J Med Genet* 1994;54:100–06

# Pleomorphic Xanthoastrocytoma of Childhood: MR Imaging and Diffusion MR Imaging Features

W. Moore, D. Mathis, L. Gargan, D.C. Bowers, L.J. Klesse, L. Margraf, and K. Koral

## ABSTRACT

**BACKGROUND AND PURPOSE:** Pleomorphic xanthoastrocytomas are rare astrocytic neoplasms of childhood and young adulthood. The purpose of this retrospective review was to evaluate MR imaging features of pediatric pleomorphic xanthoastrocytomas with an emphasis on diffusion MR imaging.

**MATERIALS AND METHODS:** Review of the neuro-oncology data base revealed 11 pediatric patients (range, 4.7–16.1 years) with pleomorphic xanthoastrocytomas with 9 of these patients having preoperative MR imaging available. Six patients had preoperative diffusion MR imaging. Demographics, histopathology slides, conventional imaging characteristics (location, cystic component, hemorrhage, enhancement, vasogenic edema, inner table scalloping), and ADC metrics (mean tumor ADC and tumor to normal brain ADC ratio) were evaluated.

**RESULTS:** Three pleomorphic xanthoastrocytomas had anaplastic features. Ten tumors were supratentorial. Two-thirds (6 of 9) of all tumors were either predominantly cystic or had cystic components, and three-fourths (6 of 8) of the supratentorial tumors had associated inner table scalloping. Seven of the 9 tumors had marked vasogenic edema (>10 mm). Mean tumoral ADC ( $n = 7$ ) was  $912 \pm 219 \times 10^{-6} \text{ mm}^2/\text{s}$  (min–max: 617–1189). The tumor to normal brain ADC ratio was  $1.14 \pm 0.26$  (min–max: 0.75–1.47).

**CONCLUSIONS:** Pleomorphic xanthoastrocytoma should be entertained in the differential diagnosis of peripheral supratentorial tumors that appear during childhood. Cysts, inner table scalloping, and marked vasogenic edema are relatively frequent features. Relatively low ADC values and ADC ratios are not uncommon in pleomorphic xanthoastrocytoma.

**ABBREVIATION:** PXA = pleomorphic xanthoastrocytoma

Pleomorphic xanthoastrocytomas (PXAs) are rare neoplasms comprising less than 1% of all astrocytic tumors.<sup>1</sup> They are more frequently encountered in childhood and young adulthood.<sup>2</sup> Although there is relatively abundant literature on the histopathology and treatment of these tumors, there are fewer reports describing the imaging characteristics of PXAs. Moreover, imaging reports dedicated solely to pediatric PXAs are rare. The histopathologic descriptor “pleomorphic” aptly applies to the radiology of PXAs as well, resulting in myriad imaging presentations, potentially complicating the preoperative diagnosis. In the past several years, we encountered PXAs displaying hemorrhage and cysts, associated with marked vasogenic edema, and solid

components showing relatively decreased water diffusion. These observations led to unnecessary inclusion of high-grade glial and embryonal tumors in differential diagnosis. Primitive neuroectodermal tumors, atypical teratoid rhabdoid tumors, and glioblastomas may present with imaging characteristics similar to those of PXAs.<sup>3,4</sup> The purpose of this retrospective study was to seek MR imaging and diffusion MR imaging features that may be helpful in correctly diagnosing pediatric PXA preoperatively.

## MATERIALS AND METHODS

The Institutional Review Board of the University of Texas Southwestern Medical Center approved this retrospective study and waived the requirement for informed consent. Review of the neuro-oncology database at Children’s Medical Center revealed 11 pediatric PXAs diagnosed between January 1998 and April 2012. The imaging, pathology, and medical records of these patients were reviewed.

Histopathologic diagnoses were confirmed according to the 2007 World Health Organization classification of central nervous system tumors by a pediatric pathologist with >20 years experience (L.M.) and by a neuropathology fellow (D.M.).

Received March 9, 2014; accepted after revision April 8.

From the Departments of Radiology (W.M., K.K.), Pathology (D.M., L.M.), and Pediatrics (D.C.B., L.J.K.), University of Texas Southwestern Medical Center, Dallas, Texas; and Departments of Radiology (K.K.), Pathology (L.M.), Pediatrics (D.C.B., L.J.K.), and Neuro-Oncology (L.G.), Children’s Medical Center, Dallas, Texas.

Please address correspondence to Korgun Koral, MD, Department of Radiology, University of Texas Southwestern Medical Center/Children’s Medical Center, 1935 Medical District Dr, Dallas, TX 75235; e-mail: korgun.koral@utsouthwestern.edu

<http://dx.doi.org/10.3174/ajnr.A4011>

## Individual patient information on demographics, histology, treatment, and outcome

Patient No.	Age (y)/ Sex	Diagnosis	ADC Value ( $\times 10^{-6}$ mm <sup>2</sup> /s)	ADC Ratio	Treatment	F/U (y)	Treatment Response	TTP (y)	F/U Results
1	4.7/F	PXA			XRT/Chemo	14.8	PD	8.6	Alive
2	4.8/M	PXA	838	1.06	Sx (3)/XRT	5.0	PD	2.7	Alive
3	7.1/F	Anap. PXA			Sx (2)/XRT/Chemo	0.5	PD	0.2	Died
4	9.3/F	PXA	928	1.24	Sx	7.7	CR	n/a	Alive
5	4.5/F	PXA	668	0.85	Sx	Lost to F/U			
6	6.9/M	PXA	1189	1.47	Sx (3)	9.6	PD	3.8	Alive
7	16.1/M	PXA	889	1.28	Sx	3.4	CR	n/a	Alive
8	6.1/M	Anap. PXA	825	0.75	Sx/XRT/Chemo	4.0	CR	n/a	Alive
9	11.6/M	PXA	762	1.32	Sx	Lost to F/U			
10	14.0/F	PXA			Sx/XRT/Chemo	8.2	PD	0.8	Died
11	13.0/M	Anap. PXA			Sx/XRT/Chemo	2.5	CR	n/a	Alive

**Note:**—Anap. indicates anaplastic; Chemo, chemotherapy; CR, complete remission; F/U, follow-up; PD, progressive disease; Sx, surgery; XRT, radiotherapy.

Of the 11 included patients, 9 had preoperative MR imaging available. Eight patients underwent scanning at our institution where 1.5T and 3T scanners were used (Philips Healthcare, Best, the Netherlands). Conventional sequences included T1-weighted spin-echo (at least 2 orthogonal planes), FLAIR, T2-weighted spin-echo (coronal and axial), and gadolinium-enhanced 3 plane T1-weighted spin-echo. Diffusion MR imaging, performed using a spin-echo sequence with  $b = 0$  and  $b = 1000$  seconds/mm<sup>2</sup>, was available in 7 patients. ADC maps were generated with a mono-exponential fit on a voxel-to-voxel basis for all imaging planes. Preoperative head CT was available in 4 patients.

Imaging studies were reviewed by a fourth year radiology resident (W.M.) and a pediatric neuroradiologist with 11 years of experience (K.K.) Tumor location, volume, and enhancement characteristics, presence of cyst(s), and presence/size of perilesional edema were evaluated in consensus. “Predominantly cystic” was defined as a solitary cyst and a smaller solid component and “multiple cysts” description was used if the tumors had more than 1 cystic component. When diffusion MR imaging was available, the solid components of the tumors were sampled by placing as many as 3 nonoverlapping ROIs on the ADC map. If tumors were large enough, 3 ROIs were used to sample the tumor more reliably. In 3 tumors with smaller solid components, only 1 region of interest could be placed on the tumor. A single ROI was placed on the normal contralateral thalamus because the thalamus provides a reliable internal control as it maintains its normal signal intensity on diffusion MR imaging even in cases of marked hydrocephalus.<sup>5</sup> Mean tumor ADC values and tumor to normal brain ADC ratios were calculated. The head CT examinations were assessed for calcifications and hemorrhage.

## RESULTS

### Patient Population

The mean age at diagnosis was 8.9 years of age (range, 4.7–16.1 years). Six (54.5%) patients were male and 5 (45.5%) were female. Three of 11 tumors (27.3%) demonstrated anaplastic features, increased mitotic activity, and often areas of necrosis. Ten of the 11 (90.9%) tumors were supratentorial. The mean follow-up was 5.1 years (range, 0.02–14.8 years). Five of 11 (45.5%) patients had evidence of recurrence or progression during follow-up. The mean time to progression was 3.2 years (range, 0.2–8.6 years). The 5-year progression-free survival rate was 49.2%. Two patients died, yielding an overall survival of 81.8% to date and a 5-year survival rate of 88.9%.

### Imaging

**CT and MR Imaging.** No calcifications were identified in the 4 PXAs where CT was available. Nine patients had preoperative MR imaging available for review. The only infratentorial PXA predominantly involved the pons and to a lesser extent, the midbrain and medulla oblongata. The preoperative tumor volumes varied from 1.73 to 249.9 cm<sup>3</sup> (mean = 88.3, SD = 101.6). On the preoperative examinations, 8 of 9 (88.9%) demonstrated intense heterogeneous enhancement of the solid component (all except the smallest tumor). Six of the 9 (66.7%) tumors were either predominantly cystic or had multiple cysts. Six of the 8 (75%) supratentorial tumors demonstrated scalloping of the inner table of the calvarium. Seven of the 9 (77.7%) patients had significant vasogenic edema (defined as  $\geq 10$  mm diameter). Three of 9 (33.3%) tumors demonstrated hemorrhage.

**Diffusion MR Imaging.** Tumoral ADC values were measured in 7 patients. The mean tumoral ADC value was  $912 \pm 219 \times 10^{-6}$  mm<sup>2</sup>/s (min–max: 617–1189). The tumor to normal brain ADC ratio was  $1.14 \pm 0.26$  (min–max: 0.75–1.47). In the 7 patients who had preoperative diffusion MR imaging available, ADC ratios could not be used to determine the recurrence or survival. Of the 6 patients without anaplastic features, 4 underwent gross total resection and did not show recurrence (Table and Fig 1). The only patient with a PXA without anaplastic features and ADC ratio  $< 1$  underwent gross total resection, but was lost to follow-up. One patient had a hippocampal and parahippocampal gyrus tumor (ADC ratio, 1.47) and underwent subtotal resections and had a progressive tumor. One patient (ADC ratio, 1.06) had progressive disease about the left middle cerebral artery after subtotal resection and underwent radiation therapy and chemotherapy (Fig 2). The only patient with PXA with anaplastic features in whom preoperative diffusion MR imaging was available (ADC ratio, 0.75) underwent gross total resection, chemotherapy, and radiation therapy (Fig 3). This patient had no signs of recurrence at 4-year follow-up.

### DISCUSSION

In this study, we report preoperative MR imaging findings of pediatric PXAs and describe the diffusion MR imaging metrics of these rare tumors. Consistent with the histopathologic descriptor “pleomorphic,” the imaging features of PXAs may be varied and generate some difficulty in the preoperative diagnosis. Although the mean age at presentation is 26 years, PXAs can be encountered in all age groups ranging from infancy to the ninth decade.<sup>2,6</sup> PXAs are overwhelm-

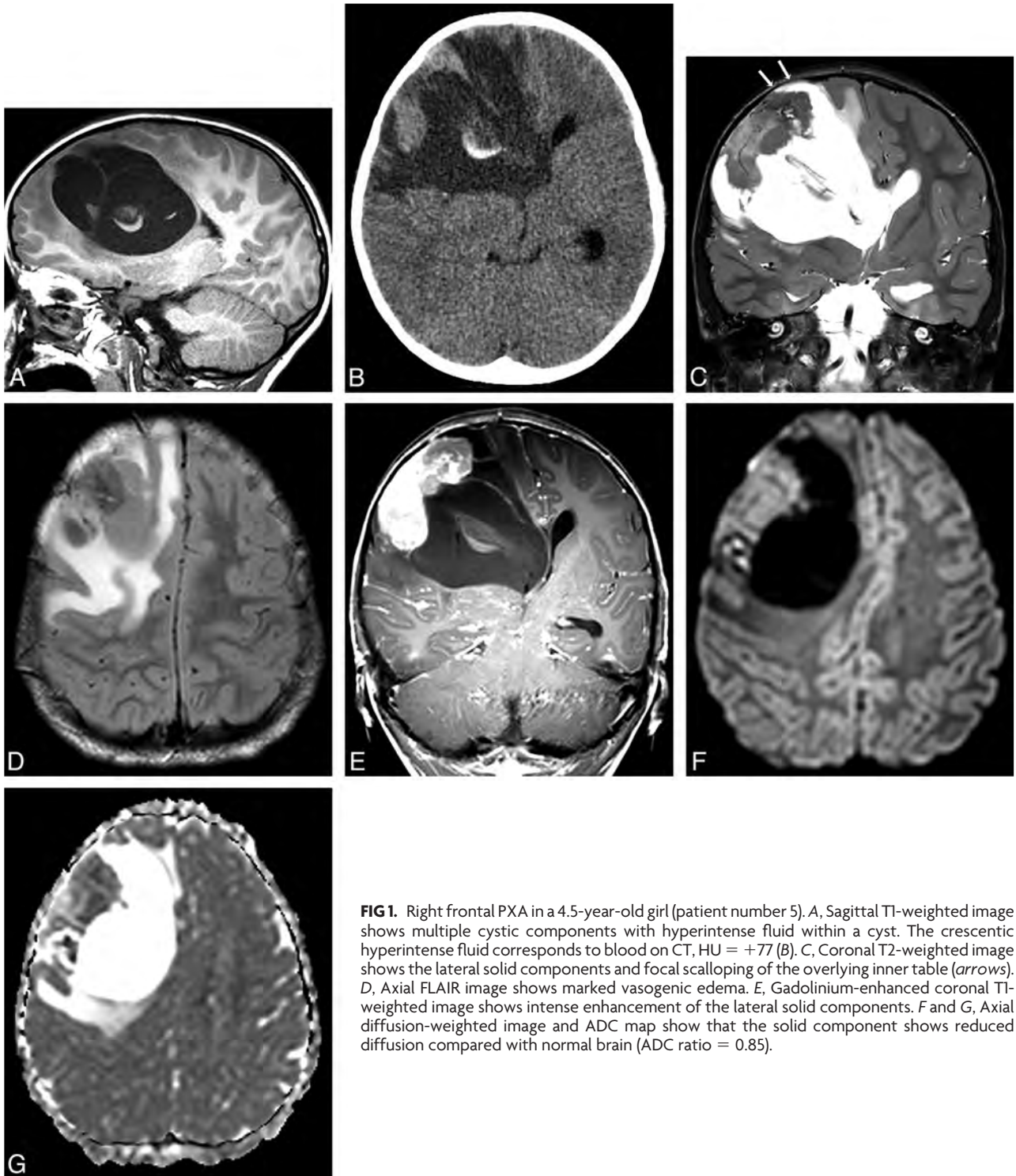


**FIG 1.** Right frontal PXA in a 4.5-year-old girl (patient number 5). *A*, Sagittal T1-weighted image shows multiple cystic components with hyperintense fluid within a cyst. The crescentic hyperintense fluid corresponds to blood on CT, HU = +77 (*B*). *C*, Coronal T2-weighted image shows the lateral solid components and focal scalloping of the overlying inner table (*arrows*). *D*, Axial FLAIR image shows marked vasogenic edema. *E*, Gadolinium-enhanced coronal T1-weighted image shows intense enhancement of the lateral solid components. *F* and *G*, Axial diffusion-weighted image and ADC map show that the solid component shows reduced diffusion compared with normal brain (ADC ratio = 0.85).

ingly supratentorial tumors (99%); in a study based upon the National Cancer Institute's Surveillance, Epidemiology, and End Results database,<sup>6</sup> only 2 cerebellar tumors were present among 214 PXAs. The only infratentorial PXA in our series was a brain stem lesion without involvement of the cerebellum. PXAs tend to be superficial in the cerebral hemispheres and 40%–50% involve the temporal lobes.<sup>2,6</sup> In the largest series where presenting symptoms were known, 71% of the patients' presenting symptoms were seizures only, which were often of long duration (median 3 years).<sup>2</sup>

According to the latest World Health Organization classification,

PXAs represent grade II tumors histologically.<sup>2</sup> A small percentage of PXAs demonstrate increased mitotic activity (defined as 5 or more mitoses per 10 high-power fields) with or without areas of necrosis and are designated as "PXA with anaplastic features."<sup>2</sup> PXAs are remarkable for a relatively favorable outcome with 5- and 10-year overall survival rates of 75%–81% and 67%–70%, respectively.<sup>2,6</sup> The survival rates in our cohort are comparable. Gross total resection of the tumor and a low mitotic rate were found to correlate positively with overall survival.<sup>2</sup> Although PXAs are generally considered indolent neoplasms, they are associated with a higher frequency of recur-

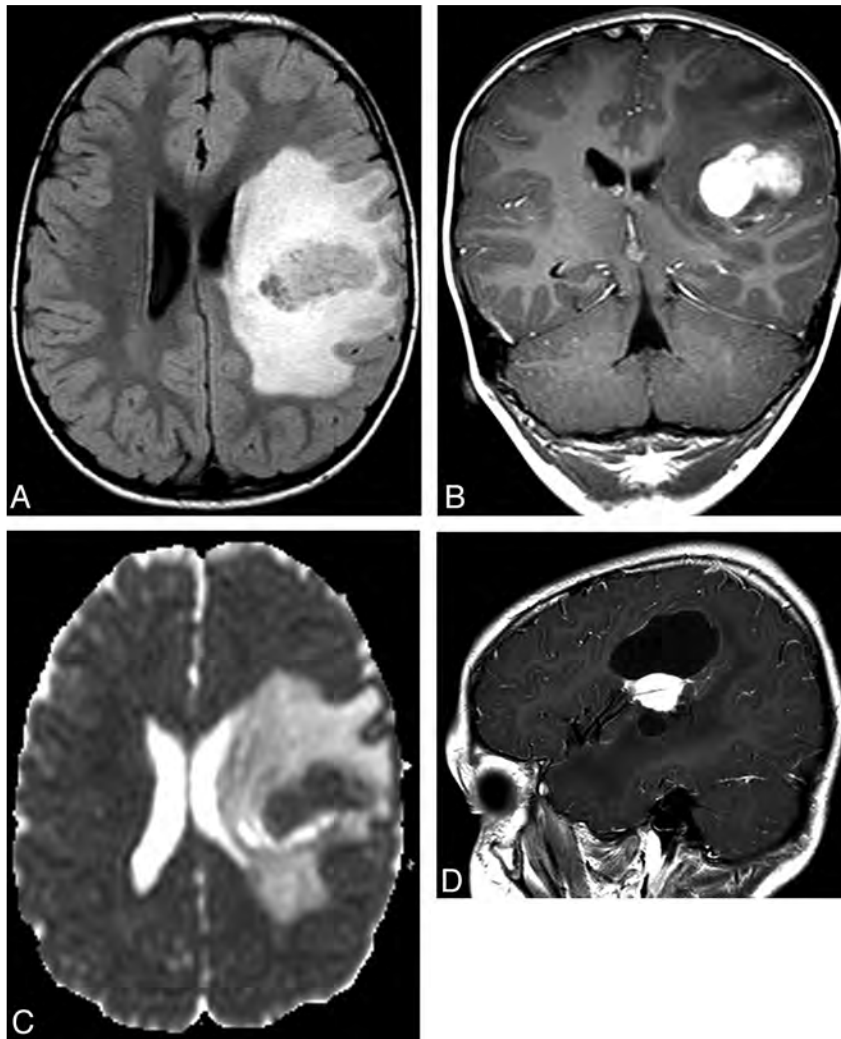


**FIG 2.** Left frontal PXA in a 4.8-year-old boy (patient number 2). *A*, Preoperative axial FLAIR image shows marked vasogenic edema. *B*, Preoperative coronal T1-weighted gadolinium-enhanced image shows intense enhancement of the lesion. *C*, The calculated preoperative ADC ratio was 1.06. *D*, The mass could not be resected completely because of its proximity to the left middle cerebral artery and showed progression over 4 years. Sagittal gadolinium-enhanced T1-weighted image shows the signal void of a middle cerebral artery branch within the enhancing mass.

rence, malignant transformation, and death, compared with other low-grade gliomas, such as pilocytic astrocytomas.<sup>6-9</sup>

Although there are imaging reports of PXAs in children and adults, dedicated pediatric imaging studies are rare and diffusion MR imaging characteristics were not previously described.<sup>10-14</sup> In 1 of the earliest MR imaging reports, Lipper et al<sup>12</sup> described imaging findings of PXA in 7 patients, 3 of whom were children. Peripheral location of PXA in the cerebral hemispheres was emphasized in this report. We identified 3 studies with >15 patients where imaging findings were described in detail.<sup>10,15,16</sup> Crespo-Rodríguez et al<sup>10</sup> described preoperative MR imaging findings in 10 children (mean age = 11.2 years, range = 9–14 years) in a publication of pediatric and adult PXAs. Eight of these tumors were cystic with a mural nodule; this feature was recognized with similar frequency in the adult population of the same study. In a dedicated pediatric PXA report, 8 of the 11 tumors had an enhancing mass with a cystic component.<sup>8</sup> Our cohort shows similarities with these reports with two-thirds of tumors being predominantly cystic or containing multiple cysts.

In our study, we found that 6 of the 8 supratentorial tumors

showed inner table scalloping. Inner table scalloping is a feature of slow-growing superficial brain tumors of childhood, such as ganglioglioma and dysembryoplastic neuroepithelial tumor.<sup>17</sup> Whereas Crespo-Rodríguez et al<sup>10</sup> reported inner table remodeling in 3 of 6 patients with PXA younger than 12 years, in the study by Yu et al,<sup>16</sup> only 1 of the 19 patients (both children and adults with an age range of 8–70 years) demonstrated calvarial remodeling.

Our findings are similar to the previously published reports in the frequency of perilesional edema; however, we recognized that marked perilesional edema, described as >10 mm, was present in 7 of our 9 PXAs. Lipper et al<sup>12</sup> reported “definite” perilesional edema (mild or moderate) in 5 of 7 cases. In the study of Crespo-Rodríguez et al,<sup>10</sup> perilesional edema was present in 2 of the 10 pediatric patients, similar to the frequency seen in their adult patients with PXA. In a more recent study that reported perilesional edema in greater detail, 31.8% (7 of 22) of the patients had edema >10 mm, while 36.4% (8/22) had edema <10 mm.<sup>15</sup> In this study, all of the 9 pediatric PXAs showed perilesional edema; in 7 patients, edema was <10 mm, and in 2 it was >10 mm.<sup>15</sup>

Hemorrhage in PXA has been described as an uncommon im-

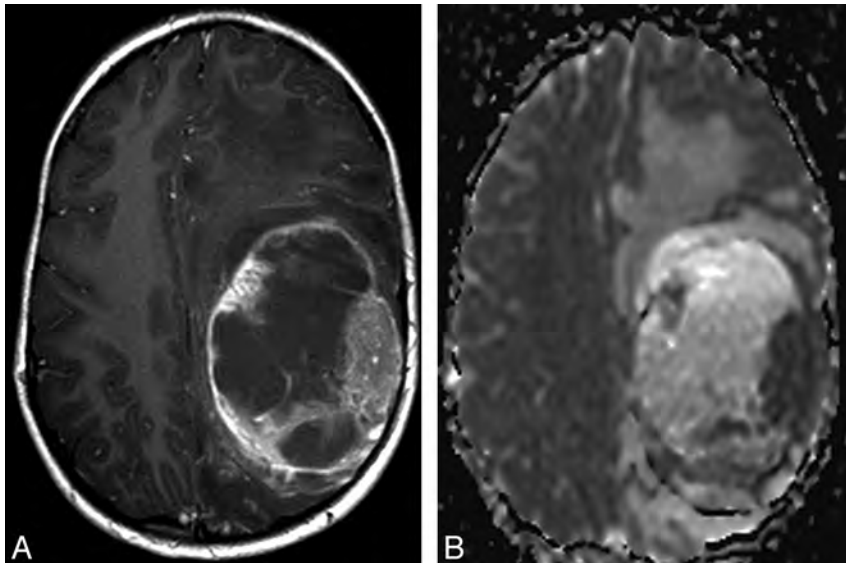


**FIG 3.** Left frontal and parietal PXA with anaplastic features in a 6.1-year-old male (patient number 8). A, Preoperative axial gadolinium-enhanced T1-weighted image shows a predominantly cystic mass with marked vasogenic edema. B, ADC ratio of the tissue corresponding to the solid enhancing tumor is 0.75.

aging feature, but was present in 33% of tumors in our series.<sup>10</sup> While hemorrhage does not seem to represent a typical feature, its presence should not dissuade the diagnosis of PXA.

Diffusion MR imaging has become an important tool in preoperative characterization of brain tumors. To our knowledge, diffusion MR imaging characteristics of PXAs have not been reported previously. In the 7 tumors where ADC values can be reliably measured, we found the mean ADC was  $912 \pm 219 \times 10^{-6} \text{ mm}^2/\text{s}$  and mean ADC ratio of the tumors was  $1.14 \pm 0.26$ . These values are lower than those of pediatric pilocytic astrocytomas and supratentorial gangliogliomas. It is important to recognize that the relatively low ADC values and ADC ratios of PXAs are not unusual characteristics and do not necessarily signify high-grade neoplasms. Although inclusion of diffusion MR imaging is a feature that distinguishes this study from the previous reports, the number of patients does not allow for making generalizations as to the survival or discrimination of PXAs with anaplastic features from those without. Future publications with emphasis on diffusion MR imaging of PXAs may be of benefit. Our study has some limitations. First, although we compiled a cohort that is comparable with other larger pediatric PXA series, the number of patients remains limited and conclusions of the study should be interpreted with caution. Second, even though this is the first report of diffusion MR imaging of PXAs, only 7 of our patients had diffusion MR imaging. Third, we had only 1 patient with a PXA with anaplastic features in whom preoperative diffusion MR imaging was available. Although the solid component of this tumor showed restricted diffusion, this was not a distinguishing characteristic from the PXAs without anaplastic features. Fourth, 2 patients were lost to follow-up, shortening the overall follow-up duration.

## CONCLUSIONS

In this study we reported preoperative imaging findings of pediatric PXAs with emphasis on diffusion MR imaging. PXA should be entertained in the differential diagnosis of peripheral cerebral hemispheric lesions with solid and cystic components associated with scalloping of the adjacent inner table. Vasogenic edema of the adjacent

white matter appears to be a common observation. Relatively lower ADC values and ADC ratios of the solid components may distinguish these tumors from other low-grade supratentorial, peripheral tumors such as gangliogliomas.

## REFERENCES

1. Giannini C, Paulus W, Louis DN, et al. **Pleomorphic xanthoastrocytoma.** In: Louis DN, Ohgaki H, Wiestler OD, et al, eds. *WHO Classification of Tumours of the Central Nervous System.* 4th ed. Lyon, France: International Agency for Research on Cancer; 2007:22–24
2. Giannini C, Scheithauer BW, Burger PC, et al. **Pleomorphic xanthoastrocytoma: what do we really know about it?** *Cancer* 1999;85:2033–45
3. Borja MJ, Plaza MJ, Altman N, et al. **Conventional and advanced MRI features of pediatric intracranial tumors: supratentorial tumors.** *AJR Am J Roentgenol* 2013;200:W483–503
4. Chang YW, Yoon HK, Shin HJ, et al. **MR imaging of glioblastoma in children: usefulness of diffusion/perfusion-weighted MR and MR spectroscopy.** *Pediatr Radiol* 2003;33:836–42
5. Gimi B, Cederberg K, Derinkuyu B, et al. **Utility of apparent diffusion coefficient ratios in distinguishing common pediatric cerebellar tumors.** *Acad Radiol* 2012;19:794–800
6. Perkins SM, Mitra N, Fei W, et al. **Patterns of care and outcomes of patients with pleomorphic xanthoastrocytoma: a SEER analysis.** *J Neurooncol* 2012;110:99–104
7. Marton E, Feletti A, Orvieto E, et al. **Malignant progression in pleomorphic xanthoastrocytoma: personal experience and review of the literature.** *J Neurol Sci* 2007;252:144–53
8. Rao AA, Laack NN, Giannini C, et al. **Pleomorphic xanthoastrocytoma in children and adolescents.** *Pediatr Blood Cancer* 2010;55:290–94
9. Tekkok IH, Sav A. **Anaplastic pleomorphic xanthoastrocytomas. Review of the literature with reference to malignancy potential.** *Pediatr Neurosurg* 2004;40:171–81
10. Crespo-Rodríguez AM, Smirniotopoulos JG, Rushing EJ. **MRI and CT imaging of 24 pleomorphic xanthoastrocytomas (PXA) and a review of the literature.** *Neuroradiology* 2007;49:307–15
11. Goncalves VT, Reis F, Queiroz Lde S, et al. **Pleomorphic xanthoastrocytoma: magnetic resonance imaging findings in a series of cases with histopathological confirmation.** *Arq Neuropsiquiatr* 2013;71:35–39
12. Lipper MH, Eberhard DA, Phillips CD, et al. **Pleomorphic xanthoastrocytoma, a distinctive astroglial tumor: neuroradiologic and pathologic features.** *AJNR Am J Neuroradiol* 1993;14:1397–404
13. Tien RD, Cardenas CA, Rajagopalan S. **Pleomorphic xanthoastrocytoma of the brain: MRI findings in six patients.** *AJR Am J Roentgenol* 1992;159:1287–90
14. Wallace DJ, Byrne RW, Ruban D, et al. **Temporal lobe pleomorphic xanthoastrocytoma and chronic epilepsy: long-term surgical outcomes.** *Clin Neurol Neurosurg* 2011;113:918–22
15. Lim S, Kim JH, Kim SA, et al. **Prognostic factors and therapeutic outcomes in 22 patients with pleomorphic xanthoastrocytoma.** *J Korean Neurosurg Soc* 2013;53:281–87
16. Yu S, He L, Zhuang X, et al. **Pleomorphic xanthoastrocytoma: MR imaging findings in 19 patients.** *Acta Radiol* 2011;52:223–28
17. Shin JH, Lee HK, Khang SK, et al. **Neuronal tumors of the central nervous system: radiologic findings and pathologic correlation.** *Radiographics* 2002;22:1177–89

# Cement Salvage of Instrumentation-Associated Vertebral Fractures

R. Xu, K. O'Connor, G. Krol, Y. Yamada, M. Bilsky, I. Laufer, and E. Lis



## ABSTRACT

**BACKGROUND AND PURPOSE:** Spinal instrumentation plays a key role in the treatment of spinal instability in patients with metastatic tumors. Poor bone quality, radiation, and diffuse osseous tumor involvement present significant challenges to spinal stabilization with instrumentation and occasionally result in postinstrumentation compression fractures. Vertebral cement augmentation has been effective in the treatment of painful tumor-related compression fractures. Our objective was to describe cement augmentation options in the treatment of vertebral compression fractures associated with spinal instrumentation in patients with metastatic tumors.

**MATERIALS AND METHODS:** Patients who underwent percutaneous vertebral cement augmentation in the treatment of instrumentation-associated vertebral compression fractures between 2005 and 2011 were included in the analysis. Only fractures that occurred within the construct or at an adjacent level were included. The change in Visual Analog Scale and need for further surgery were analyzed.

**RESULTS:** Eleven patients met the inclusion criteria, with 8 tumors located in the thoracic spine and 3 tumors in the lumbar spine. The median time between instrumented surgery and vertebral augmentation was 5 months (1–48 months) and the median follow-up after cement augmentation was 24 months (4–59 months). A total of 22 vertebrae that were either within or immediately adjacent to the surgical instrumentation underwent vertebral augmentation. All patients reported a decrease in their pain scores (mean decrease: 6 Visual Analog Scale points;  $P < .003$ ). One patient required reoperation after cement augmentation. None of the patients experienced vertebral cement augmentation–related complications.

**CONCLUSIONS:** Vertebral cement augmentation represents a safe and effective treatment option in patients with recurrent or progressive back pain and instrumentation-associated vertebral compression fractures.

**ABBREVIATIONS:** VAS = Visual Analog Scale; SRS = stereotactic radiosurgery

The role of surgery in the treatment of metastatic spinal tumors has been firmly established as an effective and safe method for spinal cord decompression and stabilization of the spine. The goals of surgery for spinal metastases remain palliative and include preservation or restoration of neurologic function and pain control. Tumor control is largely accomplished using radiation and chemotherapy. In patients with metastatic spinal tumors, spi-

nal instrumentation is required in most cases to provide spinal stability after circumferential spinal cord decompression. Spinal fixation in this patient population can be quite challenging because of extensive osteoporosis and lytic tumor destruction. Furthermore, chest wall resection may be required, further destabilizing the spine and increasing the risk of fixation failure. Prior spine radiation results in increased risk of vertebral compression fractures.<sup>1–3</sup> Failure of fixation may require interruption or delay of systemic or radiation therapy, increasing the risk of local or systemic tumor progression. Vertebral compression fractures either within or adjacent to the surgical construct often result in either recurrent or progressive back pain.

Percutaneous vertebral cement augmentation (ie, balloon kyphoplasty/vertebroplasty) has been established as a safe and effective method of quickly achieving pain control in osteoporotic and tumor-related compression fractures.<sup>4,5</sup> Cement has also been used to reinforce screws at the time of insertion.<sup>6,7</sup> However, little information exists regarding its use as a salvage technique for

Received September 9, 2013; accepted after revision April 2, 2014.

From the Departments of Neurosurgery (R.X., K.O., M.B., I.L.), Spine Tumor Center (M.B., I.L., E.L.), Radiology (G.K., E.L.), and Radiation Oncology (Y.Y.), Memorial Sloan–Kettering Cancer Center, New York, New York; Department of Neurological Surgery (M.B., I.L.), Weill Cornell Medical College, New York–Presbyterian Hospital, New York, New York; Mount Sinai School of Medicine (K.O.), New York, New York; and Department of Medical Biophysics (R.X.), Institute of Physiology and Pathophysiology, Heidelberg University, Heidelberg, Germany.

Please address correspondence to Eric Lis, MD, Department of Radiology, Memorial Sloan–Kettering Cancer Center, 1275 York Ave, New York, NY 10021; email: lise@mskcc.org

Indicates article with supplemental on-line table.

<http://dx.doi.org/10.3174/ajnr.A4037>

instrumented patients who develop recurrent back pain secondary to new vertebral compression fractures within or adjacent to their surgical construct. We report a series of patients in whom percutaneous vertebral cement augmentation was used as an initial treatment of symptomatic instrumentation or junctional fractures in place of open hardware revision.

## MATERIALS AND METHODS

### Patient Population

Patients who underwent kyphoplasty or vertebroplasty and surgery for the treatment of spinal metastatic tumors between 2005 and 2011 were included in the study. A waiver of institutional review board authorization and informed consent was obtained from the institution to collect the existing data regarding these patients. Among the 29 patients who fit these inclusion criteria, 18 patients were excluded because the postcement augmentation follow-up was less than 2 months, they underwent cement augmentation before surgical stabilization, or the cement augmentation levels were more than 1 level outside of the instrumented levels. The charts and imaging studies of the remaining 11 patients were retrospectively reviewed for tumor histology, tumor level, decompression, instrumentation and cement augmentation levels, further revision surgery, and Visual Analog Scale (VAS) scores.

### Surgery

All patients underwent separation surgery, an open surgical technique that separates epidural disease to reconstitute the thecal sac and posterior stabilization, followed by postoperative radiation therapy.<sup>8</sup> To provide circumferential thecal sac decompression at the level of epidural extension of the tumor, laminectomy with bilateral or unilateral facetectomy and resection of the ventral epidural tumor with very limited vertebrectomy were performed. Spinal stabilization was provided by posterolateral fixation at least 2 levels above and below the tumor. All patients were treated with adjuvant radiation therapy that consisted of either conventional external-beam radiation or stereotactic radiosurgery (SRS) that was selected based on tumor histology and prior radiation history.

### Cement Augmentation

All patients had cross-sectional imaging of the spine before the procedure usually consisting of MR imaging and often a CT scan. This determined which vertebrae to augment and helped in the planning of the trajectory of the introducer needles for subsequent cement augmentation. The procedure was performed under general anesthesia in the interventional radiology suite that has both fluoroscopic and CT (conebeam as well as collimated) capabilities. Both CT and fluoroscopy were used for placement of the introducer needles. The trajectory of the introducer needles was dictated by the hardware and anatomy (Fig 1). During the fluoroscopic portion of the procedure, oblique views of the spine were often required in addition to the more standard anterior-posterior and lateral views to “throw off” the hardware and to allow better visualization of the introducer needles and cement infusion. If there was any question regarding needle or cement location, an intraprocedural conebeam CT scan was obtained. Deciding between balloon kyphoplasty and vertebroplasty was determined during the procedure by needle trajectory and the anatomy. At the levels without intrapedicular screws or with only a unilateral

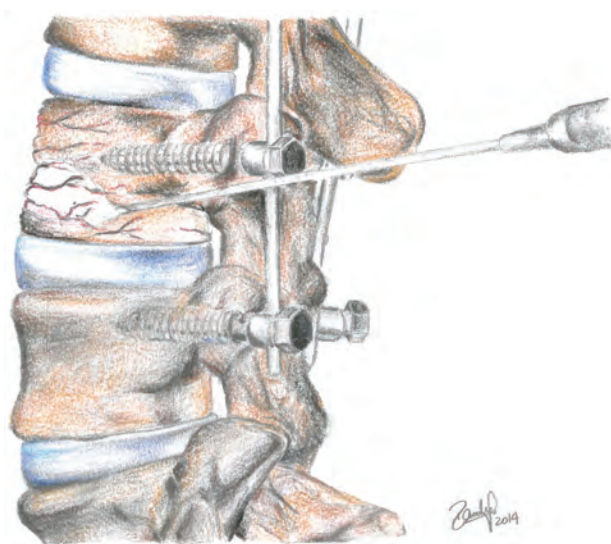


**FIG 1.** Percutaneous vertebral cement augmentation for an instrumentation-associated vertebral fracture. Schematic showing the placement of the introducer needle and cement infusion, the trajectory of the kyphoplasty needle being dictated by the presence of existing hardware, and anatomic structures.

screw, an inflatable bone tamp (Medtronic MIS, Sunnyvale, California) was used before the cement infusion (kyphoplasty). At levels with previously placed bilateral screws, the trajectory of the introducer needle was extrapedicular, often at the superior or inferior extremes of the vertebral body thereby obviating the ability to place a bone tamp. In these cases vertebroplasty was performed, usually through a curved AVAflex needle (Carefusion, Waukegan, Illinois). The use of the curved needle was particularly helpful in directing the cement into different regions of the vertebral body when surgical screws limited the position of the introducer needle.

The cement was hand injected coaxially through the introducer needle under fluoroscopic visualization, with repeat CT imaging performed if there was a question of extravasation into the spinal canal or neural foramina. The cement used was either the standard high-viscosity radiopaque polymethylmethacrylate or Cortoss bone augmentation material (Stryker Neurovascular, Fremont, California), which is a nonresorbable composite. The latter has an advantage that a small amount can be mixed on demand, which is particularly helpful if switching back and forth between CT and fluoroscopy is required.

### Data Analysis

Statistical analysis was performed using SPSS 20.0 (IBM, Armonk, New York). A Wilcoxon signed ranks test was used to compare the prekyphoplasty and postkyphoplasty VAS scores.

## RESULTS

Individual patient and treatment information are summarized in the On-line Table. The median age at time of postsurgical cement augmentation was 60 years (range: 38–71 years). Median follow-up after cement augmentation was 24 months (range: 4–59 months), and the median time between instrumentation and salvage cement augmentation was 5 months (range: 1–48 months). Eight tumors were located in the thoracic spine and the remaining 3 were located in the lumbar spine. All patients underwent cement

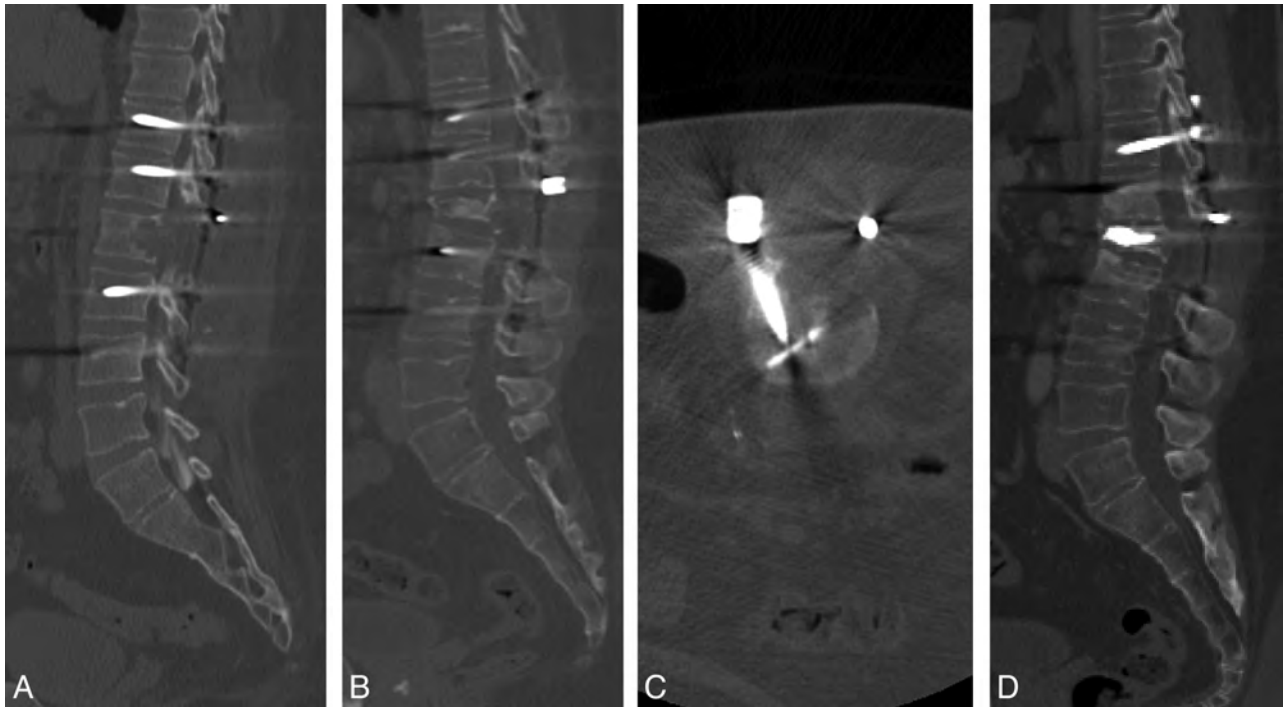


**FIG 2.** A 38-year-old man with renal cancer with L1 metastasis treated with surgical decompression followed by SRS. *A*, Reconstructed sagittal CT of the lumbar spine obtained post L1 laminectomy. *B*, Follow-up CT scan 23 months later showing a moderate L1 collapse. *C*, Intraoperative CT confirming an adequate trajectory through the L1 vertebral body. *D*, Postaugmentation CT scan showing good filling of the L1 vertebral body.

augmentation after developing new painful compression fractures. The pain rather than the radiographic finding was the indication for intervention. Eight of the cement augmentation procedures were done at the levels of the top or bottom screws or immediately adjacent to these levels. The remaining 3 patients had cement augmentation in the middle of the construct.

The mean prekyphoplasty VAS score was 8.4 (range 4–10) and postkyphoplasty score was 1.5 (range 0–5). All patients reported a decrease in their pain scores. The mean decrease in the VAS score was 6 points ( $P < .003$ ).

One patient required surgery after kyphoplasty. The patient initially underwent L1 decompression and T11–L3 stabilization for a renal cell metastasis (Fig 2*A*). One year after the initial operation, the patient developed severe back pain and was found to have a new L1 compression fracture; however, the patient's hardware appeared intact (Fig 2*B*). The patient underwent a L1 kyphoplasty with significant pain relief, from 10/10 to 1/10 (Fig 2*C*, -*D*). Five months after the kyphoplasty, the patient developed new back pain and x-rays revealed a unilateral rod fracture. The rod was replaced and the back pain resolved.

None of the patients experienced vertebral cement augmentation–related complications such as neural element compression or cement embolization.

### Case Example

A 62-year-old man with metastatic melanoma underwent single-fraction SRS (24 Gy) to L4. Three months after radiation, he developed an L4 burst fracture and mechanical radiculopathy requiring an L3–L5 posterolateral instrumentation and fusion with left L4–L5 facetectomy. One year later, the patient developed an L2 metastasis. Initially he underwent an L2 kyphoplasty; however,

because of the progression of radicular pain and posterior element instability he required extension of instrumentation to T12 and right-sided transpedicular decompression of the epidural tumor. Four years after the initial surgery, the patient developed recurrence of back pain and was noted to have a compression fracture at L4 and endplate infractions at L3 and L5 without evidence of tumor progression (Fig 3*A*). This patient underwent cement augmentation at L3–L5, resulting in significant decrease of pain symptoms (VAS 10/10 to 2/10). At L4, kyphoplasty was performed; the needle was advanced into the vertebral body via the left pedicle, and an inflatable bone tamp was used before cement infusion (Fig 3*B*, -*C*). At levels L3 and L5, where bilateral screws were present, the trajectory of the introducer needles was extrapedicular, therefore obviating the ability to place a bone tamp; instead, vertebroplasty was performed through a curved AVAflex needle. At L3, a lateral parapedicular approach was undertaken. At L5 the guide needle was inserted via a superior, extrapedicular approach and the augmentation needle was then advanced coaxially, allowing access to both the contralateral and unilateral side (Fig 3*B*, -*C*).

### DISCUSSION

The treatment of spinal metastases is performed with the palliative goals of preservation or restoration of neurologic function and spinal stability, pain control, and local tumor control. Surgery is indicated for patients with metastatic spinal tumors in the setting of spinal cord compression and spinal instability.<sup>9</sup> Instrumentation restores spinal stability after circumferential decompression and osseous infiltration by tumor. Generally patients with metastatic tumors require systemic therapy, which requires

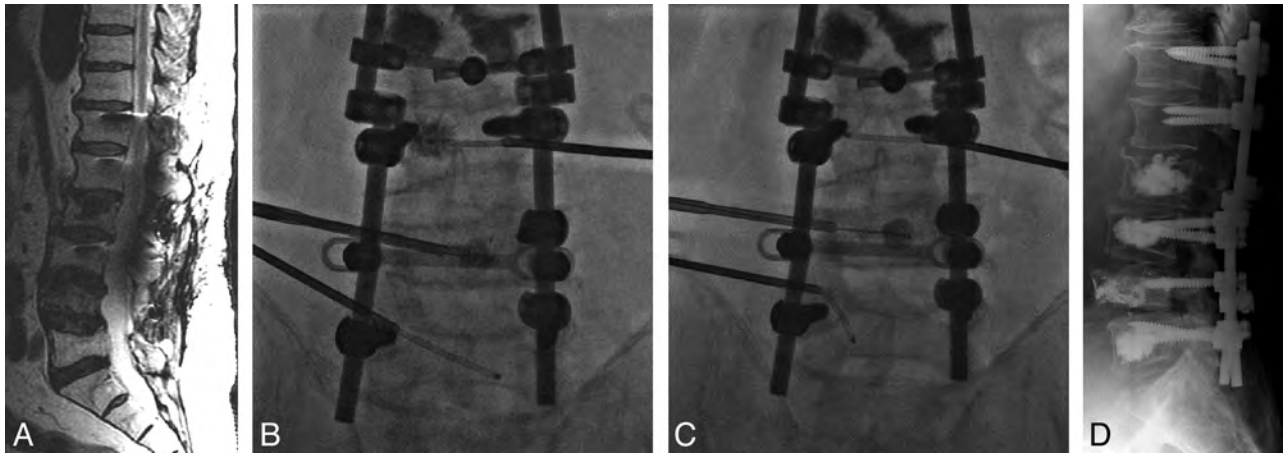


**FIG 3.** A 62-year-old man status post prior L2 kyphoplasty and radiation therapy for melanoma metastasis with subsequent recurrence and surgical decompression. *A*, The patient developed a partial collapse deformity of L4 with early endplate infractions L3 and L5 as demonstrated on MR imaging. *B*, Anterior-posterior fluoroscopic image showing an inflated bone tamp in L3, with curved needles in L3 and L5. *C*, Anterior-posterior image a few moments later showing cement infusion into L3 and L4. Notice the repositioning of the curved needle in L5. *D*, Postaugmentation sagittal x-ray demonstrating good filling of vertebral bodies.

coordination with surgery and radiation. Spinal radiation is generally administered 3–4 weeks after surgery to decrease the risk of wound dehiscence or infection. Systemic therapy is administered after radiation and is of paramount importance in preventing systemic progression of cancer. Postoperative wound complications or hardware failure may require significant delay in chemotherapy administration and may have disastrous implications, with systemic progression leading to the demise of the patient or requiring additional surgery and radiation.

While the beneficial role of surgery has been thoroughly documented in the treatment of patients with spinal metastases, these operations may be associated with a wide range of potential complications. The reported perioperative complication rate range is 19%–50%.<sup>10–12</sup> The hardware failure rate has been reported to be 2.2%–16%. Hardware-related complications include dislodgement of titanium cage, screw, hook, rod, or plate back-out, or breakage and adjacent level fractures. Generally, symptomatic hardware malfunction compromises spinal stability and requires patients to return to the operating room to replace the fractured components and often to extend the fixation to adjacent levels. In oncologic patients, multilevel tumor infiltration along with chest wall involvement further complicates the stabilization, as does underlying poor bone quality often secondary to osteoporosis and prior radiation. Avoidance of multiple hardware revisions is crucial in continuation of chemotherapy and radiation and in avoidance of high-risk reoperations.

Percutaneous vertebral cement augmentation has been established as an effective treatment for painful fractures in patients with metastatic spinal tumors.<sup>4</sup> The Spine Oncology Study Group<sup>13</sup> made a strong recommendation for the use of vertebral cement augmentation in patients with symptomatic osteolytic metastases and compression fractures. The group conducted a systematic review of the literature that confirmed that kyphoplasty or vertebroplasty consistently relieves mechanical axial pain and improves functional status. Furthermore, the investigators of the Cancer Fracture Evaluation study<sup>5</sup> randomized 134 patients with painful compression fractures to undergo kyphop-

lasty or nonsurgical management and found a significant improvement in the pain and function in the treatment group at 1-month follow-up. Complications were very rare, with 1 patient experiencing anesthesia-related non-Q-wave myocardial infarction and 1 patient developing an adjacent-level vertebral body fracture 1 day after the kyphoplasty. Thus, vertebral cement augmentation provides a safe and effective minimally invasive treatment option for cancer-related vertebral fractures that can be performed on an outpatient basis.

While the procedure of postinstrumentation vertebral body cement augmentation is similar to standard percutaneous vertebral cement augmentation procedures performed in nonsurgically stabilized patients, there are some unique technical challenges. The fixation hardware often consists of bilateral intrapedicular screws and posterior stabilization rods, which alters access to the vertebral body. The presence of pedicle screws essentially eliminates the transpedicular approach to the vertebral body. The screws within the vertebral body are typically lateral, making access to the central aspect of the vertebral body challenging. Fluoroscopic imaging is more difficult because the introducer needle tips may be obscured or silhouetted by the surgical hardware. In the lateral plane under fluoroscopy, the presence of intrapedicular screws will also obscure a portion of the spinal canal and ventral epidural space. This is of critical importance during the infusion of the cement as the posterior extent of the cement may not be readily apparent. If the vertebral body to be augmented is at the level of tumor resection, often the standard fluoroscopic imaging landmarks are absent. The pedicles and posterior elements typically have been resected and or previously destroyed by tumor. This not only makes fluoroscopic access challenging, but also the absence of the posterior elements removes the bony protection of the thecal sac. Similarly, if the costovertebral junction has been removed, the thorax is more vulnerable to penetration by the introducer needles. Multiple oblique fluoroscopic trajectories may be required to optimize the visualization of the needle trajectory and cement. If needle placement

trajectory or the posterior extent of cement is not clear with fluoroscopy, an intraprocedural conebeam CT can be obtained.

In addition to the hardware and postsurgical osseous changes, postsurgical soft tissue changes need to be considered. In particular, the presence of a paraspinal fluid collection, seroma, or pseudomeningocele will need to be avoided and require modification of the trajectory of the introducer needle. This reinforces the necessity of having a preprocedural cross-sectional imaging study to help determine the best trajectory of the augmentation needle into the collapsed vertebrae.

The current patient series documents the feasibility of percutaneous vertebral cement augmentation in the treatment of symptomatic vertebral compression fractures within or immediately adjacent to pedicle fixation constructs. The data show that cement reinforcement provides effective pain relief in instances of junctional fractures as well as fractures within the construct. Thus, in place of open hardware revision and extension, patients undergo an outpatient procedure with minimal risk of morbidity. Our report includes the results of a small series of consecutive patients who were treated with this technique, and a larger prospective cohort will be necessary to determine the optimal candidates for this treatment and to provide more generalizable outcome data. Furthermore, in some patients, the position of the instrumentation may prohibit safe cement augmentation. Cement salvage of hardware-related fractures provides a safe and well-tolerated alternative to open surgery that does not require interruption of systemic therapy.

## CONCLUSIONS

Surgery for metastatic spinal cancer is a palliative measure. Poor quality of bone and tumor progression can lead to new symptomatic compression fractures. The use of percutaneous vertebral cement augmentation in these situations can be extremely beneficial for the patient by effectively relieving pain with an outpatient procedure that does not require interruption of systemic therapy or radiation.

Disclosures: Yoshiya Yamada—UNRELATED: Consultancy: Varian Medical Systems, Speakers Bureau for the Institute for Medical Education, Comments: CME-approved lectures; Board Membership: American Brachytherapy Society; Travel/Accommodations/Meeting Expenses Unrelated to Activities Listed: American Brachytherapy Society; Grants/Grants Pending: Medtronic,\* Comments: for an image-guided brachytherapy study. Mark Bilsky—UNRELATED: Consultancy: SpineWave and

DePuy Synthes. Ilya Laufer—UNRELATED: Consultancy: SpineWave and DePuy Synthes. Eric Lis—UNRELATED: Consultancy: Medtronic; Payment for Lectures (including service on speakers' bureaus): Medtronic. \*Money paid to the institution.

## REFERENCES

1. Boehling NS, Grosshans DR, Allen PK, et al. **Vertebral compression fracture risk after stereotactic body radiotherapy for spinal metastases.** *J Neurosurg Spine* 2012;16:379–86
2. Cunha MV, Al-Omair A, Atenafu EG, et al. **Vertebral compression fracture (VCF) after spine stereotactic body radiation therapy (SBRT): analysis of predictive factors.** *Int J Radiat Oncol Biol Phys* 2012;84:e343–49
3. Rose PS, Laufer I, Boland PJ, et al. **Risk of fracture after single fraction image-guided intensity-modulated radiation therapy to spinal metastases.** *J Clin Oncol* 2009;27:5075–79
4. Fournay DR, Schomer DF, Nader R, et al. **Percutaneous vertebroplasty and kyphoplasty for painful vertebral body fractures in cancer patients.** *J Neurosurg* 2003;98:21–30
5. Berenson J, Pflugmacher R, Jarzem P, et al. **Balloon kyphoplasty versus non-surgical fracture management for treatment of painful vertebral body compression fractures in patients with cancer: a multicentre, randomised controlled trial.** *Lancet Oncol* 2011;12:225–35
6. Amendola L, Gasbarrini A, Fosco M, et al. **Fenestrated pedicle screws for cement-augmented purchase in patients with bone softening: a review of 21 cases.** *J Orthop Traumatol* 2011;12:193–99
7. Sawakami K, Yamazaki A, Ishikawa S, et al. **Polymethylmethacrylate augmentation of pedicle screws increases the initial fixation in osteoporotic spine patients.** *J Spinal Disord Tech* 2012;25:E28–35
8. Laufer I, Iorgulescu JB, Chapman T, et al. **Local disease control for spinal metastases following “separation surgery” and adjuvant hypofractionated or high-dose single-fraction stereotactic radiosurgery: outcome analysis in 186 patients.** *J Neurosurg Spine* 2013;18:207–14
9. Patchell RA, Tibbs PA, Regine WF, et al. **Direct decompressive surgical resection in the treatment of spinal cord compression caused by metastatic cancer: a randomised trial.** *Lancet* 2005;366:643–48
10. Falicov A, Fisher CG, Sparkes J, et al. **Impact of surgical intervention on quality of life in patients with spinal metastases.** *Spine* 2006;31:2849–56
11. Finkelstein JA, Zaveri G, Wai E, et al. **A population-based study of surgery for spinal metastases. Survival rates and complications.** *J Bone Joint Surg Br* 2003;85:1045–50
12. Wise JJ, Fischgrund JS, Herkowitz HN, et al. **Complication, survival rates, and risk factors of surgery for metastatic disease of the spine.** *Spine* 1999;24:1943–51
13. Mendel E, Bourekas E, Gerszten P, et al. **Percutaneous techniques in the treatment of spine tumors: what are the diagnostic and therapeutic indications and outcomes?** *Spine* 2009;34:S93–100

# Safety and Effectiveness of Sacroplasty: A Large Single-Center Experience

A.C. Gupta, R.V. Chandra, A.J. Yoo, T.M. Leslie-Mazwi, D.L. Bell, B.P. Mehta, T.L. Vanderboom, J.D. Rabinov, M. Larvie, and J.A. Hirsch



## ABSTRACT

**BACKGROUND AND PURPOSE:** Sacral insufficiency fractures are a common cause of severe low back pain and immobilization in patients with osteoporosis or cancer. Current practice guideline recommendations range from analgesia and physical therapy to resection with surgical fixation. We sought to assess the safety and effectiveness of sacroplasty, an emerging minimally invasive treatment.

**MATERIALS AND METHODS:** We performed a retrospective review of institutional databases for percutaneous sacroplasty performed between January 2004 and September 2013. Demographic and procedural data and pre- and posttreatment Visual Analog Scale, Functional Mobility Scale, and Analgesic Scale scores were reviewed. Overall response was rated by using a 4-point scale (1, complete resolution of pain; 2, improvement of pain; 3, no change; 4, worsened pain) assessed at short-term follow-up.

**RESULTS:** Fifty-three patients were included; most (83%) were female. Fracture etiology was cancer-related (55%), osteoporotic insufficiency (30%), and minor trauma (15%). No major complication or procedure-related morbidity occurred. There were statistically significant decreases in the Visual Analog Scale ( $P < .001$ ), Functional Mobility Scale ( $P < .001$ ), and Analgesic Scale scores ( $P < .01$ ) in 27 patients with recorded data: pretreatment Visual Analog Scale (median [interquartile range], 9.0 [8.0–10.0]); Functional Mobility Scale, 3.0 (2.0–3.0); and Analgesic Scale scores, 3.0 (3.0–4.0) were reduced to 3.0 (0.0–5.8), 1.0 (0.25–2.8), and 3.0 (2.0–3.8) posttreatment. When we used the overall 4-point score at a mean of 27 days, 93% ( $n = 45$ ) reported complete resolution or improvement in overall pain.

**CONCLUSIONS:** In this single-center cohort, sacroplasty was a safe and effective procedure. There were significant short-term gains in pain relief, increased mobility, and decreased dependence on pain medication.

**ABBREVIATIONS:** AS = Analgesic Scale; FMS = Functional Mobility Scale; PMMA = polymethylmethacrylate; VAS = Visual Analog Scale

Sacral insufficiency fractures are a common source of debilitating pain and immobilization in the elderly population. Typically seen in the sacral ala or S2 vertebral body, they may result from osteopenia, osteolysis from cancer metastasis (specifically postradiation therapy), or trauma.<sup>1</sup> Most commonly seen in the osteoporotic elderly female population, sacral insufficiency fractures tend to present with nonlocalized low back pain with or without radiation to the buttocks. They can be difficult to diagnose because most nondisplaced or transverse sacral fractures are not clearly identified on conventional radiology. Specifically, they require more advanced imaging with CT, MR imaging, or nuclear

bone scintigraphy for accurate diagnosis.<sup>2</sup> As a result, detection may be delayed for many weeks.<sup>1</sup>

The current standard of care is a short period of bed rest and analgesia, often with opioid analgesics. Physical therapy to facilitate an early return to mobilization is encouraged to avoid physical deconditioning and associated complications of immobilization (venous thrombosis, pulmonary embolism, and pressure sores). Surgical fixation is generally reserved for patients with displaced dorsal fractures or fracture dislocations. For some patients, a prolonged conservative approach carries significant risk of morbidity from immobilization and opioid side effects such as respiratory depression, change in mental status, and dependence.<sup>3</sup>

Percutaneous sacroplasty has emerged more recently as a therapeutic option to reduce pain and facilitate early mobilization. While there are no randomized controlled trial data to support its efficacy, observational studies have reported significant reductions in pain scores and narcotic analgesic requirements, with an acceptable safety profile.<sup>4–11</sup> Data on functional mobility outcomes are more limited. The aim of this study was to evaluate the

Received February 5, 2014; accepted after revision April 16.

From the Department of Radiology (A.C.G., A.J.Y., T.M.L.-M., D.L.B., B.P.M., T.L.V., J.D.R., M.L., J.A.H.), Massachusetts General Hospital, Harvard Medical School, Boston, Massachusetts; and Department of Radiology (R.V.C.), Monash Health, and Department of Surgery, Monash University, Melbourne, Australia.

Please address correspondence to Joshua A. Hirsch, MD, Department of Radiology, Massachusetts General Hospital, Harvard Medical School, Gray 241, 55 Fruit St, Boston, MA 02114; e-mail: jahirsch@partners.org, jahirsch@mgh.harvard.edu

<http://dx.doi.org/10.3174/ajnr.A4027>



**FIG 1.** Percutaneous CT-guided sacroplasty. Intraoperative axial CT images during PMMA injection (A and B). The needle tip position is identified by the presence of beam-hardening artifacts (arrows) with adjacent PMMA deposition. Final postprocedural coronal CT image (C) reveals satisfactory PMMA deposition (arrows), with no extravasation into the sacral neural foramina.

**Table 1: Functional Mobility Scale and Analgesic Scale<sup>13</sup>**

Score	Functional Mobility Scale	Analgesic Scale
0	Full activity	No pain medication use
1	Walking with assistance	Aspirin, acetaminophen (Tylenol), nonsteroidal anti-inflammatory drugs
2	Walking with assistance for short periods	Prescription nonnarcotics
3	Walking with assistance for activities of daily living/appointments only	Oral narcotic as needed
4	Confined to a wheelchair	Oral narcotic scheduled
5	Bedridden	Parental narcotic

Reproduced from Gupta AC, Hirsch JA, Chaudhry ZA, et al. Evaluating the safety and effectiveness of percutaneous acetabuloplasty. *J Neurointerv Surg* 2012;4:134–38, with permission from BMJ Publishing Group Ltd.

safety and effectiveness of sacroplasty in a large single-center cohort, with emphasis on overall response to pain, functional mobility, and analgesic use.

## MATERIALS AND METHODS

### Patient Cohort

Under institutional review board approval, we retrospectively reviewed institutional databases to identify percutaneous sacroplasty cases performed at our institution from January 2004 to September 2013. Patients were referred for pain relief after a poor response to conservative therapy. Chart review was performed to obtain patient demographic data and fracture etiology. In patients with non-cancer-related fractures, fracture etiology was defined as osteoporotic insufficiency unless there was a clear history of a preceding traumatic event, such as a mechanical fall. In these cases, fracture etiology was deemed traumatic. All patients were evaluated with either CT or MR imaging before the procedure to assess fracture characteristics, extent of bony involvement, and proximity to neural structures. For cancer-related fractures, only patients with osteolytic or mixed osteolytic/osteoblastic lesions were included. Patients with osteoblastic primary tumors or predominantly osteoblastic metastasis were excluded due to the anticipated difficulty of needle placement. In addition, patients with involvement of the sacroiliac joint, clear osseous breach of the sacral neural foramina, or local neural compression were also excluded. Informed consent was obtained before the procedure, and Health Insurance Portability and Accountability Act compliance was maintained.

### Technique

Procedures were performed with intravenous sedation, typically by using a combination of fentanyl and midazolam or with the patient under general anesthesia. Local anesthetic was infiltrated in the skin, subcutaneous tissues, and periosteum. Continuous x-ray fluoroscopy, CT fluoroscopy, or intermittent CT scanning

was used to place an 11-gauge AVAmax needle (CareFusion, San Diego, California) into the fracture site by using either a short-axis or posterior long-axis approach. No adjunctive cavity creation (curettage and/or balloon inflation) or tumor ablative therapies (radiofrequency ablation/laser/cryotherapy) were used. Polymethylmethacrylate (PMMA) cement (Advanced Biomaterial Systems, Chatham, New Jersey) was then mixed and injected through the trocar by using a screw injector under continuous x-ray fluoroscopic guidance or intermittent CT scanning to monitor cement deposition. For CT-guided procedures, a small volume of PMMA was injected, and then a limited CT that covered the target site was performed to ensure that there was no untoward craniocaudal cement migration before injecting further PMMA (Fig 1). Using this intermittent CT method, we aimed to prevent extravasation into the sacral neural foramina. Final postprocedural images were used to evaluate final filling of the lesion and assess technical complications.

### Outcomes

Charts were reviewed to identify procedural complication data. Significant complications were defined as cement leakage leading to permanent neurologic deficit, cauda equina syndrome, a new neurologic deficit requiring surgical intervention, or systemic complications such as pulmonary embolism or procedure-related mortality.

The Visual Analog Scale (VAS), Functional Mobility Scale (FMS), and Analgesic Scale (AS) were used for pre- and postprocedural assessments. The VAS is a widely validated pain assessment tool that correlates sketched faces with numbers from 0 to 10, with 0 representing no pain to 10 representing the worst pain the patient has ever experienced.<sup>12</sup> The FMS measures mobility of the patient, with ranges from 0 to 5, with 0 representing full activity and 5 representing a bedridden patient (Table 1). The AS assesses a patient's use of pain medication on a scale from 0 to 5, with 0 representing no medication use and 5 representing paren-

**Table 2: Four-level pain scale<sup>9</sup>**

Score	Four-Level Pain Scale
1	Complete pain resolution
2	Improvement in fracture-related pain
3	No change in pain
4	Worsening of pain after the procedure

**Table 3: Summary data for 53 patients who underwent percutaneous sacroplasty**

Characteristics	Data
Total patients	53
Age (mean) (yr)	76.4 ± 2.8
Age younger than 70 yr	13 (25%)
Age 70–79 yr	20 (38%)
Age 80–89 yr	15 (28%)
Age 90 yr or older	5 (9%)
Female	44 (83%)
Female/male ratio	5:1
Cancer-related fracture	29 (55%)
Breast cancer	9/29 (31%)
Multiple myeloma	7/29 (24%)
Colorectal cancer	6/29 (21%)
Small cell lung cancer	2/29 (7%)
Prostate cancer	1/29 (3%)
Melanoma	1/29 (3%)
Cervical cancer	1/29 (3%)
Hematologic malignancy	1/29 (3%)
Pancreatic cancer	1/29 (3%)
Osteoporotic fracture	16 (30%)
Traumatic fracture	8 (15%)
Bilateral fractures treated	44 (83%)
Sacroplasty with conscious sedation	39 (74%)
Sacroplasty under general anesthesia	14 (26%)
Sacroplasty with CT guidance	48 (91%)
Sacroplasty with fluoroscopic guidance	5 (9%)
Significant complications	0
Procedural mortality	0
Time to follow-up (days)	27 (±3.7)

tal narcotic use (Table 1). Both the FMS and the AS have been described in the evaluation of cement augmentation procedures.<sup>13</sup> Formal, documented VAS, FMS, and AS evaluations became routine during the study period and were performed between January 2007 and September 2013. A 4-level pain scale was also used to evaluate patient response to the procedure (Table 2).<sup>9</sup> The scale ranges from 1 to 4 and was used to measure patient response to the procedure following sacroplasty, where 1 represents complete resolution of pain; 2, improvement of pain; 3, no change; and 4, worsened pain following the procedure.

### Statistical Analysis

All summary statistics for continuous variables were reported as mean (±SD and range), while categorical variables were reported as percentages. VAS, FMS, and AS scores (ordinal variables) were reported as median (interquartile range). Normality was assessed by using the Kolmogorov-Smirnov test. The Wilcoxon signed rank test was performed for statistical correlation with paired testing of pre- and posttreatment scores. Statistical significance was defined as  $P < .05$ . Statistical analysis was performed with MedCalc for Windows software, Version 12.7.7 (MedCalc Software, Mariakerke, Belgium).

## RESULTS

Fifty-three patients met the study criteria. Table 3 outlines the

**Table 4: Pre- and posttreatment VAS, FMS, and AS scores reported as median (interquartile range)**

	Preprocedure	Postprocedure	P Value
Visual Analog Scale	9.0 (8.0–10.0)	3.0 (0.0–5.8)	<.001
Functional Mobility Scale	3.0 (2.0–3.0)	1.0 (0.25–2.8)	<.001
Analgesic Scale	3.0 (3.0–4.0)	3.0 (2.0–3.8)	<.01

**Table 5: Pre- and posttreatment VAS, FMS, and AS scores for noncancer fractures (osteoporotic insufficiency and traumatic cohort combined) reported as median (interquartile range)**

	Preprocedure	Postprocedure	P Value
Visual Analog Scale	9.5 (8.0–10.0)	0.0 (0.0–4.0)	<.001
Functional Mobility Scale	3.0 (1.5–3.0)	1.0 (0.0–2.0)	<.01
Analgesic Scale	3.0 (3.0–3.0)	3.0 (1.0–3.0)	.06

**Table 6: Pre- and posttreatment VAS, FMS, and AS scores for cancer-related fractures reported as median (interquartile range)**

	Preprocedure	Postprocedure	P Value
Visual Analog Scale	8.0 (8.0–10.0)	4.0 (2.3–6.0)	<.01
Functional Mobility Scale	3.0 (2.3–3.8)	2.0 (1.0–3.0)	.11
Analgesic Scale	4.0 (3.0–4.0)	4.0 (3.0–4.0)	.19

summary data for the total cohort. Mean age was 76 years; most were female (83%) patients with either cancer-related (55%) or osteoporotic insufficiency (30%) fractures. Breast carcinoma metastasis, multiple myeloma, and colorectal carcinoma metastasis accounted for three-quarters of cancer-related fractures. All traumatic fractures were the result of minor trauma, such as a mechanical fall. No patients with high-energy trauma such as a motor vehicle collision were included. Fifteen of the 53 patients had vertebral augmentation before sacroplasty; however, none had these procedures performed within 3 months of sacroplasty, and most (80%) were performed >9 months before sacroplasty.

Percutaneous sacroplasty was generally performed with the patient under conscious sedation (74%) and by using CT guidance (91%). Bilateral fractures were treated in 44 patients. For the total cohort of 53 patients with 97 sacral fractures treated, no significant complications occurred. There was no procedural mortality. Effectiveness was assessed by using the VAS, FMS, AS, and the 4-level pain scale at a mean follow-up of 27 ± 3.7 days. Pre- and posttreatment VAS, FMS, and AS scores were available for 27 patients. There were statistically significant reductions in VAS, FMS, and AS scores after sacroplasty (Table 4). Pretreatment median (interquartile range) VAS, 9.0 (8.0–10); FMS, 3.0 (2.0–3.0); and AS, 3.0 (3.0–4.0) were reduced to median posttreatment (interquartile range) VAS, 3.0 (0.0–5.8); FMS, 1.0 (0.25–2.8); and AS 3.0 (2.0–3.8). Nineteen of the 53 patients had additional pelvic fractures at the time of presentation, mostly pubic rami fractures. In this smaller cohort of patients with additional pelvic fractures, all had significant reduction in their VAS, FMS, and AS scores after sacroplasty.

Osteoporotic insufficiency fractures were combined with traumatic fractures to form the noncancer fracture cohort to facilitate comparison of outcomes according to fracture etiology. Before treatment, there was no significant difference in the VAS ( $P = .94$ ), FMS ( $P = .74$ ), or AS ( $P = .11$ ) scores between the noncancer- ( $n = 16$ ) and cancer-related fracture cohorts ( $n = 11$ ). The treatment effect of sacroplasty in the noncancer and cancer-related fracture cohorts are summarized in Tables 5 and 6.

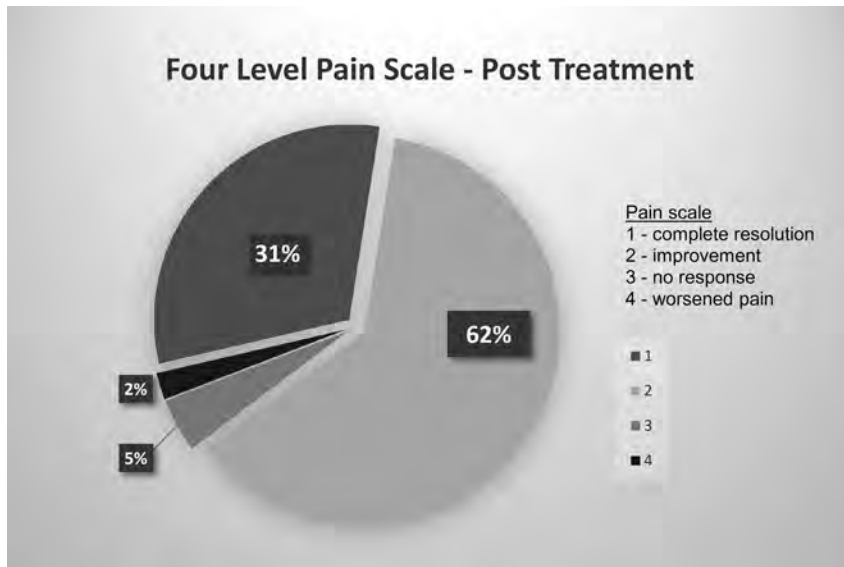


**FIG 2.** Treatment effect of sacroplasty on the 4-level pain scale scores at 1 month. Most patients (93%) reported improvement or complete resolution of pain.

The reduction in median VAS and AS scores was significantly greater for the non-cancer-related fractures ( $P = .02$  and  $P = .004$  respectively) compared with the cancer-related fractures. There were no significant differences in the reduction of median FMS in non-cancer-related and cancer-related fracture cohorts.

Four-level pain scale scores were available for 45 patients. After sacroplasty, 93% reported complete resolution or improvement in overall pain. Almost a third ( $n = 14$ ) reported complete resolution of pain. Only 2 patients had no improvement, and 1 patient had worsened pain after sacroplasty (Fig 2). Two patients underwent vertebral augmentation after sacroplasty. Both of these patients reported either improvement or complete resolution of their pain on the 4-level pain scale at short-term follow-up before new symptomatic thoracic vertebral compression fractures occurred.

## DISCUSSION

Sacral insufficiency fractures are severely debilitating to the elderly population, exacerbated by delays to diagnosis and the limited treatment options available. Percutaneous sacroplasty is a minimally invasive therapeutic strategy for patients not responding to conservative therapy with bed rest, physical therapy, and analgesics or for those who are not surgical candidates. Our results show that percutaneous sacroplasty effectively decreases pain, increases mobility, and decreases analgesic requirements in patients with sacral fractures. The quantified improvements in pain, mobility, and anesthesia are supported by the dramatic response in the 4-point scale score—almost one-third had complete resolution of their pain; 93% reported improvement or complete resolution.

To date, there have been several case series showing good outcomes following sacroplasty.<sup>4-8,14</sup> The largest multicenter cohort to date included 243 patients and showed that most patients responded positively to sacroplasty and had statistically significant decreases in pain based on the VAS.<sup>6</sup> A recent single-center cohort of 57 patients also showed reduced opioid use after sacroplasty.<sup>15</sup>

Our study confirms this treatment effect of percutaneous sacroplasty on pain and analgesic use. Postulated mechanisms of pain relief include increased structural stability in a previously weakened weight-bearing site after cement deposition and neurolysis of painful nerve fibers.<sup>16,17</sup>

There are little data on functional mobility outcomes after percutaneous sacroplasty. A single study assessed 1-month ambulation outcomes after sacroplasty by using a 3-point scale: 1, worse; 2, unchanged; and 3, improvement of ambulation. Most impressively, 80% with walking limitation experienced improvement.<sup>7</sup> We add to the emerging literature on sacroplasty by reporting quantifiable and significant short-term improvement in functional mobility by using the FMS.

In our cohort, patients with osteoporotic insufficiency or minor traumatic fractures gained greater reductions in VAS and AS scores compared with patients with cancer-related fractures. These results are similar to those from the largest multicenter cohort.<sup>6</sup> This finding may be, in part, due to the presence of additional fractures that may have impacted outcome. However, in the small cohort of patients with additional pelvic fractures (mainly pubic rami), all had a significant reduction in their VAS, FMS, and AS scores, suggesting that the presence of additional fractures did not impact the short-term effect of sacroplasty.

The treatment effectiveness for an individual patient is balanced by the procedural safety. In the large multicenter cohort of 243 patients, there were no significant cement extravasations, infections, hemorrhages, pulmonary emboli, or procedure-related deaths.<sup>6</sup> This outcome may be, in part, due to the use of CT guidance and the limitation to operators trained and experienced in vertebral augmentation techniques. Similarly, we performed most procedures (91%) under CT guidance, and we limited performance of sacroplasty to operators trained and experienced in vertebral augmentation and acetabuloplasty. No complications occurred in our cohort. We thus confirm that when performed by experienced operators, percutaneous sacroplasty is a safe procedure.

Our study has significant limitations, in particular the lack of uniform patient response in the VAS, FMS, and AS scores. Documentation of these scores became routine during the study period. However, we sought to rectify the lower rate of recorded outcome scores for VAS, FMS, and AS by including the 4-level pain scale score. The inclusion of pain improvement and pain worsening allows more useful interpretation of the patient perspective on treatment effectiveness compared with binary yes or no responses. While we have demonstrated significant short-term gains, other studies have shown durable pain reduction for up to 1.5 years.<sup>11,18,19</sup>

Ultimately, percutaneous sacroplasty should be evaluated in a

randomized controlled trial against conservative therapy with analgesia and/or surgical fixation. Until then, emerging data from our study can be included in comparative effectiveness research to define treatment appropriateness criteria for percutaneous sacroplasty and to inform health care decisions on the relative benefits and harm of the different treatment options available for patients with sacral fractures.

## CONCLUSIONS

Sacral insufficiency fractures continue to be a frequent source of pain and disability in the elderly population. Percutaneous sacroplasty effectively decreases pain, increases mobility, and decreases analgesic requirements in patients with painful sacral fractures. Complications are rare with appropriate techniques and operator experience. Percutaneous sacroplasty is an excellent treatment option for patients with painful sacral fractures not responding to conservative therapy.

Disclosures: Joshua A. Hirsch—RELATED: Consulting Fees or Honoraria: from CareFusion, a company that makes augmentation products that could be used in sacroplasty; Stocks/Stock Options: He also holds stocks/stock options in Intratech.

## REFERENCES

1. Gotis-Graham I, McGuigan L, Diamond T, et al. **Sacral insufficiency fractures in the elderly.** *J Bone Joint Surg Br* 1994;76:882–86
2. Coleman RE. **Clinical features of metastatic bone disease and risk of skeletal morbidity.** *Clin Cancer Res* 2006;12:6243s–49s
3. Babayev M, Lachmann E, Nagler W. **The controversy surrounding sacral insufficiency fractures: to ambulate or not to ambulate?** *Am J Phys Med Rehabil* 2000;79:404–09
4. Gupta AC, Yoo AJ, Stone J, et al. **Percutaneous sacroplasty.** *J Neurointerv Surg* 2012;4:385–89
5. Hirsch JA, Barr JD, Zoarski GH. **Sacroplasty: beyond the beginning.** *J Neurointerv Surg* 2013;5:395
6. Kortman K, Ortiz O, Miller T, et al. **Multicenter study to assess the efficacy and safety of sacroplasty in patients with osteoporotic sacral insufficiency fractures or pathologic sacral lesions.** *J Neurointerv Surg* 2013;5:461–66
7. Pereira LP, Clarencon F, Cormier E, et al. **Safety and effectiveness of percutaneous sacroplasty: a single-centre experience in 58 consecutive patients with tumours or osteoporotic insufficient fractures treated under fluoroscopic guidance.** *Eur Radiol* 2013;23:2764–72
8. Cho CH, Mathis JM, Ortiz O. **Sacral fractures and sacroplasty.** *Neuroimaging Clin N Am* 2010;20:179–86
9. Jha RM, Yoo AJ, Hirsch AE, et al. **Predictors of successful palliation of compression fractures with vertebral augmentation: single-center experience of 525 cases.** *J Vasc Interv Radiol* 2009;20:760–68
10. Whitlow CT, Yazdani SK, Reedy ML, et al. **Investigating sacroplasty: technical considerations and finite element analysis of polymethylmethacrylate infusion into cadaveric sacrum.** *AJNR Am J Neuroradiol* 2007;28:1036–41
11. Frey ME, Depalma MJ, Cifu DX, et al. **Percutaneous sacroplasty for osteoporotic sacral insufficiency fractures: a prospective, multi-center, observational pilot study.** *Spine J* 2008;8:367–73
12. DeLoach LJ, Higgins MS, Caplan AB, et al. **The visual analog scale in the immediate postoperative period: intrasubject variability and correlation with a numeric scale.** *Anesth Analg* 1998;86:102–06
13. Gupta AC, Hirsch JA, Chaudhry ZA, et al. **Evaluating the safety and effectiveness of percutaneous acetabuloplasty.** *J Neurointerv Surg* 2012;4:134–38
14. Trouvin AP, Alcaix D, Somon T, et al. **Analgesic effect of sacroplasty in osteoporotic sacral fractures: a study of six cases.** *Joint Bone Spine* 2012;79:500–03
15. Dougherty RW, McDonald JS, Cho YW, et al. **Percutaneous sacroplasty using CT guidance for pain palliation in sacral insufficiency fractures.** *J Neurointerv Surg* 2014;6:57–60
16. Harty JA, Brennan D, Eustace S, et al. **Percutaneous cementoplasty of acetabular bony metastasis.** *Surgeon* 2003;1:48–50
17. Richards AM, Mears SC, Knight TA, et al. **Biomechanical analysis of sacroplasty: does volume or location of cement matter?** *AJNR Am J Neuroradiol* 2009;30:315–17
18. Whitlow CT, Mussat-Whitlow BJ, Mattern CW, et al. **Sacroplasty versus vertebroplasty: comparable clinical outcomes for the treatment of fracture-related pain.** *AJNR Am J Neuroradiol* 2007;28:1266–70
19. Kamel EM, Binaghi S, Guntern D, et al. **Outcome of long-axis percutaneous sacroplasty for the treatment of sacral insufficiency fractures.** *Eur Radiol* 2009;19:3002–07

**21<sup>st</sup> Annual Blood-Brain Barrier Consortium Meeting**  
**March 19-21, 2015**  
**Skamania Lodge in Stevenson, Washington**

The 2015 Annual Blood-Brain Barrier Consortium Meeting will be held March 19-21 at Skamania Lodge in Stevenson, Washington. The meeting will include a state-of-the-art pre-clinical and clinical neuroimaging session titled "Imaging the Neurovascular Unit: Permeability, Blood Volume, and Functional Imaging". The meeting is partially funded by a National Institutes of Health R13 grant, with support from the National Cancer Institute, National Institute of Neurological Disorders and Stroke, and National Institute of Deafness and Communication Disorders, and is organized in collaboration with the International Brain Barriers Society.



For more information, please visit [www.ohsu.edu/bbb](http://www.ohsu.edu/bbb)



**Simplify**  
the MOC Process

**CMEgateway.org**



**Manage**  
your CME Credits Online



**It's Easy and Free!**

Log on to CME Gateway to:

- View or print reports of your CME credits from multiple societies from a single access point.
- Print an aggregated report or certificate from each participating organization.
- Link to SAMs and other tools to help with maintenance of certification.

**American Board of Radiology (ABR) participation!**

By activating ABR in your organizational profile, your MOC-fulfilling CME and SAM credits can be transferred to your own personalized database on the ABR Web site.

**Sign Up Today!**

go to [CMEgateway.org](http://CMEgateway.org)

**Available to Members of Participating Societies**

American Board of Radiology (ABR)	Radiological Society of North America (RSNA)
American College of Radiology (ACR)	Society of Interventional Radiology (SIR)
American Roentgen Ray Society (ARRS)	SNM
American Society of Neuroradiology (ASNR)	The Society for Pediatric Radiology (SPR)
Commission on Accreditation of Medical Physics Educational Programs, Inc. (CAMPEP)	

## Target® Detachable Coil

See package insert for complete indications, contraindications, warnings and instructions for use.

### INTENDED USE / INDICATIONS FOR USE

Target Detachable Coils are intended to endovascularly obstruct or occlude blood flow in vascular abnormalities of the neurovascular and peripheral vessels.

Target Detachable Coils are indicated for endovascular embolization of:

- Intracranial aneurysms
- Other neurovascular abnormalities such as arteriovenous malformations and arteriovenous fistulae
- Arterial and venous embolizations in the peripheral vasculature

### CONTRAINDICATIONS

None known.

### POTENTIAL ADVERSE EVENTS

Potential complications include, but are not limited to: allergic reaction, aneurysm perforation and rupture, arrhythmia, death, edema, embolus, headache, hemorrhage, infection, ischemia, neurological/intracranial sequelae, post-embolization syndrome (fever, increased white blood cell count, discomfort), TIA/stroke, vasospasm, vessel occlusion or closure, vessel perforation, dissection, trauma or damage, vessel rupture, vessel thrombosis. Other procedural complications including but not limited to: anesthetic and contrast media risks, hypotension, hypertension, access site complications.

### WARNINGS

- Contents supplied STERILE using an ethylene oxide (EO) process. Do not use if sterile barrier is damaged. If damage is found, call your Stryker Neurovascular representative.
- For single use only. Do not reuse, reprocess or resterilize. Reuse, reprocessing or resterilization may compromise the structural integrity of the device and/or lead to device failure which, in turn, may result in patient injury, illness or death. Reuse, reprocessing or resterilization may also create a risk of contamination of the device and/or cause patient infection or cross-infection, including, but not limited to, the transmission of infectious disease(s) from one patient to another. Contamination of the device may lead to injury, illness or death of the patient.
- After use, dispose of product and packaging in accordance with hospital, administrative and/or local government policy.
- **This device should only be used by physicians who have received appropriate training in interventional neuroradiology or interventional radiology and preclinical training on the use of this device as established by Stryker Neurovascular.**
- Patients with hypersensitivity to 316LVM stainless steel may suffer an allergic reaction to this implant.
- MR temperature testing was not conducted in peripheral vasculature, arteriovenous malformations or fistulae models.
- The safety and performance characteristics of the Target Detachable Coil System (Target Detachable Coils, InZone Detachment Systems,

delivery systems and accessories) have not been demonstrated with other manufacturer's devices (whether coils, coil delivery devices, coil detachment systems, catheters, guidewires, and/or other accessories). Due to the potential incompatibility of non Stryker Neurovascular devices with the Target Detachable Coil System, the use of other manufacturer's device(s) with the Target Detachable Coil System is not recommended.

- To reduce risk of coil migration, the diameter of the first and second coil should never be less than the width of the ostium.
- In order to achieve optimal performance of the Target Detachable Coil System and to reduce the risk of thromboembolic complications, it is critical that a continuous infusion of appropriate flush solution be maintained between a) the femoral sheath and guiding catheter, b) the 2-tip microcatheter and guiding catheters, and c) the 2-tip microcatheter and Stryker Neurovascular guidewire and delivery wire. Continuous flush also reduces the potential for thrombus formation on, and crystallization of infusate around, the detachment zone of the Target Detachable Coil.
- Do not use the product after the "Use By" date specified on the package.
- Reuse of the flush port/dispenser coil or use with any coil other than the original coil may result in contamination of, or damage to, the coil.
- Utilization of damaged coils may affect coil delivery to, and stability inside, the vessel or aneurysm, possibly resulting in coil migration and/or stretching.
- The fluoro-saver marker is designed for use with a Rotating Hemostatic Valve (RHV). If used without an RHV, the distal end of the coil may be beyond the alignment marker when the fluoro-saver marker reaches the microcatheter hub.
- If the fluoro-saver marker is not visible, do not advance the coil without fluoroscopy.
- Do not rotate delivery wire during or after delivery of the coil. Rotating the Target Detachable Coil delivery wire may result in a stretched coil or premature detachment of the coil from the delivery wire, which could result in coil migration.
- Verify there is no coil loop protrusion into the parent vessel after coil placement and prior to coil detachment. Coil loop protrusion after coil placement may result in thromboembolic events if the coil is detached.
- Verify there is no movement of the coil after coil placement and prior to coil detachment. Movement of the coil after coil placement may indicate that the coil could migrate once it is detached.
- Failure to properly close the RHV compression fitting over the delivery wire before attaching the InZone® Detachment System could result in coil movement, aneurysm rupture or vessel perforation.
- Verify repeatedly that the distal shaft of the catheter is not under stress before detaching the Target Detachable Coil. Axial compression or tension forces could be stored in the 2-tip microcatheter causing the tip to move during coil delivery. Microcatheter tip movement could cause the aneurysm or vessel to rupture.
- Advancing the delivery wire beyond the microcatheter tip once the coil has been detached involves risk of aneurysm or vessel perforation.
- The long term effect of this product on extravascular tissues has not been established so care should be taken to retain this device in the intravascular space.

Damaged delivery wires may cause detachment failures, vessel injury or unpredictable distal tip response during coil deployment. If a delivery wire is damaged at any point during the procedure, do not attempt to straighten or otherwise repair it. Do not proceed with deployment or detachment. Remove the entire coil and replace with undamaged product.

- After use, dispose of product and packaging in accordance with hospital, administrative and/or local government policy.

### CAUTIONS / PRECAUTIONS

- Federal Law (USA) restricts this device to sale by or on the order of a physician.
- Besides the number of InZone Detachment System units needed to complete the case, there must be an extra InZone Detachment System unit as back up.
- Removing the delivery wire without grasping the introducer sheath and delivery wire together may result in the detachable coil sliding out of the introducer sheath.
- Failure to remove the introducer sheath after inserting the delivery wire into the RHV of the microcatheter will interrupt normal infusion of flush solution and allow back flow of blood into the microcatheter.
- Some low level overhead light near or adjacent to the patient is required to visualize the fluoro-saver marker; monitor light alone will not allow sufficient visualization of the fluoro-saver marker.
- Advance and retract the Target Detachable Coil carefully and smoothly without excessive force. If unusual friction is noticed, slowly withdraw the Target Detachable Coil and examine for damage. If damage is present, remove and use a new Target Detachable Coil. If friction or resistance is still noted, carefully remove the Target Detachable Coil and microcatheter and examine the microcatheter for damage.
- If it is necessary to reposition the Target Detachable Coil, verify under fluoroscopy that the coil moves with a one-to-one motion. If the coil does not move with a one-to-one motion or movement is difficult, the coil may have stretched and could possibly migrate or break. Gently remove both the coil and microcatheter and replace with new devices.
- Increased detachment times may occur when:
  - Other embolic agents are present.
  - Delivery wire and microcatheter markers are not properly aligned.
  - Thrombus is present on the coil detachment zone.
- Do not use detachment systems other than the InZone Detachment System.
- Increased detachment times may occur when delivery wire and microcatheter markers are not properly aligned.
- Do not use detachment systems other than the InZone Detachment System.

Copyright © 2014 Stryker  
NV00009006.AA

## Trevo® XP ProVue Retrievers

See package insert for complete indications, complications, warnings, and instructions for use.

### INDICATIONS FOR USE

The Trevo Retriever is intended to restore blood flow in the neurovasculature by removing thrombus in patients experiencing ischemic stroke within 8 hours of symptom onset. Patients who are ineligible for intravenous tissue plasminogen activator (IV t-PA) or who fail IV t-PA therapy are candidates for treatment.

### COMPLICATIONS

Procedures requiring percutaneous catheter introduction should not be attempted by physicians unfamiliar with possible complications which may occur during or after the procedure. Possible complications include, but are not limited to, the following: air embolism; hematoma or hemorrhage at puncture site; infection; distal embolization; pain/headache; vessel spasm; thrombosis; dissection; or perforation; emboli; acute occlusion; ischemia; intracranial hemorrhage; false aneurysm formation; neurological deficits including stroke; and death.

### COMPATIBILITY

3x20 mm retrievers are compatible with Trevo® Pro 14 Microcatheters (REF 90231) and Trevo® Pro 18 Microcatheters (REF 90238). 4x20 mm retrievers are compatible with Trevo® Pro 18 Microcatheters (REF 90238). Compatibility of the Retriever with other microcatheters has not been established. Performance of the Retriever device may be impacted if a different microcatheter is used. The Merci® Balloon Guide Catheters are recommended for use during thrombus removal procedures. Retrievers are compatible with the Abbott Vascular DOC® Guide Wire Extension (REF 22260).

### WARNINGS

- Contents supplied STERILE, using an ethylene oxide (EO) process. Nonpyrogenic.
- To reduce risk of vessel damage, adhere to the following recommendations:
  - Take care to appropriately size Retriever to vessel diameter at

intended site of deployment.

- Do not perform more than six (6) retrieval attempts in same vessel using Retriever devices.
- Maintain Retriever position in vessel when removing or exchanging Microcatheter.
- To reduce risk of kinking/fracture, adhere to the following recommendations:
  - Immediately after unsheathing Retriever, position Microcatheter tip marker just proximal to shaped section. Maintain Microcatheter tip marker just proximal to shaped section of Retriever during manipulation and withdrawal.
  - Do not rotate or torque Retriever.
  - Use caution when passing Retriever through stented arteries.
- Do not resterilize and reuse. Structural integrity and/or function may be impaired by reuse or cleaning.
- The Retriever is a delicate instrument and should be handled carefully. Before use and when possible during procedure, inspect device carefully for damage. Do not use a device that shows signs of damage. Damage may prevent device from functioning and may cause complications.
- Do not advance or withdraw Retriever against resistance or significant vasospasm. Moving or torquing device against resistance or significant vasospasm may result in damage to vessel or device. Assess cause of resistance using fluoroscopy and if needed resheath the device to withdraw.
- If Retriever is difficult to withdraw from the vessel, do not torque Retriever. Advance Microcatheter distally, gently pull Retriever back into Microcatheter, and remove Retriever and Microcatheter as a unit. If undue resistance is met when withdrawing the Retriever into the Microcatheter, consider extending the Retriever using the Abbott Vascular DOC guidewire extension (REF 22260) so that the Microcatheter can be exchanged for a larger diameter catheter such as a DAC® catheter. Gently withdraw the Retriever into the larger diameter catheter.
- Administer anti-coagulation and anti-platelet medications per standard institutional guidelines.

### PRECAUTIONS

- Prescription only – device restricted to use by or on order of a physician.
- Store in cool, dry, dark place.
- Do not use open or damaged packages.
- Use by "Use By" date.
- Exposure to temperatures above 54°C (130°F) may damage device and accessories. Do not autoclave.
- Do not expose Retriever to solvents.
- Use Retriever in conjunction with fluoroscopic visualization and proper anti-coagulation agents.
- To prevent thrombus formation and contrast media crystal formation, maintain a constant infusion of appropriate flush solution between guide catheter and Microcatheter and between Microcatheter and Retriever or guidewire.
- Do not attach a torque device to the shaped proximal end of DOC® Compatible Retriever. Damage may occur, preventing ability to attach DOC® Guide Wire Extension.



Concentric Medical  
301 East Evelyn  
Mountain View, CA 94041



EMERGO Europe  
Molenstraat 15  
2513 BH, The Hague  
The Netherlands



Stryker Neurovascular  
47900 Bayside Parkway  
Fremont, CA 94538-6515

[stryker.com/neurovascular](http://stryker.com/neurovascular)

Date of Release: JUN/2014

EX\_EN\_US

Stryker Neurovascular  
47900 Bayside Parkway  
Fremont, CA 94538-6515

[stryker.com/neurovascular](http://stryker.com/neurovascular)  
[stryker.com/emea/neurovascular](http://stryker.com/emea/neurovascular)

Date of Release: JUN/2014

EX\_EN\_GL

Copyright © 2014 Stryker  
NV00009028.AA



## Target<sup>®</sup> Nano<sup>™</sup> DETACHABLE COILS

### Beyond Soft

The softest coil technology\* available, combined with Target Coil's consistently smooth deployment and exceptional microcatheter stability, results in an experience that is beyond soft. Designed to treat small spaces, the Target Nano Coil's incredible softness delivers increased conformability and shape adjustment.

Target Nano Coils—**Smooth and Stable** has never been so soft.

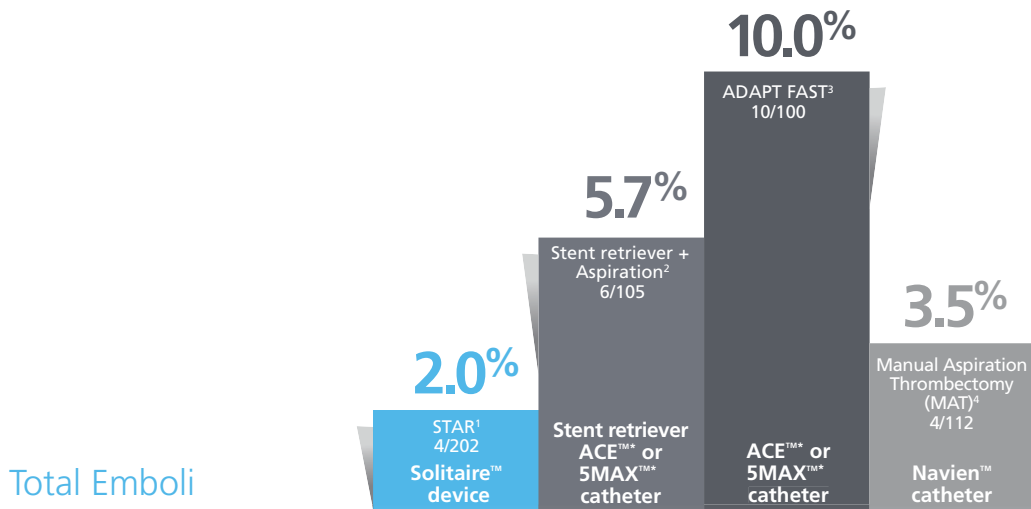
For more information, please visit [www.strykerneurovascular.com/Target](http://www.strykerneurovascular.com/Target)

**stryker**<sup>®</sup>  
Neurovascular

\*Testing performed by Stryker Neurovascular. n=3. Data are on file at Stryker Neurovascular and will be made available upon request. Bench test results may not necessarily be indicative of clinical performance.

Copyright © 2014 Stryker  
NV00009006.AA

**Stroke: Our Only Focus. Our Ongoing Promise.**



Total Emboli

## Numbers don't lie.

Using the Solitaire™ device first results in the lowest recorded instances of distal emboli, especially when compared to ADAPT.



For you, and your acute ischemic stroke patients, outcomes make all the difference. That's why evaluating and understanding the differences in the data, across multiple clinical studies, is so important to delivering the best possible outcomes and quality of life after stroke.

The Solitaire™ revascularization device has been more rigorously tested<sup>1-6</sup> than any other mechanical thrombectomy device. With consistent results showing significantly lower total emboli<sup>1-4</sup>, unrivaled\* neurological outcomes<sup>1-7</sup>, and the lowest observed mortality<sup>1-7</sup>, **the Solitaire™ device is demonstrably the fastest route to better outcomes.**

**Solitaire™ Revascularization Device**



**COVIDIEN**

\* mRS ≤ 2 over 50% in a published study.

**REFERENCES** 1. Pereira V, Gralla J, Davalos A, et al. Prospective, Multicenter, Single-Arm Study of Mechanical Thrombectomy Using Solitaire Flow Restoration in Acute Ischemic Stroke. *Stroke*. 2013;44:2802-2807. 2. Humphries W, Hoyt D, Doss VT, et al. *J NeuroIntervent Surg*. doi:10.1136/neurintsurg-2013-010986. Data self reported. 3. Turk AS, Frei D, Fiorella D, et al. *J NeuroIntervent Surg*. doi:10.1136/neurintsurg-2014-011125. Data self reported. 4. Jankowitz B, Grandhi R, Horev A, et al. *J NeuroIntervent Surg*. doi:10.1136/neurintsurg-2013-011024. Data self reported. 5. Saver JL, Jahan R, Levy EI, et al. SWIFT Trialists. Solitaire flow restoration device versus the Merci Retriever in patients with acute ischemic stroke (SWIFT): a randomized, parallel-group, non-inferiority trial. *Lancet*. 2012;380(9849):1241-1249. 6. Jahan R, Liebeskind D, Nogueira R, et al. For SWIFT Investigators. Abstract 163: TIC1 success rates in SWIFT: comparison between randomized arms and correlation to 90 day neurologic outcome. *Stroke*. 2013;44:A163. 7. Dávalos A, Pereira VM, Chapot R, et al. Solitaire Group. Retrospective multicenter study of Solitaire FR for revascularization in the treatment of acute ischemic stroke. *Stroke*. 2012;43(10):2699-2705.

The Solitaire™ revascularization device is intended to restore blood flow by removing thrombus from a large intracranial vessel in patients experiencing ischemic stroke within 8 hours of symptom onset. Patients who are ineligible for intravenous tissue plasminogen activator (IV t-PA) or who fail IV t-PA therapy are candidates for treatment. Indications, contraindications, warnings and instructions for use can be found on the product labeling supplied with each device. CAUTION: Federal (USA) law restricts this device to sale by or on the order of a physician.

COVIDIEN, COVIDIEN with Logo, and Covidien Logo are US and internationally registered trademarks of Covidien AG. TM\* Trademark of its respective owner. Other brands are trademarks of a Covidien company. ©2014 Covidien. MK1138072014A